

ABSTRACT

HEWITT, PATRICK. Organic Polyradicals and Donor-Bridge-Acceptor Biradicals: Synthesis, Characterization and Properties for Understanding Electronic Structure. (Under the direction of Dr. David A. Shultz).

Herein several topics relating to stable organic radicals will be discussed. After a general introduction, background and theory presented in Chapter I, Part A describes the theory, design, synthesis and application of several polyradicals, as discussed in Chapters II, then Part B will begin with Chapter III on the theory, design, synthesis and prior results of donor-bridge-acceptor biradicals. In this work, these biradicals will provide insights into molecular electronic structure; specifically related molecular rectification in single-molecule electronics (Chapter IV) and the electronic nature of and coupling through nonalternant π -system bridges (Chapter V).

Chapter I will focus on and describe the physical organic theory behind organic radicals and the correlation of this theory and structure-property relationships. These topics include the Pauli Exclusion Principle, Hund's rules, the Heisenberg Hamiltonian and magnetic exchange coupling. These principles will then be discussed in the context of spin polarization and the origin of the ground-state spin of organic radicals of disjoint and non-disjoint molecules. This chapter will also discuss primary characterization techniques employed in the study of organic radicals; these are electron paramagnetic resonance (EPR) and magnetometry.

Part A, Chapter II is going to discuss the history and application of radical polymers (polyradicals), including the synthesis, characterization and results of two polyradical backbones: poly(*ortho*-phenyleneethynylene) (PoPE) and poly(thiophene) (pTh). The significant synthetic progress on a third polymer, a copolymer of the radical-appended thiophene with 3-hexylthiophene as well as a polyradical for future work involving a facile synthesis are discussed in Appendix A.

Part B begins with Chapter III and will cover donor-bridge-acceptor biradical theory for semiquinone donor radicals bridged with diamagnetic linkers to nitronyl nitroxide acceptor radicals. The relevance to molecular electronics, as well as their synthesis, characterization and results in a general aspect with regard to results that predates the work reported in this document. Such topics to be discussed include the history of electron transfer, ways that electron transfer can be measured and models to evaluate and explain the observations of magnetic exchange coupling in our molecules. Former relevant results that will be discussed will be the importance of the distance dependence series donor-bridge-acceptors, how exchange coupling changes and is affected by a conjugated versus a cross-conjugated diamagnetic bridging unit and the significance of torsional dependence studies on exchange coupling.

Chapter IV concentrates on molecular rectification. The seminal literature of molecular rectification will be discussed, the influence of the frontier molecular orbitals in a rectifying device, the crucial characteristic for a rectifier and three classes of rectifiers that satisfy this characteristic with some examples. The discussion of current work in molecular rectification will conclude with ongoing challenges facing the study of molecular rectification and introduce why hetero-biradicals may be uniquely suited for studying certain attributes of molecular rectifiers. Our group's initial foray into molecular rectification and lessons learned will be discussed along with two, separate strategies for elucidating the orbital contributions to molecular rectification and their results.

Finally Chapter V focuses on a class of conjugated hydrocarbons, known as nonalternant hydrocarbons, whose electronic structure and the common analogies that describe it are still contended, and empirical studies probing it are scarce. Of this class of compounds, a member that has been investigated for its unique photophysical properties and electronic structure for

over 60 years, azulene is investigated with the hetero-biradical donor-bridge-acceptor motif. Alongside azulene, ferrocene is also investigated and these compounds are compared to the alternant hydrocarbon, phenylene (benzene) as a bridging unit.

© Copyright 2020 Patrick Hewitt

All Rights Reserved

Organic Polyradicals and Donor-Bridge-Acceptor Biradicals: Synthesis, Characterization and
Properties for Understanding Electronic Structure.

by
Patrick Hewitt

A thesis submitted to the Graduate Faculty of
North Carolina State University
in partial fulfillment of the
requirements for the Degree of
Doctor of Philosophy

Chemistry

Raleigh, North Carolina

2020

APPROVED BY:

David A. Shultz
Committee Chair

Felix N. Castellano

Christopher B. Gorman

Joshua G. Pierce

BIOGRAPHY

Patrick Hewitt was born and raised in western Pennsylvania in Indiana County by his parents, Nancy and Butch Hewitt and maternal grandmother, Wilma Tomb. He grew-up engaged from an early age creating drawing and other works of art, constructing elaborate, detailed structures out of Legos, and enjoying the challenge and strategy of chess and other games; which while frustrating at times of failure only sought to make the victories more enjoyable.

After graduating high school in 2010 and realizing that while he enjoyed the creation and puzzle-solving aspect of computer programming decided it was not something that he wanted to pursue in college, instead choosing chemistry as his major when he enrolled at Saint Vincent College in Latrobe, Pennsylvania; in an effort to satisfy a desire for evermore challenging puzzles. At Saint Vincent, he found his synthetic and physical chemistry classes and labs most enjoyable and interesting and while taking organic chemistry would spend evenings doing extra practice problems and worksheets developing synthetic schemes for fun. In Spring of his Junior year at Saint Vincent, his adviser, Steve Gravelle, asked about plans for after graduation and then suggested something that Patrick had never considered before: graduate school.

In April of 2014, Patrick got the opportunity to present his undergraduate research on stimuli-responsive polymers at the National ACS meeting held in Dallas, Texas and after graduating Saint Vincent in May, moved to Raleigh, NC to attend graduate school at North Carolina State University.

TABLE OF CONTENTS

LIST OF FIGURES	vii
LIST OF TABLES	xvii
LIST OF SCHEMES	xix
I: General Theory for Organic Radicals	1
I.1. Pauli Exclusion Principle	3
I.2. Hund's Rules.....	8
I.3. Heisenberg Hamiltonian and the Exchange Coupling Constant (<i>J</i>).....	12
I.4. Structural Considerations for Organic Radicals.....	16
I.4.1. Kekulé vs. non-Kekulé.....	16
I.4.2. Spin Ground States of Organic Biradicals.....	17
I.5. Spin Polarization.....	19
I.6. Disjoint and Non-disjoint Biradicals.....	26
I.7. Electron Paramagnetic Resonance (EPR) Spectroscopy.....	27
I.7.1. Introduction, X-band, organic radicals.....	27
I.7.2. Zeeman Splitting.....	28
I.7.3. Isotropic EPR Spectra.....	30
I.7.4. Anisotropic EPR Spectra.....	35
I.8. Magnetometry.....	40
I.9. References.....	45
PART A: Polyradicals	54
II: High Spin Organic-Based Polyradicals	54
II.1. History and Current Work.....	54
II.2. Applications of Radical Polymers.....	62
II.3. Poly(<i>ortho</i> -phenyleneethynylene) (PoPE-SQ).....	67
II.3.1. Synthesis of poly(<i>o</i> -phenyleneethynylene 4-(3-(<i>tert</i> -butyl)-4,5-bis(methoxymethoxy)benzene) (PoPE-MOM).....	70
II.3.2. Results.....	87
II.3.3. Conclusions.....	93
II.4. Cobalt Complex Synthesis.....	93
II.5. Polythiophene (pThSQ).....	97
II.5.1. Synthetic Discussion.....	99
II.5.2. Results.....	114
II.5.3. Conclusions	120
II.6. Experimental for polyradicals	122
II.6.1. PoPE-SQ	122
II.6.2. pThSQ	140
II.7. References	143
PART B. Donor-Bridge-Acceptor Biradicals for Probing Electronic Structure	169
III: Donor-Bridge-Acceptor Biradical Background	169
III.1. A Brief Historical Perspective on Electronic Coupling and Electron Transfer.....	171
III.2. Semiquinone donor-bridge-Nitronyl nitroxide acceptor (SQ-B-NN) Biradicals.....	178
III.3. Synthesis of SQ-B-NN Biradicals.....	178

III.3.1. General Synthesis.....	178
III.3.2. Preparation of Semiquinones and their Synthons.....	179
III.3.3. Preparation of Nitronylnitroxides.....	181
III.3.4. Preparation of Zn(OH)Tp ^{Cum,Me} Ancillary Ligand.....	183
III.3.5. Preparation of Bridge-NN-Elaborated Catechols and Preparation of Zinc SQ-B-NN Complexes.....	186
III.4.Characterizing Biradicals and Measuring/Evaluating Exchange Coupling.....	189
III.4.1. Electron Paramagnetic Resonance (EPR) Spectroscopy.....	190
III.4.2. Electronic Absorption Spectroscopy.....	193
III.4.3. Superconducting Quantum Interference Device (SQUID) Detected Magnetometry	194
III.4.4. X-ray Crystallography.....	197
III.5. Previous Studies of SQ-B-NN Complexes.....	198
III.5.1. Distance Dependence of Coupling: Support for the Superexchange Model...	198
III.5.2. Conjugated vs. Cross-conjugated Bridges: Implications for “Quantum Interference” Effects.....	200
III.5.3. Torsional Dependence of Electronic and Exchange Coupling in SQ-B-NN Complexes.....	204
III.5.4. Summary.....	208
III.6. References.....	210
IV: Donor-Bridge-Acceptor Biradicals for Studying Molecular Rectification.....	224
IV.1. Definition and Predictions of Conductance with Green’s Functions.....	224
IV.2. Definition of Rectification.....	228
IV.3. Theory of Molecular Rectifiers.....	229
IV.3.1. Aviram-Ratner Model.....	229
IV.3.2. HOMO and LUMO Energy Levels under a Bias.....	231
IV.3.3. Asymmetry is Essential.....	233
IV.3.4. Past Work and Examples of Rectification Ratios.....	235
IV.3.5. Challenges for Studying Molecular Rectification.....	237
IV.4. Hetero-biradicals as models for studying orbital mechanisms of molecular rectification.....	240
IV.4.1. Redefining SQ and NN as analogs of “Cathode” and “Anode”.....	242
IV.5. Results from Pyridine-Thiophene SQ-B-NN.....	242
IV.5.1. A VBCI explanation for the computed RRs and observed <i>J</i> values.....	243
IV.5.2. Designing U-type rectifiers.....	245
IV.6. Torsional Rectifiers.....	245
IV.6.1. Large Bond Torsions to Facilitate Decoupling.....	246
IV.6.2. Theory and Hypothesis.....	248
IV.6.3. Synthesis of SQ-PhMe ₂ Th-NN and NN-PhMe ₂ Th-SQ.....	249
IV.6.4. Results and Conclusions.....	262
IV.7. Cross-Conjugative Asymmetry.....	268
IV.7.1. Hypothesis.....	268
IV.7.2. Synthetic Discussion of <i>p</i> -SQ- <i>m</i> -NN and <i>m</i> -SQ- <i>p</i> -NN.....	269
IV.7.3. Results and Conclusions.....	272
IV.8. Experimental.....	275

IV.8.1. Torsional Rectifiers.....	275
IV.8.2. Cross-Conjugative Asymmetry.....	284
IV.9. References.....	290

V: Evaluation of Coupling in Donor-Bridge-Acceptor Biradicals with Nonalternant

π-System Bridges.....	296
V.1. Introduction to Azulene and Theory.....	296
V.1.1. Azulene vs. Naphthalene.....	296
V.1.2. Types of Alternant and Nonalternant Hydrocarbons.....	296
V.1.3. Electronic Structure Differences between Alternant and Nonalternant Hydrocarbons	298
V.1.4. Breakdown of Rules for Understanding Conjugation, Electron-pushing and Spin-polarization in Nonalternant Hydrocarbons.....	299
V.1.5. The Dipole Moment of a Hydrocarbon and some Small Molecules.....	303
V.1.6. Violation of Kasha's Rule.....	305
V.1.7. Organic Electronics.....	308
V.1.8. Azulene Oligomers and Polymers.....	308
V.1.9. Conductance Studies through Azulene Derivatives.....	311
V.2. Azulene Biradicals.....	314
V.2.1. 1,3-NN ₂ Az and 1,3-IN ₂ Az.....	314
V.2.2. Symmetric and Asymmetric Biradicals for Evaluating Bridge-Modulated Coupling.....	316
V.2.3. 1,3-SQ-Az-NN Synthesis.....	319
V.2.4. 1,3-SQ ₂ Az Synthesis.....	345
V.2.5. Results.....	346
V.2.6. Discussion and Conclusions about Azulene Biradicals.....	354
V.3. Ferrocene as Another Nonalternant Bridge.....	365
V.3.1. 1,3-SQ ₂ Fc Synthesis.....	365
V.3.2. 1,1'-SQ ₂ Fc Synthesis.....	370
V.3.3. 1-SQFc Synthesis.....	370
V.3.4. Ferrocene Results.....	372
V.3.5. Conclusions about Ferrocene.....	384
V.4. Nonalternant Hydrocarbon Experimental.....	385
V.4.1. Azulene Experimental.....	385
V.4.2. Ferrocene Experimental.....	398
V.5. References.....	404

APPENDICES..... 416

APPENDIX A: Proposed High Spin Polyradicals..... 417

A.1. Introduction.....	417
A.2. Progress toward the synthesis of Poly(3-hexylthiophene- <i>alt</i> -3-SQthiophene) (P3HT-ThSQ).....	418
A.3. Hypothetical High-Spin and Soluble polymer: Poly(phenanthrene semiquinone- <i>alt</i> - 3,4-dialkylthieno[2,3-b]thiophene) (pPhenSQ-XBT)	425
A.4. Experimental.....	433

A.5. References.....	436
APPENDIX B: MOM₂CatBpin – An Anthology.....	441
B.1. Introduction.....	432
B.2. Experimental.....	451
B. References.....	454
APPENDIX C: Progress Toward PhMeTh Twisted Rectifiers.....	455
C.1. Introduction.....	455
C.2. Synthetic Discussion.....	455
C.3. Experimental.....	459
C.4. References.....	464
APPENDIX D: Progress toward the Donor-Bridge-Acceptor, 1,3-SQ-Fc-NN.....	465
D.1. Synthetic Discussion.....	465
D.2. Experimental.....	475
D.3. References.....	476
APPENDIX E. Crystallographic Data.....	478

LIST OF FIGURES

Figure I-1.	Electronic wavefunctions ($\Psi_{\text{Electronic}}$) cases for bonding and antibonding orbitals.....	7
Figure I-2.	The overlap region of two orthogonal p-orbitals.....	14
Figure I-3.	Triplet and singlet configuration in a carbon atom.....	15
Figure I-4.	Resonance structures of butadiene (Kekulé).....	16
Figure I-5.	Examples of Kekulé and non-Kekulé hydrocarbons.....	16
Figure I-6.	Trimethylenemethane (TMM) and tetramethyleneethane (TME) analysis with the star convention and ground-state spin calculation.....	18
Figure I-7.	Consequences for σ and π bonding interactions between two adjacent carbon atoms based on the requirements for the electronic wavefunctions ($\Psi_{\text{Electronic}}$).....	20
Figure I-8.	TMM and TME spin polarization explaining seemingly Hund's rule violation.....	20
Figure I-9.	Allyl radical ground state molecular orbital diagram a) without and b) with dynamic spin polarization (DSP).....	21
Figure I-10.	Huckel MO diagrams of cyclobutadiene and TMM.....	23
Figure I-11.	Effect of dynamic spin polarization on the α and β spin energies in the ψ_1 of cyclobutadiene.....	24
Figure I-12.	Effect of dynamic spin polarization in TMM.....	25
Figure I-13.	Non-disjoint and disjoint molecular orbitals.....	27
Figure I-14.	Zeeman splitting diagram of the m_s energy levels of an $S = 1/2$ paramagnetic species.....	28
Figure I-15.	$S = 1/2$ EPR spectra without and with hyperfine coupling shown beside their absorbance spectra.....	29
Figure I-16.	The EPR spectra of an organic radical interacting with two equivalent $I = 1/2$ nuclei and one $I = 1$ nucleus.....	30
Figure I-17.	Pascal's triangle showing the relative signal intensities for $I = 1/2$ and $I = 1$ nuclear spins.....	31
Figure I-18.	EPR spectra, line drawings and SOMOs for nitronylnitroxides and iminonitroxide organic radicals.....	32
Figure I-19.	Zeeman splitting in an exchange coupled biradical.....	33
Figure I-20.	EPR spectra of nitronylnitroxide (NN) monoradical in the form of Cat-B-NN and the corresponding semiquinone-bridge-nitronylnitroxide (SQ-B-NN) biradical.....	34

Figure I-21.	Cubic, axial, and rhombic spin systems with definitions of D and E as well as common geometric and chemical examples.....	36
Figure I-22.	Energy diagrams for magnetic spin axes in triplet EPR spectra.....	39
Figure I-23.	A simple schematic of the sample chamber of a SQUID magnetometer.....	41
Figure I-24.	M/M_{sat} Brillouin functions for $S=1/2, 2/2, 3/2, 4/2, 5/2,$ and $6/2$. (A) full plot and (B) zoomed in to show the initial slopes.....	42
Figure I-25.	Effect of temperature on the populations of the singlet and triplet states leading to the effects on the magnetic moment for when $J > 0$ (A) and $J < 0$ (B) beside their theoretical paramagnetic susceptibility ($\chi_{para}T$) plots for different values of J	43
Figure II-1.	The synthetic route to polycarbenes used by Iwamura in 1986.....	54
Figure II-2.	Itoh's high spin polyradical with a DP = 190.....	55
Figure II-3.	Cartoon of Ferromagnetic (solid) and antiferromagnetic (dashed lines) interactions in materials.....	56
Figure II-4.	Several polyradicals synthesized by Racja et al.....	57
Figure II-5.	Triarylamminium polyradicals (a) theoretical polyradical proposed by Bushby et al. (b-d) polyradicals synthesized by Nishide et al.....	58
Figure II-6.	Several polyradicals bearing stable-organic radicals as pendant groups that have been synthesized.....	59
Figure II-7.	(a) Radicals positioned <i>meta</i> to the poly(<i>m</i> -phenyleneethynylene) backbone are going to be non-Kekulé and disjoint and (b) radicals positioned <i>ortho/para</i> to the backbone are going to give rise to a Kekulé molecule.....	60
Figure II-8.	Radical perylene-3,4:9,10- <i>bis</i> (carboximide) synthesized displaying intersystem crossing modulation.....	63
Figure II-9.	TFPB polymer prepared by Yan et al.....	64
Figure II-10.	Schematic of an organic radical battery.....	65
Figure II-11.	PoPE-SQ and PPV-SQ polymers bearing semiquinone radicals that were originally synthesized over twenty years ago. Also shows the different oxidation states of the SQ group.....	67
Figure II-12.	A trimer of the PoPE-SQML _A polymer with the “star-method” applied to determine the ground-state spin and the redox reaction of Co ^{II} and PoPE-BQ to form PoPE-SQCo ^{III} L _A	69
Figure II-13.	FT-IR spectra of the monomer (II-12) and the polymers.....	86

Figure II-14. A) Absorption spectra of II-12 and the polymers. B) Emission spectra of samples before degassing. C) Difference between emission spectra before and after degassing.....	87
Figure II-15. IR spectra of PoPE-BQ (0%), PoPE-BQ₁₄-SQ₄ (~25%), PoPE-BQ₉-SQ₉ (50%), PoPE-BQ₆-SQ₁₂ (~66%), PoPE-BQ₂-SQ₁₆ . (~100%) showing the quinone stretch at 1650 cm ⁻¹ decreasing as the concentration of semiquinone increases.....	89
Figure II-16. EPR spectra of (a) 3,5-di- <i>tert</i> -butylsemiquinone-cobalt (III) complex. Line splitting: $a_{Co}=10.00$, $a_H=3.22$ Gauss. (b) PoPE-SQ (DP = 5) that had been reacted with excess CoL_A . (c) PoPE-SQ (DP = 17-18) reacted with 0.25 equivalents of CoL_A . (d) PoPE-SQ (DP = 17-18) reacted with 1.00 equivalents of CoL_A	90
Figure II-17. EPR spectra for the trials of increasing the spin concentration in the polymer as a function of the amount of CoL_A added. (A) The EPR signal for each trial. (B) Singly integrated EPR spectra. (C) Plot of calculated amount of SQ from spin concentration vs. the amount of CoL_A added.....	91
Figure II-18. M/M_{sat} plots for PoPESQ-050 and PoPESQ-075 in polystyrene films alongside theoretical Brillouin function plots for $S = 1/2, 2/2, 3/2$ and $4/2$. Magnetic field was swept from 0.05 to 7 T while the temperature was held at 2 K.....	92
Figure II-19. Donor-bridge-acceptor (D-B-A) biradicals evaluating the exchange coupling through conjugated phenylene and thiophene oligomers.....	98
Figure II-20. A) Synthesis of pThSQ from pThBQ and CoL_A and B) spin polarization through thiophene backbone illustrating ferromagnetically coupled radicals.....	98
Figure II-21. Routes to polythiophenes.....	100
Figure II-22. Reactivity of thiophene and characteristic ¹ H-NMR splittings for substitution patterns.....	105
Figure II-23. Catalytic cycle for Direct Arylation Polymerization(DArP).....	110
Figure II-24. EPR spectra of a monomer radical (ThSQ) and four polymers that have been reacted with 0.25, 0.50, 0.75 and 1.00 eq. of CoL_A : pThSQ-025 , pThSQ-050 , pThSQ-075 and pThSQ-100 , respectively.....	115
Figure II-25. EPR spectra of ThSQ and pThSQ-025 (left) and 3,5-di- <i>tert</i> -butylsemiquinone and PoPESQ-025 (right). Both polymers are 17 or 18 units long with PDIs of 1.5 or 1.4 and are both the nominally 25% spin concentration versions.....	116
Figure II-26. M/M_{sat} plots for pThSQ-025 , pThSQ-050 and pThSQ-075 in polystyrene films alongside theoretical Brillouin function plots for $S = 1/2, 2/2, 3/2$ and $4/2$. Magnetic field was swept from 0.05 to 7 T while the temperature was held at 2 K.....	118

Figure II-27. Examples of head-tail (HT), head-head (HH) or tail-tail (TT) linkages in a tetramer of pThSQ-100 and the effect of placement of the defect in the oligomer has on the ground-state spin of the oligomer.....	119
Figure II-28. Spin concentration calibration plot.....	124
Figure III-1. A diamagnetic donor-bridge-acceptor system which gives a biradical-like state upon excitation.....	169
Figure III-2. A) Directly overlapping SOMOs giving rise to direct antiferromagnetic exchange and B) SOMOs interacting through a filled diamagnetic <i>p</i> -orbital resulting in antiferromagnetic superexchange.....	171
Figure III-3. The original “no bridge” donor-acceptor biradical, SQ-NN.....	175
Figure III-4. Interactions leading to ferromagnetic exchange in SQ-NN.....	175
Figure III-5. Interactions for conjugated SQ-B-NN molecules.....	176
Figure III-6. VBCI model state diagram illustrating electronic transitions and energy gaps, <i>U</i> , <i>K₀</i> and <i>J</i> . The ground states (^{1,3} GC) and variable temperature electronic absorption spectra with the electronic transitions from the state diagram labelled.....	177
Figure III-7. General structure of SQ donor-bridge-NN acceptor biradicals.....	178
Figure III-8. ¹ H-NMR spectra of BHA and BHA•H ₂ SO ₄ after approximately 1.5 years, from the same reduction of 2,3-dimethyl-2,3-dinitrobutane and both stored at -20 °C occasionally exposed to ambient conditions from us.....	182
Figure III-9. EPR spectra of Cat-B-NN, Cat-B-IN, SQ-B-NN and SQ-B-NN with hindered rotation.....	190
Figure III-10. Thermal ellipsoid and space-filling models of SQ-<i>m</i>Ph-NN illustrating the steric interaction between [Tp ^{Cum,Me}] ⁻ isopropyl groups and the NN.....	192
Figure III-11. Electronic absorption spectra of SQ-NN, Ph-NN and SQZnTp ^{Cum,Me}	193
Figure III-12. A) Theoretical plots of $\chi_{\text{para}}T$ vs. <i>T</i> with different <i>J</i> values, B) theoretical plots of $\chi_{\text{para}}T$ vs. <i>T</i> with different <i>J</i> values, C) experimental plot of $\chi_{\text{para}}T$ vs. <i>T</i> for a biradical with the best data fit giving a <i>J</i> = -15 cm ⁻¹ and D) experimental plot of χ_{para} vs. <i>T</i> for the same biradical giving <i>J</i> = -14 cm ⁻¹ by calculation from the temperature at which the χ_{para} is greatest.....	196
Figure III-13. SQ-B-NN biradicals with no bridge and bridged by one phenyl ring, two phenyl rings, one thiophene ring and two thiophene rings. A) exponential decay functions of the no bridge, one phenyl ring and two phenyl rings series for <i>J</i> and <i>H_{DA}</i> and B) exponential decay functions of the no bridge, one thiophene ring and two thiophene rings series for <i>J</i> and <i>H_{DA}</i>	199
Figure III-14. SQ- <i>p</i> Ph-NN and SQ- <i>m</i> Ph-NN.....	201

Figure III-15. Electronic absorption spectra of SQ-NN , SQ-<i>m</i>Ph-NN and SQ-<i>p</i>Ph-NN and summary of the dominant FMO interactions that dictate the observed sign of exchange coupling.....	203
Figure III-16. A) The series of SQ-B-NN used to evaluate the torsional dependence of exchange coupling as well as the σ -only SQ-BCO-NN and B) the consequences of torsion angles between two <i>p</i> -orbitals.....	204
Figure III-17. Experimental change coupling values <i>vs.</i> the cosine-squared of torsion angles for SQ-Ph and Ph-NN. Square-blocked grid correlates experimental $J_{SQ-B-NN}$ values with experimental SQ-Ph and Ph-NN torsion angles: $J_{SQ-B-NN} = 0.34 + 3.77 \cdot \cos^2(\phi_{SQ-Ph}) - 13.4 \cdot \cos^2(\phi_{Ph-NN}) + 179 \cdot \cos^2(\phi_{SQ-Ph}) \cdot \cos^2(\phi_{Ph-NN}) + 16.3 \cdot \cos^4(\phi_{Ph-NN})$	206
Figure III-18. Spin polarization through a conjugated π -system and for a σ -only system....	207
Figure IV-1. HOMO and LUMO of benzene with symmetry allowed <i>para</i> and symmetry forbidden <i>meta</i> connectivity.....	227
Figure IV-2. Current-voltage profile of a device that obeys Ohm's law (not a rectifier) and a device that displays non-Ohmic behavior (a molecular rectifier)	228
Figure IV-3. Molecules with a thiol donor and a nitrile acceptor and 12 double bonds: a) the donor and acceptor are strongly coupled and their Hückel orbitals are very symmetric between the donor and acceptor side (not a rectifier) b) the donor and acceptor sides are decoupled (rectifier) by an alkyl linker as shown by the DFT calculated HOMO and LUMO.....	230
Figure IV-4. Aviram-Ratner's proposed bicyclooctane (BCO) bridge to decouple a donor (TTF) from the acceptor (TCNQ).....	230
Figure IV-5. The schematic of a metal-organic-metal rectifying device where the two identical electrodes are connected via a donor-acceptor bridging unit and qualitatively illustrating the Fermi levels of the metals and the HOMO and LUMO levels of the donor and acceptor A) under no bias B) when the current flows anode-acceptor-donor-cathode and C) when the current flows anode-donor-acceptor-cathode.....	231
Figure IV-6. Schottky type rectifiers A) a cartoon of changes that can be made to make an S-type rectifier. B) Examples of S-type rectifiers.....	233
Figure IV-7. A-type unimolecular rectifiers that are the asymmetric placement of the chromophore. A) a schematic showing the asymmetric placement of the chromophore and B) several examples of A-type rectifiers.....	234
Figure IV-8. U-type unimolecular rectifiers which are considered to be "True" unimolecular rectifiers that are governed by the asymmetry of their orbitals. A) a schematic showing the asymmetric orbital segments of the acceptor (O_A) and donor (O_B) and B) example of a biphenyl-bridged device which could be a U-type molecular rectifier due to orbital asymmetry.....	235

Figure IV-9. Examples of molecular rectifiers that are a compilation of S, A and U-type rectifiers and their empirically determined RRs.....	236
Figure IV-10. Challenges for studying molecular rectification A) issues with the contact angle a molecule makes with an electrode surface that itself may have defects leading to observed rectification and B) issues with reproducibility of rectification experiments that lead to ranges of RRs being reported.....	238
Figure IV-11. A) Redefining SQ as the “anode” and NN as the “cathode”. B) Crystal structures with torsion angles and PyTh being placed between the two electrodes.....	241
Figure IV-12. A) Data for the measured and corrected exchange coupling constants of each compound with their corresponding RRs. B) The calculation used to correct the exchange coupling constants resulting in the inversion of the RR.....	243
Figure IV-13. Frontier molecular orbital interactions of the VBCI model that result in a ferromagnetically coupled biradical.....	244
Figure IV-14. Computational studies performed by Xia et al. on a molecular rectifier composed of a tetramethylbenzodioxole donor, a phenyl bridge, and a tetracyanobenzene (TCNB) acceptor. A) the schematic of TMDO-Ph-TCNB placed between two gold electrodes. B) Computational models of the rectifying device with the donor, bridge, and acceptor each in turn rotated out of the plane of the molecule by 30, 60, or 90°. C) The resulting RRs from the electron transport calculations performed on the models in B)	246
Figure IV-15. Proposed molecular rectifier: thiophene donor-phenyl acceptor dyad and the qualitative effect that torsion angle will have on the delocalization of the donor and acceptor orbitals in the HOMO and LUMO.....	247
Figure IV-16. Crystal structures of SQ-PhMe₂Th-NN and NN-PhMe₂Th-SQ	262
Figure IV-17. A) Electronic absorption spectra for SQ-PhMe₂Th-NN (blue) and NN-PhMe₂Th-SQ (red). B) Variable temperature paramagnetic susceptibility plots and fitting parameters for SQ-PhMe₂Th-NN (blue) and NN-PhMe₂Th-SQ (red).....	263
Figure IV-18. Proposed molecular rectifier possessing cross-conjugative asymmetry at the positions indicated with the green arrows beside the Hückel MO coefficients in the HOMO and LUMO.....	268
Figure IV-19. Proposed rectifiers: p-SQ-m-NN and m-SQ-p-NN and their respective SQ and NN SOMOs	269
Figure IV-20. Crystal structures providing detailed geometry data, variable temperature paramagnetic susceptibility ($\chi_{\text{para}}T$ vs. T) with exchange coupling fitting parameters J for the measured and corrected for planar molecules, and the RRs for p-SQ-m-NN and m-SQ-p-NN	273

Figure IV-21.	The Hückel-based MO description of the delocalization of the SQ SOMO through bithiophene-based cross-conjugative molecular rectifiers. A) 4'-SQ-2,2'-BTh-5-NN and 5'-SQ-2,2'-BTh-4-NN thiophene-based <i>p</i> -SQ- <i>m</i> -NN and <i>m</i> -SQ- <i>p</i> -NN analogs where the bridge subunits are conjugated and cross-conjugation is achieved through positioning of the SQ and NN. B) 5'-SQ-2,3'-BTh-5-NN and 5-SQ-2,3'-BTh-5'-NN where the bridge subunits are cross-conjugated with each other.....	274
Figure V-1.	Structures and CH ₂ Cl ₂ solutions of the C ₁₀ H ₈ isomers: azulene (left) and naphthalene (right).....	296
Figure V-2.	Examples of even-alternant, odd-alternant, and nonalternant hydrocarbons, alongside heterocycles which are not part of any of these other classifications.....	297
Figure V-3.	A) Hückel-calculated energy level diagrams for azulene and naphthalene. B) HOMO-1, HOMO, LUMO and LUMO+1 molecular orbitals for naphthalene and azulene. C) Hückel-calculated charge densities for each carbon atom of naphthalene and azulene. D) Examples of nonalternant hydrocarbons where rotational symmetry dictates atom charge densities are equivalent or not equivalent.....	298
Figure V-4.	The breakdown of some common pictorial analogies that work for alternant hydrocarbons, but not for nonalternant hydrocarbons. A) Electron/arrow-pushing to move a radical or charge around aromatic rings. B) SOMOs of 1-methylene-naphthalene and 1-methylene-azulene radicals showing discrepancies between the analogy and even low level of theory Hückel calculations. C) Application of the star method to naphthalene and spin polarization in naphthalene vs. azulene.....	300
Figure V-5.	A) Application of the atom counting model for predicting quantum interference in nonalternant hydrocarbons like azulene and alternant hydrocarbons such as benzene. B) SQ-B-NN molecules with alternant bridges that the atom counting model indicates quantum interference give $J < 0$ while those for which the atom counting model does not indicate quantum interference give $J > 0$	302
Figure V-6.	The dipole moment of azulene, other hydrocarbons, some common small molecules and a few heterocycles.....	304
Figure V-7.	A) S ₂ state absorption and emission spectrum of azulene. B) Excited state dynamics of naphthalene and azulene. C) HOMO, LUMO and LUMO+1 of azulene with orbital symmetries in the C _{2v} point group. D) Transition moment integral and the products of the symmetries of the S ₁ and S ₂ states of azulene and naphthalene.....	306
Figure V-8.	<i>poly</i> (1,3-azulene) prepared by Wang, et al. with the radical cations and resonance structures attributed to the conductivity of polymers treated with either acid or iodine.....	308

Figure V-9.	The ability of <i>poly</i> (2,6-azulene) to have the quinoidal resonance structure like other conjugated polymers, such as <i>poly</i> (phenylene) and polymers of 5-membered heterocycles containing chalcogens and pnictogens.	309
Figure V-10.	Terazulenes from Yamaguchi et al. possessing different connectivities beside their DFT calculated HOMOs, LUMOs and dipole moments.....	310
Figure V-11.	Organic molecules with heteroatoms possessing dipole moments comparable to the terazulenes from Song et al.....	310
Figure V-12.	Reported measured conductance values for the azulene derivatives synthesized by A) Xia et al. and B) Schwarz et al. with the order from greatest conductance to lowest conductance for both the measured and calculated conductance from each study.....	312
Figure V-13.	1,3-IN₂Az and 1,3-NN₂-Az	315
Figure V-14.	SQ-B-NNs as analogs of TMM (A) or TME (B) allowing for delocalization of one radical while localizing the other resulting in nondisjoint SOMOs for SQ-NN and SQ-B-NNs with conjugated bridges or disjoint SOMOs for SQ-B-NNs with cross-conjugated bridges.....	317
Figure V-15.	Disjoint, localized symmetric NN biradicals that will exhibit small exchange coupling constants.	317
Figure V-16.	Symmetrical SQ-B-SQ biradicals that are either A) cross-conjugated or B) conjugated through the bridge.	318
Figure V-17.	Assigned ¹ H-NMR spectrum of Cat-Az-CHO . Clean aromatic region with the full spectrum (<i>inset</i>) only showing residual solvent peaks.....	322
Figure V-18.	EPR spectra and simulations of the attempted deprotection of MOM₂Cat-Az-BHA with catalytic acid giving A) the crude reaction mixture. B) The spectrum of Az-NN . C) The spectrum of Az-IN . D) Treatment of the crude mixture with NaIO ₄ . E) Treatment of the crude mixture with NaIO ₄ then <i>m</i> -CPBA and F) treatment of the crude mixture with <i>m</i> -CPBA, then NaIO ₄	326
Figure V-19.	EPR spectra of A) NN-H and B) NNAuPPh₃	329
Figure V-20.	Aromatic region from the ¹ H-NMR spectrum from the reduction of BQ-Az to Cat-Az and allowing it to sit out for two days.....	338
Figure V-21.	A) Room temperature isotropic EPR spectra of Ac₂Cat-Az-NN monoradical (<i>top</i>) and 1,3-SQ-Az-NN biradical (<i>bottom</i>). B) Anisotropic EPR spectrum and simulation of 1,3-SQ-Az-NN in 2-MTHF at 125 K and the Δ _{m_s} = 2 half field transition (<i>inset</i>).....	344
Figure V-22.	Thermal ellipsoid plots (50% probability) and biradical ligand atomic numbering schemes for X-ray structures of 1,3-SQ₂Az (left) and 1,3-SQ-Az-NN (right).....	346

Figure V-23. X-band EPR spectra of 1,3-SQ₂Az (A) and 1,3-SQ-Az-NN (B) recorded at 100K and 125K, respectively in 2-methyltetrahydrofuran (2-MTHF). Simulations were executed using <i>Easyspin</i> .™.....	348
Figure V-24. Room-temperature solution spectrum of 1-SQ-Az . Dashed blue lines show additional lines due to ¹ H-hyperfine couplings.....	349
Figure V-25. Electronic absorption spectra of (A) SQ-NN , ZnSQ , Ph-NN and pSQ-Ph-NN and (B) azulene, 1-SQAz , 1-NNAz , 1,3-SQ-Az-NN and 1,3-SQ₂Az	350
Figure V-26. Magnetic susceptibility (A) Saturation magnetization plots and (B) variable temperature paramagnetic susceptibility plots for 1,3-SQ₂Az and 1,3-SQ-Az-NN	353
Figure V-27. Predicted and observed coupling in alternant hydrocarbons. (A) TMM and TME (B) symmetric, delocalized biradical (C) asymmetric one delocalized and one localized ferromagnetically and (D) antiferromagnetically coupled biradicals.....	355
Figure V-28. (A) symmetric, delocalized biradical (B) asymmetric one delocalized and one localized biradicals 1,3- through azulene.....	357
Figure V-29. Spin polarization through alternant and nonalternant hydrocarbons between two (A) symmetric, delocalized and (B) asymmetric, one delocalized and one localized radicals.....	358
Figure V-30. (A) Dominant orbital interactions for 1,3-SQ-Ph-NN and 1,4-SQ-Ph-NN. (B) HOMO and LUMO of alternant hydrocarbons: benzene and naphthalene and nonalternant hydrocarbon: azulene.....	361
Figure V-31. Atom-counting model for the presence of quantum interference.....	363
Figure V-32. Thermal ellipsoid plots (50% probability) and biradical ligand atomic numbering schemes for X-ray structures of 1,3-SQ₂Fc (top left), 1,1'-SQ₂Fc (right), and 1-SQFc (bottom left). Cumenyl groups and hydrogens have been omitted for clarity.....	372
Figure V-33. A) Room temperature isotropic spectrum of 1-SQFc in 2-MTHF. B) 110K powder spectrum of 1-SQFc . Simulations were executed using <i>Easyspin</i> .™..	374
Figure V-34. IR spectra of 1-SQFc , 1,1'-SQ₂Fc and 1,3-SQ₂Fc	375
Figure V-35. Electronic absorption spectra of (A) 1-SQFc , 1,3-SQ₂Fc and 1,1'-SQ₂Fc . (B) comparison of 1,3-SQ₂Fc spectral feature at 10000 cm ⁻¹ in DMSO and toluene.....	377
Figure V-36. Plots of paramagnetic susceptibility-temperature product ($\chi_{\text{para}} \cdot T$) vs. temperature for a crystalline sample of (A) 1,1'-SQ₂Fc and (B) 1,3-SQ₂Fc . fit to the experimental $\chi_{\text{para}} \cdot T$ data gives a antiferromagnetic exchange parameter, $J = -2 \text{ cm}^{-1}$ and $J = -15 \text{ cm}^{-1}$, respectively indicating a singlet ground state ($\mathcal{H} = -2J\hat{S}_1 \cdot \hat{S}_2$). C) Plot of paramagnetic susceptibility-	

	(χ_{para}) vs. temperature for 1,3-SQ₂Fc with $J = -14 \text{ cm}^{-1}$ by the mathematical relation between J and the temperature at which the magnetization is maximum (T_{max}).....	378
Figure V-37.	Cyclic voltammogram of 1-SQFc in MeCN with 0.1 M Bu ₄ NPF ₆	379
Figure V-38.	Cyclic voltammogram of 1,3-SQ₂Ph , SQ₂ , 1,3-SQ₂Fc , 1,1'-SQ₂Fc , 1-SQFc and 1-MOM₂CatFc in MeCN with 0.1 M Bu ₄ NPF ₆	380
Figure V-39.	Spacefilling models from the crystal structures of 1,3-SQ₂Ph , SQ₂ , 1,3-SQ₂Fc , 1,1'-SQ₂Fc , SQ₂ , and 1-SQFc . The (ZnTp ^{Cum,Me}) ⁺ ligands for each molecule are displayed horizontally. Red atoms are the oxygen atoms of the SQ . The green circle shows the six-carbon atoms of the phenyl ring bridge from 1,3-SQ₂Ph	381
Figure V-40.	Differential pulsed voltammograms of t-BuBQ , 1,3-BQ₂Ph , 1,3-BQ₂Fc , 1,1'-BQ₂Fc and 1,3-BQ₂Az collected in MeCN with 0.1 M Bu ₄ NPF ₆	383
Figure A-1.	<i>ortho</i> -lithiation directing MOM group.....	421
Figure A-2.	Polyradicals prepared by A) Yan et al. and B) Swager et al.....	425
Figure A-3.	Possible features of an ideal high-spin polyradical.....	427
Figure A-4.	Hückel SOMOs of A) phenalenyl and B) BDPA fragments from polyradicals.....	428
Figure A-5.	Proposed high-spin, soluble polyradical, pPhenSQ-XBT	429
Figure D-1.	¹ H-NMR spectra of DioxOH-Fc in DMSO-d ₆ , CDCl ₃ and aged.....	471
Figure D-2.	¹ H-NMR Spectra of CHO-Fc-I in DMSO and CDCl ₃	472
Figure D-3.	¹ H-NMR of the BHA cyclization of 1,3-CHO-Fc-Cat using the reaction conditions from Scheme D-5 taken in DMSO-d ₆ (green) and with a drop of D ₂ O added.....	474

LIST OF TABLES

<i>Table II-1.</i>	Comparison of different Wittig Olefination and subsequent dehydrohalogenation conditions; test reactions performed on the conversion of 4-bromobenzaldehyde to 4-bromophenylacetylene (II-16).....	74
<i>Table II-2.</i>	Attempted reactions for the protection of terminal aryl acetylene for II-14	77
<i>Table II-3.</i>	Conditions for test double dehydrohalogenation reactions to make II-16	80
<i>Table II-4.</i>	Conditions for test double dehydrohalogenation and hydrolysis reactions to make II-16	82
<i>Table II-5.</i>	Sonogashira polymerization reactions.....	85
<i>Table II-6.</i>	EPR data for spin concentration calculations.....	91
<i>Table II-7.</i>	Synthetic attempts to make CoL_A	96
<i>Table II-8.</i>	Evaluation of Suzuki coupling conditions to optimize the synthesis of 3-(MOM₂Cat)Th	103
<i>Table II-9.</i>	Attempted iodination conditions for the thiophene monomer.....	106
<i>Table II-10.</i>	Test iodination conditions on 2-bromothiophene.....	108
<i>Table II-11.</i>	pThCatMOM₂ DArP conditions.....	113
<i>Table II-12.</i>	DPPH calibration data.....	124
<i>Table III-1.</i>	Typical and characteristic hyperfine splitting of NN and IN monoradicals alongside a typical SQ-B-NN biradical and an SQ-B-NN biradical with hindered rotation leading to an irregular EPR spectrum.....	191
<i>Table III-2.</i>	Selected bond lengths for Cat-NN, SQ-NN and SQ.....	197
<i>Table IV-1.</i>	Attempted palladium-mediated cross-coupling conditions.....	251
<i>Table IV-2.</i>	Test aryl triazene conversion to aryl iodide.....	256
<i>Table IV-3.</i>	Aryl triazene (RN₃-PhMe₂Th) conversion to aryl iodide (I-PhMe₂Th).....	259
<i>Table IV-4.</i>	Measured <i>J</i> -values for Me _n Ph biradical complexes with torsions corrected to be a planar molecule and with all torsion angles set to those of SQ-PhMe-NN	265
<i>Table IV-5.</i>	Measured <i>J</i> values for SQ-PhMe₂Th-NN and NN-PhMe₂-SQ with torsions corrected to be a planar molecule and with all torsion angles set to the other isomer's torsion angles.....	266
<i>Table V-1.</i>	Attempted silyl protections of Br-Az-BHA	324
<i>Table V-2.</i>	Select 1,3-SQ₂-Az and 1,3-SQ-Az-NN bond lengths.....	347
<i>Table V-3.</i>	Attempted palladium-mediate cross-couplings for 1,3-(MOM₂Cat)₂Fc	368

Table V-4.	Select 1,3-SQ₂Fc , 1,1'-SQ₂Fc and 1-SQFc bond lengths.....	373
Table A-1.	Syntheses of 5-Bu₃Sn-3-(MOM₂Cat)Th	420

LIST OF SCHEMES

<i>Scheme II-1.</i> Shultz group synthetic route for pinacolyl(1,2-dimethoxymethoxy-6- <i>tert</i> -butyl-1- phenyl) boronate (MOM ₂ CatBpin).....	71
<i>Scheme II-2.</i> Monomer synthesis via the original Wittig reaction with (bromomethyl)triphenylphosphonium bromide.....	72
<i>Scheme II-3.</i> Synthetic route by alkyne formation and protection.....	73
<i>Scheme II-4.</i> Proposed mechanism for epoxide formation (red route) via Wittig olefination using ylides with leaving groups vs. the route for olefination formation (blue route).....	75
<i>Scheme II-5.</i> Protection of the terminal aryl acetylene with a tertiary alcohol and reaction with phenylacetylene used as a model compound.....	76
<i>Scheme II-6.</i> Trialkylsilyl protection of the terminal aryl acetylene. Reaction with phenylacetylene used as a model compound.....	78
<i>Scheme II-7.</i> Synthetic route to II-12 using Wittig reaction with methyltriphenylphosphonium iodide followed by bromination of the double bond and double dehydrohalogenation.....	79
<i>Scheme II-8.</i> Access to II-12 via Wittig reaction with (ethyl ester methyl)triphenylphosphonium bromide to give the ethyl propiolate; serving as the protected alkyne.....	81
<i>Scheme II-9.</i> Synthesis of II-12 via the Ohira-Bestmann reaction.....	82
<i>Scheme II-10.</i> Polymerization of II-12 followed by deprotection to the catechol (PoPE-Cat) and oxidation to the quinone polymer (PoPE-BQ).....	84
<i>Scheme II-11.</i> The synthesis of random copolymers of PoPE with SQ and BQ pendant groups with the redox reaction of a cobalt (II) complex.....	88
<i>Scheme II-12.</i> Synthesis of a cobalt (II) complex that will undergo a redox reaction with a quinone to generate a semiquinone.....	94
<i>Scheme II-13.</i> Original synthesis for pThCatMOM₂ using either A) the McCullough method or B) the GRIM polymerization.....	101
<i>Scheme III-1.</i> Synthesis of MOM ₂ CatBpin.....	179
<i>Scheme III-2.</i> Synthesis of HOPhBpin.....	180
<i>Scheme III-3.</i> The synthesis of nitronyl nitroxides from commercially available starting materials.....	181
<i>Scheme III-4.</i> Decomposition of BHA by atmospheric oxygen.....	182
<i>Scheme III-5.</i> Synthesis of Zn(OH)Tp ^{Cum,Me}	183
<i>Scheme III-6.</i> Traditional assembly of SQ-B-NN biradicals.....	187

<i>Scheme III-7.</i> Complexation of Zn(OH)Tp ^{Cum,Me} to catechol followed by aerial oxidation to SQ.....	189
<i>Scheme IV-1.</i> Proposed retrosynthetic pathway for SQ-PhMe₂Th-NN and NN-PhMe₂Th-SQ	249
<i>Scheme IV-2.</i> Original synthesis with a common intermediate for both biradicals.....	250
<i>Scheme IV-3.</i> Lithium-halogen exchange followed by borylation with i-PrOBpin.....	252
<i>Scheme IV-4.</i> Employing an aryl triazine as a masked halide.....	253
<i>Scheme IV-5.</i> Attempted cross-coupling with a less electron-rich substrate.....	254
<i>Scheme IV-6.</i> Synthesis of the common intermediate and the beginning of the divergent syntheses.....	258
<i>Scheme IV-7.</i> The final steps to the synthesis of SQ-PhMe₂Th-NN and NN-PhMe₂Th-SQ	261
<i>Scheme IV-8.</i> Retrosynthetic pathways of <i>p</i> - SQ-<i>m</i>-NN and <i>m</i> - SQ-<i>p</i>-NN	270
<i>Scheme IV-9.</i> Successful synthetic procedures for <i>p</i> - SQ-<i>m</i>-NN and <i>m</i> - SQ-<i>p</i>-NN	271
<i>Scheme V-1.</i> Generic route for all Shultz group SQ-B-NN biradicals up to this point.....	320
<i>Scheme V-2.</i> The original proposed synthesis of 1,3-SQ-Az-NN	321
<i>Scheme V-3.</i> Proposed use of silyl protecting groups for protecting Ar-BHA.....	323
<i>Scheme V-4.</i> Synthesis of NNAuPPh₃	328
<i>Scheme V-5.</i> Original proposed method for implementing NNAuPPh₃ for the synthesis of 1,3-SQ-Az-NN	330
<i>Scheme V-6.</i> A more efficient route to MOM₂Cat-Az-I	332
<i>Scheme V-7.</i> Synthesis and attempted iodination of Me₂Cat-Az	333
<i>Scheme V-8.</i> Synthesis of BQ-Az-I	334
<i>Scheme V-9.</i> Microwave synthesis of Cat-Az-BHA , oxidation with I ₂ and multiple attempted complexations with Zn(OH)Tp ^{Cum,Me}	335
<i>Scheme V-10.</i> Pd/C hydrogen reduction and subsequent protection of BQ-Az to Ac₂Cat-Az , followed by iodination.....	339
<i>Scheme V-11.</i> One-pot replacement of methoxymethyl groups with acetates.....	341
<i>Scheme V-12.</i> Synthesis of Ac₂Cat-Az-NN and 1,3-SQ-Az-NN	342
<i>Scheme V-13.</i> Test in situ acetate deprotection/ complexation.....	342
<i>Scheme V-14.</i> Synthesis of 1,3-SQ₂Az	345
<i>Scheme V-15.</i> Synthesis of 1,3-diiodoferrocene.....	366

<i>Scheme V-16.</i> Synthesis of 1,3-SQ₂Fc	369
<i>Scheme V-17.</i> Synthesis of A) 1-SQFc monoradical and B) SQ₂ dioxolene dimer.....	371
<i>Scheme A-1.</i> Retrosynthesis of P3HT-ThSQ	418
<i>Scheme A-2.</i> Synthesis of P3HT-ThCatMOM₂	419
<i>Scheme A-3.</i> Attempted polymerization of 3HT-ThCATMOM₂-Br with DArP.....	423
<i>Scheme A-4.</i> Synthetic procedure to make P3HT-ThCatMOM₂ via GRIM.....	423
<i>Scheme A-5.</i> Proposed synthesis of pPhenBQ-XBT ; precursor to pPhenSQ-XBT	431
<i>Scheme B-1.</i> Methyl protected catechol synthesis starting with guaiacol.....	441
<i>Scheme B-2.</i> Some synthetic transformations of MOM₂CatBr	442
<i>Scheme B-3.</i> Synthesis of MOM₂CatBr starting from 2- <i>tert</i> -butylphenol and making catechol via <i>ortho</i> -lithiation to a MOM protecting group.....	443
<i>Scheme B-4.</i> (A) IBX oxidation of electron-rich phenols. (B) IBX synthesis from 2-iodobenzoic acid and oxone in water.....	444
<i>Scheme B-5.</i> IBX synthesis of MOM₂CatBr and MOM₂CatBpin	445
<i>Scheme B-6.</i> PhOHBpin synthetic procedure to catechols.....	446
<i>Scheme B-7.</i> Challenging substrates for IBX oxidation of phenols.....	447
<i>Scheme B-8.</i> Phenol test reactions with IBX using different solvents.....	449
<i>Scheme B-9.</i> Redesigned synthesis using 25% MeOH/CH ₂ Cl ₂ to accelerate the IBX oxidation of phenol.....	450
<i>Scheme C-1.</i> Retrosynthesis of PhMe_nTh -bridged torsional rectifiers.....	456
<i>Scheme C-2.</i> Synthesis of PhMeTh isomers up to MOM₂Cat-B-CHO by following the procedures from Chapter IV.....	457
<i>Scheme C-3.</i> Incomplete PhMeTh -bridge isomer steps from MOM₂Cat-B-CHO to SQ-B-NN	458
<i>Scheme D-1.</i> Retrosynthesis of racemic 1,3-SQ-Fc-NN	465
<i>Scheme D-2.</i> Possible synthetic routes to the racemic mixture of 1,3-SQ-Fc-NN biradicals.....	465
<i>Scheme D-3.</i> A) lithium-halogen exchange method to make CHO-Fc and B) aggressive conditions employed for the deprotonation of ferrocene.....	467
<i>Scheme D-4.</i> Unsuccessful palladium-mediated cross-coupling reaction of iodoferrocene with NNAuPPh₃	468
<i>Scheme D-5.</i> Retrosynthesis of enantiopure 1,3-NN-Fc-SQ from CHO-Fc-I	468

<i>Scheme D-6.</i> Synthesis of enantiopure CHO-Fc-I as described by Ferber et al.....	470
<i>Scheme D-7.</i> Successful route for ferrocene-1-nitronitroxide.....	473

I. Introduction and General Theory

In 1900, Moses Gomberg first reported an organic radical, triphenylmethyl, which he postulated must have been created during his attempted synthesis of hexaphenylethane, but instead resulted in the formation of the triphenylmethyl peroxide.¹ It was not until 1957, that a stable organic radical, displaying weak ferromagnetism was discovered in crystals of galvinoxyl radicals.^{2,3} Since then a variety of stable organic radicals, such as: nitroxides, (2,2,6,6-Tetramethylpiperidin-1-yl)oxyl (TEMPO), 2,2-diphenyl-1-picrylhydrazyl (DPPH), 1,2,4-benzotriazinyl (Blatter's radical), verdazyl, aminyl, and many others and derivatives; have been discovered and studied.⁴⁻¹⁴ More recently in the past 25 years, many magnetic materials and other novel materials by incorporating organic radicals into organic or hybrid-organic materials have been synthesized and studied.¹⁵⁻²⁷ These types of materials have potential application for new organic batteries, spintronics and spin-polarized transport, semiconductors, memory storage, photovoltaics, organic light-emitting diodes (OLEDs), and other organic electronic devices.²⁸⁻⁴²

Specifically, in 1997, IBM released the first hard drive (16.8 GB) that utilized spin valves in the read heads, which revolutionized the way that information could be stored.⁴³ Information could now be encoded as the binary language of 1's and 0's on a hard disk in the form of either an electron with an up spin or down spin. Since then great advancements have been made in the development of memory storage devices, but more efficient, innovative, and cost-effective methods are necessary. Especially because according to IBM, in 2015, more than 2.5 exabytes (1 exabyte = 1 million terabytes) of information was created and stored per day necessitating the need for materials and devices with higher areal density. Through the application of fundamental understanding of redox activity, charge transport, and spintronics, new materials capable of storing and processing information will be developed.

Another area of interest is OLEDs, which have an upper limit of efficiency of 25% because only singlet excitons will emit light and according to spin statistics, only 25% of excitons formed are singlets the other 75% are triplets. However using stable, organic, high spin materials could provide a relatively inexpensive route to manipulating spin populations by facilitating intersystem crossings via radical substituents.⁴⁴

In conventional inorganic magnetic materials, the source of spin comes from electrons located in d- and f-orbitals of transition and rare earth metals and spins are coupled in three dimensions. This is a problem that must be addressed when designing organic high-spin materials.^{45,46} Since ferromagnetic coupling requires very specific intermolecular interactions, most organic radicals are only coupled in two dimensions and result in antiferromagnetic coupling in the third dimension (*z*-axis) resulting in a material with a minimized net spin. Current electronic and magnetic materials rely on rare earth or precious elements that are scarce and expensive to use which in turn raises the cost of the products in which they find application. Moving toward organic or organic-hybrid molecular electronics benefit from reduced cost of production, lighter weight and flexibility.

Two classes of organic radicals will be discussed: first the application, background and current progress into incorporating stable organic radicals onto a polymer backbone, known as polyradicals will be discussed in Chapter II; the second will be the utility of heterospin organic biradicals for the evaluation of electronic and magnetic coupling through bridging units that are of interest for molecular electronics will be discussed in Chapters III-V.

Polyradical research has been an active area of research since Mataga proposed using polycarbenes for accessing high-spin materials in 1968⁴⁷ and since then, Rajca demonstrated the synthesis of entirely organic high spin materials, some with spin quantum numbers (*S*) as high as

5000 at 10 K.^{48,49} Recently, Nishide has had success by incorporating TEMPO and galvinoxyl pendant groups into aliphatic polymer backbones to serve as anodes and cathodes, respectively, in an organic battery.^{28,35,38,50} Potential spintronics applications are possible for any spin-polarized material, but has been demonstrated by Tagami, K. et al. where by measuring current-voltage relationships and showing that through a tetramer of poly(o-phenylenevinylene) with phenoxy pendant groups, the current resulting from up spins and down spins is disproportionate.¹⁸

The second part of this document (Chapters III-V) will discuss the past, current and future work of heterospin, donor-bridge-acceptor biradicals (in the form of ligands) for evaluating molecules that are of interest to molecular electronics, which has been an active area of research in the Shultz group for over a decade.⁵¹ Stable D-B-A biradicals are effectively ground-state analogues of the charge-separated excited states encountered in photoinduced electron transfer. As such, detailed electronic studies of stable ground state donor-acceptor biradical systems provide a convenient platform for evaluating crucial electronic structure contributions to electron transport relevant to molecular electronics.

The remainder of this chapter will be devoted to the models of spin-spin interactions in high-spin organic radicals. The succeeding chapters will involve analyses of organic radicals and applications of materials incorporating organic radicals into molecular electronics. Knowledge obtained from this research will have application and relevance elsewhere, such as photovoltaics, data storage, semiconductors, OLEDs, etc.

I.1. Pauli Exclusion Principle.

Electrons are members of a class of subatomic particles known as fermions. The Pauli Exclusion Principle states that no two fermions can possess the same quantum state. Fermions

possess half-integer spins and must be completely indistinguishable from one another. The electronic state ($\Psi_{Electronic}$) for an electron is the product of several wavefunctions:

$$\Psi_{Electronic} = \psi_{MO}\psi_{spin} \quad \text{Eq. I-1}$$

where, ψ_{MO} is the spatial wavefunction, the atomic or molecular orbital that an electron occupies and ψ_{spin} is the spin wavefunction. The electronic wavefunction ($\Psi_{Electronic}$) must be antisymmetric with respect to exchange of electron “labels.” If two electrons (1 and 2) are in two molecular orbitals (a and b), the wavefunction:

$$\begin{aligned} \psi_{MO} &= \phi_a(1)\phi_b(2) \\ \phi_a(1)\phi_b(2) &\neq \pm \phi_a(2)\phi_b(1) \end{aligned}$$

is unacceptable because it is neither symmetric nor antisymmetric with respect to exchange of the two electrons and electrons 1 and 2 can be distinguished spatially; electron 1 only exists in ϕ_a and electron 2 only exists in ϕ_b .⁵² In order to make symmetrized wavefunctions, linear combinations of $\phi_a(1)\phi_b(2)$ and $\phi_a(2)\phi_b(1)$ are taken to give symmetric and antisymmetric wavefunctions, respectively, ψ_s and ψ_a :

$$\psi_s = \frac{1}{\sqrt{2}}(\phi_a(1)\phi_b(2) + \phi_a(2)\phi_b(1)) \quad \text{Eq. I-2}$$

$$\psi_a = \frac{1}{\sqrt{2}}(\phi_a(1)\phi_b(2) - \phi_a(2)\phi_b(1)) \quad \text{Eq. I-3}$$

$$P_{12}\psi_s = \frac{1}{\sqrt{2}}(\phi_a(2)\phi_b(1) + \phi_a(1)\phi_b(2)) = \psi_s$$

An operation is performed on the above wavefunctions (Eq. I-2 and I-3), this operator exchanges the two electrons and is called the permutation operator (P_{12}). When applied to equations Eq. I-2 and Eq. I-3, it yields:

$$P_{12}\psi_a = \frac{1}{\sqrt{2}}(\phi_a(1)\phi_b(2) - \phi_a(2)\phi_b(1)) = -\psi_a$$

Note that $P_{12}\psi_s = \psi_s$ and $P_{12}\psi_a = -\psi_a$, identifying symmetric and antisymmetric spatial wavefunctions.

Electron spin can be expressed as either an up spin (α) or a down spin (β) with respect to the axis of quantization. Electrons with the same spin are symmetric with respect to label exchange and electrons with opposite spins are antisymmetric with respect to label exchange.^{52,53} Statistically, there are four possibilities when considering two electrons (1 and 2) between two spin channels (α and β): $\alpha(1)\alpha(2)$, $\beta(1)\beta(2)$, $\alpha(1)\beta(2)$, and $\beta(1)\alpha(2)$. The first two are symmetric with respect to exchange and the last two are neither symmetric nor antisymmetric with respect to exchange; therefore, the electrons in these spin channels are distinguishable and are not acceptable spin functions. So, linear combinations of each must be used to make the electron spins indistinguishable from one another. The two from the linear combination with the two already acceptable spin combinations will give four wavefunctions, three will be symmetric and one will be antisymmetric with respect to exchange and they are:

$$\text{Symmetric:} \quad \alpha(1)\alpha(2); \quad \beta(1)\beta(2); \quad \frac{1}{\sqrt{2}}(\alpha(1)\beta(2) + \beta(1)\alpha(2))$$

$$\text{Antisymmetric} \quad \frac{1}{\sqrt{2}}(\alpha(1)\beta(2) - \beta(1)\alpha(2))$$

For two electrons in two spin channels, the symmetric wavefunctions are referred to as the triplet state and the antisymmetric wavefunction is referred to as the singlet state. The total spin for a system, $(S) = \sum m_s$; or the number of up spins (α) minus the number of down spins (β), divide by two. When examining a system of electrons and spins, only the unpaired electrons need to be considered when calculating S because for all paired spins: $S = \sum m_s = \frac{1}{2} - \frac{1}{2} = 0$.

In order to get the overall antisymmetric electronic wavefunctions ($\Psi_{Electronic}$), in general, is written as a Slater determinant. For a two spatial wavefunctions (ψ and ψ), two spin wavefunction system, the Slater determinant is written as follows:

$$\Psi_{Electronic} = \frac{1}{\sqrt{2}} \begin{vmatrix} \psi(1)\alpha(1) & \psi(1)\beta(1) \\ \psi(2)\alpha(2) & \psi(2)\beta(2) \end{vmatrix}$$

If the electrons were to occupy the same orbital and have the same spin, the Slater determinant would be:

$$\Psi_{Electronic} = \frac{1}{\sqrt{2}} \begin{vmatrix} \psi(1)\alpha(1) & \psi(1)\alpha(1) \\ \psi(2)\alpha(2) & \psi(2)\alpha(2) \end{vmatrix}$$

In this case the columns are the same and so the determinant would be:

$$|\Psi_{Electronic}| = \psi(1)\alpha(1)\psi(2)\alpha(2) - \psi(1)\alpha(1)\psi(2)\alpha(2) = 0$$

The determinant for a matrix with equivalent columns is zero.⁵⁴ As a result this case is mathematically impossible and coincides with the Pauli Exclusion Principle in that no two electrons may occupy the same orbital and have the same spin. A more generic form for the Slater determinant is:

$$\psi(1,2 \dots, N) = \left(\frac{1}{N!}\right)^{1/2} \begin{vmatrix} \phi_a(1) & \phi_b(1) & \dots & \phi_z(1) \\ \phi_a(2) & \phi_b(2) & \dots & \phi_z(2) \\ \vdots & \vdots & \dots & \vdots \\ \phi_a(N) & \phi_b(N) & \dots & \phi_z(N) \end{vmatrix}$$

Interchanging two rows of the matrix causes the wavefunction to change signs and if two columns are identical, then the determinant is zero. Simply put, the symmetric spatial wavefunction must be combined with the antisymmetric spin wavefunction and the antisymmetric spatial wavefunction must be combined with the symmetric spin wavefunctions as follows:

$${}^1\Psi = [\psi_{MO,s}][\psi_{spin,a}] = [\phi_a(1)\phi_b(2) + \phi_a(2)\phi_b(1)][(\alpha(1)\beta(2) - \beta(1)\alpha(2))]$$

$$\begin{aligned}
{}^3\Psi &= [\psi_{MO,a}][\psi_{Spin,s}] = [\phi_a(1)\phi_b(2) - \phi_a(2)\phi_b(1)][(\alpha(1)\beta(2) + \beta(1)\alpha(2))] \\
&= [\phi_a(1)\phi_b(2) - \phi_a(2)\phi_b(1)][\alpha(1)\alpha(2)] \\
&= [\phi_a(1)\phi_b(2) - \phi_a(2)\phi_b(1)][(\beta(1)\beta(2))]
\end{aligned}$$

As shown in Figure I-1 for the electronic wavefunctions for σ orbitals in H_2 the case where:

$\Psi_{Electronic} = S_{MO} \times A_{Spin}$, the symmetric spatial wavefunctions allow for orbital overlap and if the spatial wavefunction is symmetric, then the spin wavefunction must be antisymmetric (in line

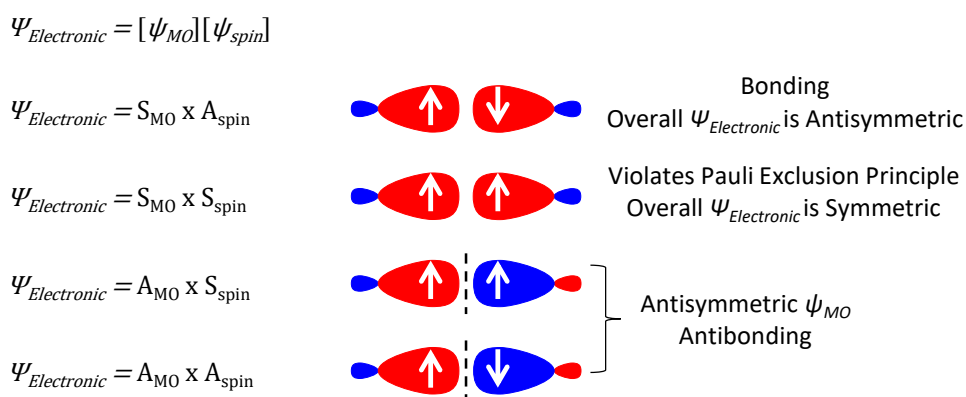


Figure I-1. Electronic wavefunctions ($\Psi_{Electronic}$) cases for bonding and antibonding orbitals with respect to they symmetries of the spatial (ψ_{MO}) and spin (ψ_{spin}) wavefunctions.

with the Pauli Principle) and the result is a bonding interaction resulting in a singlet ground state for H_2 .¹⁷ In the case where: $\Psi_{Electronic} = A_{MO} \times S_{Spin}$, the symmetric spin wavefunction would result in a high-spin triplet ground state for H_2 , however if the spin wavefunction is symmetric, then the spatial wavefunction must be antisymmetric which results in a molecular orbital with a node between the two constituent hydrogen s orbitals and that is the same as the antibonding (σ^*) orbital in H_2 . Indicating that the triplet ground state for H_2 is impossible and the singlet is indeed the ground state configuration for H_2 . For the three triplet electronic functions, the probability of finding the two electrons close together in space is essentially zero ($({}^3\Psi)^2 \approx 0$) The electrons repel each other as a result of the antisymmetric spatial wavefunction.

I.2. Hund's Rules.

Consider two, orthogonal p orbitals (p_x and p_y) occupied by electrons 1 and 2. The singlet and triplet electronic wavefunctions are:

$${}^1\Psi = \frac{1}{\sqrt{2}}[xy + yx][(\alpha\beta - \beta\alpha)]$$

$${}^3\Psi = \frac{1}{\sqrt{2}}[xy - yx][(\alpha\beta + \beta\alpha)]$$

$$= \frac{1}{\sqrt{2}}[xy - yx][\alpha\alpha]$$

$$= \frac{1}{\sqrt{2}}[xy - yx][\beta\beta]$$

The total energy for each state is given by:

$${}^x E = \frac{\langle {}^x\Psi | \hat{H} | {}^x\Psi \rangle}{\langle {}^x\Psi | {}^x\Psi \rangle} \quad \text{Eq. I-4}$$

The denominator of equation Eq. I-4 is equal to one because the two p -orbitals are orthogonal and the wavefunctions are normalized. The spin functions can be integrated separately because they do not interact with the Hamiltonian and are also equal to one because they too are normalized.⁵⁵ The energy expressions become:

$${}^1 E = \frac{1}{2} \langle xy + yx | \hat{H} | xy + yx \rangle = \frac{1}{2} (\langle xy | \hat{H} | xy \rangle + \langle xy | \hat{H} | yx \rangle + \langle yx | \hat{H} | xy \rangle + \langle yx | \hat{H} | yx \rangle)$$

$${}^3 E = \frac{1}{2} \langle xy - yx | \hat{H} | xy - yx \rangle = \frac{1}{2} (\langle xy | \hat{H} | xy \rangle - \langle xy | \hat{H} | yx \rangle - \langle yx | \hat{H} | xy \rangle + \langle yx | \hat{H} | yx \rangle)$$

Because the p orbitals can be interchanged by symmetry operations, the energy expressions can be simplified:

$$\langle xy | \hat{H} | xy \rangle = \langle yx | \hat{H} | yx \rangle \text{ and } \langle xy | \hat{H} | yx \rangle = \langle yx | \hat{H} | xy \rangle$$

$${}^1 E = \langle xy | \hat{H} | xy \rangle + \langle xy | \hat{H} | yx \rangle$$

$${}^3E = \langle xy | \hat{H} | xy \rangle - \langle xy | \hat{H} | yx \rangle$$

\hat{H} is composed of two one-electron terms (\hat{h}_1 and \hat{h}_2) and one two electron term ($1/r_{12}$) where the subscripts 1 and 2 refer to the order of the electrons in the integral.⁵⁴

$$\hat{H} = \hat{h}_1 + \hat{h}_2 + \frac{1}{r_{12}}$$

After substituting the operators and expanding the equations, the energy expressions become:

$${}^1E = \langle xy | \hat{h}_1 + \hat{h}_2 + \frac{1}{r_{12}} | xy \rangle + \langle xy | \hat{h}_1 + \hat{h}_2 + \frac{1}{r_{12}} | yx \rangle$$

$${}^1E = \langle xy | \hat{h}_1 | xy \rangle + \langle xy | \hat{h}_2 | xy \rangle + \langle xy | \frac{1}{r_{12}} | xy \rangle + \langle xy | \frac{1}{r_{12}} | yx \rangle$$

$${}^1E = \left[\langle x | \hat{h}_1 | x \rangle \langle y | y \rangle + \langle y | \hat{h}_2 | y \rangle \langle x | x \rangle + \left\langle xy \left| \frac{1}{r_{12}} \right| xy \right\rangle \right] \\ + \left[\langle x | \hat{h}_1 | y \rangle \langle y | x \rangle + \langle y | \hat{h}_2 | x \rangle \langle x | y \rangle + \left\langle xy \left| \frac{1}{r_{12}} \right| yx \right\rangle \right]$$

$${}^3E = \langle xy | \hat{h}_1 + \hat{h}_2 + \frac{1}{r_{12}} | xy \rangle - \langle xy | \hat{h}_1 + \hat{h}_2 + \frac{1}{r_{12}} | yx \rangle$$

$${}^3E = \langle xy | \hat{h}_1 | xy \rangle + \langle xy | \hat{h}_2 | xy \rangle + \langle xy | \frac{1}{r_{12}} | xy \rangle - \langle xy | \frac{1}{r_{12}} | yx \rangle$$

$${}^3E = \left[\langle x | \hat{h}_1 | x \rangle \langle y | y \rangle + \langle y | \hat{h}_2 | y \rangle \langle x | x \rangle + \left\langle xy \left| \frac{1}{r_{12}} \right| xy \right\rangle \right] \\ - \left[\langle x | \hat{h}_1 | y \rangle \langle y | x \rangle + \langle y | \hat{h}_2 | x \rangle \langle x | y \rangle + \left\langle xy \left| \frac{1}{r_{12}} \right| yx \right\rangle \right]$$

$$\langle x | \hat{h}_1 | x \rangle = \mathbf{h}_{xx}, \langle y | \hat{h}_2 | y \rangle = \mathbf{h}_{yy}, \langle x | \hat{h}_1 | y \rangle = \mathbf{h}_{xy}, \langle y | \hat{h}_2 | x \rangle = \mathbf{h}_{yx}; \mathbf{h}_{xx} = \mathbf{h}_{yy} \text{ and } \mathbf{h}_{xy} = \mathbf{h}_{yx}$$

$$S_{xx} = \langle x | x \rangle = 1, S_{yy} = \langle y | y \rangle = 1, S_{xy} = \langle x | y \rangle = \langle y | x \rangle = 0 \text{ for orthogonal orbitals.}$$

$$\left\langle xy \left| \frac{1}{r_{12}} \right| xy \right\rangle = j_{xy} \text{ and } \left\langle xy \left| \frac{1}{r_{12}} \right| yx \right\rangle = k_{xy}$$

\mathbf{h} is the resonance integral, j is the coulomb integral, k is the exchange integral, and S is the overlap integral. A key point is that the exchange integral measures the electron-electron

repulsion in the overlap region of orbitals x and y. By substituting these definitions, the energy expressions become:

$$\begin{aligned} {}^1E &= [\mathbf{h}_{xx}S_{yy} + \mathbf{h}_{yy}S_{xx} + j_{xy}] + [\mathbf{h}_{xy}S_{yx} + \mathbf{h}_{yx}S_{xy} + k_{xy}] \\ &= \mathbf{h}_{xx} + \mathbf{h}_{yy} + j_{xy} + k_{xy} \end{aligned}$$

$$\begin{aligned} {}^3E &= [\mathbf{h}_{xx}S_{yy} + \mathbf{h}_{yy}S_{xx} + j_{xy}] - [\mathbf{h}_{xy}S_{yx} + \mathbf{h}_{yx}S_{xy} + k_{xy}] \\ &= \mathbf{h}_{xx} + \mathbf{h}_{yy} + j_{xy} - k_{xy} \end{aligned}$$

$${}^1E = 2\mathbf{h}_{xx} + j_{xy} + k_{xy} \quad \text{Eq. I-5}$$

$${}^3E = 2\mathbf{h}_{xx} + j_{xy} - k_{xy} \quad \text{Eq. I-6}$$

The energy difference between the singlet and triplet states is equal to:

$$\begin{aligned} \Delta E_{ST} &= {}^1E - {}^3E = (2\mathbf{h}_{xx} + j_{xy} + k_{xy}) - (2\mathbf{h}_{xx} + j_{xy} - k_{xy}) \\ &= 2\mathbf{h}_{xx} - 2\mathbf{h}_{xx} + j_{xy} - j_{xy} + k_{xy} + k_{xy} = 2k_{xy} \quad \text{Eq. I-7} \end{aligned}$$

For two, non-orthogonal p-orbitals the energy expressions becomes:

Singlet State:

The exchange integral is never zero ($k_{xy} \geq 0$), so the triplet state is lower in energy than the singlet state by $2k_{xy}$.⁵⁴

$$\begin{aligned} {}^1E &= \frac{\langle {}^x\Psi | \hat{H} | {}^x\Psi \rangle}{\langle {}^x\Psi | {}^x\Psi \rangle} = \frac{\langle xy + yx | \hat{H} | xy + yx \rangle}{\langle xy + yx | xy + yx \rangle} \\ &= \frac{\langle xy | \hat{H} | xy \rangle + \langle xy | \hat{H} | yx \rangle + \langle yx | \hat{H} | xy \rangle + \langle yx | \hat{H} | yx \rangle}{\langle xy | xy \rangle + \langle xy | yx \rangle + \langle yx | xy \rangle + \langle yx | yx \rangle} \\ &= \frac{2(\langle xy | \hat{H} | xy \rangle + \langle xy | \hat{H} | yx \rangle)}{2(\langle xy | xy \rangle + \langle xy | yx \rangle)} = \frac{\langle xy | \hat{H} | xy \rangle + \langle xy | \hat{H} | yx \rangle}{\langle xy | xy \rangle + \langle xy | yx \rangle} \end{aligned}$$

Triplet State:

$$\begin{aligned}
{}^3E &= \frac{\langle {}^x\Psi|\hat{H}|{}^x\Psi\rangle}{\langle {}^x\Psi|{}^x\Psi\rangle} = \frac{\langle xy - yx|\hat{H}|xy - yx\rangle}{\langle xy - yx|xy - yx\rangle} \\
&= \frac{\langle xy|\hat{H}|xy\rangle - \langle xy|\hat{H}|yx\rangle - \langle yx|\hat{H}|xy\rangle + \langle yx|\hat{H}|yx\rangle}{\langle xy|xy\rangle - \langle xy|yx\rangle - \langle yx|xy\rangle + \langle yx|yx\rangle} \\
&= \frac{2(\langle xy|\hat{H}|xy\rangle - \langle xy|\hat{H}|yx\rangle)}{2(\langle xy|xy\rangle - \langle xy|yx\rangle)} = \frac{\langle xy|\hat{H}|xy\rangle - \langle xy|\hat{H}|yx\rangle}{\langle xy|xy\rangle - \langle xy|yx\rangle}
\end{aligned}$$

These expressions can be expanded and simplified by substituting \hat{H} , which is once again the sum of the one-electron terms (\hat{h}_1 and \hat{h}_2) and the two electron term ($1/r_{12}$), $j_{xy} = \left\langle xy \left| \frac{1}{r_{12}} \right| xy \right\rangle$;

$$k_{xy} = \left\langle xy \left| \frac{1}{r_{12}} \right| yx \right\rangle, \text{ and } \langle xy|xy\rangle = \langle yx|yx\rangle = 1; \langle xy|yx\rangle = \langle yx|xy\rangle = S_{xy}^2$$

Singlet State:

$$\begin{aligned}
{}^1E &= \frac{[\mathbf{h}_{xx}S_{yy} + \mathbf{h}_{yy}S_{xx} + j_{xy}] + [\mathbf{h}_{xy}S_{yx} + \mathbf{h}_{yx}S_{xy} + k_{xy}]}{1 + S_{xy}^2} \\
&= \frac{[\mathbf{h}_{xx} + \mathbf{h}_{yy} + j_{xy}] + [\mathbf{h}_{xy}S_{yx} + \mathbf{h}_{yx}S_{xy} + k_{xy}]}{1 + S_{xy}^2} \quad \text{Eq. I-8}
\end{aligned}$$

Triplet State:

$$\begin{aligned}
&= \frac{[\mathbf{h}_{xx}S_{yy} + \mathbf{h}_{yy}S_{xx} + j_{xy}] - [\mathbf{h}_{xy}S_{yx} + \mathbf{h}_{yx}S_{xy} + k_{xy}]}{1 - S_{xy}^2} \\
{}^3E &= \frac{[\mathbf{h}_{xx} + \mathbf{h}_{yy} + j_{xy}] + [\mathbf{h}_{xy}S_{yx} + \mathbf{h}_{yx}S_{xy} - k_{xy}]}{1 - S_{xy}^2} \quad \text{Eq.I-9}
\end{aligned}$$

The energy difference between the singlet and triplet states is now:

$$\begin{aligned}
\Delta E_{ST} &= \frac{[\mathbf{h}_{xx} + \mathbf{h}_{yy} + j_{xy}] + [\mathbf{h}_{xy}S_{yx} + \mathbf{h}_{yx}S_{xy} + k_{xy}]}{1 + S_{xy}^2} \\
&\quad - \frac{[\mathbf{h}_{xx} + \mathbf{h}_{yy} + j_{xy}] + [\mathbf{h}_{xy}S_{yx} + \mathbf{h}_{yx}S_{xy} - k_{xy}]}{1 - S_{xy}^2}
\end{aligned}$$

$$\Delta E_{ST} = \frac{(1 - S_{xy}^2)[\mathbf{h}_{xx} + \mathbf{h}_{yy} + j_{xy} + \mathbf{h}_{xy}S_{yx} + \mathbf{h}_{yx}S_{xy} + k_{xy}]}{(1 + S_{xy}^2)(1 - S_{xy}^2)}$$

$$- \frac{(1 + S_{xy}^2)[\mathbf{h}_{xx} + \mathbf{h}_{yy} + j_{xy} + \mathbf{h}_{xy}S_{yx} + \mathbf{h}_{yx}S_{xy} - k_{xy}]}{(1 + S_{xy}^2)(1 - S_{xy}^2)}$$

$$\Delta E_{ST} = \frac{4S_{xy}\mathbf{h}_{xy} + 2k_{xy} - 2S_{xy}^2\mathbf{h}_{xx} - 2S_{xy}^2\mathbf{h}_{yy} - 2S_{xy}^2j_{xy}}{1 - S_{xy}^4} \quad \text{Eq. I-10}$$

Now, the energies of the singlet and triplet states are dependent on the overlap integral (S) of the orbitals (atomic or molecular).

1.3. Heisenberg Hamiltonian and the Exchange Coupling Constant (J).

For a system of two singly occupied molecular orbitals (SOMOs), the Heisenberg Hamiltonian is:

$$\hat{H} = -2 \sum_{x < y} \sum J_{xy} \hat{S}_x \hat{S}_y \quad \text{Eq. I-11}$$

where J_{xy} is the exchange coupling constant between centers x and y and \hat{S}_x and \hat{S}_y are the spin operators for electrons 1 and 2.⁵⁴ The exchange coupling constant (J) can be described as the sum of two terms discussed in the previous section: the exchange integral, k , and the product of the resonance integral, β , which is a negative number, and the overlap integral, S .

$$J = 2\beta S + k \quad \text{Eq. I-12}$$

where $\beta = \langle \phi_x | \hat{H} | \phi_y \rangle$, $S = \langle \phi_x | \phi_y \rangle$, and $k = \langle xy | \frac{1}{r_{12}} | xy \rangle$.^{54,56} The spin alignment of the two

electrons in the SOMOs is given by the sign of J . When $J > 0$, the spins are aligned parallel meaning the triplet ground-state is lower in energy than the singlet (given that at this point only two SOMOs are being considered), which gives a high-spin, ferromagnetic interaction. When $J < 0$, the spins are aligned antiparallel meaning the singlet ground-state is lower in energy than the triplet, which gives a low-spin, antiferromagnetic interaction. Because $2\beta S \leq 0$ and $k > 0$, the

product of the resonance integral and the overlap integral ($2\beta S$) is the antiferromagnetic component of J , as it makes J more negative; conversely, k contributes to the ferromagnetic component of J , as it makes J more positive. So, when $2\beta S > k$, $J < 0$ and the interaction between the spins is antiferromagnetic and when $2\beta S < k$, $J > 0$ and the interaction is ferromagnetic. The energies of the singlet and triplet states are given by:

$${}^1E = 2(\alpha + \beta S) + j + k \quad \text{Eq.I-13}$$

$${}^3E = 2(\alpha - \beta S) + j - k \quad \text{Eq.I-14}$$

where $\alpha = \langle \phi_x | \hat{H} | \phi_x \rangle$, the Coulomb integral.⁵⁴ The sign changes in front of two terms when going from the expression for the energy of the singlet state vs. the triplet state: in front of βS and k . Because β is a negative number, the product βS , stabilizes the singlet state by lowering the overall energy, but the negative sign in front of βS in the triplet state energy expression will make the term positive and increase the overall energy, destabilizing the triplet. Likewise, the exchange integral is always positive and so k increases the energy of the singlet state, destabilizing it and for the triplet, the energy is stabilized by k .

$$\Delta E_{ST} = {}^1E - {}^3E = 2(\alpha + \beta S) + j + k - (2(\alpha - \beta S) + j - k)$$

$$\Delta E_{ST} = 2\alpha + 2\beta S + j + k - 2\alpha - 2\beta S - j + k$$

$$\Delta E_{ST} = 4\beta S + 2k = 2J \quad \text{Eq.I-25}$$

$$\text{If } S = 0, \text{ then: } \Delta E_{ST} = 2k = 2J$$

According to equation Eq.I-15, the difference between the singlet and triplet energies (ΔE_{ST}) is entirely dependent on the exchange coupling constant, J .⁵⁴ In the limiting case when the two SOMOs are orthogonal, ΔE_{ST} and J are entirely dependent on the exchange coupling. To make high-spin molecules the overlap integral must be minimized ($S = 0$) by constructing

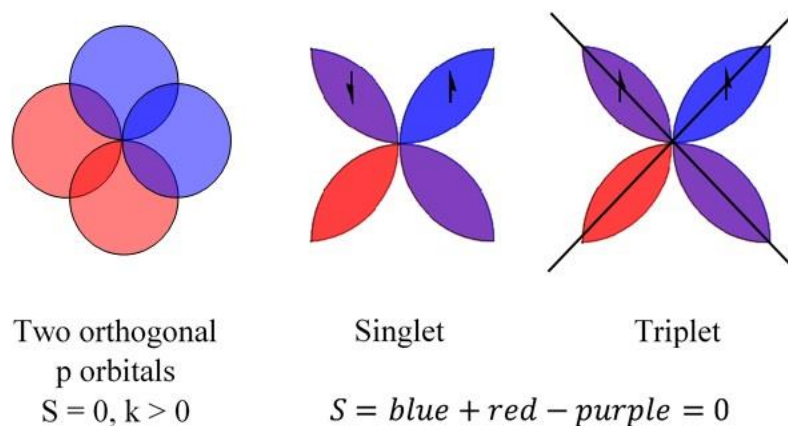


Figure I-2. The overlap region of two orthogonal p orbitals.

molecules with orthogonal SOMOs and the maximizing the exchange integral ($k \gg 0$) by allowing the SOMOs to overlap.⁵⁷ Figure I-2 shows two orthogonal p-orbitals on an atom and the region of space where those two orbitals overlap, for these orbitals the overlap integral (S) is zero, despite being significant overlap between the orbitals. In the overlap region, the blue and red areas show where the wavefunctions constructively interfere ($S > 0$) and the purple region shows where the wavefunctions destructively interfere ($S < 0$). The net result is that the constructive interference is cancelled completely by the destructive interference because the p-orbitals are orthogonal. According to Eq.I-15 the energy of the singlet state is lowered by overlap (S) because this allows for delocalization of the antiferromagnetically coupled electrons. The energy of the singlet state is increased by exchange (k) because the antiparallel spins can occupy

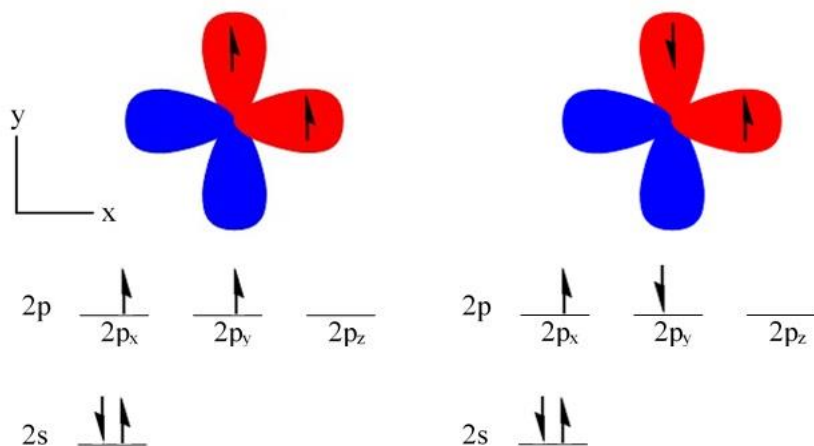


Figure I-3. Triplet and singlet configurations in a carbon atom.

this overlap region which increases its energy due to electron-electron repulsion. The triplet state is lowered because the electrons do not experience the electron-electron repulsion that the singlet configuration experiences because the parallel spins cannot occupy the overlap region at all due to the Pauli Exclusion Principle.⁵⁷ Given this information, electrons in atomic orbitals align parallel to the other unpaired electrons in the atom as shown in Figure I-3 with p_x and p_y orbitals of a carbon atom. Carbon having four valence electrons, the first two go into the 2s orbitals, it being much lower in energy than the 2p allows the electrons to pair. The two remaining electrons go into the p_x and p_y orbitals. The parallel alignment is lower in energy than the antiparallel alignment for atomic orbitals as a result of the exchange interaction.

I.4. Structural Considerations for Organic Radicals.

I.4.1. Kekulé vs. non-Kekulé. Conjugated organic compounds can be classified as either Kekulé or non-Kekulé based on the existence of closed-shell line-drawing structures. Molecules that are considered to be Kekulé have one or more resonance structures that can be represented completely with a single line-drawing structure (i.e., with neither radicals nor formal charges).

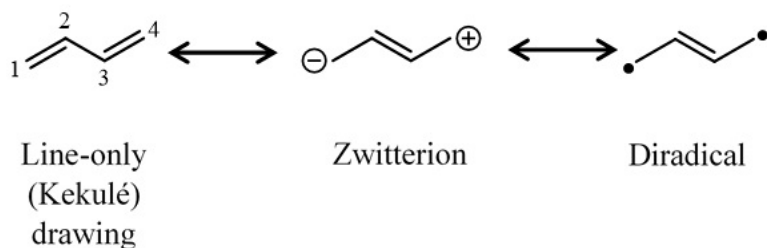


Figure I-4. Resonance structures of butadiene (Kekulé).

For example, butadiene is represented completely by the line-only drawing shown in Figure I-4.

If one were to draw the biradical or zwitterionic structures, using arrow-pushing, one could arrive at the resonance form consisting of the line-only drawing. Therefore, butadiene is

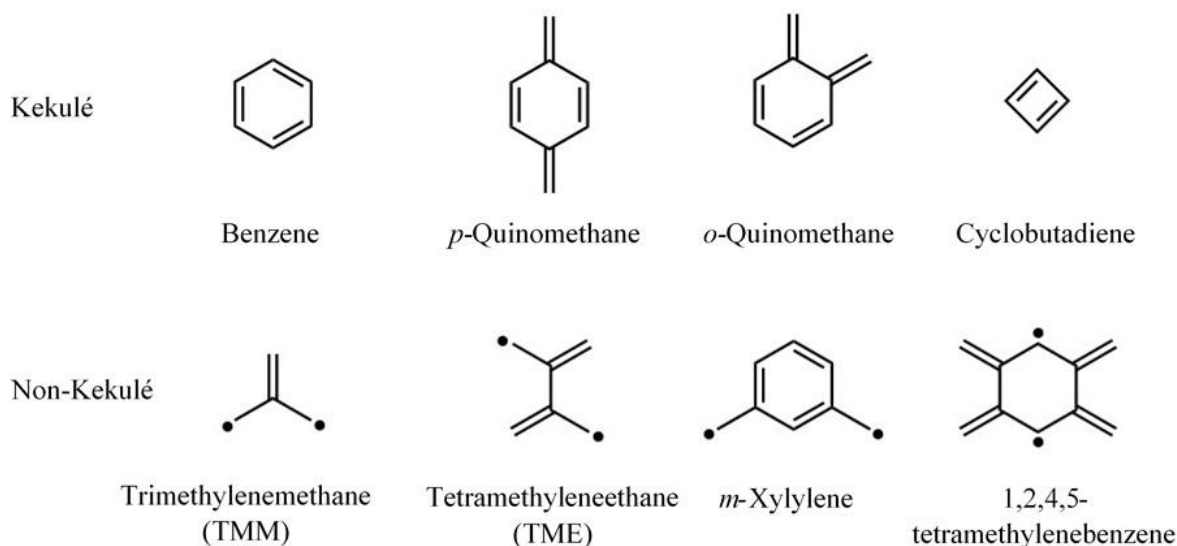


Figure I-5. Examples of Kekulé and non-Kekulé hydrocarbons.

considered to be a Kekulé structure. Benzene is a quintessential Kekulé hydrocarbon, shown in Figure I-5, as being the molecule whose structure was solved in 1865 by Friedrich August Kekulé as being drawn as a cyclohexane ring with alternating single and double bonds. Figure I-5 shows other molecules considered to be Kekulé along with non-Kekulé structures. Non-Kekulé molecules are those that lack resonance forms represented solely by line-only structures. As a consequence, non-Kekulé molecules have multiple radical centers (or charges), and the simplest examples are biradicals.¹⁷

I.4.2. Spin Ground-States of Organic Biradicals. The atomic connectivity through a given π -system dictates whether spins are coupled ferromagnetically or antiferromagnetically. To illustrate this, consider trimethylenemethane (TMM) and tetramethyleneethane (TME), Figure I-6. An alternant π -system can be defined using a convention, informally known as the “star” method, which states that if one stars every other atom in the π -system, such that the number of stars is maximized, and if no starred-atom is next to another, then the system is said to be alternant.⁵⁸ Electronic structure, bonding, and reactivity is very well understood and can be predicted for these systems.⁵⁹ Even alternant π - systems include derivatives of benzene, naphthalene, etc. If two starred-atoms or two non-starred-atoms are adjacent to each other, the system is said to be nonalternant, and the electronic structure, bonding, and reactivity in these systems is not as easily predicted, these systems include derivatives of cyclopentadienyl ions, azulene, and others. Figure I-6 shows TMM and TME starred appropriately showing that both molecules have even, alternant π systems. The stars are not only a determination of alternant vs. nonalternant, but can also be used to provide the number of non-bonding molecular orbitals (NBMOs) as well as give the ground-state spin for the biradicals. The number of NBMOs is equal to the number of p-orbitals in the π -system minus two times the number of double bonds in

the resonance structure with the highest degree of bondedness (Eq. I-16).⁶⁰ Which is to say, if this analysis were being performed on butadiene, in Figure I-4, the resonance structure that we would use would be the first (the Kekulé drawing) with two double bonds.

$$\text{No. of NBMOs} = N - 2T \quad \text{Eq.I-16}$$

where N= the number of p-orbitals in the π system and T = the number of double bonds in the molecule's highest degree of bondedness. Application of this formula on butadiene gives zero NBMOs, but for TMM and TME, the number of NBMOs in each biradical is two, which concurs with the fact that there are two radical centers. To calculate the ground-state spin (S) for biradicals (or polyradicals), S is equal to the number of starred atoms minus the number of

$$S = \frac{(n^* - n)}{2} \quad \text{Eq.I-17}$$

unstarred atoms, divided by two (Eq.I-17). where n^* = number of starred atoms and n = number of unstarred atoms. If this calculation is performed on TMM and TME in Figure I-6, then for TMM there are three starred-atoms minus one unstarred, divided by two gives $S = 1$, a triplet

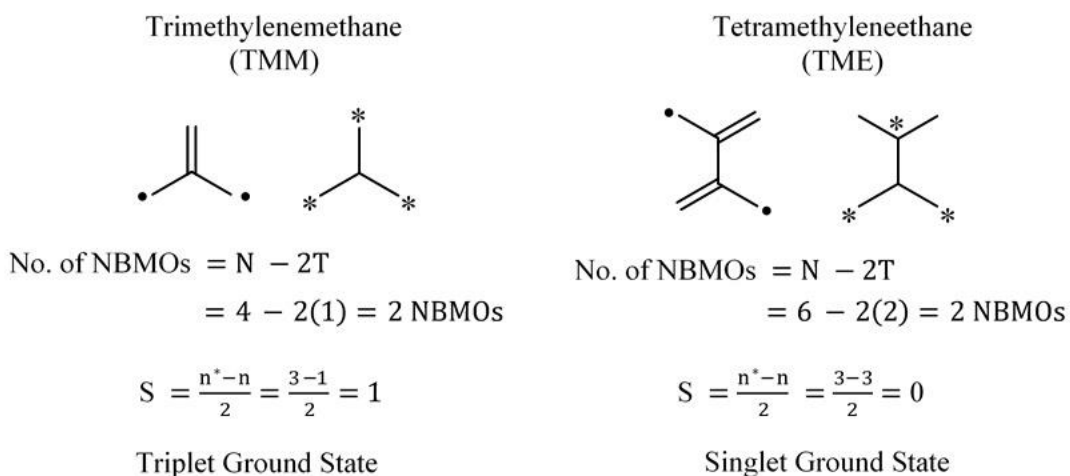


Figure I-6. Trimethylenemethane (TMM) and tetramethyleneethane (TME) analysis with the star convention and ground-state spin calculation.

ground state with the spins aligned parallel. For TME there are three starred-atoms minus three unstarred, divided by two gives $S = 0$, a singlet ground-state with the spins of the two radicals aligned antiparallel. An antiparallel spin alignment among lone electrons in degenerate orbitals is a violation of Hund's Rule, which states that the lowest energy configuration is when the spins of electrons in degenerate orbitals are aligned to give the highest spin quantum number.

I.5. Spin Polarization.

There are two models concerning spin polarization that are used to explain the ground state configurations of molecules and violations of Hund's Rule. The first way to explain this is with the spin polarization that results from the necessity of electrons in a π -system to form a bonding interaction.⁶⁰ Each p-orbital (atom) in a π -system contributes one electron to the π -system and in order to have a bonding interaction between adjacent atoms, the electrons in those orbitals must have an antiferromagnetic interaction (covalent bonding interactions are extreme examples of antiferromagnetic interactions). In Figure I-7, the interactions between two carbon atoms each with two orthogonal p-orbitals are shown. When the spatial wavefunction is symmetric, the spin wavefunction must be antisymmetric. The electrons in p_x and p_y on carbon 1 (C_1) both have down spins for reasons previously discussed and the p-orbitals and electrons on carbon 2 (C_2) satisfy the requirement for the electronic wavefunction ($\Psi_{Electronic}$) ($S_{MO} \times A_{Spin}$). This results in both σ - and π -bonding interactions and that the adjacent π -system p-orbitals have the opposite spin.⁶⁰ This can be applied to larger π -systems, adjacent carbon atoms must have opposite spins.

and node between the p_{y1} and p_{y2} orbitals. Based solely on the spatial wavefunctions these resemble σ^* and π^* orbitals, respectively. C_1 and C_2 have no bonding interaction and no π -system between them. Figure I-8 applies this method of spin polarization by labeling π system atoms as either having an α (up) spin or a β (down) spin and adjacent atoms have opposite spins. The ground-state spin can be determined by taking the absolute value of the difference between the numbers of α spin and β spins. Note that the starred atoms in the π -system in Figure I-6 corresponds to identical spins in the α -, β -labelling in Figure I-8.

The other method for explaining the ground state in biradicals is via a configuration interaction which is known as dynamic spin polarization (DSP). This method involves mixing in an excited-state of the same symmetry with the ground-state and can be understood using simple Hückel molecular orbitals. Before discussing biradicals, let's consider dynamic spin polarization in allyl radical. Equation 18 shows the mixing of the lowest excited doublet-state of the same symmetry into the allyl radical, $|\psi_1^\alpha \psi_1^\beta \psi_2^\alpha\rangle$.^{61,62} The first term in Eq.I-18 shows that mixing α

$$\Psi = \frac{1}{\sqrt{6}} \left(|\psi_3^\alpha \psi_1^\beta \psi_2^\alpha\rangle - |\psi_1^\alpha \psi_3^\beta \psi_2^\alpha\rangle - 2|\psi_1^\alpha \psi_2^\beta \psi_3^\alpha\rangle \right) \quad \text{Eq.I-18}$$

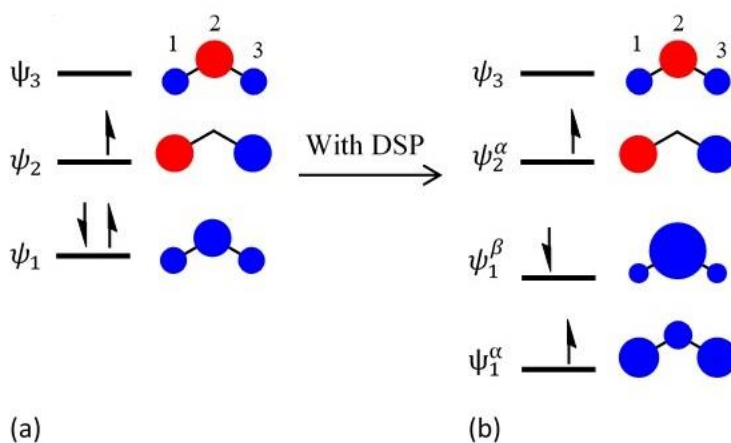


Figure I-9. Allyl radical ground state molecular orbital diagram a) without and b) with dynamic spin polarization (DSP).

spin in ψ_3 into ψ_1 with a positive sign will increase the probability of finding the electron on the terminal carbons (1 and 3) because of the α spin in ψ_2 does not allow the two electrons to appear in the same p-orbital simultaneously. Increasing the probability of finding the electrons at opposite ends of the molecule reduces the chance that the electrons will be in adjacent p-orbitals and decreases the electrostatic repulsion between the two electrons. The second term results in increase probability of finding the β spin on carbon 2 because the β can simultaneously appear in the same p orbitals as the α spins which decreases the probability of finding the β spin on carbons 1 and 3 in ψ_1 due to the α spin in ψ_2 , which lowers the Coulombic repulsion between these two electrons.⁶² The third term results in decreased electron repulsion between the electrons of opposite spins in ψ_1 and ψ_2 . The way this manifests itself in the allyl radical is that the α spin in ψ_2 results in the polarization of the ψ_1 orbital by increasing the α spin density on carbons 1 and 3 because the α spins cannot simultaneously occupy the same p orbital, restricting them to opposite sides of the molecule so that the probability of the α spins do not occupy p-orbitals on adjacent carbon atoms. This lowers the energies of the ψ_1^α and ψ_1^β by reducing the Coulombic repulsions between the α and β spins because the α spin in ψ_1 has an increased

probability of being found at the terminal carbon atoms due to the increased exchange interaction with the α spin of the ψ_2 which only has electron density on the terminal carbon atoms. This exchange further lowers the energy of the ψ_1^α orbital. The ψ_1^β orbital is only lowered due to the reduced Coulombic repulsions between the α and β spins because of the increased probability of finding the β spin on the central carbon atom to fulfill the requirement that in order to have a π bonding interaction an antiferromagnetic alignment between adjacent p orbitals is needed. The effects of dynamic spin polarization in biradicals is the same as explained in the allyl radical, however now the polarization effects of both NBMOs must be considered. The classic example of dynamic spin polarization from a Hückel MO diagram biradical is the explanations of the ground state in cyclobutadiene and TMM, the MO diagrams of both are shown in Figure I-10, without spins on the electrons in the ψ_2 and ψ_3 MOs, and these will be identified using a DSP explanation. In a biradical, DSP may be either additive or competitive. Additive means that the NBMOs polarize the orbitals in the same manner enhancing the polarizing effects, leading to a

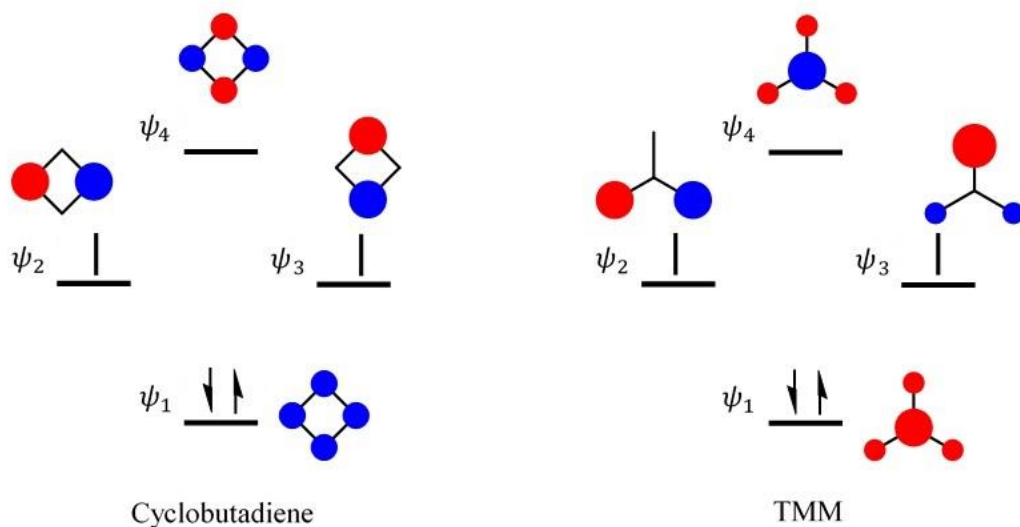


Figure I-10. Hückel MO diagrams of cyclobutadiene and TMM.

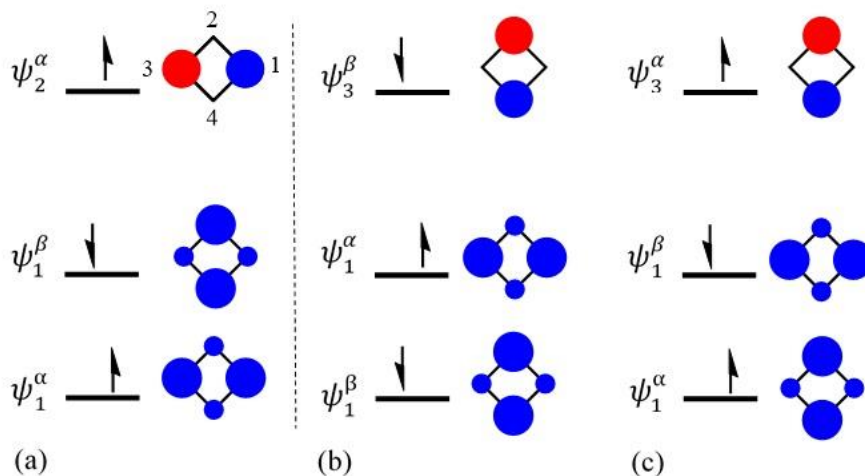


Figure I-11. Effect of dynamic spin polarization on the α and β spin energies on the ψ_1 of cyclobutadiene. lower energy state and competitive means that the NBMOs polarize the orbitals in the opposite manner and cancel out the polarizing effects.

Figure I-11a shows the effects on ψ_1 of placing one α spin electron in ψ_2 , which splits and polarizes ψ_1 into α and β orbitals, for the same reasons as discussed in the allyl radical, where the ψ_1 orbital is polarized such that there is an increased probability of finding the α spin electron in the p orbitals located on carbons 1 and 3 and the β spin has an increased probability of being found on carbons 2 and 4.^{62,63} Figure I-11b and c show the effects on ψ_1 when the second electron is placed in ψ_3 . For the triplet configuration of cyclobutadiene (a and c together), the DSP is competitive and the stabilizing effects are canceled due to the first α spin electron in ψ_2 polarizing ψ_1 to give increased α spin on carbons 1 and 3 and increased β spin on carbons 2 and 4 and the second α spin electron in ψ_3 polarizing ψ_1 to give increased α spin on carbons 2 and 4 and increased β spin on carbons 1 and 3; opposite polarizations. For the singlet configuration of cyclobutadiene (a and b together), the DSP is additive and the stabilizing effects are enhanced due to the first α spin electron in ψ_2 polarizing ψ_1 to give increased α spin on

carbons 1 and 3 and increased β spin on carbons 2 and 4, and the β spin electron in ψ_3 polarizing ψ_1 to give increased α spin on carbons 1 and 3 and increased β spin on carbons 2 and 4; same polarization. Therefore, the ground state configuration of cyclobutadiene is a singlet due to the enhanced stabilizing effects from the additive DSP.

Figure I-12 shows DSP in TMM, which has previously been mentioned to have a high-spin triplet ground state configuration. Figure I-12a shows the effects on ψ_1 of placing one α spin electron in ψ_2 , which splits and polarizes ψ_1 into α and β orbitals, where the ψ_1 orbital is polarized such that there is an increased probability of finding the α spin electron in the p orbitals located on carbons 1, 3 and 4 and the β spin has an increased probability of being found on carbon 2. Figure I-12b and c show the effects on ψ_1 when the second electron is placed in ψ_3 . For the triplet configuration of TMM (a and c together), the DSP is additive and the stabilizing effects are enhanced due to the first α spin electron in ψ_2 polarizing ψ_1 to give increased α spin on carbons 1, 3 and 4 and increased β spin on carbon 2 and the second α spin electron in ψ_3 polarizing ψ_1 to give increased α spin on carbons 1, 3 and 4 and increased β spin on carbon 2; polarization is the same. For the singlet configuration of TMM (a and b together), the DSP is

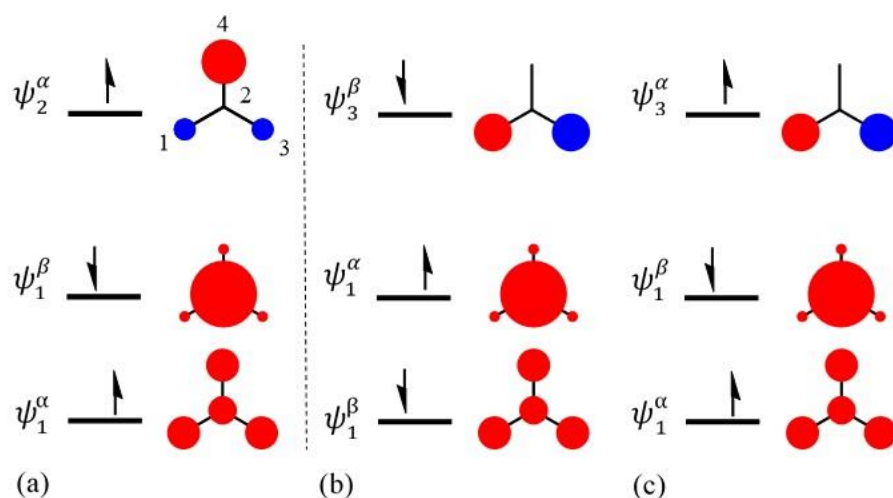


Figure I-12. Effect of dynamic spin polarization on the α and β spin energies in the ψ_1 of TMM.

competitive and the stabilizing effects are canceled due to the first α spin electron in ψ_2 polarizing ψ_1 to give increased α spin on carbons 1, 3 and 4 and increased β spin on carbon 2, and the β spin electron in ψ_3 polarizing ψ_1 to give increased α spin on carbon 2 and increased β spin on carbons 1, 3 and the enhanced stabilizing effects from the additive DSP. This method for determining ground state spin in biradical systems can be applied to other biradicals, these are the simplest cases because there is only one filled MO to take into account and this analysis can become quite complex. Therefore, the ground state configuration of TMM is a triplet due to when examining the MOs of larger molecules, DSP manifests itself in the topological configuration of the MOs and the NBMOs can be classified as either disjoint or non-disjoint.

I.6. Disjoint and Non-disjoint Biradicals.

In TMM (Figures I-10, I-12), there is electron density on both carbons 1 and 3 in both the NBMOs, ψ_2 and ψ_3 . This is called non-disjoint and as discussed before, this overlap density gives rise to a substantial exchange integral (k) and leads to the ferromagnetic alignment of the spins, i.e., a high-spin ground state in TMM, where the triplet lies below the singlet by $2k = 2j$ (Eq.I-15). In cyclobutadiene (Figures I-10, I-11), in ψ_2 there is electron density on carbons 1 and 3 and in ψ_3 the electron density is located on carbons 2 and 4.^{17,57} Such an orbital pattern is characteristic of disjoint biradicals, and leads to a negligible exchange integral (k) and to antiferromagnetic alignment of the spins and a low-spin ground state in cyclobutadiene. This classification of disjoint biradical having low-spin ground states and small singlet-triplet gaps and non-disjoint molecules having high-spin ground states and large singlet-triplet gaps holds for even-alternant π systems. Figure I-13 shows two examples each of biradicals that are disjoint and non-disjoint as can be seen by the MO diagrams of the NBMOs in each example. It is easily seen

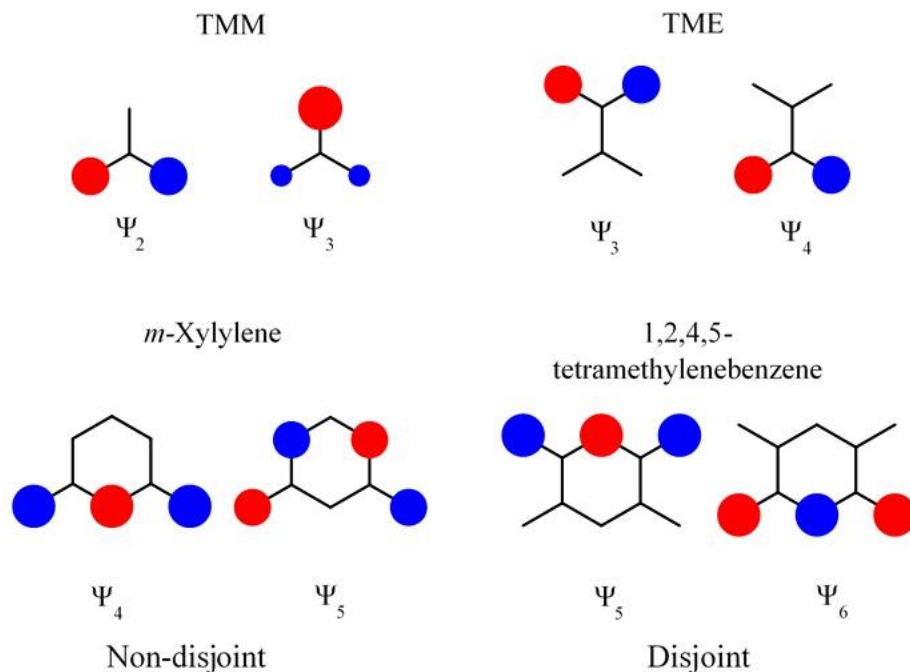


Figure I-13. Non-disjoint and disjoint molecular orbitals.

that TMM and *m*-xylylene both share electron density on common carbon atoms in each of their respective NBMOs. Indicating that they are non-disjoint and would be predicted to have a high-spin, ferromagnetically aligned ground state. In TME and 1,2,4,5-tetramethylenebenzene, the electron density in the NBMOs are located on opposite sides of the molecule and do not share any common carbon atoms. These two cases are effectively two distinct allyl radicals in the case of TME and two distinct pentadienyl radicals as is the case for 1,2,4,5-tetramethylenebenzene.

I.7. Electron Paramagnetic Resonance (EPR) Spectroscopy.

I.7.1. Introduction, X-band, organic radicals. EPR was first observed and developed by Zavoisky in 1944 as a method for studying materials with unpaired electrons and is analogous to NMR spectroscopy and has been used to study organic radicals, paramagnetic metal ions, and even bioorganic molecules such as metallo-proteins.⁶⁴ EPR is classified by the frequency of microwave radiation used and while there are wavebands that range from 1 to 360 GHz, most

commonly microwaves of approximately 9-10 GHz are used for studying organic radical species which is known as X-band EPR. To a lesser extent, Q-band with microwave frequencies of about 35 GHz can also be used, but the higher the frequency the stronger the magnetic field that is required to observe EPR transitions, which will be indicated and discussed in Eq. I-19.

I.7.2. Zeeman splitting. Zeeman splitting describes the energy changes for m_s energy levels when in a magnetic field. Figure I-14 shows the Zeeman splitting for an $S = 1/2$ paramagnetic species with increasing magnetic field. In the absence of an applied magnetic field the $m_s = \pm 1/2$ energy levels are degenerate, but as a magnetic field that is parallel with $m_s = +1/2$ and antiparallel with $m_s = -1/2$ is applied, the $+1/2$ energy level decreases in energy and the $-1/2$ energy level increases. Eq. I-19 describes the Zeeman splitting:

$$\Delta E = h\nu = g_e\mu_B B_0, \quad \text{Eq. I-19}$$

where h is Plank's constant, ν is the microwave frequency, g_e is the Landé factor, μ_B is the Bohr magneton and B_0 is the magnetic field. Eq. I-19 also describes the resonance condition for the m_s energy levels; the quantum of energy that must be absorbed in order to induce transitions between the energy levels.

The Landé factor also known as a g -factor or g -value is a unitless parameter which by analogy is compared to the chemical shift in NMR spectroscopy. The g -value for a free electron

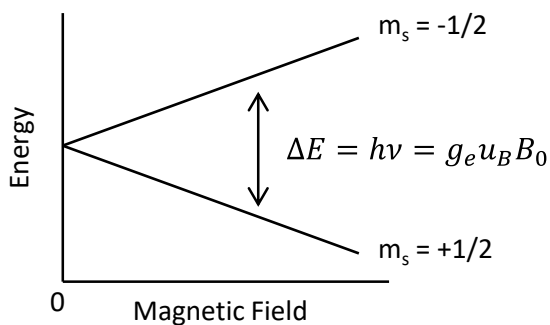


Figure I-14. Zeeman splitting diagram of the m_s energy levels of an $S = 1/2$ paramagnetic species.

is 2.00232. Most organic radicals will be close to this value and paramagnetic metal ions can have a variety of g -values. The g -values are sometimes used to identify the paramagnetic species present and the g -value can be calculated from the EPR spectrum by knowing the microwave frequency; however, the magnetic fields that come from an EPR spectrum are relative values not absolute. In order to correctly assign a g -value to a paramagnetic species a reference with a well-known g -value must be added to the EPR sample and then the x -axis is shifted to give the reference the correct g -value, just as solvent signals or ferrocene/ferrocenium are used as references for NMR or electrochemistry, respectively.

A main distinction between EPR spectroscopy and other types of spectroscopies like NMR or electronic absorption is that the spectrum comes out of the spectrometer looking like the first derivative of the absorption signal as shown in Figure I-15A. EPR spectrometers have resonators for the signals that get produced from microwaves, but even with this the signal can be very noisy and the technique that is used to improve the signal-to-noise ratio is called field modulation which involves a small field being added to the main magnetic field by the use of two modulating coils on either side of the resonator. The modulated field's phase and amplitude

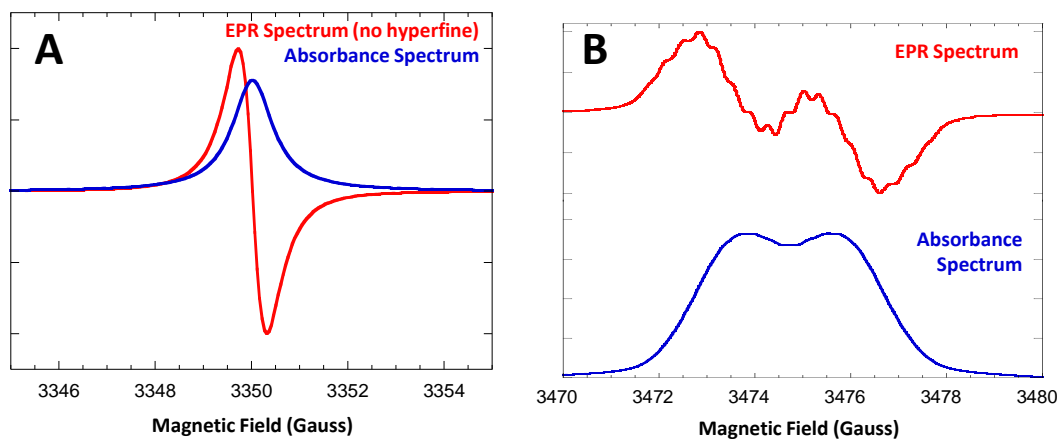


Figure I-15. A) EPR spectrum without hyperfine shown beside its absorbance spectrum. B) EPR and absorbance spectrum of an $S = 1/2$ organic radical showing a doublet of a more complex multiplet.

is compared to a reference signal and the result is that the signal-to-noise ratio is improved. Consequently, very small changes in the slope of the absorbance spectrum stand-out much more in the modulated EPR spectrum (Figure I-15B); which for all intents and purposes is a first derivative spectrum as it can be integrated to give the absorbance spectrum and integrated again to give the area under the curve which can be used in linear Beer's law-type comparisons of spin concentrations. Figure I-15B exemplifies the advantage of acquiring a field-modulated spectrum rather than the absorbance spectrum as it shows an organic radical which is a doublet of a more complex multiplet with small hyperfine couplings that can be observed in the EPR spectrum, but in the absorbance spectrum only the doublet signal can be easily detected visually.

I.7.3. Isotropic EPR Spectra. Thus far and for this section all the EPR spectra that have been shown as examples and discussed are isotropic EPR spectra. That is they are taken in fluid solutions and the EPR spectrum is an average of the various molecular orientations. This results in spectra with a high degree of inversion symmetry.

Another feature of EPR spectra is the presence of hyperfine coupling which just like in NMR spectroscopy a magnetic nucleus interacts with the magnetic fields of other magnetic

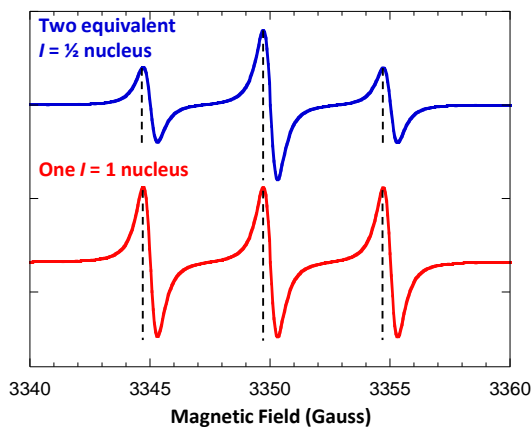


Figure I-16. The EPR spectra of an organic radical interacting with two equivalent $I = 1/2$ nuclei (Top) and the spectrum of an organic radical interacting with one $I = 1$ nucleus (Bottom) each shown with a stick drawing to help identify the intensities and peak positions.

nuclei and this results in the splitting of the observed signal, the same is true for electrons in EPR interacting with magnetic nuclei. For an electron interacting with one nucleus with a nuclear spin (I) = 1/2, like a proton, the EPR signal would be split into a doublet by following the equation $2NI + 1$ for the number of observed lines, where N is the number of equivalent nuclei and I is the nuclear spin, just like in NMR. If the radical is interacting with two equivalent protons, then the signal is a triplet ($2 \cdot 2 \cdot 1/2 + 1 = 3$) as shown in the top spectrum of Figure I-16. The bottom spectrum of Figure I-16 also shows a triplet, but this is due to the radical interacting with one $I = 1$ nucleus, like a nitrogen, rather than it interacting with two $I = 1/2$ nuclei. The key to differentiating these scenarios are the line intensities for each spectrum. Just as in $^1\text{H-NMR}$ spectroscopy, the $I = 1/2$ nuclei follow Pascal's triangle for their relative intensities, which means there should be three lines and they are in a 1:2:1 ratio with one another. For $I = 1$ nuclei, they follow a modified version of Pascal's triangle because they give 3 lines ($2 \cdot 1 \cdot 1 + 1 = 3$) for one nucleus, but each line is of equivalent intensity. So the $N = 1$ line of Pascal's triangle is 1:1:1. Both triangles for $I = 1/2$ and $I = 1$ nuclei are shown in Figure I-17 for relative intensities up to $N = 5$. Modified Pascal's triangles for nuclear spins greater than 1 can be generated as well by following the same pattern. For multiple inequivalent nuclei the signal will be split accordingly into multiplets of multiplets, an example of this will be shown in Figure I-18.

N	Relative Intensities (for $I = \frac{1}{2}$ nuclei)	Relative Intensities (for $I = 1$ nuclei)
0	1	1
1	1 : 1	1 : 1 : 1
2	1 : 2 : 1	1 : 2 : 3 : 2 : 1
3	1 : 3 : 3 : 1	1 : 3 : 6 : 7 : 6 : 3 : 1
4	1 : 4 : 6 : 4 : 1	1 : 4 : 10 : 16 : 19 : 16 : 10 : 4 : 1
5	1 : 5 : 10 : 10 : 5 : 1	1 : 5 : 15 : 20 : 45 : 51 : 45 : 20 : 15 : 5 : 1

Figure I-17. Pascal's triangle showing the relative signal intensities for $I = \frac{1}{2}$ and $I = 1$ nuclear spins.

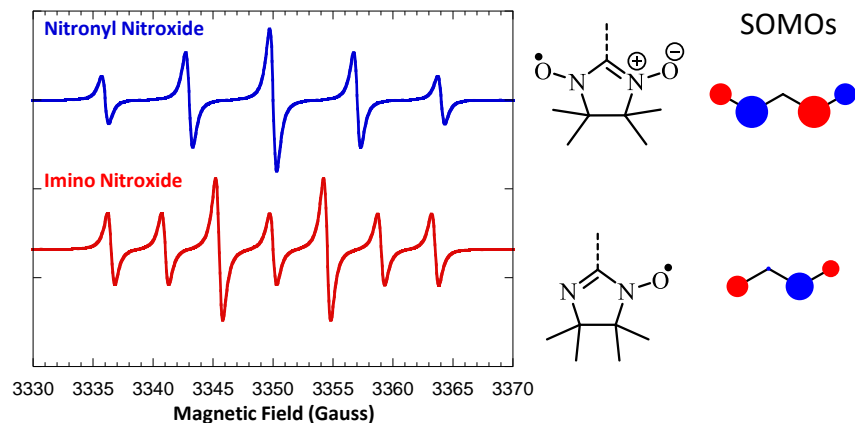


Figure I-18. EPR spectra, line drawings and SOMOs for nitronyl nitroxides and iminonitroxide organic radicals.

The observed magnitude of the hyperfine coupling (a) is proportional to the amount of spin density on that magnetic nucleus and is given by the McConnell relation:

$$a = Q\rho,$$

where a is the observed hyperfine coupling constant, ρ is the spin density and Q is an empirical constant that ranges from 2.0 to 2.5 mT.⁶⁵

Figure I-18 shows the EPR spectra of two organic radicals, the top spectrum is that of a nitronyl nitroxide and the bottom is an iminonitroxide. In terms of determining the expected EPR spectrum, it is important that we look at the SOMO of each radical because it will be the most closely related to the spin density and for the nitronyl nitroxide, in particular, the line drawing structure cannot convey the correct information. The SOMO for nitronyl nitroxide is symmetric, there is a large amount of spin on the nitrogen nuclei, a little less on the oxygens and a node going through the central carbon atom. Given this picture we can assume and observe that the EPR spectrum for nitronyl nitroxide will consist of the radical interacting with two equivalent nitrogen ($I=1$) nuclei, which should give a 5-line pattern in a 1:2:3:2:1 ratio. 99.962% of naturally occurring oxygen isotopes have a nuclear spin of zero, so no splitting is observed for

the oxygen nuclei. The iminonitroxide SOMO, just like the line drawing shows that the nitrogen nuclei are inequivalent, so for this radical we can expect that the EPR signal would be split into a 1:1:1 triplet by each nitrogen giving a triplet of triplets or nine lines. It turns out that for iminonitroxides, the hyperfine with respect to the N-O nitrogen is approximately two times that of the other nitrogen and so the observed spectrum is a seven-line pattern with two sets of overlapping lines near the middle of the spectrum. Experimentally, the nitronylnitroxide hyperfine is approximately 7 Gauss and the iminonitroxide hyperfine coupling constants are about 9 and 4.5 Gauss, given McConnell's relation we can conclude that some of the spin density has shifted from one nitrogen onto the other in the iminonitroxide, relative to the nitronylnitroxide.

So far, the organic radicals discussed are monoradicals; however, much of the later chapters involve the synthesis of biradicals or polyradicals and at minimum, EPR is used as a characterization technique. The isotropic EPR spectra of biradicals and polyradicals have a distinguishing feature if the radicals are coupled with each other and form higher spin states. For a coupled biradical, the m_s quantum numbers can be 1, 0, -1 and split as shown in Figure I-19 when placed into a magnetic field. Just like the $S = 1/2$ monoradical, one m_s level rises and one m_s level decreases in energy, but the $m_s = 0$ has not net magnetic moment and therefore is not

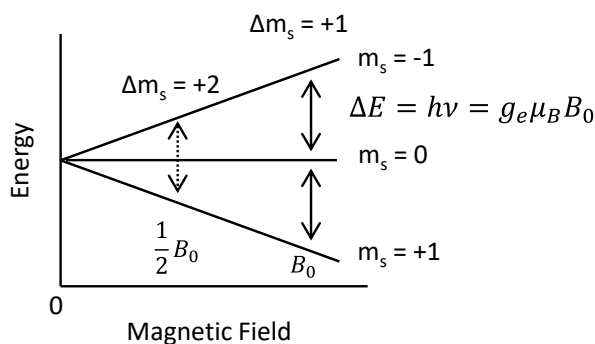


Figure I-19. Zeeman splitting in an exchange coupled biradical.

affected by Zeeman splitting. In EPR only transitions between 1-0 and -1-0 are allowed which are known as $\Delta m_s = +1$ transitions. At low temperature in frozen solution, a forbidden transition, $\Delta m_s = +2$ between the -1-1 energy levels can be observed at one-half the magnetic field as the $\Delta m_s = +1$ transitions. In the $\Delta m_s = 1$ an exchange coupled biradical manifests as the hyperfine couplings that were present in the monoradical are now half their value. Figure I-20 shows a nitronylnitroxide monoradical as one of the common intermediates (Cat-B-NN) during the synthesis of semiquinone-bridge-nitronylnitroxide (SQ-B-NN) biradicals that will be described in greater detail in Chapter 3. As mentioned previously, nitronylnitroxide (NN) hyperfine coupling from the nitrogen nuclei is approximately 7 Gauss as is shown for Cat-B-NN and when the semiquinone (SQ) is introduced into the molecule, the EPR spectrum of the biradical still shows the characteristic 5-line pattern for the NN, but now the hyperfine coupling is effectively half at about 3.5-4 Gauss. This trend in hyperfine coupling for monoradicals, biradicals and polyradicals follows the pattern of $a_{obs} = a_{mono} / N$, where a_{obs} and a_{mono} are the observed hyperfine coupling and the hyperfine coupling in the monoradical, respectively and N is the number of exchange coupled radicals in the system allowing for higher spin states. So for a biradical it is half the monoradical and for a triradical it would be one-third the monoradical

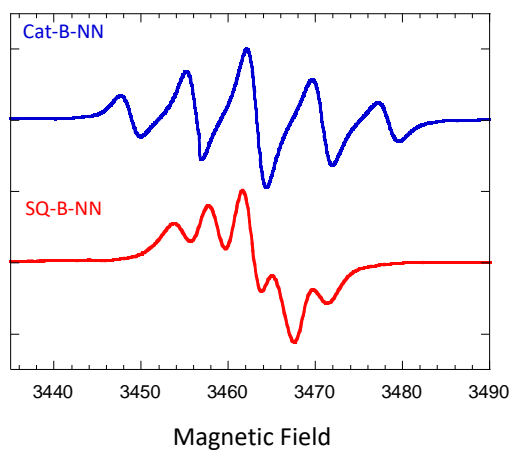


Figure I-20. EPR spectra of nitronylnitroxide (NN) monoradical in the form of Cat-B-NN and the corresponding semiquinone-bridge-nitronylnitroxide (SQ-B-NN) biradical.

hyperfine coupling, and so on. g -values and hyperfine couplings, the latter of which indicates the spin density distribution is most of the information that can be acquired from isotropic EPR of mono-, bi- and polyradicals.

I.7.4. Anisotropic EPR Spectra. Further information can be gleaned by hindering the rotation of the molecules which is most easily accomplished by immobilizing the molecules in a frozen glass or more uncommonly a polymer film. Alternatively, single crystals can be rotated and EPR spectra acquired. However, this is more amenable to paramagnetic inorganic species, not organic radicals and because this work does not include paramagnetic inorganic species, the EPR spectra of single crystals will not be discussed, but the principles that will be discussed are the same.

The EPR spectra that arise from immobilized organic radicals are anisotropic and have weaker signals than the corresponding isotropic EPR because of the many molecular orientations that are present when a sample is frozen, only a relative few will have one of their three principle axes (x,y,z) oriented with the magnetic field of the spectrometer, whereas in a fluid solution molecular rotation allows molecules to rotate in and out of orientation, thus averaging the anisotropic features together into one signal.

Anisotropic EPR spectra allow for the extraction of zero-field splitting parameters, D and E which describe the electronic geometry of the spin system. D is used to describe the energy deviation of the z axis from the x and y axes and E describes the deviation of the x and y axes from each other. D can be a negative value, but this only has consequences for the spectrum at liquid helium temperatures and the assignment of the x and y axes is arbitrary so E will be positive for one and negative for the other, but is usually only discussed in terms of being the absolute value. Because the zero-field splitting parameters provide insight into the electronic

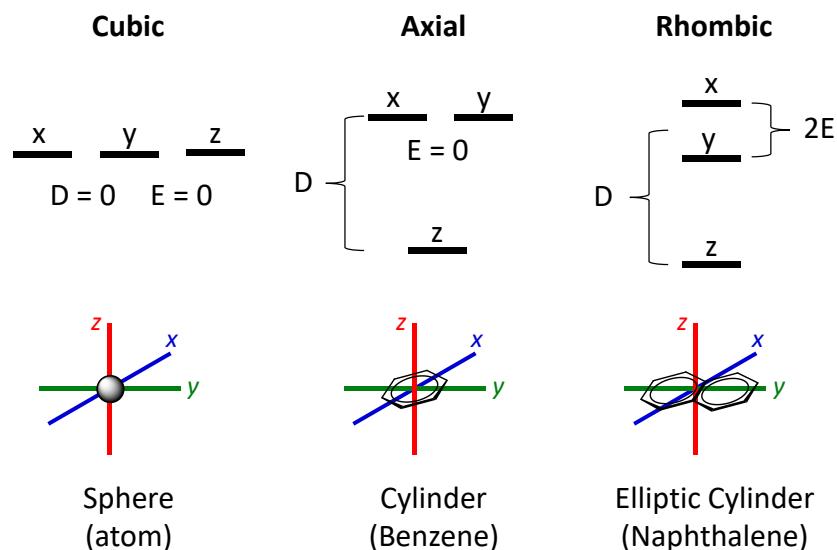


Figure I-21. Cubic, axial, and rhombic spin systems with definitions of D and E as well as common geometric and chemical examples.

geometry, D varies inversely with the cube of the interelectronic distance.⁶⁶ Several cases are shown in Figure I-21 for the electronic geometry. The first case is where D and E are both equal to zero and the frozen solution. Examples of this would be a sphere or an atom and is known as a cubic spin system. The EPR spectrum will appear as a singlet because the x , y and z axes are not split from each other because the electronic geometry is the same along each axis. The second case is when the electronic geometry is the same along the x and y axes, but different in the z -axis. The classic examples are a cylinder or benzene for a molecular example. This is known as axial geometry and the splitting of the x and y energy levels from z is described by D . E will be equal to zero because x and y are the same. The last case is when $D \neq 0$ and $E \neq 0$, this is known as a rhombic spin system and is geometrically an elliptic cylinder or naphthalene where the electronic distribution along the three axes is $x \neq y \neq z$. In this case, D describes the energy difference from the z axis and the mean of the energy difference between the x and y axes and E describes the energy separation of the x and y axes from D . In other words the x energy level is $D + E$ and the y energy level is $D - E$. Recall that the x and y axis labels are arbitrary so the

respective axis energies could easily be reversed. The only requirement is that the axes be assigned so that $D > 3E$.

D and E are described by the magnetic dipole operator, \mathcal{H}_D which is:⁶⁷

$$\mathcal{H}_D = g_e^2 \mu_B^2 \sum_{i>j} \left\{ \frac{S_i \cdot S_j}{r_{ij}^3} - \frac{3(r_{ij} \cdot S_i)(r_{ij} \cdot S_j)}{r_{ij}^5} \right\} \quad \text{Eq. I-20}$$

where S_i is the spin operator of electron i and r_{ij} is the interelectronic vector. In terms of the components of the total spin angular momentum S and consequently terms of D and E , Eq. I-20 can be transformed to:⁶⁶

$$\mathcal{H}_D = - \left[\frac{1}{3} D - E \right] S_x^2 - \left[\frac{1}{3} D + E \right] S_y^2 + \frac{2}{3} D S_z^2 \quad \text{Eq. I-21}$$

where x , y and z are the principle axis coordinate system. Adding a term for the Zeeman energy can be added to give the complete Hamiltonian as:

$$\mathcal{H} = \mu_B \mathbf{H} g \mathbf{S} + D S_z^2 + E (S_x^2 - S_y^2) - \frac{2}{3} D \quad \text{Eq. I-22}$$

\mathbf{H} is the external magnetic field. The matrix for Eq. I-22 for an $S = 1$ system with $m_s = +1, 0, -1$ is:

$$\begin{bmatrix} (D/3) + \mu_B \mathbf{H} g n & \mu_B \mathbf{H} g (l - im)/\sqrt{2} & E \\ \mu_B \mathbf{H} g (l + im)/\sqrt{2} & -2D/3 & \mu_B \mathbf{H} g (l - im)/\sqrt{2} \\ E & \mu_B \mathbf{H} g (l + im)/\sqrt{2} & (D/3) - \mu_B \mathbf{H} g n \end{bmatrix} \quad \text{Eq. I-23}$$

where l , m , and n are the direction cosines of the external field with respect to the magnetic axes of the triplet.⁶⁶ Initially disregarding D and E and assuming an isotropic g tensor, the eigenvalues of Eq. I-23 are $\pm \mu_B \mathbf{H} g$ and 0. Then the zero-field splitting parameters are introduced as a perturbation to the +1, 0 and -1 energy levels of the triplet to give:

$$W'_1 = g\mu_B H + \left(\frac{D}{2}\right)\left(n^2 - \frac{1}{3}\right) + \left[\frac{l^2 - m^2}{2}\right]E$$

$$W'_0 = D\left(\frac{1}{3} - n^2\right) - [l^2 - m^2]E \quad \text{Eq. I-24}$$

$$W'_{-1} = g\mu_B H + \left(\frac{D}{2}\right)\left(n^2 - \frac{1}{3}\right) + \left[\frac{l^2 - m^2}{2}\right]E$$

Because only 0-1 and -1-0 transitions are allowed and the microwave frequency is constant, the field at which a transition occurs is given as:

$$H_{0-1, -1-0} = H_r = H_0 \pm \left[\frac{D' - 3E'}{2}\right]l^2 + \left[\frac{D' + 3E'}{2}\right]m^2 + D'n^2 \quad \text{Eq. I-25}$$

where resonance for an isolated monoradical ($S = 1/2$) occurs at $H_0 = hv/g\mu_B$ and $D' = D/g\mu_B$.

With \mathbf{H} parallel to x , y or z magnetic axis absorptions will occur at $H_r = H_0 \pm (D' - 3E')/2$,

$\pm(D' + 3E')/2$, or $\pm D'$.⁶⁶ Therefore, for a rhombic spin system there should be six features, two

for each axis, the two features for the z -axis will be separated by $2D$, the features for either the x

or y will be separated by $D+3E$ and the other will be separated by $D-3E$ as shown in Figure I-22.

Figure I-22A shows the principle magnetic axes with each axis oriented parallel to the external magnetic field ($H_{x,y \text{ or } z}$) and the effect that has on the x , y , and z energy levels in each case. When

the z -axis is parallel to the external magnetic field, the z energy level remains unperturbed and

the x and y energy levels split according to Eq. I-24. The resonant conditions for the 1-0 and -1-0

transitions occur and the distance between them is equal to $2D$, this distance is indicated by the

red dashed line. If the y -axis is parallel to the external magnetic field, the y energy level remains

unperturbed and the x and z energy levels split. The resonant conditions now will occur at $\pm(D-3E)/2$ as defined by Eq. I-25 and the green dashed line indicates the distance separating the two

resonances as $D-3E$. Finally, aligning the external magnetic field with the x -axis will split the y

and z energy levels and leave the x unperturbed. The resonant conditions in this case will occur

by Eq. I-25 at $\pm(D+3E)/2$ and be separated by a distance of $D+3E$ as indicated by the blue dashed line. It is important to mention that magnetic field is on the x -axis of these plots, the figure does not perfectly depict the scenario for an isotropic g tensor, if it did, the features would

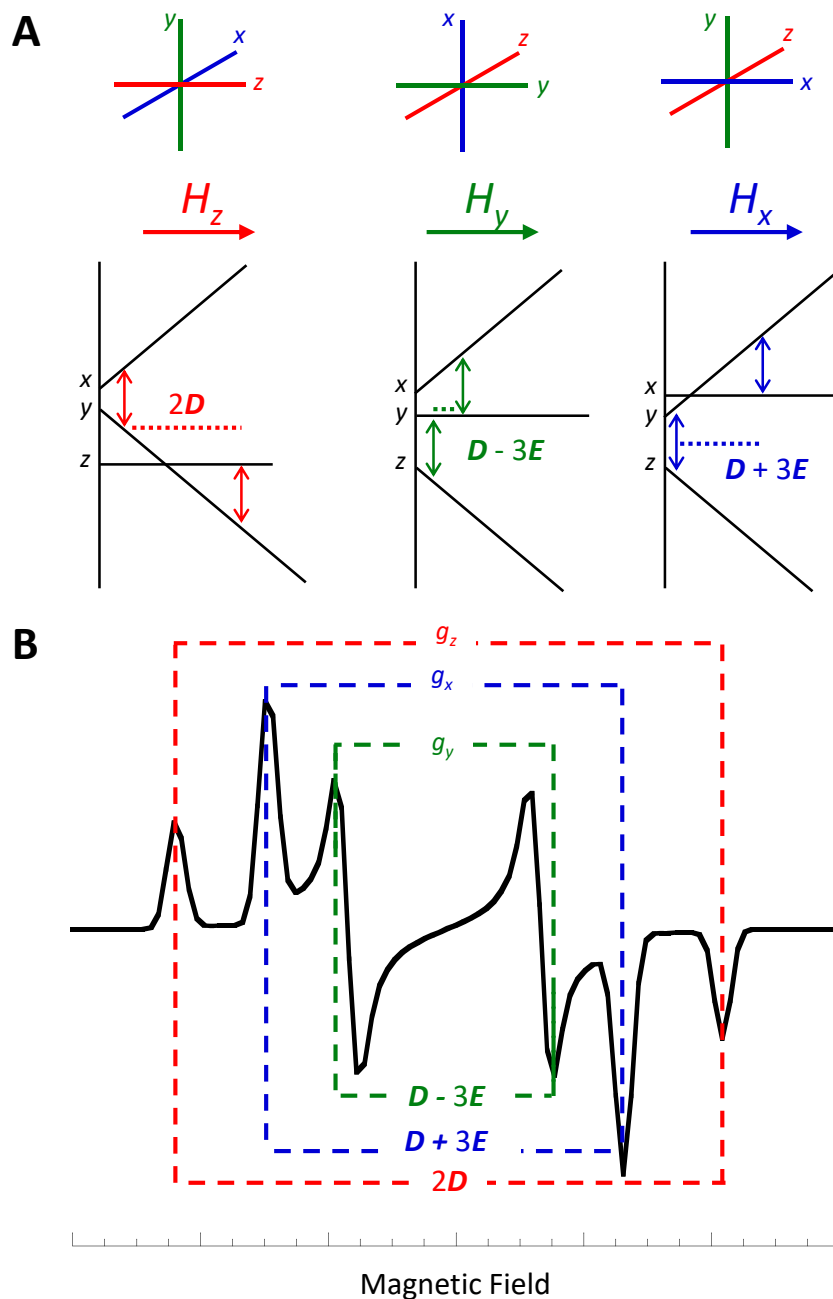


Figure I-22. (A) the alignment of each of the magnetic axes of the triplet with respect to the external magnetic field and the consequences for the x , y , and z energy levels in each case. (B) how the energy diagrams and resonant conditions manifest themselves in the anisotropic spectrum of a biradical.

be symmetrically placed about $H_0 = h\nu/g\mu_B$ as shown in Figure I-22B. However, if measured, Figure I-22A's dashed lines are consistent with their assigned gaps of $2D$, $D+3E$ and $D-3E$. Ultimately, the goal is to bridge the gap between the theory and the observed spectrum and Figure I-22B illustrates the gaps between the resonant conditions for each of the principle axes: $2D$, $D-3E$ and $D+3E$ for an isotropic g tensor ($g_x = g_y = g_z$). Asymmetry in the spectrum gets introduced if $g_x \neq g_y \neq g_z$.

I.8. Magnetometry.

In general, magnetometry is the study of magnetism and magnetometers measure the direction, strength or change of a magnetic field at a particular location. The term magnetometer is a device for measuring magnetism and ranges, but is not limited to, from the most simple, a compass that detects the Earth's magnetic field, to a Gouy balance that detects the changes in mass of a sample that is suspended in a magnetic field where diamagnetic samples are repelled from the field and paramagnetic samples are attracted; even more sensitive and elaborate set-ups of SQUID (superconducting quantum interference device) magnetometers which are capable of detecting very small magnetic fields in samples and utilize variable temperature experiments to analyze magnetic susceptibility. Because this work utilizes SQUID magnetometry, this experimental set-up, instrument and data analysis will be discussed.

SQUID magnetometers have superconducting coils and generate magnetic fields up to 7 Tesla so cryogenic temperatures are required for SQUID operation, typically liquid helium is used. As a result the outer piece of a squid magnetometer is a Dewar that stores the cryogenic liquid which is used to cool the sample chamber as well as the magnet. A simple schematic of the sample chamber of a SQUID magnetometer is shown in Figure I-23 which involves the sample placed inside of a plastic straw which is then passed through the SQUID's

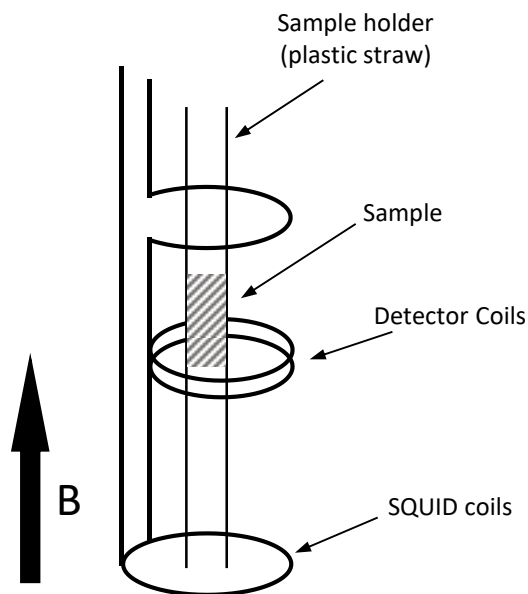


Figure I-23. A simple schematic of the sample chamber of a SQUID magnetometer.

superconducting coils while a magnetic field is applied to align the spins in a paramagnetic sample and the movement of the magnetized sample through the coils results in modulation of the current which is detected by the detector coils. The current changes are translated into the magnetic response of the sample. Every data point collected during a SQUID experiment goes through this process several times which are then averaged.

Either the magnetic field or temperature are the two variables that are modulated during a SQUID experiment, while the other variable is held constant. Holding the temperature constant while the magnetic field is varied is used for determining saturation magnetization (M_{sat}) which is when the applied magnetic field cannot increase the magnetization of the sample any further and is defined by the equation:

$$M_{sat} = Ng_e\mu_B S \quad \text{Eq. I-26}$$

where N is the number of particles, g_e is the Landé factor, μ_B is the Bohr magneton and S is the spin of the system. Calculating M_{sat} allows for the determination of S for a sample for a paramagnetic species with a ferromagnetically coupled ground state. The caveat is that because

magnetometry is not spectroscopy any impurities present in the sample are not differentiated and the result of the experiment would be an average of all the paramagnetic species, weighted appropriately for those that are higher or lower spin than the sample. Regardless the magnetization (M) of the sample can be calculated for any temperature (T) and magnetic field (H) combination if the ground-state spin (S) is known by Eq. I-27:

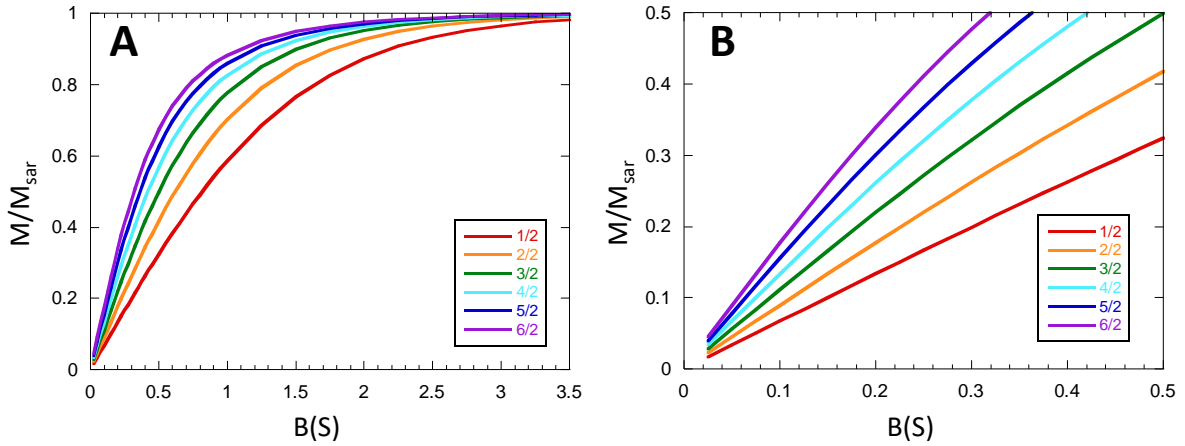


Figure I-24. M/M_{sat} Brillouin functions for $S=1/2, 2/2, 3/2, 4/2, 5/2$, and $6/2$. (A) full plot and (B) zoomed in to show the initial slopes.

$$M_{sat} = Ng_e\mu_B SB_S(x) \quad \text{Eq. I-27}$$

where $B_S(x)$ is the corresponding Brillouin function:

$$B_S(x) = \frac{1}{S} \left[\left(S + \frac{1}{2} \right) \coth \left[\left(S + \frac{1}{2} \right) x \right] - \frac{1}{2} \coth \left(\frac{x}{2} \right) \right] \quad \text{Eq. I-28}$$

where $x = g_e\mu_B H/kT$. If M/M_{sat} is plotted for experimental data with an unknown ground-state spin (S), then the Brillouin functions for magnetization can be plotted alongside it and compared to determine the average ground state spin for the sample. Figure I-24 shows the Brillouin functions for $S = 1/2$ through $6/2$. Because M_{sat} is being used the plots asymptotically approach 1. However, depending on S the initial slope changes (Figure I-24B) and this can be helpful for determining the average ground-state spin of a sample which is a technique used in Chapter II.

Holding the temperature constant and sweeping the magnetic field gives information pertaining to the strength of the magnetism of the sample, but holding the magnetic field constant and sweeping the temperature provides insights into the strength of the interactions leading to the observed ground-state spin. This type of experiment is known as magnetic susceptibility. The

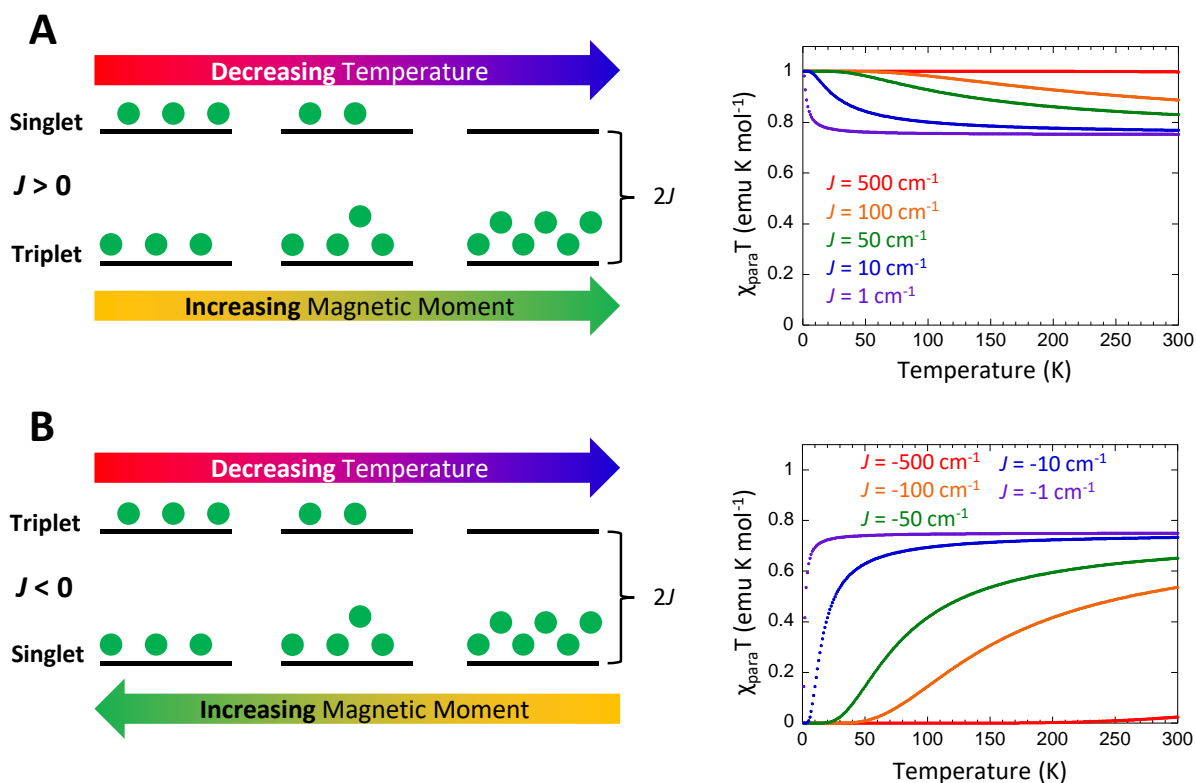


Figure I-25. Effect of temperature on the populations of the singlet and triplet states leading to the effects on the magnetic moment for when $J > 0$ (A) and $J < 0$ (B) beside their theoretical paramagnetic susceptibility ($\chi_{\text{para}} T$) plots for different values of J .

energy gap between the singlet and triplet states (ΔE_{ST}) is equivalent to $2J$ and as defined by the Heisenberg-Dirac-Van Vleck Hamiltonian:

$$\hat{H}_{ij} = -2J_{ij}\hat{S}_i\hat{S}_j \quad \text{Eq. I-29}$$

The triplet state has a net magnetic moment where the singlet state does not. Therefore, $2J > 0$ when the triplet state is lower in energy than the singlet state and as the system's temperature

decreases the triplet state will become more populated and the magnetization of the sample will increase (Figure I-25A). Conversely, $2J < 0$ when the singlet state is lower in energy than the triplet state and the system's temperature decreases the singlet state will become more populated and the magnetization of the sample will decrease (Figure I-25B). χ_{para} is the paramagnetic susceptibility and can be modelled with Eq. I-30.

$$\chi_{para} = \frac{g^2 0.125 \text{ emu K/mol}}{T} \left(\frac{6}{e^{\frac{-2J_{DA}}{k_B T}} + 3} \right) \quad \text{Eq. I-30}$$

Figure I-25 also has $\chi_{para} T$ plotted for various values of J . These plots illustrate that it is relatively easy to differentiate between ferromagnetically and antiferromagnetically coupled radicals because even when J is small ($|J| < 5 \text{ cm}^{-1}$), the sign of J can still be determined at lower temperatures when $J > 0$, $\chi_{para} T$ increases and for $J < 0$, $\chi_{para} T$ decreases toward 0 emu K mol^{-1} . However, it becomes more difficult to differentiate between small changes in magnitude for two values of J of the same sign. From these theoretical plots, absolute values of J that are less than 10 cm^{-1} have data that are very similar and this can become convoluted when other data corrections are required to fit experimental data. SQUID magnetometry will be revisited later in Chapter III in the context of donor-bridge-acceptor biradicals and then implemented in the data collection and analyses of Chapters IV and V.

I.9 References.

- (1) Gomberg, M. An Instance of Trivalent Carbon: Triphenylmethyl. *J. Am. Chem. Soc.* **1900**, 22 (11), 757–771.
- (2) Coppinger, G. M. A Stable Phenoxy Radical Inert to Oxygen. *J. Am. Chem. Soc.* **1957**, 79 (2), 501–502. <https://doi.org/10.1021/ja01559a073>.
- (3) Kharasch, M. S.; Joshi, B. S. Reactions of Hindered Phenols. II. Base-Catalyzed Oxidations of Hindered Phenols *. *J. Org. Chem.* **1957**, 22 (11), 1439–1443. <https://doi.org/10.1021/jo01362a034>.
- (4) Prokhorov, A.; Fedorov, V. Antiferromagnetism of Free Radicals. *Sov. Phys. JETP-USSR* **1963**, 16 (6), 1489–1492.
- (5) Lebedev, O. L.; Kazarnovskii, S. N. TEMPO. *Zhur. Obs. Khim.* **1960**, 30 (5), 1631–1635.
- (6) Shu, C.; Zhang, H.; Olankitwanit, A.; Rajca, S.; Rajca, A. High-Spin Diradical Dication of Chiral π -Conjugated Double Helical Molecule. *J. Am. Chem. Soc.* **2019**, 141 (43), 17287–17294. <https://doi.org/10.1021/jacs.9b08711>.
- (7) Lanfranc de Panthou, F.; Luneau, D.; Laugier, J.; Rey, P.; de Panthou, F. L.; Luneau, D.; Laugier, J.; Rey, P. Crystal Structures and Magnetic Properties of a Nitronyl Nitroxide and of Its Imino Analog. Crystal Packing and Spin Distribution Dependence of Ferromagnetic Intermolecular Interactions. *J. Am. Chem. Soc.* **1993**, 115 (20), 9095–9100. <https://doi.org/10.1021/ja00073a027>.
- (8) Moore, R. F.; Waters, W. A. Some Products Formed from Phenolic Inhibitors during the Autoxidation of Cumene. *J. Chem. Soc.* **1954**, 243–246. <https://doi.org/10.1007/s13398-014-0173-7.2>.
- (9) Tamura, M.; Nakazawa, Y.; Shiomi, D.; Nozawa, K.; Hosokoshi, Y.; Ishikawa, M.;

- Takahashi, M.; Kinoshita, M. Bulk Ferromagnetism in the β -Phase Crystal of the p-Nitrophenyl Nitronyl Nitroxide Radical. *Chem. Phys. Lett.* **1991**, *186*, 401–404.
[https://doi.org/10.1016/0009-2614\(91\)90198-I](https://doi.org/10.1016/0009-2614(91)90198-I).
- (10) Turek, P.; Nozawa, K.; Shiomi, D.; Awaga, K.; Inabe, T.; Maruyama, Y.; Kinoshita, M. Ferromagnetic Coupling in a New Phase of the P-Nitrophenyl Nitronyl Nitroxide Radical. *Chem. Phys. Lett.* **1991**, *180* (4), 327–331. [https://doi.org/10.1016/0009-2614\(91\)90328-7](https://doi.org/10.1016/0009-2614(91)90328-7).
- (11) Allemand, P. M.; Fite, C.; Srdanov, G.; Keder, N.; Wudl, F.; Canfield, P. On the Complexities of Short Range Ferromagnetic Exchange in a Nitronyl Nitroxide. *Synth. Met.* **1991**, No. 41–43, 3291–3295. [https://doi.org/10.1016/0379-6779\(91\)91290-Q](https://doi.org/10.1016/0379-6779(91)91290-Q).
- (12) Brown, T. H.; Anderson, D. H.; Gutowsky, H. S. Spin Densities in Organic Free Radicals. *J. Chem. Phys.* **1960**, *33* (3), 720. <https://doi.org/10.1063/1.1731246>.
- (13) Gallagher, N. M.; Bauer, J. J.; Pink, M.; Rajca, S.; Rajca, A. High-Spin Organic Diradical with Robust Stability. *J. Am. Chem. Soc.* **2016**, *138* (30), 9377–9380.
<https://doi.org/10.1021/jacs.6b05080>.
- (14) Gallagher, N.; Zhang, H.; Junghoefer, T.; Giangrisostomi, E.; Ovsyannikov, R.; Pink, M.; Rajca, S.; Casu, M. B.; Rajca, A. Thermally and Magnetically Robust Triplet Ground State Diradical. *J. Am. Chem. Soc.* **2019**, *141* (11), 4764–4774.
<https://doi.org/10.1021/jacs.9b00558>.
- (15) Shultz, D. A.; Hollomon, M. G. Preparation and EPR Spectroscopic Investigation of Conjugated Oligomers Containing Semiquinone Repeat Units. *Chem. Mater.* **2000**, *12* (2), 580–585. <https://doi.org/10.1021/cm9907155>.
- (16) Li, F.; Zhang, Y.; Kwon, S. R.; Lutkenhaus, J. L. Electropolymerized Polythiophenes Bearing Pendant Nitroxide Radicals. *ACS Macro Lett.* **2016**, *5* (3), 337–341.

- <https://doi.org/10.1021/acsmacrolett.5b00937>.
- (17) Rajca, A. Organic Diradicals and Polyradicals: From Spin Coupling to Magnetism? *Chem. Rev.* **1994**, *94* (4), 871–893. <https://doi.org/10.1021/cr00028a002>.
- (18) Tagami, K.; Tsukada, M. Spintronic Transport through Polyphenoxyl Radical Molecules. *J Phys Chem B* **2004**, *108* (20), 6441–6444. <https://doi.org/10.1021/jp037953e>.
- (19) Zhang, K.; Monteiro, M. J.; Jia, Z. Stable Organic Radical Polymers: Synthesis and Applications. *Polym. Chem.* **2016**, *7* (36), 5589–5614.
<https://doi.org/10.1039/C6PY00996D>.
- (20) Nishide, H.; Takahashi, M.; Takashima, J.; Pu, Y. J.; Tsuchida, E. Acyclic and Cyclic Di- and Tri(4-Oxyphenyl-1,2-Phenyleneethynylene)s: Their Synthesis and Ferromagnetic Spin Interaction. *J. Org. Chem.* **1999**, *64* (20), 7375–7380.
<https://doi.org/10.1021/jo990575i>.
- (21) Kaneko, T.; Iwamura, K.; Nishikawa, R.; Teraguchi, M.; Aoki, T. Synthesis of Sequential Poly(1,3-Phenyleneethynylene)-Based Polyradicals and through-Space Antiferromagnetic Interaction of Their Solid State. *Polymer (Guildf)*. **2014**, *55* (5), 1097–1102.
<https://doi.org/10.1016/j.polymer.2014.01.019>.
- (22) Murata, H.; Miyajima, D.; Nishide, H. A High-Spin and Helical Organic Polymer: Poly{[4-(Dianisylaminium)Phenyl]Acetylene}. *Macromolecules* **2006**, *39* (19), 6331–6335. <https://doi.org/10.1021/ma060773t>.
- (23) Itoh, T.; Jinbo, Y.; Hirai, K.; Tomioka, H. Preparation of Poly(Phenyl)Acetylenes Having Diazo Groups and Magnetic Characterization of Poly(Carbene). *J. Am. Chem. Soc.* **2005**, *127* (6), 1650–1651. <https://doi.org/10.1021/ja0455345>.
- (24) Nishide, H.; Maeda, T.; Oyaizu, K.; Tsuchida, E. High-Spin Polyphenoxyl Based on Poly

- (1, 4-Phenyleneethynylene). *J. Org. Chem.* **1999**, No. 6, 7129–7134.
- (25) Nishide, H.; Kaneko, T.; Nii, T.; Katoh, K.; Tsuchida, E.; Lahti, P. M. Poly(Phenylenevinylene)-Attached Phenoxyl Radicals: Ferromagnetic Interaction through Planarized and π -Conjugated Skeletons. *J. Am. Chem. Soc.* **1996**, *118* (40), 9695–9704. <https://doi.org/10.1021/ja961721u>.
- (26) Murata, H.; Takahashi, M.; Namba, K.; Takahashi, N.; Nishide, H. A High-Spin and Durable Polyradical: Poly (4-Diphenylaminium-1, 2-Phenylenevinylene). *J. Org. Chem.* **2004**, No. 69, 631–638.
- (27) Juetten, M. J.; Buck, A. T.; Winter, A. H. A Radical Spin on Viologen Polymers: Organic Spin Crossover Materials in Water. *Chem. Commun. (Camb)*. **2014**, *51*, 5516–5519. <https://doi.org/10.1039/c4cc07119k>.
- (28) Suga, T.; Ohshiro, H.; Ugita, S.; Oyaizu, K.; Nishide, H. Emerging N-Type Redox-Active Radical Polymer for a Totally Organic Polymer-Based Rechargeable Battery. *Adv. Mater.* **2009**, *21* (16), 1627–1630. <https://doi.org/10.1002/adma.200803073>.
- (29) Nakahara, K.; Iriyama, J.; Iwasa, S.; Suguro, M.; Satoh, M.; Cairns, E. J. Al-Laminated Film Packaged Organic Radical Battery for High-Power Applications. *J. Power Sources* **2007**, *163* (2), 1110–1113. <https://doi.org/10.1016/j.jpowsour.2006.10.003>.
- (30) Létard, J.-F.; Guionneau, P.; Goux-Capes, L. Towards Spin Crossover Applications. In *Spin Crossover in Transition Metal Compounds III*; 2004; Vol. 1, pp 221–249. <https://doi.org/10.1007/b95429>.
- (31) Boehme, C.; Lupton, J. M. Challenges for Organic Spintronics. *Nat. Nanotechnol.* **2013**, *8* (9), 612–615. <https://doi.org/10.1038/nnano.2013.177>.
- (32) Sato, O.; Tao, J.; Zhang, Y.-Z. Control of Magnetic Properties through External Stimuli.

- Angew. Chemie Int. Ed.* **2007**, *46* (13), 2152–2187.
<https://doi.org/10.1002/anie.200602205>.
- (33) Tomlinson, E. P.; Hay, M. E.; Boudouris, B. W. Radical Polymers and Their Application to Organic Electronic Devices. *Macromolecules* **2014**, *47* (18), 6145–6158.
<https://doi.org/10.1021/ma5014572>.
- (34) Calzolari, A.; Chen, Y.; Lewis, G. F.; Dougherty, D. B.; Shultz, D. A.; Buongiorno Nardelli, M. Complex Materials for Molecular Spintronics Applications: Cobalt Bis(Dioxolene) Valence Tautomers, from Molecules to Polymers. *J. Phys. Chem. B* **2012**, *116* (43), 13141–13148.
- (35) Nishide, H.; Iwasa, S.; Pu, Y. J.; Suga, T.; Nakahara, K.; Satoh, M. Organic Radical Battery: Nitroxide Polymers as a Cathode-Active Material. *Electrochim. Acta* **2004**, *50* (2-3 SPEC. ISS.), 827–831. <https://doi.org/10.1016/j.electacta.2004.02.052>.
- (36) Janoschka, T.; Hager, M. D.; Schubert, U. S. Powering up the Future: Radical Polymers for Battery Applications. *Adv. Mater.* **2012**, *24* (48), 6397–6409.
<https://doi.org/10.1002/adma.201203119>.
- (37) Nakahara, K.; Oyaizu, K.; Nishide, H. Organic Radical Battery Approaching Practical Use. *Chem. Lett.* **2011**, *40* (3), 222–227. <https://doi.org/10.1246/cl.2011.222>.
- (38) Yonekuta, Y.; Susuki, K.; Oyaizu, K.; Honda, K.; Nishide, H. Battery-Inspired, Nonvolatile, and Rewritable Memory Architecture: A Radical Polymer-Based Organic Device. *J. Am. Chem. Soc.* **2007**, *129* (46), 14128–14129.
<https://doi.org/10.1021/ja075553p>.
- (39) Nakahara, K.; Iriyama, J.; Iwasa, S.; Suguro, M.; Satoh, M.; Cairns, E. J. Cell Properties for Modified PTMA Cathodes of Organic Radical Batteries. *J. Power Sources* **2007**, *165*

- (1), 398–402. <https://doi.org/10.1016/j.jpowsour.2006.11.044>.
- (40) Mike, J. F.; Lutkenhaus, J. L. Recent Advances in Conjugated Polymer Energy Storage. *J. Polym. Sci. Part B Polym. Phys.* **2013**, *51* (7), 468–480.
<https://doi.org/10.1002/polb.23256>.
- (41) Nakahara, K.; Iriyama, J.; Iwasa, S.; Suguro, M.; Satoh, M.; Cairns, E. J. High-Rate Capable Organic Radical Cathodes for Lithium Rechargeable Batteries. *J. Power Sources* **2007**, *165* (2), 870–873. <https://doi.org/10.1016/j.jpowsour.2006.11.045>.
- (42) Waters, D. P.; Joshi, G.; Kavand, M.; Limes, M. E.; Malissa, H.; Burn, P. L.; Lupton, J. M.; Boehme, C. The Spin-Dicke Effect in OLED Magnetoresistance. *Nat Phys* **2015**, *11* (11), 910–914.
- (43) Parkin, S.; Wolf, S. A.; Harris, J. S.; Zhang, S.; Smith, D. J. The Application of Spintronics <http://www-03.ibm.com/ibm/history/ibm100/us/en/icons/spintronics/> (accessed Jan 1, 2016).
- (44) Köhler, A.; Bäessler, H. Triplet States in Organic Semiconductors. *Mater. Sci. Eng. R Reports* **2009**, *66* (4–6), 71–109. <https://doi.org/10.1016/j.mser.2009.09.001>.
- (45) Miller, J. S.; Epstein, A. J. Organic and Organometallic Molecular Magnetic Materials—Designer Magnets. *Angew. Chem. Int. Ed. Engl.* **1994**, *33* (4), 385–415.
<https://doi.org/10.1002/anie.199403851>.
- (46) Miller, J. S. Organic- and Molecule-Based Magnets. *Mater. Today* **2014**, *17* (5), 224–235.
<https://doi.org/10.1016/j.mattod.2014.04.023>.
- (47) Mataga, N. Possible “Ferromagnetic States” of Some Hypothetical Hydrocarbons. *Theor. Chim. Acta* **1968**, *10* (4), 372–376. <https://doi.org/10.1007/BF00526505>.
- (48) Rajca, A. Magnetic Ordering in an Organic Polymer. *Science*. **2001**, *294* (5546), 1503–

1505. <https://doi.org/10.1126/science.1065477>.
- (49) Rajca, A.; Rajca, S.; Wongsriratanakul, J. Very High-Spin Organic Polymer: π -Conjugated Hydrocarbon Network with Average Spin of $S \geq 40$. *J. Am. Chem. Soc.* **1999**, *121* (26), 6308–6309. <https://doi.org/10.1021/ja990881d>.
- (50) Oyaizu, K.; Nishide, H. Radical Polymers for Organic Electronic Devices: A Radical Departure from Conjugated Polymers? *Adv. Mater.* **2009**, *21* (22), 2339–2344. <https://doi.org/10.1002/adma.200803554>.
- (51) Kirk, M. L.; Shultz, D. A.; Depperman, E. C.; Brannen, C. L. Donor-Acceptor Biradicals as Ground State Analogues of Photoinduced Charge Separated States. *J. Am. Chem. Soc.* **2007**, *129* (7), 1937–1943. <https://doi.org/10.1021/ja065384t>.
- (52) Wertz, D. W.; Shultz, D. A. *Advanced Inorganic Chemistry II: Applications of Group Theory to Bonding and Spectroscopy*, 8th ed.; 2014.
- (53) Rajca, A. From High-Spin Organic Molecules to Organic Polymers with Magnetic Ordering. *Chem. - A Eur. J.* **2002**, *8* (21), 4834–4841. [https://doi.org/10.1002/1521-3765\(20021104\)8:21<4834::AID-CHEM4834>3.0.CO;2-E](https://doi.org/10.1002/1521-3765(20021104)8:21<4834::AID-CHEM4834>3.0.CO;2-E).
- (54) Kollmar, C.; Kahn, O. A Heisenberg Hamiltonian for Intermolecular Exchange Interaction: Spin Delocalization and Spin Polarization. *J. Chem. Phys.* **1993**, *98* (1), 453. <https://doi.org/10.1063/1.464639>.
- (55) Kahn, O. O. *Molecular Magnetism*; VCH Publishers Inc.: New York, 1993.
- (56) Kollmar, C.; Kahn, O. Ferromagnetic Spin Alignment in Molecular Systems: An Orbital Approach. *Acc. Chem. Res.* **1993**, *26* (5), 259–265. <https://doi.org/10.1021/ar00029a006>.
- (57) Rajca, A. The Physical Organic Chemistry of Very High-Spin Polyradicals. In *Advances in Physical Organic Chemistry*; 2005; Vol. 40, pp 153–199.

- [https://doi.org/10.1016/S0065-3160\(05\)40004-0](https://doi.org/10.1016/S0065-3160(05)40004-0).
- (58) Coulson, C. A.; Rushbrooke, G. S.; Coulson, C. A. Mathematical Proceedings of the Cambridge Cambridge Philosophical Society : *Math. Proc. Cambridge Philos. Soc.* **1940**, *36* (02), 193–200. <https://doi.org/10.1017/S0305004100017163>.
- (59) Dewar, M. J. S.; Dougherty, R. C. *The PMO Theory of Organic Chemistry*; Plenum Press: New York, 1975.
- (60) Ovchinnikov, A. A. Multiplicity of the Ground State of Large Alternant Organic Molecules with Conjugated Bonds. *Theor. Chim. Acta* **1978**, *47* (4), 297–304. <https://doi.org/10.1007/BF00549259>.
- (61) Teki, Y.; Matsumoto, T. Theoretical Study of Dynamic Electron-Spin-Polarization via the Doublet-Quartet Quantum-Mixed State and Time-Resolved ESR Spectra of the Quartet High-Spin State. *Phys. Chem. Chem. Phys.* **2011**, *13* (13), 5728–5746. <https://doi.org/10.1039/c0cp01752c>.
- (62) Borden, W. T. Can a Square or Effectively Square Singlet Be the Ground State of Cyclobutadiene? *J. Am. Chem. Soc.* **1975**, *97* (21), 5968–5970.
- (63) Kollmar, H.; Staemmler, V. A Theoretical Study of the Structure of Cyclobutadiene. *J. Am. Chem. Soc.* **1977**, *99* (11), 3583–3587.
- (64) Atherton, N. M. (Neil M. *Principles of Electron Spin Resonance*; Ellis Horwood PTR Prentice Hall: New York, 1993.
- (65) McConnell, H. M. Indirect Hyperfine Interactions in the Paramagnetic Resonance Spectra of Aromatic Free Radicals. *J. Chem. Phys.* **1956**, *24* (4), 764–766. <https://doi.org/10.1063/1.1742605>.
- (66) Wasserman, E.; Snyder, L. C.; Yager, W. A. ESR of the Triplet States of Randomly

Oriented Molecules. *J. Chem. Phys.* **1964**, *41* (6), 1763–1772.

<https://doi.org/10.1063/1.1726156>.

- (67) Heisenberg, W. Über Die Spektren von Atomsystemen Mit Zwei Elektronen. *Zeitschrift für Phys.* **1926**, *39* (7–8), 499–518. <https://doi.org/10.1007/BF01322090>.

PART A. Polyradicals

II. High Spin Organic-Based Polyradicals

II.1. History and current work.

Implementing non-disjoint, non-Kekulé molecules into polymers as a way of creating ferromagnetically-coupled, high spin materials was proposed nearly five decades ago, and since then an extensive amount of work has been done to create such polymers and materials.¹⁻⁶ Mataga's proposal from 1968 suggested using carbenes as the route for accessing high-spin materials because carbene monomer units provide a spin quantum number of $S = 1$, two spins for each unit as they consist of a carbon atom that has two half-filled p orbitals and the exchange coupling between neighboring carbenes is large.¹ By 1986, Iwamura had developed and implemented a synthetic methodology for accessing polycarbenes, which involved the photolysis of polydiazocompounds which could be produced from polyketones using hydrazine, that

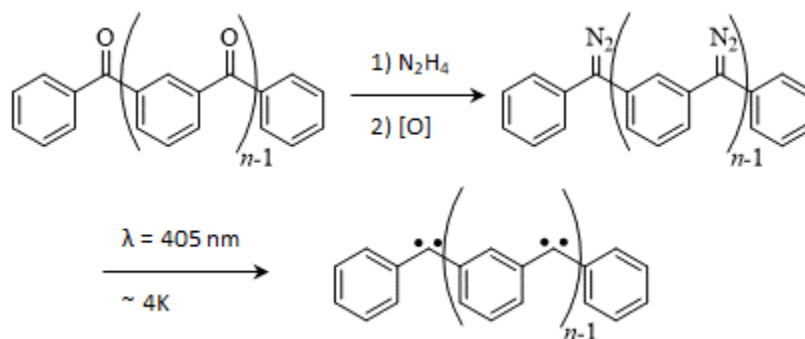


Figure II-1. The synthetic route to polycarbenes used by Iwamura in 1986.

produced polycarbenes which were found to be in the high-spin ground state (Figure II-1).⁷

High-spin ground state results from the delocalization of one of the electrons in the half-filled p orbitals, the other electron is localized due to its orthogonality with the π -system. While these carbenes produced high spin polyradical, they are highly unstable. The photolysis needed to be conducted under an inert atmosphere at 4.2 K in the EPR cavity in order to collect the spectra before the carbenes reacted. Itoh used carbene pendant groups as a route for synthesizing a high

spin polymer with a poly(vinylene) backbone with an average molecular weight of 86 000 corresponding to a degree of polymerization of 190.⁸ The delocalized electron of a diaryl carbene has thermodynamic stability, which is stabilizing radicals by delocalization. This carbene also implemented neighboring bromines and methyl groups in order to afford some kinetic stability to the carbene, which is employing bulky functional groups to shield the radical and reduce its ability to react. They succeeded in generating carbenes that persisted for several days as long as

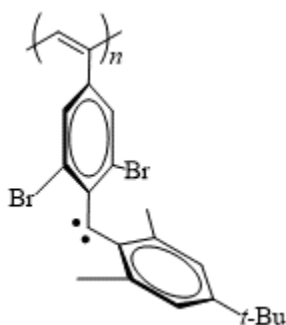


Figure II-2. Itoh's high spin polyradical with a DP = 190.⁸

they are kept in an inert atmosphere at 5-10 K.⁸ The polycarbene shown in Figure II-2 displays a much lower spin multiplicity than would be predicted, which implies either the generation of the triplet carbenes was incomplete or there are many antiferromagnetic interactions, as the authors note, the latter is probably due to intermolecular antiferromagnetic interactions between the polymer chains, given that the diazo stretch disappeared in IR after irradiation. Inter- and intramolecular interactions leading to antiferromagnetic coupling in a bulk material is an ever present ubiquitous issue that must be addressed when attempting to make high spin materials.⁹⁻¹⁴

Figure II-3 shows how non-Kekule, non-disjoint polyradicals can give rise to a bulk antiferromagnetic interaction despite being ferromagnetically coupled within the polymer chain. Figure II-3a shows a typical example of mono-organic radicals in a crystal structure. The solid is dominated by antiferromagnetic, through-space interactions between the NBMOs of adjacent

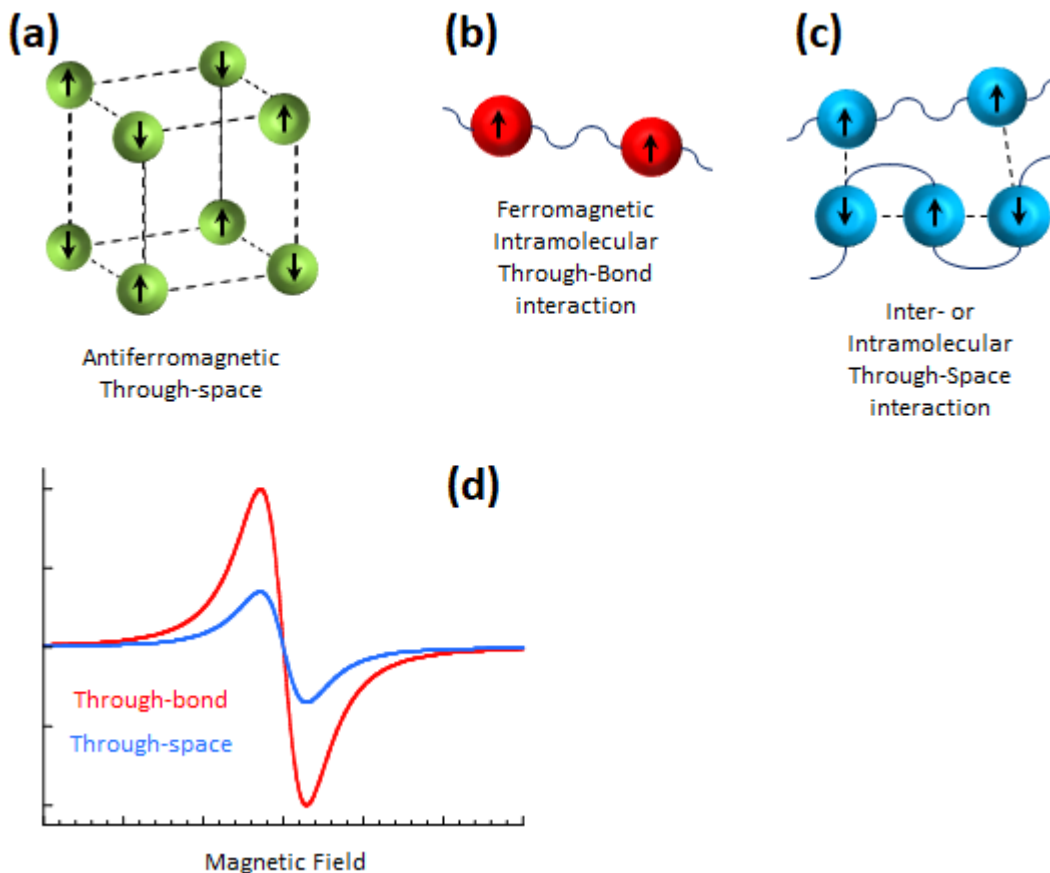


Figure II-3. Ferromagnetic (solid) and antiferromagnetic (dashed lines) interactions in materials. **A)** Most organic radicals suffer from net antiferromagnetic interactions in solid phase. **B)** Ferromagnetic coupling for isolated, non-Kekulé, non-disjoint polyradicals. **C)** Types of antiferromagnetic interactions in polyradicals. **D)** EPR spectra of theoretical polyradicals from **B** (red) and **C** (blue).

molecules, note that in the cartoon model in (a), each electron in each circle, representing a molecule (NBMO), has the opposite spin as its nearest neighbors. Of course, there are some notable exceptions to mono-organic radicals that exhibit ferromagnetic coupling in the solid, such as crystals of galvinoxyl and *p*-nitrophenyl nitronylnitroxide.¹⁵⁻¹⁸ These examples arise from the orthogonality between adjacent NBMOs in the crystal structure. Figure II-3b shows two radical units of a polyradical which is through-bond ferromagnetically coupled and is free from intra- and intermolecular through-space interactions. Figure II-3c shows radical repeat units in a polymer that have the ground-state spin lowered due to antiferromagnetic through-space intra- and intermolecular, horizontal and vertical dashed lines, respectively, which arises from non-

orthogonal overlap of the NBMOs in three-dimensional space. Figure II-3d shows an example EPR spectrum of (b) (red) and (c) (blue) assuming equal concentrations of radicals in each sample, the signal is stronger for (b) than (c) because the ground state spin is not being lowered due to antiferromagnetic interactions and is maximized by the intended ferromagnetic coupling and so (b) has more paramagnetic character. This through-bond ferromagnetic vs. through-space antiferromagnetic interactions were demonstrated by Winter et al. using radical cation viologen-containing polymers, where a macrocycle, cucurbituril, was added to a solution of the polymer to non-covalently separate the viologen radicals and manifested in an increase in the EPR signal intensity.¹⁹ Separating the viologen units from each other allowed the ferromagnetic, through-bond (σ -system, in this case), to govern more of the system and increase the ground-state spin.

Much of the early work for designing high-spin polymers was done by implementing triarylmethyl radicals into organic networks, Rajca made several such polyradicals (Figure II-4)

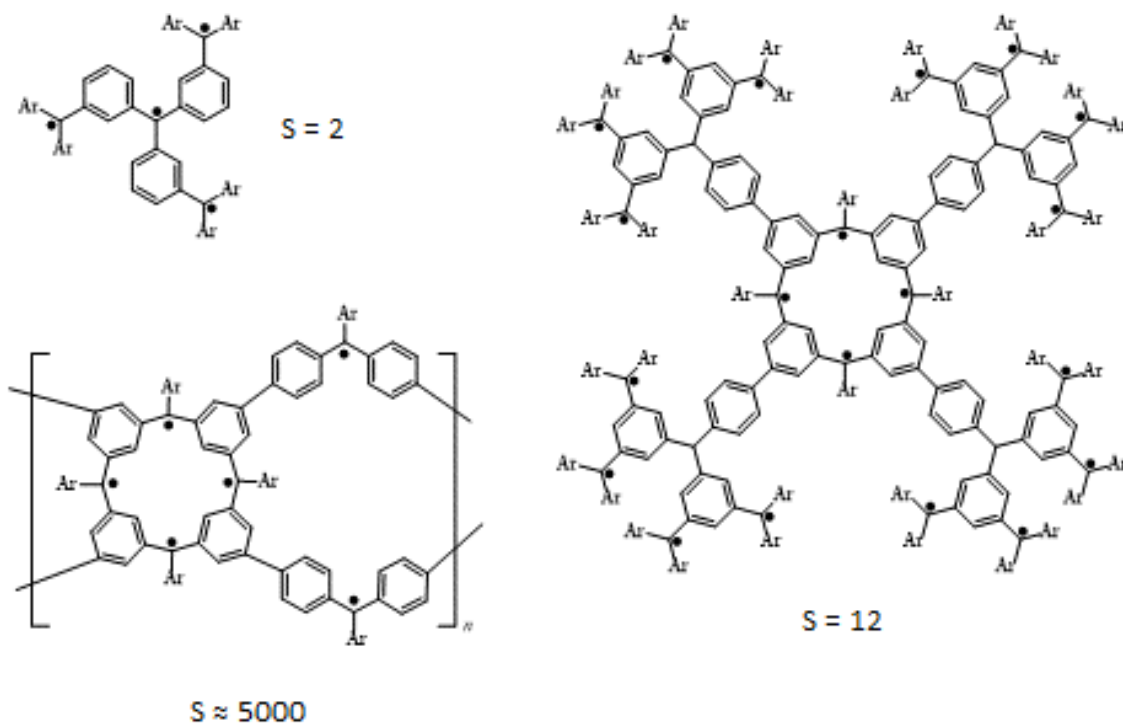


Figure II-4. Several polyradicals synthesized by Rajca et al.

in the 1990s of varying spins: $S = 2, 6, 12, 5000$.^{20–24} These polyradicals were synthesized with ever increasing numbers of spins all the way to the $S = 5000$ at 10 K polyradical shown in Figure II-4, which is the highest number of spins in an organic-based material. Unfortunately, many of these polyradicals lack the ability to be implemented in applications due to thermal instability, oxygen sensitivity, and complex synthetic procedures required for preparation.^{20,24–27} For example, the dendritic polyradical with $S = 12$, shown in Figure II-4 was prepared, like most, through a stepwise series of lithium-halogen exchanges, then lithium-metal exchange, followed by palladium-mediated cross-coupling reactions. The polyradical was generated from its carbanion precursor via oxidation by Na/K alloy conducted at 170 K in an inert atmosphere. Annealing this polyradical at room temperature for 30 min resulted in an EPR signal 30% of the original value.²⁷ The stability issue of triarylmethyl monomer repeat units has been attempted to be circumvented by using triarylaminium radical cations in their place.^{14,28–30} Triarylaminium radicals are structurally similar to triarylmethyl radicals with the exception that their radical centers are nitrogen-centered radical cations, the more electronegative nitrogen affords the radical more stability and retains the thermodynamic stability from the delocalization into the aryl rings.²³ Bushby et al. proposed a theoretical high-spin polymer of triarylaminium radical

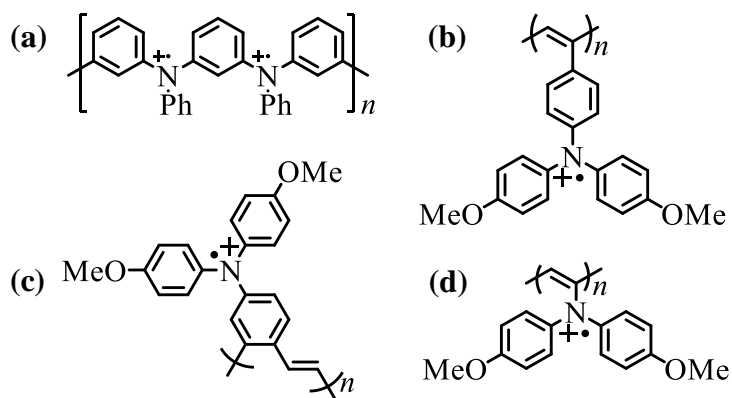


Figure II-5. Triarylaminium polyradicals (a) theoretical polyradical proposed by Bushby et al. (b-d) polyradicals synthesized by Nishide et al.

cations (Figure II-5a), initially thought to be robust, however attempts to make a tetramer of the polyradical with all four nitrogen atoms oxidized failed.³⁰ The oxidation potential for the next oxidation was too high and only up to the consecutive diradical could be formed. Nishide et al. has synthesized polyradicals (Figure II-5b-d) other than finding that (b) and (d) form chiral helical polymers in solution, (b-d) indeed have much better stability than the triarylmethyl analogs, with half-lives at room temperature in powder form of one month when phosphorous hexafluoride (PF_6^-) is used as a counter ion and only two weeks when BF_4^- is used, and (b-d) also had relatively high spin concentrations of 0.98, 0.89, 0.96, respectively.^{14,31} A great number of

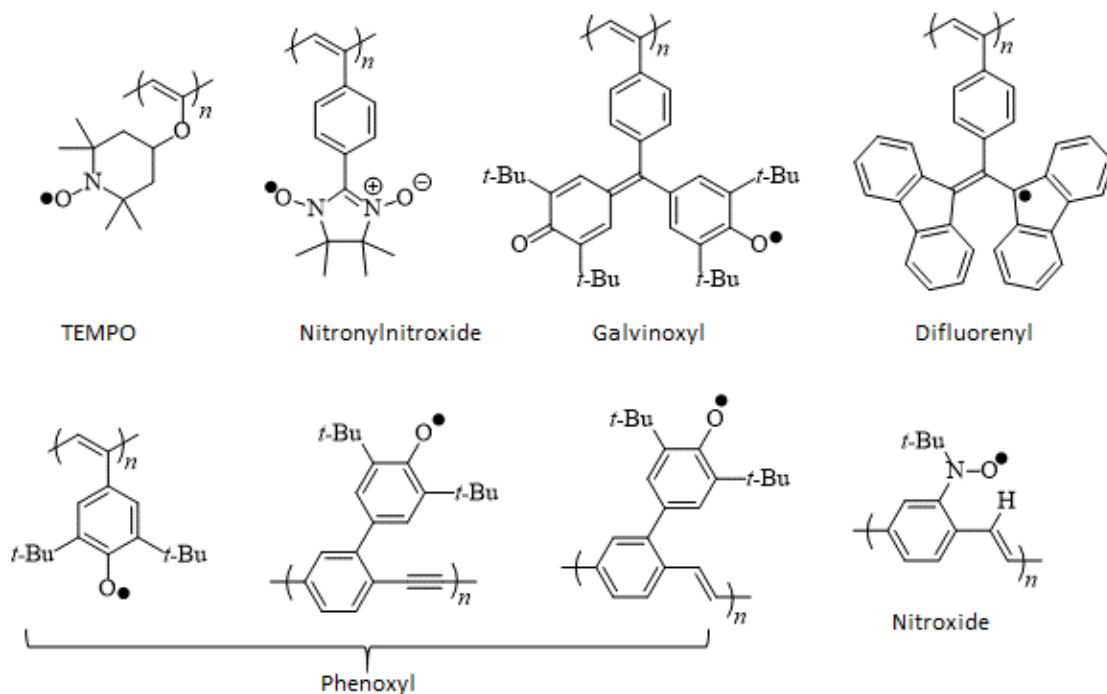


Figure II-6. Several polyradicals bearing stable-organic radicals as pendant groups that have been synthesized.

polyradicals have been synthesized using a variety of known stable organic radicals: galvinoxyl, nitroxides, phenoxyl, TEMPO, and their derivatives, just to name a few (Figure II-6).^{2,9,32-37} The polymers shown in Figure II-6 are representative of the types of organic radical substituents and the types of conjugated polymers that are used as backbones. The top row and the first polymer

in Figure II-6 shows that poly(vinylene) is a common conjugated polymer backbone to use when designing polyradicals, due to the facility of the polymerization which is to start with the monomer unit containing a terminal alkyne followed by the polymerization with a rhodium catalyst in an organic base.^{2,31,33} The poly(*p*-phenylvinylene) and poly(*p*-phenylethynylene) backbones are also fairly common in literature, the syntheses gain another level of complexity because monomer units must be synthesized that are functionalized with both a the alkyne/alkene and an aryl halide or other leaving group for either a Heck or Sonogashira polymerization.^{9,32,34,37,38} In terms of device applications, the vinylene versions of these polymers are more appealing than the ethynylene due to more efficient charge transport through alkene π -systems rather than alkyne.³⁹ There are a few examples of the *ortho* and *meta* versions of these polymer chains in literature.^{9,32,38,40,41} The *meta* versions of these polymers are typically undesirable when attempting to make high-spin polymers because it is impossible to make a *meta*-phenyl-linked homopolymer with radical pendant groups due to the positioning of the radical in the positions left on a phenyl ring after the *meta* linkages are considered (Figure II-7a). If the radical is *meta* to the backbone linkages, the radicals will be non-Kekulé and disjoint leading to antiferromagnetic coupling between neighboring units. If the radical is *ortho/para* to

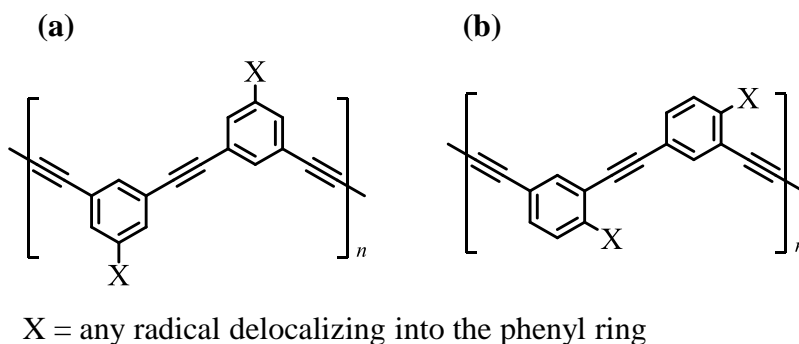


Figure II-7. (a) Radicals positioned *meta* to the poly(*m*-phenyleneethynylene) backbone are going to be non-Kekulé and disjoint and (b) radicals positioned *ortho/para* to the backbone are going to give rise to a Kekulé molecule.

the backbone linkages, the molecule will be a Kekulé hydrocarbon (i.e. no NBMOs) as shown in Figure II-7b. Although there are examples of poly(*m*-phenyleneethynylene) radical polymers bearing TEMPO and galvinoxyl radicals, but TEMPO and galvinoxyl lack pathways for delocalization into the backbone, so the connectivity would be disjoint and lead to antiferromagnetic coupling anyway.^{9,40} Of the radicals used in the conjugated polymers shown in Figure II-6, only the phenoxyl and nitroxide polymers will lead to high-spin polyradicals because both of these organic radicals can delocalize into the backbone.^{34,42,43} However, polymers bearing nitroxide pendant groups have most of their spin density localized across the N-O bond and typically exhibit through-space antiferromagnetic coupling and high-spin polymers of these have not yet been synthesized and the nitroxide polyradical shown is unstable and decomposes due to the radical reacting with the shown-alkene hydrogen atom.⁴³ As mentioned before, TEMPO does not have a path for delocalization into the conjugated polymer due to the having the spin localized across the N-O bond and being isolated on either side by sp³ hybridized carbons.⁴³ Nitronylnitroxides are localized in the pendant group due to a node at the central carbon in the SOMO which has been determined both by Hückel MO Theory and by DFT calculations.⁴⁴ Galvinoxyl and the difluorenyl polyradicals, similar to nitronylnitroxide, are more stable analogs of TMM and also bear a node at their central carbons in their SOMOs, preventing delocalization into the conjugated backbone, and will be dominated via through-space antiferromagnetic interactions between pendant groups.^{32,35} In recent years, the use of conjugated polymer backbones and delocalized polyradicals to lead to ferromagnetic coupling has diminished in favor of easily synthesized and high degree of polymerization aliphatic polymer backbones with a focus on the redox activity of organic radicals rather than their potential for spin alignment.

II.2. Applications of Radical Polymers.

Originally polyradicals were touted as being a novel class of materials with the sole purpose of designing inexpensive, light-weight, flexible replacements for inorganic magnetic materials.^{3,7,45} While polyradicals can and have found application in a variety of devices and materials, they are probably not going to be replacing inorganic materials any time soon. Particularly when it is considered that in an inorganic magnet, if for example, is made from a d-block metal, at best there can be five, spin-aligned electrons per atom contrast that with the simplest diradical, TMM, there are two, ferromagnetically coupled electrons per ten atoms (four carbon, six hydrogen) and TMM is unstable and requires more atoms in the π -system to provide it with thermodynamic stability (i.e. galvinoxyl, 72 atoms). Also, as discussed previously, bulk ferromagnetic character in a purely organic material at room temperature is, thus far unheard of due to antiferromagnetic through-space interactions between adjacent organic radicals in the solid state.^{3,11,15,16}

Despite this, polyradicals may be able to find application in spintronics.⁴⁶⁻⁴⁹ Calzolari et al. designed organic-inorganic hybrid, valence tautomeric molecules that with the incorporation of semiquinones as pendant groups undergo reversible 5/2 high-spin to 1/2 low-spin transitions.⁴⁶ Tagami et al. have measured the contributions of charge transport as a function of up and down spins through poly(4-phenoxy-1,2-phenylenevinylene) oligomers.⁴⁸ The phenoxy radicals are ferromagnetically coupled and were examined as bridges between two electrodes and displayed spin polarized transport. They found that the down spins carried the current more consistently and at higher current than the up spins in region of 0.1 to 0.2 V, and at voltages greater than 0.2 V, the up spins carried the majority of the current and the up spins current saturated approximately 2.6 times higher than that of the down spins. The ability of polyradicals to selectively filter spins at varying voltages would be of great interest when designing spintronic

devices, such as spin valves or spin filters. Along these lines, organic memory storage devices are of increasing interest to make lighter, smaller, and flexible devices to be used as dielectric media to replace silicon dioxide along with inorganic semiconductor-based transistors.⁵⁰⁻⁵³

The advancement of OLED technology is limited by spin statistics which indicate that 75% of electrically generated excited states are going to be triplets, unfortunately OLEDs are designed based on the fluorescence emission from singlet states, which means that the upper limit to efficiency for such devices is 25%.^{47,54,55} Which means that either phosphorescent LEDs (PhoLEDs) need to be developed or the singlet population needs increased by enhancing the intersystem crossing from the triplet to the singlet state. Wasielewski et al. have synthesized nitroxide and TEMPO perylene-3,4:9,10-bis(carboximides) (Figure II-8) which are capable of inducing electron exchange intersystem crossing mechanisms, which allows manipulations of the spin populations.⁵⁶⁻⁵⁸ In these molecules two charge recombination pathways are present, one which results in slow recombination affecting 25% and a fast recombination pathway affecting the other 75% of the spin populations. The nitroxide version has a greater influence on the control over the spin populations due to the delocalization of the radical into the phenyl ring,

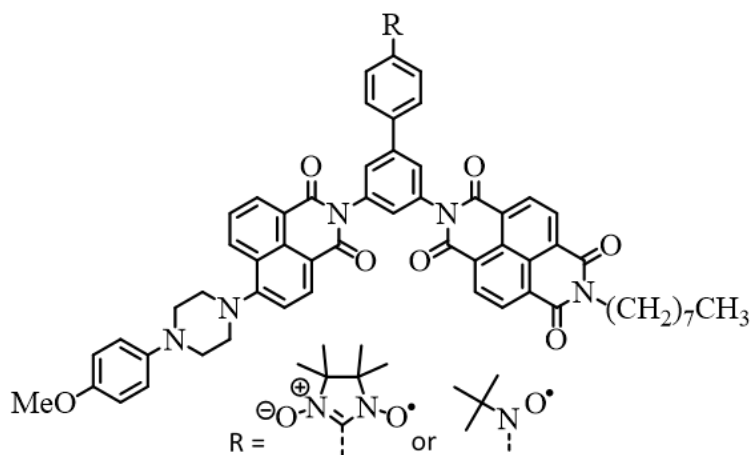


Figure II-8. Radical perylene-3,4:9,10-bis(carboximide) synthesized displaying intersystem crossing modulation.

whereas the nitronylnitroxide spin is localized.⁵⁷ Therefore, it is conceivable introducing a delocalized stable organic radical incorporated into a luminescent conjugated polymer used in an OLED device could in facilitate the modulation of the spin populations.

Recently, due to increased demand for new materials with photovoltaic properties, a few polyradicals have been prepared with this application in mind.^{10,59,60} There is already a variety of research in the field concerning conjugated polymers, but the utilization of radicals for the conversion of solar energy to assist in charge mobility in photovoltaic devices is largely untouched.^{59,61-74} Phenalenyl is of interest due to its electronic absorption spectrum that resembles the solar spectrum, the corresponding radicals are somewhat stable due to the delocalization around the phenalenyl rings, and the radicals are neutral so there are not counter

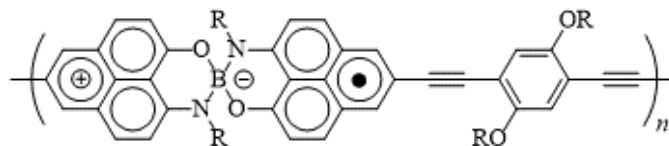


Figure II-9. TFPB polymer prepared by Yan et al.

ions.⁷⁵ Two polyradicals incorporating phenalenyl radicals into the pendant groups have been synthesized with poly(1,4-phenyleneethynylene) and polythiophene backbones with degrees of polymerization of 15 and 12 units, respectively. In solid state the poly(1,4-phenyleneethynylene) was found to be quite robust, showing no signs of decomposition in the EPR spectrum after one month, however in solution, for the same amount of time, the EPR spectrum of this polymer required magnification of 600 times in order to be able to detect the signal. A third phenalenyl polyradical incorporates the radical units directly into the backbone which allows the radicals to delocalize throughout the main chain of the polymer and exhibit stronger spin coupling with neighboring radical units.¹⁰ This polymer is a tetrakis[3,5-bis(trifluoromethyl)phenyl]borate (TFPB) (Figure II-9) which was synthesized using a Sonogashira cross-coupling reaction and the resulting polymer was then reduced with cobaltocene to give the polyradical with a degree of

polymerization of eight units which is stable in air at room temperature as a solid for weeks, exhibited ferromagnetic coupling between adjacent phenalenyl units giving a ground state spin of $S = 4$, and displayed reversible redox behavior.

The redox capability of radical repeat units is of vital interest because a radical can usually be either reversibly reduced or oxidized to act as a cathode or anode, respectively. However, one field where the redox capability of polyradicals is already being implemented is fabrication of organic batteries, the first known application of polyradical for energy storage systems was published in 2002 with the synthesis of *poly*(TEMPO methacrylate) (PTMA) and from there the field expanded into the search for stable organic radical pendant groups with aliphatic polymer backbones.⁷⁶ Delocalization of the radicals into the backbone and spin alignment are unnecessary features of these types of materials because the NBMOs of the organic radicals are just acting as sites for electrons or holes, the identity of the spin does not

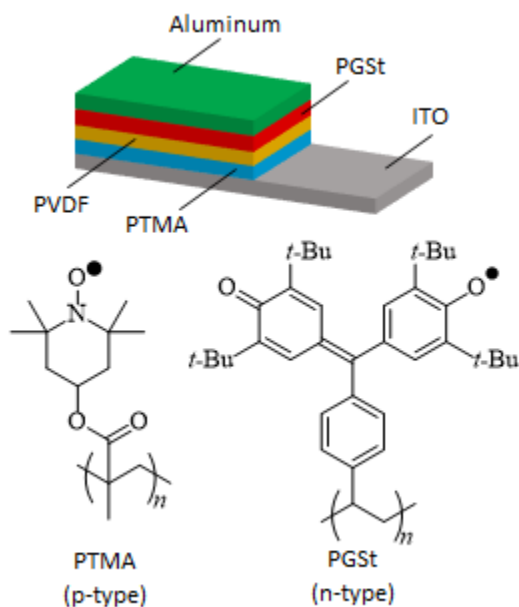


Figure II-10. Schematic of an organic radical battery with *poly*(TEMPO methacrylate) (PTMA) as the anode and *poly*(galvinoxyl styrene) (PGSt) as the cathode, separated by polyvinylidene fluoride (PVDF). Layers are not drawn to scale.

matter. Radicals can either be characterized as p-type or n-type depending on whether they are easily oxidized or reduced, respectively. Organic radicals such as TEMPO, nitroxide, and PROXYL are p-type because they are more easily oxidized than reduced because their radical lacks delocalization to provide stability, and radicals like galvinoxyl, phenoxyl and triarylaminium are more easily reduced than oxidized because their radicals are delocalized, making them n-type.⁴ Two common polyradicals that are used to make batteries are PTMA which is a n-type polyradical and serves as the cathode and *poly*(galvinoxyl styrene) (PGSt) which is a p-type polyradical and serves as the anode. Figure II-10 shows a schematic of an organic radical battery utilizing PTMA and PGSt. The device has the anode, consisting of indium tin oxide (ITO) with a layer of PTMA, the p-type material, and the cathode consisting of aluminum with a layer of PGSt. The two electrodes are assembled together by insulating them with a layer of polyvinylidene fluoride (PVDF) between them.⁷⁷ Making batteries from organic polyradicals have several advantages when compared to current inorganic salts used to make batteries that include: solution-based synthesis, relative inexpensive manufacturing, lightweight, they are modifiable, and have fast redox activity which leads to fast charging times.^{5,78-82} Also, radicals are more useful than ion for electrodes because the neutral radicals do not require counter ions.²⁹ A PTMA/carbon cathode and graphite anode device has been fabricated that is approximately the size of a business card, weighing about 20 g and is less than 4.5 mm thick and four of these connected in series operates a 200 W desktop computer without an additional power source.^{83,84} A clear indication of the potential energy storage capacity of these materials and the possibilities for the limited volume requirements. Stability is always a question when dealing with radicals, but these polymers show remarkable stability to time and reversible redox reactions. PTMA has been shown to survive more than a year in aprotic solutions of 1.0M

lithium hexafluorophosphate (LiPF_6), which is the salt that is used in Li-ion batteries.^{85,86} PGSt has also been shown to have stability when undergoing continuous redox cycling, showing only 5% deterioration after 500 CV cycles.⁷⁹ Despite the advances that have been made toward making purely organic batteries, there is still work to be done because many of these polyradicals suffer from incomplete oxidation resulting in about 70-80% of the radicals being formed.^{76,78}

II.3. Poly(*ortho*-phenyleneethynylene) (PoPE-SQ).

Even with decades of work for designing polyradicals for various applications and a variety of stable organic radicals being utilized, there is very little work with using semiquinone radicals which offer some novel features in comparison with other organic radicals. Such as the ability to incorporate metals into the polymer chain using the semiquinones as chelating ligands.⁸⁷⁻⁹⁰ Using semiquinones as ligands to bind metal cations allows for the incorporation of ancillary ligands on the metal ions to change the electronic or physical structure of the polymer

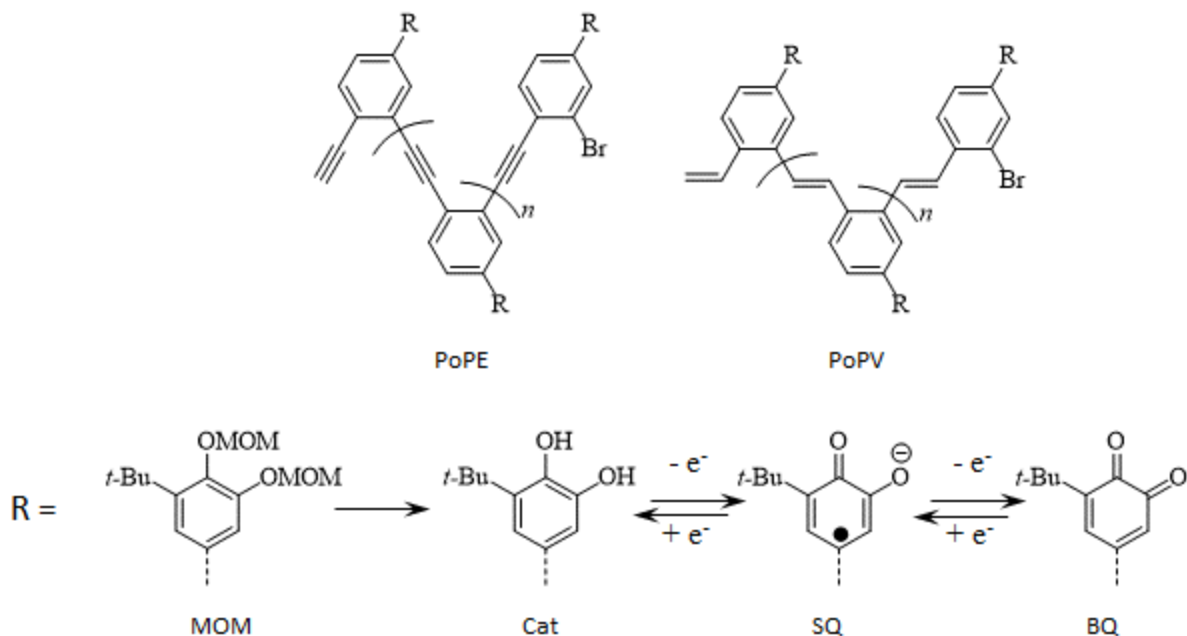


Figure II-11. PoPE and PPV polymers bearing semiquinone radicals that were originally synthesized over twenty years ago. Also shows the different oxidation states of the R group. After being deprotected to form the catechol (Cat) a one electron oxidation forms the semiquinone (SQ) and another one electron oxidation forms the benzoquinone (BQ).

and tailor the properties to suit the application, or use semiquinones to crosslink neighboring polymer chains. The polymer presented in this work is in continuance of a project that was initially started in the group over twenty years ago. The original synthesis, electrochemistry and some EPR data have been published on this polymer and includes the *poly*(1,2-phenyleneethynylene) (**PoPE**) and the *poly*(1,2-phenylenevinylene) (**PoPV**) polymers bearing semiquinone radical repeat units, both are shown in Figure II-11.³⁸ The synthesis of the **PoPE** gave oligomers with degrees of polymerization of 22-25 units and the **PoPV** gave oligomers of only about 8 units. The work that is being presented, only the **PoPE** was synthesized due to it being believed to be the easier one to synthesize and providing oligomers of higher degrees of polymerization.

First to mention the structural features of the polymer that make it coincide with the previous polyradicals that have been synthesized and then to mention the features that make it unique. First of all, the **PoPE** backbone is directly linked to the π -system of the semiquinone, which allows the semiquinone radical density to delocalize through the conjugated polymer backbone which provides thermodynamic stability for the semiquinones, which are also afforded some kinetic stability by the *tert*-butyl groups. Figure II-12a shows a trimer of the polyradical and has Ovchinnikov's "star method" applied to determine the ground-state spin of the system to show the high-spin ordering in the polyradical.⁹¹ Here the semiquinones are and can be treated like methylene radicals because the radicals only have one pathway into the conjugated backbone to make the molecule non-Kekulé. If the stars are placed starting at one of the semiquinone carbons α to the **PoPE** backbone, and starring every other carbon in the π -system, there are fifteen starred atoms and twelve unstarred atoms, which gives a ground-state spin of 3/2 for the trimer: one up spin radical for each monomer unit.

In the original work, the semiquinones were generated from the catechol using bulk electrolysis which resulted in the oligomers becoming insoluble before 25% of the coulombs had passed, which means no more than 25% of the catechol repeat units had been reduced to the semiquinone.³⁸ These semiquinones were also very unstable, given that semiquinones are radical anions, they require a counter ion to stabilize them and depending on the counter ion they can be very reactive which is the case here where they were stabilized by a tetraalkylammonium cation.

In this work, a cobalt (II) complex to react with the **PoPE-BQ** polymer and for the BQ

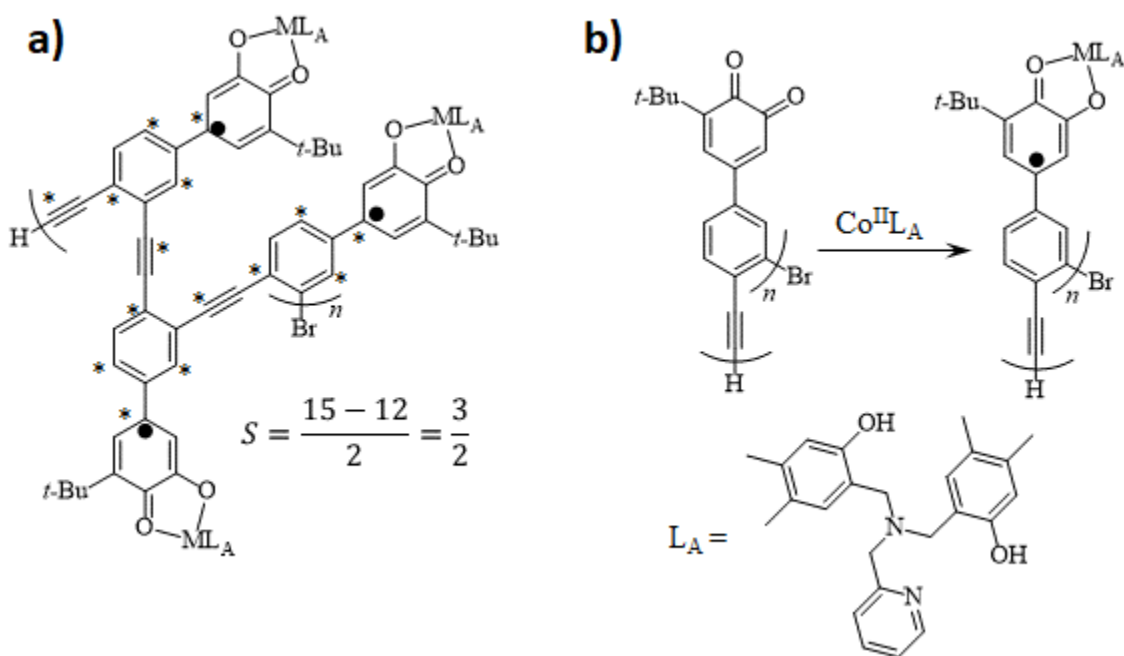


Figure II-12. a) A trimer of the **PoPE-SQML_A** polymer with the “star-method” applied to determine the ground-state spin. SQ are treated like methylene radicals appended to the backbone b) redox reaction of **Co^{II}** and **PoPE-BQ** to form **PoPE-SQCo^{III}L_A**.

and the cobalt to undergo a redox reaction to generate a **PoPE-SQ-Co^{III}** polymer as shown in Figure II-12b. Cobalt (II) was selected due to it having a stable $M^x - e^- \rightarrow M^{x+1}$ state and capability to go through this redox reaction with a benzoquinone moiety. The ancillary ligand, **L_A**, was selected to be polydentate in order to afford more stability to the **Co^{II}L_A** complex and the resulting **PoPE-SQ** by resisting the discoordination of σ -bonding substituents and having enough steric bulk to force the SQ monomer units away from each other to decrease the probability that

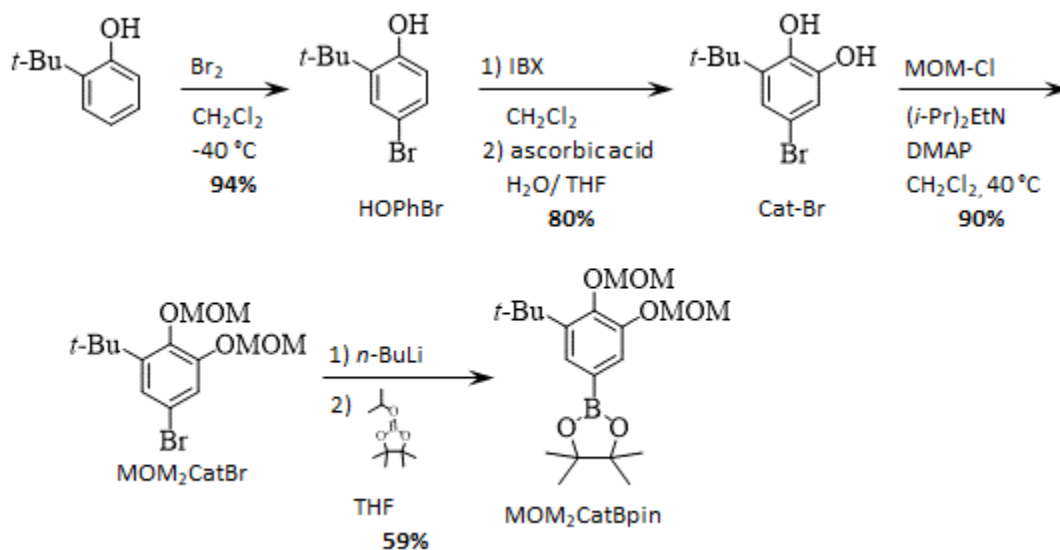
the NBMOs will have a through-space antiferromagnetic interactions. It is conceivable, that another ligand could be used to tailor the electronic or structural properties of the polymer or use an ancillary ligand that will cross-link polymer chains together.

Finally, there is great utility in using semiquinone repeat units which have the capability of chelating a variety of metal ions and are known to participate in several electronic phenomena, such as mixed valence states, valence tautomerism, and spin-crossover phenomena.^{46,87,90,92–96} These properties allows for introducing new properties and tailoring of resulting polymers' redox activity, three-dimensional structure, conductivity, magnetic interactions, and photophysical properties.

II.3.1. Synthesis of poly(o-phenylene ethynylene 4-(3-(*tert*-butyl)-4,5-bis(methoxymethoxy)-benzene) (PoPE-MOM).

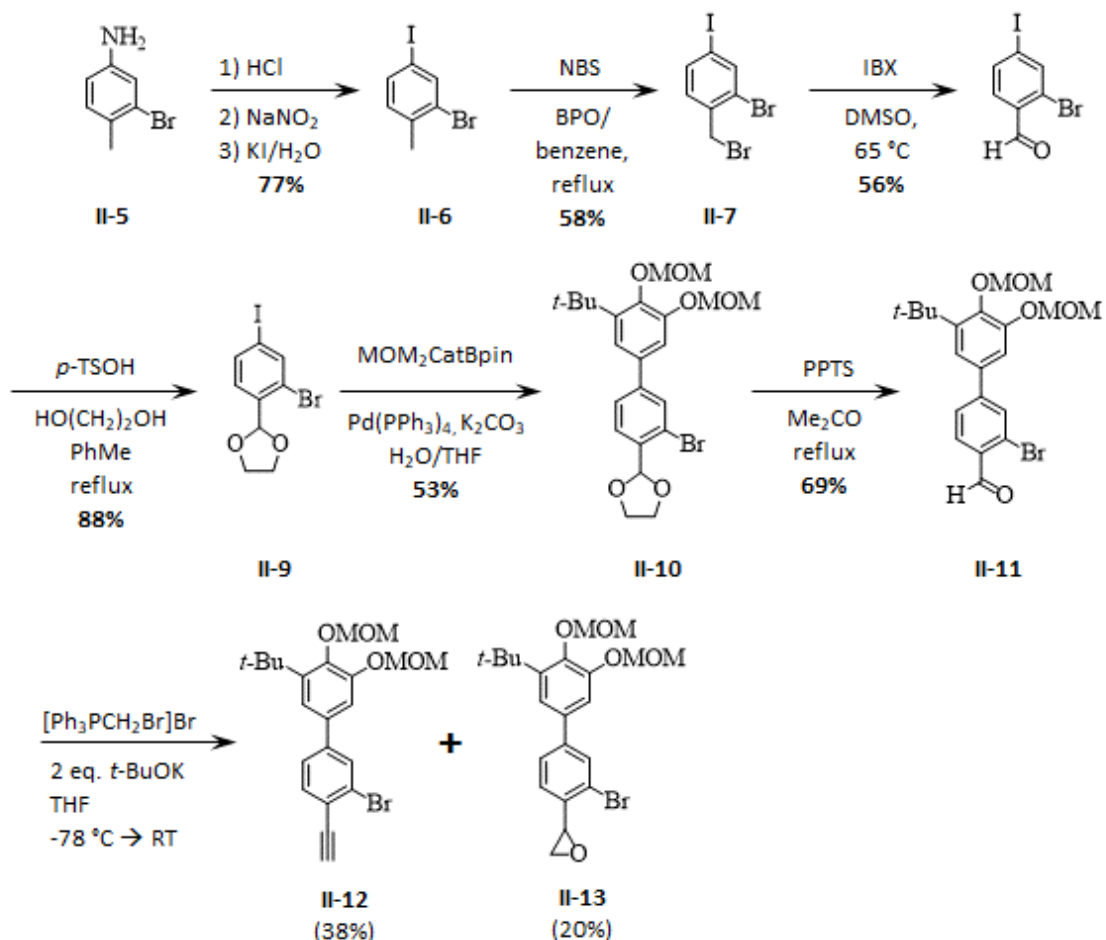
The synthesis of **PoPE-MOM** was designed based on the Shultz group's protocol for the synthesis of MOM₂CatBpin from Scheme II-1. This synthesis is integral for the donor-bridge-acceptor projects in the group and was utilized in the monomer synthesis for the preparation of the side-chain semiquinones for the conjugated polymer backbone. The synthesis of MOM₂CatBpin implements the bromination of the aromatic ring of 2-*tert*-butylphenol to make HOPhBr. Then the phenol is oxidized via an IBX-mediated oxidation to the quinone, which can then be reduced to the catechol (Cat-Br).⁹⁷ The catechol is then protected with methoxymethyl (MOM) protecting groups to make MOM₂CatBr, which is both to prevent the oxidation from ambient conditions back to the quinone and for the subsequent lithium-halogen exchange with *n*-BuLi for the installation of the boron pinacolate to make MOM₂CatBpin.

Scheme II-1. Shultz group synthetic route for pinacolyl(1,2-dimethoxymethoxy-6-*tert*-butyl-1- phenyl) boronate (MOM₂CatBpin).



As mentioned previously, the original polymer synthesis as presented in Scheme II-2 presented significant reproducibility problems. The main issue arose in steps involving the Wittig olefination of **II-11** to **II-12** using (bromomethyl)triphenylphosphonium bromide and the subsequent dehydrohalogenation to give the alkyne (**II-12**). This reaction resulted in variable and significant (variable 20-50%) impurities of an epoxide (**II-13**). This presented two problems to the monomer synthesis: 1) low yielding reactions due to the loss of starting material to the side product, which limited the amount of monomer that could be synthesized, and 2) the products of the reaction: **II-12** and **II-13** are very difficult to separate by column chromatography across a variety of solvent mixtures and compositions. Scheme II-3 was proposed as an alternative with the intent of the separation of the alkyne (**II-14**) from the epoxide (**II-15**) easier than the separation of **II-12** from **II-13**. The alkyne (**II-14**) could then be protected either with a tertiary alcohol or trialkylsilyl protecting group, the protected alkyne could then be subjected to the Suzuki coupling with MOM₂CatBpin followed by deprotection to give the monomer (**II-12**). With column chromatography **II-14** could be isolated as a colorless solid; however, yields were

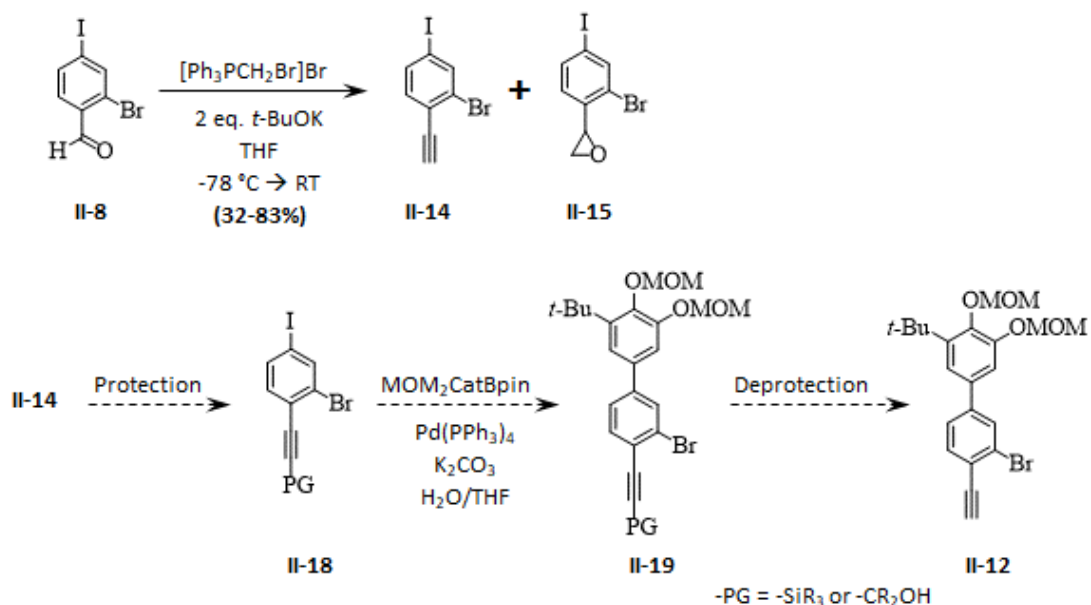
Scheme II-2. Monomer synthesis via the original Wittig reaction with (bromomethyl)triphenylphosphonium bromide.



still low and sporadic (30-40%, at best) due to the epoxide (**II-15**) formation. In an attempt to combat the formation of the epoxide impurities, the Wittig reaction was performed on 4-bromobenzaldehyde, as a model compound, to make 4-bromophenylacetylene (**II-16**) and reduce the amount of 2-(4-bromophenyl)oxirane (**II-17**) impurity.

Initially, the conditions of the reaction, such as time in between ylide formation and the introduction of the second equivalent of base, and whether the aldehyde was present during or added after the formation of the ylide. The results of these attempts (Table II-1) are that the epoxide formation followed no discernable pattern with these variables. Epoxide formation during Wittig olefination reactions where the ylide contains a leaving group alpha to the alkene-

Scheme II-3. Synthetic route by alkyne formation and protection.

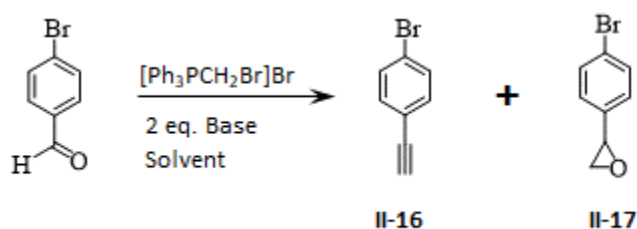


forming carbon atom is known and investigated by Arimoto, et al. and their proposed mechanism is shown in Scheme II-4.⁹⁸ This article suggested a method for reducing the formation of the epoxide by quenching the cold reaction with BF₃•Et₂O. In this case, for the conversion of 4-bromobenzaldehyde to **II-16** (Table II-1, entry 7) resulted in ~50% epoxide (**II-17**) impurity. Based on Scheme II-4 there are two points at which the epoxide formation may be able to be effected. The base can be changed to hinder the nucleophilic attack of the anion on the phosphonium ion in the second structure (on the red route). This anion in Arimoto, et al. is methoxide because their reactions were quenched with methanol.⁹⁸ In our case, this anion could latter option is unlikely, given that all Wittig reactions were carried out with anhydrous THF and the crude ¹H-NMR spectrum of the reaction mixture still shows epoxide formation comparable with the worked-up reactions. Therefore, assuming the proposed mechanism is correct, *tert*-butoxide is either be *tert*-butoxide or hydroxide, which could come from water added during work-up. This is the probable anion to contribute to the mechanism. To test this, a reaction was

carried-out using sodium hydride to act as both the base to form the ylide and to perform the dehydrohalogenation (Table II-1, entry 8). The impurity based on the integration of the epoxide protons is 11%. Despite efficient conversion of the aldehyde, sodium hydride did not allow for efficient dehydrohalogenation, there was trans-alkene as the major product, which normally will undergo *cis*-elimination with *tert*-butoxide.

The other step in the mechanism that can be used to manipulate epoxide formation is the equilibrium between the oxaphosphetane and the betaine. Implementing a more non-polar solvent would, in theory, shift equilibrium toward the uncharged oxaphosphetane by

Table II-1. Comparison of different Wittig Olefination and subsequent dehydrohalogenation conditions; test reactions performed on the conversion of 4-bromobenzaldehyde to 4-bromophenylacetylene (**II-16**).



Entry	Base	Solv.	Time between 1 st eq. base and 2 nd eq. base	Aldehyde added separately?	Epoxide ^a	Notes
1	2 eq. <i>t</i> -BuOK	THF	1h	Yes	~24%	
2^b	2 eq. <i>t</i> -BuOK	THF	1h	No	~50%	38% yield
3^b	2 eq. <i>t</i> -BuOK	THF	1h	Yes	<10%	54% yield
4	2 eq. <i>t</i> -BuOK	THF	1.5h	No	~30%	
5^c	2 eq. <i>t</i> -BuOK	THF	1.5h	Yes	~30%	
6	2 eq. <i>t</i> -BuOK	THF	Added together	Yes	~40%	
7	2 eq. <i>t</i> -BuOK	THF	1h	Yes	52%	Quenched with BF ₃ •Et ₂ O
8	2 eq. NaH	THF	1h	Yes	11 %	Alkene remaining
9	2 eq. <i>t</i> -BuOK	Et ₂ O	1h	Yes	14 %	
10^b	NaH/ <i>t</i> -BuOK	Et ₂ O	1h	Yes	1-2 %	28% yield, poor conversion.

All reactions were carried out at -78 °C and warmed to RT before addition of second equivalent of base.

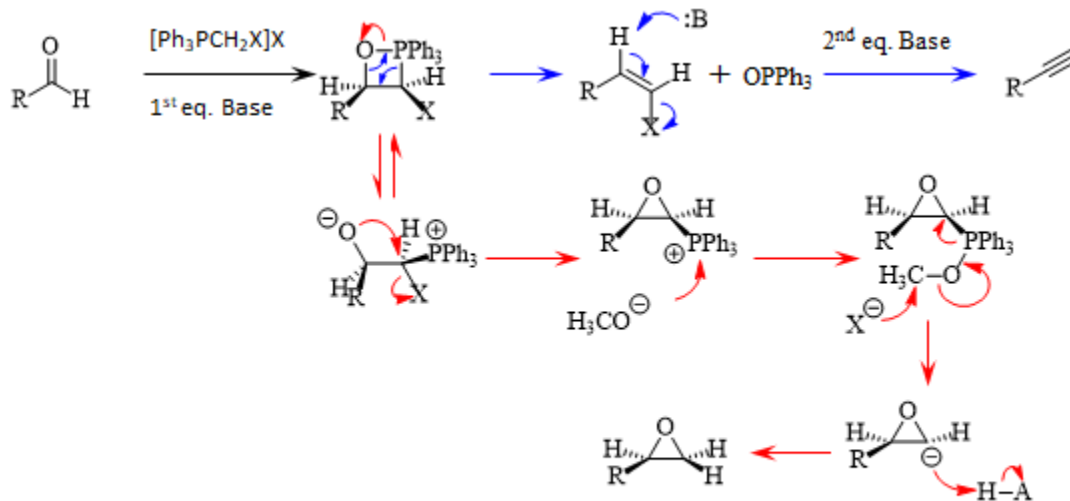
^a Epoxide formation is based on the integration of the epoxide protons in ¹H-NMR and alkyne and alkene protons.

^b Yields given are after column chromatography.

^c Reactions performed on 8 used these conditions and yields ranged from 32-83%.

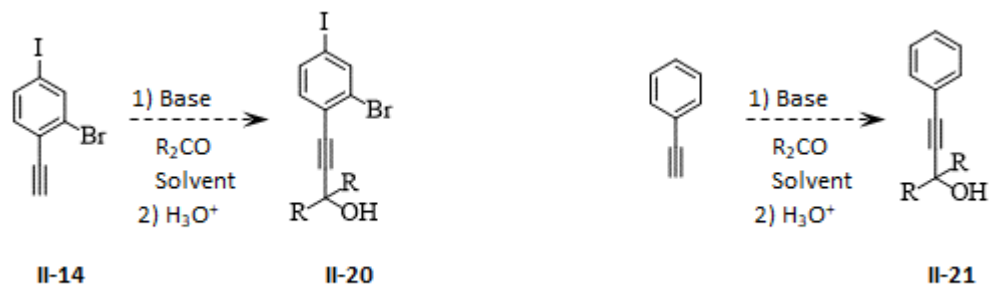
destabilizing the betaine, allowing the reaction to proceed through olefination rather than epoxidation. This hypothesis was tested by performing the reaction in Et₂O with two equivalents of potassium *tert*-butoxide as the base. Et₂O was selected because it was more non-polar than

Scheme II-4. Proposed mechanism for epoxide formation (red route) via Wittig olefination using ylides with leaving groups vs. the route for olefination formation (blue route).



THF, but would still allow for some solubility for the phosphonium salt, which has poor solubility in THF and would be poorer in a more non-polar solvent. The result (Table II-1, entry 9), was a higher impurity of epoxide than was experienced when using sodium hydride as the base (14%), but the aldehyde was fully converted to alkyne. Another reaction was carried out in Et₂O using sodium hydride as the first equivalent of base required to form the ylide and potassium *tert*-butoxide as the second equivalent of base for the dehydrohalogenation reaction. This reaction (Table II-1, entry 10) resulted in 1-2% epoxide impurity, the rest being alkyne.

Scheme II-5. Protection of the terminal aryl acetylene with a tertiary alcohol and reaction with phenylacetylene used as a model compound.



Unfortunately, this reaction only gave 28% yield due to incomplete conversion of the aldehyde, this was probably due to the combined poor solubilities of the phosphonium salt and sodium hydride in Et_2O . Attempting to modulate the epoxide formation was abandoned after these attempts in favor of continuing with the best yielding procedure (Table II-1, entry 5) for the synthesis of **II-14**.

For the protection of the terminal aryl acetylene, the Favorskii reaction to use a ketone as to form a tertiary alcohol protecting group was attempted first (Scheme II-5), given its simplicity and can be performed with acetone, acting as a relatively inexpensive protecting reagent.⁹⁹ In order to get the reagents and conditions appropriate for **II-14**, phenylacetylene was employed as a model compound. Protecting terminal acetylenes should be relatively straightforward: deprotonate the acetylene, then the acetylide will nucleophilically attack either the carbonyl carbon of a ketone or the silicon of a trialkylsilyl halide or equivalent; displacing the halide in an S_N2 reaction.

A variety of conditions, bases, solvents, and protecting reagents were implemented to try to protect the aryl acetylene (Table II-2). First, the Favorskii reaction was attempted. A problem that was encountered using Favorskii reactions was an aldol condensation side reaction. This is to be expected to some extent given the literature pK_a values for phenylacetylene and α -methyl protons to a carbonyl are 28.8 and 19-20, respectively. In these reactions, much of the ketone protecting reagent was consumed by this side reaction. Some of the test reactions provided yields

Table II-2. Attempted reactions for the protection of terminal aryl acetylene for **II-14**.

Entry	Protecting Reagent	Other Reagents	Solvent(s)/ Conditions	Phenylacetylene Test Reactions ^a	Reaction with II-14 ^a
1	acetone	LDA	THF	Aldol Cond.	little product ^d 10-20%
2	2-butanone	<i>t</i> -BuOK	DMSO	72%	15-20%
3	2-butanone	NaH	DMSO	Aldol Cond.	
4	10 eq. 2-butanone	NaH	DMSO	Aldol Cond.	
5	2-butanone	Bu ₄ NOH, NaOH	H ₂ O/PhF, 48 h	No Reaction	
6	2-butanone	Bu ₄ NOH, NaOH	H ₂ O/Et ₂ O, 48 h	~20%	
7	2-butanone	Bu ₄ NOH, NaOH	H ₂ O/Toluene, 48 h	~50%	little product ^d
8	2-butanone	Bu ₄ NOH, NaOH	H ₂ O/CH ₂ Cl ₂ , 72 h	little product ^d	
9	2-butanone	LDA	THF	Aldol Cond.	10-20%
10	2-butanone	<i>t</i> -BuOK	DMSO	~70%	~10%
11	2-butanone	CuI, TEA, KOH	DMSO, 100 KO	No Reaction	
12	TMS-Cl	Zn(OTf) ₂ , Et ₃ N	DCM	78%	No reaction
13	TMS-Cl	NaH/DMSO	THF	~20% ^a	
14	TMS-Cl	NaH	THF	~30% ^a	No reaction
15	TMS-Cl	NaH	DMSO	No reaction	
16	TMS-Cl	<i>t</i> -BuOK	DMSO	No reaction ^c	
17	TMS-Cl	LDA	THF	~60%	¹ H-NMR aromatic region complex ^b

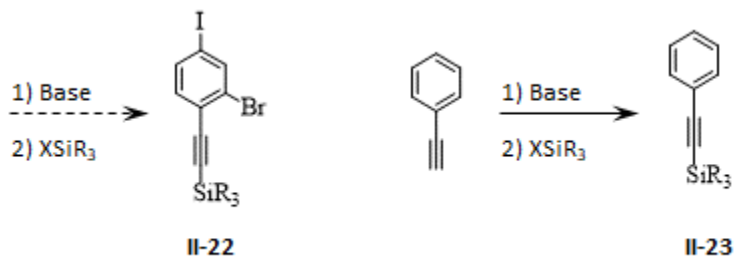
^a Percentages are conversion estimated from ¹H-NMR.

^b Side reactions occurred; very little product present.

^c ¹H-NMR indicated that it worked once, but could not be replicated

^d "little product" means less than 10% conversion by ¹H-NMR

Scheme II-6. Trialkylsilyl protection of the terminal aryl acetylene. Reaction with phenylacetylene used as a model compound.

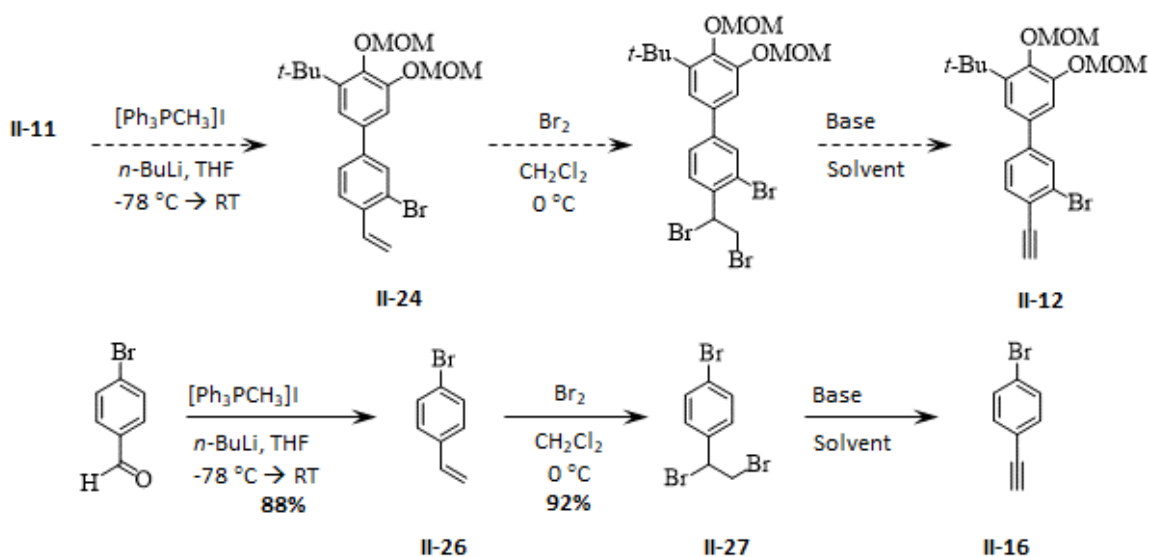


between 50-70% and were attempted on **II-14** (Table II-2, entries 2, 7, and 10). Unfortunately, these reactions performed more poorly giving lower yields (10-20%), which is undesirable for a protecting step, especially following the Wittig reaction which typically gave yields < 40%.

The next method is shown in Scheme II-6 and was to try the protection using chlorotrimethylsilane (Table II-2, entries 12-17). These reactions were mostly unsuccessful, even those that showed some promise with the model compound such as Table II-2, entries for **II-12**¹⁰⁰ and **II-17**, giving 78 and 60% yields, respectively, but did not work when applied to **II-14** or without giving side products. These issues are most likely related to the aryl halides given that it is the only difference between **II-14** and phenylacetylene. Entry 12 resulted in simply no reaction with only starting material present, while entry 17 resulted in many side products. Possibly the result of the aryl halides exchanging with the lithium from LDA. After attempts to

protect **II-14** were unsuccessful, the next strategy was to change how the alkyne was synthesized. Given that the phosphonium salt, (bromomethyl)triphenylphosphonium bromide, was the source of the low-yielding Wittig reaction, the synthetic scheme was altered to the strategy presented in Scheme II-7. This strategy consists of a Wittig reaction with methyltriphenylphosphonium iodide followed by bromination across the double bond with subsequent double dehydrohalogenation to give **II-12**. The formation of this ylide required a stronger base than potassium *tert*-butoxide, so *n*-BuLi was used, and the olefin product (**II-26**)

Scheme II-7. Synthetic route to **II-12** using Wittig reaction with methyltriphenylphosphonium iodide followed by bromination of the double bond and double dehydrohalogenation.



was then brominated and **II-28** was synthesized in good overall yield (84%). The conversion from the dibrominated product (**II-25**) to **II-12** required more synthetic method development and 1-bromo-4-(1, 2-dibromoethyl)benzene (**II-27**) was used as a model to make **II-16**, the results of these tests are shown in Table II-3. None of the bases that were attempted showed any of the desired product in $^1\text{H-NMR}$.

A literature search revealed that for the model compound provided access to the ethyl propiolate via the ethyl 2,3-dibromophenylpropanoate.^{37,101,102} This strategy seemed to have

Table II-3. Conditions for test double dehydrohalogenation reactions to make **II-16**.

Entry	2.5 eq. Base	Solvent	Temperature	Results
1	<i>t</i> -BuOK	THF	RT	No desired product
2	KOH	EtOH	RT	No desired product
3	K ₂ CO ₃	DMSO	RT	No desired product
4	<i>t</i> -BuOK	THF	Reflux	No desired product
5	KOH	EtOH	Reflux	No desired product
6	K ₂ CO ₃	DMSO	Reflux	No desired product

“No desired product” means that the alkyne proton was not observed in ¹H-NMR. All conditions resulted in at least the reaction that generated the *trans*-alkene (**II-27**). At higher temperatures other signals appeared in the NMR spectra.

some promise for dehydrohalogenation. The ethyl propiolate can be hydrolyzed to give the propiolic acid, which in theory, if the conditions are right, an anion could be stabilized by the acetylide, which would allow for decarboxylation to give a terminal alkyne. As shown in Scheme II-8, the alkyl propiolate could be generated, then Suzuki coupled to MOM₂CatBpin, followed by saponification and decarboxylation of the alkyl propiolate (**II-32**). **II-31** could be synthesized from **II-8** in high yield in comparison to the synthesis of the terminal alkyne **II-14**. The facile synthesis of **II-28** was performed with another Wittig reaction using (ethyl ester methyl)triphenylphosphonium bromide and under very mild conditions for the reaction: K₂CO₃ as the base to form the ylide, the reaction was biphasic in CH₂Cl₂ and water, and under ambient conditions and provided a 94% yield after filtering through a pad of silica to give a mixture of *trans* and *cis* alkenes in a 88:12 ratio. Both alkenes were subject to bromination which gave a mixture of two sets of diastereomers each with an enantiomer which arose from the anti bromination across the double bond on each alkene isomer to give **II-29** as a pure product of

isomers in a 96% yield. For the double dehydrohalogenation to generate the alkyl propionate, two equivalents of base were used initially; however, instead of both dehydrohalogenations occurring consecutively, one anti-elimination occurred and then the ester was hydrolyzed, which generally afforded little if any of the ethyl propionate. Therefore, an excess of base (3.5 eq.) was used to complete the conversion to propionic acid (**II-30**), which exhibited carbon-carbon triple bond and carbonyl stretches in the IR spectrum at 2206 and 1662 cm^{-1} , respectively. Table II-4 summarizes the bases and conditions to complete the conversion, with entry 4 being the first set of conditions that successfully provided the desired product. Given that palladium can catalyze decarboxylative cross-coupling reactions, the propionic acid (**II-30**) needed to be reprotected, to give **II-31**, before being subjected to Suzuki conditions.^{103,104} After the successful Suzuki

Scheme II-8. Access to **II-12** via Wittig reaction with (ethyl ester methyl)triphenyl-phosphonium bromide to give the ethyl propionate; serving as the protected alkyne.

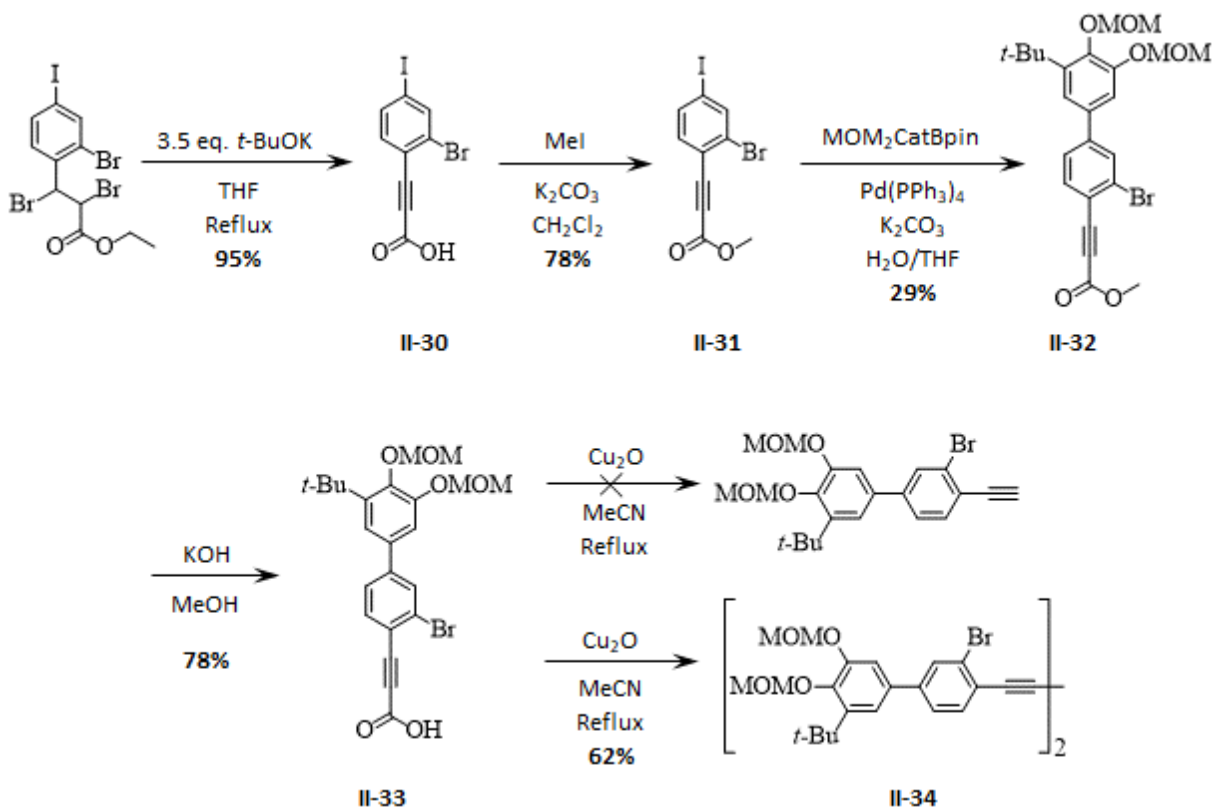


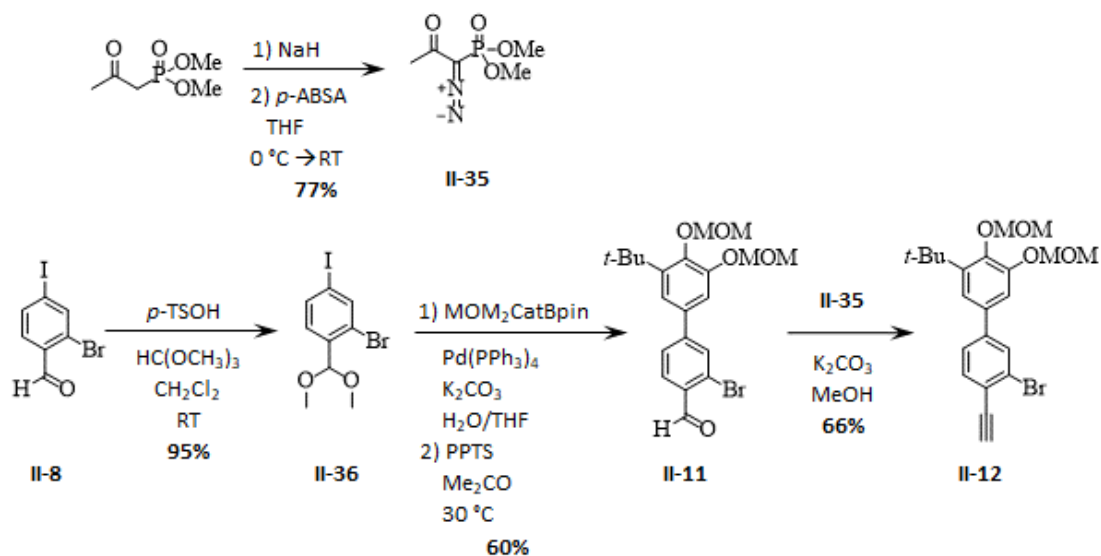
Table II-4. Conditions for test double dehydrohalogenation and hydrolysis reactions to make **II-16**.

Entry	3.5 eq. Base	Solvent	Temperature	Results
1	K ₂ CO ₃	DMSO	Reflux	Product mixture
2	KOH	DMSO	Reflux	Product mixture
3	NaH	EtOH	Reflux	Product mixture
4	KOH	EtOH	Reflux	Product mixture
5	t-BuOK	THF	Reflux	95%

“Product mixture” is a mixture of intermediates consisting of trans-alkenes both the cinnamic acid and ester.

coupling to give **II-32**, which was then deprotected with NaOH in methanol to give **II-33**. To get **II-12** it was then stirred with Cu₂O in MeCN at reflux under anaerobic, anhydrous conditions, with the intent of decarboxylation, which worked successfully in 70% yield as a test reaction with 3-(4-bromophenyl)propionic acid.^{105–107} However, when applied to **II-33**, the result was not **II-12**, the spectra resembled **II-12**, but with the ¹H-NMR missing the alkyne proton at δ = 3.42

Scheme II-9. Synthesis of **II-12** via the Ohira-Bestmann reaction.

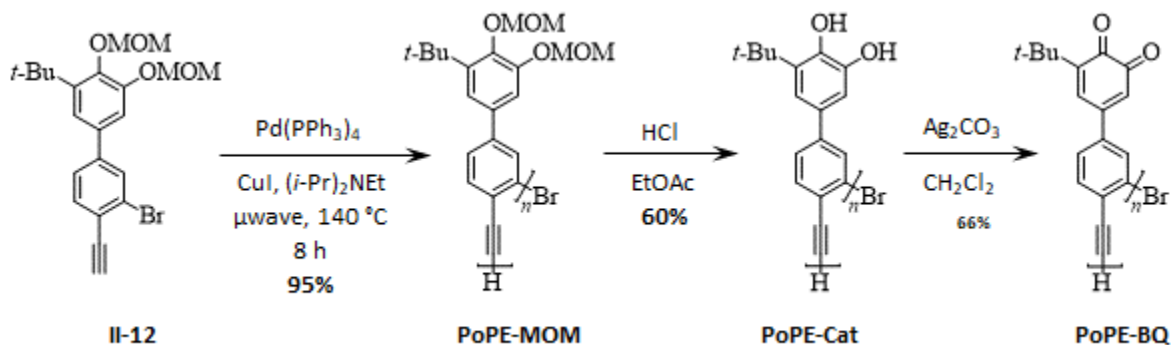


and a weak carbon-carbon triple bond stretch in the IR spectrum at, which **II-12** does not exhibit. These data suggest that the product of the reaction is the diyne **II-34**. Unfortunately, the dimerization of propiolic acids with a copper (I) salt is a known name reaction, known as a Hay coupling, and have been used in the synthesis of diynes.^{103,104,108} Hay couplings require an oxidant, the oxidant under these conditions is unknown. The MeCN was degassed by a stream of nitrogen for 24 h and the reaction was assembled in an air-free glovebox. After the unsuccessful decarboxylation, a different reagent was proposed for an old reaction.

For the conversion of **II-11** to **II-12**, the Ohira-Bestmann reaction was considered (Scheme II-9), which required the synthesis of dimethyl (1-diazo-2-oxopropyl)phosphonate (the Ohira-Bestmann reagent, **II-35**), which can be done so in a 77% yield and can be stored cool (-20 °C) without decomposition..^{109,110} Scheme II-9 also has the pre-Suzuki coupled aldehyde protecting group changed from the ethylene glycol acetal (**II-9**) changed to a dimethyl acetal (**II-36**). The reason for this change is that after the Suzuki coupling the deprotection of **II-10** always resulted in the loss of one of the MOM protecting groups, which needed to be reprotected and resulted in lower yields and more complicated separations. Going from **II-8** to **II-11** with **II-9** and **II-10** as intermediates is a 36% overall yield, but going from **II-8** to **II-11** with **II-36** as the intermediate followed by deprotection before work-up of the Suzuki coupling gives a 54% overall yield.

When **II-35** is used on **II-11** using anhydrous K₂CO₃, and anhydrous, degassed MeOH under anaerobic conditions, **II-12** is obtained as the only product on TLC above the baseline (10% EtOAc/hexanes).^{109,111} After passing the crude material through a pad of deactivated silica, **II-12** is obtained in 66% yield as a colorless solid.

Scheme II-10. Polymerization of **II-12** followed by deprotection to the catechol (**PoPE-Cat**) and oxidation to the quinone polymer (**PoPE-BQ**).



The Sonogashira polymerization (Scheme II-10) of **II-12** was initially conducted with literature precedent, with $\text{Pd(PPh}_3)_2\text{Cl}_2$, CuI in 1:1 Et_3N :pyridine at reflux with conventional heating methods.³⁸ When this method was attempted, gel permeation chromatography (GPC) indicated a monodisperse oligomer with an average molecular weight (M_n) corresponding to a degree of polymerization (DP) of pentamers. This result was confirmed via MALDI-TOF mass spectrometry. A decamer would be the lower limit of what would be a suitable DP, 15-20 units would be better. Therefore, a series of polymerizations with varying reaction conditions were attempted to try to increase the DP; Table II-5 shows the results of these trials. Initially conventional heating methods were used to heat the Sonogashira polymerization reactions, however none of the trials provided any polymers with a DP above a hexamer. In order to

achieve DP higher than six, a microwave reactor was employed to achieve higher temperatures and shorter reaction times. Different amine bases were used, Hunig's base is has been shown to be one of the better bases for microwaved Sonogashira reactions and the catalyst, Pd(PPh₃)₂Cl₂ was swapped for Pd(PPh₃)₄ over concerns that the initial reduction of the palladium (II) catalyst by the reductive elimination of dimerized starting material was leading to polymers (oligomers) that may have head-to-head or tail-to-tail linkages, which in the semiquinone polymer would result in antiferromagnetic coupling somewhere in the middle of the polymer chain and lower the overall spin quantum number. The best trial in the series was entry 8, using the palladium (0) catalyst with Hunig's base as the solvent in the microwave reactor (T= 140 °C, μwave power = 140 W) which gave PoPE-MOM with an average molecular weight (M_n) of 6.1 kDa, corresponding to a DP of 17-18 with a polydispersity index (PDI) of 1.35. The ¹H-NMR spectrum of PoPE-MOM was similar to the monomer, II-12, but showed broader signals in the aromatic, methyl and methylene MOM, and *tert*-butyl group regions, characteristic of a

Table II-5. Sonogashira polymerization reactions.

Entry	Catalyst	Solvent*	Temp.	Time (h)	Method	M _n (DP)	M _w (DP)	PDI
1	Pd(PPh ₃) ₂ Cl ₂	1:1 Et ₃ N: Pyr	Reflux	24	Conventional	1800 (~5)	1900 (5-6)	1.10
2	Pd(PPh ₃) ₂ Cl ₂	1:1 Et ₃ N: Pyr	Reflux	48	Conventional	1800 (~5)	1900 (5-6)	1.10
3	Pd(PPh ₃) ₂ Cl ₂	Piperidine	106 °C	24	Conventional	1781 (~5)	2013 (5-6)	1.13
4	Pd(PPh ₃) ₂ Cl ₂	3:2 Et ₃ N: THF	Reflux	6	Microwave (100 W)	2414 (6-7)	3111 (8-9)	1.29
5	Pd(PPh ₃) ₂ Cl ₂	Et ₃ N	90 °C	6	Microwave (100 W)	3742 (10-11)	4853 (13-14)	1.30
6	Pd(PPh ₃) ₄	(<i>i</i> -pr) ₂ NH	85 °C	6	Microwave (110 W)	4111 (11-12)	5148 (14-15)	1.25
7	Pd(PPh ₃) ₄	(<i>i</i> -pr) ₂ NEt	140 °C	6	Microwave (130 W)	5316 (~15)	6530 (18-19)	1.23
8	Pd(PPh ₃) ₄	(<i>i</i> -pr) ₂ NEt	140 °C	8	Microwave (140 W)	6147 (17-18)	8297 (23-24)	1.35

* In all cases the base for the Sonogashira reaction is the solvent

monomer. The terminal alkyne proton signal was obscured by the methyl MOM signals and significantly smaller given the oligomer chain length. The FT-IR spectrum showed alkyl and aromatic C-H stretches, looking similar to the monomer, but a reduced alkyne C-H stretch.

After polymerization the **PoPE-MOM** was deprotected using aqueous 12 M HCl in EtOAc to give the catechol polymer (**PoPE-Cat**) (Scheme II-10). The $^1\text{H-NMR}$ showed the loss of the MOM groups. The FT-IR spectrum showed a broad O-H stretch from 3500-3100 cm^{-1} and a stronger aromatic C-O stretch at 1594 cm^{-1} (Figure II-13). The **PoPE-Cat** then underwent a two electron oxidation with Fetizon's reagent to give the quinone polymer (**PoPE-BQ**) which the $^1\text{H-NMR}$ spectrum was not diagnostic given that only the catechol protons changed and did not appear in the $^1\text{H-NMR}$ spectrum of **PoPE-Cat**.¹¹² The FT-IR spectrum showed the loss of the O-H stretch and showed a quinone C=O stretch at 1658 cm^{-1} . **PoPE-BQ** can undergo a one electron reduction (Scheme II-11) to give the semiquinone radical polymer (**PoPE-SQ**) using either electrochemical or chemical means.³⁸ To make **PoPE-SQ**, a stable metal complex capable of

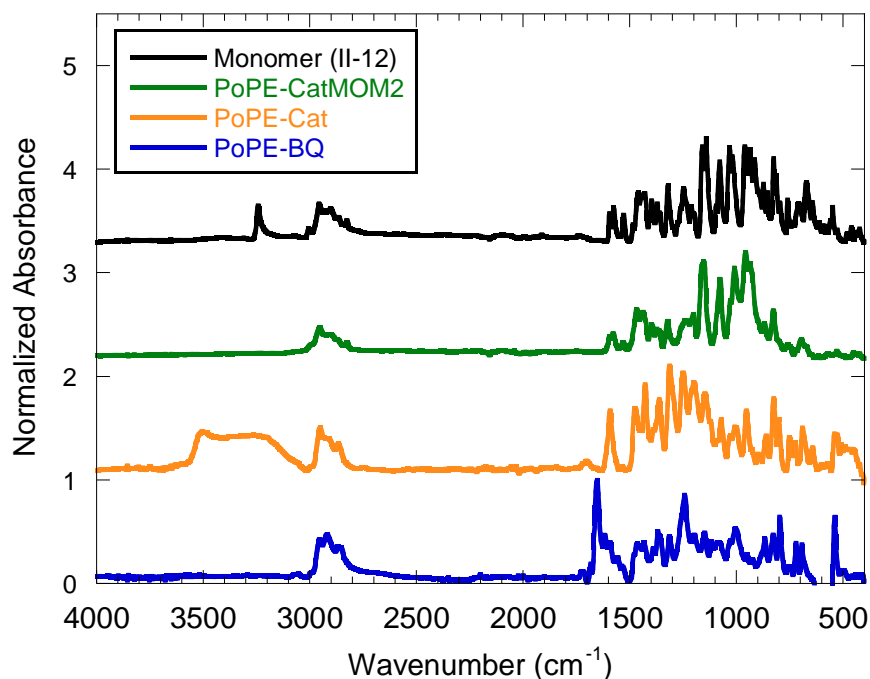


Figure II-13. FT-IR spectra of the monomer (**II-12**) and the polymers.

undergoing a one electron oxidation was required to reduce the benzoquinones to semiquinones and to stabilize the semiquinone. The synthesis of PoPE-SQ from the polymer precursor, PoPE-BQ using the cobalt (II) complex, CoL_A, the synthesis for which will be discussed in Chapter II.4, was conducted in a nitrogen atmosphere in 1 mL of anhydrous, degassed CH₂Cl₂. The resulting highly colored solutions were stirred overnight and then transferred directly into EPR tubes for spectroscopic data.

II.3.2. Results.

Absorption and Emission Studies of the PoPE Polymers The photophysical properties of the PoPE polymers were examined for fluorescence and phosphorescence. Figure II-14a shows

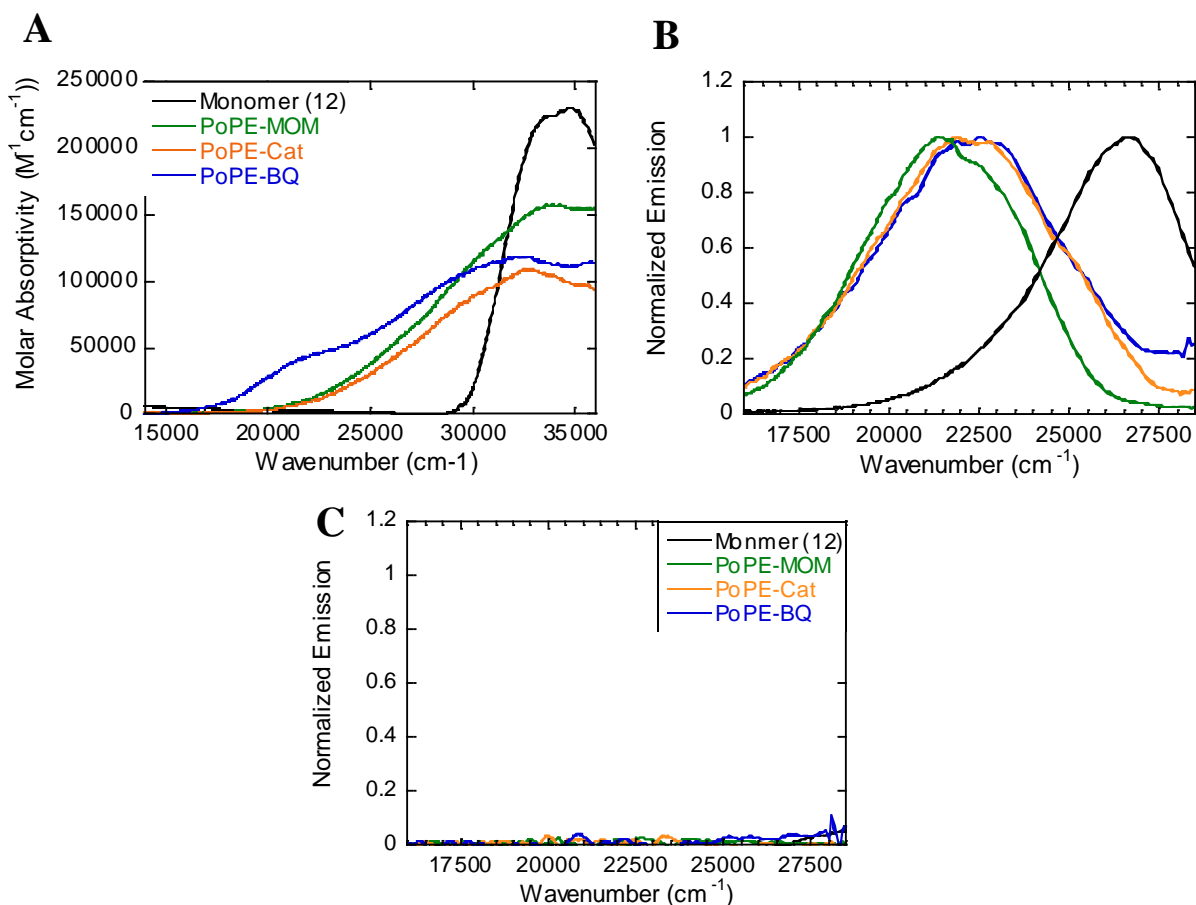


Figure II-14. A) Absorption spectra of **II-12** and the polymers. B) Emission spectra of samples before degassing. C) Difference between emission spectra before and after degassing.

the electronic absorption profiles of the monomer (**II-12**) and the **PoPE** polymers. The monomer only absorbed in the UV region with a $\lambda_{\text{max}} = 34720 \text{ cm}^{-1}$, when polymerized and the conjugation length increased the polymers began to absorb at lower wavenumbers giving a $\nu_{\text{max}} = 33333 \text{ cm}^{-1}$ for **PoPE-MOM**. The removal of the MOM protecting groups caused another bathochromic shift for **PoPE-Cat** and **PoPE-BQ** giving $\nu_{\text{max}} = 32787$ and 32362 cm^{-1} , respectively. The emission spectra displayed in Figure II-14b were collected in aerated CH_2Cl_2 to give $\nu_{\text{max}} = 26596, 21413, 21888, 22555 \text{ cm}^{-1}$ for **II-12**, **PoPE-MOM**, **PoPE-Cat** and **PoPE-BQ**, respectively. Figure II-14c shows the result when these samples were degassed and emission spectra recollected, and the spectra pre-degassing were subtracted from the degassed spectra. The emission spectra only shows noise across all four samples, indicating that if there is any phosphorescence at room temperature, it is below the instrument's limit of detection.

Generation of Random Copolymers: PoPE-SQ_xBQ_{1-x}. As discussed previously the SQ units on the polymer can be chemically generated by a redox reaction of the BQ polymer with a cobalt (II) complex (**CoL_A**) as shown in Scheme II-11. This scheme also shows that by controlling the equivalents of **CoL_A** added to **PoPE-BQ**, the mole fraction of the polymer that is SQ can be controlled.

Scheme II-11. The synthesis of random copolymers of **PoPE** with **SQ** and **BQ** pendant groups with the redox reaction of a cobalt (II) complex.

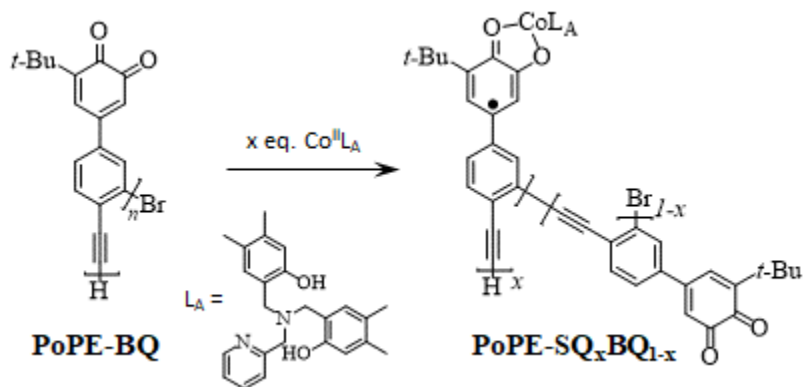


Figure II-15 shows the IR spectra for **PoPE-BQ** (0%) alongside when it is reacted with 0.25, 0.5, 0.75 and 1.00 eq. of **CoL_A**. As can be seen, as the equivalents of **CoL_A** increase, the quinone stretch decreases. Figure II-16a shows the simulated and experimental EPR spectrum of 3,5-di-*tert*-butylsemiquinone-cobalt(III) complex as a model compound for the monomer repeat units. The spectrum shows an eight-line splitting pattern due to the cobalt nucleus ($I = 7/2$) of $a_{Co} = 10.00$ Gauss and a proton hyperfine with $a_H = 3.22$. Figure II-16b-d shows the EPR spectra of two **PoPE-SQ** oligomers, b) has a M_n corresponding to five repeat units and has been reacted

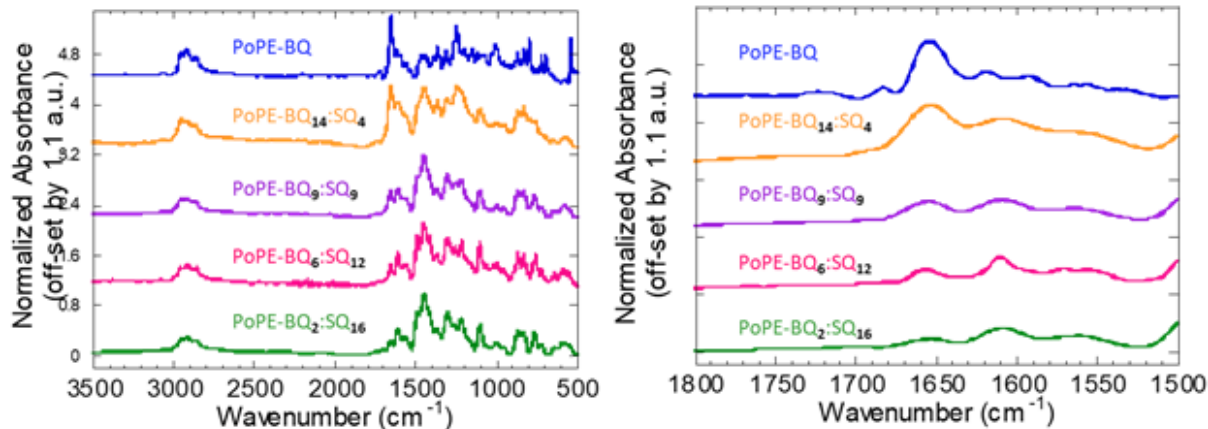


Figure II-15. IR spectra of **PoPE-BQ** (0%), **PoPE-BQ₁₄-SQ₄** (~25%), **PoPE-BQ₉-SQ₉** (50%), **PoPE-BQ₆-SQ₁₂** (~66%), **PoPE-BQ₂-SQ₁₆** (~100%) showing the quinone stretch at 1650 cm^{-1} decreasing as the concentration of semiquinone increases.

with an excess of **CoL_A** and c) has an M_n corresponding to 17-18 repeat units and has been reacted with 0.25 equivalents of **CoL_A** in each case some of the cobalt and proton hyperfine can still be identified. As the $DP = 17-18$ oligomer has more **CoL_A** added to it, the EPR spectra become featureless as can be seen in Figure II-16d when 1.0 equivalents of **CoL_A** is added to generate the **PoPE-SQ**. Table II-6 shows the results of determining the spin concentration of the **PoPE-SQ** oligomers by addition of **CoL_A**. The calculated spin concentration in **PoPE-SQ** was a close match with the theoretical 85% of the theoretical for entries 1 and 3, 100% for entry 2, and

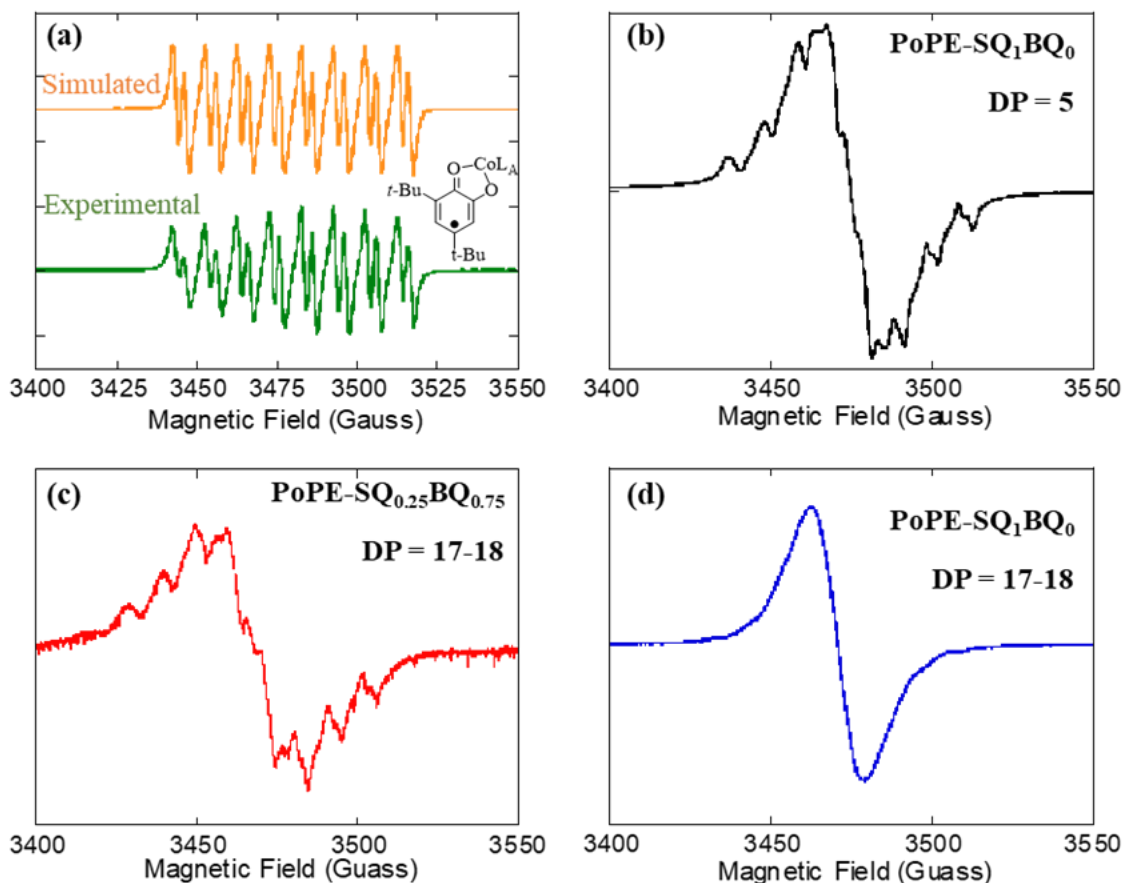


Figure II-16. EPR spectra of (a) 3,5-di-*tert*-butylsemiquinone-cobalt (III) complex. Line splitting: $a_{Co} = 10.00$, $a_H = 3.22$ Gauss. (b) **PoPE-SQ** (DP = 5) that had been reacted with excess **CoL_A**. (c) **PoPE-SQ** (DP = 17-18) reacted with 0.25 equivalents of **CoL_A**. (d) **PoPE-SQ** (DP = 17-18) reacted with 1.00 equivalents of **CoL_A**.

91% for entry 4. Figure II-17a shows the EPR signal from the entries in Table II-6, which show increasing signal intensity as more **CoL_A** is added to generate **PoPE-SQ**. Figure II-17b shows the resulting absorption spectra of the EPR signals, making it easy to see the absorption intensity increasing going from entry 1 to 4. Figure II-17c shows the correlation between the amount of SQ

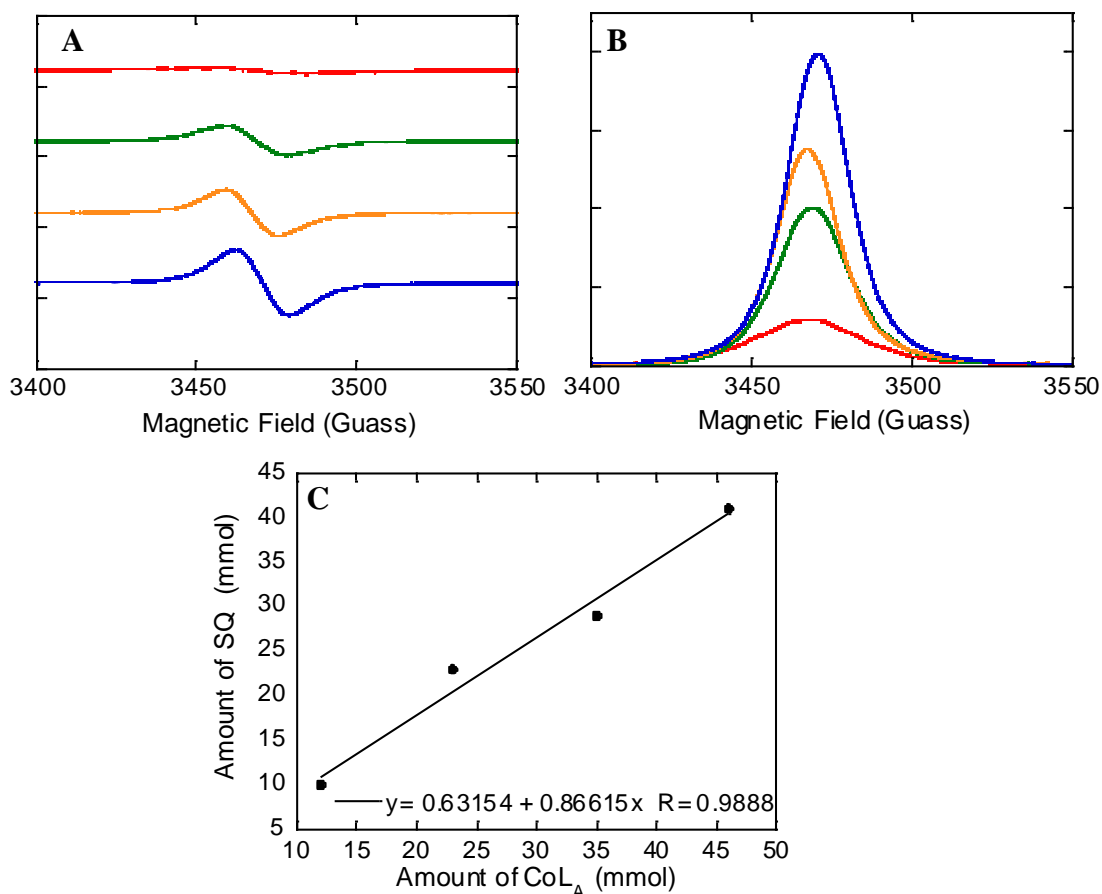


Figure II-17. EPR spectra for the trials of increasing the spin concentration in the polymer as a function of the amount of **CoL_A** added. (A) The EPR signal for each trial. (B) Singly integrated EPR spectra. (C) Plot of calculated amount of SQ from spin concentration vs. the amount of **CoL_A** added.

as a function of **CoL_A** added, which shows that the signal response to the generation of semiquinones on the backbone was relatively linear, with an R^2 value of 0.9888. This indicates that the through-space intra- or intermolecular antiferromagnetic interactions had minimal effect on the paramagnetic character of the sample. This potentially could be due to the use of the bulky

Table II-6. EPR data for spin concentration calculations.

Entry	PoPE (μmol)	CoL _A (μmol)	Theor. SQ spin concentration per repeat unit	Calc. SQ spin concentration per repeat unit
1	45	12	0.26	0.22
2	45	23	0.51	0.51
3	45	35	0.77	0.64
4	45	46	1.00	0.91

ancillary ligand, **II-39**, which could be providing enough steric bulk to keep the semiquinones apart and allow the intended through-bond ferromagnetic high-spin alignment to dominate the sample.

Magnetometry. Figure II-18 shows the SQUID magnetometry data for **PoPESQ-050** and **PoPESQ-075** alongside the theoretical Brillouin functions for $S = 1/2, 2/2, 3/2$ and $4/2$. As can be seen, the plots of both **PoPESQ** seem to follow the $S = 1/2$ Brillouin function with only slight variation at weaker field strengths. This would indicate that the high-spin coordinated coupling is not observed for the polyradicals that have been cast into polystyrene films. This could be due to the polymer chains possibly having aggregated when the polystyrene films were drying and if the chains are close enough, weak antiferromagnetic through-space interactions between the chains could be lowering the overall spin of the system. This was similarly observed for the **pThSQ** polyradicals and will be discussed further in **II.5.2**.

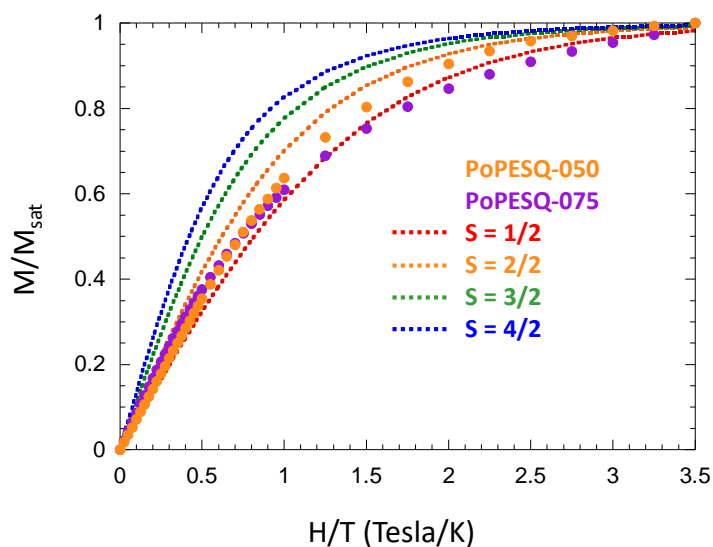


Figure II-18. M/M_{sat} plots for **PoPESQ-050** and **PoPESQ-075** in polystyrene films alongside theoretical Brillouin function plots for $S = 1/2, 2/2, 3/2$ and $4/2$. Magnetic field was swept from 0.05 to 7 T while the temperature was held at 2 K.

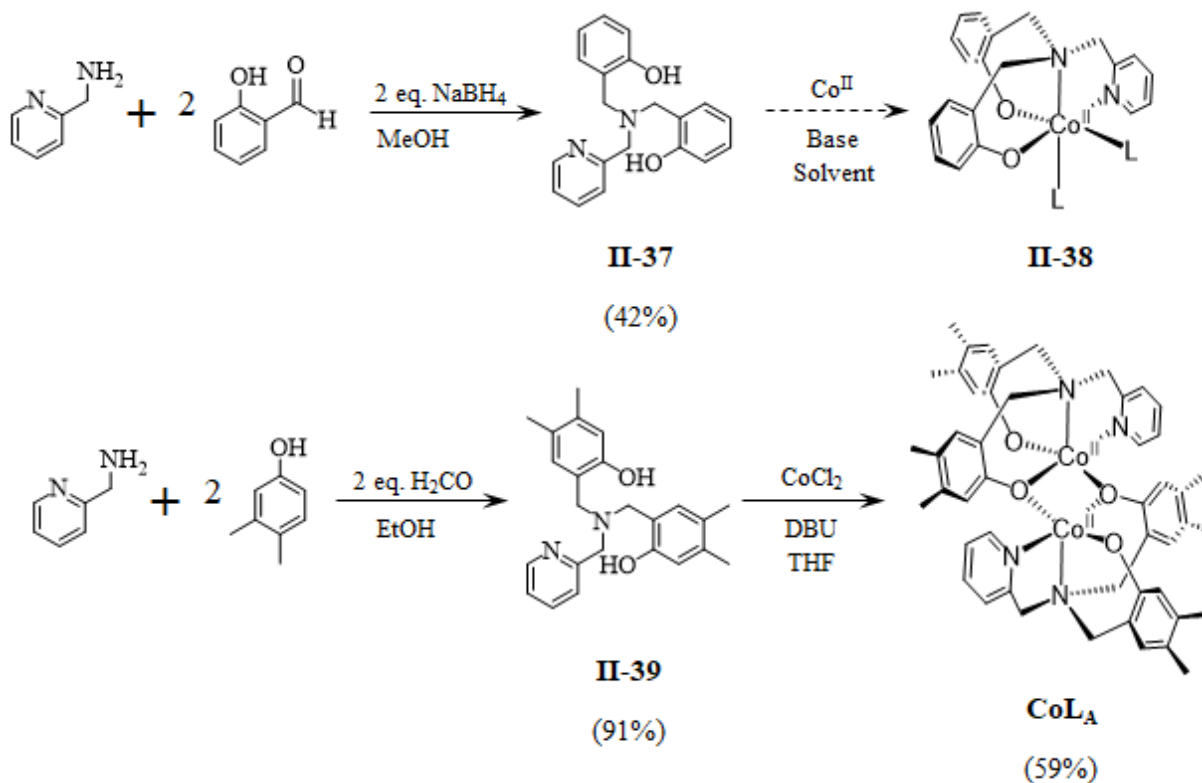
II.3.3. Conclusions.

The **PoPE-MOM** polymer was synthesized using a Sonogashira polymerization with from the corresponding terminal alkyne monomer **II-12**, which was generated using the Ohira-Bestmann reaction. The **PoPE-SQ** was synthesized by the reduction of the precursor, **PoPE-BQ** which was in turn synthesized from the oxidation of **PoPE-Cat** after the deprotection of **PoPE-MOM**. In order to synthesize the **PoPE-SQ** oligomers a cobalt (II) complex, **CoL_A** was synthesized. The **PoPE-MOM**, **PoPE-Cat**, and **PoPE-BQ** displayed fluorescence emission, but no phosphorescence emission was detected. The **PoPE-SQ** oligomers had varying spin concentrations as a function of the amount of **CoL_A** added, which gave an R² value of 0.9888, a linear correlation, which is an indication that the **PoPE-SQ** does not experience many through-space antiferromagnetic interactions and that there was high conversion of **PoPE-BQ** into the corresponding **PoPE-SQ**.

II.4. Synthesis of Cobalt Complex (CoL_A)

Scheme II-12 shows the attempted syntheses of two cobalt complexes (**II-38** and **CoL_A**) and the syntheses of their ancillary ligands (**II-37** and **II-39**). The original attempts to synthesize a cobalt (II) complex were with the ligand (**II-37**). The reaction is conducted in several steps: first the reductive amination of one equivalent of salicylaldehyde with 2-(aminomethyl)pyridine, a work-up, then the second reductive amination with the second equivalent of salicylaldehyde, which is then purified by flash chromatography and recrystallized to give a yield of 42%. Table II-7 shows attempts to use this ligand to make the cobalt (II) complex (**II-38**) were unsuccessful, in that conditions were not found to facilitate the crystallization of the complex. After these

Scheme II-12. Synthesis of a cobalt (II) complex that will undergo a redox reaction with a quinone to generate a semiquinone.



attempts ligand was changed to **II-39** to have the 3,4-dimethyl phenol groups instead of just the phenol in hopes this would help with packing in a crystal structure and that crystals of the dinuclear cobalt (II)-cobalt (II) complex had already been synthesized in literature.¹¹³ Ligand **II-39** was synthesized via a specific case of a Mannich reaction conducted with phenols and primary aryl amines.¹¹⁴ The one-pot reaction is carried out in refluxing ethanol with 2-(aminomethyl)pyridine and two equivalents of both 3, 4-dimethylphenol and formaldehyde. The product, which precipitates, is filtered, washed and recrystallized to give a 91% yield of **II-39**. Table II-7 shows the attempts to make **CoL_A**, the reaction becoming purple in color and according to literature precedent, giving a purple solid indicated formation of the cobalt (II)

ligand complex; a brown color indicated oxidation and the formation of a mixed valent cobalt(II)-cobalt(III) complex.^{113,115} Many of the entries in Table II-7 yielded a purple solution, but either upon exposure to air or standing over time, would become highly colored, indicating decomposition or oxidation to cobalt(III).¹¹⁵ Entry 10 seemed promising, but the elemental analysis indicated that there were other substances present. Analysis of the chemical equation and mass percent from the EA suggested that the excess mass was due to some amount of triethylammonium perchlorate, which was not consistent across samples. This is an issue because a working, consistent molecular mass is required for whatever cobalt complex is used. The remaining entries in Table II-7 are attempts to remove the resulting salt. Entry 24 is the successful removal of most, if not all of the resulting salt from the reaction according to

Table II-7. Synthetic attempts to make **CoL_A**.

Entry	Cobalt (II)	Ligand	Base	Solvent(s)	Results
1	Co(ClO ₄) ₂ •6H ₂ O	II-37	Et ₃ N	CH ₂ Cl ₂	Purple crystals, will not recrystallize.
2	CoCl ₂ •6H ₂ O	II-37	Na ₂ CO ₃	MeCN	decomposition
3	Co(OAc) ₂ •4H ₂ O	II-37		MeCN	No color change; No Reaction
4	Co(OAc) ₂ •4H ₂ O	II-37	Et ₃ N	MeCN	No color change; No Reaction
5	Co(OAc) ₂ •4H ₂ O	II-37	Et ₃ N	MeCN/ CH ₂ Cl ₂	decomposition
6	Co(ClO ₄) ₂ •6H ₂ O	II-37	DABCO	CH ₂ Cl ₂	Purple soln., and solid after removing solvent, but turned dark red when trying to precipitate from EtOAc/CH ₂ Cl
7	Co(ClO ₄) ₂ •6H ₂ O	II-37	DBU	CH ₂ Cl ₂	decomposition
8	Co(ClO ₄) ₂ •6H ₂ O	II-37	Cs ₂ CO ₃	CH ₂ Cl ₂	Pink solid, not very soluble in anything, not crystallizing
9	Co(ClO ₄) ₂ •6H ₂ O	II-37	Et ₃ N	CH ₂ Cl ₂	Purification problems
10	Co(ClO ₄) ₂ •6H ₂ O	II-39	Et ₃ N	CH ₂ Cl ₂	Tiny purple crystals, EA says other stuff present works with quinone reaction, turns orange/brown in solvent over time: EtOH > MeOH > THF > MeCN > EtOAc > CH ₂ Cl ₂
11	CoSO ₄ •7H ₂ O	II-39	Et ₃ N	CH ₂ Cl ₂ /H ₂ O	decomposition
12	CoSO ₄ •7H ₂ O	II-39	Et ₃ N	CH ₂ Cl ₂ /H ₂ O	decomposition
13	Co(ClO ₄) ₂ •6H ₂ O	II-39		CH ₂ Cl ₂	decomposition
14 ^a	CoSO ₄ •7H ₂ O	II-39		CH ₂ Cl ₂	Turned purple; not replicable
15 ^a	Co(ClO ₄) ₂ •6H ₂ O	II-39	KOH	CH ₂ Cl ₂	decomposition
16 ^a	CoCl ₂	II-39		CH ₂ Cl ₂ /H ₂ O	No color change; No Reaction
17 ^a	CoCl ₂	II-39		MeCN/THF	decomposition
18 ^a	CoCl ₂	II-39		THF	No color change
19 ^a	CoCl ₂	II-39		Me ₂ CO	decomposition
20 ^a	CoCl ₂	II-39		MeOH	No color change; No Reaction
21 ^a	CoCl ₂	II-39		CH ₂ Cl ₂ / DMSO	No color change; No Reaction
22	Co(OAc) ₂ •4H ₂ O	II-39	NaOH	1:1 MeOH: PhMe	Purple solid
23	CoSO ₄ •7H ₂ O	II-39	NaH	THF	decomposition
24 ^b	CoCl ₂	II-39	DBU	CH ₂ Cl ₂ / THF	Purple solid

^a The sodium salt of the ligand was used

^b Elemental analysis indicates the product is cobalt and the ligand without any other ligands or solvent molecules. The complex most likely exists as a dimer or larger polymeric structure.

elemental analysis. Using an excess of DBU to deprotonate **II-39** and CoCl₂ as the cobalt (II)

source results in forming the salt of DBU and HCl, which is slightly soluble in the solvent

mixture CH₂Cl₂. However, adding Et₂O results in the precipitation of both **CoL_A** and the salt.

Which can then be filtered and washed with H₂O to remove the salt, leaving **CoL_A** as a purple solid. Despite extensive efforts to recrystallize **CoL_A**, crystals sufficient for x-ray crystallography were not obtained.

II.5. Polythiophene (pThSQ).

The **PoPE-MOM**, **PoPE-Cat**, **PoPE-BQ** series was a starting point for the synthesis of semiquinone radical polymers; however, there are other potentially more interesting polymers to make. First of all, the **PoPE** series did not show any phosphorescence which made attempting to modulate the singlet-triplet excited state intersystem crossing, as Wasielewski et al. did with nitroxide and TEMPO in the excited state of a chromophore, difficult if not impossible to measure.⁵⁶⁻⁵⁸ Also, **PoPEs** are known to form a coiled helical structure in solution as the lowest energy conformation, which could provide non-orthogonal overlap for the NBMOs of the semiquinone repeat units, resulting in a through-space antiferromagnetic interaction which is lowering the ground state of **PoPE-SQ**.^{9,14,41,116,117} Furthermore, any coiled or bent structure in the **PoPE** backbone would induce bond torsions which would further weaken the through-bond coupling.¹¹⁸

Having the semiquinone radicals appended to a polythiophene backbone would allow for stronger exchange coupling between radical moieties on adjacent thiophene rings. It has been shown that the exchange coupling, as given by the exchange coupling parameter, J , the magnitude which shows the strength of the exchange coupling. Through one thiophene ring is +220 cm⁻¹ in comparison with +100 cm⁻¹ for one phenyl ring, through two thiophene rings J is +108 cm⁻¹ and two phenyl rings is +20 cm⁻¹ as shown in Figure II-19.¹¹⁹ Meaning that the spin

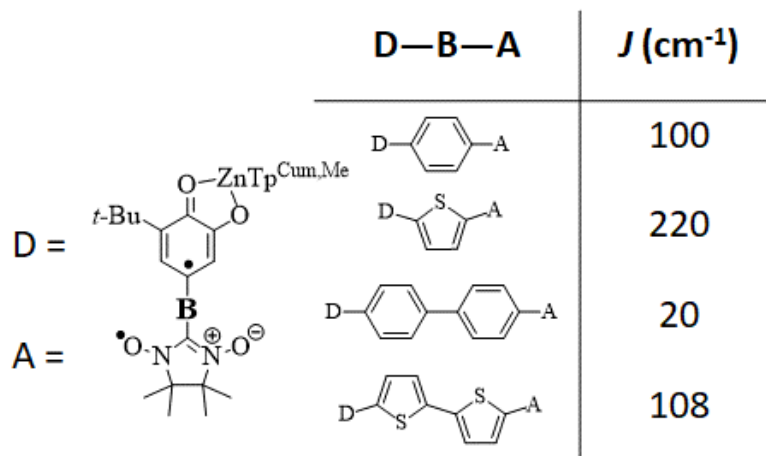


Figure II-19. Donor-bridge-acceptor (D-B-A) biradicals evaluating the exchange coupling through conjugated phenylene and thiophene oligomers.

alignment through polythiophene will be stronger and the high spin alignment will persist through more of the polymer backbone, which should make such a polymer more resistant to incomplete oxidations (incomplete reduction in our case) that would ordinarily make a radical disjoint and result in antiferromagnetic coupling.

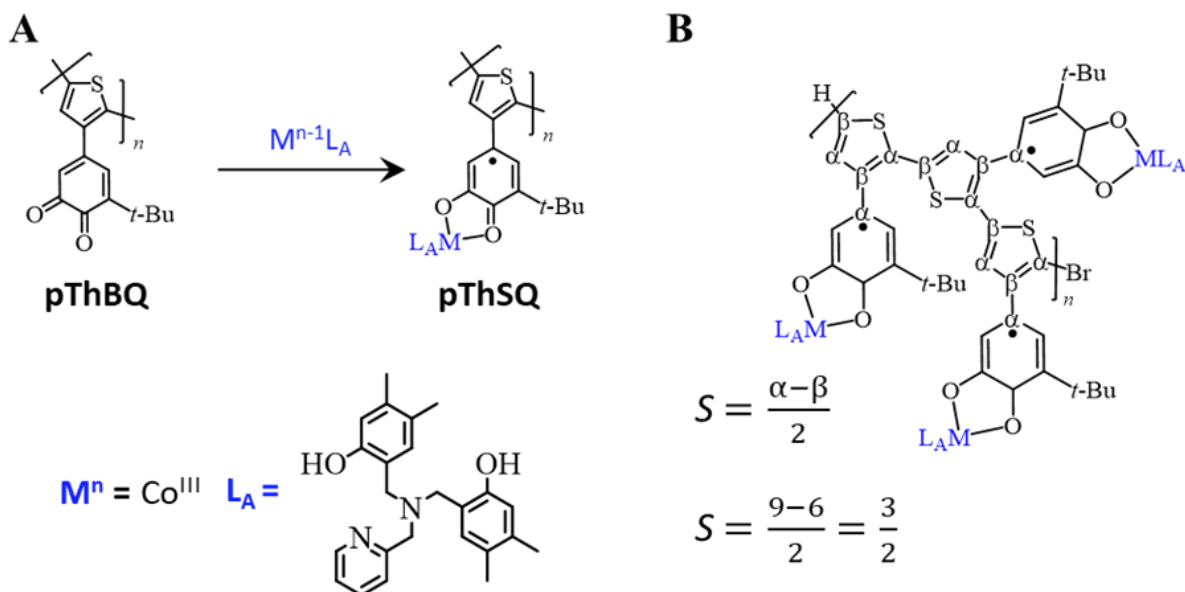


Figure II-20. A) Synthesis of **pThSQ** from **pThBQ** and **CoL_A** and B) spin polarization through thiophene backbone illustrating that the three spin-1/2 electrons are ferromagnetically coupled.

As shown in Figure II-20A, **pThSQ** can be made from the corresponding quinone polymer (**pThBQ**) by the redox reaction with **CoL_A** just as the **PoPE-SQ** polymers were synthesized. Figure II-20B shows the spin polarization using α and β to indicate either up or down spins, respectively, in the π -system to illustrate that in theory, because thiophene acts like a perturbed butadiene the semiquinone radicals should all be spin aligned, ferromagnetically coupled.

Polythiophenes are of great interest in the development of a variety of organic electronic devices due to their extended conjugation and charge transport capabilities.^{71,120–122} Several polythiophenes bearing radical repeat units have been synthesized before including those with phenoxyl, verdazyl and nitroxide radicals.^{2,42,123,124} Once again, the introduction of semiquinone repeat units would afford numerous opportunities for tailoring the polymer properties.

II.5.1. Synthetic Discussion.

Synthesis of poly(3-(3-(tert-butyl)-4,5-bis(methoxymethoxy)phenyl)thiophene) (*pThCatMOM₂*). The original proposed synthesis (Scheme II-13) for **pThCatMOM₂** followed possible literature precedents for the synthesis of poly(3-substituted thiophenes). Figure II-21 shows a summary of polymerization strategies that have been employed for 3-substituted polythiophenes. The simplest method is an oxidative polymerization using FeCl₃ which proceeds via a one electron transfer from thiophene to make the thiophene radical cations which polymerize with each other and liberate HCl and give up to 90% head-to-tail configuration.^{42,125–127} This has limited scope for our system which incorporates the MOM₂Cat moiety, which would have the MOMs quickly deprotected by the acidic conditions; although Nishide et al. successfully employed this method in the synthesis of 3-phenoxy radical substituted

polythiophenes by using acetate protecting groups.^{42,124} The other issue is the up to 90% head-to-tail configuration which depending on where in the polymer chain a tail-to-tail or head-to-head linkage occurs would be very detrimental to the desired ferromagnetic coupling. The Grignard metathesis polymerization (GRIM), Reike, McCullough, Suzuki and Stille polymerizations offer basic conditions to prevent MOM deprotection and better control for head-to-tail couplings with varying degrees of monomer and polymerization condition complexity.¹²⁸ The GRIM and McCullough methods were deemed to be the simplest and most efficient, given that the criteria for a polymerization reaction were 1) a relatively few steps for monomer synthesis, in comparison to **PoPECatMOM₂** 2) give as long of polymers as possible to get many spins in the system. To make the Suzuki and Stille monomers, either deprotonation or halogenation/lithium-halogen exchange at the 5-position and quenching with an appropriate boron or tin reagent would be necessary in comparison with the GRIM and Reike or McCullough methods which offer

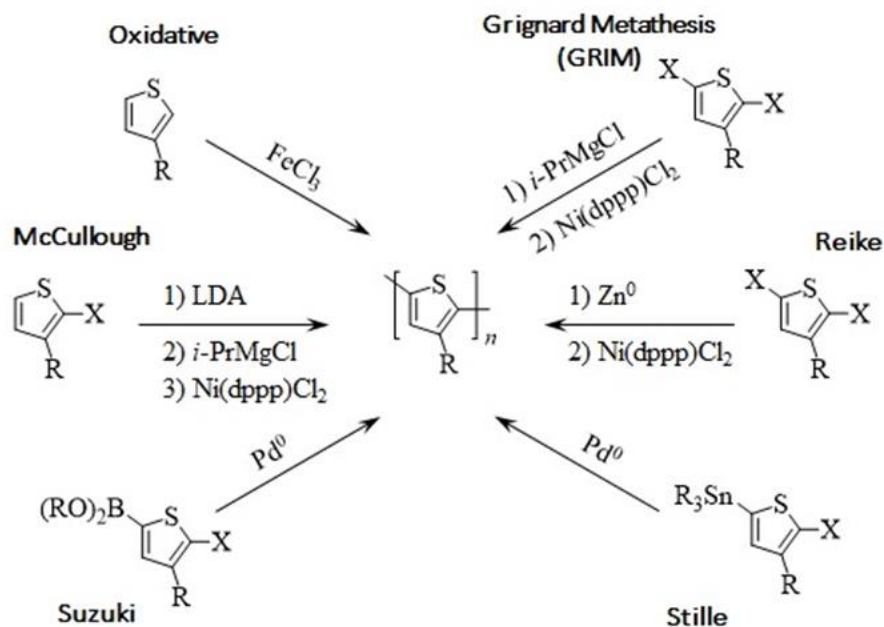
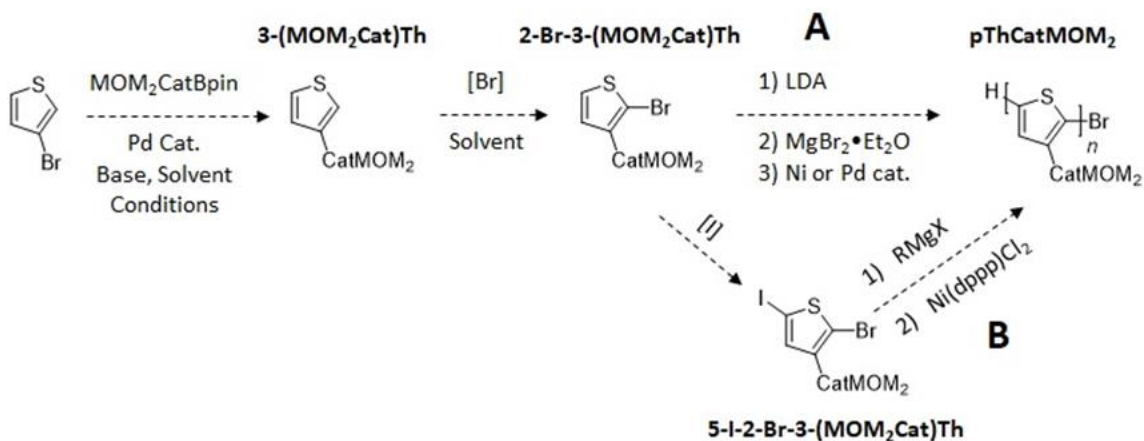


Figure II-21. Routes to polythiophenes.

polymerization from either the magnesium-halogen exchanged or deprotonated species, respectively.

As shown in Scheme II-13, the monomer synthesis first involves the functionalization of thiophene at the 3-position, in this case, 3-bromothiophene is Suzuki coupled with $\text{MOM}_2\text{CatBpin}$ to give **3-(MOM₂Cat)Th** and then selectively brominated at the 2-position.¹²⁹ **2-Br-3-(CatMOM₂)Th** can then follow Scheme II-13, route A: the McCullough method for polymerizing 2-halo-3-substituted thiophenes or Scheme II-13, route B; where the monomer is

Scheme II-13. Original synthesis for **pThCatMOM₂** using either A) the McCullough method or B) the GRIM polymerization.



then selectively iodinated at the 5-position and then subjected to the GRIM conditions to afford the polythiophene. The McCullough method is a one-pot method, where LDA deprotonates the substituted thiophene at the 5-position, the lithiated species is then metathesized with magnesium, which is then polymerized by Kumada coupling with the halogenated 2-position and the magnesiated 5-position to give a regioregular polymer coupled in head-to-tail fashion. As previously mentioned, head-to-tail coupling for most cross-conjugated polyradicals is imperative in order to preserve the ferromagnetic coupling between radical substituents.

The Suzuki coupling to make **3-(MOM₂Cat)Th** was carefully evaluated for conditions that would consistently produce high yielding, pure material because as it is the first step and the synthesis of MOM₂CatBpin requires several days to complete, proceeding from this point unhindered by low yields or lengthy purification was important. Table II-8 shows the analysis of this Suzuki coupling. The first entry of Table II-8 produced the desired compound, but as indicated by the 65 and 31% yields, it was inconsistent. Entry 2 shows a significant reduction in reaction temperature, at only 30 °C it is slightly above room temperature. This was to facilitate the coupling under mild temperatures where, ideally the yield would be more consistent without losing material to undesired side products. Unfortunately, the three day reaction time and still a low yield of 39% made this unsuitable. Entry 3 returns to elevated reaction temperature, but changes the base to non-nucleophilic K₂CO₃, which should also be milder than the strong bases, KOH or KO^tBu. This reaction still resulted in a low yield of 41%. The following trials implemented toluene/water mixtures, which have been widely employed in Suzuki couplings for decades instead of THF, which is known to be susceptible to auto-oxidation by atmospheric oxygen to form peroxides, which was considered to be a contributing factor to the inconsistent yield of entry 1; as well as other cross-couplings that had implemented THF and proven to be H₂O at 80 °C and the palladium catalyst was changed from Pd(dppf)Cl₂ to Pd(PPh₃)₄ because using a palladium (II) catalyst without a means of reduction to palladium (0) will inevitably lead to at least one side product; homo-coupled biaryl from whichever species contains the metal or inconsistent over long reaction times. Entry 4 used toluene and 2.5% of the reaction volume in boron moiety. However, after 20 hours of reaction time, no reaction was observed. This reaction solvent was much more nonpolar than previous trials which was thought to be inhibiting the reaction in that the palladium cycle involves charged transition states which would be stabilized

by a more polar solvent mixture and polar reagents during ligand substitution and transmetalation steps must be soluble enough to get to the catalytic reaction center. To this end, water and THF were added to the existing reaction to increase the polarity, which resulted in the highest yielding coupling yet in entry 5. The higher yield was also contributed to using toluene to help solubilize the nonpolar reaction components which also need to be able to react with catalytic center. The base was also changed from K_2CO_3 to Na_2CO_3 , which may also have had some effect. Proceeding with this intermediate polarity solvent mixture and Na_2CO_3 , entry 6 lead

Table II-8. Evaluation of Suzuki coupling conditions to optimize the synthesis of **3-(MOM₂Cat)Th**.

Entry	Catalyst	Base	Solvent	Temp	Time (h)	Results
1	0.01 eq. Pd(dppf)Cl ₂	2 eq. KO ^t Bu	10% H ₂ O/ THF (0.64 M)	Reflux	24	65%, 31%
2	0.01 eq. Pd(dppf)Cl ₂	2 eq. KOH	10% H ₂ O/ THF (0.62 M)	30 °C	72	39%
3	0.01 eq. Pd(dppf)Cl ₂	2 eq. K ₂ CO ₃	10% H ₂ O/ THF (0.49 M)	Reflux	48	41%
4	0.02 eq. Pd(PPh ₃) ₄	2 eq. Na ₂ CO ₃	2.5% H ₂ O/PhMe (0.26 M)	80 °C	20	No Rxn
5	0.02 eq. Pd(PPh ₃) ₄	2 eq. Na ₂ CO ₃	14% H ₂ O/ 29% THF/ 57% PhMe (0.15 M)	80 °C	48	78%
6	0.02 eq. Pd(PPh ₃) ₄	2 eq. Na ₂ CO ₃	17% H ₂ O/ 17% THF/ 66% PhMe (0.11 M)	80 °C	48	94%, 76%, 69%, 85%
7	0.02 eq. Pd(PPh ₃) ₄	2 eq. Na ₂ CO ₃	25% H ₂ O/PhMe (0.43 M)	80 °C	24	No Rxn
8 ^a	0.02 eq. Pd(PPh ₃) ₄	2 eq. Na ₂ CO ₃	25% H ₂ O/PhMe (0.43 M)	80 °C	18	93%, 97%, 95%, 97%, 88%, 87%

^aThese conditions are the same as “No Rxn” entry 7, but 10% Bu₄NBr has been added as a phase transfer catalyst

to several high yielding reactions, but still suffered from inconsistency with yields ranging from 69-94%; this was still being attributed to THF and long reaction time. Entry 7 was similar to entry 4, but the amount of water was increased from 2.5% to 25% to help solubilize the Na₂CO₃

and other polar species. However, like entry 4, after 24 hours, showed no sign of reaction by TLC. The lack of reaction was attributed to toluene and water being immiscible, which THF must have facilitated their mixing in entries 5 and 6 to produce the desired compound in moderate to high yields. Tetrabutylammonium bromide (Bu_4NBr), a phase transfer catalyst was added to the existing reaction in entry 7 to give entry 8, with the hope that it would help shuttle the necessary polar reactive species into the organic layer and facilitate the reaction in the primarily nonpolar solvent. When the reaction was checked 18 hours later, it was complete, free from side products and produced a 93% yield. These reaction conditions have been repeated several times, consistently giving high yields (> 90%) and relatively pure material after just an aqueous work-up and filtration. The actual reaction time for entry 8 completion has been determined to be in the vicinity of 5 hours.

The next reaction from Scheme II-13 is to selectively brominate the 3-substituted thiophene at the 2-position. This reaction was completed with either pyridinium bromide perbromide (HPyrBr_3) or NBS in either MeOH or MeCN with KOAc or NaHCO_3 present during bromination to prevent the loss of the MOM groups due to transient HBr. The best results were obtained by NBS with KOAc in MeOH.

A couple notes on thiophene reactivity and identification, as shown in Figure II-22, the 2 and 5 positions of thiophene are much more reactive than either the 3 or 4 positions and will undergo electrophilic aromatic substitution and deprotonation. 3-substituted thiophenes are reactive toward electrophilic aromatic substitution at the 2-position; only when R is strongly electron withdrawing, will substitution occur at the 5-position.¹³⁰ Conversely, subjecting 3-substituted thiophenes to strong bases, such as butyl lithium or LDA will cause deprotonation at the 5-position; this is not as selective and some deprotonation at the 2-position can occur, but the

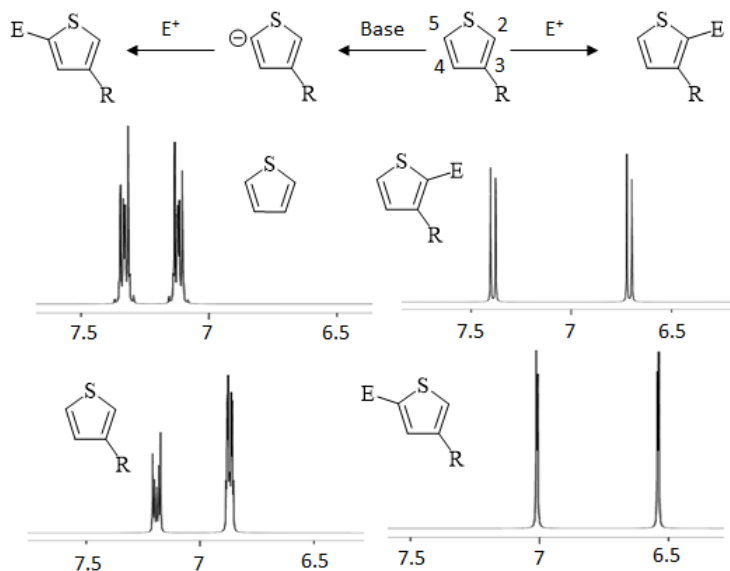


Figure II-22. Reactivity of thiophene and characteristic $^1\text{H-NMR}$ splittings for substitution patterns.

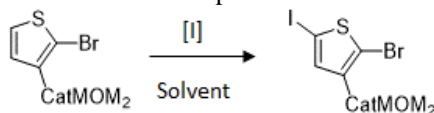
extent depends on the electronics of the group at the 3-position.¹³⁰ Figure II-22 also shows that $^1\text{H NMR}$ is very effective for determining the substitution pattern of thiophene. Unsubstituted thiophene's protons are AA'BB' in Pople notation and give rise to two complex multiplets. Adding a group at the 3-position has the 4 and 5 protons *ortho* coupled with each other and then each are differently *meta* coupled to the 2-position proton. 2,3-substitution eliminates the *meta* coupling from the 4 and 5 protons and 3,5-substituted eliminates the *ortho* coupling from the 4 and 2 positions. It is worth mentioning that thiophene *ortho* and *meta* coupling constants are smaller than their phenyl analogs.

The first attempts at polymerization employed the McCullough method which was performed several times and no polymerization was observed. Upon quenching the reaction after deprotonation with CH_3OD , deuteration was observed at the desired position; however, only ca. 15% of the monomer was converted. The lack of observed polymer was attributed to the low degree of deprotonation. Route B in Scheme II-13, the GRIM method, was pursued, which

involves iodination of the existing monomer, **2-Br-3-(MOM₂Cat)Th**, at the 5-position.

Iodination at the 5-position of thiophene of 2,3-substituted thiophenes is usually accomplished with I₂ and PhI(OAc)₂ or *N*-iodosuccinimide (NIS).^{131,132} Table II-9 shows the attempts to iodinate **2-Br-3-(MOM₂Cat)Th** at the 5-position. Following previously reported procedure¹³², I₂ and PhI(OAc)₂ were employed in chloroform at room temperature. As shown in Table II-9 entries 1-3, room temperature did not produce a reaction in this case, elevated temperature began to produce some product, but extended length of time resulted in no more product, but the MOM protecting groups began to decompose. Entries 4 and 5 attempted NIS, which is also used to iodinate thiophenes, but not as extensively as I₂/PhI(OAc)₂. NIS was completely unreactive to **2-Br-3-(MOM₂Cat)Th** even at elevated temperature and so further attempts were made to get

Table II-9. Attempted iodination conditions for the thiophene monomer.



Entry	Iodination Reagent	Other reagents	Solvent	Temp (°C)	Time (h)	Result
1	I ₂	PhI(OAc) ₂	CHCl ₃ (0.1M)	0→RT	6	No Rxn
2	I ₂	PhI(OAc) ₂	CHCl ₃ (0.1M)	RT→60	24	1:3 ^a
3	I ₂	PhI(OAc) ₂	CHCl ₃ (0.1M)	RT→60	96	1:2 ^{a,b}
4	NIS		THF (0.1M)	RT	18	No Rxn
5	NIS		THF (0.1M)	Reflux	24	No Rxn ^b
6	I ₂	PhI(OAc) ₂ , Pyr ^c	CHCl ₃ (0.1M)	Reflux	48	2:1 ^d
7	I ₂	PhI(OAc) ₂	THF (0.1M)	RT	13	45%
8	I ₂	PhI(OAc) ₂	THF (0.1M)	RT	16	No Rxn
9	I ₂	PhI(OAc) ₂	THF (0.1M)	40	48	No Rxn
10	I ₂	PhI(OAc) ₂	CH ₂ Cl ₂ (0.06M)	0→RT	12	1:1 ^d
11	I ₂	PhI(OCOCF ₃) ₂	CH ₂ Cl ₂ (0.06M)	0→RT	48	2:1 ^{a,b}

^a Product:Starting material ratio

^b MOMs are deprotecting

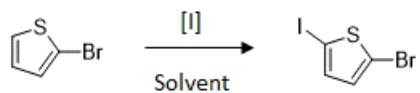
^c Pyr = 3,5-di-*tert*-butyl-4-methylpyridine

^d Not Product and not starting material and intractable reaction mixture

$I_2/PhI(OAc)_2$ to produce the desired compound more efficiently. Given that the MOMs were decomposing under some of the iodination conditions, a similar strategy was used from the previous step to brominate **3-(MOM₂Cat)Th**, which was to use some base to absorb any transient acid that could lead to the decomposition of the MOMs. For this, 2,6-di-*tert*-butyl-4-methylpyridine was implemented. This led to a reaction that produced some product along with another compound, whose ¹H NMR was inconsistent with 2,6-di-*tert*-butyl-4-methylpyridine, product, starting material or deprotected starting material. This was attributed to some iodination of 2,6-di-*tert*-butyl-4-methylpyridine. Changing the solvent from $CHCl_3$ to THF in entry 7, led to the first successful full conversion of **2-Br-3-(MOM₂Cat)Th** to **5-I-2-Br-3-(MOM₂Cat)Th**; albeit 45% yield. Unfortunately, upon scale-up in entry 8, the reaction did not proceed at all. Subsequent attempts to get the reaction to proceed in the same conditions failed, including slightly elevated temperatures and longer reaction times. The solvent was changed again to CH_2Cl_2 which once again led to a mixture of product and starting material. Finally, the oxidant was changed to $PhI(OCOCF_3)_2$, which is a much more reactive version of $PhI(OAc)_2$; however, this also proceeded to give the mixture of product to starting material.

Table II-10 shows test reactions involving 2-bromothiophene as a model compound in different reaction conditions. These attempts were to find iodination conditions that proceeded cleanly and also in the presence of base to protect the MOMs. As can be seen in Table II-10, only the baseline reaction in entry 1 worked and did very quickly (ca 20 min); indicated by depletion of iodine color and confirmed by ¹H NMR as all reactions were performed on a small scale in CDCl₃ for easy analysis. Attempts to add bases to react with any transient acid that could deprotect the MOMs ended with either the undesired, evident reaction of the base with the

Table II-10. Test iodination conditions on 2-bromothiophene.



Iodination Reagent	Other reagents	Base	Solvent	Result
I ₂	PhI(OCOCF ₃) ₂		CDCl ₃ (0.06M)	Total conversion in 20 min
I ₂	PhI(OCOCF ₃) ₂	Pyr ^a	CDCl ₃ (0.06M)	Pyr reacts with something, no desired reaction
I ₂	PhI(OCOCF ₃) ₂	DBU	CDCl ₃ (0.06M)	No Rxn
I ₂	PhI(OCOCF ₃) ₂	Et ₃ N	CDCl ₃ (0.06M)	No Rxn
I ₂	PhI(OCOCF ₃) ₂	KOAc	CDCl ₃ (0.06M)	No Rxn

^aPyr = 3,5-di-*tert*-butyl-4-methylpyridine

iodination conditions or no reaction at all being observed. Near this time, a C-H activation method for head-to-tail polymerizing thiophenes became known to us, which alleviated the need to get this iodination reaction to proceed reliably. These iodination reactions needed to be revisited in Appendix A, where it was discovered that the reaction worked in CDCl₃, but not in CHCl₃. This was probably not due to the identity of the solvent, but rather the CDCl₃ was not as old as CHCl₃ and that the hypohalite that is formed during the oxidation of I₂ by PhI(OAc)₂ is an extremely reactive electrophile and any reactive impurities in the solvent kill the reaction. This

would explain the one successful reaction in THF, which failed in subsequent reactions, given that THF is known to not be air stable. Therefore, it is recommended to use solvents that have been purified immediately prior to use or employ a more stable solvent that would be free from such impurities.

Direct arylation polymerization (DArP), a C-H activation polymerization of aromatic monomers was receiving considerable attention as an atom efficient, economical means to synthesize polythiophenes and other aromatic polymers.^{81,133–160} DArP, with respect to thiophenes, takes advantage of the fact that the 5-position is the most acidic proton on the thiophene ring and under the right conditions, the C-H bond can be polarized enough for palladium (II) to insert. Figure II-23 shows the generic monomer for DArP, the general reaction conditions and the catalytic cycle. As can be seen, the monomer for DArP is the 2-halo-3-substituted thiophene or the already synthesized, **2-Br-3-(MOM₂Cat)Th** for **pThSQ**. DArP is not only used for polythiophenes.^{137,139,158,159,140,146,150,151,154–157} Reaction conditions for DArP typically use Pd(OAc)₂ as a pre-catalyst, a carboxylate which acts as a ligand to facilitate the weakening of the C-H bond, a base which is used to regenerate the carboxylate and a polar organic solvent, such as DMF, DMAc or DMSO.^{136,143,144,151} Thompson et al. examined the effects of different carboxylates on poly(3-hexylthiophene) yield, molecular weight, regioregularity, PDI and other characteristics.¹⁴⁴ Thompson et al. settled on using pivalic acid as their carboxylate of choice, not having pivalic acid readily available for the synthesis of pThCatMOM₂, stearic acid and adamantane carboxylic acid (AdCO₂H) were used as a viable alternatives.^{136,143,152} Table II-11 shows the reaction scheme and various reaction conditions that were attempted in order to arrive at the highest possible molecular weight, best yield and lowest

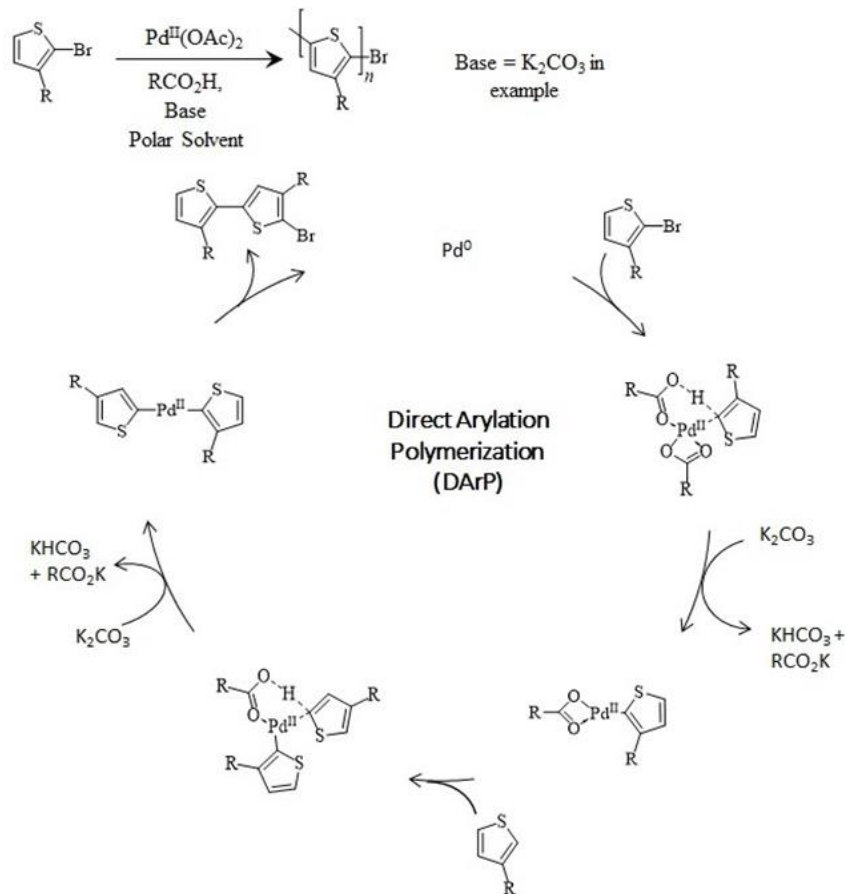


Figure II-23. Reaction conditions and catalytic cycle for Direct Arylation Polymerization (DAP).

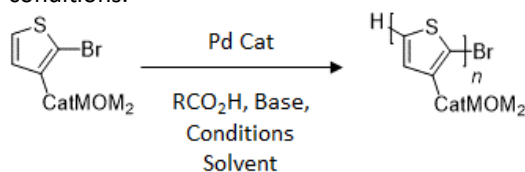
PDI. The first attempt at DAP with ThCatMOM₂ met with success in Table II-11, entry 1 using Pd(OAc)₂ precatalyst, stearic acid as the carboxylate, DMF as solvent and at 70 °C for 24 h to give a polymer with a degree of polymerization (DP) of 17 units. Unfortunately, this was only in an 18% yield. The future attempts were to further increase the DP since a DP around 20 units was what **PoPE-CatMOM₂** provided and to increase the yield. Following entries exchanged DMF as the solvent for DMAc which has better thermal stability so that the reactions could be carried out at elevated temperatures without the risk of decomposing solvent and getting undesired or unpredictable consequences. As a result, entry 2's yield doubled to 36% relative to entry 1 at over double the reaction temperature and three times as long. The DP also increased to 31 units, unfortunately the PDI increased to 4.36 and this material was too insoluble to continue

with the synthesis of **pThSQ**; once it was precipitated as **pThCatMOM₂** it could not be dissolved again. Meaning that there was a maximum limit to the DP of the polymer in order to carry the synthesis further. Entry 3 was used to reduce the DP and was carried out at 120 °C for 48 h. This afforded a DP = 18 units and also served to increase the yield to 52%, which is most likely a result of the lower DP and not as much polymer became insoluble material that just precipitated in the reaction. Subsequent attempts in entries 4 and 5 were unsuccessful. Entry 4 attempted to use microwave heating and resulted in a black solution, which is believed to be catalyst decomposition and no polymeric material. Entry 5 was the same as entry 2 with the exception the reaction time was 24 h instead of 72 h, intending to take advantage of the elevated temperature of entry 2, but reduce the DP by giving the polymerization less time to occur. Unfortunately, this was unsuccessful as it generated a copious amount of dark insoluble material, which is thought to be polymerization to the point of insolubility. However, if this is true, this indicated that the temperature seemed to be primarily responsible for the DP, not necessarily excessive time. Keeping this in mind, the remainder of the entries were aimed at keeping the temperature lower and varying other experimental parameters to modulate the polymerization's yield and PDI. Entries 6-9 changed Pd(OAc)₂ to Pd(PPh₃)₄. Interestingly, entry 6 was successful and provided the same DP as entry 2, unfortunately this is too large to be used in subsequent syntheses, but it provided this DP at much lower temperature (160 vs 90 °C) with a different catalyst. Entry 7 attempted to use the solvent combination of 1:3 H₂O:PhMe that was very successful for our Suzuki couplings; however, for the DArP reaction this did not work, probably due to lack of polarity in the solvent to facilitate the weakening of the thiophene's 5-position C-H bond. Entry 8 returned to DMAc and is the only entry to change the base from K₂CO₃ to Cs₂CO₃; however, this reaction outright failed. Entry 9 changed to a different polar solvent,

DMPU which also outright failed. Given that the only successful entry with Pd(PPh₃)₄ was entry 6 and the result was very similar to entry 2 with Pd(OAc)₂, entries 10-12 returned to Pd(OAc)₂ as the precatalyst, but changed the carboxylate to AdCO₂H. Thompson et al. had used pivalic acid due to alkyl branching at the carbon α to the carbonyl.¹⁴⁴ Their studies indicated that tertiary branched acids were superior to primary branched acids because the C-H activation of DARP could occur at the 4-position on thiophene, instead of the desired 5-position.¹⁴⁴ This would lead to branched polymers that could cross-link with others, which increases the molecular weight, but decreases solubility, decreases the yield and for cross-conjugated polyradicals, allow for conjugation and overall lowering of the ground state spin. Hypothesizing that using a tertiary acid may help increase the yield, AdCO₂H was used instead of linear stearic acid. Entry 10 met with failure using AdCO₂H at 125 °C for 20 h and did not produce any material of sufficient mass to precipitate when the reaction was dripped into MeOH. Reattempting the polymerization at 100 °C for 18 h in entry 11 met with the greatest success in Table II-11 that gave a polymer with DP = 17 so that it was soluble and in a 79% yield. Entry 12 was a reattempt of entry 10 with

slightly less time and provided contradicting results with a DP = 16 and yield of 30% against entry 10's material that was too low of molecular weight to precipitate. Entry 11 provided enough material to continue on in the synthesis and no further attempts were tried and would be the starting point for future attempts to use DArP with polythiophenes with appended CatMOM₂.

Table II-11. pThCatMOM₂ DArP conditions.



Entry	Catalyst	Carboxylate	Solvent	Temp/ Time	Results
1	Pd(OAc) ₂	CH ₃ (CH ₂) ₁₆ CO ₂ H	DMF	70 °C/ 24h	M _n = 5.58 kDa; DP = 17; PDI = 1.41; 18% yield
2 ^a	Pd(OAc) ₂	CH ₃ (CH ₂) ₁₆ CO ₂ H	DMAc	160 °C/ 72h	M _n = 8.78 kDa; DP = 31; PDI = 4.36; 36% yield
3	Pd(OAc) ₂	CH ₃ (CH ₂) ₁₆ CO ₂ H	DMAc	120 °C/ 48h	M _n = 5.18 kDa; DP = 18; PDI = 1.22; 52% yield
4 ^b	Pd(OAc) ₂	CH ₃ (CH ₂) ₁₆ CO ₂ H	DMAc	100 °C/ 1h	Black solution, no precipitate
5 ^a	Pd(OAc) ₂	CH ₃ (CH ₂) ₁₆ CO ₂ H	DMAc	160 °C/ 24h	Dark insoluble solid
6 ^a	Pd(PPh ₃) ₄	CH ₃ (CH ₂) ₁₆ CO ₂ H	DMAc	90 °C/ 24h	M _n = 8.66 kDa; DP = 31; PDI = 1.46; 11% yield
7	Pd(PPh ₃) ₄	CH ₃ (CH ₂) ₁₆ CO ₂ H	25% H ₂ O/ PhMe	90 °C/ 24h	No Color change; No Reaction
8 ^c	Pd(PPh ₃) ₄	CH ₃ (CH ₂) ₁₆ CO ₂ H	DMAc	90 °C/ 24h	No Color change; No Reaction
9	Pd(PPh ₃) ₄	AdCO ₂ H	DMPU	90 °C/ 24h	No Reaction; Black precipitate (catalyst decomp.)
10	Pd(OAc) ₂	AdCO ₂ H	DMAc	125 °C/ 20h	Very low molecular weight material; doesn't precipitate from MeOH
11	Pd(OAc) ₂	AdCO ₂ H	DMAc	100 °C/ 24h	M _n = 5.72 kDa; DP = 17; PDI = 1.50; 79% yield
12	Pd(OAc) ₂	AdCO ₂ H	DMAc	125 °C/ 18h	M _n = 5.38 kDa; DP = 16; PDI = 1.56; 30% yield

Typical conditions: monomer:catalyst ratio = 100:1; 0.3 eq. of Carboxylate; 2 eq. of K₂CO₃

^a Very poor solubility; could not continue

^b Microwave heating was used

^c Cs₂CO₃ was the base

From pThCatMOM₂, the MOMs were removed with aqueous HCl in THF and the catechol polymer was oxidized to the pThBQ with NaIO₄ in water and acetone. The catechol polymer was never fully isolated and dried because it was found that if it was concentrated to dryness it could not be redissolved. **pThBQ** had slight solubility in CH₂Cl₂, but not much else and was purified before complexation with **CoL_A** by another precipitation into MeOH and drying.

II.5.2. Results.

EPR spectroscopy. Figure II-24 shows the EPR spectra from the monomer radical, ThSQ, and 0.25, 0.50, 0.75 and 1 eq. of Co^{II}L_A added to 1 eq. of pThBQ and stirred for 24 h in CH₂Cl₂ to ensure completion of the complexation and redox reaction. As can be seen, ThSQ shows a doublet of octets, corresponding to the proton hyperfine ($a = 3.1$ Gauss) and the cobalt nuclear spin of $7/2$ ($a = 10.3$ Gauss). **3,5-di-tert-butylsemiquinone-cobalt (III) complex displayed proton and cobalt hyperfine of** When radicals are generated in the polymer the EPR spectra change, one change was seen with the PoPE-SQ polymers where the hyperfine became broadened and/or merged into a featureless singlet for the 25, 50, 75 and 100% polymers. This featureless singlet is probably the result of multiple polymer chains of different lengths that result in slightly different g values and superimpose the various EPR spectra on top of one

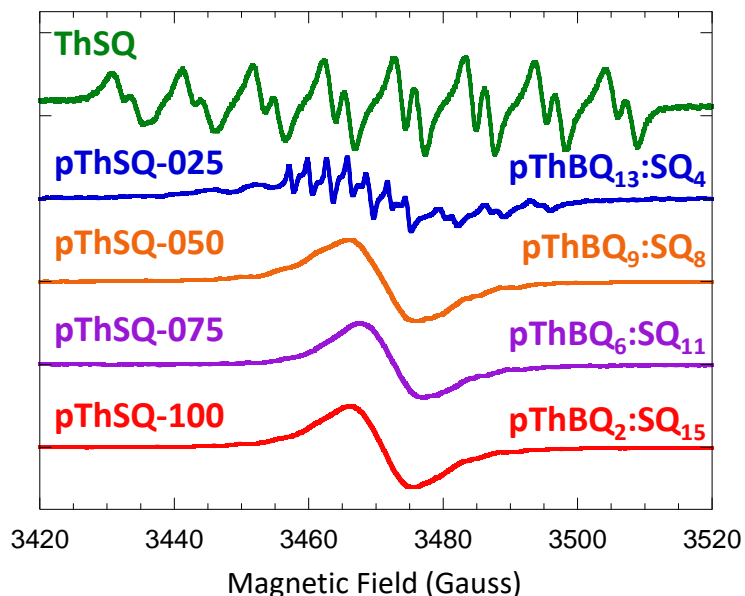


Figure II-24. EPR spectra of a monomer radical (ThSQ) and four polymers that have been reacted with 0.25, 0.50, 0.75 and 1.00 eq. of CoLA: pThSQ-025, pThSQ-050, pThSQ-075 and pThSQ-100, respectively.

another. In the pThSQ series there are two other related changes occurring between the polymers and the monomeric ThSQ. This is most easily seen in pThSQ-025 where the spectral width narrows and smaller hyperfine coupling constants are observed according to the hyperfine coupling as a fraction of the number of coupled radicals (a/N). So, in ThSQ if the hyperfine coupling with respect to the proton is 3.1, then in a biradical it should be $3.1/2 \approx 1.55$ Gauss and the cobalt hyperfine coupling would be $10.3/2 \approx 5.15$ Gauss. This fractionating of the hyperfine coupling leads to an overall smaller spectral width and is indicative of higher order states in the polyradicals: triplets, quartets, etc. In Figure II-25, these hyperfine couplings are analyzed via stick diagrams to show hyperfine coupling constants that can be ascertained in the spectrum of pThSQ-025 beside those for the monomer ThSQ (upper left of Figure II-25). The EPR spectrum of ThSQ has green lines (10.3 Gauss) showing the hyperfine coupling with respect to the cobalt nucleus and purple lines with respect to the proton hyperfine (3.1 Gauss). The EPR spectrum for pThSQ-025, the outer lines and on the right-hand side of the spectrum, hyperfine couplings of

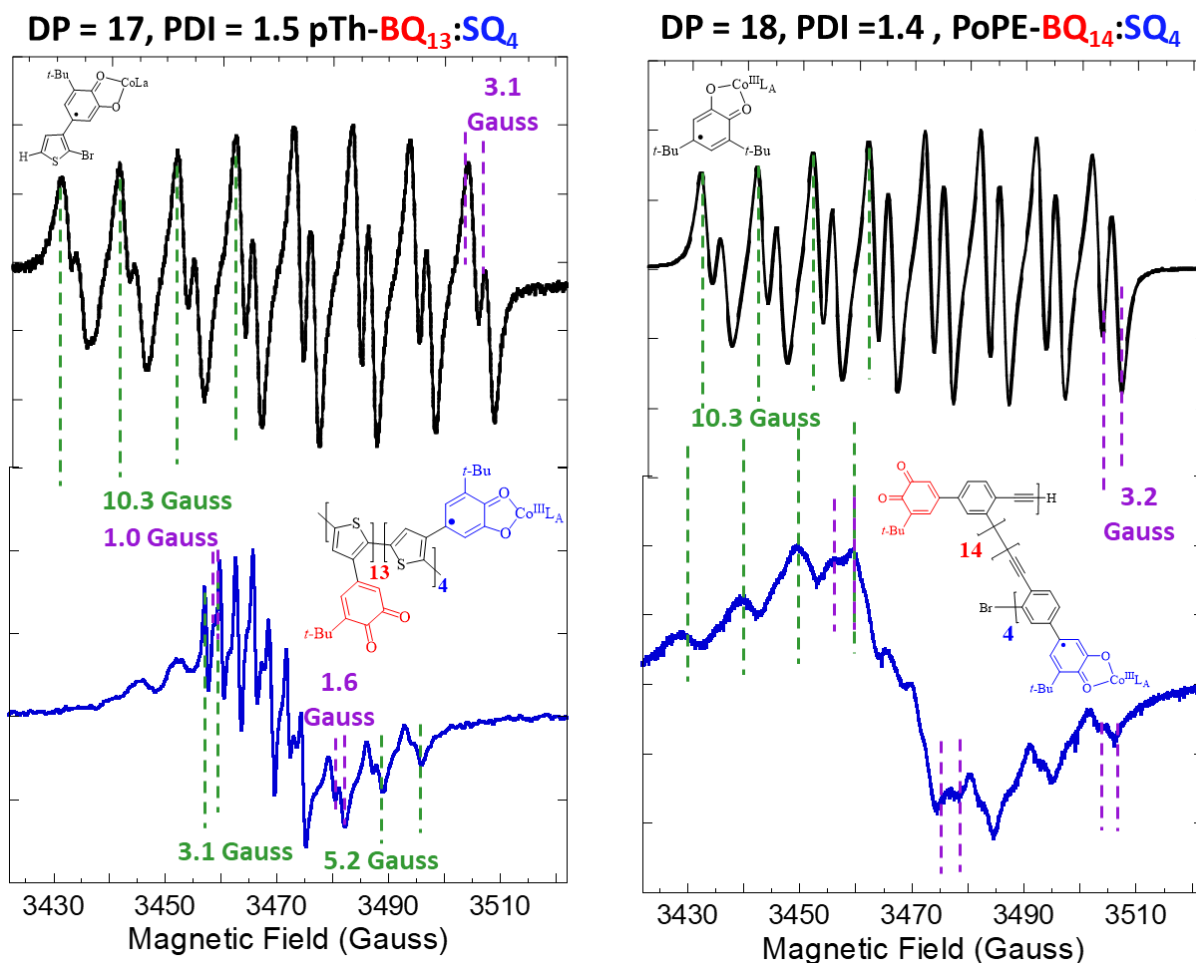


Figure II-25. EPR spectra of **ThSQ** and **pThSQ-025** (left) and **3,5-di-tert-butylsemiquinone** and **PoPESQ-025** (right). Both polymers are 17 or 18 units long with PDIs of 1.5 or 1.4 and are both the nominally 25% spin concentration versions.

5.2 and 1.6 Gauss can be deciphered, which are for all intents and purposes 5.15 and 1.55 Gauss; which would correspond to two semiquinone radicals interacting through the polymer chain. Nearer to the center of the spectrum, hyperfine couplings of approximately 3.1 and 1.0 Gauss can be identified which would correspond to the hyperfine coupling constants for cobalt and the proton due to the interaction with three radicals interacting with the nuclei. This is particularly interesting because this is a polymer that only has 25% of its individual monomer units as radicals. From its EPR spectrum, pThSQ-025 is dominated by bi- and tri-radicals, which means for a polymer where only a random 3-4 of the units out of 17 are radicals, the radicals are not

only delocalized, but these few radicals are most likely interacting with each other across multiple units. For comparison, the right-hand side of Figure II-25 shows the spectra of 3,5-di-*tert*-butylsemiquinone-cobalt (III) complex and the corresponding **PoPESQ-025** polymer. Unsurprisingly, 3,5-di-*tert*-butylsemiquinone-cobalt (III) complex also exhibits the doublet of octets corresponding to the proton and cobalt hyperfine coupling with hyperfine coupling constants of 3.2 and 10.3 Gauss, very similar to **ThSQ**. **PoPESQ-025** (bottom right of Figure II-25) displays hyperfine coupling as well from the constituent monomers containing the proton and cobalt nuclei. However, in this case the 3.2 and 10.3 Gauss hyperfine coupling that was observed in 3,5-di-*tert*-butylsemiquinone-cobalt (III) complex is still the dominant species in the **PoPESQ-025** polyradical; indicating that the semiquinone radicals are not interacting strongly with each other.

In Figure II-24, the EPR spectra of the 50, 75 and 100% **pThSQ** polyradicals no longer have ascertainable hyperfine coupling constants very similar to the EPR spectra of 50, 75 and 100% **PoPESQ** polyradicals and are relatively featureless singlets. **pThSQ-050** has some residual biradical or triradical signal remaining on the outer spectrum, but is mostly the singlet. The difference between the **PoPESQ** and **pThSQ** polyradicals is that the **PoPESQ** polyradicals are featureless singlets with the same spectral width, probably resulting from the varying *g*-values of differing polymer lengths. The **pThSQ** polyradicals continue to noticeably decrease in spectral width going from **ThSQ** to **pThSQ-075**; **pThSQ-100** does not visibly seem to decrease any further from **pThSQ-075**.

Magnetometry. Figure II-26 shows the SQUID magnetometry data for **pThSQ-025**, **pThSQ-050** and **pThSQ-075** alongside the theoretical Brillouin functions for $S = 1/2, 2/2, 3/2$ and $4/2$. As can be seen, the plots of all three **pThSQ** seem to follow the $S = 1/2$ Brillouin

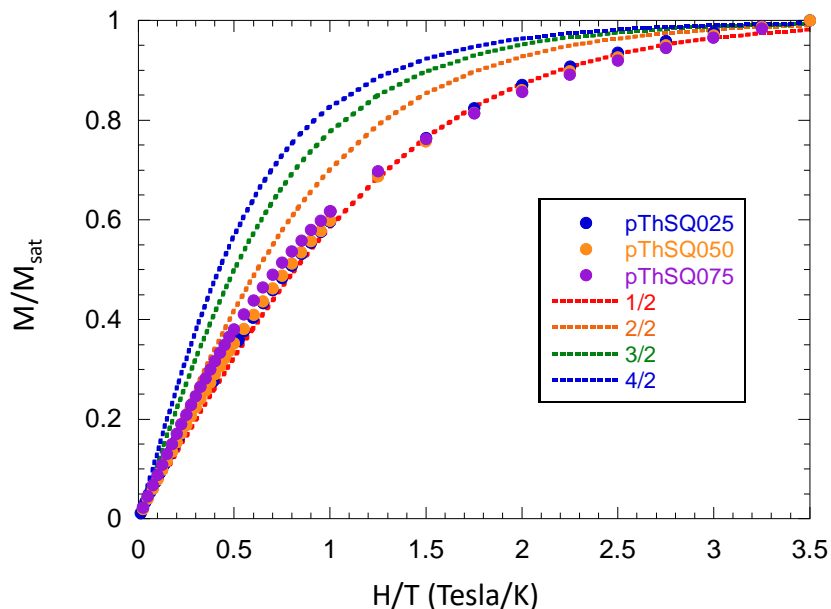


Figure II-26. M/M_{sat} plots for **pThSQ-025**, **pThSQ-050** and **pThSQ-075** in polystyrene films alongside theoretical Brillouin function plots for $S = 1/2, 2/2, 3/2$ and $4/2$. Magnetic field was swept from 0.05 to 7 T while the temperature was held at 2 K.

function with only slight variation at weaker field strengths. This would indicate that the high-spin coordinated coupling is not observed for the polyradicals that have been cast into polystyrene films. This was similarly observed for the **PoPESQ** polyradicals. This could be due to the polymer chains possibly having aggregated when the polystyrene films were drying and if the chains are close enough, weak antiferromagnetic through-space interactions between the chains could be lowering the overall spin of the system. Alternatively, there could be a high number of head-head (HH) or tail-tail (TT) couplings rather than the desired head-tail (HT), in which two or more separate ferromagnetically coupled segments of one polymer chain cancel each other out. Figure II-27 illustrates the effect of defects in a tetramer of **pThSQ-100**, where there are three bonds between monomers in the oligomer. Blue bonds represent the desired HT linkages that give rise to ferromagnetic coupling between radicals and red bonds represent either HH or TT defects that lead to antiferromagnetic coupling. Because there are three bonds, all the

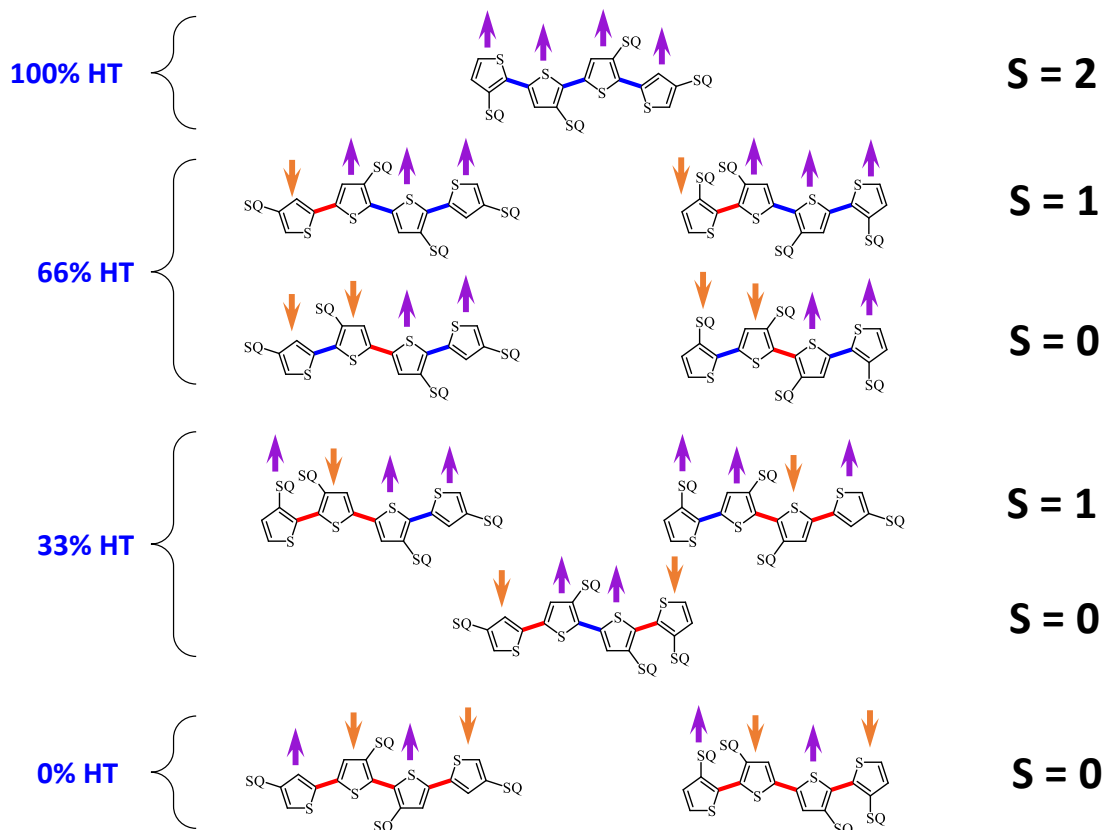


Figure II-27. Examples of head-tail (HT), head-head (HH) or tail-tail (TT) linkages in a tetramer of pThSQ-100 and the effect of placement of the defect in the oligomer has on the ground-state spin of the oligomer.

bonds can be 100% HT linkages or 66% HT linkages with the 66% HT having two options depending on where the HH or TT linkages is found along the polymer chain. In the 100% HT linkages, the ground-state spin of the system will be $S = 2$ with four spin 1/2 unpaired electrons all ferromagnetically coupled with each other. The middle example of 66% HT linkages where the HH or TT defect is observed at the end of the oligomer gives an $S = 1$ because three 1/2 spins are ferromagnetically coupled with each other, but antiferromagnetically coupled with the end unit ($S = 3/2 - 1/2 = 1$); still a non-zero net ground-state spin. The worst case-scenario for a high-spin polymer is the bottom example of 66% HT linkages where the HH or TT defect is somewhere in the middle of the polymer so that most or all of the 1/2 spins cancel each other out. Here each set of two thiophene units on each side are ferromagnetically coupled with each other, but antiferromagnetically coupled with the other set because the defect is in the middle, which

results in a minimized ground state spin or in this oligomer, $S = 2/2 - 2/2 = 0$; a net zero ground state spin. Only 33% HT linkages will also result in either an $S = 1$ or $S = 0$ ground state spin, depending on the location of the defect and 0% HT linkages will only result in a ground state spin, $S = 0$. As can be seen from the examples given in Figure II-27, one or more defects, depending on location in the conjugated polymer backbone can have deleterious effects on the outcome of the ground state spin of the polyradical if a high-spin polyradical is intended.

II.5.3. Conclusions.

Several polyradicals of metallo-semiquinone-containing polythiophenes have been synthesized by the redox-complexation reaction of $\text{Co}^{\text{II}}\text{L}_A$ with the corresponding quinone polymer, **pThBQ**, which was in turn synthesized from the **2-Br-3-(MOM₂Cat)Th** by direct arylation polymerization (DAP) with $\text{Pd}(\text{OAc})_2$ as a precatalyst and AdCO_2H as the carboxylate to facilitate the weakening of thiophene's 5-position C-H bond similar to preparations of polythiophenes by Thompson et al.^{136,143,144,152} The EPR spectra of **ThSQ**, **pThSQ-025**, **pThSQ-050**, **pThSQ-075** and **pThSQ-100** indicated higher order radicals, such as at least bi- and triradicals that could be observed in just **pThSQ-025** and the observed spectral narrowing of **pThSQ-050**, **pThSQ-075** and **pThSQ-100** suggests that these polyradicals were interacting with each other more than **pThSQ-025**.

The EPR spin concentration measurements that were performed on **PoPE-SQ** were unsuccessful for **pThSQ**. **pThSQ-025** and **pThSQ-075** were approximately consistent relative to each other, but the **pThSQ-050** and **pThSQ-100** were an order of magnitude signal intensity greater. Attempts to replicate the syntheses of the polyradicals were challenging and may provide an explanation for the disparate results between the 25 and 75% polyradicals versus the 50 and 100% polyradicals. During attempted replication of the syntheses, there was a large amount of

each of the polyradicals that were insoluble and depending on length of the polymer, some redox/complexation reactions were largely unsuccessful and only provided noisy singlet signals in EPR. The EPR signals that were obtained and were reported are probably the result of a small fraction of **pThSQ** that were soluble. Regardless, the conclusions about the splitting of the hyperfine coupling constants being indicative to polyradicals rather than isolated monoradicals and correspondingly the observed spectral narrowing are still valid despite the poor solubility, which are that polythiophene allows for enough delocalization and coupling between radicals to allow the semiquinones to interact with each other. A sample of **pThSQ** where the semiquinone-quinone copolymers could be successfully generated, measured without solubility issues and/or cast onto substrates or have other analyses performed would need to be less than 17 units with a low PDI. Several attempts to synthesize **pThCatMOM₂** with DPs low enough to be soluble, but still isolatable were unsuccessful. However, the information that was provided from the EPR studies on these polymers that lacked sufficient solubility, particularly **pThSQ-025**, provided an alternative strategy to resist insolubility and provide a high spin polymer with decent coupling between radicals.

Alkyl chains are a common technique to afford solubility to macromolecules. Thiophene copolymers with alkyl chains at either just the 3 or 3 and 4 positions of thiophene have been utilized to afford better solubility to growing polymer chains during polymerization or to provide easier solution manipulation of resulting polymers.¹⁶¹ From the EPR spectrum of **pThSQ-025** it was observed that metallo-semiquinone pendant groups on a polythiophene could interact with each other to afford at least a majority bi- and triradicals in a polymer that was 17 units long with a random distribution of those units being radicals. This would suggest, by probability, that many of these radicals were able to interact over two or more diamagnetic thiophene units to provide

the observed fractionating of the hyperfine coupling constants that were observed in a monoradical of the monomer, ThSQ. Given this, a trade-off for in a 100% of the BQ units being converted to SQ would be to have an alternating copolymer where every other unit would have a SQ radical and the units in between the radicals would be thiophenes with alkyl groups appended in order to provide the greater solubility. In theory, the trade-off would be that fewer units could be radicals for increased solubility which could overall provide a much higher working molecular weight which may overall have more units that are radicals. Appendix A shows the synthetic progress that was made toward this polymer and recommends what could be synthetically simpler polymer via the Stille copolymerization of two symmetric monomers to provide a high spin, soluble polyradical in only 4 synthetic steps to protected-catechol-like copolymer.

II.6. Experimental for polyradicals

II.6.1. PoPE-SQ.

Experimental

General Considerations. Reagents and solvents were purchased from commercial sources and used as received unless otherwise noted. ^1H and ^{13}C NMR spectra were recorded on a Varian Mercury 400 MHz spectrometer at room temperature. ^1H and ^{13}C chemical shifts are listed in parts per million (ppm) and are referenced to residual protons or carbons of the deuterated solvents, respectively. Reactions where microwave irradiation is listed as the heat source were performed on a CEM Discover system. Infrared spectra were recorded on a Brüker Vertex 80v spectrometer with Brüker Platinum ATR attachment. Elemental analyses were performed by Atlantic Microlab Inc. for CHN analysis and replicated when possible.

GPC Analysis. Measurements of oligomeric materials were obtained on a Shimadzu Scientific Instrument using LC-20AD pump. Anhydrous THF was used as the eluent at a flow rate of 1 mL/min on a Jordi-gel DVB column. Column specifications are pores of 1000 Å, length of 250 mm, and ID of 10 mm. Molecular weights were determined by GPC using narrow polystyrene standards with $M(p)$ 250-70,000 by Fluka Analytical bought from Sigma-Aldrich. Samples were prepared by dissolving a few mg of sample in 1 mL of anhydrous THF then passed through a 25 mm syringe filter with w/ 0.2 μm membrane.

Electronic Absorption Spectroscopy. Electronic absorption spectra were recorded on a Shimadzu UV-3600 UV-Visible Spectrophotometer instrument in spectroscopic grade, anhydrous CH_2Cl_2 as solvent.

Emission Spectroscopy. Emission and excitation data were collected using an Edinburgh Instruments FLS980 series emission spectrophotometer. Samples were prepared in spectroscopic grade, anhydrous CH_2Cl_2 and collected in quartz cuvettes.

EPR Spectroscopy. Spectra were recorded on an IBM ER200D-SRC EPR spectrometer in anhydrous, degassed CH_2Cl_2 and collected in 3 mm quartz EPR tubes.

Spin concentration determination.

A calibration plot for the determination of spin concentration in the polymer was made by making a calibration plot of the doubly integrated EPR signal as a function of concentration of DPPH radical in mmol/mL (Figure II-28). Five standards of DPPH were prepared in an inert

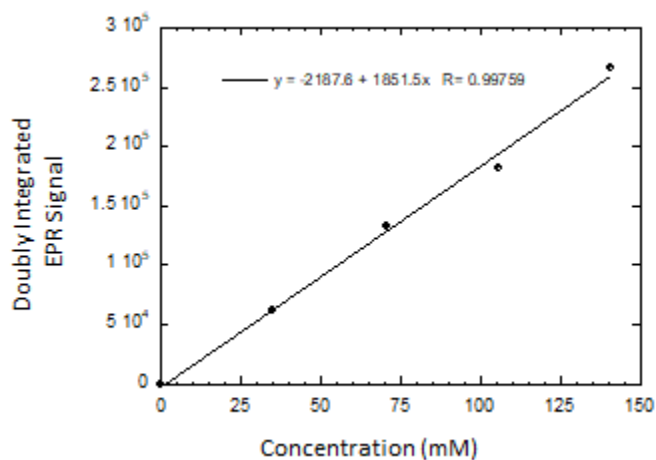


Figure II-28. Spin concentration calibration plot.

atmosphere by making solutions of 0, 14, 28, 42, and 56 mg of DPPH in 1 mL of degassed, anhydrous CH₂Cl₂. The EPR spectra were collected in 3mm quartz EPR sealed-tubes with a sweep time of 20 s and generated from the average of five scans. The data was processed by correcting the signal data for entry 5 in Table II-12 for the change in the gain by multiplying the signal by the ratio of the two gain values (2.0/1.25). The EPR signals for all standards were

Table II-12. DPPH calibration data.

Entry	Amount of DPPH (mg)	Conc. of DPPH in 1 mL CH ₂ Cl ₂ (mM)	Gain (*10 ²)	Area (Doubly integrated EPR signal)
1	0	0	2.0	0.0000
2	14	35	2.0	6.1476*10 ⁴
3	28	71	2.0	1.3241*10 ⁵
4	42	106	2.0	1.8243*10 ⁵
5	56	141	1.25	2.6633*10 ⁵

* Amplitude modulation must and was kept constant at 0.16.

integrated once to give the absorption spectra, then a baseline correction was performed by subtracting a straight line generated from the endpoints of the spectra (data points at x = 3422

and 3522 Gauss). The baseline-corrected absorption spectra were then integrated to give the area under the curve. These areas were plotted as a function of concentration of DPPH and then fitted with a linear line of regression.

4-Bromo-2-(*tert*-butyl)phenol (BrPhOH).³⁸ To a 250 mL round-bottom flask was added 2-(*tert*-butyl)phenol (20.0 g, 133 mmol) of with 100 mL of dichloromethane and cooled to -40 °C. To this solution was added bromine (18.6 g, 133 mmol), dropwise. Once the addition of bromine was complete, the reaction was allowed to stir for another hour, after which 50 mL of H₂O was added and allowed to stir for 0.5 h. The reaction was then washed with NaHCO₃ and NaCl three times and extracted three times with diethyl ether. The organic extracts were dried with Na₂SO₄, filtered, and then the solvent was removed in vacuo to yield a clear, slightly pink tinted oil (27.9 g, 94% yield). ¹H NMR (300 MHz, CDCl₃, δ ppm): δ = 7.36 (d, *J* = 2.4 Hz, 1H), 7.16 (dd, *J* = 8.4, 2.4 Hz, 1H), 6.46 (d, *J* = 8.4 Hz, 1H), 4.88 (s, 1H), 1.39 (s, 9H).

5-Bromo-3-(*tert*-butyl)benzene-1,2-diol (CatBr).³⁸ Compound BrPhOH (5.01 g, 21.9 mmol) was added to a 250 mL round-bottom flask along with 60 mL of dichloromethane. 2-Iodoxybenzoic acid (8.00 g, 28.6 mmol) of was added and the reaction was stirred in the dark at room temperature for 48 h. After which the reaction was diluted with 100 mL of diethyl ether, washed with NaHCO₃ and NaCl three times. The organic layer was extracted, dried with Na₂SO₄, filtered, and solvent was removed under reduced pressure. The resulting dark red oil was then re-dissolved in 100 mL THF and placed under nitrogen. 5.07 g (28.4 mmol) of ascorbic acid, dissolved in 15 mL of H₂O was added and the solution was allowed to stir for 2 h. The reaction was then diluted with EtOAc and washed with NaCl. The organic layer was separated, dried with Na₂SO₄, filtered and solvent was removed in vacuo pressure to give an orange oil

(4.29 g, 80%). $^1\text{H NMR}$ (300 MHz, CDCl_3 , δ ppm): $\delta = 6.97$ (d, $J = 1.9$ Hz, 1H), 6.87 (d, $J = 1.9$ Hz, 1H), 1.38 (s, 9H).

5-Bromo-1-(*tert*-butyl)-2,3-bis(methoxymethoxy)benzene (MOM_2CatBr).³⁸ To a 0 °C cooled solution, under nitrogen, of CatBr (5.35 g, 21.8 mmol) in 40 mL of dichloromethane was added a catalytic amount of 4-dimethylaminopyridine and 16.9 g (130 mmol) of $\text{N,N}'$ -diisopropylethylamine were added and the reaction was stirred at 0 °C for 10 minutes before 6.80 g (84.3 mmol) of methoxymethyl chloride was added. The solution was stirred at 0 °C for another 15 minutes, then was heated to reflux for 15 h. The reaction was cooled, diluted with EtOAc, neutralized with NH_4Cl and washed with NaCl. The organic layer was extracted and dried with Na_2SO_4 , filtered and solvent was removed in vacuo to give a red oil (6.51 g, 90%) of. $^1\text{H NMR}$ (300 MHz, CDCl_3 , δ ppm): $\delta = 7.19$ (d, $J = 2.4$ Hz, 1H), 7.10 (d, $J = 2.4$ Hz, 1H), 5.17 (s, 2H), 5.15 (s, 2H), 3.64 (s, 3H), 3.50 (s, 3H), 1.39 (s, 9H).

Pinacolyl(1,2-dimethoxymethoxy-6-*tert*-butyl-1-phenyl) boronate ($\text{MOM}_2\text{CatBpin}$).³⁸ To an oven-dried 50 mL round-bottom flask was added **3** (3.28 g, 9.84 mmol) and was purge-pumped three times, filling with nitrogen on the final cycle. **3** was dissolved in 20 mL of anhydrous THF and cooled to -78 °C. *n*-BuLi (4.60 mL, 12.2 mmol, 2.65 M) was added dropwise over 20 minutes and was allowed to stir 0.5 h after the addition was complete. Isopropoxy boronic acid pinacol ester (2.80 mL, 13.7 mmol) was added dropwise and allowed to stir 0.5 h at -78 °C and then warmed to room temperature and allowed to stir a further 18 h. The reaction was filtered through a layer of celite and washed with EtOAc. The solvent was removed and the residue was purified by flash chromatography (deactivated silica gel, gradient 2-20% EtOAc/hexanes) to give $\text{MOM}_2\text{CatBpin}$ (2.19 g, 5.76 mmol, 59%) as a yellow oil. TLC: $R_f = 0.48$ (10% EtOAc/

hexanes). $^1\text{H NMR}$ (300 MHz, CDCl_3 , δ ppm): $\delta = 7.47$ (d, $J = 2.4$ Hz, 1H), 7.40 (d, $J = 2.4$ Hz, 1H), 5.24 (s, 2H), 5.21 (s, 2H), 3.65 (s, 3H), 3.52 (s, 3H), 1.44 (s, 9H), 1.26 (s, 12H).

2-Bromo-4-iodotoluene (II-6).³⁸ To a 250 mL round-bottom flask containing 3-bromo-4-methylaniline (10.0 g, 53.7 mmol) of was added 60 mL of 12 M HCl and 100 mL of H_2O , the solution was heated to dissolve white precipitate. This solution was cooled to 0 °C before adding sodium nitrite (4.05 g, 58.7 mmol) of dissolved in 10 mL of H_2O , dropwise. The solution was stirred at 0 °C for 1 h. Then, 9.48 g (57.1 mmol) of potassium iodide, dissolved in 7 mL of H_2O , dropwise. The resulting red solution was stirred at 0 °C for 1 h, was then placed in an oil bath heated to 90 °C for 45 minutes. The reaction was cooled to room temperature, then neutralized with NaHCO_3 , washed with $\text{Na}_2\text{S}_2\text{O}_3$, and extracted three times with diethyl ether. The extracts were dried with Na_2SO_4 , filtered and solvent was removed in vacuo. The red oil was purified via SiO_2 chromatography with 100% hexanes as eluent to give a colorless oil (12.2 g, 41.1 mmol, 77%). TLC: $R_f = 0.8$ (100% hexanes). $^1\text{H NMR}$ (300 MHz, CDCl_3 , δ ppm): $\delta = 7.86$ (d, $J = 1.8$ Hz, 1H), 7.50 (dd, $J = 8.1, 1.8$ Hz, 1H), 6.95 (d, $J = 8.1$ Hz, 1H), 2.34 (s, 3H).

2-Bromo-4-iodobenzyl bromide (II-7).³⁸ Under nitrogen, N-bromosuccinimide (8.80 g, 49.4 mmol) and benzoyl peroxide (1.01 g, 4.17 mmol) of was added to a stirring solution of **II-5** (12.2 g, 41.2 mmol), dissolved in 25 mL of anhydrous benzene contained in a 100 mL round-bottom flask. The solution was heated to reflux for 20 h. 25 mL of H_2O and 50 mL of saturated NaHCO_3 solution were added and the reaction was stirred for 15 minutes before extracting three times with diethyl ether. The extract was dried with Na_2SO_4 , filtered and solvent was removed in vacuo, producing a red oil (6.42 g, 73%). $^1\text{H NMR}$ (300 MHz, CDCl_3 , δ ppm): $\delta = 7.93$ (d, $J = 1.8$ Hz, 1H), 7.62 (dd, $J = 8.1, 1.8$ Hz, 1H), 7.17 (d, $J = 8.1$ Hz, 1H), 4.53 (s, 2H).

2-Bromo-4-iodobenzaldehyde (II-8).³⁸ Compound **II-5** (15.5 g, 41.2 mmol) was added to an oven-dried 100 mL round-bottom flask and dissolved in 50 mL of anhydrous DMSO and placed in the dark under nitrogen. 2-Iodoxybenzoic acid (11.4 g, 40.8 mmol) was added and the reaction was heated to 65 °C for 18 h. The reaction was cooled to room temperature and saturated solution of NaHCO₃ was added until the foaming stopped and stirred for 10 minutes. 100 mL of diethyl ether was added and stirred for 15 minutes after which the organic layer was extracted, dried with Na₂SO₄, filtered, and the solvent was removed in vacuo. Removal of solvent yielded a sticky, yellow solid, which was placed in a medium frit and washed with hexanes to give **II-7** as an off-white solid (6.39 g, 20.6 mmol, 50%). ¹H NMR (300 MHz, CDCl₃, δ ppm): δ = 10.28 (s, 1H), 8.60 (d, *J* = 1.5 Hz, 1H), 7.78 (dd, *J* = 8.1, 1.5 Hz, 1H), 7.60 (d, *J* = 8.1 Hz, 1H).

2-(4-Iodo-2-bromophenyl)-1,3-dioxolane (II-9).³⁸ Compound **II-8** (1.00 g, 3.23 mmol), ethylene glycol (0.400 mL, 7.16 mmol), and *p*-TSOH (73 mg, 0.38 mmol) and 40 mL of toluene were added to a 50 mL oven-dried, round-bottom flask with a Dean-Stark apparatus and heated to reflux for 24 h. The reaction was cooled to room temperature, concentrated and diluted with Et₂O. The organic layer was washed with aqueous NaHCO₃ and NaCl. The organic layer was extracted and dried with Na₂SO₄, filtered, and solvent was removed in vacuo to give a solid tan product (1.0 g, 2.9 mmol, 88%). ¹H NMR (300 MHz, CDCl₃, δ ppm): δ = 7.92 (d, *J* = 1.5 Hz, 1H), 7.67 (dd, *J* = 8.1, 1.5 Hz, 1H), 7.31 (d, *J* = 8.1 Hz, 1H), 6.01 (s, 1H), 4.10 (dd, *J* = 15.7, 3.5 Hz, 4H).

2-(3-bromo-3'-(*tert*-butyl)-4',5'-bis(methoxymethoxy)-[1,1'-biphenyl]-4-yl)-1,3-dioxolane (II-10).³⁸ An oven-dried 50mL round-bottom flask was charged with 1.00 g (2.63 mmol) of MOM₂CatBpin and 1.39 g (3.92 mmol) **II-9**, purge-pumped three times, filled with nitrogen and

0.141 g (0.122 mmol) of Pd(PPh₃)₄ was added under an inert atmosphere. 10 mL of degassed THF and 4.00 mL of aqueous 2M K₂CO₃, then equipped with a nitrogen-purged reflux condenser, the flask was shielded from light, placed in a sand bath and heated to reflux for 48 h. Reaction was cooled to room temperature, diluted with Et₂O, and washed with aqueous NaCl. The organic layer was separated, dried with Na₂SO₄, filtered, and solvent was removed. The crude oil was purified by flash chromatography (deactivated silica gel, 1-35% EtOAc/ hexanes) and the third band was collected and solvent was removed to give **II-10** as a yellow oil (0.673 g, 1.39 mmol, 53%). TLC: R_f = 0.40 (deactivated silica gel, 10% EtOAc/ hexanes). ¹H NMR (300 MHz, CDCl₃, δ ppm): δ = 7.73 (d, *J* = 1.8 Hz, 1H), 7.63 (d, *J* = 8.1 Hz, 1H), 7.50 (dd, *J* = 8.1, 1.8 Hz, 1H), 7.21 (d, *J* = 1.8 Hz, 1H), 7.18 (d, *J* = 1.8 Hz, 1H), 5.25 (s, 1H), 5.24 (s, 1H), 4.15 (dd, *J* = 15.7, 3.5 Hz, 4H), 3.68 (s, 3H), 3.54 (s, 3H), 1.47 (s, 12H).

2-Bromo-4-(3'-*tert*-butyl-4', 5'-dimethoxymethoxyphenyl)benzaldehyde (II-11).³⁸ To an oven-dried 50 mL round-bottom flask was added MOM₂CatBpin (1.45 g, 3.81 mmol) and **II-36** (1.40 g, 3.92 mmol) and purge-pumped three times, filling with nitrogen on the final cycle. Pd(PPh₃)₄ (219 mg, 0.190 mmol) was added. 20 mL of anhydrous, degassed THF was added and degassed aqueous K₂CO₃ (4.00 mL, 8.00 mmol, 2 M) was added via syringe. The flask was equipped with a nitrogen-purged reflux condenser and heated to 65 °C in the dark for 28 h. The reaction was cooled, washed with aqueous NaCl, and then extracted with diethyl ether. The organic layer was dried with Na₂SO₄, filtered and then the solvent was removed. The residue was dissolved in acetone and a catalytic amount of PPTS was added, heated to 30 °C and stirred for 48 h. After the deprotection was complete, the solvent was removed in vacuo and the residue was purified with flash chromatography (deactivated silica gel, 2-20% EtOAc/ hexanes) to give **II-9**

as a yellow oil (1.01 g, 2.31 mmol, 60%). ¹H NMR (300 MHz, CDCl₃, δ ppm): δ = 10.37 (s, 1H), 7.95 (d, *J* = 8.1 Hz, 1H), 7.90 (d, *J* = 1.5 Hz, 1H).

2-Bromo-1-ethynyl-4-(3'-*tert*-butyl-4',5'-dimethoxymethoxy)biphenyl (II-12).³⁸ Compound **II-9** (1.04 g, 2.38 mmol) and 694 mg (5.02 mmol) of K₂CO₃ was added to an oven-dried round bottom flask and purge-pumped three times, then 6 mL of anhydrous methanol was added and the contents were stirred until they dissolved. 606 mg (3.15 mmol) of dimethyl (1-diazo-2-oxopropyl)phosphonate, dissolved in 3 mL of anhydrous methanol via cannula transfer. The reaction was stirred for 2 h, then the solvent was removed in vacuo. The residue was washed with aqueous NH₄Cl and NaCl. The product was extracted with diethyl ether, which was then dried with Na₂SO₄, filtered, then the solvent was removed. The brown oil was purified via flash chromatography (deactivated silica gel, 2-20% EtOAc/hexanes) to give **II-12** as a colorless solid (681 mg, 1.57 mmol, 66%). ¹H NMR (300 MHz, CDCl₃, δ ppm): δ = 7.77 (d, *J* = 1.5 Hz, 1H), 7.56 (d, *J* = 6.0 Hz, 1H), 7.46 (dd, *J* = 6.0, 1.5 Hz, 1H), 7.23 (d, *J* = 1.5 Hz, 1H), 7.19 (d, *J* = 1.5 Hz, 1H), 5.27 (s, 2H), 5.25 (s, 2H), 3.69 (s, 3H), 3.55 (s, 3H), 3.43 (s, 1H), 1.48 (s, 9H). ¹³C NMR (400 MHz, CDCl₃, δ ppm): δ = 150.7, 146.6, 144.1, 143.4, 134.4, 133.9, 130.9, 126.0, 125.9, 122.7, 119.6, 113.5, 99.3, 95.6, 82.4, 82.2, 57.8, 56.6, 35.5, 30.7. FTIR (neat): 3288, 2953, 2903, 2869, 2826, 1736, 1596, 1577, 1530, 1466, 1447, 1436, 1428, 1399, 1372, 1322, 1239, 1201, 1152, 1077, 1010, 956, 939, 831, 764, 724, 682, 548 cm⁻¹.

2-Bromo-4-iodophenylacetylene (II-14).¹⁶² (Bromomethyl)triphenylphosphonium bromide (**II-8**, 0.716 g, 2.31 mmol) and 1.01 g (2.31 mmol) of were added to a 100 mL oven-dried, round-bottom flask and purge-pumped three times, filling with nitrogen on the last cycle. Added 30 mL of anhydrous, degassed THF and cooled to -78 °C. Added 0.272 g (2.42 mmol) of *t*-BuOK suspended in 15 mL of THF and stirred for 1.5 h at -78 °C. The reaction was warmed to room

temperature and added 0.269 g (2.40 mmol) of *t*-BuOK, suspended in 15 mL of THF via cannula transfer. Reaction was stirred for 24 h at room temperature. Reaction was poured into about 50 mL of aqueous NH₄Cl, then diluted with Et₂O. The organic layer was washed with saturated aqueous NaCl, separated, and dried with Na₂SO₄. The layer was filtered and solvent was removed in vacuo. The crude brown oil was purified via flash chromatography (silica gel, 100% hexanes) to give **II-14** as a colorless solid (0.590 g, 1.93 mmol). TLC: R_f = 0.46. ¹H NMR (300 MHz, CDCl₃, δ ppm): δ = 7.96 (d, *J* = 1.5 Hz, 1H), 7.60 (dd, *J* = 8.4, 1.5 Hz, 1H), 7.22 (d, *J* = 8.4 Hz, 1H), 3.43 (s, 1H).

Example for Favorskii Reaction: 3-methyl-1-phenylpent-1-yn-3-ol (II-21).¹⁶³

Phenylacetylene (195 mg, 1.91 mmol) and 161 mg (2.23 mmol) of 2-butanone were added to 10 mL of DMSO. 42 mg (0.37 mmol) of *t*-BuOK was suspended in 5 mL of DMSO and added dropwise, via cannula to the reaction mixture, which turned dark red. The reaction was stirred at room temperature for 3 h. After completion, the reaction was then poured into NH₄Cl, washed with NaCl and extracted with Et₂O. The organic layer was separated and dried with Na₂SO₄, filtered and solvent was removed to give **II-21** as a yellow oil (0.24 g, 1.4 mmol, 72%). This method was adapted for other trials by changing the ketone, base, solvent, reaction time, and temperature. ¹H NMR (300 MHz, CDCl₃, δ ppm): δ = 7.42 (m, 2H), 7.29 (m, 3H), 1.80 (q, *J* = 6.9 Hz, 2H), 1.57 (s, 3H), 1.11 (t, *J* = 6.9 Hz, 3H).

Example of trimethylsilyl protection reaction: trimethyl(phenylethynyl)silane (II-23).¹⁶⁴

Diisopropylamine (215 mg, 2.13 mmol) was added to an oven-dried, nitrogen-purged, round-bottom flask and 15 mL of anhydrous, degassed THF was added. The flask was cooled to -78 °C. 0.900 mL (1.80 mmol) of 2.2 M *n*-BuLi was added via syringe. The reaction was stirred for 5 min. at -78 °C, and then warmed to room temperature. The reaction flask, containing LDA, was

cooled to $-78\text{ }^{\circ}\text{C}$ and added to a $-78\text{ }^{\circ}\text{C}$ reaction flask containing 205 mg (2.00 mmol) of phenylacetylene and 223 mg (2.05 mmol) of chlorotrimethylsilane and stirred for 20 h. The reaction was monitored via TLC, upon completion, the solvent was removed in vacuo. The residue was washed with water and NaCl. The product was extracted with Et_2O , separated, and dried with Na_2SO_4 , filtered and the solvent was removed to give **II-23** as a yellow oil (0.188 g, 1.08 mmol, 60%). This method was adapted for other trials by changing the base, solvent, and reaction time. ^1H NMR (300 MHz, CDCl_3 , δ ppm): $\delta = 7.47$ (m, 2H), 7.33 (m, 3H), 0.250 (s, 9H).

4-Bromostyrene (II-26).¹⁶⁵ (Methyl)triphenylphosphonium iodide (281 mg, 0.692 mmol) was suspended in 20 mL of anhydrous, degassed THF. The suspension was cooled to $-78\text{ }^{\circ}\text{C}$ and 0.310 mL (0.682 mmol) of 2.2 M of *n*-BuLi were added dropwise and allowed to stir 5 min. 300 mg (0.686 mmol) of **II-11** in 5 mL THF were added via cannula to the dark, yellow solution. The reaction was allowed to stir for 2 h, then quenched with aqueous NH_4Cl , and extracted with Et_2O . The organic layer was dried with Na_2SO_4 , filtered, and the solvent was removed in vacuo. The crude brown oil was filtered through a pad of deactivated silica with 100% hexanes as eluent, solvent was removed in vacuo to give a clear oil with a slightly yellow tint (242 mg, 81%). ^1H NMR (300 MHz, CDCl_3 , δ ppm): $\delta = 7.44$ (dd, $J = 6.6, 1.8$ Hz, 2H), 7.26 (dd, $J = 6.6, 1.8$ Hz, 2H), 6.65 (dd, $J = 17.7, 10.8$ Hz, 1H), 5.74 (d, $J = 17.7$ Hz, 1H), 5.27 (d, $J = 10.8$ Hz, 1H).

1-Bromo-4-(1,2-dibromoethyl)benzene (II-27).¹⁶⁵ Compound **II-26** (509 mg, 2.78 mmol), dissolved in 3 mL of CH_2Cl_2 was cooled to $0\text{ }^{\circ}\text{C}$. 0.130 mL (2.89 mmol) of Br_2 was added via syringe dropwise. Upon completion, the reaction was allowed to stir at $0\text{ }^{\circ}\text{C}$ for 1 h and then warmed to room temperature. Aqueous $\text{Na}_2\text{S}_2\text{O}_3$ was added and allowed to stir until the color

disappeared. The organic layer was washed with brine, extracted and dried with MgSO₄. The solvent was removed in vacuo to give a white solid (877 mg, 92%). ¹H NMR (300 MHz, CDCl₃, δ ppm): δ = 7.40 (dd, *J* = 6.6, 1.8 Hz, 2H), 7.30 (dd, *J* = 6.6, 1.8 Hz, 2H), 5.14 (dd, *J* = 10.5, 5.4 Hz, 1H), 4.06 (m, 2H).

(Ethyl ester methyl)triphenylphosphonium bromide.¹⁶⁶ To a solution of 5.01 g (19.1 mmol) of triphenylphosphine in 30 mL of toluene was added 2.40 mL (21.7 mmol) of ethyl bromoacetate was added and heated to reflux and stirred under nitrogen for 2 h after which a white precipitate formed. The precipitate was filtered and washed with toluene and dried under vacuum to afford a white solid (7.44 g, 91%). ¹H NMR (300 MHz, CDCl₃, δ ppm): δ = 7.95-7.26 (m, 15H), 5.62 (d, *J* = 13.8 Hz, 2H), 4.05 (q, *J* = 7.2 Hz, 2H), 1.07 (t, *J* = 7.2 Hz, 3H).

Ethyl-(E)-3-(2-bromo-4-iodophenyl) acrylate (II-28).¹⁶⁷ 0.997 g (3.22 mmol) of **II-27**, 1.527 g (3.56 mmol) of (ethyl ester methyl)triphenylphosphonium bromide, and 0.577 g (4.17 mmol) of K₂CO₃, and 20 mL of CH₂Cl₂ and 20 mL of water were stirred at room temperature for 4 h. After completion the reaction was quenched with aqueous NH₄Cl and washed with brine. The organic layer was extracted, dried with Na₂SO₄, filtered and solvent was removed in vacuo to give the crude brown oil, which was filtered through a layer of silica using 10% EtOAc/hexanes as eluent. The solvent was removed to afford **II-28** as a white solid (1.15 g, 94%). ¹H NMR (300 MHz, CDCl₃, δ ppm): δ = 7.91 (d, *J* = 1.5 Hz, 1H), 7.89 (d, *J* = 15.6 Hz, 1H), 7.59 (dd, *J* = 8.4, 1.5 Hz, 1H), 7.24 (d, *J* = 8.4 Hz, 1H), 6.33 (d, *J* = 15.6 Hz, 1H), 4.24 (q, *J* = 6.9 Hz, 2H), 1.31 (t, *J* = 6.9 Hz, 3H).

Ethyl 2,3-dibromo-3-(2-bromo-4-iodophenyl)propanoate (II-29).¹⁶⁸ 1.15 g (3.02 mmol) of **II-28** was dissolved in 20 mL of CH₂Cl₂ and cooled to 0 °C. 0.140 mL (3.11 mmol) of Br₂ was

added dropwise via syringe. The reaction was allowed to stir at 0 °C for 2 h then warmed to room temperature. Aqueous Na₂S₂O₃ was added and stirred until the orange-red color disappeared. The organic layer was washed with brine, separated, and dried with Na₂SO₄. The organic layer was filtered and the solvent was removed in vacuo to afford **II-29** as a white solid (1.54 g, 94%). ¹H NMR (300 MHz, CDCl₃, δ ppm): δ = 7.95 (d, *J* = 1.8 Hz, 1H), 6.68 (dd, *J* = 8.1, 1.8 Hz, 1H), 7.18 (d, *J* = 8.1 Hz, 1H), 5.83 (d, *J* = 11.1 Hz, 1H), 4.80 (d, *J* = 11.1 Hz, 1H), 3.84 (q, *J* = 7.2 Hz, 2H), 1.35 (t, *J* = 7.2 Hz, 3H).

3-(2-bromo-4-iodophenyl)propionic acid (II-30).¹⁶⁸ *t*-BuOK (1.12 g, 9.97 mmol) was added to a solution of **II-29** (1.54 g, 2.85 mmol) dissolved in 30 mL of THF and heated to reflux under nitrogen for 20 h. The reaction was allowed to cool to room temperature and 50 mL of Et₂O was added and acidified with 2M HCl. The organic layer was separated, dried with Na₂SO₄, filtered, and solvent was removed in vacuo to give **II-30** as a tan solid (0.880 g, 88%). ¹H NMR (300 MHz, DMSO-*d*₆, δ ppm): δ = 8.20 (d, *J* = 1.8 Hz, 1H), 7.83 (dd, *J* = 8.1, 1.8 Hz, 1H), 7.46 (d, *J* = 8.1 Hz, 1H).

Methyl 3-(2-bromo-4-iodophenyl)propiolate (II-31).¹⁶⁹ K₂CO₃ (0.416 g, 3.01 mmol) was added to a solution of **II-30** (0.880 g, 2.51 mmol) and methyl iodide (0.392 g, 2.76 mmol) in 6 mL of DMSO and stirred at room temperature for 3 h. The reaction was washed with water and brine and extracted with Et₂O. The organic layer was dried with MgSO₄, filtered, and solvent was removed in vacuo to give **31** as a tan solid (0.786 g, 78%). ¹H NMR (300 MHz, CDCl₃, δ ppm): δ = 7.99 (d, *J* = 1.8 Hz, 1H), 7.65 (dd, *J* = 8.1, 1.8 Hz, 1H), 7.27 (d, *J* = 8.1 Hz, 1H), 3.85 (s, 3H).

Methyl 3-(3-bromo-3'-(*tert*-butyl)-4',5'-bis(methoxymethoxy)-[1,1'-biphenyl]-4-

yl)propiolate (II-32). Pd(PPh₃)₄ (53 mg, 0.046 mmol) was added to a nitrogen-purged, round-bottom flask containing 366 mg (0.962 mmol) of **II-4** and 351 mg (0.962 mmol) of **II-31**. 10 mL of anhydrous, degassed THF and 2.0 mL (4.0 mmol) of 2M K₂CO₃ solution were added. The flask was protected from the light and heated to reflux with an attached, nitrogen-purged condenser for 21 h. The reaction was cooled to room temperature and washed with brine, and extracted with Et₂O. The organic layer was dried with MgSO₄, filtered and solvent was removed in vacuo to give a crude dark oil. The product was purified with flash chromatography (deactivated silica gel, 2-15% EtOAc/hexanes) to give **II-32** as a tan solid (116 mg, 29%).

TLC: R_f = 0.23 (10% EtOAc/ hexanes). ¹H NMR (300 MHz, CDCl₃, δ ppm): δ = 7.80 (d, *J* = 1.5 Hz, 1H), 7.63 (d, *J* = 7.8 Hz, 1H), 7.50 (dd, *J* = 7.8, 1.5 Hz, 1H), 7.24 (d, *J* = 2.4 Hz, 1H), 7.19 (d, *J* = 2.4 Hz, 1H), 5.27 (s, 2H), 3.87 (s, 3H), 3.68 (s, 3H), 3.54 (s, 3H), 1.48 (s, 9H). ¹³C NMR (400 MHz, DMSO-d₆, δ ppm): δ = 154.3, 150.6, 146.8, 145.1, 144.1, 135.1, 133.3, 131.0, 126.9, 125.9, 120.1, 119.6, 113.4, 99.2, 95.5, 84.6, 84.4, 57.7, 56.5, 53.0, 35.4, 30.5.

3-(3-Bromo-3'-(*tert*-butyl)-4',5'-bis(methoxymethoxy)-[1,1'-biphenyl]-4-yl)propionic acid

(II-33). Compound **II-33** (116 mg (0.236 mmol)) was added to a 10 mL solution of KOH in methanol and stirred at room temperature for 8 h. The solvent was removed in vacuo, then diluted with Et₂O and washed with water and acidified with 2 M HCl solution. The ether layer was separated and dried with Na₂SO₄, filtered and solvent was removed to give **II-33** as a light yellow oil (88 mg, 78%). ¹H NMR (300 MHz, CDCl₃, δ ppm): δ = 7.77 (d, *J* = 1.5 Hz, 1H), 7.61 (d, *J* = 8.1 Hz, 1H), 7.47 (dd, *J* = 8.1, 1.5 Hz, 1H), 7.22 (d, *J* = 2.1 Hz, 1H), 7.19 (d, *J* = 2.1 Hz, 1H), 5.26 (s, 2H), 5.24 (s, 2H), 3.67 (s, 3H), 3.54 (s, 3H), 1.47 (s, 9H).

1,4-Bis(3-bromo-3'-(*tert*-butyl)-4',5'-bis(methoxymethoxy)-[1,1'-biphenyl]-4-yl)buta-1,3-diyne (II-34) (Attempted decarboxylation to synthesize **II-12**). Cu₂O (55 mg, 0.38 mmol) was added to a nitrogen-purged, anhydrous solution of **II-33** (88 mg (0.18 mmol) in 10 mL of MeCN and heated to reflux with stirring for 15 h. The reaction was quenched with aqueous NH₄Cl and stirred. The product was extracted with Et₂O and the organic layer was washed with brine, separated, and dried with Na₂SO₄, and filtered. The solvent was removed in vacuo to give the crude product, which was purified with flash chromatography (deactivated silica gel, 5-20% EtOAc/hexanes) to give **II-34** as a yellow oil. TLC: R_f = 0.14 (10% EtOAc/hexanes). ¹H NMR (300 MHz, CDCl₃, δ ppm): δ = 7.77 (d, *J* = 1.5 Hz, 1H), 7.56 (d, *J* = 6.0 Hz, 1H), 7.46 (dd, *J* = 6.0, 1.5 Hz, 1H), 7.19 (d, *J* = 1.5 Hz, 1H), 7.14 (d, *J* = 1.5 Hz, 1H), 5.27 (s, 2H), 5.25 (s, 2H), 3.70 (s, 3H), 3.55 (s, 3H), 1.48 (s, 9H).

Dimethyl (1-diazo-2-oxopropyl)phosphonate (II-35).¹¹¹ Compound **II-35** was prepared according to literature procedure.¹⁰⁹ To a nitrogen-purged, cooled (0 °C) solution of dimethyl (2-oxopropyl)phosphonate (2.02 g, 12.2 mmol) of in 15 mL of anhydrous, degassed THF NaH (0.606 g, 15.2 mmol) suspended in 5 mL of THF was added dropwise via cannula and allowed to stir for 1 h. Then, 4-acetamidobenzenesulfonyl azide (*p*-ABSA) (3.22 g, 13.4 mmol) dissolved in 5 mL of THF was added while the reaction was at 0 °C. The reaction was allowed to warm to room temperature overnight. The opaque light brown suspension was filtered and washed with 800 mL of 25% Et₂O/ pet. ether, then the filtrate was removed in vacuo to afford **II-35** as a yellow oil (1.80 g, 77%). ¹H NMR (300 MHz, CDCl₃, δ ppm): δ = 3.85 (d, *J* = 12.0 Hz, 6H), 2.28 (s, 3H).

2-Bromo-1-(dimethoxymethyl)-4-iodobenzene (II-36).³⁸ Compound **II-6** (2.43 g, 7.85 mmol) and *p*-toluenesulfonic acid (138 mg, 0.725 mmol) was dissolved in 20 mL of THF in an oven-

dried 50 mL round-bottom flask and placed under nitrogen. Trimethyl orthoformate was added via syringe and stirred for 6 h. After reaction was complete, solvent was removed in vacuo to give 2.51 g (7.03 mmol, 95%) to give **II-36** as an orange oil. ¹H NMR (300 MHz, DMSO-d₆, δ ppm): δ = 7.99 (d, *J* = 1.2 Hz, 1H), 7.77 (dd, *J* = 8.1, 1.2 Hz, 1H), 7.28 (d, *J* = 8.1 Hz, 1H), 5.40 (s, 1H), 3.27 (s, 6H).

2-[Bis(2-hydroxybenzyl)aminomethyl]pyridine (II-37).¹⁷⁰ Compound **II-37** was prepared according to literature procedure.¹¹⁵ Salicylaldehyde (0.228 g, 1.87 mmol) was added to a solution of 2-aminomethylpyridine (0.101 g, 0.934 mmol) in 10 mL of MeOH and stirred under ambient conditions for 2 h to make a bright yellow solution indicating formation of the imine. Then, NaBH₄ (0.109 g, 2.88 mmol) was added slowly and stirred for 1 h. The solvent was removed in vacuo and 10 mL of water was added and neutralized with AcOH. The product was extracted with 30 mL of CH₂Cl₂ and the organic layer was dried with Na₂SO₄. The organic layer was filtered and the solvent was removed to give an oil which was then redissolved in 10 mL of MeOH and salicylaldehyde (0.228 g, 1.87 mmol) was added and stirred for another 2 h. Then, NaBH₄ (0.106 g, 2.80 mmol) was added slowly and stirred for 1 h. The solvent was removed in vacuo, then 10 mL of water was added and neutralized with AcOH. The product was extracted with 30 mL of CH₂Cl₂ and the organic layer was dried with Na₂SO₄. The organic layer was filtered and the solvent was removed to give a crude product as an off-white solid, which was purified by flash chromatography (silica gel, 100% CH₂Cl₂ followed by 100% EtOAc after the 1st band eluted) and then recrystallized from CH₂Cl₂ to give 0.251 g (42%) of **II-37** as colorless crystals. ¹H NMR (300 MHz, CDCl₃, δ ppm): δ = 10.16 (s, 2H), 8.54 (d, *J* = 5.1 Hz, 1H), 7.78 (dd, *J* = 7.5, 1.5 Hz, 1H), 7.39 (d, *J* = 7.2 Hz, 1H), 7.30 (dd, *J* = 7.5, 1.5 Hz, 1H), 7.17 (d, *J* = 7.5 Hz, 2H), 7.07 (m, 2H), 6.73 (m, 4H), 3.74 (s, 2H), 3.65 (s, 4H).

6,6'-(((Pyridin-2-ylmethyl)azanediyl)bis(methylene))bis(3,4-dimethylphenol) (II-39).¹¹³

Compound **II-39** was prepared according to literature procedure.¹¹³ A 150 mL EtOH solution containing 11.32 g (92.67 mmol) of 3,4-dimethylphenol, 5.20 g (48.1 mmol) of 2-aminomethylpyridine and 8.00 mL (98.6 mmol) of 37% formaldehyde/H₂O was heated to reflux for 18 h. A white precipitate formed which was filtered and washed with H₂O and then purified by recrystallization from CH₂Cl₂ to give 15.8 g (91%) of **II-39** as colorless crystals. ¹H NMR (300 MHz, CDCl₃, δ ppm): δ = 10.47 (s, 2H), 8.65 (d, *J* = 5.1 Hz, 1H), 7.70 (dd, *J* = 5.1, 1.8 Hz, 1H), 7.27 (d, *J* = 12.6 Hz, 1H), 7.12 (d, *J* = 7.8 Hz, 1H), 6.80 (s, 2H), 6.70 (s, 2H), 3.86 (s, 2H), 3.75 (s, 4H), 2.18 (s, 6H), 2.15 (s, 6H).

6,6'-(((Pyridin-2-ylmethyl)azanediyl)bis(methylene))bis(3,4-dimethylphenoxy) Cobalt (II)

(CoL_A). A solution of DBU (4.00 mL, 26.7 mmol) of and **II-39** (2.00 g, 5.32 mmol) dissolved in 40 mL of THF was added dropwise via addition funnel to a vigorously-stirring royal blue solution of 0.750 g (5.78 mmol) of CoCl₂ in 60 mL of THF. The solution is allowed to stir 1 h after the addition is complete and then 200 mL of Et₂O is added. The light purple precipitate is filtered and washed first with Et₂O and then with H₂O. The purple solid is collected by washing with CH₂Cl₂ and then removing the solvent in vacuo to give 1.37 g (59%) of **CoL_A** as a purple solid. Elemental analysis: Calculated (C: 66.51, H: 6.05, N: 6.46), Found (C: 66.07, H: 6.23, N: 6.48).

Poly(1,2-phenyleneethynylene-4-(3'-*tert*-butyl-4',5'-dimethoxymethoxycatechol)) (PoPE-

MOM).³⁸ To a nitrogen-purged, oven-dried Schlenk tube containing **II-12** (610 mg (1.41 mmol), in an inert atmosphere, was added Pd(PPh₃)₄ (81 mg, 0.07 mmol) of and CuI (27 mg, 0.14 mmol) and sealed with a stopcock and septum. Degassed, anhydrous ethyldiisopropylamine (8 mL) was added via syringe through the septum. The Schlenk tube was placed inside a CEM Discover

microwave reactor and heated with 150 W to 140 °C for 8 h. The solvent was removed in vacuo, and the polymer was redissolved in minimal CH₂Cl₂ (2-3 mL) and precipitated into 40 mL of MeOH. The precipitate was placed in a centrifuge for five minutes at 3000 RPM, then decanted. The orange solid was dried under vacuum to give 481 mg (79%) of **PoPE-MOM**. ¹H NMR (300 MHz, CDCl₃, δ ppm): δ = 8.0-6.9 (m, 5H), 5.44-5.03 (bs, 4H), 3.82-3.28 (bs, 6H), 1.75-1.19 (bs, 9H). ¹³C NMR (400 MHz, DMSO-d₆, δ ppm): δ = 149.7, 145.8, 142.7, 131.2, 128.5, 118.3, 112.8, 98.5, 94.6, 56.9, 55.9, 34.7, 30.0. FTIR (neat): 2952, 2906, 2828, 1594, 1578, 1470, 1442, 1396, 1369, 1322, 1239, 1202, 1159, 1075, 1007, 958, 936, 869, 825, 828, 760, 696, 575, 538, 454, 436, 424 cm⁻¹.

Poly(1,2-phenyleneethynylene-4-(3'-tert-butyl-4',5'-catechol)) (PoPE-Cat).³⁸ **PoPE-MOM** (481 mg) of was dissolved in 50 mL of EtOAc and 2 drops of 12 M HCl was added and stirred for 48 h. The solvent was removed in vacuo to give of **PoPE-Cat**.

¹H NMR (300 MHz, CDCl₃, δ ppm): FTIR (neat): 3558-3035, 2955, 2916, 2866, 1554, 1578, 1478, 1428, 1361, 1313, 1250, 1200, 1150, 1072, 1029, 952, 862, 827, 800, 750, 723, 690, 642, 543, 523 cm⁻¹.

Poly(1,2-phenyleneethynylene-4-(3'-tert-butyl-4',5'-benzoquinone)) (PoPE-BQ).³⁸ **PoPE-Cat** was dissolved in 25 mL of CH₂Cl₂ and Fetizon's reagent (Ag₂CO₃/celite) was added and stirred in the dark for 2 h. The reaction was filtered through a layer of celite and washed with CH₂Cl₂, the solvent from the filtrate was removed to give **PoPE-BQ** as a solid. ¹H NMR (300 MHz, CDCl₃, δ ppm): FTIR (neat): 3558-3035, 2955, 2916, 2858, 1656, 1619, 1594, 1558, 1480, 1470, 1438, 1392, 1367, 1313, 1243, 1197, 1150, 1077, 1029, 1005, 867, 832, 793, 720, 693, 537 cm⁻¹.

Poly(1,2-phenyleneethynylene-4-(3'-tert-butyl-4',5'-semiquinone)) (PoPE-SQ). PoPE-BQ (12 mg, 0.045 mmol) and an appropriate amount of CoL_A (5, 10, 15, and 20 mg) were dissolved in 1 mL of anhydrous, degassed CH₂Cl₂ and stirred overnight in a nitrogen atmosphere. The solutions were then transferred into 3 mm quartz EPR tubes for analysis. All samples gave broad, featureless EPR spectra.

II.6.2. pThSQ

3-(3-(tert-butyl)-4,5-bis(methoxymethoxy)phenyl)thiophene (3-(MOM₂Cat)Th).

MOM₂CatBpin (1.892 g, 4.980 mmol), Na₂CO₃ (1.094 g, 10.32 mmol) and Bu₄NBr (0.160 g, 0.496 mmol) were added to a 50 mL round-bottom flask, which was then purge-pumped three times with nitrogen and Pd(PPh₃) (97 mg, 0.084 mmol) was added. Toluene (9 mL), 3 mL of water and 3-bromothiophene (0.52 mL, 5.6 mmol) were added via syringe and a nitrogen-purged, water-cooled reflux condenser was attached and the contents were heated to 85 °C for 20 h. The reaction was cooled to room temperature, diluted with ca. 50 mL of EtOAc and washed with 50 mL of brine two times. The organic layer was separated, dried with MgSO₄ and concentrated under reduced pressure. The crude brown oil was purified by deactivate silica gel column chromatography with 10% EtOAc/hexanes to afford the title compound as a colorless to light yellow oil (1.6 g, 97%). ¹H NMR (400MHz, acetone-d₆) δ = 7.62 (dd, *J* = 0.8, 3.1 Hz, 1 H), 7.53 (dd, *J* = 3.1, 5.1 Hz, 1 H), 7.44 (dd, *J* = 0.8, 5.1 Hz, 1 H), 7.36 (d, *J* = 2.0 Hz, 1 H), 7.30 (d, *J* = 2.0 Hz, 1 H), 5.29 (s, 2 H), 5.25 - 5.21 (s, 2 H), 3.65 - 3.58 (s, 3 H), 3.54 - 3.47 (s, 3 H), 1.48 - 1.44 (s, 9 H). ¹³C NMR (101 MHz, acetone-d₆) δ = 151.9, 146.9, 144.2, 132.3, 127.7, 127.7, 121.2, 119.7, 114.4, 100.4, 96.7, 58.2, 57.1, 36.4, 31.5. HRMS (HESI) calculated for C₁₈H₂₄O₄S [M + H] 337.14681, found 337.14657.

2-bromo-3-(3-(tert-butyl)-4,5-bis(methoxymethoxy)phenyl)thiophene (2-Br-3-

(MOM₂Cat)Th). 3-(MOM₂Cat)Th (1.93 g, 5.99 mmol) was dissolved in ca. 75 mL of MeOH with NaHCO₃ (10.32 g, 12.28 mmol), the reaction mixture was placed under nitrogen and cooled to -78 °C. Then pyridinium bromide perbromide (1.932 g, 6.04 mmol) was added to the -78 °C mixture as a solid and was stirred for 15 min at -78 °C. The flask was removed from the cold bath and was allowed to warm to room temperature. It was stirred for ½ hour and then 50 mL of H₂O were added and the reaction was transferred to a separatory funnel. The reaction was extracted with Et₂O, separated and the solvent was removed under reduced pressure. The crude brown oil was diluted with Et₂O and washed with brine. Separated the organic layer, dried with Na₂SO₄ and concentrated under reduced pressure. The colorless product was crystallized twice from heptane by use of an existing seed crystal to give the title compound as colorless crystals (1.16 g, 54%). ¹H NMR (400MHz, CDCl₃) δ = 7.29 (d, *J* = 5.5 Hz, 1 H), 7.25 (d, *J* = 2.3 Hz, 1 H), 7.22 (d, *J* = 2.3 Hz, 1 H), 7.04 (d, *J* = 5.9 Hz, 1 H), 5.26 (s, 2 H), 5.22 (s, 2 H), 3.68 (s, 3 H), 3.54 (s, 3 H), 1.49 (s, 9 H). ¹³C NMR (101MHz, CDCl₃) δ = 149.8, 145.4, 143.1, 140.9, 129.6, 129.0, 125.7, 121.1, 115.0, 108.1, 99.0, 95.4, 57.5, 56.3, 35.3, 30.5. HRMS (HESI) calculated for C₁₈H₂₃BrO₄S [M + H] 415.05732, Found 415.05678.

Poly(3-(3-(tert-butyl)-4,5-bis(methoxymethoxy)phenyl)thiophene) (pThCatMOM₂). 2-Br-3-(MOM₂Cat)Th (324 mg, 0.780 mmol), 1-adamantanecarboxylic acid (45 mg, 0.25 mmol), and K₂CO₃ (333 mg, 2.41 mmol) were added to a 10 mL oven-dried round-bottom flask and purge-pumped three times; backfilling with nitrogen. 1.5 mL of a 5 mM solution of Pd(OAc)₂ in DMAc was added via syringe. A nitrogen-purged reflux condenser was attached and the solution was heated to 115 °C for 24 h. The reaction was cooled to room temperature and precipitated into MeOH (ca. 40 mL) and centrifuged at 3500 rpm for 10 min. The solvent was decanted and the

solid was dried under a stream of nitrogen. The crude solid was Soxhlet first with MeOH, then with hexanes and finally the product was collected with CHCl₃ and concentrated to afford the product as an orange-red powder. ¹H NMR (400MHz, CDCl₃) δ = 7.20 - 6.81 (m, 3 H), 5.22 (br. s., 2 H), 5.11 (br. s., 2 H), 3.62 (s, 3 H), 3.44 (br. s., 3 H), 1.38 (br. s., 9 H). ¹³C NMR (101MHz, CDCl₃) δ = 150.1, 145.5, 143.2, 139.4, 134.1, 130.7, 130.2, 129.4, 121.9, 115.2, 99.0, 95.4, 57.5, 56.2, 35.2, 30.5.

Poly(3-(3'-*tert*-butyl-4',5'-benzoquinone)thiophene) (PTh-BQ). PTh-CatMOM₂ (481 mg) was dissolved in 50 mL of EtOAc and 2 drops of 12 M HCl was added and stirred for 24 h. The solvent was concentrated, but not to dryness due to very poor solubility, under reduced pressure to give of PTh-Cat which was carried into the next reaction without further purification. PTh-Cat was redissolved in 25 mL of CH₂Cl₂ and Fetizon's reagent (Ag₂CO₃/celite) was added and stirred in the dark for 2 h. The reaction was filtered through a layer of celite and washed with CH₂Cl₂, the solvent from the filtrate was removed to give PTh-BQ as a solid. ¹H NMR (400MHz, CD₂Cl₂) δ = 7.26 (br. s., 1 H), 6.65 (br. s., 1 H), 6.53 (br. s., 1 H), 1.12 (br. s., 9 H) FTIR (neat): 3050-2860, 1706, 1657, 1355, 1271, 1240, 1217, 862, 791, 737, 537 cm⁻¹.

Poly(3-(3'-*tert*-butyl-4',5'-semiquinone)thiophene) (PTh-SQ). PTh-BQ (20 mg, 0.081 mmol) and an appropriate amount of CoL_A (8, 17, 26, and 35 mg) were dissolved in 5 mL of anhydrous, degassed CH₂Cl₂ and stirred overnight in a nitrogen atmosphere. The solutions were then transferred into 3 mm quartz EPR tubes under nitrogen for analysis. FTIR (neat) of PTh-SQ where 35 mg (1 eq.) of CoL_A was used: 2993-2832, 1664, 1358-1197, 1092-996, 843, 553 cm⁻¹.

II.7. References.

- (1) Mataga, N. Possible “Ferromagnetic States” of Some Hypothetical Hydrocarbons. *Theor. Chim. Acta* **1968**, *10* (4), 372–376. <https://doi.org/10.1007/BF00526505>.
- (2) Zhang, K.; Monteiro, M. J.; Jia, Z. Stable Organic Radical Polymers: Synthesis and Applications. *Polym. Chem.* **2016**, *7* (36), 5589–5614. <https://doi.org/10.1039/C6PY00996D>.
- (3) Miller, J. S.; Epstein, A. J. Organic and Organometallic Molecular Magnetic Materials—Designer Magnets. *Angew. Chem. Int. Ed. Engl.* **1994**, *33* (4), 385–415. <https://doi.org/10.1002/anie.199403851>.
- (4) Tomlinson, E. P.; Hay, M. E.; Boudouris, B. W. Radical Polymers and Their Application to Organic Electronic Devices. *Macromolecules* **2014**, *47* (18), 6145–6158. <https://doi.org/10.1021/ma5014572>.
- (5) Janoschka, T.; Hager, M. D.; Schubert, U. S. Powering up the Future: Radical Polymers for Battery Applications. *Adv. Mater.* **2012**, *24* (48), 6397–6409. <https://doi.org/10.1002/adma.201203119>.
- (6) Rajca, A. Organic Diradicals and Polyradicals: From Spin Coupling to Magnetism? *Chem. Rev.* **1994**, *94* (4), 871–893. <https://doi.org/10.1021/cr00028a002>.
- (7) Iwamura, H. High-Spin Polycarbenes as Models for Organic Ferromagnets. *Pure Appl. Chem.* **1986**, *58* (1), 187–196. <https://doi.org/10.1351/pac198658010187>.
- (8) Itoh, T.; Jinbo, Y.; Hirai, K.; Tomioka, H. Preparation of Poly(Phenyl)Acetylenes Having Diazo Groups and Magnetic Characterization of Poly(Carbene). *J. Am. Chem. Soc.* **2005**, *127* (6), 1650–1651. <https://doi.org/10.1021/ja0455345>.

- (9) Kaneko, T.; Abe, H.; Teraguchi, M.; Aoki, T. Folding-Induced Through-Space Magnetic Interaction of Poly(1,3-Phenyleneethynylene)-Based Polyradicals. *Macromolecules* **2013**, *46* (7), 2583–2598. <https://doi.org/Doi.10.1021/Ma302314n>.
- (10) Yan, W.; Wan, X.; Xu, Y.; Lv, X.; Chen, Y. A Phenalenyl-Based Neutral Stable π -Conjugated Polyradical. *Synth. Met.* **2009**, *159* (17–18), 1772–1777. <https://doi.org/10.1016/j.synthmet.2009.05.025>.
- (11) Kaneko, T.; Iwamura, K.; Nishikawa, R.; Teraguchi, M.; Aoki, T. Synthesis of Sequential Poly(1,3-Phenyleneethynylene)-Based Polyradicals and through-Space Antiferromagnetic Interaction of Their Solid State. *Polymer (Guildf)*. **2014**, *55* (5), 1097–1102. <https://doi.org/10.1016/j.polymer.2014.01.019>.
- (12) Morisaki, Y.; Ishida, T.; Chujo, Y. Synthesis and Optical Properties of Novel Through-Space [Pi]-Conjugated Polymers Having a Dithia[3.3]Metacyclophane Skeleton in the Main Chain. *Polym J* **2003**, *35* (6), 501–506.
- (13) Verhoeven, J. W.; Pasma, P. The Relative Sign of Through-Bond and through-Space Interactions - Sigma-Assistance of Cyclization and Intramolecular Hydrogen Transfer. *Tetrahedron* **1981**, *37* (5), 943–947. [https://doi.org/10.1016/S0040-4020\(01\)97664-1](https://doi.org/10.1016/S0040-4020(01)97664-1).
- (14) Murata, H.; Miyajima, D.; Nishide, H. A High-Spin and Helical Organic Polymer: Poly{[4-(Dianisylaminium)Phenyl]Acetylene}. *Macromolecules* **2006**, *39* (19), 6331–6335. <https://doi.org/10.1021/ma060773t>.
- (15) Williams, D. E. The Structure of Galvinoxyl, a Stable Phenoxyl Radical. *Mol. Phys.* **1968**, *16* (2), 145–151. <https://doi.org/10.1080/00268976.1969.10310426>.

- (16) Turek, P.; Nozawa, K.; Shiomi, D.; Awaga, K.; Inabe, T.; Maruyama, Y.; Kinoshita, M. Ferromagnetic Coupling in a New Phase of the P-Nitrophenyl Nitronyl Nitroxide Radical. *Chem. Phys. Lett.* **1991**, *180* (4), 327–331. [https://doi.org/10.1016/0009-2614\(91\)90328-7](https://doi.org/10.1016/0009-2614(91)90328-7).
- (17) Tamura, M.; Nakazawa, Y.; Shiomi, D.; Nozawa, K.; Hosokoshi, Y.; Ishikawa, M.; Takahashi, M.; Kinoshita, M. Bulk Ferromagnetism in the β -Phase Crystal of the p-Nitrophenyl Nitronyl Nitroxide Radical. *Chem. Phys. Lett.* **1991**, *186*, 401–404. [https://doi.org/10.1016/0009-2614\(91\)90198-I](https://doi.org/10.1016/0009-2614(91)90198-I).
- (18) Allemand, P. M.; Fite, C.; Srdanov, G.; Keder, N.; Wudl, F.; Canfield, P. On the Complexities of Short Range Ferromagnetic Exchange in a Nitronyl Nitroxide. *Synth. Met.* **1991**, No. 41–43, 3291–3295. [https://doi.org/10.1016/0379-6779\(91\)91290-Q](https://doi.org/10.1016/0379-6779(91)91290-Q).
- (19) Juetten, M. J.; Buck, A. T.; Winter, A. H. A Radical Spin on Viologen Polymers: Organic Spin Crossover Materials in Water. *Chem. Commun.* **2015**, *51* (25), 5516–5519. <https://doi.org/10.1039/C4CC07119K>.
- (20) Rajca, A.; Utamapanya, S. Toward Organic-Synthesis of a Magnetic Particle - Dendritic Polyradicals with 15 and 31 Centers for Unpaired Electrons. *J. Am. Chem. Soc.* **1993**, *115* (9), 10688–10694.
- (21) Veciana, J.; Rovira, C.; Crespo, M. I.; Armet, O.; Domingo, V. M.; Palacio, F. Stable Polyradicals with High-Spin Ground States. 1. Synthesis, Separation, and Magnetic Characterization of the Stereoisomers of 2,4,5,6-Tetrachloro-Alpha, Alpha, Alpha', Alpha'-Tetrakis(Pentachlorophenyl)-m-Xylylene Biradical. *J. Am. Chem. Soc.* **1991**, *113* (7), 2552–2561. <https://doi.org/10.1021/ja00007a033>.
- (22) Rajca, A. The Physical Organic Chemistry of Very High-Spin Polyradicals. In *Advances*

in Physical Organic Chemistry; 2005; Vol. 40, pp 153–199.

[https://doi.org/10.1016/S0065-3160\(05\)40004-0](https://doi.org/10.1016/S0065-3160(05)40004-0).

- (23) Rajca, A. From High-Spin Organic Molecules to Organic Polymers with Magnetic Ordering. *Chem. - A Eur. J.* **2002**, *8* (21), 4834–4841. [https://doi.org/10.1002/1521-3765\(20021104\)8:21<4834::AID-CHEM4834>3.0.CO;2-E](https://doi.org/10.1002/1521-3765(20021104)8:21<4834::AID-CHEM4834>3.0.CO;2-E).
- (24) Rajca, A.; Rajca, S.; Wongsriratanakul, J. Very High-Spin Organic Polymer: π -Conjugated Hydrocarbon Network with Average Spin of $S \geq 40$. *J. Am. Chem. Soc.* **1999**, *121* (26), 6308–6309. <https://doi.org/10.1021/ja990881d>.
- (25) Rajca, A.; Utamapanya, S.; Thayumanavan, S. Poly(Arylmethyl) Octet ($S = 7/2$) Heptaradical and Undecet ($S = 5$) Decaradical. *J. Am. Chem. Soc.* **1992**, *114* (5), 1884–1885. <https://doi.org/10.1021/ja00031a055>.
- (26) Rajca, A. Magnetic Ordering in an Organic Polymer. *Science* (80-.). **2001**, *294* (5546), 1503–1505. <https://doi.org/10.1126/science.1065477>.
- (27) Rajca, S.; Rajca, A.; Wongsriratanakul, J.; Butler, P.; Choi, S. Organic Spin Clusters. A Dendritic-Macrocyclic Poly(Arylmethyl) Polyradical with Very High Spin of $S = 10$ and Its Derivatives: Synthesis, Magnetic Studies, and Small-Angle Neutron Scattering. *J. Am. Chem. Soc.* **2004**, *126* (22), 6972–6986. <https://doi.org/10.1021/ja031548j>.
- (28) Bushby, R. J.; Taylor, N.; Williams, R. A. High-Spin Polymers. *J. Mater. Chem.* **2007**, *17*, 955–964. <https://doi.org/10.1039/b612798n>.
- (29) Oyaizu, K.; Nishide, H. Radical Polymers for Organic Electronic Devices: A Radical Departure from Conjugated Polymers? *Adv. Mater.* **2009**, *21* (22), 2339–2344.

<https://doi.org/10.1002/adma.200803554>.

- (30) Bushby, R. J.; Kilner, C. A.; Taylor, N.; Vale, M. E. Disjoint and Coextensive Amminium Radical Cations: A General Problem in Making Amminium Radical Cation Based High-Spin Polymers. *Tetrahedron* **2007**, *63* (46), 11458–11466.

<https://doi.org/10.1016/j.tet.2007.08.038>.

- (31) Murata, H.; Takahashi, M.; Namba, K.; Takahashi, N.; Nishide, H. A High-Spin and Durable Polyradical: Poly (4-Diphenylaminium-1, 2-Phenylenevinylene). *J. Org. Chem.* **2004**, No. 69, 631–638.

- (32) Nishide, H.; Hozumi, Y.; Nii, T.; Tsuchida, E. Poly (1 , 2-Phenylenevinylene) s Bearing Nitronyl Nitroxide and Galvinoxyl at the 4-Position : π -Conjugated and σ -Type Polyradicals with a Triplet Ground State. *Macromolecules* **1997**, *30* (14), 3986–3991.

<https://doi.org/10.1021/ma970217m>.

- (33) Miura, Y.; Matsumoto, M.; Ushitani, Y.; Teki, Y.; Takui, T.; Itoh, K. Magnetic and Optical Characterization of Poly(Ethynylbenzene) with Pendant Nitroxide Radicals. *Macromolecules* **1993**, No. 26, 6673–6675.

- (34) Kaneko, T.; Makino, T.; Miyaji, H.; Onuma, A.; Teraguchi, M.; Aoki, T. A Poly(9,10-Anthryleneethynylene)-Based Polyradical Designed to Be a Ladder-like Ferromagnetic Spin Coupling Network. *Polyhedron* **2003**, *22* (14–17), 1845–1850.

[https://doi.org/10.1016/S0277-5387\(03\)00251-1](https://doi.org/10.1016/S0277-5387(03)00251-1).

- (35) Nishide, H.; Kaneko, T.; Tsuchida, E.; Yoshioka, N.; J, P. M. L. Magnetic Characterization and Computational Modeling of Poly(Phenylacetylene)s Bearing Stable Radical Groups. *Macromolecules* **1994**, *27*, 3082–3086.

- (36) Nishide, H.; Maeda, T.; Oyaizu, K.; Tsuchida, E. High-Spin Polyphenoxy Based on Poly (1,4-Phenyleneethynylene). *J. Org. Chem.* **1999**, No. 6, 7129–7134.
- (37) Nishide, H.; Takahashi, M.; Takashima, J.; Pu, Y. J.; Tsuchida, E. Acyclic and Cyclic Di- and Tri(4-Oxyphenyl-1,2-Phenyleneethynylene)s: Their Synthesis and Ferromagnetic Spin Interaction. *J. Org. Chem.* **1999**, *64* (20), 7375–7380.
<https://doi.org/10.1021/jo990575i>.
- (38) Shultz, D. A.; Hollomon, M. G. Preparation and EPR Spectroscopic Investigation of Conjugated Oligomers Containing Semiquinone Repeat Units. *Chem. Mater.* **2000**, *12* (2), 580–585. <https://doi.org/10.1021/cm9907155>.
- (39) Frey, J. E.; Andrews, A. M.; Ankoviac, D. G.; Beaman, D. N.; Du Pont, L. E.; Elsner, T. E.; Lang, S. R.; Zwart, M. A. O.; Seagle, R. E.; Torreano, L. A. Charge-Transfer Complexes of Tetracyanoethylene with Cycloalkanes, Alkenes, and Alkynes and Some of Their Aryl Derivatives. *J. Org. Chem.* **1990**, *55* (2), 606–624.
<https://doi.org/10.1021/jo00289a041>.
- (40) Matsuda, K.; Stone, M. T.; Moore, J. S. Helical Pitch of m-Phenylene Ethynylene Foldamers by Double Spin Labeling. *J. Am. Chem. Soc.* **2002**, *124* (40), 11836–11837.
<https://doi.org/10.1021/ja027437m>.
- (41) Ray, C. R.; Moore, J. S. Supramolecular Organization of Foldable Phenylene Ethynylene Oligomers. *Advances in Polymer Science.* 2005, pp 91–149.
https://doi.org/10.1007/11593980_7.
- (42) Miyasaka, M.; Yamazaki, T.; Tsuchida, E.; Nishide, H. Regioregular Polythiophene with Pendant Phenoxy Radicals: A New High-Spin Organic Polymer. *Macromolecules* **2000**,

- 33 (22), 8211–8217. <https://doi.org/10.1021/ma000993l>.
- (43) Nishide, H. High-Spin Alignment in Pi-Conjugated Polyradicals: A Magnetic Polymer. *Adv. Mater.* **1995**, *7* (11), 937–941.
- (44) Zheludev, A.; Barone, V.; Bonnet, M.; Delley, B.; Grand, A.; Ressouche, E.; Rey, P.; Subra, R.; Schweizer, J. Spin Density in a Nitronyl Nitroxide Free Radical. Polarized Neutron Diffraction Investigation and Ab Initio Calculations. *J. Am. Chem. Soc.* **1994**, *116* (5), 2019–2027. <https://doi.org/10.1021/ja00084a048>.
- (45) Iwamura, H.; Koga, N. Studies of Organic Diradicals, Oligoradicals, and Polyradicals by Means of Their Bulk Magnetic-Properties. *Acc. Chem. Res.* **1993**, *26* (6), 346–351.
- (46) Calzolari, A.; Chen, Y.; Lewis, G. F.; Dougherty, D. B.; Shultz, D. A.; Buongiorno Nardelli, M. Complex Materials for Molecular Spintronics Applications: Cobalt Bis(Dioxolene) Valence Tautomers, from Molecules to Polymers. *J. Phys. Chem. B* **2012**, *116* (43), 13141–13148.
- (47) Boehme, C.; Lupton, J. M. Challenges for Organic Spintronics. *Nat. Nanotechnol.* **2013**, *8* (9), 612–615. <https://doi.org/10.1038/nnano.2013.177>.
- (48) Tagami, K.; Tsukada, M. Spintronic Transport through Polyphenoxyl Radical Molecules. *J Phys Chem B* **2004**, *108* (20), 6441–6444. <https://doi.org/10.1021/jp037953e>.
- (49) Gallagher, N. M.; Olankitwanit, A.; Rajca, A. High-Spin Organic Molecules. *J. Org. Chem.* **2015**, *80* (3), 1291–1298. <https://doi.org/10.1021/jo502505r>.
- (50) Horiuchi, S.; Tokura, Y. Organic Ferroelectrics. *Nat. Mater.* **2008**, *7* (5), 357–366. <https://doi.org/10.1038/nmat2137>.

- (51) Ye, H.-Y.; Zhang, Y.; Noro, S.; Kubo, K.; Yoshitake, M.; Liu, Z.-Q.; Cai, H.-L.; Fu, D.-W.; Yoshikawa, H.; Awaga, K.; Xiong, R.-G.; Nakamura, T. Molecule-Displacive Ferroelectricity in Organic Supramolecular Solids. *Sci. Rep.* **2013**, *3* (1), 2249. <https://doi.org/10.1038/srep02249>.
- (52) Ouyang, J.; Chu, C.-W.; Szmanda, C. R.; Ma, L.; Yang, Y. Programmable Polymer Thin Film and Non-Volatile Memory Device. *Nat. Mater.* **2004**, *3* (12), 918–922. <https://doi.org/10.1038/nmat1269>.
- (53) Bandyopadhyay, A.; Pal, A. J. Large Conductance Switching and Memory Effects in Organic Molecules for Data-Storage Applications. *Appl. Phys. Lett.* **2003**, *82* (8), 1215–1217. <https://doi.org/10.1063/1.1555263>.
- (54) McCamey, D. R.; Seipel, H. a; Paik, S.-Y.; Walter, M. J.; Borys, N. J.; Lupton, J. M.; Boehme, C. Spin Rabi Flopping in the Photocurrent of a Polymer Light-Emitting Diode. *Nat. Mater.* **2008**, *7* (9), 723–728. <https://doi.org/10.1038/nmat2252>.
- (55) Kulkarni, A. P.; Tonzola, C. J.; Babel, A.; Jenekhe, S. A. Electron Transport Materials for Organic Light-Emitting Diodes. *Chem. Mater.* **2004**, *16*, 4556–4573.
- (56) Giacobbe, E. M.; Mi, Q.; Colvin, M. T.; Cohen, B.; Ramanan, C.; Scott, A. M.; Yeganeh, S.; Marks, T. J.; Ratner, M. A.; Wasielewski, M. R. Ultrafast Intersystem Crossing and Spin Dynamics of Photoexcited Perylene-3,4:9,10-Bis(Dicarboximide) Covalently Linked to a Nitroxide Radical at Fixed Distances. *J. Am. Chem. Soc.* **2009**, *131* (10), 3700–3712. <https://doi.org/10.1021/ja808924f>.
- (57) Chernick, E. T.; Mi, Q.; Vega, A. M.; Lockard, J. V.; Ratner, M. A.; Wasielewski, M. R. Controlling Electron Transfer Dynamics in Donor–Bridge–Acceptor Molecules by

- Increasing Unpaired Spin Density on the Bridge. *J. Phys. Chem. B* **2007**, *111* (24), 6728–6737. <https://doi.org/10.1021/jp068741v>.
- (58) Chernick, E. T.; Casillas, R.; Zirzmeier, J.; Gardner, D. M.; Gruber, M.; Kropp, H.; Meyer, K.; Wasielewski, M. R.; Guldi, D. M.; Tykwinski, R. R. Pentacene Appended to a TEMPO Stable Free Radical: The Effect of Magnetic Exchange Coupling on Photoexcited Pentacene. *J. Am. Chem. Soc.* **2014**, *137*, 857–863. <https://doi.org/10.1021/ja510958k>.
- (59) Lv, X.; Mao, J.; Liu, Y.; Huang, Y.; Ma, Y.; Yu, A.; Yin, S.; Chen, Y. A Neutral Stable and Soluble Polymer Radical with Low Band Gap and Its Photovoltaic Application. *Macromolecules* **2008**, *41* (3), 501–503. <https://doi.org/10.1021/ma7025572>.
- (60) Wan, X.; Lv, X.; He, G.; Yu, A.; Chen, Y. Synthesis of Neutral Stable Polyradicals and Their Application on Photovoltaic Devices. *Eur. Polym. J.* **2011**, *47* (5), 1018–1030. <https://doi.org/10.1016/j.eurpolymj.2011.02.017>.
- (61) Brabec, C. J.; Gowrisanker, S.; Halls, J. J. M.; Laird, D.; Jia, S.; Williams, S. P. Polymer-Fullerene Bulk-Heterojunction Solar Cells. *Adv. Mater.* **2010**, *22* (34), 3839–3856. <https://doi.org/10.1002/adma.200903697>.
- (62) Tang, A.; Zhan, C.; Yao, J. A Series of Quinoidal Methyl-Dioxocyano-Pyridine Based π -Extended Narrow-Bandgap Oligomers for Solution-Processed Small-Molecule Organic Solar Cells. *Chem. Mater.* **2015**, 150611083812007. <https://doi.org/10.1021/acs.chemmater.5b01350>.
- (63) Jin, E.; Du, C.; Wang, M.; Li, W.; Li, C.; Wei, H.; Bo, Z. Dibenzothiophene-Based Planar Conjugated Polymers for High Efficiency Polymer Solar Cells. *Macromolecules* **2012**, *45* (19), 7843–7854. <https://doi.org/10.1021/ma301622g>.

- (64) Warnan, J.; El Labban, A.; Cabanetos, C.; Hoke, E. T.; Shukla, P. K.; Risko, C.; Brédas, J. L.; McGehee, M. D.; Beaujuge, P. M. Ring Substituents Mediate the Morphology of PBDTPD-PCBM Bulk-Heterojunction Solar Cells. *Chem. Mater.* **2014**, *26* (7), 2299–2306. <https://doi.org/10.1021/cm500172w>.
- (65) Zhou, H.; Yang, L.; Liu, S.; You, W. A Tale of Current and Voltage: Interplay of Band Gap and Energy Levels of Conjugated Polymers in Bulk Heterojunction Solar Cells. *Macromolecules* **2010**, *43* (24), 10390–10396. <https://doi.org/10.1021/ma101646r>.
- (66) Earmme, T.; Hwang, Y. J.; Murari, N. M.; Subramaniyan, S.; Jenekhe, S. A. All-Polymer Solar Cells with 3.3% Efficiency Based on Naphthalene Diimide-Selenophene Copolymer Acceptor. *J. Am. Chem. Soc.* **2013**, *135* (40), 14960–14963. <https://doi.org/10.1021/ja4085429>.
- (67) Silvestri, F.; Marrocchi, A. Acetylene-Based Materials in Organic Photovoltaics. *Int. J. Mol. Sci.* **2010**, *11* (4), 1471–1508. <https://doi.org/10.3390/ijms11041471>.
- (68) Zhang, J.; Zhang, Y.; Fang, J.; Lu, K.; Wang, Z.; Ma, W.; Wei, Z. Conjugated Polymer–Small Molecule Alloy Leads to High Efficient Ternary Organic Solar Cells. *J. Am. Chem. Soc.* **2015**, *137* (25), 8176–8183. <https://doi.org/10.1021/jacs.5b03449>.
- (69) Zheng, H.; Gu, C.; Zhu, Q.; Bao, X.; Wen, S.; Qiu, M.; Zhu, D.; Sun, M.; Yang, R. Thiophene π -Bridge Effect on Photovoltaic Performances of Dithienosilole and Bithiazole Backboned Polymers. *J. Appl. Polym. Sci.* **2015**, 42798–42806. <https://doi.org/10.1002/app.42798>.
- (70) Günes, S.; Neugebauer, H.; Sariciftci, N. S. Conjugated Polymer-Based Organic Solar Cells. *Chem. Rev.* **2007**, *107* (4), 1324–1338. <https://doi.org/10.1021/cr050149z>.

- (71) Haid, S.; Mishra, A.; Uhrich, C.; Pfei, M.; Peter, B. Dicyanovinylene-Substituted Selenophene À Thiophene Co-Oligomers for Small-Molecule Organic Solar Cells. *Chem. Mater.* **2011**, *23*, 4435–4444.
- (72) Haid, S.; Mishra, A.; Weil, M.; Uhrich, C.; Pfeiffer, M.; Bäuerle, P. Synthesis and Structure – Property Correlations of Dicyanovinyl-Substituted Oligoselenophenes and Their Application in Organic Solar Cells. *Adv. Funct. Mater.* **2012**, *22*, 4322–4333. <https://doi.org/10.1002/adfm.201201018>.
- (73) Nakamura, T.; Fujitsuka, M.; Araki, Y.; Ito, O.; Ikemoto, J.; Takimiya, K.; Aso, Y.; Otsubo, T. Photoinduced Electron Transfer in Porphyrin-Oligothiophene-Fullerene Linked Triads by Excitation of a Porphyrin Moiety. *J. Phys. Chem. B* **2004**, *108* (30), 10700–10710. <https://doi.org/10.1021/jp049122u>.
- (74) Kim, J.-H.; Kim, H. U.; Kang, I.-N.; Lee, S. K.; Moon, S.-J.; Shin, W. S.; Hwang, D.-H. Incorporation of Pyrene Units to Improve Hole Mobility in Conjugated Polymers for Organic Solar Cells. *Macromolecules* **2012**, *45* (21), 8628–8638. <https://doi.org/10.1021/ma301877q>.
- (75) Hou, Y.; Wang, H.; Li, Z.; Liu, Y.; Wan, X.; Xue, X.; Chen, Y.; Yu, A. Organic Radicals Based on Phenalenyl and Verdazyl Units. *Tetrahedron Lett.* **2011**, *52* (28), 3670–3673. <https://doi.org/10.1016/j.tetlet.2011.05.031>.
- (76) Nakahara, K.; Iwasa, S.; Satoh, M.; Morioka, Y.; Iriyama, J.; Suguro, M.; Hasegawa, E. Rechargeable Batteries with Organic Radical Cathodes. *Chem. Phys. Lett.* **2002**, *359* (5–6), 351–354. [https://doi.org/10.1016/S0009-2614\(02\)00705-4](https://doi.org/10.1016/S0009-2614(02)00705-4).
- (77) Yonekuta, Y.; Susuki, K.; Oyaizu, K.; Honda, K.; Nishide, H. Battery-Inspired,

- Nonvolatile, and Rewritable Memory Architecture: A Radical Polymer-Based Organic Device. *J. Am. Chem. Soc.* **2007**, *129* (46), 14128–14129.
<https://doi.org/10.1021/ja075553p>.
- (78) Nishide, H.; Iwasa, S.; Pu, Y. J.; Suga, T.; Nakahara, K.; Satoh, M. Organic Radical Battery: Nitroxide Polymers as a Cathode-Active Material. *Electrochim. Acta* **2004**, *50* (2-3 SPEC. ISS.), 827–831. <https://doi.org/10.1016/j.electacta.2004.02.052>.
- (79) Suga, T.; Ohshiro, H.; Ugita, S.; Oyaizu, K.; Nishide, H. Emerging N-Type Redox-Active Radical Polymer for a Totally Organic Polymer-Based Rechargeable Battery. *Adv. Mater.* **2009**, *21* (16), 1627–1630. <https://doi.org/10.1002/adma.200803073>.
- (80) Nyholm, L.; Nyström, G.; Mihranyan, A.; Strømme, M. Toward Flexible Polymer and Paper-Based Energy Storage Devices. *Adv. Mater.* **2011**, *23* (33), 3751–3769.
<https://doi.org/10.1002/adma.201004134>.
- (81) Mike, J. F.; Lutkenhaus, J. L. Recent Advances in Conjugated Polymer Energy Storage. *J. Polym. Sci. Part B Polym. Phys.* **2013**, *51* (7), 468–480.
<https://doi.org/10.1002/polb.23256>.
- (82) Baker, W. J.; Ambal, K.; Waters, D. P.; Baarda, R.; Morishita, H.; van Schooten, K.; McCamey, D. R.; Lupton, J. M.; Boehme, C. Robust Absolute Magnetometry with Organic Thin-Film Devices. *Nat. Commun.* **2012**, *3* (May), 898.
<https://doi.org/10.1038/ncomms1895>.
- (83) Nakahara, K.; Iriyama, J.; Iwasa, S.; Suguro, M.; Satoh, M.; Cairns, E. J. Al-Laminated Film Packaged Organic Radical Battery for High-Power Applications. *J. Power Sources* **2007**, *163* (2), 1110–1113. <https://doi.org/10.1016/j.jpowsour.2006.10.003>.

- (84) Nakahara, K.; Iriyama, J.; Iwasa, S.; Suguro, M.; Satoh, M.; Cairns, E. J. Cell Properties for Modified PTMA Cathodes of Organic Radical Batteries. *J. Power Sources* **2007**, *165* (1), 398–402. <https://doi.org/10.1016/j.jpowsour.2006.11.044>.
- (85) Nakahara, K.; Iriyama, J.; Iwasa, S.; Suguro, M.; Satoh, M.; Cairns, E. J. High-Rate Capable Organic Radical Cathodes for Lithium Rechargeable Batteries. *J. Power Sources* **2007**, *165* (2), 870–873. <https://doi.org/10.1016/j.jpowsour.2006.11.045>.
- (86) Nakahara, K.; Oyaizu, K.; Nishide, H. Organic Radical Battery Approaching Practical Use. *Chem. Lett.* **2011**, *40* (3), 222–227. <https://doi.org/10.1246/cl.2011.222>.
- (87) Boone, S. R.; Purser, G. H.; Chang, H.; Lowery, M. D.; Hendrickson, D. N.; Pierpont, C. G. Magnetic Exchange Interactions in Semiquinone Complexes of Iron . Structural and Magnetic Properties Of. *J. Am. Chem. Soc.* **1989**, *111* (6), 2292–2299.
- (88) Shultz, D. a.; Kumar, R. K.; Bin-Salamon, S.; Kirk, M. L. Valence Tautomerization and Exchange Coupling in a Cobalt–Nitronyl Nitroxide–Semiquinone Complex. *Polyhedron* **2005**, *24* (16–17), 2876–2879. <https://doi.org/10.1016/j.poly.2005.03.016>.
- (89) Shultz, D. A.; Vostrikova, K. E.; Bodnar, S. H.; Koo, H.-J. H.-J.; Whangbo, M.-H. M.-H.; Kirk, M. L.; Depperman, E. C.; Kampf, J. W. Trends in Metal-Biradical Exchange Interaction for First-Row M(II)(Nitronyl Nitroxide-Semiquinone) Complexes. *J. Am. Chem. Soc.* **2003**, *125* (6), 1607. <https://doi.org/10.1021/ja020715x>.
- (90) Chaudhary, A.; Patra, R.; Rath, S. P. Binding of Catechols to Iron(III)-Octaethylporphyrin: An Experimental and DFT Investigation. *Eur. J. Inorg. Chem.* **2010**, No. 33, 5211–5221. <https://doi.org/10.1002/ejic.201000707>.

- (91) Ovchinnikov, A. A. Multiplicity of the Ground State of Large Alternant Organic Molecules with Conjugated Bonds. *Theor. Chim. Acta* **1978**, 47 (4), 297–304.
<https://doi.org/10.1007/BF00549259>.
- (92) Shultz, D. A.; Vostrikova, K. E.; Bodnar, S. H.; Koo, H.; Whangbo, M.; Kirk, M. L.; Depperman, E. C.; Kampf, J. W. Trends in Metal-Biradical Exchange Interaction for First-Row M. *J. Am. Chem. Soc.* **2007**, No. 11, 1607–1617.
- (93) Shultz, D. A. Valence Tautomerism in Dioxolene Complexes of Cobalt. In *Magnetism: Molecules to Materials II*; Miller, J. S., Drillon, M., Eds.; 2003; pp 281–306.
<https://doi.org/10.1002/9783527620548.ch8a>.
- (94) Hendrickson, D. N.; Pierpont, C. G. MOF78-Valence Tautomeric Transition Metal Complexes. *Top. Curr. Chem.* **2004**, 234, 63–95. <https://doi.org/10.1007/b95413>.
- (95) Mulyana, Y.; Alley, K. G.; Davies, K. M.; Abrahams, B. F.; Moubaraki, B.; Murray, K. S.; Boskovic, C. Dinuclear Cobalt(II) and Cobalt(III) Complexes of Bis-Bidentate Naphthoquinone Ligands. *Dalt. Trans.* **2014**, 43 (6), 2499–2511. <https://doi.org/10.1039/C3DT52811A>.
- (96) Ruf, M.; Noll, B. C.; Groner, M. D.; Yee, G. T.; Pierpont, C. G. Pocket Semiquinonate Complexes of Cobalt(II), Copper(II), and Zinc(II) Prepared with the Hydrotris(Cumenylmethylpyrazolyl)Borate Ligand. *Inorg. Chem.* **1997**, 36 (21), 4860–4865. <https://doi.org/10.1021/ic970244t>.
- (97) Magdziak, D.; Rodriguez, A. A.; Van De Water, R. W.; Pettus, T. R. R. Regioselective Oxidation of Phenols to o -Quinones with o -Iodoxybenzoic Acid (IBX). *Org. Lett.* **2002**, 4 (2), 285–288. <https://doi.org/10.1021/ol017068j>.

- (98) Arimoto, H.; Kaufman, M. D.; Kobayashi, K.; Qiu, Y.; Smith III, A. B. Anomalous Epoxide Formation Upon Wittig Olefination With 1-Iodoethyl Triphenylphosphonium Ylide. *Synlett* **1998**, 07, 765–767. <https://doi.org/10.1055/s-1998-1770>.
- (99) Favorskii, A. E.; Skosarevskii, M. P. Favorskii Reaction. *Russ. Khim. Ob-va.* **1900**, 32, 652.
- (100) Jiang, H.; Zhu, S. Silylation of 1-Alkynes with Chlorosilanes Promoted by Zn(OTf)₂: An Efficient Way to the Preparation of Alkynylsilanes. *Tetrahedron Lett.* **2005**, 46 (3), 517–519. <https://doi.org/10.1016/j.tetlet.2004.10.175>.
- (101) Newman, M. S.; Merrill, S. H. Synthesis of a Series of Substituted Phenylpropionic Acids. *J. Am. Chem. Soc.* **1955**, 77 (21), 5549–5551. <https://doi.org/10.1021/ja01626a033>.
- (102) Jacobsen, E. N.; Deng, L.; Furukawa, Y.; Martínez, L. E. Enantioselective Catalytic Epoxidation of Cinnamate Esters. *Tetrahedron* **1994**, 50 (15), 4323–4334. [https://doi.org/10.1016/S0040-4020\(01\)89369-8](https://doi.org/10.1016/S0040-4020(01)89369-8).
- (103) Liu, D. X.; Li, F. L.; Li, H. X.; Gao, J.; Lang, J. P. Synthesis of 1,4-Diarylsubstituted 1,3-Diynes through Ligand-Free Copper-Catalyzed Oxidative Decarboxylative Homocoupling of Aryl Propionic Acids. *Tetrahedron* **2014**, 70 (14), 2416–2421. <https://doi.org/10.1016/j.tet.2014.02.022>.
- (104) Li, T.; Sun, P.; Yang, H.; Zhu, Y.; Yan, H.; Lu, L.; Mao, J. Copper-Catalyzed Decarboxylative Coupling of Aryl Halides with Alkynyl Carboxylic Acids Performed in Water. *Tetrahedron* **2012**, 68 (32), 6413–6419. <https://doi.org/10.1016/j.tet.2012.06.003>.
- (105) Kolarovič, A.; Fáberová, Z. Catalytic Decarboxylation of 2-Alkynoic Acids. *J. Org.*

- Chem.* **2009**, 74 (18), 7199–7202. <https://doi.org/10.1021/jo901377b>.
- (106) Landgree, J. A.; Rynbrandt, R. H.; The, O. F. Synthesis and Solvolysis. *J. Org. Chem.* **1966**, 2075 (August), 2585–2593.
- (107) Park, K.; Palani, T.; Pyo, A.; Lee, S. Synthesis of Aryl Alkynyl Carboxylic Acids and Aryl Alkynes from Propiolic Acid and Aryl Halides by Site Selective Coupling and Decarboxylation. *Tetrahedron Lett.* **2012**, 53 (7), 733–737.
<https://doi.org/10.1016/j.tetlet.2011.11.117>.
- (108) Hay, A. S. Oxidative Coupling of Acetylenes. III. *J. Org. Chem.* **1962**, 27 (9), 3320–3321. <https://doi.org/10.1021/jo01056a511>.
- (109) Müller, S.; Liepold, B.; Roth, G. J.; Bestmann, H. J. An Improved One-Pot Procedure for the Synthesis of Alkynes from Aldehydes. *Synlett* **1996**, 1996 (06), 521–522.
<https://doi.org/10.1055/s-1996-5474>.
- (110) Ohira, S. Methanolysis of Dimethyl (1-Diazo-2-Oxopropyl) Phosphonate: Generation of Dimethyl (Diazomethyl) Phosphonate and Reaction with Carbonyl Compounds. *Synth. Commun.* **1989**, 19 (3–4), 561–564. <https://doi.org/10.1080/00397918908050700>.
- (111) Roth, G.; Liepold, B.; Müller, S.; Bestmann, H. Further Improvements of the Synthesis of Alkynes from Aldehydes. *Synthesis (Stuttg.)* **2004**, No. 1, 59–62.
<https://doi.org/10.1055/s-2003-44346>.
- (112) Fetizon, M.; Balogh, V.; Golfier, M. Oxidations with Silver Carbonate/Celite. V. Oxidations of Phenols and Related Compounds. *J. Org. Chem.* **1971**, 36 (10), 1339–1341.
<https://doi.org/10.1021/jo00809a004>.

- (113) Labisbal, E.; Rodr, L.; Souto, O.; Sousa-pedrares, A.; Garc, A.; Orallo, F.; Romero, J.; Sousa, A.; Matilde, Y. Electrochemical Synthesis and Structural Characterization of Co (II), Ni (II) and Cu (II) Complexes of N , N -Bis (4 , 5-Dimethyl-2-Hydroxybenzyl) - N - (2-Pyridylmethyl) Amine †. *Dalt. Trans.* **2009**, 8644–8656.
<https://doi.org/10.1039/b907539a>.
- (114) Mannich, C.; Krösche, W. Ueber Ein Kondensationsprodukt Aus Formaldehyd, Ammoniak Und Antipyrin. *Arch. Pharm. (Weinheim)*. **1912**, 250 (1), 647–667.
<https://doi.org/10.1002/ardp.19122500151>.
- (115) Singh, R.; Banerjee, A.; Gordon, Y.; Rajak, K. K. Binuclear Cobalt(II/II) and Cobalt(II/III) Chelates with O₂N₂ Ligands: Synthesis, Structure and Magnetic Studies. *Transit. Met. Chem.* **2009**, 34 (6), 689–694. <https://doi.org/10.1007/s11243-009-9249-1>.
- (116) Khan, A.; Hecht, S. Poly(Ortho-Phenylene Ethynylene)s: Synthetic Accessibility and Optical Properties. *J. Polym. Sci. Part A Polym. Chem.* **2006**, 44 (5), 1619–1627.
<https://doi.org/10.1002/pola.21238>.
- (117) Blatchly, R. A.; Tew, G. N. Theoretical Study of Helix Formation in Substituted Phenylene Ethynylene Oligomers. *J. Org. Chem.* **2003**, 68 (15), 8780–8785.
- (118) Stasiw, D. E.; Zhang, J.; Wang, G.; Dangi, R.; Stein, B. W.; Shultz, D. A.; Kirk, M. L.; Wojtas, L.; Sommer, R. D. Determining the Conformational Landscape of σ and π Coupling Using Para -Phenylene and “Aviram–Ratner” Bridges. *J. Am. Chem. Soc.* **2015**, 137 (29), 9222–9225. <https://doi.org/10.1021/jacs.5b04629>.
- (119) Kirk, M. L.; Shultz, D. A.; Stasiw, D. E.; Lewis, G. F.; Wang, G.; Brannen, C. L.; Sommer, R. D.; Boyle, P. D. Superexchange Contributions to Distance Dependence of

- Electron Transfer/Transport: Exchange and Electronic Coupling in Oligo(Para-Phenylene)- and Oligo(2,5-Thiophene)-Bridged Donor-Bridge-Acceptor Biradical Complexes. *J. Am. Chem. Soc.* **2013**, *135* (45), 17144–17154.
<https://doi.org/10.1021/ja4081887>.
- (120) Salzner, U. Effect of Donor–Acceptor Substitution on Optoelectronic Properties of Conducting Organic Polymers. *J. Chem. Theory Comput.* **2014**, *10* (11), 4921–4937.
<https://doi.org/10.1021/ct500816c>.
- (121) Reuter, L. G.; Bonn, A. G.; Stückl, A. C.; He, B.; Pati, P. B.; Zade, S. S.; Wenger, O. S. Charge Delocalization in a Homologous Series of α,α - Bis(Dianisylamino)-Substituted Thiophene Monocations. *J. Phys. Chem. A* **2012**, *116* (27), 7345–7352.
<https://doi.org/10.1021/jp303989t>.
- (122) Zahedi, E.; Pangh, A. Superlattices and Microstructures The Comparative Study in Transport Properties of Furan , Thiophene and Selenophene Dithiols in Nano Electronic. *Superlattices Microstruct.* **2011**, *50* (4), 386–399.
<https://doi.org/10.1016/j.spmi.2011.08.001>.
- (123) Li, F.; Zhang, Y.; Kwon, S. R.; Lutkenhaus, J. L. Electropolymerized Polythiophenes Bearing Pendant Nitroxide Radicals. *ACS Macro Lett.* **2016**, *5* (3), 337–341.
<https://doi.org/10.1021/acsmacrolett.5b00937>.
- (124) Miyasaka, M.; Yamazaki, T.; Tsuchida, E.; Nishide, H. Magnetic and Electrical Properties of Poly (3-Radical-Substituted Thiophene) S. *Polyhedron* **2001**, *20*, 1157–1162.
- (125) Knuuttila, P.; Oy, N.; Korvola, J. Polymerization of 3-Alkylthiophenes w i t h FeCl₃. **1992**, *33* (7), 1559–1562.

- (126) Miyasaka, M.; Yamazaki, T.; Tsuchida, E.; Nishide, H. Magnetic and Electrical Properties of Poly(3-Radical-Substituted Thiophene)S. *Polyhedron* **2001**, *20* (11–14), 1157–1162. [https://doi.org/10.1016/S0277-5387\(01\)00588-5](https://doi.org/10.1016/S0277-5387(01)00588-5).
- (127) Niemi, V. M.; Knuuttila, P.; Österholm, J.-E.; Korvola, J. Polymerization of 3-Alkylthiophenes with FeCl₃. *Polymer (Guildf)*. **1992**, *33* (7), 1559–1562. [https://doi.org/http://dx.doi.org/10.1016/0032-3861\(92\)90138-M](https://doi.org/http://dx.doi.org/10.1016/0032-3861(92)90138-M).
- (128) Osaka, I.; Mccullough, R. D. Advances in Molecular Design and Synthesis of Regioregular Polythiophenes. *Acc. Chem. Res.* **2008**, *41* (9), 1202–1214. <https://doi.org/10.1021/ar800130s>.
- (129) Hoffmann, K. J.; Carlsen, P. H. J. Study of an Efficient and Selective Bromination Reaction of Substituted Thiophenes. *Synth. Commun.* **1999**, *29* (9), 1607–1610. <https://doi.org/10.1080/00397919908086142>.
- (130) Tanaka, S.; Tamba, S.; Tanaka, D.; Sugie, A.; Mori, A. Synthesis of Well-Defined Head-to-Tail-Type Oligothiophenes by Regioselective Deprotonation of 3-Substituted Thiophenes and Nickel-Catalyzed Cross-Coupling Reaction. *J. Am. Chem. Soc.* **2011**, *133* (42), 16734–16737. <https://doi.org/10.1021/ja205953g>.
- (131) Peeters, H.; Jivanescu, M.; Stesmans, A.; Pereira, L. M. C.; Dillemans, L.; Locquet, J.-P. P.; Van Bael, M. J.; Persoons, A.; Koeckelberghs, G. Influence of the Bulkiness of the Substituent on the Aggregation and Magnetic Properties of Poly(3-Alkylthiophene)S. *J. Polym. Sci. Part A Polym. Chem.* **2014**, *52* (1), 76–86. <https://doi.org/10.1002/pola.26973>.
- (132) Holcombe, T. W.; Woo, C. H.; Kavulak, D. F. J.; Thompson, B. C.; Fréchet, J. M. J. All-Polymer Photovoltaic Devices of Poly(3-(4-n-Octyl)-Phenylthiophene) from Grignard

- Metathesis (GRIM) Polymerization. *J. Am. Chem. Soc.* **2009**, *131* (40), 14160–14161.
<https://doi.org/10.1021/ja9059359>.
- (133) Wakioka, M.; Takahashi, R.; Ichihara, N.; Ozawa, F. Mixed-Ligand Approach to Palladium-Catalyzed Direct Arylation Polymerization: Highly Selective Synthesis of π -Conjugated Polymers with Diketopyrrolopyrrole Units. *Macromolecules* **2017**, *50* (3), acs.macromol.6b02679. <https://doi.org/10.1021/acs.macromol.6b02679>.
- (134) Kuwabara, J.; Yamazaki, K.; Yamagata, T.; Tsuchida, W.; Kanbara, T.; Wang, F.; Horie, M.; Kanbara, T.; Kanbara, T. The Effect of a Solvent on Direct Arylation Polycondensation of Substituted Thiophenes. *Polym. Chem.* **2015**, *6* (6).
<https://doi.org/10.1039/C4PY01387E>.
- (135) Homyak, P. D.; Liu, Y.; Harris, J. D.; Liu, F.; Carter, K. R.; Russell, T. P.; Coughlin, E. B. Systematic Fluorination of P3HT: Synthesis of P(3HT-Co-3H4FT)s by Direct Arylation Polymerization, Characterization, and Device Performance in OPVs. *Macromolecules* **2016**, *49* (8), 3028–3037. <https://doi.org/10.1021/acs.macromol.6b00386>.
- (136) Rudenko, A. E.; Latif, A. A.; Thompson, B. C. Influence of β -Linkages on the Morphology and Performance of DARp P3HT–PC 61 BM Solar Cells. *Nanotechnology* **2014**, *25* (1), 014005. <https://doi.org/10.1088/0957-4484/25/1/014005>.
- (137) Bura, T.; Blaskovits, J. T.; Leclerc, M. Direct (Hetero)Arylation Polymerization: Trends and Perspectives. *J. Am. Chem. Soc.* **2016**, *138* (32), 10056–10071.
<https://doi.org/10.1021/jacs.6b06237>.
- (138) Chang, S.-W.; Waters, H.; Kettle, J.; Kuo, Z.-R.; Li, C.-H.; Yu, C.-Y.; Horie, M. Pd-Catalysed Direct Arylation Polymerisation for Synthesis of Low-Bandgap Conjugated

- Polymers and Photovoltaic Performance. *Macromol. Rapid Commun.* **2012**, *33* (22), 1927–1932. <https://doi.org/10.1002/marc.201200368>.
- (139) Bura, T.; Beaupré, S.; Légaré, M.-A.; Quinn, J.; Rochette, E.; Blaskovits, J. T.; Fontaine, F.-G.; Pron, A.; Li, Y.; Leclerc, M. Direct Heteroarylation Polymerization: Guidelines for Defect-Free Conjugated Polymers. *Chem. Sci.* **2017**, *8* (5). <https://doi.org/10.1039/C7SC00589J>.
- (140) Grenier, F.; Goudreau, K.; Leclerc, M. Robust Direct (Hetero)Arylation Polymerization in Biphasic Conditions. *J. Am. Chem. Soc.* **2017**, *139* (7), 2816–2824. <https://doi.org/10.1021/jacs.6b12955>.
- (141) Morin, P.-O.; Bura, T.; Leclerc, M. Realizing the Full Potential of Conjugated Polymers: Innovation in Polymer Synthesis. *Mater. Horizons* **2016**, *3* (1), 11–20. <https://doi.org/10.1039/C5MH00164A>.
- (142) Morin, P. O.; Bura, T.; Sun, B.; Gorelsky, S. I.; Li, Y.; Leclerc, M. Conjugated Polymers à La Carte from Time-Controlled Direct (Hetero)Arylation Polymerization. *ACS Macro Lett.* **2015**, *4* (1), 21–24. <https://doi.org/10.1021/mz500656g>.
- (143) Gobalasingham, N. S.; Noh, S.; Thompson, B. C. Palladium-Catalyzed Oxidative Direct Arylation Polymerization (Oxi-DArP) of an Ester-Functionalized Thiophene. *Polym. Chem.* **2016**, *7* (8), 1623–1631. <https://doi.org/10.1039/C5PY01973G>.
- (144) Rudenko, A. E.; Thompson, B. C. Influence of the Carboxylic Acid Additive Structure on the Properties of Poly(3-Hexylthiophene) Prepared via Direct Arylation Polymerization (DArP). *Macromolecules* **2015**, *48* (3), 569–575. <https://doi.org/10.1021/ma502131k>.

- (145) Kuwabara, J.; Fujie, Y.; Maruyama, K.; Yasuda, T.; Kanbara, T. Suppression of Homocoupling Side Reactions in Direct Arylation Polycondensation for Producing High Performance OPV Materials. *Macromolecules* **2016**, *49* (24).
<https://doi.org/10.1021/acs.macromol.6b02380>.
- (146) Rossi, R.; Bellina, F.; Lessi, M.; Manzini, C. Cross-Coupling of Heteroarenes by C-H Functionalization: Recent Progress towards Direct Arylation and Heteroarylation Reactions Involving Heteroarenes Containing One Heteroatom. *Advanced Synthesis and Catalysis*. January 13, 2014, pp 17–117. <https://doi.org/10.1002/adsc.201300922>.
- (147) Ackermann, L.; Vicente, R.; Kapdi, A. R. Transition-Metal-Catalyzed Direct Arylation of (Hetero)Arenes by C-H Bond Cleavage. *Angewandte Chemie - International Edition*. December 21, 2009, pp 9792–9826. <https://doi.org/10.1002/anie.200902996>.
- (148) Zhang, J.; Kang, L. J.; Parker, T. C.; Blakey, S. B.; Luscombe, C. K.; Marder, S. R. Recent Developments in C–H Activation for Materials Science in the Center for Selective C–H Activation. *Molecules*. 2018. <https://doi.org/10.3390/molecules23040922>.
- (149) Kumada, T.; Nohara, Y.; Kuwabara, J.; Kanbara, T. Direct Arylation Polycondensation of Thienothiophenes with Various Dibromoarylenes. *Bull. Chem. Soc. Jpn.* **2015**, *88* (11), 1530–1535. <https://doi.org/10.1246/bcsj.20150235>.
- (150) Wakioka, M.; Ichihara, N.; Kitano, Y.; Ozawa, F. A Highly Efficient Catalyst for the Synthesis of Alternating Copolymers with Thieno[3,4-c]Pyrrole-4,6-Dione Units via Direct Arylation Polymerization. *Macromolecules* **2014**, *47* (2), 626–631.
<https://doi.org/10.1021/ma4023668>.
- (151) Wakioka, M.; Nakamura, Y.; Montgomery, M.; Ozawa, F. Remarkable Ligand Effect of

- P(2-MeOC₆H₄)₃ on Palladium-Catalyzed Direct Arylation. *Organometallics* **2015**, *34* (1). <https://doi.org/10.1021/om501052g>.
- (152) Rudenko, A. E.; Wiley, C. A.; Stone, S. M.; Tannaci, J. F.; Thompson, B. C. Semi-Random P3HT Analogs via Direct Arylation Polymerization. *J. Polym. Sci. Part A Polym. Chem.* **2012**, *50* (18), 3691–3697. <https://doi.org/10.1002/pola.26175>.
- (153) Ackermann, L.; Vicente, R.; Kapdi, A. Transition-Metal-Catalyzed Direct Arylation of (Hetero)Arenes by C–H Bond Cleavage. *Angew. Chemie Int. Ed.* **2009**, *48* (52), 9792–9826. <https://doi.org/10.1002/anie.200902996>.
- (154) Wakioka, M.; Ishiki, S.; Ozawa, F. Synthesis of Donor-Acceptor Polymers Containing Thiazolo[5,4-d]Thiazole Units via Palladium-Catalyzed Direct Arylation Polymerization. *Macromolecules* **2015**, *48* (22), 8382–8388. <https://doi.org/10.1021/acs.macromol.5b01822>.
- (155) Hayashi, S.; Togawa, Y.; Kojima, Y.; Koizumi, T. Direct Arylation of Fluoroarenes toward Linear, Bent-Shaped and Branched π -Conjugated Polymers: Polycondensation Post-Polymerization Approaches. *Polym. Chem.* **2016**, *7* (36), 5671–5686. <https://doi.org/10.1039/C6PY01237J>.
- (156) Yu, S.; Liu, F.; Yu, J.; Zhang, S.; Cabanetos, C.; Gao, Y.; Huang, W. Eco-Friendly Direct (Hetero)-Arylation Polymerization: Scope and Limitation. *J. Mater. Chem. C* **2017**, *5* (1). <https://doi.org/10.1039/C6TC04240F>.
- (157) Facchetti, A.; Vaccaro, L.; Marrocchi, A. Semiconducting Polymers Prepared by Direct Arylation Polycondensation. *Angew. Chemie Int. Ed.* **2012**, *51* (15), 3520–3523. <https://doi.org/10.1002/anie.201200199>.

- (158) Yamazaki, K.; Kuwabara, J.; Kanbara, T. Detailed Optimization of Polycondensation Reaction via Direct C-H Arylation of Ethylenedioxythiophene. *Macromol. Rapid Commun.* **2013**, *34* (1), 69–73. <https://doi.org/10.1002/marc.201200550>.
- (159) Kuwabara, J.; Yasuda, T.; Choi, S. J.; Lu, W.; Yamazaki, K.; Kagaya, S.; Han, L.; Kanbara, T. Direct Arylation Polycondensation: A Promising Method for the Synthesis of Highly Pure, High-Molecular-Weight Conjugated Polymers Needed for Improving the Performance of Organic Photovoltaics. *Adv. Funct. Mater.* **2014**, *24* (21), 3226–3233. <https://doi.org/10.1002/adfm.201302851>.
- (160) Pouliot, J.-R.; Grenier, F.; Blaskovits, J. T.; Beaupré, S.; Leclerc, M. Direct (Hetero)Arylation Polymerization: Simplicity for Conjugated Polymer Synthesis. *Chem. Rev.* **2016**, *116* (22), 14225–14274. <https://doi.org/10.1021/acs.chemrev.6b00498>.
- (161) McCullough, R. D. The Chemistry of Conducting Polythiophenes. *Adv. Mater.* **1998**, *10* (2), 93–116. [https://doi.org/10.1002/\(SICI\)1521-4095\(199801\)10:2<93::AID-ADMA93>3.0.CO;2-F](https://doi.org/10.1002/(SICI)1521-4095(199801)10:2<93::AID-ADMA93>3.0.CO;2-F).
- (162) Miljanić, O. S.; Holmes, D.; Vollhardt, K. P. C. 1,3,6,9,12,14,17,20-Octaethynyltetrabenz[a,b,f,j,k,o]-4,5,10,11,15,16,21,22-Octadehydro[18]Annulene: A Carbon-Rich Hydrocarbon. *Org. Lett.* **2005**, *7* (18), 4001–4004. <https://doi.org/10.1021/ol051572x>.
- (163) Bigi, F.; Carloni, S.; Maggi, R.; Muchetti, C.; Sartori, G. Zeolite-Induced Heterodimino Reaction. Regioselective Synthesis of 2 H -1-Benzopyrans from Phenols and α -Alkynols. *J. Org. Chem.* **1997**, *62* (20), 7024–7027. <https://doi.org/10.1021/jo970690y>.
- (164) Tanaka, K.; Hagiwara, Y.; Noguchi, K. Rhodium-Catalyzed Regio- and Enantioselective

- Intermolecular [4+2] Carbocyclization of 4-Alkynals with N,N-Dialkyl Acrylamides. *Angew. Chem. Int. Ed. Engl.* **2005**, *44* (44), 7260–7263.
<https://doi.org/10.1002/anie.200502380>.
- (165) Chen, W.; Tao, H.; Huang, W.; Wang, G.; Li, S.; Cheng, X.; Li, G. Hantzsch Ester as a Photosensitizer for the Visible-Light-Induced Debromination of Vicinal Dibromo Compounds. *Chem. - A Eur. J.* **2016**, *22* (28), 9546–9550.
<https://doi.org/10.1002/chem.201601819>.
- (166) Li, J.; Liu, Y.; Li, C.; Jia, X. Silver Hexafluoroantimonate-Catalyzed Three-Component [2+2+1] Cycloadditions of Allenates, Dual Activated Olefins, and Isocyanides. *Adv. Synth. Catal.* **2011**, *353* (6), 913–917. <https://doi.org/10.1002/adsc.201000795>.
- (167) Avery, T. D.; Caiazza, D.; Culbert, J. A.; Taylor, D. K.; Tiekink, E. R. T. 1,2-Dioxines Containing Tethered Hydroxyl Functionality as Convenient Precursors for Pyran Syntheses. *J. Org. Chem.* **2005**, *70* (21), 8344–8351. <https://doi.org/10.1021/jo050806n>.
- (168) Chen, J.; Chen, T.; Hu, Q.; Puntener, K.; Ren, Y.; She, J.; Du, Z.; Scalone, M. Practical Asymmetric Hydrogenation-Based Synthesis of a Class-Selective Histone Deacetylase Inhibitor. *Org. Process Res. Dev.* **2014**, *18* (12), 1702–1713.
<https://doi.org/10.1021/op500250b>.
- (169) Reimer, M.; Tobin, E. Certain Reactions of P-Bromocinnamic Acid. *J. Am. Chem. Soc.* **1941**, *63* (9), 2490–2493. <https://doi.org/10.1021/ja01854a051>.
- (170) Wong, Y.-L.; Yan, Y.; Chan, E. S. H. H.; Yang, Q.; Mak, T. C. W. W.; Ng, D. K. P. P. Cis-Dioxo-Tungsten(VI) and -Molybdenum(VI) Complexes with N₂O₂ Tetradentate Ligands: Synthesis, Structure, Electrochemistry and Oxo-Transfer Properties. *J. Chem.*

Soc. Dalt. Trans. **1998**, No. 18, 3057–3064. <https://doi.org/10.1039/a804425b>.

PART B: Donor-Bridge-Acceptor Biradicals for Probing Electronic Structure

III. Donor-Bridge-Acceptor (DBA) Biradicals Overview

Donor-bridge-acceptor molecules are fundamentally relevant to and allow for the rational design of new photovoltaics, electron transfer/transport devices, OLEDs, and spintronic devices and systems.¹⁻²³ Electron transfer and the interactions among unpaired electrons -- exchange coupling -- are entwined and crucial concepts that aid in the design of these molecular electronic

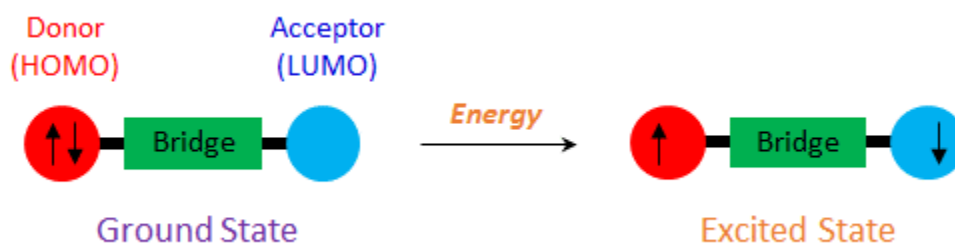


Figure III-1. A diamagnetic donor-bridge-acceptor system which gives a biradical-like state upon excitation.

devices. The study of these types of donor-bridge-acceptor systems facilitates understanding of structure-property relationships that are necessary to guide the design of novel devices for these applications.

Donor-bridge-acceptor biradicals are uniquely-suited to study and provide insights into the design and function of these materials, as Figure III-1 shows a diamagnetic donor-bridge-acceptor system which gives a biradical-like excited state. Provided the bridge allows for sufficient coupling of the donor and the acceptor, a unique $D \rightarrow A$ electronic transition exists. The orbitals involved in this electronic transition are the HOMO(donor) and the LUMO(acceptor). In the ground state of a DBA triad, the donor's HOMO is filled and the acceptor's LUMO is unoccupied, but when a photon of sufficient energy is absorbed, an electron from the HOMO(donor) "moves through the bridge" to the LUMO(acceptor) to give the D^+BA^- charge-separated excited state of the donor-bridge-acceptor system. In addition to the absorption

of a photon, a voltage bias between two electrodes can result in electron flow from donor to acceptor through the bridge. Thus, DBA molecules form the basis for understanding electron transfer as well as electron transport in single-molecule devices.

A critical characteristic of the D^+BA^- excited state is that both the donor cation and the acceptor anion possess unpaired electron spins: the HOMO(donor) and LUMO(acceptor) are now both singly-occupied molecular orbitals (SOMOs). Consequently, the donor-bridge-acceptor biradicals prepared in our group are *excited state analogs* of D^+BA^- charge-separated excited states.²⁴ Since our DBA biradicals are stable ground-state species, both the molecular and electronic structures can be probed with high resolution to reveal detailed structure-property relationships relevant to electron transfer and electron transport.

There are other ways to study electronic structure and properties of DBA systems. Because of the utility of charge-separated excited states in photoredox catalysis, solar energy conversion, and photovoltaics, there are a plethora of papers describing photo-induced energy/electron transfer in DBA molecules.^{4,8,9,11,15,23,25-27} Single molecule devices sandwiched between biased metallic electrodes can also be evaluated within the DBA construct.²⁸⁻³⁰ These analyses are imperative to understanding the properties of these materials and their behaviors; however, they do not readily allow for detailed structure-property relationships to be developed because, *e.g.*, excited states are short-lived and are not amenable to an intense evaluation of their physical structure. By the same token, the inability to probe the detailed structure of a single molecule device has led to a statistical approach to determining single-molecule conductance values that requires hundreds or thousands of individual measurements.³¹⁻³⁴ Utilizing stable organic biradicals allows for the precise analysis of the geometry of the bridging unit and its effects on the electronic communication between the donor and acceptor. Furthermore, bridged

organic radicals, as opposed to two bridged-metal ions, simplifies and limits the interactions to typically one dominant pathway, the π -system. By contrast, in DBA systems comprised of bridged-metal ions, each with possibly five d-orbitals contributing to the interactions through the bridge, it is far more challenging to disentangle coupling pathways and provide a straightforward, structural explanation for the observed properties.^{35–40}

III.1. A Brief Historical Perspective on Electronic Coupling and Electron Transfer.

Electron transfer is a fundamental and ubiquitous process that occurs in the most chemical redox reactions; the most complex electronic devices such as photovoltaics, spintronics, rectifiers,^{3–12,14–16,23} and others; and it is an essential life-sustaining process in biological systems, such as photosystems for the photosynthesis of plants, generation of ATP from the electron transport chain, Cytochrome P450 and many others.^{1,2,13,17–22,41} As a result,

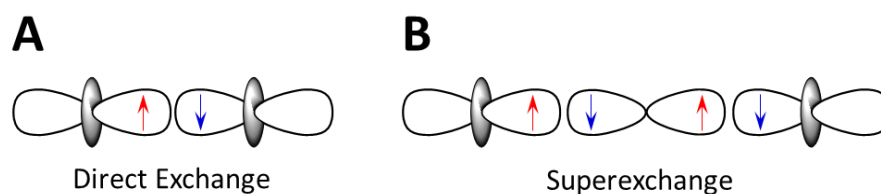


Figure III-2. A) Directly overlapping SOMOs giving rise to direct antiferromagnetic exchange and B) SOOMOs interacting through a filled diamagnetic p -orbital resulting in antiferromagnetic superexchange.

understanding electron transfer is vitally important to the development of new molecular devices and understanding biology at its most fundamental chemical and physical level, and there have been several descriptions and evaluations of electron transfer.^{13,36,41–46} Electronic- and exchange coupling are interrelated and crucial to electron transfer and understanding the underlying mechanisms of electron transfer and transport.^{26,45,46}

The origins of our understanding of electron spin exchange in molecules comes from the descriptions of bridged-metal ion species. Figure III-2A shows a schematic of direct exchange

which is where the two half-filled orbitals are interacting with each other directly giving rise to an antiferromagnetic interaction. Figure III-2B shows a simple diagram of superexchange, a term arising from the model for correlation of two spins on metal atoms that are bridged by a diamagnetic atom. The Goodenough-Kanamori rules, provide a more rigorous description of magnetic exchange interactions between metal ions joined by diamagnetic bridges.^{38,39,47} Anderson provided a foundation for the observed superexchange interaction by relating the effective exchange integral (J_{eff}) to the repulsive energy (U) which for a metal, is the observed activation energy for conduction in the d -band; and the transfer integral (b) resulting in the following Eq. III-1:

$$J_{eff} = \frac{2b^2}{U} \quad \text{Eq. III-1}$$

Anderson then rewrites the transfer integral (b) in terms of d -orbitals for all possible combinations of orbitals in terms of the crystal field splitting parameter and calculates the exchange integrals for various octahedral, oxo-bridged metal centers from estimates of repulsive (U) and transfer (b) integrals. He points out that while his estimations may be inaccurate, it is the intention of electrons to have antiparallel spins in order to spread out into overlapping orbitals.^{35,36}

McConnell expanded the electronic coupling (H_{DA}) to accommodate donor-acceptor systems where the donor and acceptor are not directed interacting, but rather are separated by one or more bridging units as shown in Eq. III-2:

$$H_{DA} = \frac{H_{DB}H_{BA}}{\Delta\varepsilon_{DB}} \left(\frac{H_{BB}}{\Delta\varepsilon_{DB}} \right)^{N-1} \quad \text{Eq. III-2}$$

where H_{DA} , H_{DB} , H_{BA} and H_{BB} are the electronic coupling matrix elements between donor-acceptor, donor-bridge, bridge-acceptor and bridge-bridge (for multiple units).⁴⁵ Note that for only one bridging unit the bridge-bridge term becomes 1 due to the absence of any bridge-bridge interaction. Also, note that McConnell's model takes into account the relevant energy gap in the system is that between the donor and the bridge, and by doing so has the same mathematical form as the Anderson description, Eq. III-1.

The electronic coupling matrix element, H_{DA} is a crucial factor in electron transfer rate constants and in conductance in single-molecule devices. Marcus provided a theoretical treatment of electron transfer reactions in 1956⁴³ and then expanded upon that theory from 1965⁴⁴ to 1985⁴¹ relating it more to chemistry and biology and introducing Eq. III-3, which describes the rate of electron transfer, k_{ET} between a donor and acceptor:

$$k_{ET} = \frac{2\pi}{\hbar} \frac{|H_{DA}|^2}{(4\pi\lambda_{DA}RT)^{1/2}} \exp\left(\frac{(\Delta G_{DA}^0 + \lambda_{DA})^2}{4\pi\lambda_{DA}RT}\right), \quad \text{Eq. III-3}$$

where ΔG_{DA}^0 is the standard free energy for the electron transfer process, λ_{DA} is the reorganization parameter and H_{DA} is the electronic coupling matrix element.⁴¹ Landauer^{42,48} described conductance (g) in single molecule devices and Nitzan upon Marcus and Landauer's work by correlating the rate of electron transfer with conductance.⁴⁶ Ratner and Wasielewski^{26,27} provided experimental and computational results that were in general agreement with Nitzan's work. Landauer's work related to the theory of conductance is shown as Eq. III-4:

$$g = \frac{e^2}{\pi\hbar} \Gamma_{RB} \Gamma_{LB} |G_{DA}|^2 \quad \text{Eq. III-4}$$

Where the Γ are the widths of the D and A levels due to coupling with the right- and left electrodes, and G_{DA} is the bridge Green's function.⁴⁹⁻⁵² In the limit weak coupling between the

bridge and the rest of the system, G_{DA} in Eq. III-4 is proportional to H_{DA} in Eq. III-3. Nitzan's work showing $g \sim k_{ET}$ is significant in that it relates to seemingly disparate experimental quantities (k_{ET} and g) to the square of the electronic coupling matrix element (H_{DA}^2). These results in conjunction with Anderson's relation of the exchange coupling constant (J) to electronic coupling (H_{DA}^2) and McConnell's expression of electronic coupling between a donor and acceptor mediated by a bridging unit, allow for a thorough foundation for the evaluation of the electronic structure of our SQ-B-NN complexes. By determining the exchange coupling constants (J) of our biradical complexes and providing tangible theoretical and empirical evidence for relating our results to the understanding of conductance in molecular devices and to electron transfer rates in charge-separated excited states in donor-bridge-acceptor systems.^{1,2,13,17-22}

III.2. Semiquinone donor-bridge-Nitronylnitroxide acceptor (SQ-B-NN) Biradicals.

The remainder of this chapter and document will be focused on evaluating electronic coupling provided by different diamagnetic bridge fragments using the structural motif: semiquinone (SQ; $S = \frac{1}{2}$ radical as a zinc(II) complex) donor-Bridge-nitronylnitroxide (NN; $S = \frac{1}{2}$ radical) acceptor (SQ-B-NN) triads in which covalent bonds connect the bridge to both the donor and acceptor. Specifically, the SQ-NN magnetic exchange parameter ($J_{SQ-B-NN}$), determined experimentally, will be used as a means of evaluating the electronic coupling (H) through a bridge to provide insights into electron transport processes that are of relevance to the development of molecular devices.^{3-12,14-16,23} This complex provides a theoretical and empirical basis for subsequent studies of SQ-B-NN complexes and will be discussed in the following sections with the results from various projects in our group.⁵³⁻⁵⁵

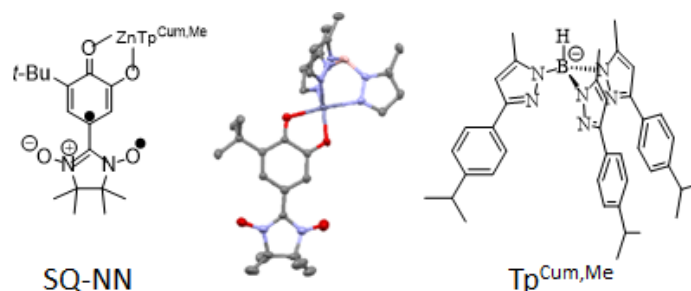


Figure III-3. The original “no bridge” donor-acceptor biradical, SQ-NN.

The parent donor-bridge-acceptor complex has the SQ donor and NN acceptor directly bonded to each other (SQ-NN) and the SQ is charge-balanced by the diamagnetic zinc II hydro(*tris*(cumenyl-methylpyrazolyl)borate [$\text{Tp}^{\text{Cum,Me}}$] $^-$) ligand as shown in Figure III-3. The magnetic coupling constant, J , which as defined represents the singlet-triplet gap ($\Delta E_{\text{ST}} = 2J$) and for SQ-NN $J = 550 \text{ cm}^{-1}$ indicating the radicals are strongly ferromagnetically-coupled. In the C_{2v} point group, the SQ SOMO has b_2 symmetry and the NN SOMO has a_2 symmetry; thus they are orthogonal and cannot directly interact. However, they can interact via the NN LUMO which

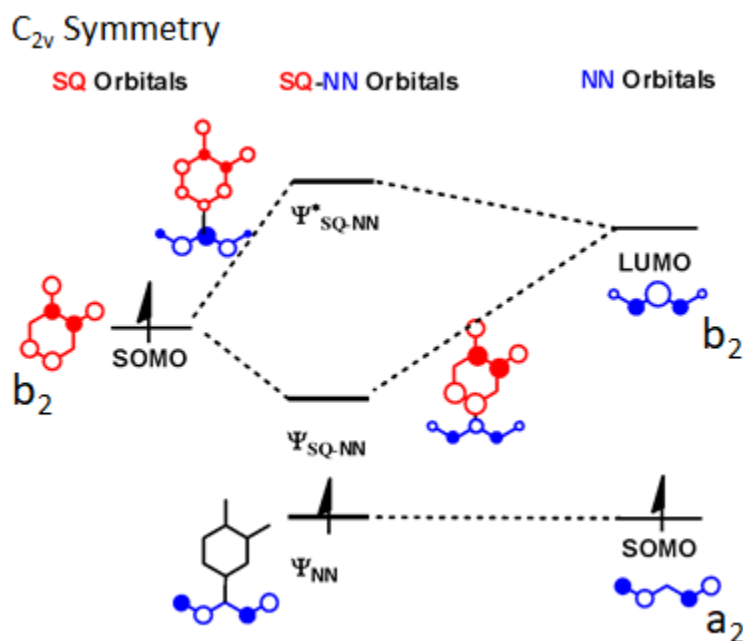


Figure III-4. Interactions leading to ferromagnetic exchange in SQ-NN.

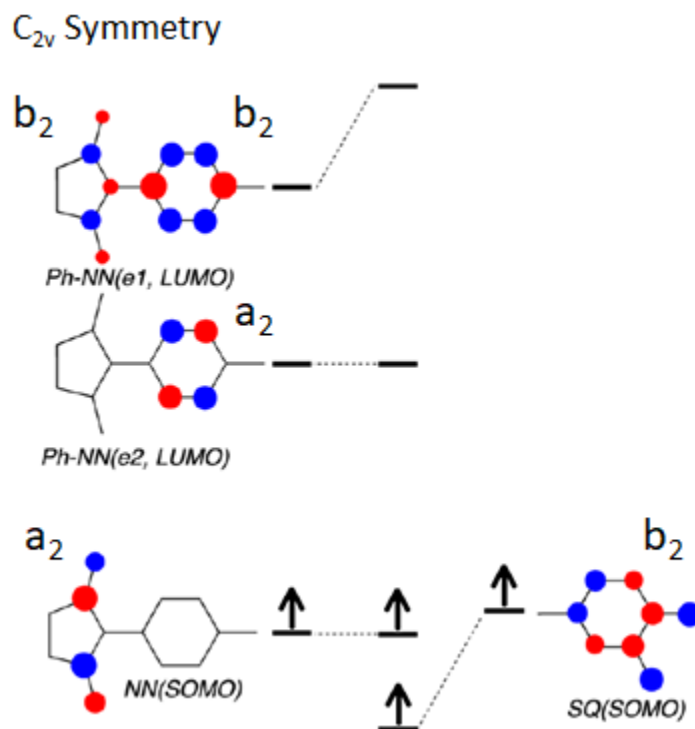


Figure III-5. Interactions for conjugated SQ-B-NN molecules.

has b_2 symmetry to result in SQ- and NN spins occupying two orthogonal, non-disjoint molecular orbitals which will give rise to ferromagnetic coupling as per Hund's first rule (Figure III-4). A similar diagram can be drawn for a *para*-phenylene-bridged biradical (SQ-Ph-NN) as shown in Figure III-5. In it the NN's LUMO mixes with one of the doubly degenerate e sets of the phenyl LUMO to make a new molecular orbital which then has the appropriate symmetry to interact with the SQ SOMO.²⁸ This complex gives ferromagnetic coupling with $J = +100 \text{ cm}^{-1}$. These interactions between the SQ SOMO and NN LUMO or NN-bridge LUMO is also spectroscopically observable by the $SQ_{\text{SOMO}} \rightarrow NN_{\text{LUMO}}$ transition observed at about 23000 cm^{-1} for SQ-NN and 25000 cm^{-1} for SQ-Ph-NN (the latter is shown in Fig. III-6B).

An alternative to the MO model above uses mixing of specific electronic states to evaluate exchange coupling, and provides a straightforward model for evaluating $H_{DA} = H_{SQ-B}$.

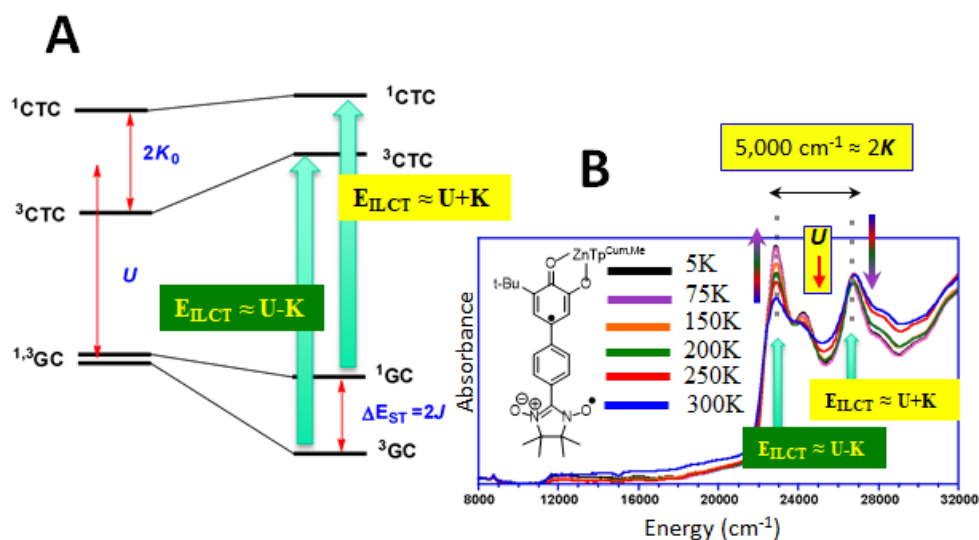


Figure III-6. A) VBCI model state diagram illustrating electronic transitions and energy gaps, U , K_0 and J . The ground states (^1GC , ^3GC) arise from the NN-SOMO¹SQ-SOMO¹NN-LUMO⁰ configuration, while the SQ \rightarrow NN CT excited states (^1CTC , ^3CTC) arise from the NN-SOMO¹SQ-SOMO⁰NN-LUMO¹ configuration. B) Variable temperature electronic absorption spectra with the electronic transitions from the state diagram labelled. The intensity of the band near 23,000 cm^{-1} increases as the temperature is lowered, while that of the band near 28,000 cm^{-1} decreases with decreasing temperature. Thus, these are assigned to a $^3\text{GC} \rightarrow ^3\text{CTC}$ and $^1\text{GC} \rightarrow ^1\text{CTC}$, respectively. Since $J \ll K$, the former is ignored in the energies, E_{ILCT} .

$_{\text{NN}}$. This model is known as the valence bond configuration interaction (VBCI) model and provides insights into the mechanism from parameters that provided by magnetometry and from these spectroscopically observable band rather than only by the aid of calculations.²⁴ Figure III-6A shows the VBCI model for the SQ-B-NN system. The state diagram on the left-side shows the energy levels of the ground and excited state in the absence of the excited state configurational interaction. Here the ground state triplet and singlet states are derived from the NN-SOMO¹SQ-SOMO¹NN-LUMO⁰ configuration, and are degenerate in first-order, therefore $J = 0 \text{ cm}^{-1}$. The excited state singlet- and triplet states arise from the NN-SOMO¹SQ-SOMO⁰NN-LUMO¹ configuration, and are split by $2K$ where K is the exchange integral that was discussed in the context of Hund's rule, and destabilizes the singlet state relative to the triplet.

$$2J_{DA} = \frac{2H_{DA}^2 K}{U^2 - K^2} \quad \text{Eq. III-5}$$

With an electronic absorption spectrum and an exchange coupling constant determined, H_{DA}^2 may be calculated from Eq. III-5 by filling in the appropriate terms for U , K , and J_{DA} . These results show that the SQ and NN radicals can interact via the LUMO of the NN to give relatively strong magnetic coupling and that when a bridge is between the SQ and the NN, the bridge LUMO is vitally important to the superexchange pathway that gives rise to the observed coupling in conjugated biradicals of SQ-B-NN.

III.3. Synthesis of SQ-B-NN Biradical Studies.

III.3.1. General Synthesis.

Shultz group donor-bridge-acceptor (DBA) biradical ligands and complexes share key structural components^{24,29,30,54,56,57} consisting of nitronyl nitroxide (NN) acceptors, diamagnetic bridges, and semiquinone (SQ) donors which are chelated to diamagnetic zinc (II) complex ion. The latter is the $[\text{Tp}^{\text{Cum,Me}}\text{Zn}^{\text{II}}]^+$ ligand as shown in Fig. III-7. The $[\text{Tp}^{\text{Cum,Me}}]^-$ ligand's steric bulk

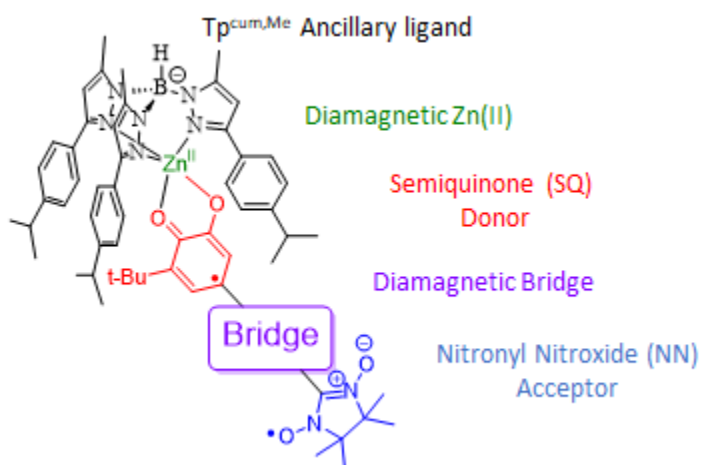
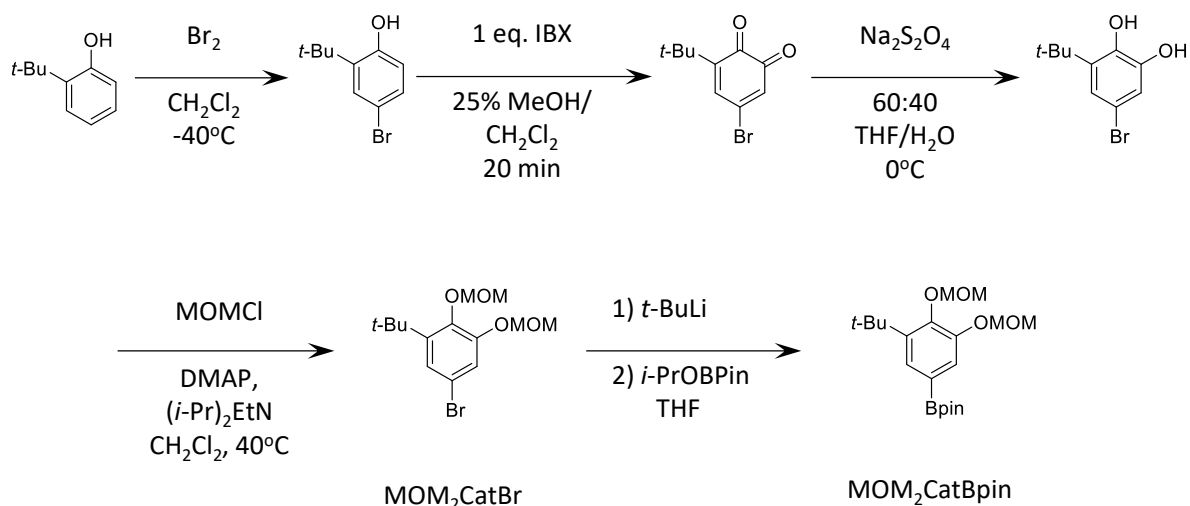


Figure III-7. General structure of SQ donor-bridge-NN acceptor biradicals.

Scheme III-1. Synthesis of MOM₂CatBpin



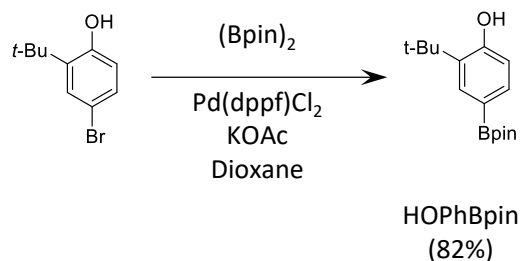
and SQ-encapsulating cumenyl groups insulate the semiquinone radicals from each other. The [Tp^{Cum,Me}Zn^{II}]⁺ complex ion was originally used by Ruf and Pierpont et al. to prepare metal complexes of 3,5-di-*tert*-butylsemiquinone,⁵⁸ and aids in analysis of magnetic data by severely attenuating intermolecular interactions. Thus, the strongest magnetic interactions in crystalline samples are intramolecular rather than being convoluted with intermolecular interactions. The [Tp^{Cum,Me}]⁻ ligand also has a -1 charge and counterbalances the combined 1+ charge on zinc(II) semiquinone. The d¹⁰ Zn²⁺ ion is both diamagnetic and NMR inactive and so contributes to neither paramagnetic susceptibility nor to EPR spectroscopy. The bridge unit can be any synthetically viable fragment. The syntheses of the precursors to the SQ, NN and zinc ancillary ligand are described in the following sections followed by the common preparation routes of the DBA biradical complexes.

III.3.2. Preparation of Semiquinones and Their Synthons.

For our purposes, the semiquinone precursor is typically a catechol which is installed onto the bridge using palladium-mediated cross-coupling methods.^{29,30,56} Given that catechols can chelate metal ions and are sensitive to oxidation, they must be protected. Scheme III-1 shows

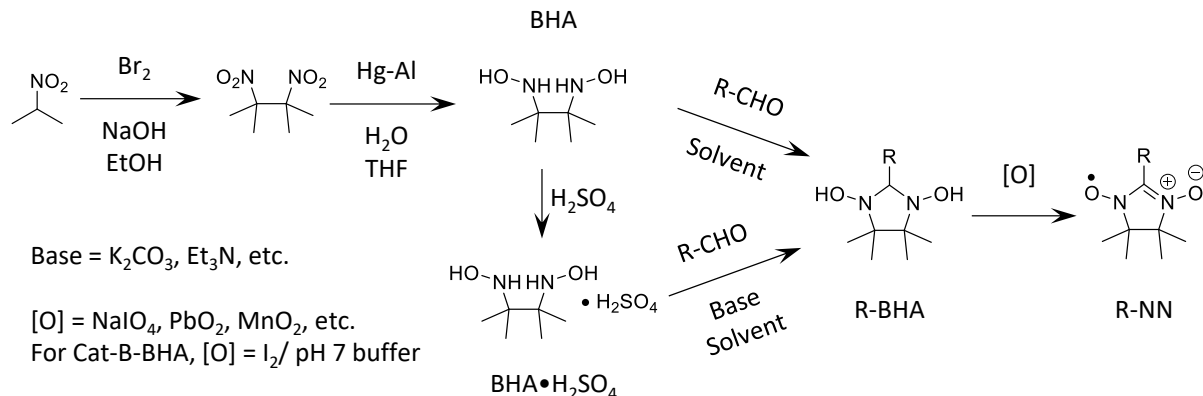
the synthesis of MOM₂CatBpin which is one reagent that can be used in a Suzuki coupling to give the methoxymethyl- (MOM) protected precursor catechol. This is the same reagent (**II-4**) whose synthesis was described in Chapter II; however, the synthesis described here is an

Scheme III-2. Synthesis of HOPhBpin.



improved method which gives higher yields, greater purities, and requires shorter reaction times. A full description of the synthesis methods used to prepare MOM₂CatBpin in the Shultz group over the years is provided in Appendix A. The newest synthesis of MOM₂CatBpin starts with the bromination of commercially-available 2-*tert*-butyl phenol, followed by reaction with IBX in 25% MeOH/CH₂Cl₂, to provide selectively, the *ortho*-quinone as described in Magdziak et al.⁵⁹ The quinone is then reduced with Na₂S₂O₄ in H₂O/THF to 4-bromo-6-*tert*-butylcatechol. The catechol is then protected by reaction with excess methoxymethylchloride to give MOM₂CatBr. MOM₂CatBpin is then synthesized via lithium-halogen exchange of MOM₂CatBr with two equivalents of *t*-BuLi, followed by quenching with *i*-PrOBpin. Purifying MOM₂CatBpin after aqueous work-up is achieved by precipitation from pentane at -20 °C overnight (seeded with a grain of previously prepared, solid MOM₂CatBpin) to provide MOM₂CatBpin as a colorless solid. Purification by column chromatography often results in yellow oils which will solidify upon standing at low temperature; however, this solid can be precipitated several times from pentane to arrive at a colorless solid.

Scheme III-3. The synthesis of nitronyl nitroxides from commercially available starting materials.



As an alternative to oxidation of 4-bromo-6-*tert*-butylphenol to the *ortho*-quinone it can be cross-coupled with *bis*(pinacolato)diboron in the presence of $Pd(dppf)Cl_2$ and $KOAc$ in *p*-dioxane, as shown in Scheme III-2 to give HOPhBpin which can then be oxidized with IBX and subsequently reduced with $Na_2S_2O_4$ *after* it has been installed onto a bridge fragment.^{29,30,56}

III.3.3. Preparation of Nitronylnitroxides.

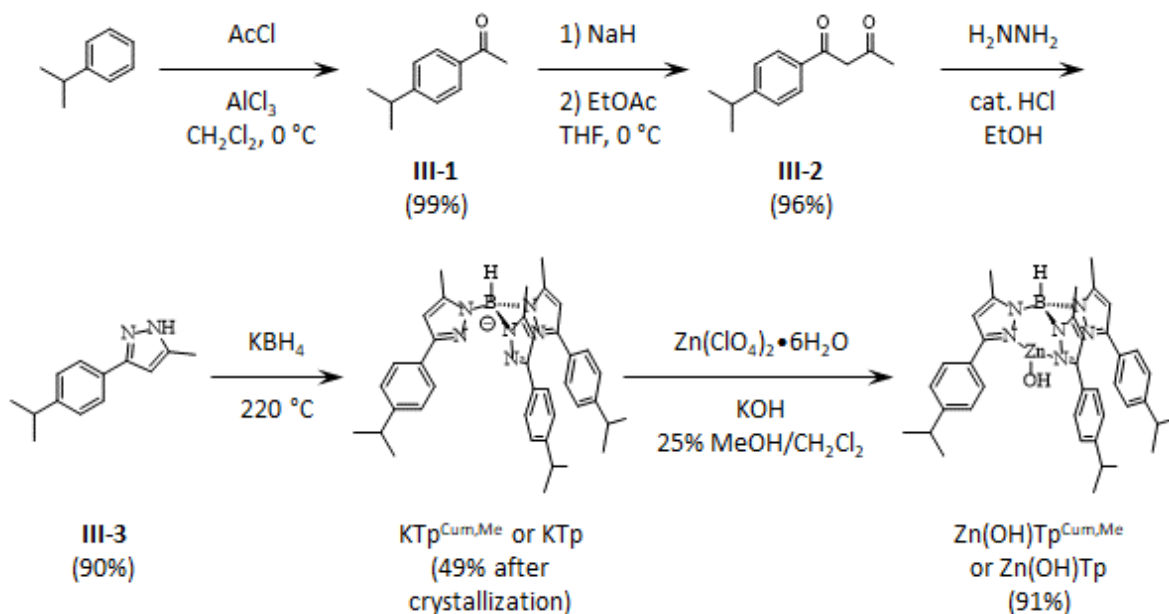
The synthesis of NNs from commercially-available starting materials is shown in Scheme III-3. The “Ulmann synthesis”^{60,61} starts with the dimerization reaction of 2-nitropropane with aqueous $NaOH$ and Br_2 in $EtOH$ to give 2,3-dimethyl-2,3-dinitrobutane which is then reduced with mercury-aluminum amalgam with water in THF ^{62,63} to give *N,N'*-(2,3-dimethylbutane-2,3-diyl)bis(hydroxylamine) (BHA) which can be condensed with an aldehyde.⁶¹ BHA can also be doubly protonated to give the bis(hydroxylammonium) sulfate salt ($BHA \cdot H_2SO_4$) which can be condensed with an aldehyde in the presence of a base, such as K_2CO_3 or Et_3N . This begs the question of why convert BHA into $BHA \cdot H_2SO_4$ if the sulfate salt must be used in the presence of base? Figure III-8 shows the NMR spectra of BHA (top) and $BHA \cdot H_2SO_4$ (bottom) after sitting in a capped vial for approximately 18 months. As can be seen, the $BHA \cdot H_2SO_4$ has higher purity as determined by the amount of acetone oxime decomposition product, due to either slightly

Given that these $^1\text{H-NMR}$ were taken nearly 1.5 years after preparation, it can be generally assumed that over a period of at least months both BHA and $\text{BHA}\cdot\text{H}_2\text{SO}_4$ have good shelf-life, but that of $\text{BHA}\cdot\text{H}_2\text{SO}_4$ may be longer.

III.3.4. Preparation of $\text{Zn}(\text{OH})\text{Tp}^{\text{Cum,Me}}$ Ancillary Ligand.

The synthesis of the hydro(*tris*(cumenyl-methylpyrazolyl)borate zinc ion was first reported by Vahrenkamp et al. and is shown in Scheme III-5 with some slight modifications to the original procedure.⁶⁴ The first step is the Friedel-Crafts acylation of cumene with acetyl chloride/ AlCl_3 . The original procedure⁶⁵ conducted this reaction in carbon disulfide (CS_2) rather than CH_2Cl_2 ; however we use CH_2Cl_2 due to its lower toxicity and flammability. An unexpected, but pleasant effect of using CH_2Cl_2 in place of CS_2 was that the resulting 4-isopropylacetophenone (**III-1**) from the Friedel-Crafts acylation was visibly more colorless. Samples from multiple syntheses and researchers showed that those from CS_2 were yellow oils

Scheme III-5. Synthesis of $\text{Zn}(\text{OH})\text{Tp}^{\text{Cum,Me}}$.



whereas samples from CH_2Cl_2 were much lighter in color and nearly colorless; probably indicative of greater purity; although no analysis other than $^1\text{H-NMR}$ was performed to confirm this.

The next reaction is the Claisen condensation of 4-isopropylacetophenone with EtOAc. This reaction was originally performed by preparing NaOEt from ethanol and hexane-washed NaH (to remove the mineral oil) in THF, then adding the acetophenone, followed by EtOAc. After a general literature search on Claisen condensation reactions, it was revealed that they could be carried out with either alkoxides or with just NaH as the base in THF. Those that were run with only NaH, generally benefitted from higher yields. This also simplified the reaction procedure because NaOEt did not need to be prepared, NaH could be loaded into an oven-dried round-bottom flask and suspended in THF, and then 4-isopropylacetophenone could be added dropwise in THF via cannula, stirred for ca. 1 h and then EtOAc in THF could be added dropwise and the reaction stirred overnight. The work-up procedure was also modified because after stirring overnight, copious amounts of precipitate were present in THF due to the formation of the salt of the β -diketone product (pK_a of this aryl malonic ester probably 7-9; 1-phenylbutane-1,3-dione is $\text{pK}_a = 8.23$). To ensure complete deprotonation and precipitation, the reaction solution was diluted with Et_2O and stirred with 1 mL of H_2O which caused more precipitate to form and should protonate any enolate of unreacted starting material. This was then filtered and washed with Et_2O until the filter cake was nearly colorless in order to remove any unreacted starting material and any remaining mineral oil from NaH. Given this work-up strategy, the initial reaction set-up was simplified because now the NaH did not need to be washed with anhydrous hexanes to remove the mineral oil, as it would just be washed away with organic solvent during filtration. The malonate is suspended in biphasic water and Et_2O , then 12

M HCl is added until the solid all dissolves and the aqueous layer is acidic to pH paper. The product (**III-2**) is then extracted from the organic layer. Yields from NaOEt ranged from 60-70%, but yields from NaH routinely exceed 85%, use less solvent and take less time.

The condensation of the β -diketone (**III-2**) with hydrazine monohydrate is performed in EtOH with catalytic aqueous HCl to give the crude pyrazole (**III-3**), which is then crystallized and/or sublimed at ca. 60 °C under high vacuum (150-50 mTorr) to give **III-3** as a colorless solid, in good yields of 80-90%.

The pyrazole (**III-3**) is heated with one-third equivalent of KBH_4 to ca. 220 °C, by which point the pyrazole has melted and hydrogen gas is evolved as three pyrazole units become bound to the boron. This melt reaction requires scrupulously anhydrous and air-free conditions in order to work well. Another subtle point is that this reaction should be performed with a glass stir bar because Teflon begins to deteriorate around 260 °C. Melt reactions performed with Teflon stir bars will usually attain a darker color (gray, dark brown, black) and the stir bar will be forever changed and be similar in color to the reaction. This decomposition may also affect the success of the reaction because Teflon stir bar reactions tend to give a variety of yields; including reactions with no desired product. Reactions performed with glass stir bars will consistently give upper 30s-50% yields of $\text{KTp}^{\text{Cum,Me}}$ after recrystallization from MeCN. Characterization of $\text{KTp}^{\text{Cum,Me}}$ is primarily by $^1\text{H-NMR}$, but this *should not* be the only form of characterization. $^1\text{H-NMR}$ should be used to assess the *purity* of $\text{KTp}^{\text{Cum,Me}}$, not necessarily the identity because pyrazole (**III-3**), $\text{KTp}^{\text{Cum,Me}}$ and mono- and di-coordinated pyrazole borohydrides have very similar chemical shifts and slight solvent impurities can shift them to so that they resemble those of the other compounds. The IR spectrum of $\text{KTp}^{\text{Cum,Me}}$ should show a *single*, B-H stretch at 2649 cm^{-1} . Additional B-H stretches would indicate the presence of mono- or di-coordinated

pyrazole borohydrides. The final important piece of characterization for $\text{KTp}^{\text{Cum,Me}}$ is the melting point at 123 °C.⁶⁴ By comparison, pyrazole (**III-3**) has a melting point of ~95 °C.

The final reaction to prepare $\text{Zn(OH)Tp}^{\text{Cum,Me}}$ is the substitution reaction of potassium with zinc. This is accomplished by combining $\text{KTp}^{\text{Cum,Me}}$, KOH and $\text{Zn(ClO}_4)_2 \cdot 6\text{H}_2\text{O}$ in 25% MeOH/ CH_2Cl_2 and stirring, usually overnight, as prescribed by Ruf and Vahrenkamp.⁶⁴ During the course of the reaction the product is produced with the aid of Le Chatelier's principle. The product, $\text{Zn(OH)Tp}^{\text{Cum,Me}}$ is in equilibrium with $\text{KTp}^{\text{Cum,Me}}$, but precipitation of the KClO_4 by-product pushes the equilibrium to make more $\text{Zn(OH)Tp}^{\text{Cum,Me}}$. Ergo, this solvent mixture is very important to the success of the reaction; too much MeOH will lead to impure $\text{Zn(OH)Tp}^{\text{Cum,Me}}$, but not enough MeOH will not allow the KOH to be solubilized to make the $\text{Zn(OH)Tp}^{\text{Cum,Me}}$. The work-up of this reaction takes advantage of the solubilities of both $\text{Zn(OH)Tp}^{\text{Cum,Me}}$, KOH, and KClO_4 . The reaction is diluted with CH_2Cl_2 to precipitate excess KOH, $\text{Zn(ClO}_4)_2 \cdot 6\text{H}_2\text{O}$, and KClO_4 , then filtered. To the filtrate, is added MeOH which when concentrated under reduced pressure, removing first the CH_2Cl_2 , followed by precipitation of $\text{Zn(OH)Tp}^{\text{Cum,Me}}$, which is removed by filtration. Importantly, the reaction mixture should not be concentrated to dryness because there are $\text{KTp}^{\text{Cum,Me}}$, side products, and/or other impurities in solution.

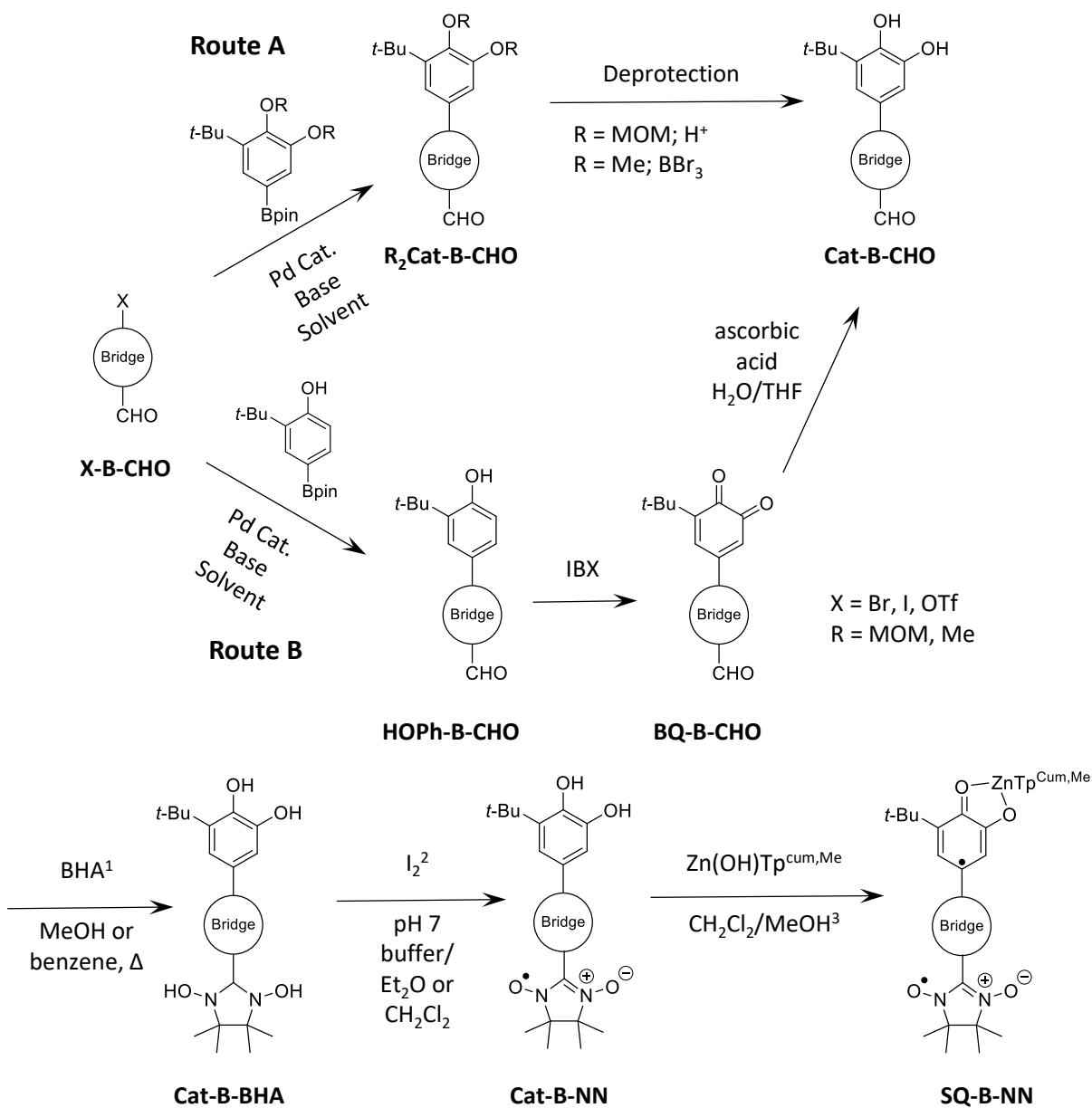
III.3.5. Preparation of Bridge-NN-Elaborated Catechols, and Preparation of Zinc SQ-B-NN Complexes.

Scheme III-6 shows the synthetic procedure that yields the D-B-A biradical complexes. In the simplest form, assuming that the bridge is already in the form of X-B-CHO, where X is any leaving group for a palladium-mediated cross-coupling, is either route A or route B. In route A, X-B-CHO is usually Suzuki-coupled with $\text{MOM}_2\text{CatBpin}$, although this could be $\text{Me}_2\text{CatBpin}$ or any suitably-protected catechol with any main group organometallic amenable to

palladium cross-couplings. Then the catechol is deprotected with catalytic acid, BBr_3 or other reagent for deprotection arriving at Cat-B-CHO .

In route B, X-B-CHO is Suzuki-coupled with HOPhBpin to give the resulting phenol-bridge-aldehyde (HOPh-B-CHO), this is then oxidized using IBX to the quinone and reduced to

Scheme III-6. Traditional assembly of SQ-B-NN biradicals.



¹ $\text{BHA} \cdot \text{H}_2\text{SO}_4 / \text{K}_2\text{CO}_3$ can be substituted for BHA

² NaIO_4 was used for no bridge SQ-NN . This requires a buffer at a slightly lower pH (~6)

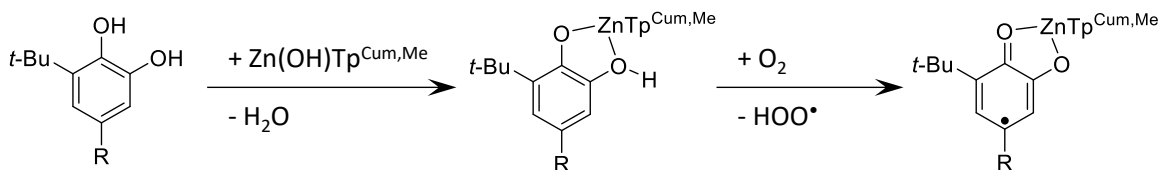
³Bases can accelerate rate of complexation by deprotonating the catechol. K_2CO_3 , KOH

the catechol with ascorbic acid to give the common intermediate to both routes, Cat-B-CHO. While $\text{Na}_2\text{S}_2\text{O}_4$ is quite effective for the reduction of quinones to catechols, it should be avoided in the presence of aldehydes due to formation of the aldehyde-sulfite adduct. All Shultz group biradicals up to this point have gone through the common intermediate, Cat-B-CHO.^{24,30,56,57,66} From here, the aldehyde is condensed with BHA or $\text{BHA}\cdot\text{H}_2\text{SO}_4/\text{base}$ in either MeOH or benzene to give Cat-B-BHA. The penultimate step to biradical complex syntheses is to selectively oxidize the condensed *bis*(hydroxylamine) to NN without oxidizing the catechol to quinone or decomposing the NN to imino nitroxide (IN). This has been accomplished for nearly all biradicals with iodine in either Et_2O or CH_2Cl_2 in the presence of pH = 7 phosphate buffer. The only exception thus far is the original, “no bridge,” **Cat-NN**, the oxidation of which was achieved with NaIO_4 in $\text{Et}_2\text{O}/\text{water}$ over 2 h according to Shultz, Bodnar and Vostrikova et al.⁵⁵ However, using water alone as solvent is not advised because of the pH-sensitive nature of the proton-coupled redox reactions of BHA adducts. Attempts to prepare **Cat-NN** with NaIO_4 in $\text{Et}_2\text{O}/\text{water}$, resulted in conversion of **Cat-BHA** straight to **BQ-NN** in approximately 30 seconds. Further investigations are needed to make NaIO_4 a viable alternative to iodine, but using a ca. pH = 6 buffer allows for selective conversion of **Cat-BHA** to **Cat-NN**. Using a pH = 7 buffer results in no oxidation of either the catechol or the BHA to BQ or NN, respectively. When using iodine, it is best to titrate the **Cat-B-BHA** solution and carefully monitor the reaction via EPR spectroscopy and TLC, as well as by solution color because too much iodine results in decomposition of NN to IN.

The final step in biradical synthesis is to complex the **Cat-B-NN** with $\text{Zn(OH)Tp}^{\text{Cum,Me}}$ and aerial oxidation the complexed catechol to semiquinone as shown in Scheme III-7. The complexations have been conducted in a mixture of CH_2Cl_2 and MeOH because the complexed $\text{Cat-ZnTp}^{\text{Cum,Me}}$ and $\text{SQ-ZnTp}^{\text{Cum,Me}}$ precipitate from MeOH. Base may be used to pre-deprotonate the catechol for complexation, but may cause issues with some bridge-NNs, but it is unclear whether these compounds failed due to the presence of base or other issues with starting materials, complexation or oxidation.

III.4. Characterizing Biradicals and Measuring/Evaluating Exchange Coupling.

Evaluating exchange coupling for SQ-B-NN systems requires several steps in order to make correlations between structure-property relationships meaningful. Several of these techniques were discussed in the context of superexchange and the VBCI model, such as *Scheme III-7*. Complexation of $\text{Zn(OH)Tp}^{\text{Cum,Me}}$ to catechol followed by aerial oxidation to SQ.



electronic absorption spectroscopy and variable-temperature magnetic susceptibility experiments that are performed using a SQUID magnetometer. These experiments as well as the roles of both EPR spectroscopy and X-ray crystallography in the context of characterizing SQ-B-NN complexes is presented in the following sections.

III.4.1. Electron Paramagnetic Resonance (EPR) Spectroscopy.

Chapter I introduced the use of EPR spectroscopy as a characterization and analytical tool for paramagnetic metal ions and organic radicals. In the synthesis of SQ-B-NN biradical complexes it is primarily used for characterization in the final two steps of synthesis when radicals become introduced into the structure and the utility of NMR methods is negligible. EPR spectroscopy allows for quick analysis and reaction-progress monitoring for species that, at times, can be unstable and result in decomposition if allowed to remain too long in their reaction solutions. Figure III-9 summarizes the utility of EPR for evaluating biradical syntheses, and shows a typical spectrum of a Cat-B-NN with a 1:2:3:2:1 5-line nitrogen hyperfine pattern, split by ~ 7.6 Gauss by two equivalent, $I = 1$ ^{14}N nuclei. A successful reaction that produces only NN radicals should exhibit EPR spectra both during and after oxidation of Cat-B-BHA, that is free from any additional EPR-active species. Figure III-9B shows the EPR spectrum of Cat-B-IN that exhibits the hyperfine pattern characteristic of two inequivalent ^{14}N nuclei present in the imino

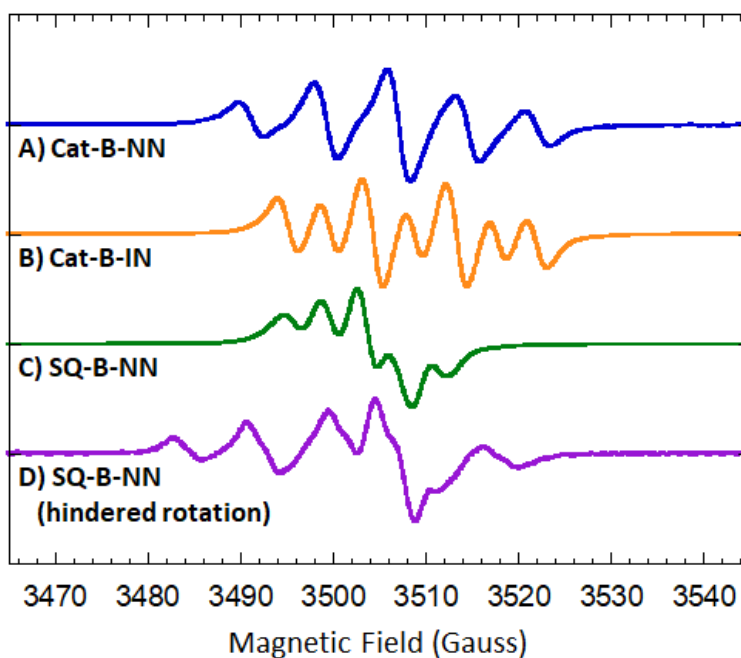


Figure III-9. EPR spectra of **A)** Cat-B-NN, **B)** Cat-B-IN, **C)** SQ-B-NN and **D)** SQ-B-NN with hindered rotation.

Table III-1. Typical and characteristic hyperfine splitting of NN and IN monoradicals alongside a typical SQ-B-NN biradical and an SQ-B-NN biradical with hindered rotation leading to an irregular EPR spectrum.

Entry	Splitting	Additional Splitting
A) Cat-B-NN (<i>p</i> -Cat- <i>m</i> -NN)	7.6 Gauss	
B) Cat-B-IN (<i>p</i> -Cat- <i>m</i> -IN)	9.1 Gauss	4.3 Gauss
C) SQ-B-NN (<i>p</i> -SQ- <i>m</i> -NN)	3.8 Gauss	
D) SQ-B-NN (hindered rotation) (1,3-SQ-Az-NN)	~8.6 Gauss*	~5.4 Gauss*

* These splittings are more variable depending on the specific SQ-B-NN and this has also been observed in biradicals of *m*-phenylenes and 1,7-naphthalenes.

nitroxide: overlapping triplet of triplets with $a_{N1} = 9.1$ and $a_{N2} = 4.3$ Gauss. Formation of IN is observed either when an excess of iodine is used to oxidize Cat-B-BHA, or when Cat-B-BHA undergoes dehydration to yield the imino nitroxide precursor. This dehydration can result from either excessive heat during cyclization or prolonged storage. Confirming the structure of Cat-B-BHA by *e.g.*, $^1\text{H-NMR}$ prior to oxidation (if it had been stored for some time), oxidizing the Cat-B-BHA shortly after isolation, and/or checking the EPR spectrum during oxidation are the most effective ways to prevent the accidental and undesired synthesis of Cat-B-IN. Occasionally, weak EPR signals of this species can be observed in a sample that is predominantly Cat-B-NN but usually is not a problem as it can be removed by precipitation and/or crystallization. Figure III-9C shows the EPR spectrum of SQ-B-NN biradical complex. This spectrum still exhibits the 5-line pattern for the two equivalent nitrogen nuclei, but due to the presence of exchange coupling between NN and the covalently-attached SQ the hyperfine coupling appears in the spectrum as $a_N/2$ ($7.6/2 \sim 3.8$ Gauss)⁶⁷ as shown in Table III-1. It should be noted that due to different relaxation times of mono- and biradicals, if there is a mixture of the two in the EPR sample, the monoradical's concentration will be exaggerated in comparison to that of the

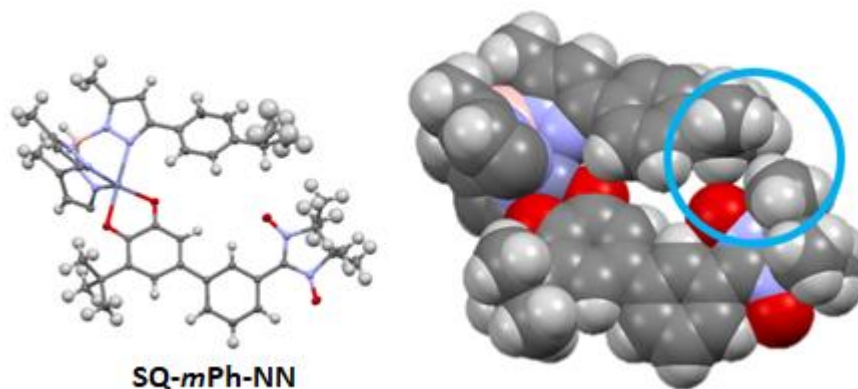


Figure III-10. Thermal ellipsoid and space-filling models of **SQ-*mPh*-NN** illustrating the steric interaction between (Tp^{Cum,Me})⁻ isopropyl groups and the NN.

biradical and a spectrum of the pure biradical complex may not be obtainable until after precipitation or crystallization. Figure III-9D shows an isotropic room temperature spectrum of a biradical when the NN and SQ sterically interact. In such cases, hindered bond rotations result in a second-order spectrum.⁶⁸ At first glance, it appears as though the SQ-B-NN has been incompletely oxidized or decomposition is occurring, but any biradical displaying a spectrum like this should be further investigated with TLC and variable-temperature EPR experiments.⁵⁷ Figure III-10 shows the crystal structure in thermal ellipsoids and space-filling models of **SQ-*mPh*-NN** where this was first observed. As seen in the space-filling model, the NN's methyl groups and one oxygen “touch” the isopropyl groups of the ancillary [Tp^{Cum,Me}]⁻ ligand. If the EPR sample is warmed above room temperature, the characteristic 5-line pattern of an SQ-B-NN biradical grows in at the expense of the more complicated, second-order spectrum.⁶⁸ In addition, the sample can be frozen and the triplet powder spectrum observed. In such spectra, fine structure appears according to the zero-field splitting parameters (D and E), and a $\Delta m_s = 2$, half-field transition, may be observed to confirm the successful synthesis of the SQ-B-NN.⁵⁷

III.4.2. Electronic Absorption Spectroscopy.

As mentioned in Chapter III.3, electronic absorption spectroscopy is necessary in order to solve for H_{DA}^2 by obtaining K_0 and U and implementing Eq. III-5. The most important characterization data that electronic absorption spectroscopy provides is the $SQ_{SOMO} \rightarrow B-NN_{LUMO}$ transition which is bridge dependent, but often appears near 24000 cm^{-1} .²⁴ As shown in Fig. III-11 the original SQ-NN spectrum alongside its constituent Ph-NN and 3,5-di-*tert*-

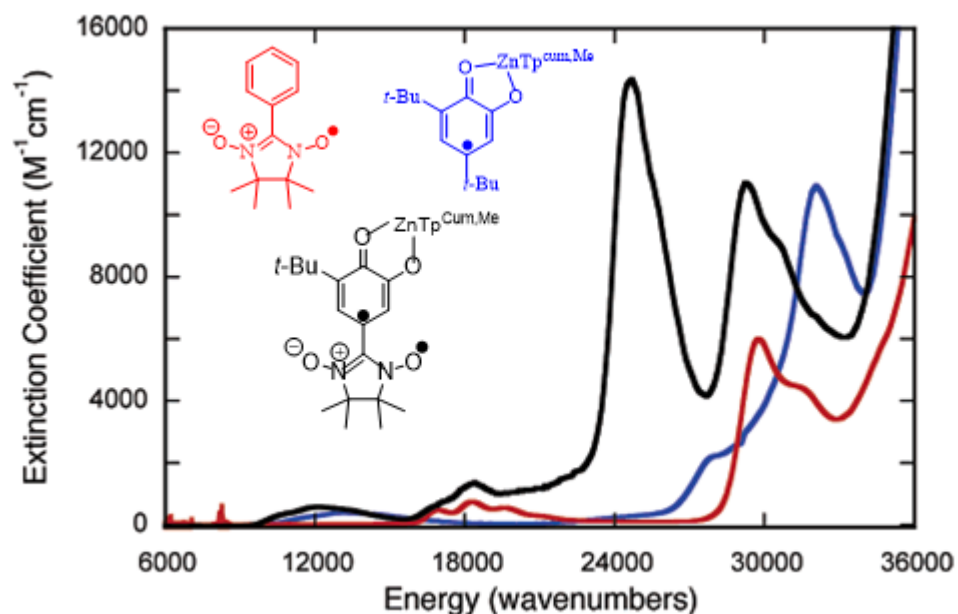


Figure III-11. Electronic absorption spectra of SQ-NN, Ph-NN and $SQZnTp^{Cum,Me}$. The band around 24000 cm^{-1} in SQ-NN appears in neither Ph-NN nor in $Tp^{Cum,Me}ZnSQ$ spectra and is the $SQ_{SOMO} \rightarrow (Bridge)NN_{LUMO}$.

butylsemiquinone ($Tp^{Cum,Me}ZnSQ$) absorption spectra. The SQ-NN complex has similar bands to the constituent chromophores, but an “extra” transition at 24000 cm^{-1} which is absent in the SQ PhNN spectra. So for any *conjugated* SQ-B-NN, this band is a vital piece of spectroscopic data to confirm the presence of the biradical complex.

III.4.3. Superconducting Quantum Interference Device- (SQUID) Detected Magnetometry.

As mentioned previously, the energy gap between the singlet and triplet states (ΔE_{ST}) is equivalent to $2J$ as defined by the Heisenberg-Dirac-Van Vleck Hamiltonian in Chapter I. The triplet state has a net magnetic moment whereas the singlet state does not. Therefore, when $2J > 0$ and the triplet state is lower in energy than the singlet state, the magnetization of the sample ($M = \chi_{para} \cdot H$, where χ_{para} is the paramagnetic susceptibility, M is the magnetization and H is the applied magnetic field), will increase as the sample temperature decreases because the triplet state population increases according to the Boltzmann distribution. Conversely, if $2J < 0$ and the singlet state is lower in energy than the triplet state, then the magnetization of the sample will decrease as the sample temperature decreases because the singlet state population increases according to the Boltzmann distribution. The paramagnetic susceptibility, χ_{para} , can be modelled using Eq. III-6.⁶⁹

$$\chi_{para} = \frac{g^2 0.125 \text{ emuK/mol}}{T} \left(\frac{6}{e^{\frac{-2JDA}{k_B T}} + 3} \right) \quad \text{Eq. III-6}$$

Figure III-12A has $\chi_{para} T$ plotted for various values of J . These plots illustrate that it is relatively easy to differentiate between ferromagnetically- and antiferromagnetically coupled radicals because even when J is small ($|J| < 5 \text{ cm}^{-1}$), the sign of J can still be determined at lower temperatures where $J > 0$, $\chi_{para} T$ increases toward $1 \text{ emu} \cdot \text{K} \cdot \text{mol}^{-1}$ and for $J < 0$, $\chi_{para} T$ decreases toward $0 \text{ emu} \cdot \text{K} \cdot \text{mol}^{-1}$. However, it becomes more difficult to differentiate between small changes in magnitude for two values of J of the same sign. From these theoretical plots, absolute values of J that are less than 10 cm^{-1} have very similar data and this can become convoluted when other corrections are required to fit experimental data. Also, as can be seen for both ferromagnetically- and antiferromagnetically coupled biradicals $\chi_{para} T$ tends toward 0.75

emu•K•mol⁻¹ at high temperatures as $k_B T \gg 2J$, the populations of the singlet and triplet states become nearly equivalent. Mathematically solving for Eq. III-6 at high temperature gives:

$$\lim_{T \rightarrow \infty} \chi_{para} = \lim_{T \rightarrow \infty} \frac{g^2 0.125 \text{ emu} \cdot \text{K/mol}}{T} \left(\frac{6}{e^{\frac{-2JDA}{k_B T}} + 3} \right) = (2)^2 0.125 \left(\frac{6}{1+3} \right) = 0.75 \text{ emu} \cdot \text{K/mol}$$

Eq.III-7

Figure III-12B shows plots of χ_{para} vs. temperature. The important features to note are that for ferromagnetically coupled biradicals ($J > 0$), χ_{para} asymptotically increases as the temperature approaches 0 K, but for antiferromagnetically coupled biradicals ($J < 0$), χ_{para} increases and reaches a maximum at a specific temperature and then decreases sharply at lower temperatures. A simple relation (Eq. III-7)⁶⁹ exists between this temperature of the maximum χ_{para} value and J that can be used to help confirm the fit of the $\chi_{para} T$ vs. T data for an antiferromagnetically coupled biradical:

$$|J| = k T_{max} = 1.599; \text{ where } k = 0.695 \text{ cm}^{-1} \text{K}^{-1} \quad \text{Eq. III-8}$$

Figure III-12C and D show plots of $\chi_{para} T$ vs. T and χ_{para} vs. T , respectively for the same antiferromagnetically coupled biradical. Figure III-11C is fit with using Eq. III-6 to give $J = -15 \text{ cm}^{-1}$ and Fig. III-12D determines $T_{max} = 25.8 \text{ K}$ and solves with Eq. III-7 to give $J = -14 \text{ cm}^{-1}$, which are in good agreement. Typically, fits of $\chi_{para} T$ vs. T have errors of $\pm 1-2 \text{ cm}^{-1}$ because of data manipulation, the error that comes from weighing 1-10 mg samples for which $|\chi_{dia}|$ (the

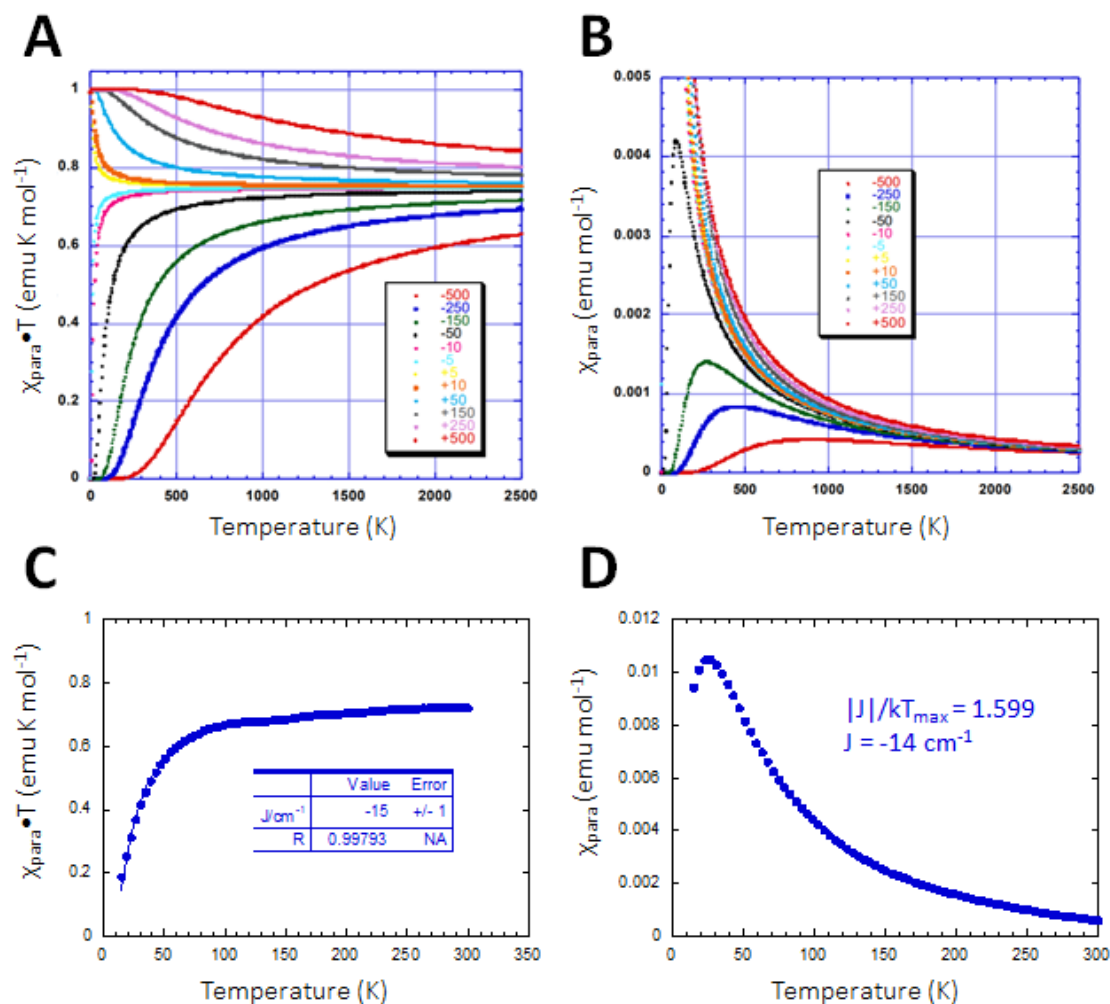


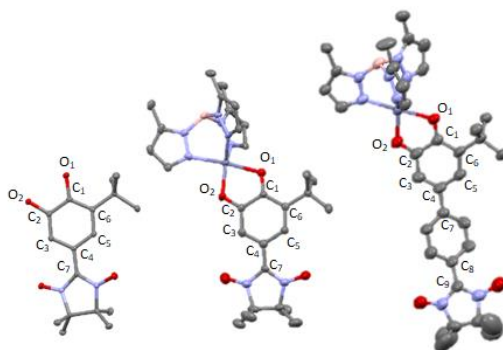
Figure III-12. A) Theoretical plots of $\chi_{\text{para}}T$ vs. T with different J values, B) theoretical plots of $\chi_{\text{para}}T$ vs. T with different J values, C) experimental plot of $\chi_{\text{para}}T$ vs. T for a biradical with the best data fit giving a $J = -15 \text{ cm}^{-1}$ and D) experimental plot of χ_{para} vs. T for the same biradical giving $J = -14 \text{ cm}^{-1}$ by calculation from the temperature at which the χ_{para} is greatest.

absolute value of the diamagnetic susceptibility correction) $\gg |\chi_{\text{para}}|$, particularly at higher temperatures: in comparison to paramagnetic metal ions, SQ-B-NN biradical complexes have a very small magnetic moments per molar mass.

III.4.4. X-ray Crystallography.

X-ray crystallography and obtaining crystal structures from SQ-B-NN biradical complexes are the crux of Shultz group research of structure-property relationships in donor-bridge-acceptor systems. From a crystal structure, detailed geometric data, such as bond lengths, torsion angles and inter-radical distances can be gathered and correlated with J values determined from fits of variable-temperature magnetic susceptibility data. For characterization purposes, crystal structures provide bond lengths to ensure the semiquinone oxidation state as opposed to, e.g., a protonated catechol. Table III-2 shows the bond lengths of Cat-NN versus SQ-NN and SQ-*p*-Ph-NN. As can be seen from the table the most diagnostic bond lengths are the carbon-oxygen bond lengths which should be 1.26-1.27 and 1.30 Å for a semiquinone. The bond

Table III-2. Selected bond lengths for Cat-NN, SQ-NN and SQ.



Bonds	Cat-NN bond lengths (Å)	SQ-NN bond lengths (Å)	SQ- <i>p</i> Ph-NN bond lengths (Å)
C ₁ -O ₁	1.37	1.27	1.26
C ₂ -O ₂	1.37	1.29	1.31
C ₁ -C ₂	1.41	1.48	1.47
C ₂ -C ₃	1.38	1.41	1.40
C ₃ -C ₄	1.41	1.39	1.38
C ₄ -C ₅	1.40	1.45	1.42
C ₅ -C ₆	1.39	1.35	1.36
C ₁ -C ₆	1.40	1.45	1.42
C ₄ -C ₇	1.46	1.44	1.47
C ₈ -C ₉			1.46

lengths around the semiquinone rings change as well; C₁-C₂, C₂-C₃, C₄-C₅ and C₁-C₆ all increase relative to the catecholate while C₃-C₄ and C₅-C₆ decrease.⁷⁰

III.5. Previous Studies of SQ-B-NN Complexes.

Of the biradical complexes that have been prepared following the SQ-B-NN motif, several series of compounds have been highlighted to describe the role of the bridge in electronic coupling, validate the mechanism of coupling, and illustrate properties relevant to fields of molecular electronics, spintronics, and photovoltaics.

III.5.1. Distance Dependence of Coupling: Support for the Superexchange Model.

The hallmark of superexchange coupling is its exponential dependence on distance between donor and acceptor, and our SQ-B-NN complexes were used to illustrate such a relationship.²⁹ Figure III-13 shows SQ-NN complexes with (*para*-phenylene)_n and 2,5-thiophene)_n bridges (*n* = 0-2). Phenylene and thiophene bridges are of continuing interest as components of molecular electronic, photovoltaic, and spintronic devices.^{7,14,71-78} The exponential decrease in both the electronic (*H*) and exchange (*J*) couplings is in accord with a superexchange model. The SQ-NN complex has a triplet ground state with *J* = +550 cm⁻¹, whereas the complexes with one (SQ-Ph-NN) and two (SQ-Ph₂-NN) phenyl rings between the SQ and NN, the exchange coupling decreases to +100 and +20 cm⁻¹, respectively. For (thiophene)_n bridges one (SQ-Th-NN) and two (SQ-Th₂-NN) rings give exchange couplings of +220 and +108 cm⁻¹, respectively. From these results we see that coupling by (2,5-thiophene)_n bridges are less attenuated by distance than are the couplings by (*para*-phenylene)_n. In fact, exchange coupling through two thiophene rings (+108 cm⁻¹) is comparable to that provided by one phenyl ring (100 cm⁻¹). Figures III-13A and B show plots of each biradical's exchange

coupling constant over the no bridge exchange coupling constant (J/J_{SQNN}) or the corresponding electronic coupling matrix element ($H_{DA}/H_{DA,SQNN}$) as a function of the distance between the radicals as determined from crystal structures for phenylene (Fig. III-13A) and thiophene (Fig. III-13B). These data points can be fit with an exponential decay function, where the coefficient in the exponent is known as the decay constant (β) which describes the distance dependence of both the magnetic exchange coupling constant and electronic matrix element.^{79,80} The value for β for the phenylene series, $\beta = 0.39$ is close to what has been experimentally determined by *para*-

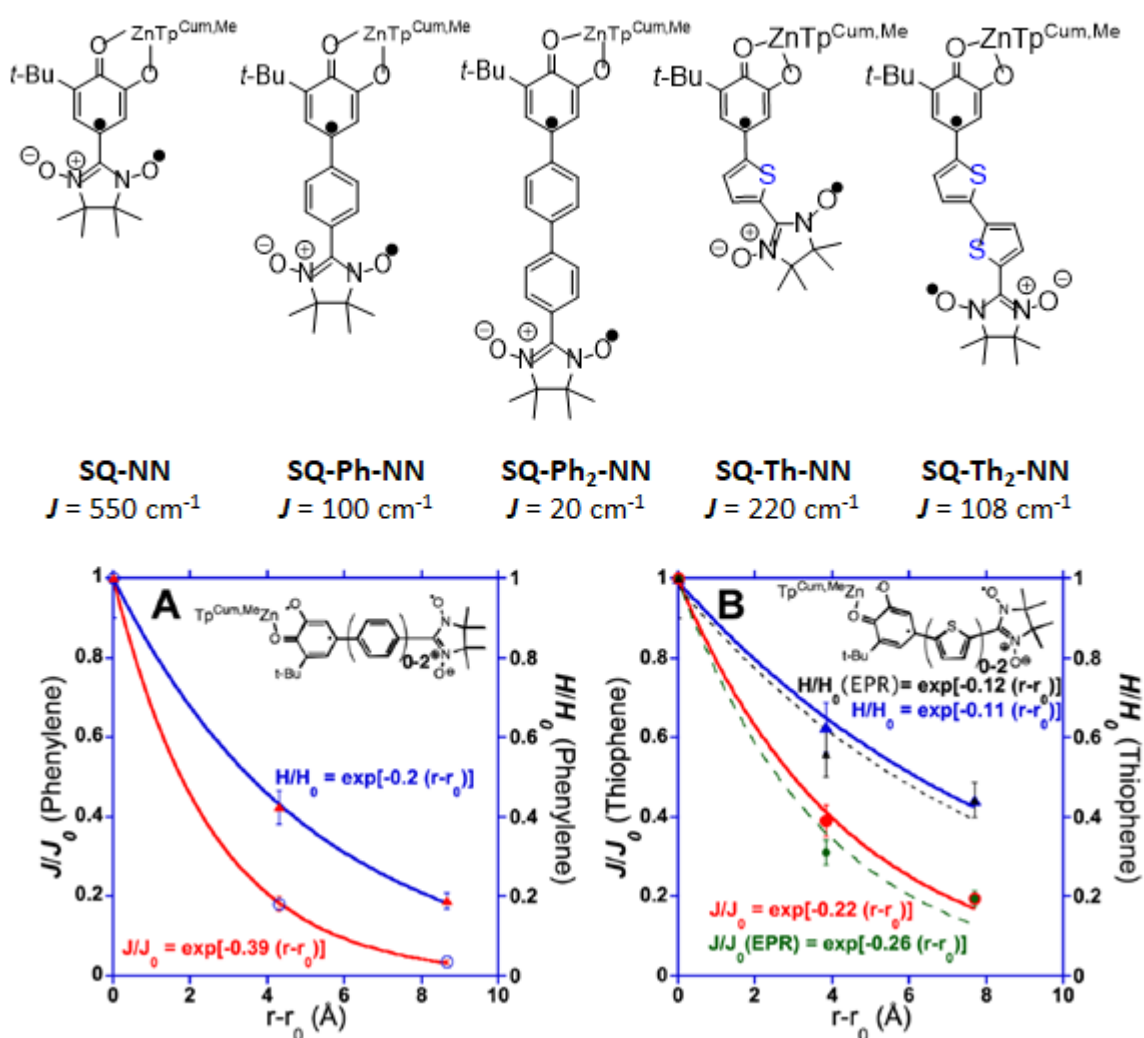


Figure III-13. SQ-B-NN biradicals with no bridge and bridged by one phenyl ring, two phenyl rings, one thiophene ring and two thiophene rings. A) exponential decay functions of the no bridge, one phenyl ring and two phenyl rings series for J and H_{DA} and B) exponential decay functions of the no bridge, one thiophene ring and two thiophene rings series for J and H_{DA} .

phenylenes bridged between two metal electrodes ($\beta = 0.41$),⁷⁹ by electron transfer from a zinc (II) porphyrin system ($\beta = 0.4$)⁸⁰ and for donor-phenylene-acceptor systems determined by charge separation rates ($\beta = 0.46$).⁸¹

This work⁶⁶ provided β values for *oligo*(1,4-phenylene) and for *oligo*(2,5-thiophene) which are benchmark variables when discussing transport in molecular wires in molecular electronics,^{7,14,71,73-78} illustrated that the energy gap between the electronic coupling matrix element of the donor-bridge (H_{DB}) and bridge-acceptor (H_{BA}) is vitally important for a given donor-bridge-acceptor system, rather than the bridge-bridge element (H_{BB}), and validated the use of a superexchange model to describe the coupling between SQ and NN through a bridge. Additionally, any future biradicals with phenylene or thiophene-like bridges can be discussed within this context, allowing us to make broad comparisons across classes of molecules to the specific nature of electronic coupling through the bridge.

III.5.2. Conjugated vs. Cross-conjugated Bridges: Implications for “Quantum Interference” Effects.

Another set of SQ-B-NN complexes is shown in Fig. III-14, and are SQ-1,4-phenylene-NN (**SQ-*p*Ph-NN**) and SQ-1,3-phenylene-NN (**SQ-*m*Ph-NN**). Donors and acceptors on a phenyl ring that are either *ortho* or *para* to each other are conjugated and by definition electrons can be resonance delocalized from the donor to the acceptor. However, donors and acceptors on a phenyl ring that are *meta* to each other will be cross-conjugated and resonance delocalization is impossible. Physicists view cross-conjugation as destructive interference of different

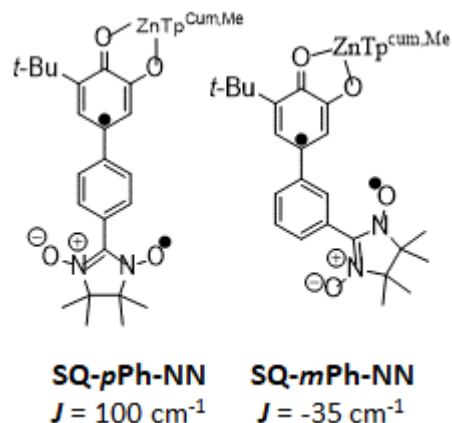


Figure III-14. SQ-*p*Ph-NN and SQ-*m*Ph-NN.

delocalization pathways, and the term “quantum interference” was coined.^{82–86} In molecular electronics, conjugative pathways lead to conductance (defined as 1/resistance), while quantum interference pathways lead to far weaker conductance and as discussed in Chapter II, conjugated systems are of great interest for designing charge carrying molecules and polymers whereas cross-conjugated systems break this feature; nevertheless both constructs are of interest in molecular electronics.^{7,11,81,87–90} As can be seen in Fig. III-14 and as mentioned previously, **SQ-*p*Ph-NN** exhibits an exchange coupling constant, $J = +100 \text{ cm}^{-1}$. On the other hand, **SQ-*m*Ph-NN** displays an exchange coupling constant of $J = -35 \text{ cm}^{-1}$. A conjugated SQ-B-NN triad results in ferromagnetically coupled radicals (positive J), while for a cross-conjugated SQ-B-NN triad, antiferromagnetically (negative J) is observed. So the SQ-B-NN motif gives two key pieces of information when evaluating a bridge: (1) the *magnitude* of the exchange coupling constant which indicates how strongly the radicals are coupled, and (2) the *sign* of the exchange coupling constant reveals how the spins are coupled, either parallel or antiparallel giving rise to a triplet or singlet ground state, respectively. Thus, it is noteworthy that magnitude of the coupling constant is lower **SQ-*m*Ph-NN** compared to that of **SQ-*p*Ph-NN**. This is consistent with studies of photo-

induced charge separated studies where the rate of charge separation in conjugated DBA systems is ~30 times faster than in cross-conjugated systems.^{26,91}

As was gleaned from our distance dependence work,²⁹ the key parameter to electronic coupling was H_{DA} in a long distance superexchange pathway, so to understand observed coupling in a cross-conjugated system, we must understand the electronic origin of the antiferromagnetic J within the framework of our superexchange (VBCI) model. According to electron transfer theory, the rate constant varies with H_{DA}^2 , so $H_{DA}(\text{cross-conjugated}) \approx H_{DA}(\text{conjugated})/(30)^{1/2}$.⁵⁷ Therefore, cross-conjugated bridges should have weaker exchange coupling constants compared to their isomeric conjugated analogs. Understanding of the mechanism by which the exchange coupling is antiferromagnetic in cross-conjugated systems requires spectroscopy and DFT calculations, and a complete discussion is beyond the scope of this section. However, a brief explanation into the relevant spectroscopic results and conclusions from the DFT calculations are as follows. Figure III-15A shows the electronic absorption spectra for **SQ-*p*Ph-NN**, **SQ-*m*Ph-NN**, and **SQNN**. As mentioned previously, conjugated SQ-B-NNs exhibit the $\text{SQ}_{\text{SOMO}} \rightarrow \text{B-NN}_{\text{LUMO}}$ charge transfer bands. For SQ-NN this band is about 25000 cm^{-1} and for **SQ-*p*Ph-NN** this band is at 23500 cm^{-1} ; however, this transition is absent in **SQ-*m*Ph-NN**. Given that the excited state involved in this transition provides the pathway that results in ferromagnetically coupled spins, its absence in the **SQ-*m*Ph-NN** spectrum suggests this ferromagnetic contribution is absent, opening the door to alternative mechanisms that result in antiferromagnetic J in cross-conjugated systems. Complex **SQ-*m*Ph-NN** instead has a stronger band at 28000 cm^{-1} than **SQ-NN** or **SQ-*p*Ph-NN**, which is attributed to the $\text{Ph-NN}_{\text{HOMO}} \rightarrow \text{Ph-NN}_{\text{LUMO}}$. DFT calculations

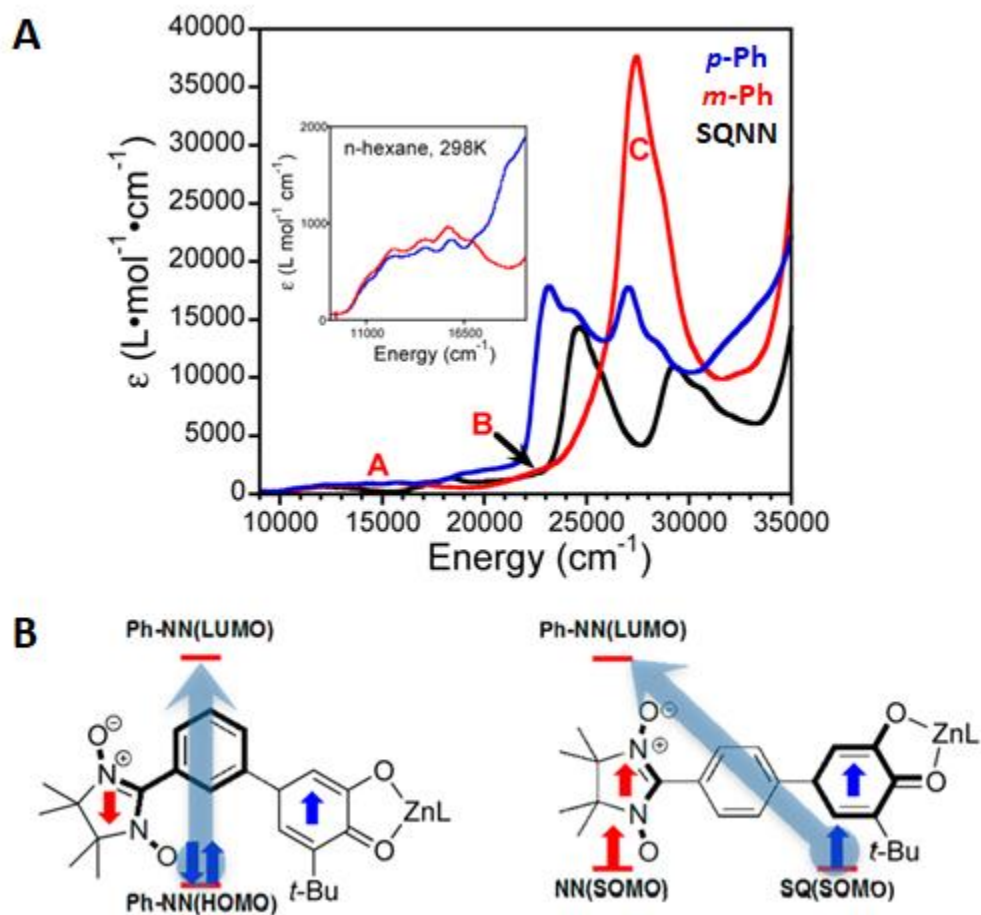


Figure III-15. A) Electronic absorption spectra of SQ-NN, SQ-*m*Ph-NN and SQ-*p*Ph-NN. B) Summary of the dominant FMO interactions that dictate the observed sign of exchange coupling.

revealed that the dominant pathway for the radicals to interact with each other in a cross-conjugated system was through the excited state involved in this transition. Figure III-15B visually summarizes the dominant superexchange mechanism in both conjugated and cross-conjugated SQ-B-NNs. For conjugated SQ-B-NNs, the $SQ_{SOMO} \rightarrow Ph-NN_{LUMO}$ is the dominant superexchange pathway while for cross-conjugated systems the $Ph-NN_{HOMO} \rightarrow Ph-NN_{LUMO}$ is the dominant superexchange pathway.²⁸

III.5.3. Torsional Dependence of Electronic and Exchange Coupling in SQ-B-NN Complexes.

Complexes.

A final series of **SQ-B-NNs** that have been synthesized are shown in Fig. III-16A and were designed to detail the modulation of coupling by torsion angles between the SQ donor and bridge (θ_{DB}) and between the bridge and NN acceptor (θ_{BA}). The overlap of adjacent *p*-orbitals varies as a cosine function⁵⁶ and Fig. III-16B shows the interactions of two *p*-orbitals connected by a sigma bond, at the extrema: 0° torsion angle and a 90° torsion angle.

Complexes were prepared with different numbers and positions of methyl groups to cause rotation of one or both of the SQ and NN groups. Complexes **SQ-MePh-NN** and **SQ-PhMe-NN** only have one methyl each either on the SQ or NN side of the phenyl ring, respectively, and as a

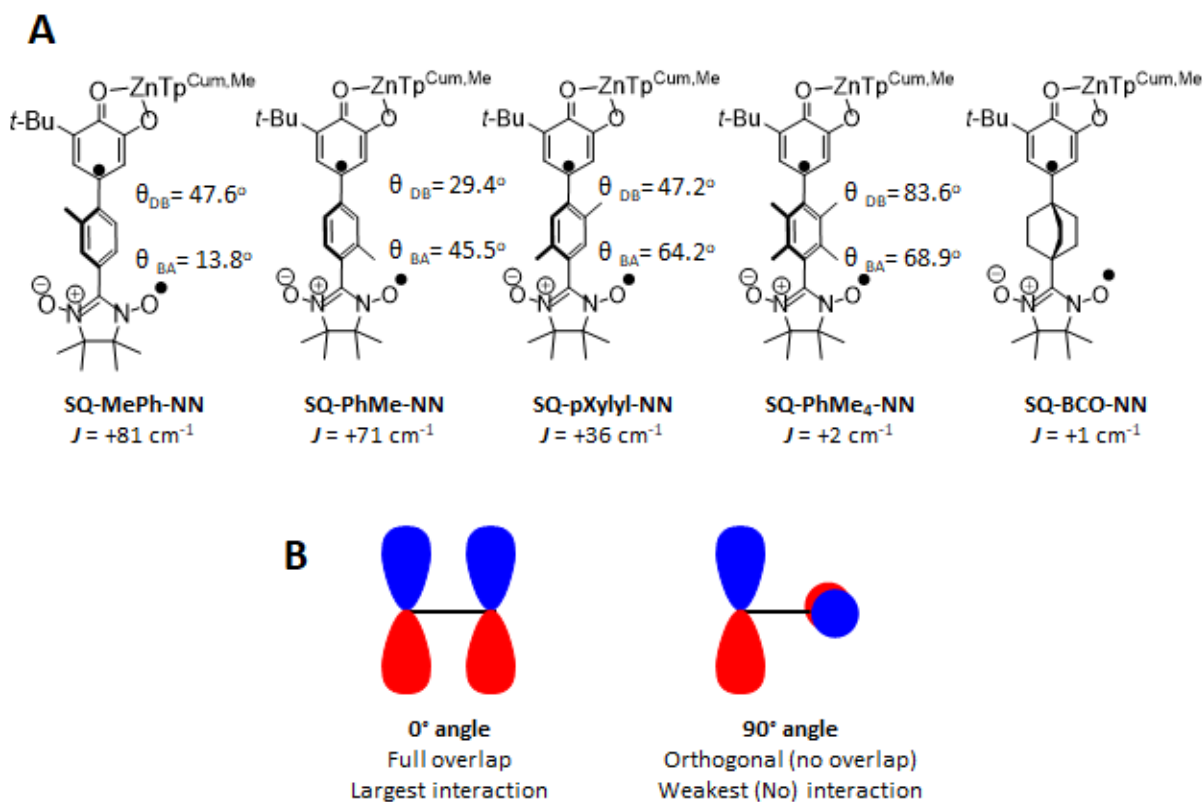


Figure III-16. A) The series of SQ-B-NN used to evaluate the torsional dependence of exchange coupling as well as the σ -only **SQ-BCO-NN** and B) the consequences of torsion angles between two *p*-orbitals.

result the magnetic exchange coupling was determined to be +81 and +71 cm^{-1} , respectively. **SQ-PhMe-NN** is less than **SQ-MePh-NN** because the torsion angle on the side of the molecule that does not have the methyl are not the same, **SQ-MePh-NN** is 13.8° on the side of the NN and **SQ-PhMe-NN** is 29.4° on the side of the SQ, so the decreased planarity and conjugation of **SQ-PhMe-NN** results in a lower coupling constant. When there is a methyl on each side of the phenyl ring to twist both the SQ (47.2°) and NN (64.2°) out as in **SQ-pXylyl-NN**, the coupling constant decreases further to 36 cm^{-1} , and when tetramethylbenzene is used as the bridge in **SQ-PhMe₄-NN**, the torsion angles further increase to 83.6° and 68.9° for the SQ and NN, respectively, and the exchange coupling constant is driven to only 2 cm^{-1} . Now, the donor and acceptor are not completely 90° and so they are not fully decoupled from each other, there is still some contribution to the coupling from the π -system.

Figure III-17 shows a 3D plot of the exchange coupling constant, J as a function of $\cos^2 \phi_{\text{SQ}}$; the torsion angle between the donor and bridge, and $\cos^2 \phi_{\text{NN}}$; the torsion angle between the acceptor and bridge. The surface of the plot was calculated by with CASSCF calculations, but the data points showing each of the SQ-B-NNs are the experimentally determined J values from fitting variable temperature magnetic susceptibility data.⁵⁶ As can be seen from the plot the data points agree well with the calculated surface with a correlation described by $R^2 = 0.899$. Given the strong correlation between the calculated surface and the experimental data, this work allows the torsion angles of any other SQ-bridge-NN biradicals to be corrected for to determine the exchange coupling if the molecule were completely planar. The caveat is that the greater the torsion angle the less accurate the correction to planarity becomes.

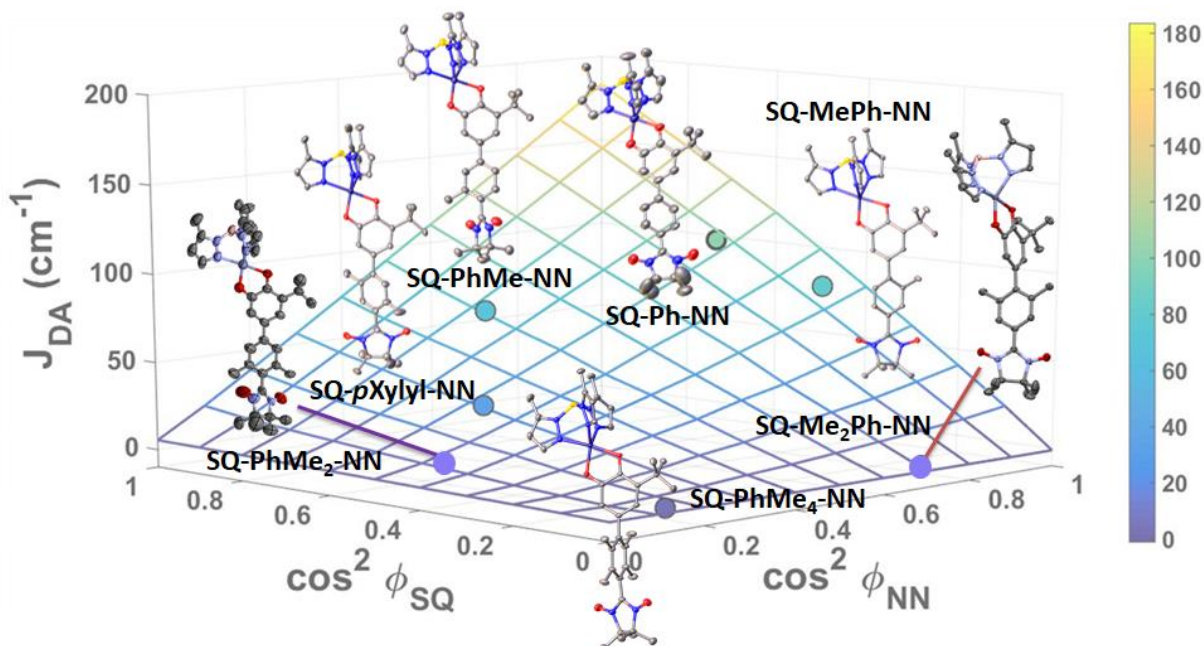


Figure III-17. Experimental change coupling values vs. the cosine-squared of torsion angles for SQ-Ph and Ph-NN. Square-blocked grid correlates experimental $J_{SQ-B-NN}$ values with experimental SQ-Ph and Ph-NN torsion angles: $J_{SQ-B-NN} = 0.34 + 3.77 \cdot \cos^2(\phi_{SQ-Ph}) - 13.4 \cdot \cos^2(\phi_{Ph-NN}) + 179 \cdot \cos^2(\phi_{SQ-Ph}) \cdot \cos^2(\phi_{Ph-NN}) + 16.3 \cdot \cos^4(\phi_{Ph-NN})$.

To fully understand the coupling through a bridge when the π system is completely decoupled from the donor and acceptor was to make a bridge that did not have a π system as in **BCO** where the bridge is bicyclo[2.2.2]octane. The only way the donor and acceptor radicals can interact through this molecule is through the σ system. Bicyclo[2.2.2]octane is the best bridge for this purpose because contributions of the constituent SOMOs into the σ system of bicyclooctane will always be the same, no matter how the bridging unit rotates with respect to donor and acceptor orbitals. This is due to the σ bonds being 120° apart from each other and the contribution of the SOMOs to each σ pathway being a linear combination of the \cos^2 and \sin^2 dependence of the SOMO p orbital with each σ orbital and $\cos^2\phi + \sin^2\phi = 1$. The exchange coupling through this σ -only bridge is not zero, it is $+1 \text{ cm}^{-1}$, and the σ system provides a mechanism for the radicals to couple. The mechanism of spin polarization through the σ system is shown alongside the spin polarization through the π system in Fig. III-18. The description of spin polarization through the π system was described in Chapter I, where the requirement for two

p orbitals to have a π -bonding interaction is that they have the same symmetry and for their electrons to be of opposite spins and this can be seen in Fig. III-18 as the spin polarization works its way around to each donor- and acceptor-bridged orbital. The spin polarization through the σ -only system is expressed via the same requirement in order to have a σ -bonding interaction is to have the two σ orbitals to have the same symmetry and have opposite spins. The interaction between two electrons each in a p-orbitals that are orthogonal with each other on a single atom is also discussed in Chapter I and comes from Hund's rule. Due to the stabilizing energy from the exchange integral (k) when two electrons have aligned spins, each set of orthogonal p-orbitals in the σ -system on each atom will have the same electron spins which will be opposite spin from

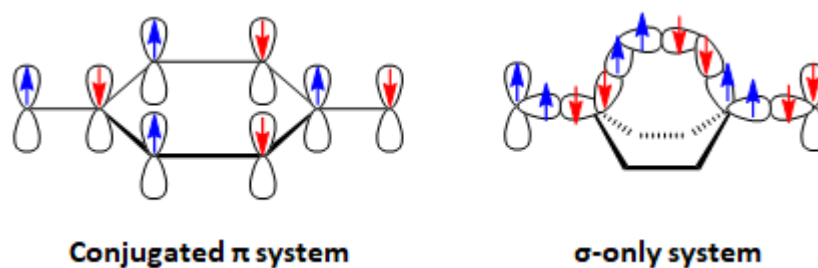


Figure III-18. Spin polarization through a conjugated π -system and through a σ -only system.

the orbitals on the neighboring atoms that they are forming a σ bond with. As a result, the spin polarization works its way around to each donor- and acceptor-bridged orbital the same as the π system does. As can be determined from this analogy and experimentally determined exchange coupling constants, a conjugated π system and this σ -only, bicyclooctane system will both give rise to ferromagnetic coupling when a SQ and NN are bridged by one of these systems. This result also allowed for the determination that the contribution to electronic through the π system is approximately 13 times that of the σ -system.⁵⁶

III.5.4. Summary

To conclude the introduction into donor-bridge-acceptor biradicals, several significant studies for future biradicals utilizing the SQ-B-NN motif were summarized which included relevant concepts that will be utilized and referenced in the subsequent chapters. The distance dependence studies validated the use of a superexchange model to describe the electronic coupling between a donor and acceptor radical through a diamagnetic bridging unit by demonstrating that the exchange coupling between the two organic radicals follows an exponential decay law with distance between the radicals and the decay constant (β) for *oligo*(phenylenes) matches closely with the decay constant for other *oligo*(phenylenes) determined by break-junction conductance and photo-induced charge transfer studies.⁶⁶ The exponential decay of the exchange coupling with distance also provided a means for evaluating other phenylene and thiophene systems for distance between the radicals in order to deconvolute the underlying mechanism for the electronic contributions to coupling between two radicals. The study of the coupling and mechanistic differences between the conjugated bridge, *para*-phenylene (SQ-*m*Ph-NN) and the cross-conjugated bridge, *meta*-phenylene (SQ-*m*Ph-NN) allows for greater evaluation of diamagnetic bridges.⁵⁷ From the magnetic exchange coupling constant (J) two pieces of information are determined by both the magnitude and sign of J . Magnitude is apparent in that the greater the coupling the stronger the interaction. A $J > 0$ by definition means that the ground state of the biradical is a triplet for a ferromagnetically coupled biradical and a $J < 0$ means that the biradical has a singlet ground state and the radicals are antiferromagnetically coupled. Finally, the study of torsional dependence now allows for the correction of J values by adjusting it by a product of $\cos^2\phi$ of the torsion angles and allowed for

the determination that the electronic coupling through the π -system is 13 times greater than the σ -system.⁵⁶

III.6. References.

- (1) Carmeli, I.; Kumar, K. S.; Heifler, O.; Carmeli, C.; Naaman, R. Spin Selectivity in Electron Transfer in Photosystem I. *Angew. Chemie Int. Ed.* **2014**, *53* (34), 8953–8958. <https://doi.org/10.1002/anie.201404382>.
- (2) Hartings, M. R.; Kurnikov, I. V.; Dunn, A. R.; Winkler, J. R.; Gray, H. B.; Ratner, M. A. Electron Tunneling through Sensitizer Wires Bound to Proteins. *Coord. Chem. Rev.* **2010**, *254* (3–4), 248–253. <https://doi.org/10.1016/j.ccr.2009.08.008>.
- (3) Ashwell, G. J.; Urasinska, B.; Tyrrell, W. D. Molecules That Mimic Schottky Diodes. *Phys. Chem. Chem. Phys.* **2006**, *8* (28). <https://doi.org/10.1039/b604092f>.
- (4) Heitzer, H. M.; Marks, T. J.; Ratner, M. A. Molecular Donor–Bridge–Acceptor Strategies for High-Capacitance Organic Dielectric Materials. *J. Am. Chem. Soc.* **2015**, *137* (22), 7189–7196. <https://doi.org/10.1021/jacs.5b03301>.
- (5) Freudenberg, J.; Jansch, D.; Hinkel, F.; Bunz, U. H. F. Immobilization Strategies for Organic Semiconducting Conjugated Polymers. *Chem. Rev.* **2018**, *118* (11), 5598–5689. <https://doi.org/10.1021/acs.chemrev.8b00063>.
- (6) Nishide, H.; Iwasa, S.; Pu, Y. J.; Suga, T.; Nakahara, K.; Satoh, M. Organic Radical Battery: Nitroxide Polymers as a Cathode-Active Material. *Electrochim. Acta* **2004**, *50* (2-3 SPEC. ISS.), 827–831. <https://doi.org/10.1016/j.electacta.2004.02.052>.
- (7) Schubert, C.; Margraf, J. T.; Clark, T.; Guldi, D. M. Molecular Wires-Impact of π -Conjugation and Implementation of Molecular Bottlenecks. *Chemical Society Reviews*. The Royal Society of Chemistry February 10, 2015, pp 988–998. <https://doi.org/10.1039/c4cs00262h>.

- (8) Oberhumer, P. M.; Huang, Y. S.; Massip, S.; James, D. T.; Tu, G.; Albert-Seifried, S.; Beljonne, D.; Cornil, J.; Kim, J. S.; Huck, W. T. S.; Greenham, N. C.; Hodgkiss, J. M.; Friend, R. H. Tuning the Electronic Coupling in a Low-Bandgap Donor-Acceptor Copolymer via the Placement of Side-Chains. *J. Chem. Phys.* **2011**, *134* (2004), 0–7. <https://doi.org/10.1063/1.3562936>.
- (9) Beverina, L.; Pagani, G. A. Pi-Conjugated Zwitterions as Paradigm of Donor-Acceptor Building Blocks in Organic-Based Materials. *Acc. Chem. Res.* **2014**, *47* (2), 319–329. <https://doi.org/10.1021/ar4000967>.
- (10) Prieto-Ruiz, J. P.; Miralles, S. G.; Prima-García, H.; López-Muñoz, A.; Riminucci, A.; Graziosi, P.; Aeschlimann, M.; Cinchetti, M.; Dediu, V. A.; Coronado, E. Enhancing Light Emission in Interface Engineered Spin-OLEDs through Spin-Polarized Injection at High Voltages. *Adv. Mater.* **2019**, 1806817. <https://doi.org/10.1002/adma.201806817>.
- (11) Mehmood, U.; Al-Ahmed, A.; Hussein, I. A. Review on Recent Advances in Polythiophene Based Photovoltaic Devices. *Renewable and Sustainable Energy Reviews*. Pergamon May 1, 2016, pp 550–561. <https://doi.org/10.1016/j.rser.2015.12.177>.
- (12) Ajayaghosh, A. Donor–Acceptor Type Low Band Gap Polymers: Polysquaraines and Related Systems. *Chem. Soc. Rev.* **2003**, *32* (4), 181–191. <https://doi.org/10.1039/B204251G>.
- (13) Marcus, R. A. An Internal Consistency Test and Its Implications for the Initial Steps in Bacterial Photosynthesis. *Chem. Phys. Lett.* **1988**, *146* (1–2), 13–22. [https://doi.org/10.1016/0009-2614\(88\)85041-3](https://doi.org/10.1016/0009-2614(88)85041-3).
- (14) Köhler, A.; Bässler, H. Triplet States in Organic Semiconductors. *Mater. Sci. Eng. R*

- Reports* **2009**, *66* (4–6), 71–109. <https://doi.org/10.1016/j.mser.2009.09.001>.
- (15) Chernick, E. T.; Mi, Q.; Vega, A. M.; Lockard, J. V.; Ratner, M. A.; Wasielewski, M. R. Controlling Electron Transfer Dynamics in Donor–Bridge–Acceptor Molecules by Increasing Unpaired Spin Density on the Bridge. *J. Phys. Chem. B* **2007**, *111* (24), 6728–6737. <https://doi.org/10.1021/jp068741v>.
- (16) Weiss, E. A.; Chernick, E. T.; Wasielewski, M. R. Modulation of Radical Ion Pair Lifetimes by the Presence of a Third Spin in Rodlike Donor-Acceptor Triads. *J. Am. Chem. Soc.* **2004**, *126* (8), 2326–2327. <https://doi.org/10.1021/ja039395n>.
- (17) Brookes, J. C. Quantum Effects in Biology: Golden Rule in Enzymes, Olfaction, Photosynthesis and Magnetodetection. *Proc. R. Soc. A Math. Phys. Eng. Sci.* **2017**, *473* (2201), 20160822. <https://doi.org/10.1098/rspa.2016.0822>.
- (18) Takano, Y.; Numata, T.; Fujishima, K.; Miyake, K.; Nakao, K.; Grove, W. D.; Inoue, R.; Kengaku, M.; Sakaki, S.; Mori, Y.; Murakami, T.; Imahori, H. Optical Control of Neuronal Firing: Via Photoinduced Electron Transfer in Donor-Acceptor Conjugates. *Chem. Sci.* **2016**, *7* (5), 3331–3337. <https://doi.org/10.1039/c5sc04135j>.
- (19) Moser, C. C.; Keske, J. M.; Warncke, K.; Farid, R. S.; Dutton, P. L. Nature of Biological Electron Transfer. *Nature* **1992**, *355* (6363), 796–802. <https://doi.org/10.1038/355796a0>.
- (20) Bond, A. M. Chemical and Electrochemical Approaches to the Investigation of Redox Reactions of Simple Electron Transfer Metalloproteins. *Inorganica Chim. Acta* **1994**, *226* (1–2), 293–340. [https://doi.org/10.1016/0020-1693\(94\)04082-6](https://doi.org/10.1016/0020-1693(94)04082-6).
- (21) Meade, T. J.; Kayyem, J. F. Electron Transfer through DNA: Site-Specific Modification

- of Duplex DNA with Ruthenium Donors and Acceptors. *Angew. Chemie Int. Ed. English* **1995**, *34* (3), 352–354. <https://doi.org/10.1002/anie.199503521>.
- (22) Holmlin, R. E.; Dandliker, P. J.; Barton, J. K. Charge Transfer through the DNA Base Stack. *Angew. Chemie Int. Ed. English* **1997**, *36* (24), 2714–2730. <https://doi.org/10.1002/anie.199727141>.
- (23) Freeman, D. M. E.; Musser, A. J.; Frost, J. M.; Stern, H. L.; Forster, A. K.; Fallon, K. J.; Rapidis, A. G.; Cacialli, F.; McCulloch, I.; Clarke, T. M.; Friend, R. H.; Bronstein, H. Synthesis and Exciton Dynamics of Donor-Orthogonal Acceptor Conjugated Polymers: Reducing the Singlet–Triplet Energy Gap. *J. Am. Chem. Soc.* **2017**, *139* (32), 11073–11080. <https://doi.org/10.1021/jacs.7b03327>.
- (24) Kirk, M. L.; Shultz, D. A.; Depperman, E. C.; Brannen, C. L. Donor-Acceptor Biradicals as Ground State Analogues of Photoinduced Charge Separated States. *J. Am. Chem. Soc.* **2007**, *129* (7), 1937–1943. <https://doi.org/10.1021/ja065384t>.
- (25) Liu, C.; Wang, K.; Gong, X.; Heeger, A. J. Low Bandgap Semiconducting Polymers for Polymeric Photovoltaics. *Chemical Society Reviews*. 2016, pp 4825–4846. <https://doi.org/10.1039/c5cs00650c>.
- (26) Ricks, A. B.; Solomon, G. C.; Colvin, M. T.; Scott, A. M.; Chen, K.; Ratner, M. A.; Wasielewski, M. R. Controlling Electron Transfer in Donor-Bridge-Acceptor Molecules Using Cross-Conjugated Bridges. *J. Am. Chem. Soc.* **2010**, *132* (43), 15427–15434. <https://doi.org/10.1021/ja107420a>.
- (27) Ratner, M. A Brief History of Molecular Electronics. *Nature Nanotechnology*. Nature Publishing Group June 5, 2013, pp 378–381. <https://doi.org/10.1038/nnano.2013.110>.

- (28) Kirk, M. L.; Shultz, D. A.; Stasiw, D. E.; Habel-rodriguez, D.; Stein, B.; Boyle, P. D. Biradical : Mechanistic Implications for Quantum Interference Effects. **2013**.
- (29) Kirk, M. L.; Shultz, D. A.; Stasiw, D. E.; Lewis, G. F.; Wang, G.; Brannen, C. L.; Sommer, R. D.; Boyle, P. D. Superexchange Contributions to Distance Dependence of Electron Transfer/Transport: Exchange and Electronic Coupling in Oligo(Para-Phenylene)- and Oligo(2,5-Thiophene)-Bridged Donor-Bridge-Acceptor Biradical Complexes. *J. Am. Chem. Soc.* **2013**, *135* (45), 17144–17154. <https://doi.org/10.1021/ja4081887>.
- (30) Kirk, M. L.; Shultz, D. A.; Zhang, J.; Dangi, R.; Ingersol, L.; Yang, J.; Finney, N. S.; Sommer, R. D.; Wojtas, L. Heterospin Biradicals Provide Insight into Molecular Conductance and Rectification. *Chem. Sci.* **2017**, *8* (8), 5408–5415. <https://doi.org/10.1039/C7SC00073A>.
- (31) Parashar, S.; Srivastava, P.; Pattanaik, M. Effect of Electrode Materials on Transport Properties of Asymmetric Biphenyl Molecular Junctions. *Solid State Commun.* **2014**, *191*, 54–58. <https://doi.org/10.1016/j.ssc.2014.04.019>.
- (32) Venkataraman, L.; Klare, J. E.; Nuckolls, C.; Hybertsen, M. S.; Steigerwald, M. L. Dependence of Single-Molecule Junction Conductance on Molecular Conformation. *Nature* **2006**, *442* (7105), 904–907. <https://doi.org/10.1038/nature05037>.
- (33) Kondo, H.; Nara, J.; Kino, H.; Ohno, T. Dependence of the Conduction of a Single Biphenyl Dithiol Molecule on the Dihedral Angle between the Phenyl Rings and Its Application to a Nanorectifier. *J. Chem. Phys.* **2008**, *128* (6), 064701. <https://doi.org/10.1063/1.2828531>.

- (34) Del Nero, J.; de Souza, F. M.; Capaz, R. B. Molecular Electronics Devices: A Short Review. *J. Comput. Theor. Nanosci.* **2010**, *7* (3), 503–516.
<https://doi.org/10.1166/jctn.2010.1386>.
- (35) Anderson, P. W. Antiferromagnetism. Theory of Superexchange Interaction. *Phys. Rev.* **1950**, *79* (2), 350–356. <https://doi.org/10.1103/PhysRev.79.350>.
- (36) Anderson, P. W. New Approach to the Theory of Superexchange Interactions. *Phys. Rev.* **1959**, *115* (1), 2–13. <https://doi.org/10.1103/PhysRev.115.2>.
- (37) Brown, T. H.; Anderson, D. H.; Gutowsky, H. S. Spin Densities in Organic Free Radicals. *J. Chem. Phys.* **1960**, *33* (3), 720. <https://doi.org/10.1063/1.1731246>.
- (38) Kanamori, J. Superexchange Interaction and Symmetry Properties of Electron Orbitals. *J. Phys. Chem. Solids* **1959**, *10* (2–3), 87–98. [https://doi.org/10.1016/0022-3697\(59\)90061-7](https://doi.org/10.1016/0022-3697(59)90061-7).
- (39) Goodenough, J. B. An Interpretation of the Magnetic Properties of the Perovskite-Type Mixed Crystals $\text{La}_{1-x}\text{Sr}_x\text{CoO}_3$. *J. Phys. Chem. Solids* **1958**, *6* (2–3), 287–297.
[https://doi.org/10.1016/0022-3697\(58\)90107-0](https://doi.org/10.1016/0022-3697(58)90107-0).
- (40) Rajca, A.; Coupling, S.; State, G.; Wroclawska, P. Organic Diradicals and Polyradicals: From Spin Coupling to Magnetism? *Chem. Rev.* **1994**, *94*, 871.
- (41) Marcus, R. A.; Sutin, N. Electron Transfers in Chemistry and Biology. *BBA Reviews On Bioenergetics*. Elsevier August 1, 1985, pp 265–322. [https://doi.org/10.1016/0304-4173\(85\)90014-X](https://doi.org/10.1016/0304-4173(85)90014-X).
- (42) Landauer, R. Electrical Resistance of Disordered One-Dimensional Lattices. *Philos. Mag.*

- 1970**, *21* (172), 863–867. <https://doi.org/10.1080/14786437008238472>.
- (43) Marcus, R. A. On the Theory of Oxidation-Reduction Reactions Involving Electron Transfer. I. *J. Chem. Phys.* **1956**, *24* (5), 966–978. <https://doi.org/10.1063/1.1742723>.
- (44) Marcus, R. A. On the Theory of Electron-Transfer Reactions. VI. Unified Treatment for Homogeneous and Electrode Reactions. *J. Chem. Phys.* **1965**, *43* (2), 679–701. <https://doi.org/10.1063/1.1696792>.
- (45) McConnell, H. M.; Chesnut, D. B. Theory of Isotropic Hyperfine Interactions in π -Electron Radicals. *J. Chem. Phys.* **1958**, *28* (1), 107–117. <https://doi.org/10.1063/1.1744052>.
- (46) Nitzan, A. A Relationship between Electron-Transfer Rates and Molecular Conduction †. *J. Phys. Chem. A* **2001**, *105* (12), 2677–2679. <https://doi.org/10.1021/jp003884h>.
- (47) Goodenough, J. B. Theory of the Role of Covalence in the Perovskite-Type Manganites [La,M(II)]MnO₃. *Phys. Rev.* **1955**, *100* (2), 564–573. <https://doi.org/10.1103/PhysRev.100.564>.
- (48) Landauer, R. Spatial Variation of Currents and Fields Due to Localized Scatterers in Metallic Conduction. *IBM J. Res. Dev.* **2000**, *44* (1), 251–259. <https://doi.org/10.1147/rd.441.0251>.
- (49) Tsuji, Y.; Stuyver, T.; Gunasekaran, S.; Venkataraman, L. The Influence of Linkers on Quantum Interference: A Linker Theorem. *J. Phys. Chem. C* **2017**, *121* (27), 14451–14462. <https://doi.org/10.1021/acs.jpcc.7b03493>.
- (50) Priyadarshy, S.; Skourtis, S. S.; Risser, S. M.; Beratan, D. N. Bridge-mediated Electronic

- Interactions: Differences between Hamiltonian and Green Function Partitioning in a Non-orthogonal Basis. *J. Chem. Phys.* **1996**, *104* (23), 9473–9481.
<https://doi.org/10.1063/1.471690>.
- (51) Combescot, R. A Direct Calculation of the Tunnelling Current. III. Effect of Localized Impurity States in the Barrier. *J. Phys. C Solid State Phys.* **1971**, *4* (16), 2611–2622.
<https://doi.org/10.1088/0022-3719/4/16/026>.
- (52) Caroli, C.; Combescot, R.; Nozieres, P.; Saint-James, D. Direct Calculation of the Tunneling Current. *J. Phys. C Solid State Phys.* **1971**, *4* (8), 916–929.
<https://doi.org/10.1088/0022-3719/4/8/018>.
- (53) Shultz, D. A.; Vostrikova, K. E.; Bodnar, S. H.; Koo, H.-J. H.-J.; Whangbo, M.-H. M.-H.; Kirk, M. L.; Depperman, E. C.; Kampf, J. W. Trends in Metal-Biradical Exchange Interaction for First-Row M(II)(Nitronyl Nitroxide-Semiquinone) Complexes. *J. Am. Chem. Soc.* **2003**, *125* (6), 1607. <https://doi.org/10.1021/ja020715x>.
- (54) Kirk, M. L.; Shultz, D. A.; Depperman, E. C.; Habel-Rodriguez, D.; Schmidt, R. D. Spectroscopic Studies of Bridge Contributions to Electronic Coupling in a Donor-Bridge-Acceptor Biradical System. *J. Am. Chem. Soc.* **2012**, *134* (18), 7812–7819.
<https://doi.org/10.1021/ja300233a>.
- (55) Shultz, D. A.; Bodnar, S. H.; Vostrikova, K. E.; Kampf, J. W. Synthesis and Structure of a Complex Having a Quartet Ground State with Three Entirely Different Spin Carriers: Nitronyl Nitroxide, o-Semiquinone, and CuII. *Inorg. Chem.* **2000**, *39* (26), 6091.
<https://doi.org/10.1021/ic0009122>.
- (56) Stasiw, D. E.; Zhang, J.; Wang, G.; Dangi, R.; Stein, B. W.; Shultz, D. A.; Kirk, M. L.;

- Wojtas, L.; Sommer, R. D. Determining the Conformational Landscape of σ and π Coupling Using Para -Phenylene and “Aviram–Ratner” Bridges. *J. Am. Chem. Soc.* **2015**, *137* (29), 9222–9225. <https://doi.org/10.1021/jacs.5b04629>.
- (57) Kirk, M. L.; Shultz, D. A.; Stasiw, D. E.; Habel-Rodriguez, D.; Stein, B.; Boyle, P. D. Electronic and Exchange Coupling in a Cross-Conjugated D-B-A Biradical: Mechanistic Implications for Quantum Interference Effects. *J. Am. Chem. Soc.* **2013**, *135* (39), 14713–14725. <https://doi.org/10.1021/ja405354x>.
- (58) Ruf, M.; Noll, B. C.; Groner, M. D.; Yee, G. T.; Pierpont, C. G. Pocket Semiquinone Complexes of Cobalt(II), Copper(II), and Zinc(II) Prepared with the Hydrotris(Cumenylmethylpyrazolyl)Borate Ligand. *Inorg. Chem.* **1997**, *36* (21), 4860–4865. <https://doi.org/10.1021/ic970244t>.
- (59) Magdziak, D.; Rodriguez, A. A.; Van De Water, R. W.; Pettus, T. R. R. Regioselective Oxidation of Phenols to o -Quinones with o -Iodoxybenzoic Acid (IBX). *Org. Lett.* **2002**, *4* (2), 285–288. <https://doi.org/10.1021/ol017068j>.
- (60) Ullman, E. F.; Call, L.; Osiecki, J. H. Stable Free Radicals. VIII. New Imino, Amidino, and Carbamoyl Nitroxides. *J. Org. Chem.* **1970**, *35* (11), 3623–3631. <https://doi.org/10.1021/jo00836a008>.
- (61) Ullman, E. F.; Osiecki, J. H.; Boocock, D. G. B.; Darcy, R. Studies of Stable Free Radicals. *J. Am. Chem. Soc.* **1972**, 7049–7059. <https://doi.org/10.1021/ja00775a031>.
- (62) Rajca, A.; Pink, M.; Mukherjee, S.; Rajca, S.; Das, K. 1,3-Alternate Calix[4]Arene Nitronyl Nitroxide Tetraradical and Diradical: Synthesis, X-Ray Crystallography, Paramagnetic NMR Spectroscopy, EPR Spectroscopy, and Magnetic Studies. *Tetrahedron*

- 2007, 63 (44), 10731–10742. <https://doi.org/10.1016/j.tet.2007.07.051>.
- (63) Shimono, S.; Tamura, R.; Ikuma, N.; Takimoto, T.; Kawame, N.; Tamada, O.; Sakai, N.; Matsuura, H.; Yamauchi, J. Preparation and Characterization of New Chiral Nitronyl Nitroxides Bearing a Stereogenic Center in the Imidazolyl Framework. *J. Org. Chem.* **2004**, 69 (2), 475–481. <https://doi.org/10.1021/jo0354443>.
- (64) Ruf, M.; Vahrenkamp, H. Small Molecule Chemistry of the Pyrazolylborate-Zinc Unit TpCum,MeZn. *Inorg. Chem.* **1996**, 35 (22), 6571–6578. <https://doi.org/10.1021/ic960335a>.
- (65) Swamer, F. W.; Hauser, C. R. Claisen Acylations and Carbethoxylations of Ketones and Esters by Means of Sodium Hydride. *J. Am. Chem. Soc.* **1950**, 72 (3), 1352–1356. <https://doi.org/10.1021/ja01159a074>.
- (66) Kirk, M. L.; Shultz, D. A.; Stasiw, D. E.; Lewis, G. F.; Wang, G.; Brannen, C.; Sommer, R. D.; Boyle, P. D. Superexchange Contributions to Distance Dependence of Electron Transfer / Transport : Exchange- and Electronic Coupling in Oligo (Para- Complexes. 1–32.
- (67) Kirk, M. L.; Shultz, D. A.; Habel-Rodriguez, D.; Schmidt, R. D.; Sullivan, U. Hyperfine Interaction, Spin Polarization, and Spin Derealization as Probes of Donor-Bridge-Acceptor Interactions in Exchange-Coupled Biradicals. *J. Phys. Chem. B* **2010**, 114 (45), 14712–14716. <https://doi.org/10.1021/jp102955j>.
- (68) Weil, J. A.; Bolton, J. R.; Wertz, J. E. *Electron Paramagnetic Resonance: Elementary Theory and Practical Applications*; John Wiley & Sons, Ltd: New York, 1994.

- (69) Kahn, O. O. *Molecular Magnetism*; VCH Publishers Inc.: New York, 1993.
- (70) Pierpont, C. G.; Lange, C. W. The Chemistry of Transition Metal Complexes Containing Catechol and Semiquinone Ligands. In *Progress in Inorganic Chemistry*; John Wiley & Sons, Ltd, 1994; Vol. 41, pp 331–442. <https://doi.org/10.1002/9780470166420.ch5>.
- (71) Günes, S.; Neugebauer, H.; Sariciftci, N. S. Conjugated Polymer-Based Organic Solar Cells. *Chem. Rev.* **2007**, *107* (4), 1324–1338. <https://doi.org/10.1021/cr050149z>.
- (72) Remmers, M.; Müller, B.; Martin, K.; Räder, H.-J.; Köhler, W. Poly(p-Phenylene)s. Synthesis, Optical Properties, and Quantitative Analysis with HPLC and MALDI–TOF Mass Spectrometry. *Macromolecules* **1999**, *32* (4), 1073–1079. <https://doi.org/10.1021/ma981260s>.
- (73) Eng, M. P.; Albinsson, B. The Dependence of the Electronic Coupling on Energy Gap and Bridge Conformation – Towards Prediction of the Distance Dependence of Electron Transfer Reactions. *Chem. Phys.* **2009**, *357* (1–3), 132–139. <https://doi.org/10.1016/j.chemphys.2008.12.004>.
- (74) Baker, W. J.; McCamey, D. R.; Van Schooten, K. J.; Lupton, J. M.; Boehme, C. Differentiation between Polaron-Pair and Triplet-Exciton Polaron Spin-Dependent Mechanisms in Organic Light-Emitting Diodes by Coherent Spin Beating. *Phys. Rev. B - Condens. Matter Mater. Phys.* **2011**, *84* (16), 1–7. <https://doi.org/10.1103/PhysRevB.84.165205>.
- (75) Malissa, H.; Kavand, M.; Waters, D. P.; van Schooten, K. J.; Burn, P. L.; Vardeny, Z. V.; Saam, B.; Lupton, J. M.; Boehme, C. Organic Electronics. Room-Temperature Coupling between Electrical Current and Nuclear Spins in OLEDs. *Science* **2014**, *345* (6203),

- 1487–1490. <https://doi.org/10.1126/science.1255624>.
- (76) Wenger, O. S. How Donor-Bridge-Acceptor Energetics Influence Electron Tunneling Dynamics and Their Distance Dependences. *Acc. Chem. Res.* **2010**, *44* (1), 25–35. <https://doi.org/10.1021/ar100092v>.
- (77) Seidler, A.; Svoboda, J.; Dekoj, V.; Chocholoušová, J. V.; Vacek, J.; Stará, I. G.; Starý, I. The Synthesis of π -Electron Molecular Rods with a Thiophene or Thieno[3,2-b]Thiophene Core Unit and Sulfur Alligator Clips. *Tetrahedron Lett.* **2013**, *54* (22), 2795–2798. <https://doi.org/10.1016/j.tetlet.2013.03.084>.
- (78) Dellsperger, S.; Do, F.; Smith, P.; Weder, C. Synthesis and Optical Properties of Novel Poly (p -Phenylene Ethynylene) S. **2000**, *198*, 192–198.
- (79) David J. Wold, †; Rainer Haag, ‡; Maria Anita Rampi, *,§ and; C. Daniel Frisbie*, †. Distance Dependence of Electron Tunneling through Self-Assembled Monolayers Measured by Conducting Probe Atomic Force Microscopy: Unsaturated versus Saturated Molecular Junctions. **2002**. <https://doi.org/10.1021/JP013476T>.
- (80) Helms, A.; Heiler, D.; McLendon, G. Electron Transfer in Bis-Porphyrin Donor-Acceptor Compounds with Polyphenylene Spacers Shows a Weak Distance Dependence. *J. Am. Chem. Soc.* **1992**, *114* (15), 6227–6238. <https://doi.org/10.1021/ja00041a047>.
- (81) Weiss, E. A.; Ahrens, M. J.; Sinks, L. E.; Gusev, A. V.; Ratner, M. A.; Wasielewski, M. R. Making a Molecular Wire: Charge and Spin Transport through Para-Phenylene Oligomers. *J. Am. Chem. Soc.* **2004**, *126* (17), 5577–5584. <https://doi.org/10.1021/ja0398215>.

- (82) Baer, R.; Neuhauser, D. Phase Coherent Electronics: A Molecular Switch Based on Quantum Interference. *J. Am. Chem. Soc.* **2002**, *124* (16), 4200–4201.
<https://doi.org/10.1021/ja016605s>.
- (83) Patoux, C.; Coudret, C.; Launay, J.-P.; Joachim, C.; Gourdon, A. Topological Effects on Intramolecular Electron Transfer via Quantum Interference. *Inorg. Chem.* **1997**, *36* (22), 5037–5049. <https://doi.org/10.1021/ic970013m>.
- (84) Hansen, T.; Solomon, G. C.; Andrews, D. Q.; Ratner, M. A. Interfering Pathways in Benzene: An Analytical Treatment. *J. Chem. Phys.* **2009**, *131* (19), 1–13.
<https://doi.org/10.1063/1.3259548>.
- (85) Valkenier, H.; Guédon, C. M.; Markussen, T.; Thygesen, K. S.; Molen, S. J. Van Der; Hummelen, J. C. Cross-Conjugation and Quantum Interference: A General Correlation? *Phys. Chem. Chem. Phys.* **2013**, *16* (2), 653–662. <https://doi.org/10.1039/C3CP53866D>.
- (86) Solomon, G. C. Cross-Conjugation and Quantum Interference. In *Cross Conjugation: Dendralene, Radialene and Fulvene Chemistry*; Wiley-VCH Verlag GmbH & Co. KGaA: Weinheim, Germany, 2016; Vol. 16, pp 397–412.
<https://doi.org/10.1002/9783527671182.ch11>.
- (87) Gehring, P.; Thijssen, J. M.; van der Zant, H. S. J. Single-Molecule Quantum-Transport Phenomena in Break Junctions. *Nat. Rev. Phys.* **2019**, *1* (6), 381–396.
<https://doi.org/10.1038/s42254-019-0055-1>.
- (88) Xin, N.; Guan, J.; Zhou, C.; Chen, X.; Gu, C.; Li, Y.; Ratner, M. A.; Nitzan, A.; Stoddart, J. F.; Guo, X. Concepts in the Design and Engineering of Single-Molecule Electronic Devices. *Nat. Rev. Phys.* **2019**, *1* (3), 211–230. <https://doi.org/10.1038/s42254-019-0022->

x.

- (89) Guldi, D. M.; Nishihara, H.; Venkataraman, L. Molecular Wires. *Chem. Soc. Rev.* **2015**, *44* (4), 842–844. <https://doi.org/10.1039/C5CS90010G>.
- (90) Li, G.; Chang, W. H.; Yang, Y. Low-Bandgap Conjugated Polymers Enabling Solution-Processable Tandem Solar Cells. *Nature Reviews Materials*. Nature Publishing Group August 25, 2017, p 17043. <https://doi.org/10.1038/natrevmats.2017.43>.
- (91) Thompson, A. L.; Ahn, T.-S.; Thomas, K. R. J.; Thayumanavan, S.; Martínez, T. J.; Bardeen, C. J. Using Meta Conjugation To Enhance Charge Separation versus Charge Recombination in Phenylacetylene Donor–Bridge–Acceptor Complexes. *J. Am. Chem. Soc.* **2005**, *127* (47), 16348–16349. <https://doi.org/10.1021/ja054543q>.

IV. Donor-Bridge-Acceptor Biradicals for Studying Molecular Rectification.

The field of molecular rectification has been studied for over 40 years since the seminal work by Aviram and Ratner.¹ As a result, there is a substantial amount of material; much of which is purely theoretical or computational and based on Greene's functions,²⁻⁵ and their utility in computing electron flow (conductance) through molecules. Because the work presented in this chapter primarily involves the synthesis of molecules designed for studying current rectification by molecules that span metallic electrodes, and is supplemented by theory and computation, much of the computational work that has been reported for rectification is not going to be discussed in the introductory sections of this chapter; rather those studies that have involved empirical observations and molecular structure-property relationships will be presented. However, Tsuji et al. have related Green's functions to the symmetries of molecular orbitals as a means to predict the conductance through single molecules and this will be discussed first as it provides a theoretical basis for the qualitative discussion of rectification and conductance based on molecular orbitals from Hückel calculations which are consistent with DFT-level calculations. The objective here is to provide an overview of molecular current rectification using molecular orbital explanations as well as important design features and discuss results from devices that have been reported in the literature.

IV.1. Definition and Predictions of Conductance with Green's Functions.

Tsuji et al. have proposed a symmetry rule for electron transport properties of single molecules from the analysis of Green's function in terms of the Hückel molecular orbitals which are consistent with more quantitative DFT calculations. There are some necessary conditions: 1) the coupling between the molecule and electrodes must be weak, 2) there is electron-hole symmetry in the orbital energies of the molecular orbital coefficients and 3) the Fermi level is

located at the midgap of the HOMO and the LUMO.⁶ As discussed in Chapter I, the conductance according to Landauer for a single molecule device with a molecule bridging two gold electrodes is given as:

$$g = \frac{2e^2}{h} T(E_F) \quad \text{Eq. IV-1}$$

where $2e^2/h$ is the quantum conductance, T is the transmission probability and E_F is the Fermi energy. The transmission probability can be calculated according to:^{7,8}

$$T(E) = \text{Tr}[\Gamma_L(E)G^R(E)\Gamma_R(E)G^A(E)] \quad \text{Eq. IV-2}$$

where G^R (G^A) and Γ_L (Γ_R) represent retarded (advanced) Green's function (a mathematical tool for solving complex differential equations) and the broadening function for the left (right) electrode, respectively.^{9,10} The broadening function is defined as

$$\Gamma_{L(R)} = i[\Sigma_{L(R)}^R - \Sigma_{L(R)}^A] \quad \text{Eq. IV-3}$$

where $\Sigma_{L(R)}^{R/A}(E)$ is the self-energy matrix for the left (right) electrode and given by $\Sigma_{L(R)}^{R/A} = \tau_{L(R)}^\dagger \mathbf{g}_{L(R)}^{R/A} \tau_{L(R)}$, where $\mathbf{g}_{L(R)}^{R/A}$ is the Green's function of the left (right) electrode and $\tau_{L(R)}$ is the molecule-electrode interaction.^{11,12} Only the nearest neighbor interactions between the molecule and electrode are considered and so the retarded and advanced Green's functions are written as:

$$G^{R/A}(E) = [I - G^{(0)R/A}(E)\Sigma^{R/A}(E)]^{-1} G^{(0)R/A} \quad \text{Eq. IV-4}$$

Where I is the unit matrix and $\mathbf{G}^{(0)R/A}$ is the zeroth Green's function, which is the Green's function of the molecule.^{10,11,13} The orbital symmetry rule is derived from the zeroth Green's function. According to Eq. IV-4 for weakly-coupled systems the Green's functions is approximately proportional to the zeroth Green's function. The conductance increases with an enhancement of the zeroth Green's function at the Fermi level. At the Fermi level the matrix elements of the zeroth Green's function, $G_{rs}^{(0)R/A}$ which describes the propagation of the

tunneling electron from one side denoted with r to another side denoted with s through the orbitals in a non-interacting molecule can be written as:

$$G_{rs}^{(0)}(E_F) = \sum_k \frac{C_{rk} C_{sk}^*}{E_F - \epsilon_k \pm i\eta} \quad \text{Eq. IV-5}$$

Where C_{rk} is the k th MO coefficient at the r th atomic orbital in an orthogonal basis, ϵ_k is the k th MO energy and η is an infinitesimal number determined by a relationship between the local density of states and the imaginary part of Green's function.⁶ Eq. IV-5 shows the correlation between the MOs and Green's function and allows for the prediction of conductance from the molecular orbitals. In Eq. IV-6 the contributions from the HOMO and LUMO are written as:

$$\frac{C_{rHOMO} C_{sHOMO}^*}{E_F - \epsilon_{HOMO} \pm i\eta} + \frac{C_{rLUMO} C_{sLUMO}^*}{E_F - \epsilon_{LUMO} \pm i\eta} \quad \text{Eq. IV-6}$$

The contributions from the frontier molecular orbitals are significant in the zeroth Green's function since the denominators of Eq. IV-6 are the smallest of all the terms of Eq. IV-5 because of the vicinity of the Fermi level. The HOMO-1 and LUMO+1 should not be important in electron transport since these orbitals are far away from the Fermi level and barely contribute to the zeroth Green's function.^{6,12} With the reversal of the signs between denominators, the orbital symmetry rule for conductance requires 1) the two atoms in which the orbital amplitudes of the HOMO and LUMO are significant should be connected to the electrodes and 2) the atoms in which the sign of the product of the molecular orbital expansion coefficients in the HOMO is different from that in the LUMO should be connected to the electrodes.

For example, the conductance and electron transport are relatively strong when the electrodes are connected *para* through a benzene ring and relatively weak when connected *meta* through a benzene ring. In Figure IV-1 the doubly degenerate HOMO and LUMO orbitals are shown for benzene and the colors of the orbitals alongside the inscribed + and - signs indicate

the relative signs of the wavefunctions. The e_{2g}^1 and e_{2u}^1 orbitals of the HOMO and LUMO, respectively, have significant orbital amplitudes when electrodes are connected to the 1 and 4 positions, thus satisfying the first requirement for the orbital symmetry rule. The second requirement of different signs for the product of the molecular orbital coefficients can be satisfied for 1,4-connectivity by determining the relative signs of the products of the wavefunction coefficients for the HOMO and LUMO which will give a negative for the HOMO and a positive for the LUMO. For *meta* connectivity at the 1,3 positions, both positions have

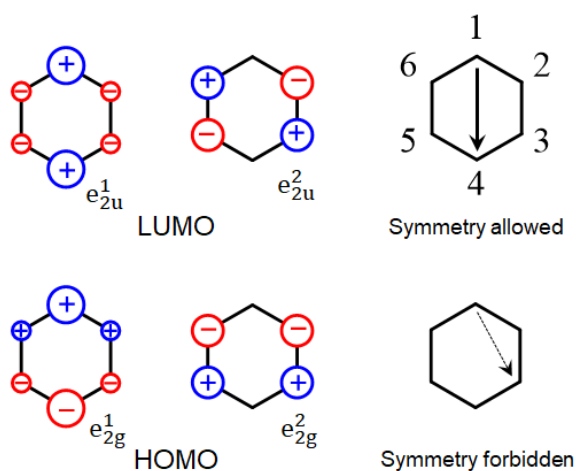


Figure IV-1. HOMO and LUMO of benzene with symmetry allowed *para* and symmetry forbidden *meta* connectivity.

significant orbital amplitude, but the sign of the product of the molecular orbital coefficients for the 1,3 positions in the HOMO and LUMO are both negative; failing to meet the second requirement of orbital symmetry. The e_{2g}^2 and e_{2u}^2 orbitals of the HOMO and LUMO can be ignored in both cases because there is zero orbital amplitude at the 1 and 4 positions due to the nodal plane.

IV.2. Definition of Rectification.

Current rectification using molecules has been studied for over 40 years and is defined as a change in the current (I)-voltage (V) profile with the direction of the applied bias.¹ Rectifiers display non-Ohmic behavior; meaning that their I - V profiles do not obey Ohm's law: $I = V/R$, where I is current, V is voltage, and R is resistance. Figure IV-2 shows the I - V plot of a device that obeys Ohm's law which (left; a linear correlation), and on the right a rectifying device (non-Ohmic behavior).¹⁴ For the rectifying device, the positive direction (voltage > 0) shows

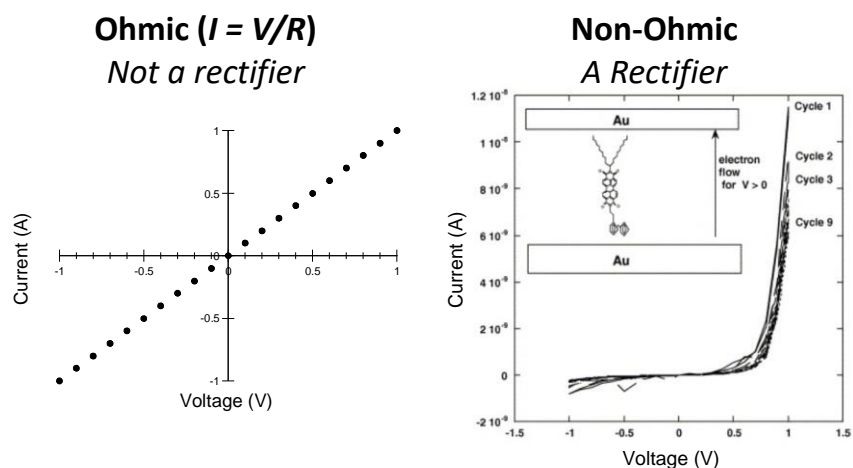


Figure IV-2. Current-voltage profile of a device that obeys Ohm's law (not a rectifier) and a device that displays non-Ohmic behavior (a molecular rectifier) from ref. 14.

measured currents that are higher in magnitude than those for corresponding voltages in the negative direction (voltages < 0); indicating that the current flows more efficiently through the molecule one direction versus the reverse direction. Rectifiers suggest that the direction of the current flow should be from anode to acceptor and donor to cathode and not *vice versa* and the performance of the device is measured by the ratio of the conductance (g) in the forward and reverse directions, known as the rectification ratio (RR) = $g_{forward}/g_{reverse}$.

IV.3. Theory of Molecular Rectifiers.

IV.3.1. Aviram-Ratner Model.

In 1974, Aviram and Ratner published an article on their hypothesis for the design and synthesis of molecular rectifiers – thus giving birth to the concept of molecular electronics.¹ At the time, crystals of organic charge transfer solids comprised of tetracyanoquinodimethane (TCNQ) and tetrathiafulvalene (TTF) were shown to be semiconductors and possibly superconductors at cryogenic temperatures.¹⁵ From these results, Aviram and Ratner theorized that current-voltage relationships should be evaluated for molecules of interest for electronic circuitry and that those molecules should have similar characteristics and emulate p-n junctions as those in solid state rectifiers (p-side is electron poor and the n-side is electron rich). For a molecule this means the presence of a dipole or appending either electron donating or electron withdrawing substituents that will enhance a molecule's donor or acceptor capabilities. If a donor and acceptor are allowed to interact strongly (i.e., they are strongly coupled), then a single, *delocalized* HOMO will exist that spans both donor and acceptor and rectification will be negligible. Therefore, the donor and acceptor moieties must be decoupled from each other by some structural perturbation or by virtue of the π -system. The suggestion from the 1974 article was to decouple the donor and acceptor using a σ -only bridge that spans the donor and acceptor. For example, consider Figure IV-3, which shows dodecahexaene with a thiol (a donor group) and nitrile (an acceptor group) end groups. This molecule is a fully-conjugated polyene and the Hückel HOMO and LUMO are shown as well in Figure IV-3. The HOMO and LUMO are fully delocalized, and are symmetric with each other as the coefficients on thiol side are similar to those on the nitrile side. Comparing the fully conjugated polyenes frontier molecular orbitals to the DFT calculated orbitals of the essentially the same molecule, but with a C₄H₈ bridge

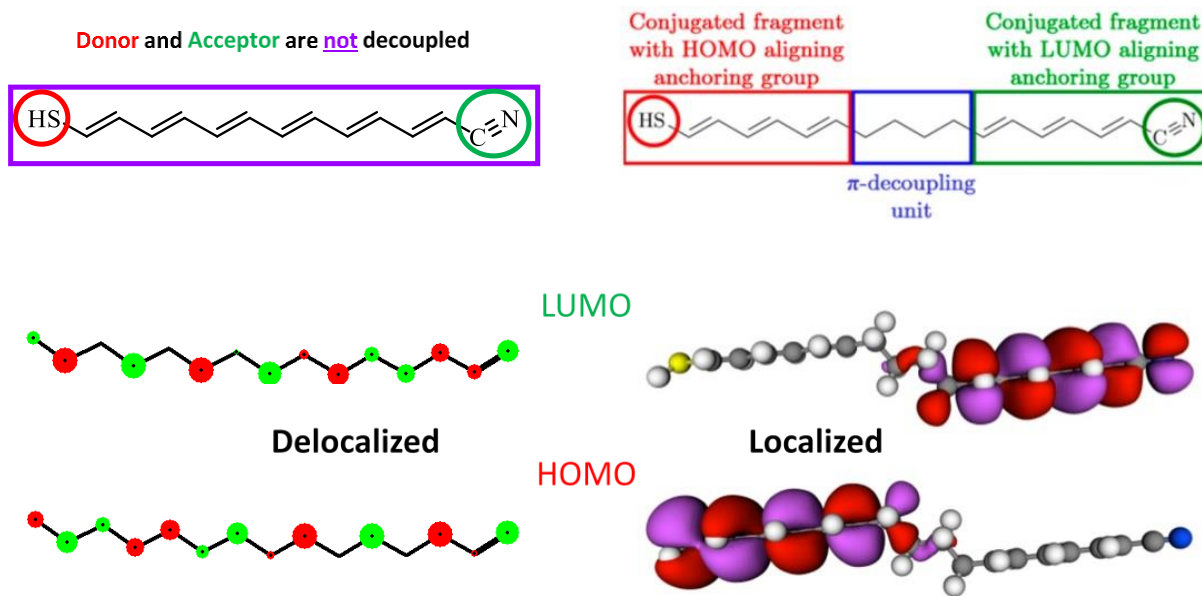


Figure IV-3. Molecules with a thiol donor and a nitrile acceptor and 12 double bonds: a) the donor and acceptor are strongly coupled and their Hückel orbitals are very symmetric between the donor and acceptor side (**not a rectifier**) b) the donor and acceptor sides are decoupled (**rectifier**) by an alkyl linker as shown by the DFT calculated HOMO and LUMO from ref 16.

decoupling unit between the thiol donor side and the nitrile acceptor side of the molecule.¹⁶ Now, the HOMO is localized on the donor side of the molecule and the LUMO is localized on the acceptor side of the molecule; the donor and acceptor have been effectively decoupled using a saturated alkyl bridge. Thus, while the polyene on the left is not a rectifier, the molecule on the right with decoupled donor and acceptor is. The bridging unit that was proposed by Aviram and Ratner is bicyclooctane as it would provide a σ -only system while maintaining

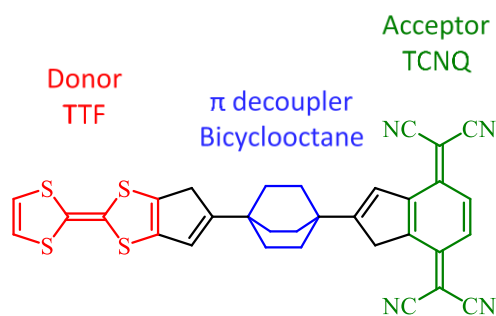


Figure IV-4. Aviram-Ratner's proposed bicyclooctane (BCO) bridge to decouple a donor (TTF) from the acceptor (TCNQ).

distance/geometry because every pathway through bicyclooctane is the same due to the rotational geometry (Figure IV-5).¹

IV.3.2. HOMO and LUMO Energy Levels under a Bias.

The HOMO and LUMO levels of the donor and acceptor dictate the bias direction and the magnitude of the rectifying behavior of the system.¹⁶ Figure IV-5 shows schematics of what happens to the donor and acceptor frontier MO energies when placed between two electrodes in the absence of a bias and with a bias in either direction. In Figure IV-5a there is no applied bias, so the Fermi levels of the electrodes (shown in gold) are equal in energy (assuming the electrodes are identical metals). The donor and acceptor are bridging the two electrodes and their frontier molecular orbitals are shown. The donor's HOMO is closer in energy to its electrode's Fermi level than the acceptor's HOMO with its corresponding electrode. Conversely, the acceptor's LUMO is closer in energy to its electrodes Fermi level than the donor's LUMO with its corresponding electrode. That is, the donor is electron-rich and has energy levels that are

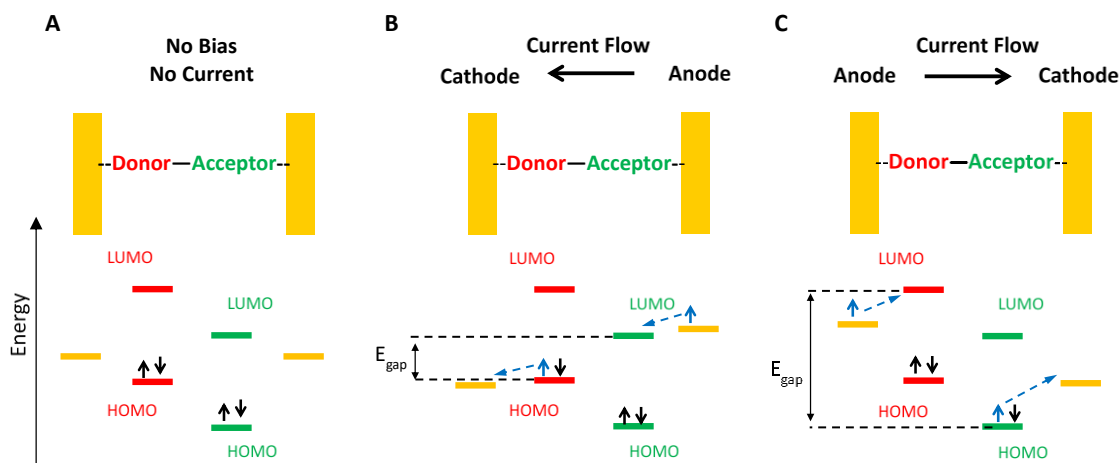


Figure IV-5. The schematic of a metal-organic-metal rectifying device where the two identical electrodes are connected via a donor-acceptor bridging unit and qualitatively illustrating the Fermi levels of the metals and the HOMO and LUMO levels of the donor and acceptor A) under no bias B) when the current flows anode-acceptor-donor-cathode and C) when the current flows anode-donor-acceptor-cathode.

higher in energy than those of the electron-poor acceptor. Conversely, the LUMO of the electron poor acceptor is lower than that of the electron rich acceptor.

In Figure IV-5b there is an applied bias so that the left electrode becomes the cathode and the right electrode becomes the anode which changes their respective Fermi levels. The anode's Fermi level raises while the cathode's Fermi level decreases depending on the applied bias. The acceptor LUMO will accept electrons from the anode (shown by the blue electron with the arrow indicating the orbital that it travels through) and the donor HOMO will donate electrons to the cathode (shown by the other blue electron with the arrow). Note that this is exergonic both overall and for individual steps. The energy difference between the HOMO and LUMO involved during the charge transport is known as the gap energy (E_{gap}). When E_{gap} is small, a smaller bias is required for current flow and when E_{gap} is large, a larger bias is required for current flow. The final step of the process (not shown) is recombination of the electron in the acceptor LUMO with the hole in the donor's HOMO to allow the process to begin again. Figure IV-5c illustrates the scenario when reverse bias is applied. Now, the left electrode becomes the anode and the right electrode is the cathode and their Fermi levels increase and decrease, respectively. For current to flow, the donor must accept electrons from the anode into its LUMO and the acceptor must donate electrons from its HOMO to the cathode; these processes are endergonic which means a greater bias is required in order to overcome these energy barriers and allow current to flow through the system. It should be noted that in this simplified diagram, the HOMO and LUMO levels of the donor and acceptor stayed the same, but in reality, their energies will change under applied biases. This is known as Fermi level pinning effect: covalently bonding a donor and acceptor to an electrode means that the donor and acceptor are now electronically coupled to their respective electrodes and when the energy levels (Fermi levels) of the electrode are

changed, the energy levels of the molecule attached to the metallic electrodes change. When the Fermi levels increase or decrease, the molecular orbitals of the molecule will “follow” them by either increasing or decreasing, respectively.

IV.3.3. Asymmetry is Essential.

In order for metal-organic-metal assemblies to display rectifying behavior, asymmetry within the donor-acceptor bridging unit is necessary.¹⁷ This is commonly understood as a dipole and in order to have a dipole the molecule must lack an inversion center; ergo asymmetry.

Within this motif, molecular rectifiers are partitioned into three categories depending on the type of asymmetry they possess. These include asymmetric Schottky barriers (S-type), asymmetric placement of the chromophore (A-type), and those that are considered to be “true” unimolecular rectifiers, which have orbital asymmetry (U-type).

A Schottky barrier is a potential energy barrier for electrons that is at a metal-semiconductor junction. In order to have an asymmetric Schottky barrier this potential energy must be different at one electrode versus the other.¹⁷ This can mean either the chemical constitution of the electrodes are different or that the connecting groups are different. Figure IV-6A depicts a cartoon illustrating these differences. The left image shows two different metals and

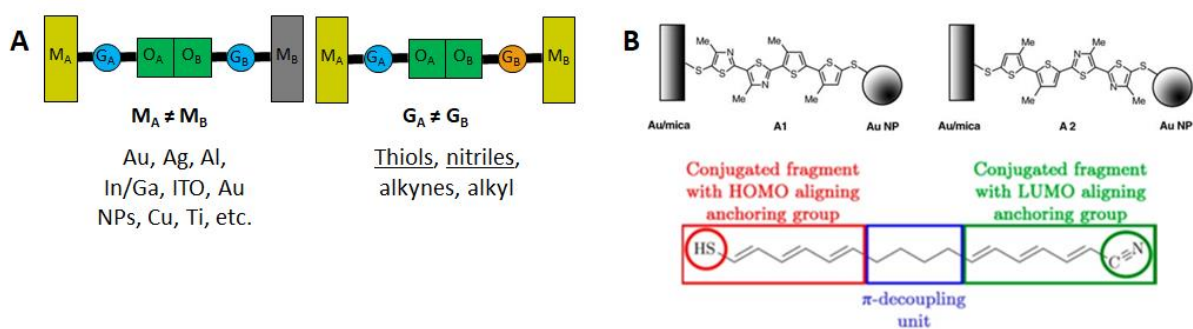


Figure IV-6. Schottky type rectifiers **A)** a cartoon of changes that can be made to make an S-type rectifier. **B)** Examples of S-type rectifiers.

the right image shows that the linking groups are different. Figure IV-6B shows an example of an S-type molecular rectifier.¹⁴ In this case the linking units are the same, both thiol linkers, but the electrodes are different; one side is a gold substrate and the other is a gold nanoparticle. These particular molecules have RRs of 5.3 and 4.8, respectively.¹⁴

A-type molecular rectifiers are defined as those that have asymmetric placement of their chromophore.¹⁷ Typically these are amphipolar molecules and so the donor-acceptor π -system makes up one side or portion of the molecule and the rest is comprised of an alkyl chain which places the much more electronically-active conjugated system of the molecule significantly closer to one electrode allowing electrons to pass to the donor-acceptor more easily than the other side. Figure IV-7A illustrates these differences, where the only difference in the rectifying device is that one side has a lengthy “alkyl chain” connecting the electrode to the conjugated moiety (represented as green squares). In practice, A-type rectifiers may also have characteristics of S- and U-type rectifiers. Figure IV-7B shows some examples of A-type molecular rectifiers

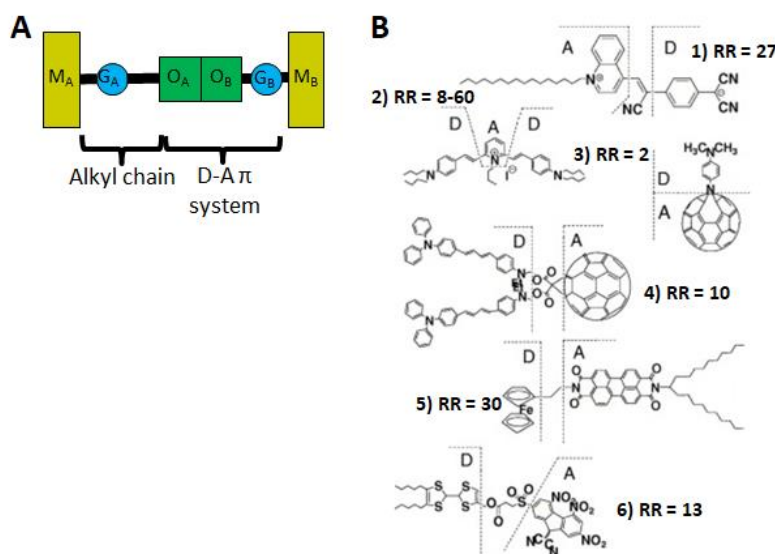


Figure IV-7. A-type unimolecular rectifiers that are the asymmetric placement of the chromophore. **A)** a schematic showing the asymmetric placement of the chromophore and **B)** several examples of A-type rectifiers.

found in Metzger, et al.¹⁷ While the electroactive moieties and structures vary for each of these examples, each has at least a donor and acceptor moiety and an alkyl chain (except Figure IV-7B.4) on one side of the molecule.

The final type of molecular rectifier are the U-type rectifiers. These are considered to be the only “true” unimolecular rectifiers because their rectification comes from the inherent electronic asymmetry of the orbitals.¹⁷ These are very rarely encountered and good examples, free from other rectifying characteristics, such as those of S- and A-type rectifiers, are scarce.

Figure IV-8A uses a cartoon illustration to demonstrate that it is only the orbital system, as

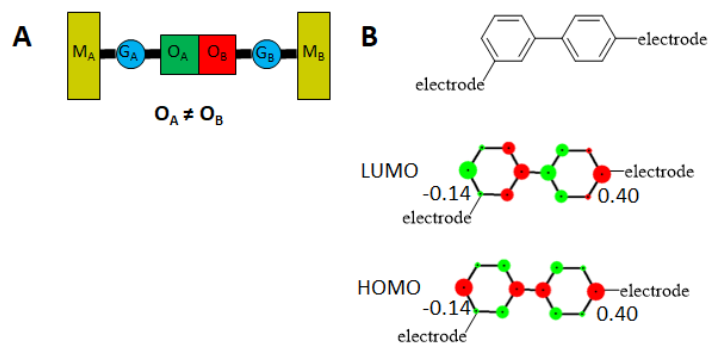


Figure IV-8. U-type unimolecular rectifiers which are considered to be “True” unimolecular rectifiers that are governed by the asymmetry of their orbitals. **A)** a schematic showing the asymmetric orbital segments of the acceptor (O_A) and donor (O_B) and **B)** example of a biphenyl-bridged device which could be a U-type molecular rectifier due to orbital asymmetry.

indicated by red and green, that has the asymmetric structure and the example (Figure IV-8B) uses an orbital diagram of the HOMO and LUMO of biphenyl which at the electrode connection points have different orbital coefficients.

IV.3.4. Past Work and Examples of Rectification Ratios.

Figure IV-9 shows some examples of molecular current rectifying systems. These examples are all some mixture of S, A and U-type rectifiers. For example, the rectifier on the top left labelled 1 is S-type in that it has asymmetric contact points due to one side’s contact point being the

malononitrile anion and the other side being the pentadecyl chain which will inevitably result in different Schottky barriers. By the same features of the connection points, the pentadecyl chain pushes the acceptor-donor unit away from one electrode and closer to the other, ergo asymmetric placement of the chromophore and would be considered an A-type rectifier. This example is also a U-type rectifier because given its zwitterionic character of the pyridinium cation being overall-charge balanced by the malononitrile anion on the other side of the molecule, the orbital coefficients closer to the cation should be larger in the LUMO of the molecule and the orbital coefficients nearer to the anion should be larger in the HOMO of the molecule. The decoupling unit here the nitrile-appended *trans*-alkene, which also is cross-conjugated with respect to the anion, donor unit. These are a few examples of rectifiers that have been studied and literature has

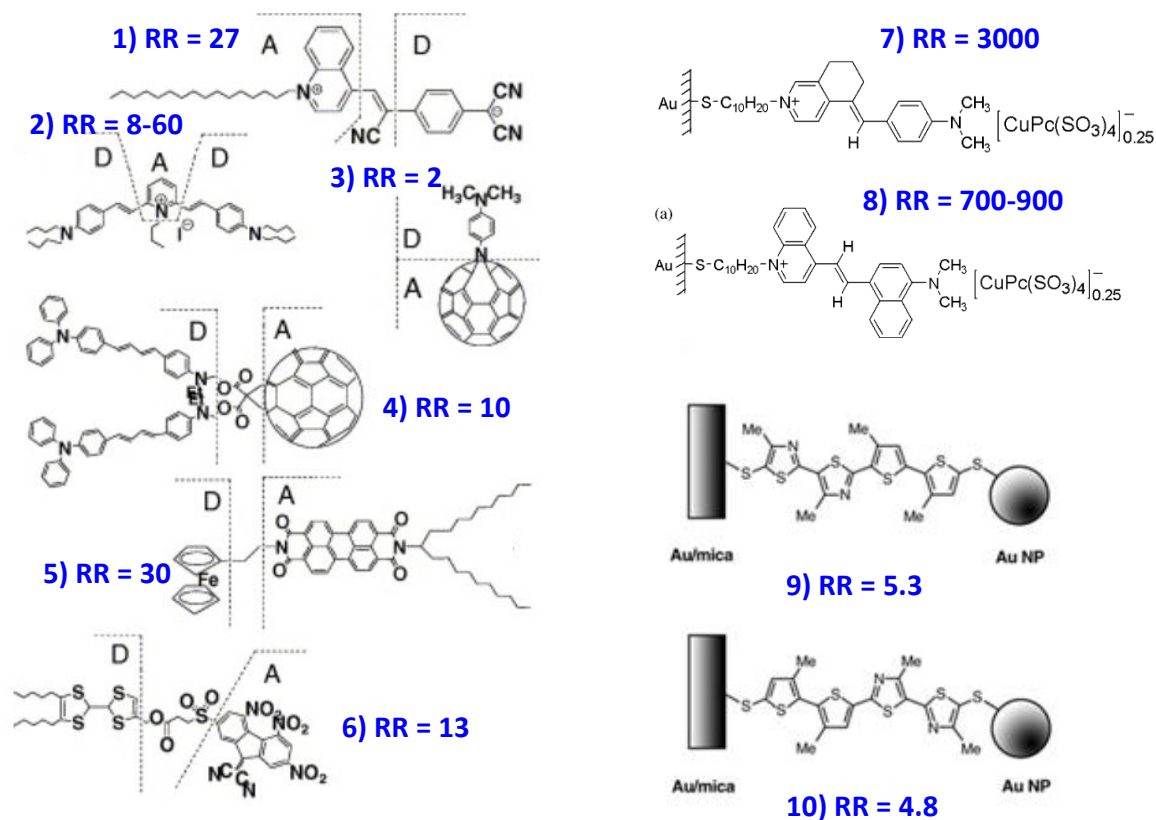


Figure IV-9. Examples of molecular rectifiers that are a compilation of S, A and U-type rectifiers and their empirically determined RRs.

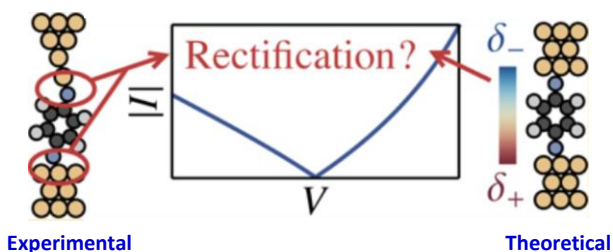
similar examples,^{5,18,19} but very few of these examples examine only one-type of rectifying behavior and currently we have found no empirical examples where only U-type molecular rectifying behavior is evaluated.

One last important point illustrated in Figure IV-9 is that many of the RRs (RR) shown in blue beside each molecule, are $< \sim 10$ with the exception of a few salts (examples 7 and 8).

IV.3.5. Challenges for Studying Molecular Rectification.

Molecular rectifiers are primarily studied either through the use of break-junction conductance studies where the rectifier is sandwiched between two gold or other metallic electrodes and under a bias, current is passed from one electrode to the other and then the bias is reversed and the current measured. These types of measurements are performed over thousands of cycles and averaged because when molecules are sandwiched between electrodes, the electrode surfaces themselves may have defects or statistically the contact geometry the rectifier makes with the electrode surface varies. Figure IV-10A illustrates this where the theoretical, idealized break-junction conductance device has two electrodes with free-from-defect surfaces and the rectifying bridge between them is binds to the surfaces in a perpendicular geometry. On the experimental side of Figure IV-10A, the electrodes are different due to a defect which would inherently change the Schottky barrier, creating an unintentional S-type rectifier, and the contact angle that the rectifying bridge makes with the two electrode surfaces is non-ideal which could unintentionally enhance current flow in one direction over the other. Contact geometry is an ongoing issue with the study of molecular rectifiers because this geometry and the preferred

A Contact Angle and Contacts on Metal Surface



B Reproducibility and Error

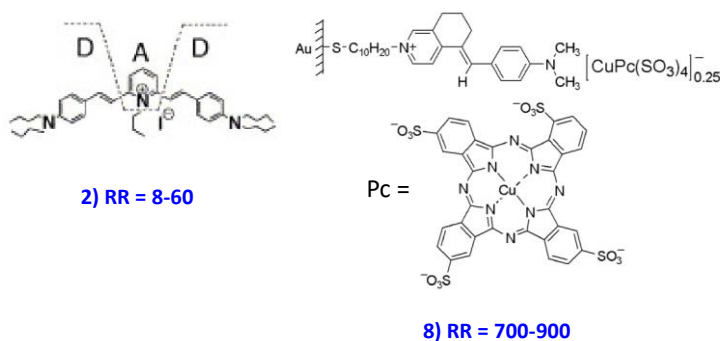


Figure IV-10. Challenges for studying molecular rectification **A)** issues with the contact angle a molecule makes with an electrode surface that itself may have defects leading to observed rectification and **B)** issues with reproducibility of rectification experiments that lead to ranges of RRs being reported.

geometry for conduction are usually unknown, and thus thousands of measurements are averaged to account for various defects and contact geometries. A final geometric problem is that the relationship between the forward and reverse biases are assessed by calculations that typically only use one, precise geometry.^{16,17} Going back to Figure IV-10A, while this experimental device might display rectifying behavior, it may not be due to the structural motif that was intended to be studied. So, how can molecular rectification be studied when there are unaccountable defects present in devices that could attenuate or enhance rectification?

Figure IV-10B demonstrates the issue of reproducibility and error by using two of the examples shown in Figure IV-9 which have RRs (RR) that span a large range of values. Example 8 is anywhere between 700-900 times greater current in one direction through the molecule

verses the other.²⁰ Example 2 is potentially more extreme since it covers nearly an order of magnitude (RR = 8-60); so at minimum this rectifier for bias versus counter bias is 8 times greater or at maximum it is 60 times greater.¹⁷ For designing molecular rectifiers to be used in a device, this is unhelpful because the device's function may be greatly altered by this large of a difference.

Another challenge for molecular rectification is that most solid-state rectifiers have $RR \sim 10^5$ whereas most molecular rectifiers have $RR \sim 10$ or less (with the exception of salts shown in Figure IV-9).

To summarize, there are three types of molecular rectifiers depending on the asymmetric unit: S, A and U-type. Most molecular rectifying devices are a mixture of these three types, but there are many examples of S and A-type. U-type rectifiers, which are considered the only "true" molecular rectifiers, are due to inherent orbital asymmetry; however, pure examples of these types of rectifiers that are void of S and A-type attributes are nearly non-existent in current literature. Also, current avenues to study molecular rectification suffers from some limitations in that for break-junction conductance studies the surface of the electrodes and the geometry of the bridging molecule are imperative to the outcome of the experiments and these are parameters are unique to each device, even variation in one device and these cannot be quantified. Consequentially, the reported RRs are averages of thousands of experiments and so reproducibility can be a problem with some RRs being reported as ranges rather than absolute numbers. Conversely, when calculations are used to evaluate these systems, precise and typically single geometries are used which may not be consistent with empirical results.

IV.4. Hetero-biradicals as models for studying orbital mechanisms of molecular rectification.

Break-junction conductance and computational studies are the most common methods for studying rectification through molecules, but as mentioned when molecules are sandwiched between two electrodes the geometry that the bridge makes with the two electrodes may not be known and may not be precise and this leads to several issues such as: 1) rectification arising from variations in contact angles, rather than the electronic structure of the molecule of interest 2) the need for many experiments that may result in large ranges for empirically-determined RRs. Aviram and Ratner's original proposed molecular rectifiers involved a donor-bridge-acceptor molecule.¹ A molecule that has an inherent bias from donor to acceptor, but which are decoupled by a bridge in order to promote molecular orbital asymmetry with the HOMO being donor-centered and the LUMO being acceptor-centered.

From Landauer's work with single molecule device conductance (g), Anderson's description of donor-acceptor electronic coupling (J) and Ratner and Nitzan's relating conductance and electronic coupling to the electronic coupling matrix element (H_{DA}^2), hetero-spin biradicals offer an opportunity to study molecular rectification in terms of exchange coupling (J), which has been shown to be proportional to H_{DA}^2 , just as conductance (g) is also proportional to H_{DA}^2 . Hetero-spin biradicals offer an opportunity to study the elusive U-type rectifiers, the "true" molecular rectifiers;^{1,16,17} those that operate due only to inherent orbital asymmetry, without the intentional or unintentional interference of S- and A-rectifier attributes. Two different, stable radicals appended to either end of a molecule will have their own inherent bias due to having SOMOs that will have different energies, which by can be analogous to the bias between two electrodes.²¹ The covalent bonds will serve as the "contact" points of the

bridging molecule to the two different radicals which serve as surrogates of biased electrodes. In this instance the two radicals will be SQ and NN and for an asymmetric bridge, synthesizing the two isomers: SQ-B-NN and NN-B-SQ would serve as the forward and reverse biases.²¹ With the SQ-B-NN motif, crystal structures are obtained for all compounds meaning that very precise geometric data is obtained and can be correlated or corrected for from previous studies^{22,23} in order to elucidate the contributions to the electronic coupling and by analogy, molecular

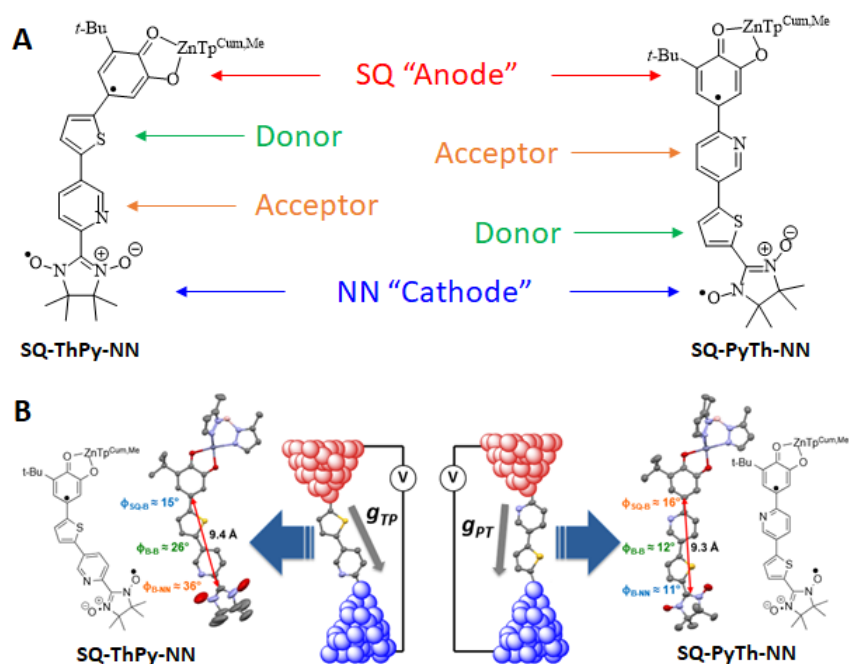


Figure IV-11. A) Redefining SQ as the “anode” and NN as the “cathode”. B) Crystal structures with torsion angles and **PyTh** being placed between the two electrodes.

rectification, of different molecules with a specific, known geometry. The first two molecules synthesized as rectifier analogs are shown in Figure IV-11A where the molecular rectifier being evaluated is the pyridine-thiophene (**PyTh** or **ThPy**). This molecule was chosen because the calculated dipole of **PyTh** is 1.94 Debye,²¹ which is one of the proposed requirements from Aviram and Ratner’s 1974 paper.¹

IV.4.1. Redefining SQ and NN as Analogs of “Cathode” and “Anode,” Respectively.

In order to discuss our SQ-B-NN biradicals in the terms that are encountered in rectification literature, we must redefine the constituents of our molecules. For a device composed of a molecular rectifier there is a donor, acceptor, a bridge, a cathode and an anode. As discussed in Chapter III, SQ-B-NN biradicals are defined as donor-bridge-acceptor molecules because the donor SQ SOMO lies higher in energy than the acceptor NN SOMO, so there is a directionality from the donor SQ to the acceptor NN.²¹ Donor and acceptors are ubiquitous for discussing rectification; however, in SQ-B-NN molecules, the SQ must be redefined as the anode and the NN as the cathode because for electrodes electrons flow from the anode to the cathode as shown in Figure IV-11A. The “donor” and “acceptor” segments of these molecules are the thiophene and pyridine, respectively, because the thiophene HOMO is higher in energy than the pyridine HOMO. Keep in mind that for rectifying devices, the direction of the bias for a strong current from Figure IV-5 is from the anode to the acceptor LUMO to the donor HOMO then to the cathode. Figure IV-11B shows **PyTh** both as the crystal structures of the biradicals showing the bond torsions between SQ-B, B-B, and B-NN as well as **PyTh** (as the dithiol) placed between an anode and cathode for electronic transport calculations.²¹

IV.5. Results from Pyridine-Thiophene SQ-B-NN.

The fitting of variable temperature magnetic susceptibility plots of **SQ-PyTh-NN** and **SQ-ThPy-NN** provided measured exchange coupling parameters of 51.2 cm^{-1} and 56.5 cm^{-1} , respectively. This results in a $RR = 0.91$ ($0.91^{-1} = 1.1$). In comparison to most of the examples from Figure IV-9, this is a very small RR and a RR of 1 would indicate no rectification. Therefore, **PyTh** seems to exhibit negligible rectification.²¹ Because of the previous work demonstrating the dependence of the exchange coupling on the torsion angles through the

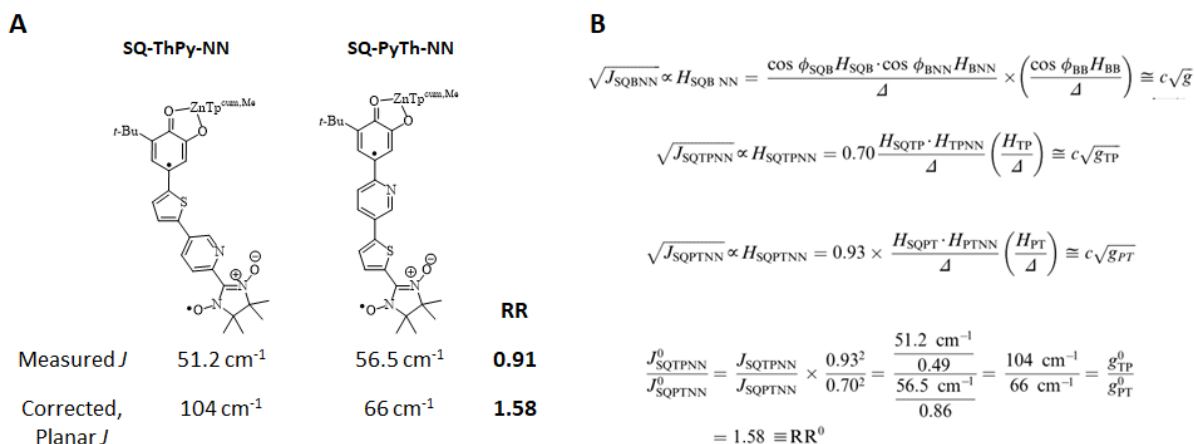


Figure IV-12. A) Data for the measured and corrected exchange coupling constants of each compound with their corresponding RRs. B) The calculation used to correct the exchange coupling constants resulting in the inversion of the RR.

molecule, the exchange coupling constants for these two compounds can be corrected to estimate the exchange coupling constants for the planar molecules.²³ When these exchange parameters are corrected, the planar forms of **SQ-PyTh-NN** and **SQ-ThPy-NN** have exchange coupling constants of +104 cm⁻¹ and +66 cm⁻¹, which gives a RR of 1.58 as shown in Figure IV-12A. This is still not a large RR when compared to the other examples from Figure IV-9, but correcting for torsion angles by a product of cosines (Figure IV-12B) resulted in an inversion of the RR: $J_{SQPyThNN}/J_{SQThPyNN} = 0.91$ vs. 1.58; indicating with torsions **SQ-ThPy-NN** is coupled more strongly than **SQ-PyTh-NN**, but in the planar molecules, the opposite is true.²¹ This study demonstrates the significant effects that torsion angles can have on the RRs.

IV.5.1. A VBCI explanation for the computed RRs and observed J values.

The resulting RR from the exchange coupling constants of the asymmetric bridge with a large dipole moment (1.94 Debye) was unexpectedly low because the large dipole moment was one of the proposed requirements for a molecular rectifier as described by Aviram and Ratner's 1974 paper. The rationale for this result can be explained in the context of the valence bond

configuration interaction (VBCI) model that is used to describe the observed ferromagnetic coupling between the SQ and NN through a conjugated, alternant hydrocarbon (Figure IV-13). The primary interaction in the VBCI model responsible for ferromagnetic coupling is the SQ SOMO \rightarrow NN-B LUMO excited configuration which configurationally mixes with the ground state. Thus, the orbital nature of the NN-B LUMO plays a critical role in the magnitude of the exchange coupling. Despite the bridge being composed of two different heterocycles, the HOMO and LUMO of **PyTh** have highly symmetric distribution of orbital coefficients in the wavefunctions at the connecting carbon atoms at both the Hückel MO theory and DFT computational levels as indicated by the purple arrows showing the connection points in Figure IV-13. Consequently, the coupling for both isomers, **SQ-PyTh-NN** and **SQ-ThPy-NN** are nearly

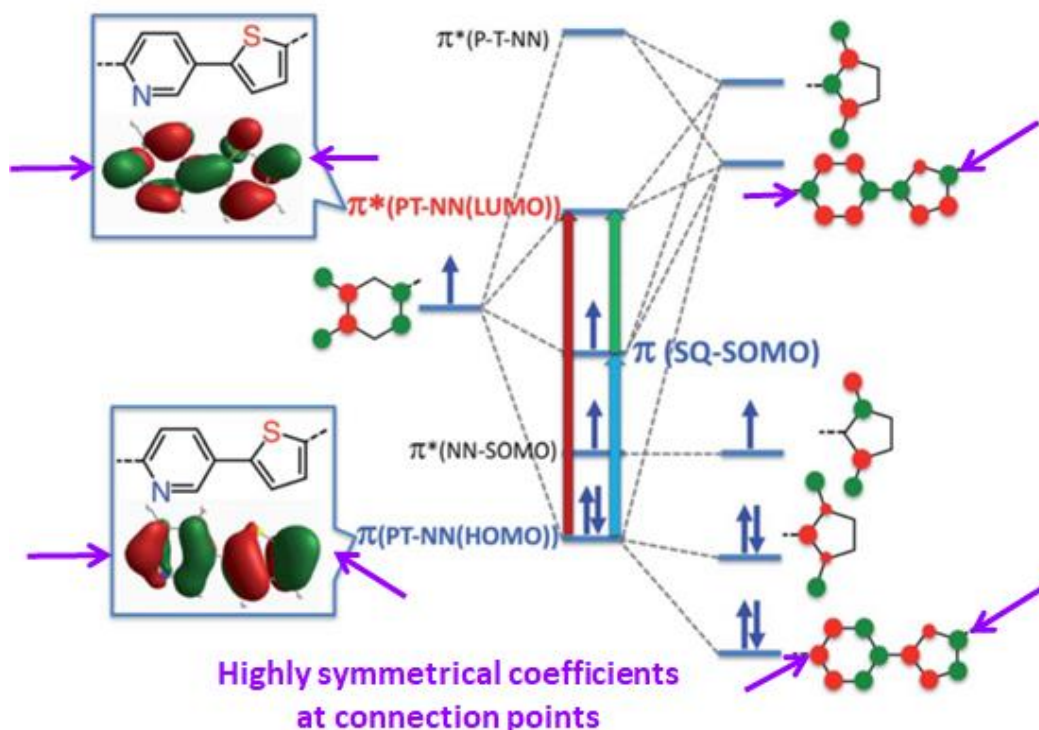


Figure IV-13. Frontier molecular orbital interactions of the VBCI model that result in a ferromagnetically coupled biradical. The purple arrows show the carbon atoms where the **PyTh** connects to the SQ and NN, which by Hückel MO theory and by DFT calculations are shown to be highly symmetric with each other in the HOMO and LUMO.

identical, and the low RR (and ratio of J -values) is attributed to the very similar orbital coefficients at the connection points.

In this initial study of utilizing hetero-biradicals to study molecular rectification, computational modelling and calculations were used to compare the observed RRs by magnetic exchange coupling parameters to computed conductance. Transport calculations on Au_{*n*}-S--**PyTh**-S-Au_{*n*} at a potential equal to the “molecular” bias ($E_{\text{bias}} = \pm E_{\text{SQ} \rightarrow \text{B-NN}}$) provided a RR for the forward and reverse biases to be 1.24 in comparison with 1.58; showing good agreement between the RRs from variable magnetic susceptibility and electron transport calculations.²¹ The orbital coefficient symmetry between the respective “donor” thiophene and “acceptor” pyridine orbitals was due to the 12° and 26° bond torsions between the two fragments were insufficient to act as the π -system decoupling unit and instead the molecular orbital of the bridging unit acted as a single donor orbital; as described by Aviram and Ratner.¹

IV.5.2. Designing U-type Rectifiers.

SQ-PyTh-NN and **SQ-ThPy-NN** did not display strong rectifying behavior as indicated by the low RRs 0.91 for the empirical and 1.58 for the “corrected,” planar molecules. Because the low RR was attributed to the similarity of the orbital coefficients, the next several attempts at designing U-type molecular rectifiers were aimed at synthesizing molecules with asymmetric LUMO coefficients at the SQ-B and B-NN connecting carbon atoms, and lacked a strong dipole.

IV.6. Torsional Rectifiers.

Our initial introduction into molecular rectification with **PyTh** resulted in a low RR due to the torsion angle between the pyridine and thiophene not being great enough to effectively decouple them from each other resulting in the linear combination of their orbitals to act as a

single donor orbital due to the lack of a π -system decoupling unit, as described by Aviram and Ratner while dictating the necessary structural features for a molecular rectifier.¹

IV.6.1. Large Bond Torsions to Facilitate Decoupling.

Several groups have investigated computationally the effect that adding torsion angles into a molecule which is bridging two electrodes will have on the conductance and the rectifying behavior of the device.^{2,3,24,25} Xia, et al. investigated a donor-bridge-acceptor molecule comprised of tetramethylbenzodioxole (TMDO) as the donor, tetracyanobenzene (TCNB) as the acceptor, and a phenyl bridging the two, between two gold electrodes as shown in Figure IV-14A.²⁵ For their computational studies they studied the effect of rotating each of the three constituents out of plane by either 30, 60, or 90° (Figure IV-14B) with the rest of the molecule. Figure IV-14C shows the results of the RRs for the forward and reverse biases for each case where the donor, bridge, or acceptor was rotated out of plane by the specified angle. TMDO-Ph-

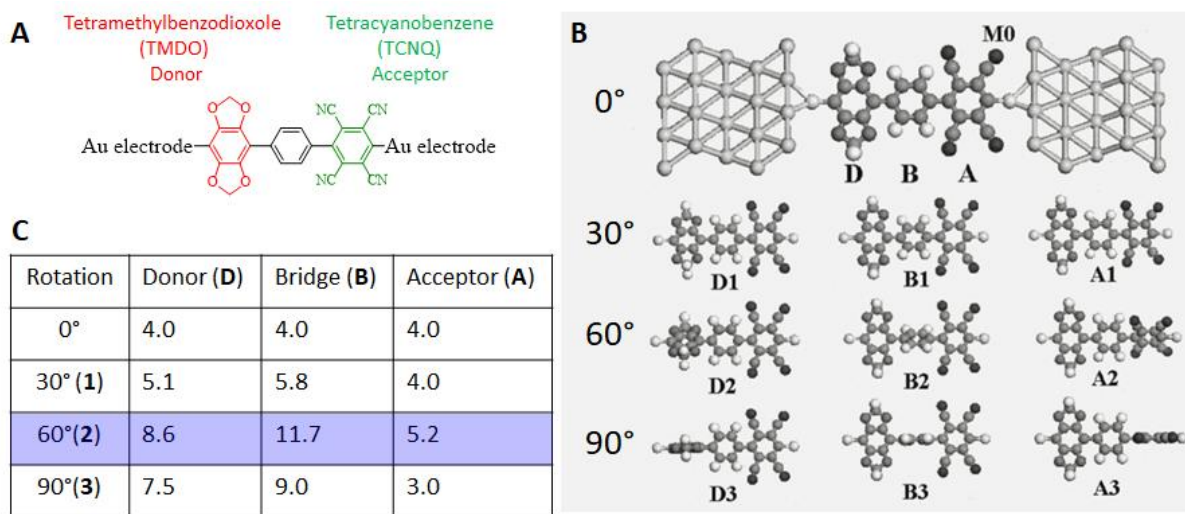


Figure IV-14. Computational studies performed by Xia et al. on a molecular rectifier composed of a tetramethylbenzodioxole donor, a phenyl bridge, and a tetracyanobenzene (TCNB) acceptor. **A**) the schematic of TMDO-Ph-TCNB placed between two gold electrodes. **B**) Computational models of the rectifying device with the donor, bridge, and acceptor each in turn rotated out of the plane of the molecule by 30, 60, or 90°. **C**) The resulting RRs from the electron transport calculations performed on the models in **B**).

TCNB is already a molecular rectifier possessing the donor and acceptor pieces and a dipole, so the baseline calculation is for the completely planar molecule which results in a RR of 4.0 as shown in the first row of the table in Figure IV-14C. The thing to note about their data is that the greatest modulation of RRs occurred at 60° rotation. Logically, the greater the rotation the less planar the molecule is and thus the more the donor and acceptor fragments will become decoupled, but as the angle proceeds past a certain point, the advantageous effect of the rotation begins to become diminished. As Aviram and Ratner pointed out, if the donor and acceptor become completely decoupled, the molecule will not display rectifying behavior. To this end, it is interesting to note, that at 90° for the TCNQ acceptor, the calculated RR is lower than the planar molecule. The other thing to point out is that for each angle they modeled, the rotation of the bridging unit had the greatest effect on the RR with the greatest modulation at 60° with a RR of 11.7. These results underscore the impact that torsions can have for a molecular rectifier and

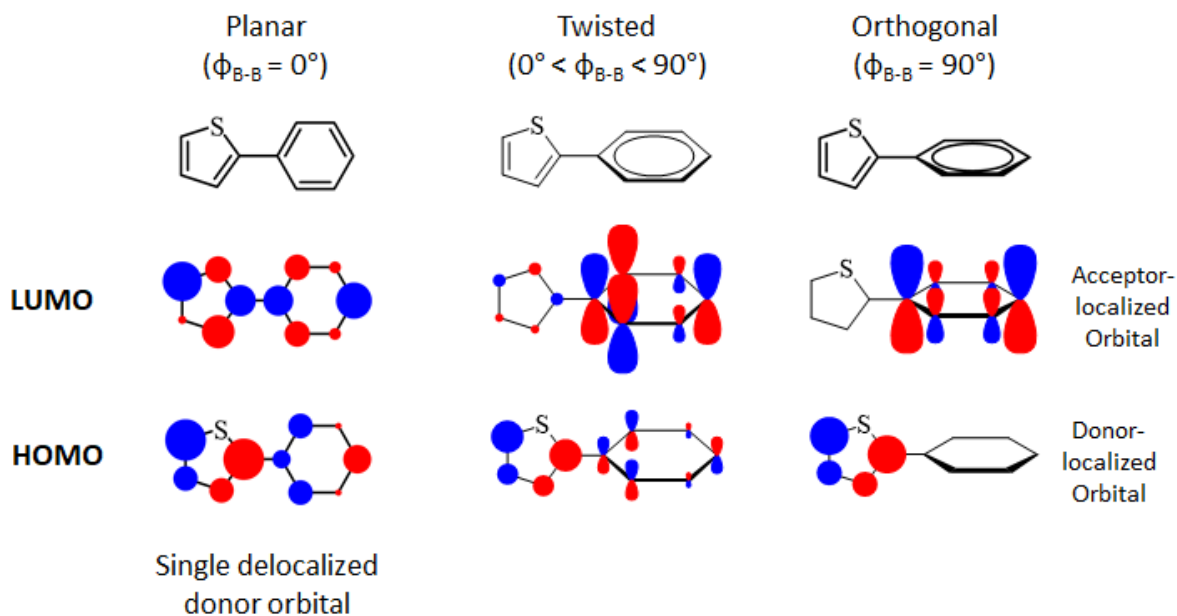


Figure IV-15. Proposed molecular rectifier: thiophene donor-phenyl acceptor dyad and the qualitative effect that torsion angle will have on the delocalization of the donor and acceptor orbitals in the HOMO and LUMO.

that it is the internal torsion angles of the bridge that have the greatest effect on the conductance through the device.²⁶

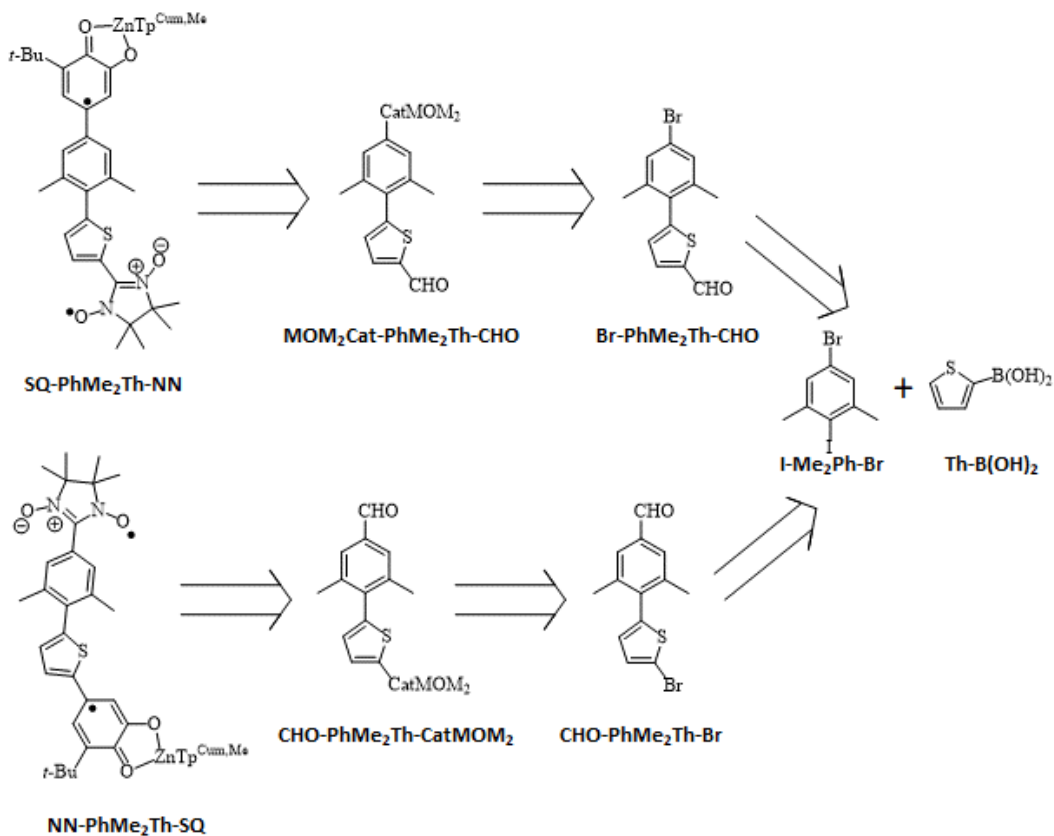
IV.6.2. Theory and Hypothesis.

In order to effect rectification in **PyTh**, we need to introduce some (less than 90°) rotation between the pyridine and thiophene rings as shown in Figure IV-15. The next set of molecules designed swapped the pyridine acceptor to phenyl in order to facilitate the available synthetic pathway. As indicated by previous studies²⁵, the planar molecule has a fully delocalized HOMO and LUMO which is a linear combination of the donor and acceptor constituent orbitals. As the molecule begins to get rotated between 0 and 90° as shown in Figure IV-15, the HOMO of the molecule begins to look more like the donor's HOMO and less like the acceptor and the LUMO begins to look more like the acceptor and less like the donor. Their π -systems are approaching decoupled, but are still conjugated to allow current flow or in this case exchange coupling. Finally, when the donor and acceptor are rotated to 90°, their π -systems are orthogonal and the HOMO is donor-localized and the LUMO is acceptor-localized. It should be mentioned that no quantitative conclusions should be drawn from the diagrams in Figure IV-15 because the planar molecule is based upon Hückel molecular orbital calculations as are the twisted and orthogonal models which are merely meant to be qualitative to illustrate the effect of rotation.

IV. 6.3. Synthesis of proposed SQ-PhMe₂Th-NN and NN-PhMe₂Th-SQ rectifiers.

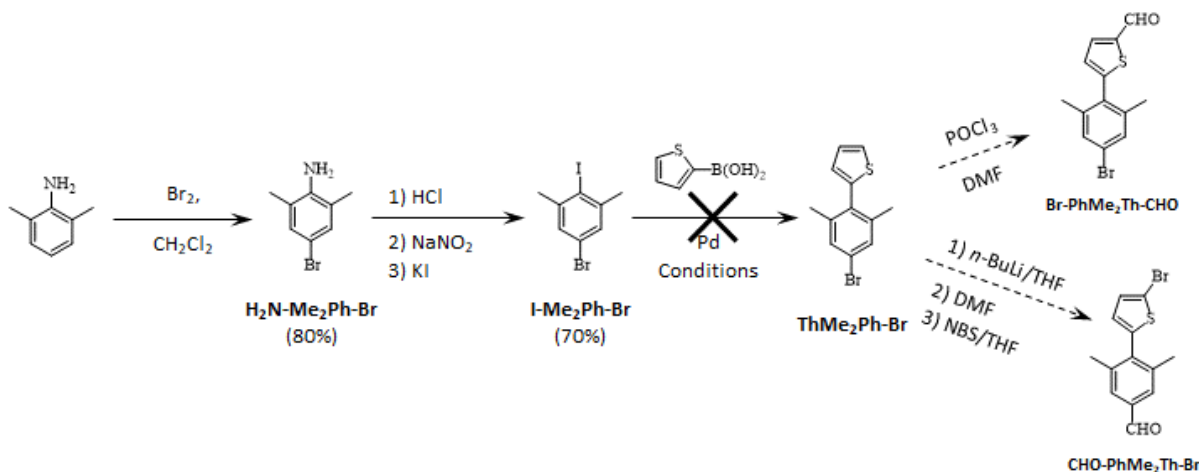
The two proposed molecules, **SQ-PhMe₂Th-NN** and **NN-PhMe₂Th-SQ**, to achieve rectification through twisting the thiophene and phenyl ring out of plane with each other are shown in Scheme IV-1 with their proposed retrosynthetic routes. In these molecules, methyl groups on either side of the phenyl-thiophene bond are used to twist the thiophene ring out of plane with the phenyl ring. The retrosynthesis is very familiar to the general synthetic pathway for all currently synthesized SQ-B-NN biradicals introduced in Chapter III, where the biradical is accessible in four steps from MOM₂Cat-B-CHO, which comes directly from a Suzuki coupling of MOM₂CatBpin with halo-bridge-aldehyde (X-B-CHO). The original method to arrive at Br-B-CHO for both isomers had common starting materials: 5-bromo-2-iodo-1,3-dimethylbenzene (**I-**

Scheme IV-1. Proposed retrosynthetic pathway for **SQ-PhMe₂Th-NN** and **NN-PhMe₂Th-SQ**.



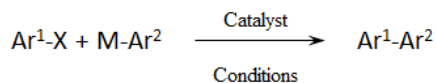
Me₂Ph-Br) and 2-thienylboronic acid (**Th-B(OH)₂**). To this end, **Th-B(OH)₂** is commercially available, but **I-Me₂Ph-Br** must be synthesized according to Scheme IV-2 by the bromination of 2,6-dimethylaniline, followed by diazotization-iodination. From here, **I-Me₂Ph-Br** is Suzuki coupled with **Th-B(OH)₂**, with the intent that the aryl iodide is the more reactive leaving group. However, this reaction did not produce the desired product, nor any other product; only starting material was present. Several attempts were made with different reaction conditions which are displayed in entries 1-6 of Table IV-1. Entry 2 and 3 tried to use the thienyl pinacol boronic ester (**Th-Bpin**) in with the hypothesis that the boronic acid did not have sufficient solubility to react

Scheme IV-2. Original synthesis with a common intermediate for both biradicals.



in the 25% H_2O /toluene mixture and entry 3 attempted using a more reactive catalyst Pd(dppf)Cl_2 , as well; both reactions failed. Entry 4 continued with the solubility hypothesis and tried THF and H_2O mixture, but this was not the issue. Entries 5 and 6 attempted Kumada coupling reactions by making the Grignard reagent of 2-bromothiophene (**Th-MgBr**) and using

Table IV-1. Attempted palladium-mediated cross-coupling conditions.



Entry	Aryl Halide (Ar ¹ -X)	Metal coupling unit M-Ar ²	Conditions	Result
1 ^a	I-Me₂Ph-Br	Th-B(OH)₂	Pd(PPh ₃) ₄ , Na ₂ CO ₃ Bu ₄ NBr, 25% H ₂ O/ toluene	No Reaction
2 ^a	I-Me₂Ph-Br	Th-Bpin	Pd(PPh ₃) ₄ , Na ₂ CO ₃ Bu ₄ NBr, 25% H ₂ O/ toluene	No Reaction
3 ^a	I-Me₂Ph-Br	Th-Bpin	Pd(dppf)Cl ₂ , Na ₂ CO ₃ Bu ₄ NBr, 25% H ₂ O/ toluene	No Reaction
4 ^a	I-Me₂Ph-Br	Th-B(OH)₂	Pd(PPh ₃) ₄ , Na ₂ CO ₃ 25% H ₂ O/ THF	No Reaction
5 ^a	I-Me₂Ph-Br	Th-MgBr	Ni(dppp)Cl ₂ , THF	No Reaction
6 ^a	I-Me₂Ph-Br	Th-MgBr	Pd(PPh ₃) ₄ , THF	No Reaction
7 ^b	RN₃-PhMe₂Br	Th-B(OH)₂	Pd(PPh ₃) ₄ , Na ₂ CO ₃ Bu ₄ NBr, 25% H ₂ O/ toluene	No Reaction
8 ^c	I-Me₂Ph-CHO	Th-B(OH)₂	Pd(PPh ₃) ₄ , K ₃ PO ₄ 25% H ₂ O/ THF	No Reaction
9 ^b	RN₃-PhMe₂Br	Th-B(OH)₂	PEPPSI- <i>i</i> Pr ^d , base ^e , solvents ^f	No Reaction
10 ^b	RN₃-PhMe₂Br	Th-Bpin	Pd(dppf)Cl ₂ , Na ₂ CO ₃ Bu ₄ NBr, 25% H ₂ O/ toluene	46, 51%

^a Substrates from **Scheme IV-4**

^b Substrates from **Scheme IV-6**

^c Substrates from **Scheme IV-7**

^d PEPPSI-*i*Pr was prepared by literature procedure of Organ, M. et al.

^e bases attempted were Na₂CO₃ and K₂CO₃

^f Solvents were 25% H₂O/toluene, 25% H₂O/THF, and *i*-PrOH

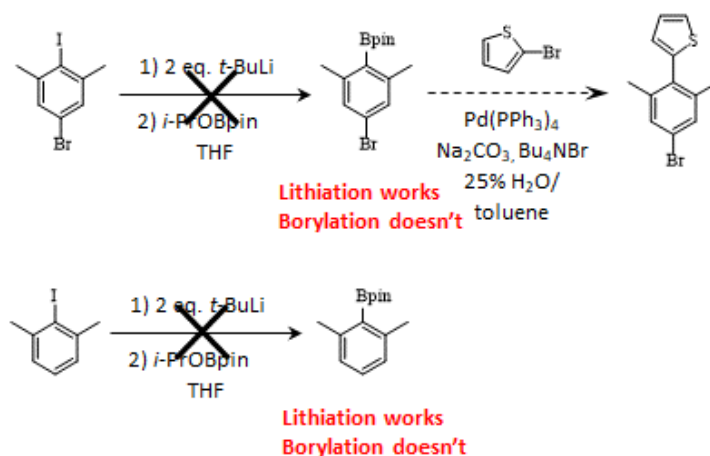
two different catalysts: Ni(dppp)Cl₂ and Pd(PPh₃)₄ for entries 5 and 6, respectively. Given that changing the metal-aryl compound did not have any effect on the reaction, attention shifted from the thiophene to the aryl halide.

Scheme IV-3 sought to swap the molecules that were the aryl halide and the aryl-metal and so **I-Me₂Ph-Br** was attempted to be lithium-halogen exchanged using *tert*-butyl lithium and then quenching with *i*-PrOBpin. The desired product was not formed, but instead ¹H-NMR

revealed that the iodide had been removed as intended and then protonated. Just to ensure there were no issues with attempting to do this with a dihalide, the same reaction was performed on 2-iodo-1,3-dimethylbenzene which had the same result. This seemed to indicate that there was some issue with having the aryl iodide between two methyl groups.

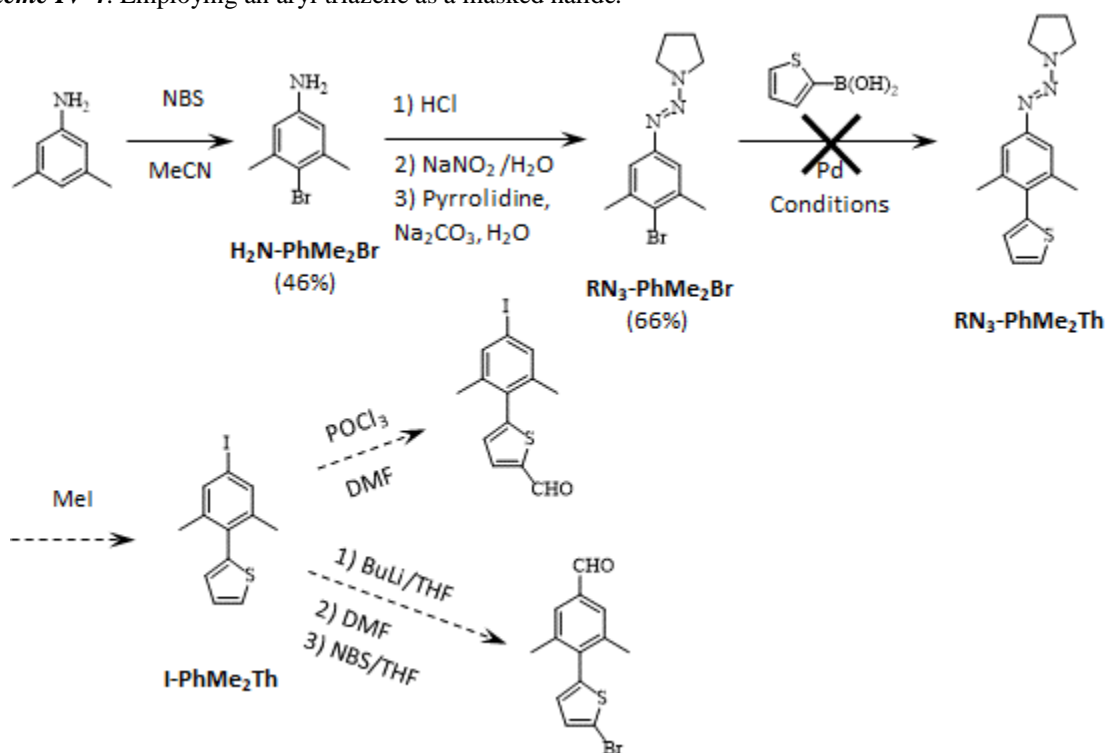
Aryl iodides are known to have peculiar behavior in Suzuki couplings and tend to result in much lower yields and reactivity at milder temperatures than aryl bromides, so the next strategy was to have the aryl halide be a bromide.²⁷ Scheme IV-4 started by brominating 3,5-dimethylaniline at the 4-position with NBS, which only provided a 46% yield after several

Scheme IV-3. Lithium-halogen exchange followed by borylation with *i*-PrOBpin.



recrystallizations from hexanes due to the presence of the 2-brominated and di-brominated side products. This route employs an aryl triazene to serve as a kind of protected-halide during the cross-coupling and then the triazene can be decomposed and replaced with an iodide for a future cross-coupling. The conversion of the aniline (**H₂N-PhMe₂Br**) to the aryl triazene (**RN₃-PhMe₂Br**) is accomplished via diazotization, then quenching with a secondary amine in the presence of base. The triazene precipitates and can be collected via filtration, followed by recrystallization from ethanol by using literature procedures as a reference.²⁸ However, the cross-coupling presented in Table IV-1 entry 7 still only provided the starting materials.

Scheme IV-4. Employing an aryl triazene as a masked halide.



Hypothesizing that the electronics of the aryl halide was not conducive to oxidative addition because no reactions were occurring, Scheme IV-5 was introduced to make a less electron-rich aryl halide; thus weakening the C-X bond for oxidative addition to the palladium by making **I-Me₂Ph-CHO**. Unfortunately, this scheme would only give one of the desired biradicals, but if it was successful, it may provide insights to facilitating one of the previous discussed schemes or a new scheme to access the other isomer. **I-Me₂Ph-CHO** needed to be synthesized and was done so from **H₂N-Me₂PhBr** by converting the aniline to the aryl triazene (**RN₃-Me₂PhBr**), which then underwent lithium-halogen exchange and quenching with DMF to give the corresponding aldehyde (**RN₃-Me₂Ph-CHO**). The triazene was then decomposed and replaced with an iodide which provided only 33% yield in iodomethane in an oil bath at 130 °C for 24 h, but a 51% yield in an oil bath at 70 °C for 48 h; either way, the Suzuki coupling still did not work as shown in Table IV-1 entry 8.

Scheme IV-5. Attempted cross-coupling with a less electron-rich substrate.

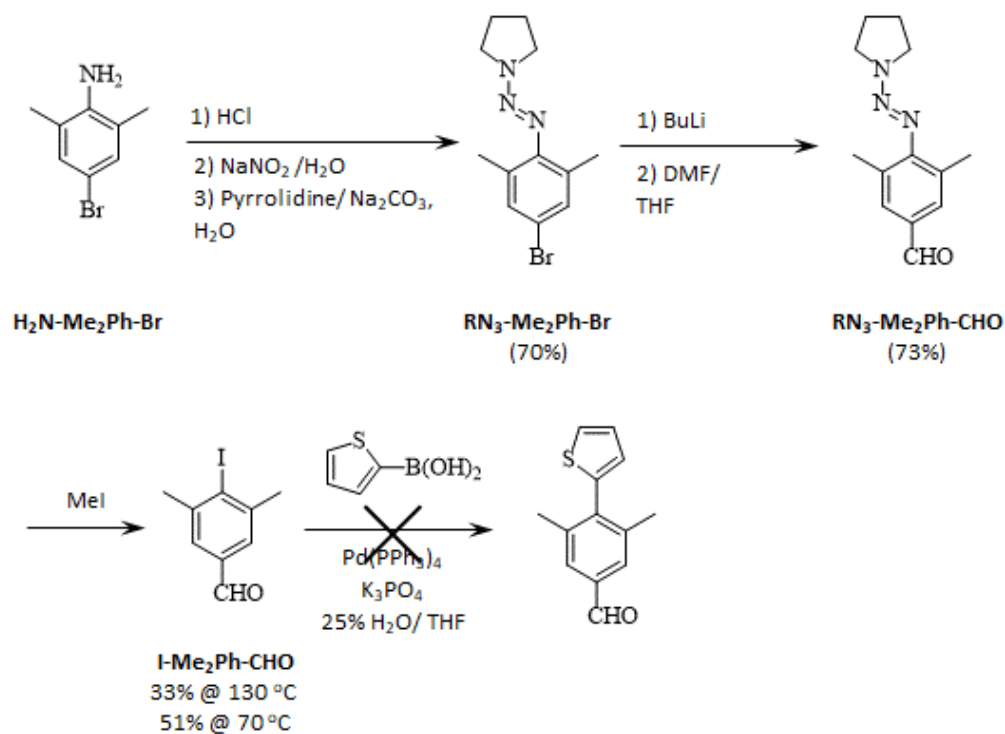


Table IV-1 entry 9 is actually composed of six trials with different solvents and bases, none of which worked, but this entry attempted using the PEPPSI-*i*Pr catalyst prepared by Organ, M. et al. which has been reported as a highly reactive catalyst for difficult substrates, such as those that are sterically-encumbered or have low reactivity such as aryl chlorides.^{29,30} While the synthesis of the PEPPSI-*i*Pr catalyst is fairly straightforward and high-yielding, it was not an effective catalyst for this transformation.

Through trial and error, Table IV-1 entry 10, which follows Scheme IV-4 with aryl triazene ($\text{RN}_3\text{-PhMe}_2\text{Br}$) and **Th-Bpin** with Pd(dppf)Cl_2 produced a successful synthesis of $\text{RN}_3\text{-PhMe}_2\text{Th}$, albeit in 46 and 51% yield over two trials. Despite the yield, the reaction was reproducible and producing pure product after column chromatography. This particular cross-coupling reaction had some other oddities to it as well even after it was successfully making the product. For example, it did not seem to matter how much **Th-Bpin** was used because it would

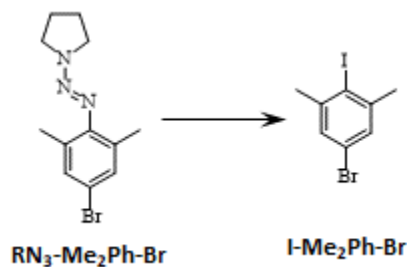
always be consumed and leave no trace on crude $^1\text{H-NMR}$ or TLC. This actually exploited because the reaction could be run with 1.2-1.5 eq. of **Th-Bpin** to ensure full conversion of **RN₃-PhMe₂Br** to the coupled product (**RN₃-PhMe₂Th**), the latter two were nearly coincident in a variety of TLC conditions. It is assumed that under the conditions of the Suzuki coupling, **Th-Bpin** is not very stable and the excess was decomposing into something that was either volatile and evaporated during the work-up, did not run on TLC or was taken into the aqueous layer during extraction. Another peculiarity was the dependence of the yield on the amount of phase-transfer catalyst (Bu_4NBr) used. Every other cross-coupling in this document that uses Bu_4NBr used 0.1 eq., which worked quite well, but when 0.1 eq. were used this cross-coupling's yields of **RN₃-PhMe₂Th** were 46, 51 and 23%, but if 0.05 eq. of Bu_4NBr were used the yields of **RN₃-PhMe₂Th** were 66, 81 and 82%.

The next synthetic issue was one that was subtly introduced in Scheme IV-5 as the effective decomposition of aryl triazenes into their corresponding aryl iodides. The first two trials from Scheme IV-5 resulted in 33 and 51% yields by stirring for 24 h at 130 °C and 48 h at 70 °C, respectively. The best yielding (> 90%) of these types of reactions are performed with iodomethane with iodine sometimes added and in sealed tubes for 16 h or more. Sealed tubes are necessary because iodomethane boils at 42 °C and most of these reactions are run above 100 °C; therefore, a significant amount of pressure must accumulate inside the reaction vessel in order to allow the temperature to proceed so high above the boiling point, which means it is difficult to know the actual reaction temperature. It is quite conceivable that in both trials of Scheme IV-5, neither were at the correct temperature and that could be the origin of the lower yields. The question was how to get the temperature high enough in a low boiling point solvent. Sometimes higher boiling point solvents, such as diiodomethane are used to achieve these higher

temperatures, but then it must be removed. **RN₃-Me₂PhBr** was used as a test compound in Table IV-2 which attempted various temperatures in iodomethane for entries 1,3-5, tetrachloroethane for entry 2 and with iodine present for entries 2-5. Entries 3 and 5 resulted in decent yields of 69 and 65%, but nowhere near the reported > 90% for some substrates.³¹⁻³⁵

Hypothesizing that insufficient temperature was still the issue, the thought that was using the microwave reactor, which possesses an IR thermometer to determine the temperature and will continuously irradiate the reaction with microwaves to keep the reaction at the specified temperature, could be the solution. Other benefits to microwave irradiation is that this reaction mechanism is dependent on the decomposition of the triazene liberating the aryl radical that

Table IV-2. Test aryl triazene conversion to aryl iodide.



Entry	Solvent	Reagents	Temp. (°C)	Time	Yield
1	Mel		130	12 h	44%
2	C ₂ H ₄ Cl ₂	I ₂	90	16 h	41%
3	Mel	I ₂	120	14 h	69%
4	Mel	I ₂	50	15 h	30%
5	Mel	I ₂	130	18 h	65%
6	Mel	I ₂	120 (μwave)	30 min	98%
7	Mel	I ₂	120 (μwave)	10 min	98%
8	Mel		120 (μwave)	10 min	Incomplete
9	Mel		120 (μwave)	30 min	98%

forms a bond with an iodide from either molecular iodine or the solvent.²⁸ Heating in an oil bath is a form of conductive heating. The energy must be transferred from the hot plate to the oil bath through the glass of the sealed tube to the iodomethane solvent and then to the aryl triazene. In radiative heating with microwaves, the aryl triazene can have energy transferred to it directly, dependent on its dipole. Entries 6-9 show the advantage of using the microwave irradiation for the decomposition of aryl triazenes to synthesize their corresponding aryl iodides. For the test compound, **RN₃-Me₂PhBr**'s conversion to **I-Me₂PhBr**, 10 minutes in the microwave with iodomethane and iodine at 120 °C was all that was necessary to obtain a 98% yield after elution through a silica pad with hexanes. The test reaction could be complete in 30 minutes at 120 °C in the absence of iodine with only the solvent as the iodine source with the same yield (entry 9).

Table IV-3 shows the results when this procedure was attempted on the conversion of the desired substrate (**RN₃-PhMe₂Th**) to the corresponding aryl iodide (**I-PhMe₂Th**). As can be seen by entries 1 and 2, the same temperature (120 °C) and even longer time than that used in Table IV-2 entry 9 that produced a 98% yield of the test compound was insufficient for the conversion of **RN₃-PhMe₂Th** to **I-PhMe₂Th**. Only after iodine was included and the temperature was increased to 130 °C did the reaction complete and provide the same yield. It was found that further increasing the temperature to 150 °C allowed for the exclusion of molecular iodine as a reagent and allowed iodomethane to function as the iodine source and provide a 99% yield after elution through a silica pad with hexanes.

Scheme IV-6 shows the finalized conditions for the synthesis of the common intermediate, **I-PhMe₂Th**, to the synthesis of both biradicals and the first two steps of the divergent syntheses to their respective biradicals. A few other modifications were made to the synthetic procedure which are worth mentioning, but not discussing in great detail. First, the bromination of 3,5-dimethylaniline that provided a 46% yield and provided the *ortho*-brominated and di-bromo side products, greatly benefitted from a three-step procedure to **H₂N-PhMe₂Br**, rather than a single bromination step with NBS. The highly active ring due to the aryl amine was deactivated by first protecting the amine with an acetate via acetic anhydride in the presence of Et₃N, then brominating with NBS in MeCN at room temperature, followed by hydrolysis of the

Scheme IV-6. Synthesis of the common intermediate and the beginning of the divergent syntheses.

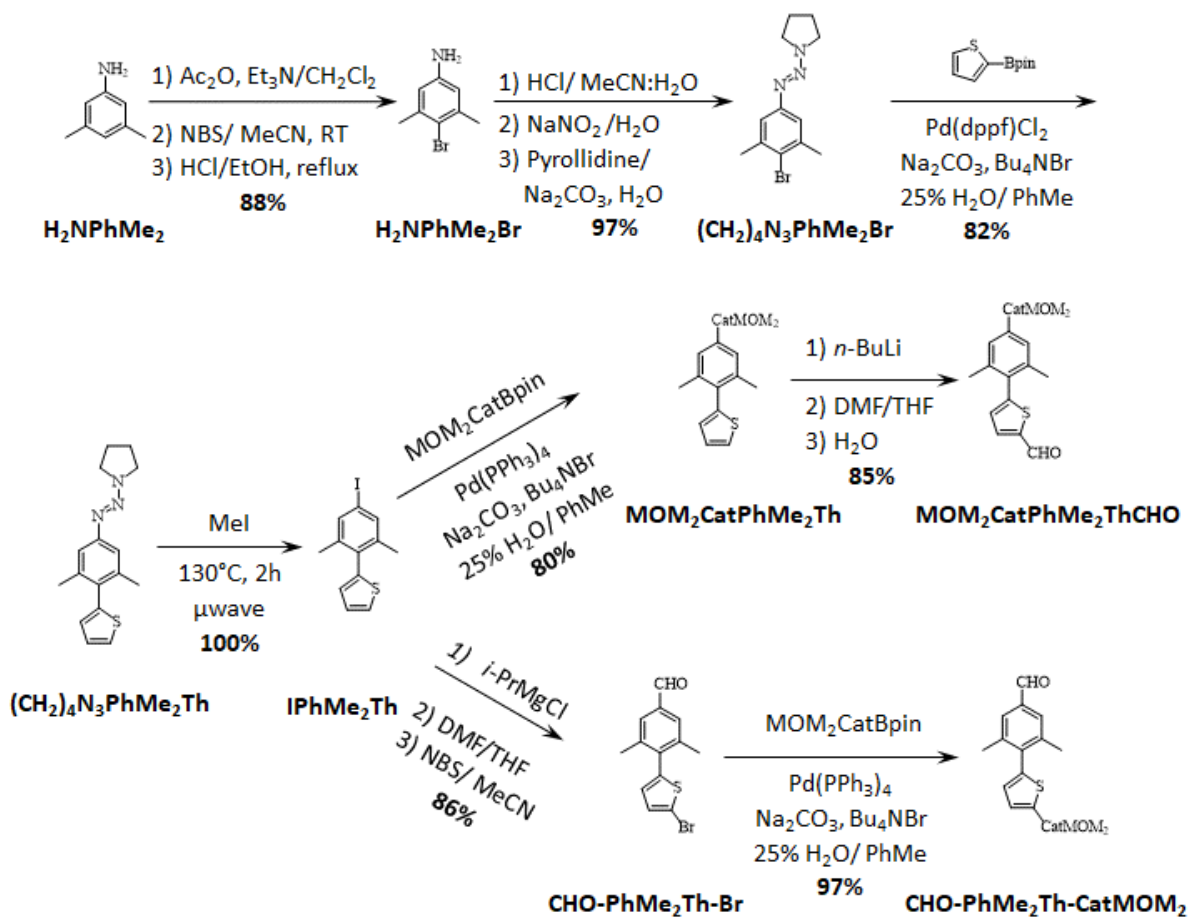
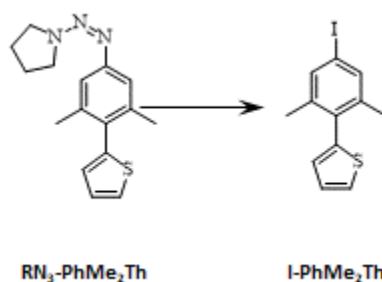


Table IV-3. Aryl triazene (**RN₃-PhMe₂Th**) conversion to aryl iodide (**I-PhMe₂Th**).



Entry	Solvent	Reagents	Temp. (°C)	Time	Yield
1	MeI		120 (μwave)	45 min	Incomplete
2	MeI		120 (μwave)	1.25 h	Incomplete
3	MeI	I ₂	130 (μwave)	30 min	98%
4	MeI		150 (μwave)	30 min	99%

acetate group in alcoholic HCl at reflux to give the desired product pure after filtration and work-up with NaOH in an 88% yield. Second, the synthesis of aryl triazenes from their corresponding anilines was discovered to be greatly improved by employing a 1:1 MeCN:H₂O mixture as the solvent during the initial diazotization step which facilitated the solubility of the resulting diazonium salt, and then pouring the diazonium salt solution into chilled, pyrrolidine and excess Na₂CO₃ in 3x the diazonium salt solution's volume of water. This last step results in the precipitation of pure aryl triazene as a solid and pyrrolidine is a better choice for the secondary amine than diisopropylamine or diethylamine because its aryl triazenes tend to be solids, rather than the possibility of oils that other secondary amines can make. Regardless the yield for the synthesis of the aryl triazene (**RN₃-PhMe₂ThBr**) was increased from 66% to 98%. Otherwise the Suzuki coupling and aryl triazene conversion to aryl iodide, **I-PhMe₂Th**, were performed as discussed.

From **I-PhMe₂Th**, the synthetic schemes diverge toward their respective biradicals. The original plan was to employ a Vilsmeier-Haack reaction to install an aldehyde directly onto the

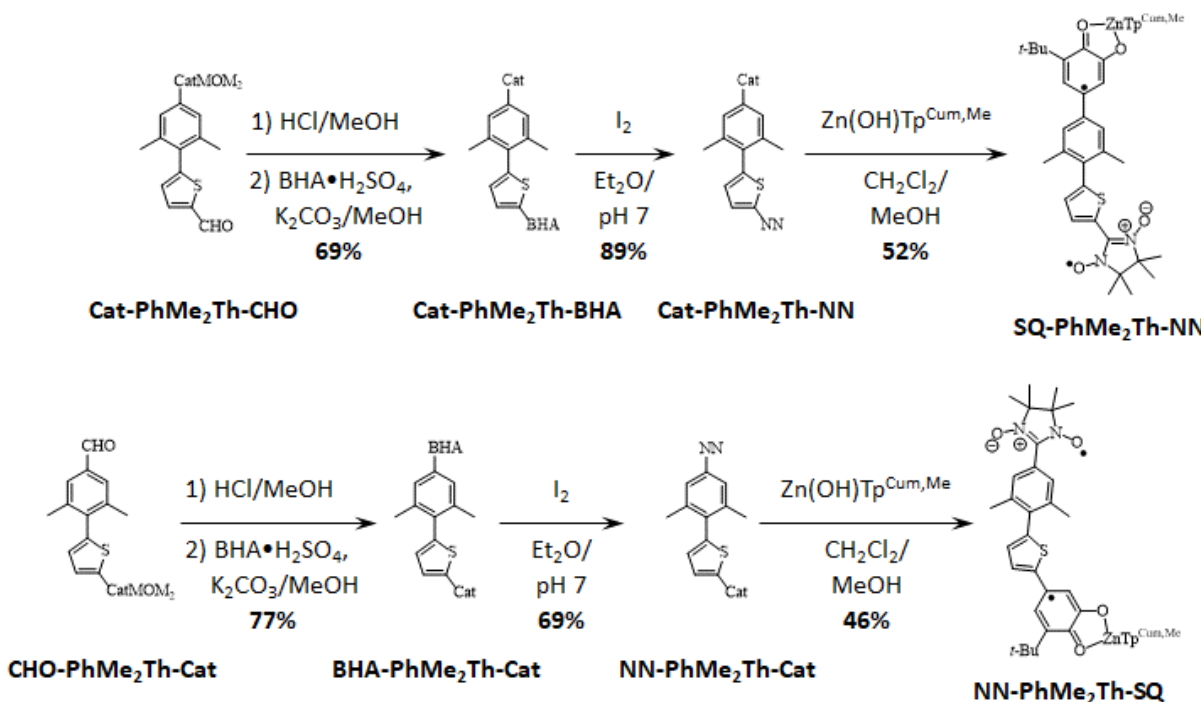
thiophene ring at the electron-rich 5-position to get **I-PhMe₂Th-CHO**; fitting the motif X-B-CHO which is a common intermediate in SQ-B-NN biradical syntheses. However, after multiple attempts and the same Vilsmeier-Haack reagents successfully formylating another substrate (azulene) in > 80% yield, it was decided that **I-PhMe₂Th** was unreactive under these conditions. Instead **I-PhMe₂Th** was taken directly into a Suzuki coupling with MOM₂CatBpin to make **MOM₂Cat-PhMe₂Th** and then this compound had its thiophene 5-position deprotonated with *n*-BuLi and quenched with DMF to afford **MOM₂Cat-PhMe₂Th-CHO**. An important intermediate for the synthesis of **SQ-PhMe₂Th-NN**.

As may be noted, for the Suzuki coupling, Pd(OAc)₂ was used as the pre-catalyst rather than a more traditional Pd(PPh₃)₄, Pd(dppf)Cl₂ or Pd(PPh₃)₂Cl₂. This is because and was noticed that Suzuki couplings with aryl iodides displayed sluggish/poor reactivity, variable yields, and/or the generation of side products. Ho et al. investigated the reactivity of aryl bromides and aryl iodides in Suzuki couplings under various conditions and with different palladium catalysts, they discovered that aryl bromides worked well under a variety of conditions, but aryl iodides performed similarly as described above when in the presence of phosphine ligands.²⁷ Two methods for avoiding these issues were to perform the reactions at higher temperatures above 100 °C to restore reactivity or use catalysts that did not have phosphine ligands. Given reaction solvents that are still easily removed and the formation of azeotropes of some with water, it was difficult to get the reaction temperature high enough to give good reactivity and was much easier to use Pd(OAc)₂ in H₂O/THF at milder temperature. H₂O/THF is the preferred solvent for the substrates presented in this document when using Pd(OAc)₂ because using H₂O/toluene mixtures results in very little conversion due to palladium plating out on the sides of the flask. THF probably stabilizes the active catalyst that Pd(OAc)₂ forms.

Along path of the synthesis of **NN-PhMe₂Th-SQ**, **I-PhMe₂Th** is first converted to **CHO-PhMe₂Th** by employing magnesium-halogen exchange with *i*-PrMgCl and then quenching with DMF. Magnesium-halogen rather than lithium-halogen exchange was used for this conversion because as was mentioned above during the synthesis of **MOM₂Cat-PhMe₂Th-CHO**, butyl lithium was used to deprotonate the thiophene, the Grignard reagent is milder and selectively undergoes the magnesium-iodide exchange without any side products to give **CHO-PhMe₂Th**. This compound is pure enough and is taken directly into the bromination with NBS in MeCN to give the key intermediate, **CHO-PhMe₂-Br** in 86% overall yield. From here it was Suzuki coupled with MOM₂CatBpin to give **CHO-PhMe₂Th-CatMOM₂** in 90% yield.

Now, the syntheses of both biradicals are to **MOM₂Cat-B-CHO**, the final steps of the reaction are shown in Scheme IV-7. The steps for both syntheses follow standard procedures, first the methoxymethyl groups are deprotected by catalytic HCl in methanol, followed by

Scheme IV-7. The final steps to the synthesis of **SQ-PhMe₂Th-NN** and **NN-PhMe₂Th-SQ**.



condensation of the aldehydes with BHA•H₂SO₄ with K₂CO₃ in methanol to give Cat-B-BHA. The NN monoradicals are made by oxidation of the previous compound by titration with I₂ in diethyl ether with 1 M pH 7 phosphate buffer. Finally, the Cat-B-NNs are complexed with Zn(OH)Tp^{Cum,Me} and then aerial oxidized to the corresponding SQ to give the biradicals: **SQ-PhMe₂Th-NN** and **NN-PhMe₂Th-SQ**.

IV. 6.4. Results and Conclusions.

Crystallography. Figure IV-16 shows the crystal structures of **SQ-PhMe₂Th-NN** and **NN-PhMe₂Th-SQ**. Most notably in the crystal structures of the torsional rectifiers is the large intra-bridge torsion between the thiophene and the dimethylphenyl of 82 and 68°. This was somewhat concerning because from our own studies the exchange coupling decreases with increased torsion angle²³ and as Aviram and Ratner stated that a donor and acceptor that have been completely decoupled will not display any rectification.¹ So with a potentially small difference between exchange coupling constants and due to the large torsion angles it was questionable how much greater than 1 the rectification ratio would be. It was however, convenient that the other torsion angles between the SQ-bridge and NN-bridge were comparable

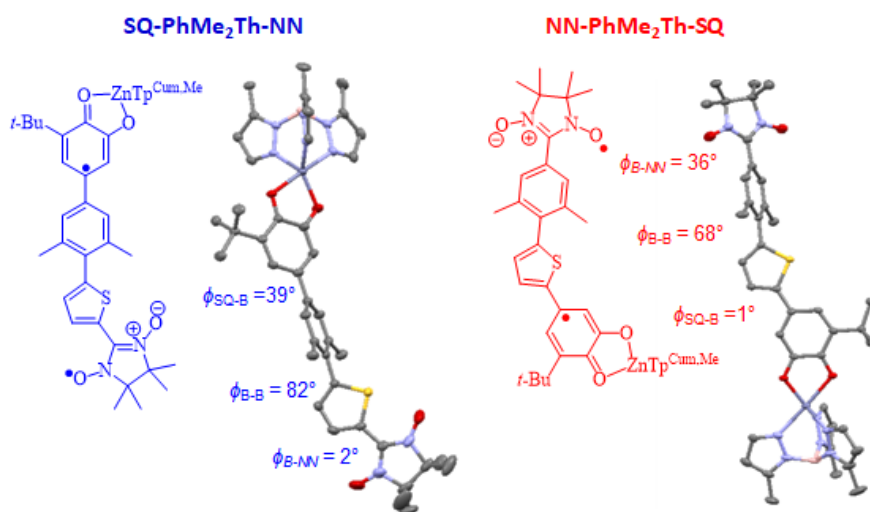


Figure IV-16. Crystal structures of **SQ-PhMe₂Th-NN** and **NN-PhMe₂Th-SQ**.

to the NN-bridge and SQ-bridge, respectively, of the other isomer; assuming that a torsion between the SQ-bridge or NN-bridge have approximately the same effect on the magnitude of the exchange coupling.

Electronic Absorption Spectra and Magnetometry. Figure IV-17A shows the electronic absorption spectra of **SQ-PhMe₂Th-NN** (blue) and **NN-PhMe₂Th-SQ** (red) which are in accord with those of the Me_nPh-bridged biradical complexes where the rotation of the acceptor results in greater hypso- and hypochromic shifting of the SQ→NN transition than rotation of the donor. Figure IV-17B shows the fitted variable temperature magnetic susceptibility plots for both isomers. **SQ-PhMe₂Th-NN** gives a $J = +2 \text{ cm}^{-1}$ and **NN-PhMe₂Th-SQ** gives a $J = +11 \text{ cm}^{-1}$. These results are consistent with what would be expected for the two molecules with high intra-bridge torsions of 82 and 68° with the higher exchange coupling constant coinciding with the smaller torsion angle. This is also reasonable in the context of the distance dependence of coupling for SQ-B -NN where the bridge is 5,5'-connectivity through 2,2'-bithiophene ($J = +108 \text{ cm}^{-1}$), and for 4,4'-connectivity through 1,1'-biphenyl, $J = +20 \text{ cm}^{-1}$. When the bridge is pyridine-thiophene, $J \sim +50 \text{ cm}^{-1}$, so the J -values for **SQ-PhMe₂Th-NN** and **NN-PhMe₂Th-SQ**

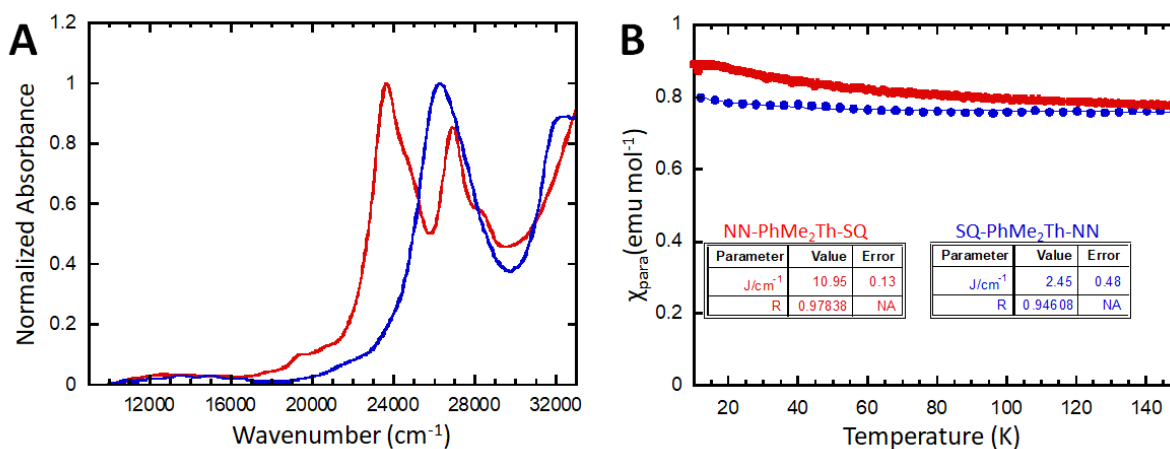
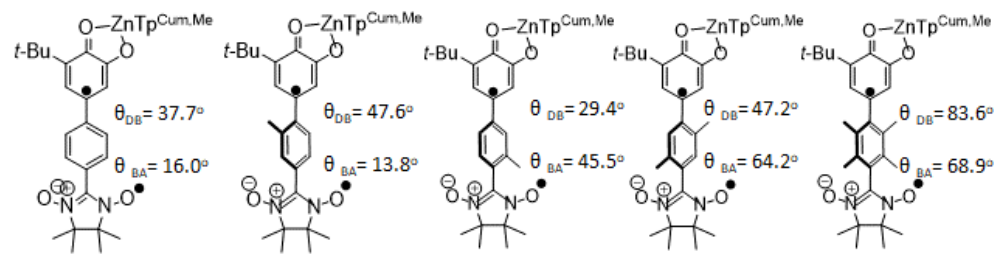


Figure IV-17. A) Electronic absorption spectra for **SQ-PhMe₂Th-NN** (blue) and **NN-PhMe₂Th-SQ** (red). B) Variable temperature paramagnetic susceptibility plots and fitting parameters for **SQ-PhMe₂Th-NN** (blue) and **NN-PhMe₂Th-SQ** (red).

are reasonable given the large torsion angles.^{21,22} For the pyridine-thiophene rectifiers the torsion angles could be corrected by dividing the measured exchange coupling constant by the square of the product of the cosine of each torsion angle to give the exchange coupling for a planar molecule.^{21,23}

In the case of **SQ-PhMe₂Th-NN** and **NN-PhMe₂Th-SQ** the larger torsion angles cannot be so easily corrected. Table IV-4 shows the methylated-phenyl-bridged complexes from our 2015 *J. Am. Chem. Soc.* paper²³ on torsional dependence of exchange coupling, with their torsion angles between donor-bridge (θ_{DB}) and bridge-acceptor (θ_{DA}). The first row showing the exchange coupling constants as given by the fitted variable temperature magnetic susceptibility data. As can be seen the greater the torsion angles, the weaker the coupling. If these exchange coupling constants are corrected by dividing by the square of the product of the cosine of the torsion angles, it gives the exchange coupling for a totally planar molecule (second row). Considering **SQ-Ph-NN** should have the most unadulterated torsion angles and exchange coupling its corrected J -value should essentially be a theoretical maximum for phenylene bridges with this SQ-B-NN motif and all other phenylene bridges with only alkyl substituents should be close to this value of +172 cm⁻¹. As can be seen in the table, while **SQ-Ph-NN** had the highest measured J value, it has the lowest “corrected” J value. The isomers **SQ-MePh-NN** and **SQ-PhMe-NN** have the closest corrected J values to planar **pSQ-Ph-NN**, but are still nearly 20 cm⁻¹

Table IV-4. Measured J -values for Me_nPh biradical complexes with torsions corrected to be a planar molecule and with all torsion angles set to those of **SQ-PhMe-NN**.



	SQ-Ph-NN	SQ-MePh-NN	SQ-PhMe-NN	SQ-pXylyl-NN	SQ-PhMe₄-NN
Measured J	+100 cm ⁻¹	+81 cm ⁻¹	+71 cm ⁻¹	+36 cm ⁻¹	+2 cm ⁻¹
Planar molecule J	+172 cm ⁻¹	+189 cm ⁻¹	+190 cm ⁻¹	+411 cm ⁻¹	+1240 cm ⁻¹
Set to SQ-PhMe-NN angles J	+64 cm ⁻¹	+70 cm ⁻¹	+71 cm ⁻¹	+154 cm ⁻¹	+463 cm ⁻¹

higher. They are in good agreement with each other in that they were 10 cm⁻¹ different for measured J -values but are nearly equal in the theoretical absence of torsion angles. However, as the torsion angles become greater the over-correction becomes more extreme as seen in **SQ-pXylyl-NN** which is corrected to +411 cm⁻¹ and is approaching the parent compound **SQ-NN**'s $J = +550$ cm⁻¹ and for **SQ-PhMe₂-NN** the over-correction is absurd giving a $J = +1240$ cm⁻¹. As can be seen from this series, the larger the torsion angle used in the correction, the greater the over-correction. Given the size of the over-correction between **SQ-Ph-NN** and the isomers **SQ-MePh-NN** and **SQ-PhMe-NN**, it is probably likely that the corrected $J = +172$ cm⁻¹ for **SQ-Ph-NN** is over-corrected given that it has an SQ-Ph torsion angle of ~38°.

The last row of **Table IV-4** is not something that was investigated in either the 2015 *J. Am. Chem. Soc.* or 2017 *Chem. Sci.* articles.^{21,23} The last row consists of corrected J -values, but if the torsion angles are all “set to the same values.” For this row of data, the torsion angles are all normalized to those of **SQ-PhMe-NN** (29.4 and 45.5°) which is done by dividing each measured J -value by the square of the products of the cosines of their respective torsion angles

and then multiplying by the square of the products of the cosines of the torsion angles of **SQ-PhMe-NN**. The intent was that the over-correction that gets introduced by larger torsion angles in the denominator could be reduced by a large torsion angle in the numerator. Comparing **SQ-MePh-NN** and **SQ-PhMe-NN**, this strategy seems to work relatively well when the difference between the measured torsion angles are close to those to which they are being set. When **SQ-MePh-NN** and **SQ-PhMe-NN** both have torsion angles of 29.4 and 45.5°, **SQ-PhMe-NN** remains unchanged since it already has these angles, but **SQ-MePh-NN** is lowered from $J = +81 \text{ cm}^{-1}$ to $J = +70 \text{ cm}^{-1}$ which is very close to **SQ-PhMe-NN**'s $J = +71 \text{ cm}^{-1}$. As the torsion angles get much smaller or larger than 29.4 and 45.5° the J values become either under- or over-corrected. It should be pointed out mathematically, the ratio of J -values for corrected compounds is nearly the same for whatever correcting strategy, but one correction may give more realistic J -values by virtue of a smaller correction.

Table IV-5 shows the measured and corrected exchange coupling constants for **SQ-PhMe₂Th-NN** and **NN-PhMe₂Th-SQ** alongside the rectification ratios. The rectification ratio ($J_{\text{NN-PhMe}_2\text{Th-SQ}}/J_{\text{SQ-PhMe}_2\text{Th-NN}}$) for the uncorrected J -values is 5.5. Attempting to correct the J -values for that of two planar molecules results in the over-correction as discussed above because **SQ-PhMe₂Th-NN** with the intra-bridge torsion of 82° gives $J = +170 \text{ cm}^{-1}$ and **NN-PhMe₂Th-**

Table IV-5. Measured J values for **SQ-PhMe₂Th-NN** and **NN-PhMe₂Th-SQ** with torsions corrected to be a planar molecule and with all torsion angles set to the other isomer's torsion angles.

	SQ-PhMe₂Th-NN	NN-PhMe₂Th-SQ	Rectification Ratio^a
Measured J	+2 cm^{-1}	+11 cm^{-1}	5.5 (0.18)
Planar molecule J	+170 cm^{-1}	+120 cm^{-1}	0.70 (1.4)
All set to the other isomer's angles J	+16 cm^{-1}	+1.4 cm^{-1}	0.088 (11)

^a Rectification Ratio = $J_{\text{NN-PhMe}_2\text{Th-SQ}}/J_{\text{SQ-PhMe}_2\text{Th-NN}}$ (Inverse Rectification Ratio = $J_{\text{SQ-PhMe}_2\text{Th-NN}}/J_{\text{NN-PhMe}_2\text{Th-SQ}}$)

SQ with the intra-bridge torsion of 68° gives $J = +120 \text{ cm}^{-1}$. Given that **SQ-ThTh-NN** has a $J = +108 \text{ cm}^{-1}$ and has torsion angles of 14.8 , 30.6 and 3.7° and the pyridine-thiophene rectifier isomers have $J = \sim +50 \text{ cm}^{-1}$, these values of $+170$ and $+120 \text{ cm}^{-1}$ are too large to be realistic for the planar molecules.^{21,22} Implementing the strategy of setting the two isomers' torsion angles to the other's at least provided reasonable values of $J = +16 \text{ cm}^{-1}$ and $+1.4 \text{ cm}^{-1}$ for **SQ-PhMe₂Th-NN** and **NN-PhMe₂Th-SQ**, respectively. Although given the tendency for over-correction, **SQ-PhMe₂Th-NN** should probably be lower and **NN-PhMe₂Th-SQ** a little higher which indicates both molecules are in good agreement with each other if possessing the other isomer's torsion angles. These torsion-set corrected J -values give a rectification ratio ($J_{\text{SQ-PhMe}_2\text{Th-NN}} / J_{\text{NN-PhMe}_2\text{Th-SQ}}$) of 11 (since rectification ratios are normally reported as numbers greater than one). Rectification ratios of 5.5 and 11 reflects what is probably this issue of over-correction. As such, any numbers derived from torsion corrections with large torsion angles should be scrutinized and used only to make qualitative statements about the magnitude or directionality of the coupling.

Through the utilization of torsion angles we were able to realize a higher rectification (5.5) ratio than was displayed by the **PyTh**-bridged rectifiers (1.1). However, a definitive conclusion is complicated by the different conformations of each isomer; most notably the intra-bridge torsion angles that are 68° for one isomer and 82° for the other. In addition to **SQ-PhMe₂Th-NN** and **NN-PhMe₂Th-SQ**, progress on the synthesis of **PhMeTh**-bridged rectifiers which should have a smaller intra-bridge torsion is discussed in APPENDIX C.

IV.7. Cross-Conjugative Asymmetry.

IV.7.1. Hypothesis

The next strategy for attempting to synthesize molecular rectifiers was to choose a molecule that possessed a large disparity between the wavefunction coefficients at the connecting carbon atoms, and quantum interference effects with respect to rectification in single molecule devices has been investigated and suggested as a viable mechanism for rectification.^{3,36} To this end, biphenyl, shown in Figure IV-18 with its HOMO and LUMO, was chosen as the simplest bridge to examine. The coefficients at the 4,4'-positions are the same with a Hückel MO

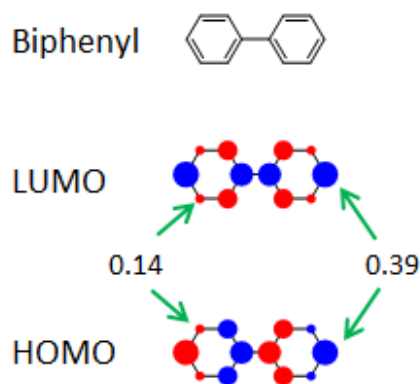


Figure IV-18. Proposed molecular rectifier possessing cross-conjugative asymmetry at the positions indicated with the green arrows beside the Hückel MO coefficients in the HOMO and LUMO.

coefficients of 0.39, but they are different from the 3,3',5, and 5' positions with a Hückel MO coefficients of 0.14. The two isomers to be synthesized are those shown in Figure IV-19: one where the SQ is conjugated with both phenyl rings and the NN is *meta* to the second phenyl ring (*p*-SQ-*m*-NN) and the other isomer where the SQ is conjugated with one phenyl ring and *meta* to the second phenyl ring while the NN is *para* to the second phenyl ring (*m*-SQ-*p*-NN). The SOMOs of both the NN and the delocalized SQ are shown in Figure IV-19. These isomers were thought to provide a larger RR because in *p*-SQ-*m*-NN the SQ SOMO can delocalize down into the ring that is directly bonded to the NN while in *m*-SQ-*p*-NN the SQ SOMO can only

delocalize into the first ring and is cross-conjugated with the second ring; thus separating keeping the radicals further apart. While it has been mentioned, it is important to note that in both isomers the SQ and the NN are cross-conjugated with each other which will result in antiferromagnetic coupling to give a singlet ground state.³⁷

IV.7.2. Synthetic discussion of *p*-SQ-*m*-NN and *m*-SQ-*p*-NN.

The retrosynthesis of both isomers is shown in Scheme IV-8, where the SQ-B-NN is synthesized from the immediate precursor Cat-B-NN by complexation with Zn(OH)Tp^{Cum,Me} followed by aerial oxidation. The Cat-B-NNs can be synthesized from MOM₂Cat-B-CHO by cleavage of the methoxymethyl groups with catalytic aqueous acid, followed by condensation and oxidation. The MOM₂Cat-B-CHO is easily accessible from Br-B-CHO, which in this case the syntheses and spectral data for both the *p*-Br-*m*-CHO³⁸ and *m*-Br-*p*-CHO³⁹ are known.

The syntheses are shown in Scheme IV-9 which proceeded as proposed. *p*-Br-*m*-CHO and *m*-Br-*p*-CHO were both synthesized by modified literature procedures in order to afford a better yield. The risk of using a symmetrically substituted aryl halide or aryl boronic alcohol or ester in a Suzuki coupling or any other palladium-mediate cross-coupling and intending to get

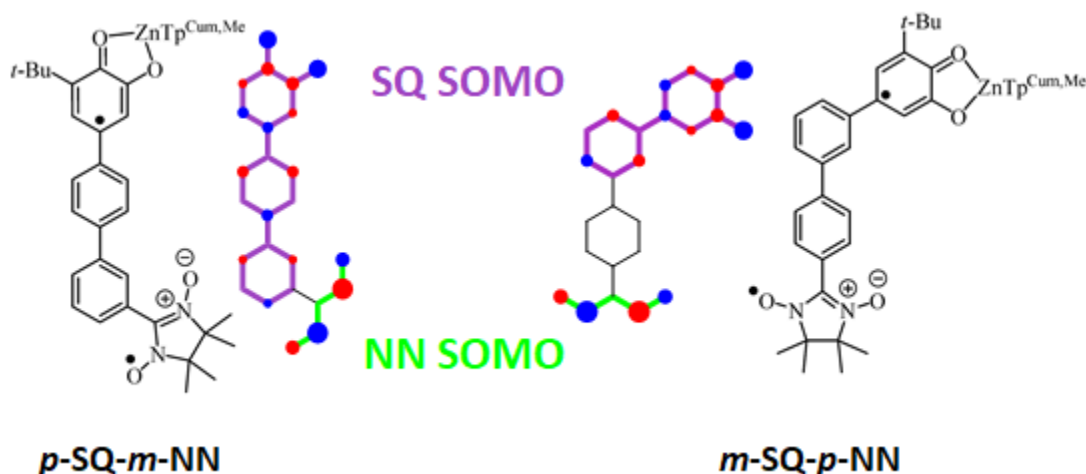
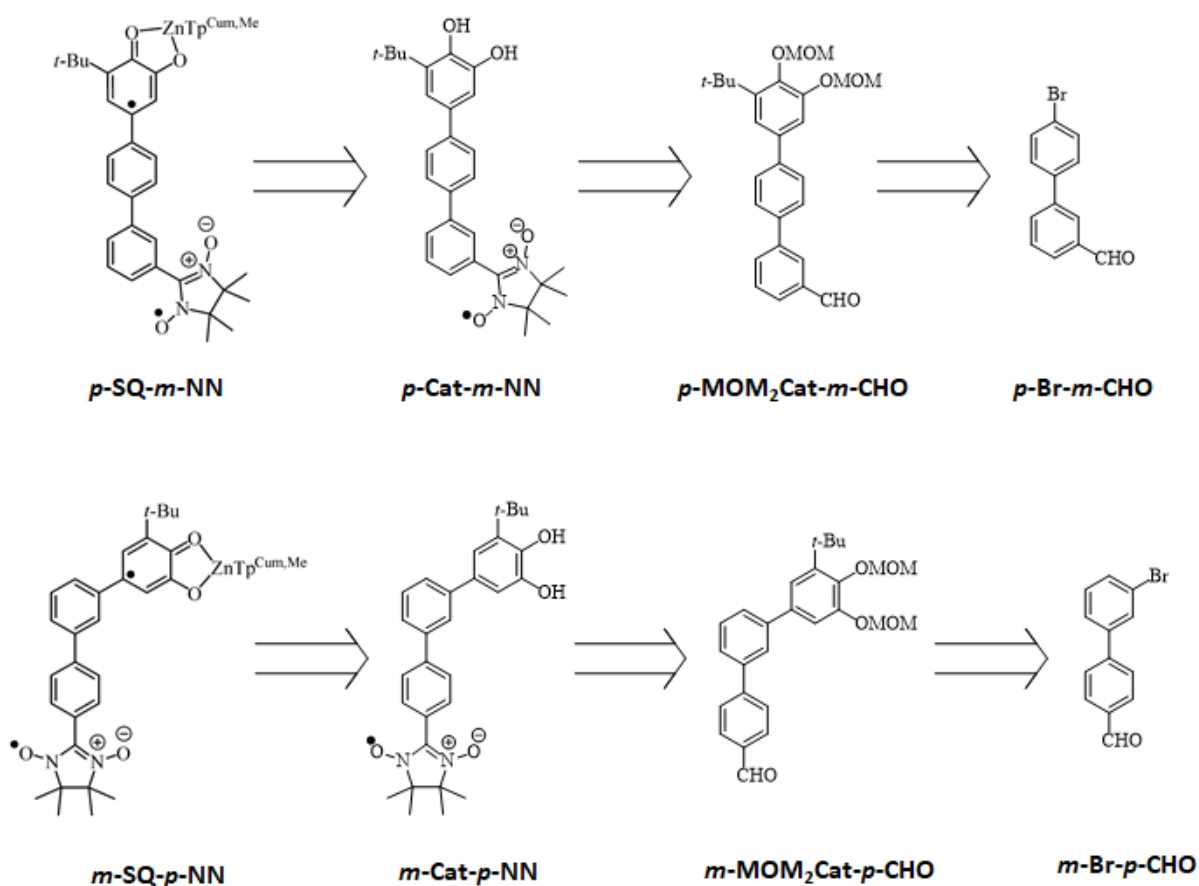


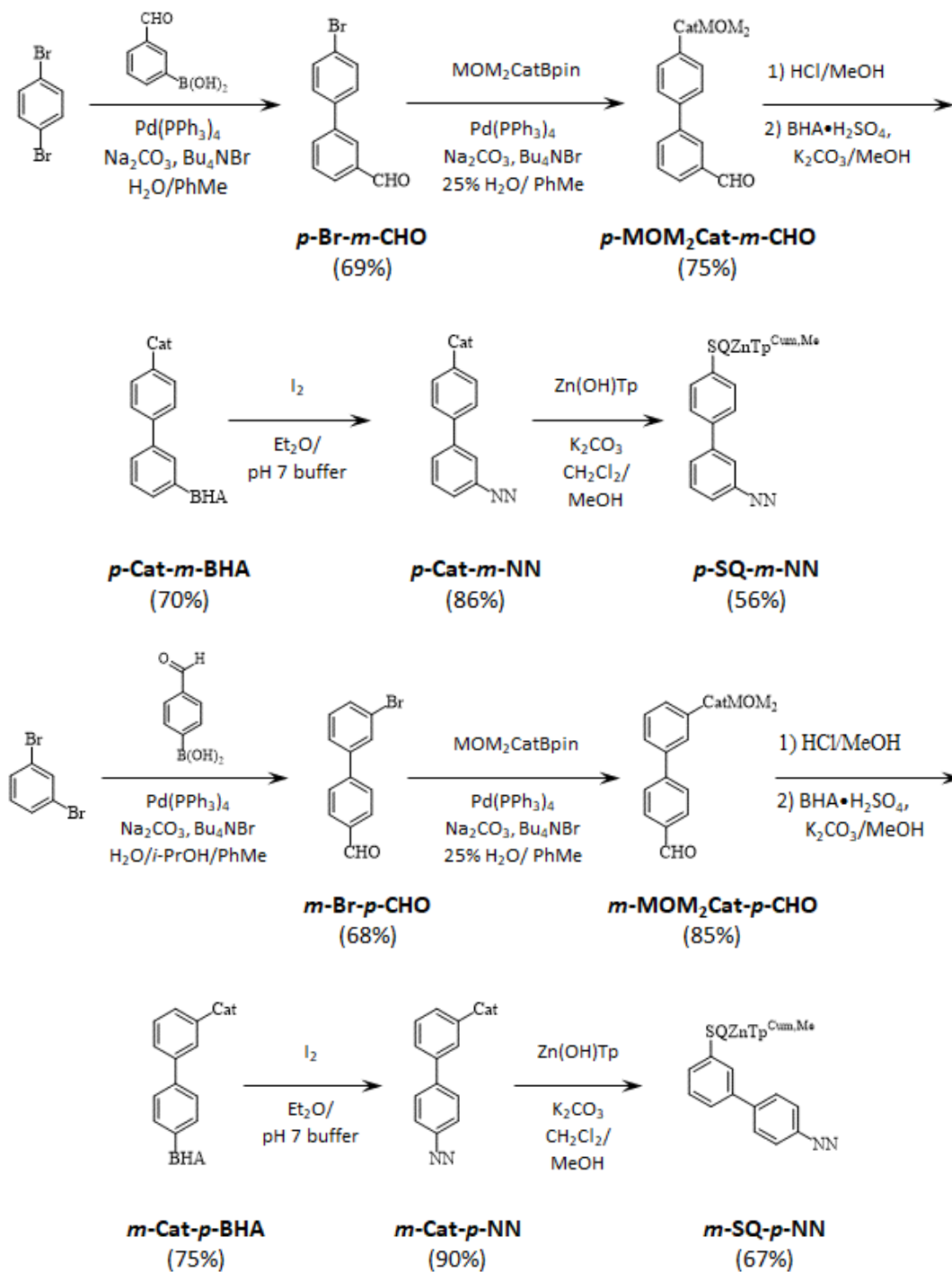
Figure IV-19. Proposed rectifiers: *p*-SQ-*m*-NN and *m*-SQ-*p*-NN and their respective SQ and NN SOMOs.

Scheme IV-8. Retrosynthetic pathways of *p*-SQ-*m*-NN and *m*-SQ-*p*-NN.



the asymmetrically-substituted, mono-coupled product is that there will inevitably be some amount of symmetrically-coupled product. The initial syntheses of both *p*-Br-*m*-CHO and *m*-Br-*p*-CHO provided yields of *ca.* 30%, with the rest being the terphenyl side product. This was countered by sheer probability by using three equivalents of both 1,4-dibromobenzene and 1,3-dibromobenzene to synthesize *p*-Br-*m*-CHO and *m*-Br-*p*-CHO in 69% and 68% yields, respectively. Both of these starting materials had high R_f values on TLC, so the excess eluted first from the columns and was recycled. If a higher yield was desired, more equivalents of both starting materials could be used to further drive-up the yield. MOM₂CatBpin and another Suzuki coupling was used to install the MOM₂Cat onto both bridges using preferred conditions of Pd(PPh₃)₄, Na₂CO₃ in 1:3 H₂O:toluene with 0.1 eq. of Bu₄NBr as a phase transfer catalyst. From

Scheme IV-9. Successful synthetic procedures for *p*-SQ-*m*-NN and *m*-SQ-*p*-NN.

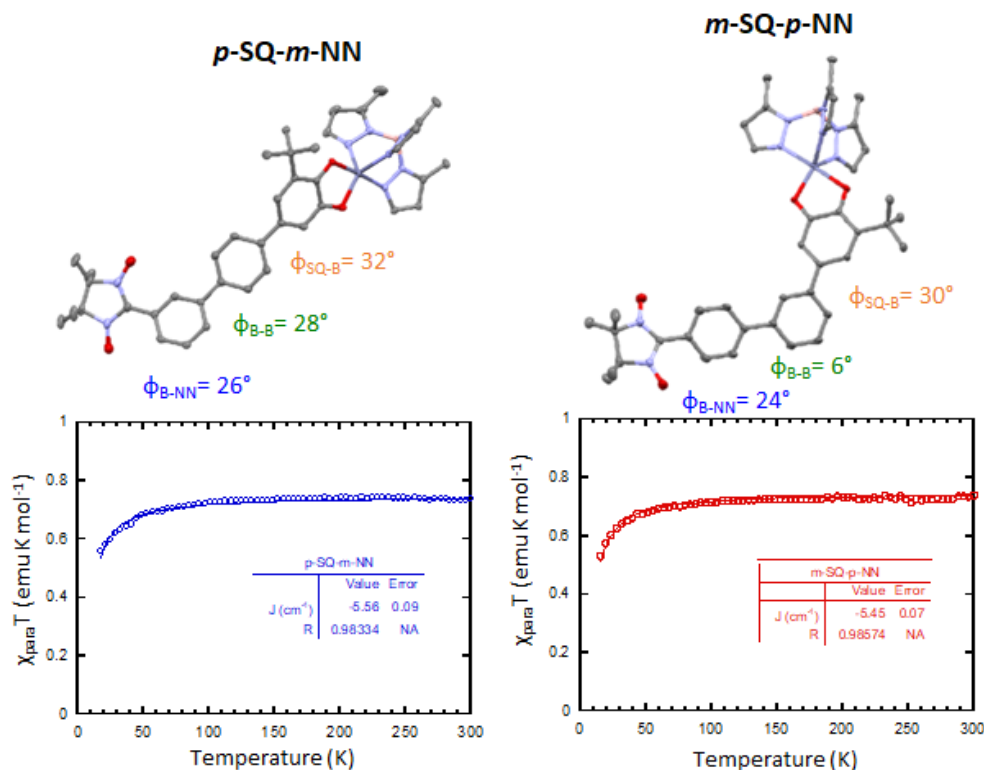


the MOM₂Cat-B-CHO, aqueous HCl in methanol was used to cleave the methoxymethyl groups and then this compound was taken directly into condensation with BHA•H₂SO₄ in methanol, using 1 eq. of K₂CO₃ to free-base the BHA. The Cat-B-BHA were both purified by precipitation

of the condensation's reaction solution into stirring brine to afford white to off-white solids of both *p-Cat-m-BHA* and *m-Cat-p-BHA*. These compounds are not indefinitely stable and were then taken into the oxidation conditions with I₂ to make the monoradical NN compounds. Finally, complexation of both Cat-B-NNs was performed with Zn(OH)Tp^{Cum,Me}.

IV.7.3 Results and Conclusions.

Variable temperature paramagnetic susceptibility measurements of *p-SQ-m-NN* and *m-SQ-p-NN* resulted in the $\chi_{\text{para}}T$ vs. T plots shown in Figure IV-20. When these data were fit, the magnetic exchange coupling parameter J , was -5.6 and -5.5 cm⁻¹ for *p-SQ-m-NN* and *m-SQ-p-NN*, respectively. As can be seen from the data, the singlet-triplet gap can be assumed to be relatively small by the relatively flat slope at $\chi_{\text{para}}T \approx 0.75$ emu K mol⁻¹ until low temperature where the paramagnetic susceptibility dips toward zero for the antiferromagnetically coupled biradicals in both cases. The RR for the uncorrected molecules is $J_{p\text{-SQ-}m\text{-NN}}/J_{m\text{-SQ-}p\text{-NN}} = -5.6$ cm⁻¹/ -5.5 cm⁻¹ = 1. The measured values of J are the same because 1) the calculated error from the fits allow them to overlap and 2) the error associated with weighing milligrams of material for molecules that are over 1.1 kDa with only two unpaired electrons. These molecules are not rectifiers either, the RR improves a little when the J values are corrected for by the torsions in the molecules by a product of the cosines squared as made possible by our previous work.^{21,23}



	<i>p</i> -SQ- <i>m</i> -NN	<i>m</i> -SQ- <i>p</i> -NN	Rectification Ratio
Measured J	-5.6 cm^{-1}	-5.5 cm^{-1}	1.02
Corrected, Planar J	12 cm^{-1}	8.9 cm^{-1}	1.35

Figure IV-20. Crystal structures providing detailed geometry data, variable temperature paramagnetic susceptibility ($\chi_{\text{para}}T$ vs. T) with exchange coupling fitting parameters J for the measured and corrected for planar molecules, and the RRs for *p*-SQ-*m*-NN and *m*-SQ-*p*-NN

The corrected J values for the planar molecules are 12 and 8.9 cm^{-1} to give a RR of 1.35. From our investigations, it does not seem as though cross-conjugative asymmetry through biphenyl is an effective method for achieving high RRs, but other structures may show improved results.

Since cross-conjugative asymmetry with biphenyl did not provide exchange couplings that were different enough to give a discernable rectification ratio, it is possible that the same strategy with bithiophenes may be more successful because coupling through conjugated pathways in bithiophenes ($J = +108 \text{ cm}^{-1}$) is much greater than through biphenyl ($J = +20 \text{ cm}^{-1}$).

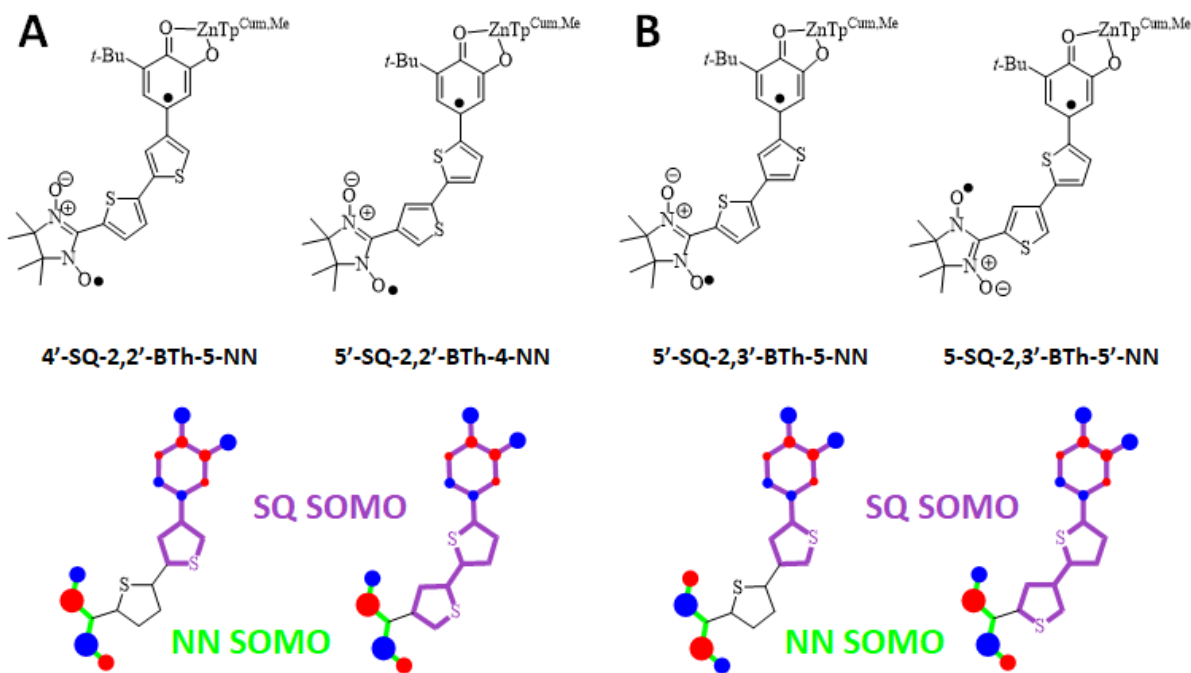


Figure IV-21. The Hückel-based MO description of the delocalization of the SQ SOMO through bithiophene-based cross-conjugative molecular rectifiers. **A)** 4'-SQ-2,2'-BTh-5-NN and 5'-SQ-2,2'-BTh-4-NN thiophene-based *p*-SQ-*m*-NN and *m*-SQ-*p*-NN analogs where the bridge subunits are conjugated and cross-conjugation is achieved through positioning of the SQ and NN. **B)** 5'-SQ-2,3'-BTh-5-NN and 5-SQ-2,3'-BTh-5'-NN where the bridge subunits are cross-conjugated with each other.

¹).²² Figure IV-21A shows two 2,2'-bithiophene isomers that follows the same pattern as *p*-SQ-*m*-NN and *m*-SQ-*p*-NN where the SQ is either conjugated through one thiophene ring or two. Interestingly, another set of isomers can be made for bithiophene that results in cross-conjugation between the SQ and NN, but it is the thiophene-thiophene bond that is involved in causing the two radicals to be cross-conjugated (Figure IV-21B). This set of isomers has no phenylene analog and would provide insight into the importance of the length of conjugation of a bridge on electronic coupling and molecular rectification.

IV.8. EXPERIMENTAL.

IV.8.1. Torsional Rectifiers.

4-Bromo-3,5-dimethylaniline (H₂N-PhMe₂Br) was prepared according to literature precedent.⁴⁰

E-1-((4-bromo-3,5-dimethylphenyl)diazenyl)pyrrolidine (RN₃-PhMe₂Br). To a 50 mL round-bottom flask was added **H₂N-PhMe₂Br** (4.036 g, 20.17 mmol) and 40 mL of a 1:1 ratio of MeCN:H₂O. To this solution, 5 mL of 12 M HCl was added and the reaction mixture was cooled to -10 °C in an acetone/ice bath. In 3 mL of H₂O, 1.531 g (22.19 mmol) of NaNO₂ was added dropwise so that the temperature remained below 5 °C. After addition, the reaction was stirred for 30 minutes and then poured into a solution of pyrrolidine (2.7 mL, 33 mmol), Na₂CO₃ (10.89 g, 102.7 mmol), and 60 mL of H₂O at 0 °C. The mixture was stirred at 0 °C for 15 minutes and then warmed to room temperature and stirred for 30 minutes. The mixture was then filtered through a Büchner funnel with filter paper and washed with water. The yellow-orange solid was collected with Et₂O, dried with Na₂SO₄ and concentrated under reduced pressure to give the title compound (5.69 g, 100%) of as a yellow-orange solid. ¹H NMR (400 MHz, CDCl₃) δ = 7.15 (s, 2 H), 3.78 (br. s., 4 H), 2.51 - 2.33 (m, 6 H), 2.12 - 1.95 (m, 4 H). ¹³C NMR (101 MHz, CDCl₃) δ = 149.7, 138.3, 123.4, 120.0, 50.5, 46.6, 23.8. HRMS (ESI) m/z: [M+H]⁺ Calculated for C₁₂H₁₆BrN₃ 282.06004; Found 282.06018.

E-1 -((3,5-dimethyl-4-(thiophen-2-yl)phenyl)diazenyl)pyrrolidine (RN₃-PhMe₂Th). To a 50 mL round-bottom flask was added 4,4,5,5-tetramethyl-2-(thiophen-2-yl)-1,3,2-dioxaborolane (2.45 g, 11.7 mmol), **RN₃-PhMe₂Br** (2.99 g, 10.6 mmol), Na₂CO₃ (3.39 g, 32.0 mmol), and Bu₄NBr (0.181 g, 0.561 mmol). The flask was purge-pumped three times into the glovebox

where Pd(dppf)Cl₂•CH₂Cl₂ (0.255 g, 0.312 mmol) was added. The flask was sealed with a rubber septum, removed from the glovebox and 7 mL of deoxygenated water and 20 mL of deoxygenated toluene were added via syringe. A nitrogen-purged, water-cooled reflux condenser was attached, and the reaction was heated to 80 °C for 18 h. The reaction was cooled to room temperature, transferred to a separatory funnel, diluted with ca. 50 mL of EtOAc, and washed with 2x 50 mL of brine. The organic layer was separated, dried with Na₂SO₄ and concentrated under reduced pressure. The residue was purified with flash chromatography (silica gel, 10% EtOAc/hexanes) to give the title compound (2.470 g, 82%) of as an orange solid. ¹H NMR (400MHz, CDCl₃) δ = 7.39 (dd, *J* = 5.1, 1.2 Hz, 1 H), 7.21 (s, 2 H), 7.13 (dd, *J* = 5.1, 3.5 Hz, 1 H), 6.85 (dd, *J* = 3.1, 1.2 Hz, 1 H), 3.83 (br. s., 4 H), 2.20 (s, 6 H), 2.05 (br. s., 4 H). ¹³C NMR (101MHz, CDCl₃) δ = 150.7, 141.5, 138.7, 130.5, 126.8, 126.3, 125.1, 119.0, 49.0, 23.6, 20.9. HRMS (ESI) *m/z*: [M+H]⁺ Calculated for C₁₆H₁₉N₃S 286.13724; Found 286.13696.

2-(4-iodo-2,6-dimethylphenyl)thiophene (I-PhMe₂Th). To an oven-dried 10 mL microwave vessel was added **RN₃-PhMe₂Th** (0.676 g, 2.37 mmol), iodomethane (3 mL, 20 eq.), and I₂ (0.602 g, 2.37 mmol). The solution was then fitted with a Teflon microwave cap and purged with nitrogen for 10 minutes. The microwave vessel was then placed into the microwave and heated to 130 °C for 2 h. The reaction was cooled to room temperature and the volatiles were removed under reduced pressure. The resulting highly-colored residue was loaded onto a silica pad and eluted with hexanes. The hexanes were placed in a separatory funnel and washed with a saturated solution of Na₂S₂O₃, then the organic layer was separated, dried with Na₂SO₄ and concentrated under reduced pressure to afford the title compound (0.700 g, 94%) of as a colorless solid. ¹H NMR (400MHz, CDCl₃) δ = 7.49 (s, 2 H), 7.40 (dd, *J* = 5.1, 1.2 Hz, 1 H), 7.12 (dd, *J* = 5.1, 3.5

Hz, 1 H), 6.81 (dd, $J = 3.5, 1.2$ Hz, 1 H), 2.11 (s, 6 H). ^{13}C NMR (101MHz, CDCl_3) $\delta = 140.4, 139.9, 136.0, 133.6, 127.1, 126.3, 125.6, 94.2, 20.4$. HRMS (ESI) m/z : $[\text{M}+\text{H}]^+$ Calculated for $\text{C}_{26}\text{H}_{32}\text{O}_4\text{S}$ 314.96989; Found 314.96981.

2-(3'-(tert-butyl)-4',5'-bis(methoxymethoxy)-3,5-dimethyl-[1,1'-biphenyl]-4-yl)thiophene

(MOM₂Cat-PhMe₂-Th). To a 10 mL round-bottom flask was added **I-PhMe₂Th** (0.231 g, 0.735 mmol), MOM₂CatBpin (0.265 g, 0.697 mmol), Na_2CO_3 (0.228 g, 2.15 mmol), and Bu_4NBr (25 mg, 0.078 mmol). The flask was purge-pumped three times into the glove box where $\text{Pd}(\text{PPh}_3)_4$ (10 mg, 8.7 μmol) of was added. The flask was sealed with a rubber septum, removed from the glovebox, and 0.5 mL of deoxygenated H_2O and 1.5 mL of deoxygenated toluene were added via syringe. A water-cooled, nitrogen-purged reflux condenser was attached and the contents were heated to 85 °C for 16 h. The reaction was cooled to room temperature, transferred to a separatory funnel, diluted with ca. 8 mL of Et_2O and then washed with ca. 8 mL of brine. The organic layer was separated, dried with Na_2SO_4 , and concentrated under reduced pressure. The residue was purified by flash chromatography (deactivated silica gel, 10% EtOAc /hexanes) to give the title compound (0.224 g, 69%) of as a colorless oil. ^1H NMR (400MHz, CD_2Cl_2) $\delta = 7.42$ (dd, $J = 5.1, 1.2$ Hz, 1 H), 7.28 (s, 2 H), 7.25 (d, $J = 2.0$ Hz, 1 H), 7.24 (d, $J = 2.0$ Hz, 1 H), 7.14 (dd, $J = 5.1, 3.5$ Hz, 1 H), 6.86 (dd, $J = 3.1, 1.2$ Hz, 1 H), 5.24 (s, 2 H), 5.23 (s, 2 H), 3.65 (s, 3 H), 3.52 (s, 3 H), 2.19 (s, 6 H), 1.47 (s, 9 H); ^{13}C NMR (101MHz, CDCl_3) $\delta = 150.2, 145.5, 143.4, 141.1, 138.7, 136.0, 132.8, 127.0, 126.4, 126.4, 126.0, 125.3, 119.4, 113.5, 99.0, 95.4, 57.5, 56.2, 35.2, 30.5, 20.9$; HRMS (ESI) m/z : $[\text{M}+\text{Na}]^+$ Calculated for $\text{C}_{26}\text{H}_{32}\text{O}_4\text{S}$ 441.19135; Found 441.19080.

5-(3'-(tert-butyl)-4',5'-bis(methoxymethoxy)-3,5-dimethyl-[1,1'-biphenyl]-4-yl)thiophene-2-carbaldehyde (MOM₂Cat-PhMe₂-Th-CHO). To a 25 mL oven-dried round-bottom flask was added **MOM₂Cat-PhMe₂-Th** (0.511 g, 1.16 mmol) and the flask was subjected to three purge-pump cycles; filling with nitrogen. 15 mL of anhydrous THF was added and the solution was cooled to -78 °C. *n*-BuLi in hexanes (1.4 mL, 3.5 mmol) was added dropwise and stirred for 1 h at -78 °C. Then anhydrous DMF (0.29 mL, 3.8 mmol) was added dropwise and stirred for 0.5 h at -78 °C, then warmed to room temperature and stirred for ca. 12 h. The reaction was quenched with 1 mL of H₂O and stirred for 0.5 h. The reaction was transferred to a separatory funnel washed with brine and extracted with Et₂O. The organic layer was separated, dried with Na₂SO₄ and concentrated under reduced pressure to give the title compound (0.46 g, 85%) of as a colorless oil. ¹H NMR (400MHz, CDCl₃) δ = 9.91 (s, 1 H), 7.79 (d, *J* = 3.5 Hz, 1 H), 7.29 (s, 2 H), 7.26 (d, *J* = 2.3 Hz, 1 H), 7.22 (d, *J* = 2.3 Hz, 1 H), 6.96 (d, *J* = 3.5 Hz, 1 H), 5.26 (s, 2 H), 5.24 (s, 2 H), 3.67 (s, 3 H), 3.53 (s, 3 H), 2.20 (s, 6 H), 1.48 (s, 9 H). ¹³C NMR (101MHz, CDCl₃) δ = 182.9, 152.2, 150.4, 145.8, 144.0, 143.6, 142.0, 138.0, 136.9, 135.6, 131.4, 128.3, 126.3, 119.5, 113.5, 99.1, 95.4, 57.6, 56.4, 35.3, 30.6, 20.9. HRMS (ESI) *m/z*: [M+H]⁺ Calculated for C₂₇H₃₂O₅S 469.20432; Found 469.20366.

2-(5-(3'-(tert-butyl)-4',5'-dihydroxy-3,5-dimethyl-[1,1'-biphenyl]-4-yl)thiophen-2-yl)-4,4,5,5-tetramethylimidazolidine-1,3-diol (Cat-PhMe₂-Th-BHA). The MOM groups were removed by stirring **MOM₂Cat-PhMe₂Th-CHO** (0.379 g, 0.809 mmol) in 1 mL of 12 M HCl and 4 mL of MeOH for 16 h. The reaction was transferred to a separatory funnel, diluted with Et₂O and washed with brine. The organic layer was separated, dried with Na₂SO₄ and concentrated under reduced pressure and the residue was used without further purification. To

the residue was added BHA•H₂SO₄ (0.228 g, 0.926 mmol) and anhydrous K₂CO₃ (88 mg, 0.64 mmol). The flask was capped with a septum and purge-pumped three times; back-filling with nitrogen. The 7 mL of anhydrous, deoxygenated MeOH was added and the contents were stirred for 48 h. The mixture was then poured into ca. 200 mL of stirring brine, then filtered. The solid was collected by dissolving it with Et₂O. The Et₂O was dried with Na₂SO₄, then concentrated under reduced pressure to afford a white solid of the title compound (0.19 g, 59%). ¹H NMR (400MHz, DMSO-d₆) δ = 9.50 (s, 1 H), 8.19 (s, 1 H), 8.04 (s, 2 H), 7.23 (s, 2 H), 7.12 - 7.04 (m, 1 H), 6.94 (br. s., 1 H), 6.90 (br. s., 1 H), 6.76 - 6.65 (m, 1 H), 4.78 (s, 1 H), 2.17 (s, 6 H), 1.39 (s, 9 H), 1.08 (s, 6 H), 1.05 (s, 6 H). HRMS (ESI) m/z: [M+H]⁺ Calculated for C₂₈H₃₆N₂O₄S 497.24685; Found 497.24688.

(Cat-PhMe₂-Th-NN). Iodine (76 mg, 0.30 mmol) dissolved in ca. 3 mL of Et₂O was added dropwise to a solution of **Cat-PhMe₂Th-BHA** (150 mg, 0.294 mmol) in 10 mL of Et₂O and 1 M, pH 7 phosphate buffer. After the addition of iodine, the reaction was transferred to a separatory funnel, washed quickly with 5 mL of saturated Na₂S₂O₃ solution which was quickly removed, then the organic layer was washed twice with 5 mL of brine each time. The organic layer was separated, dried with Na₂SO₄ and concentrated under reduced pressure to afford a green residue (130 mg, 89%) that was used without further purification. HRMS (ESI) m/z: [M+H]⁺ Calculated for C₂₉H₃₅N₂O₄S 508.23903; Found 508.23898.

(SQ-PhMe₂-Th-NN). NN-PhMe₂Th-Cat (49 mg, 0.097 mmol) was combined with Zn(OH)Tp^{Cum,Me} (67 mg, 0.097 mmol), sealed with a septum and purge-pumped three times; back-filling with nitrogen. 5 mL each of deoxygenated, anhydrous CH₂Cl₂ and MeOH were

added via syringe and stirred at room temperature for 2 h under nitrogen. Then the septum was removed and the reaction was stirred in open air for 18 h, then concentrated under reduced pressure until precipitate was forming and then placed into a dry ice bath for 10 min. The precipitate was then filtered, collected with CH₂Cl₂ and concentrated under reduced pressure to afford the crude product (59 mg, 52%). X-ray quality crystals were grown from slow-evaporation from a concentrated solution of the title compound from EtOH/EtOAc. IR (solid) ν (cm⁻¹): 2552 (w, -BH). HRMS (ESI) m/z: [M+H]⁺ Calculated for C₆₈H₇₉BN₈O₄SZn 1179.54023; Found 1179.53931.

3,5-dimethyl-4-(thiophen-2-yl)benzaldehyde (CHO-PhMe₂-Th). To a solution of **I-PhMe₂-Th** (0.400 g, 1.27 mmol) of in ca. 8 mL of anhydrous THF at -10 °C, under nitrogen, was added *i*-PrMgCl in THF (3.2 mL; 2 M, 6.4 mmol) dropwise and stirred for 1 h. Then, anhydrous DMF (0.60 mL, 7.8 mmol) of was then added dropwise and stirred for 0.5 h at -10 °C and then warmed to room temperature and stirred overnight. The reaction was poured into ca. 50 mL of H₂O and stirred for 15 min. Then, 50 mL of hexanes was added and stirred an additional 10 min. The mixture was transferred to a separatory funnel and extracted with 50 mL each of hexanes and then twice with a 50/50 mixture of Et₂O/hexanes. The organic extracts were combined, dried with Na₂SO₄ and concentrated under reduced pressure to give the title compound (0.262 g, 95%) as a white solid and used in the next step without further purification. ¹H NMR (400MHz, CDCl₃) δ = 10.00 (s, 1 H), 7.62 (s, 2 H), 7.44 (dd, *J* = 5.1, 1.2 Hz, 1 H), 7.15 (dd, *J* = 5.1, 3.5 Hz, 1 H), 6.85 (dd, *J* = 3.5, 1.2 Hz, 1 H), 2.23 (s, 6 H); HRMS (ESI) m/z: [M+H]⁺ Calculated for C₁₃H₁₂OS 217.06816; Found 217.06815.

4-(5-bromothiophen-2-yl)-3,5-dimethylbenzaldehyde (CHO-PhMe₂-Th-Br). To a 50 mL round-bottom flask was added **CHO-PhMe₂-Th** (0.301 g, 1.39 mmol) and ca. 20 mL of MeCN. NBS (0.249 g, 1.40 mmol) was added. After being stirred for 2 h at room temperature the reaction mixture was concentrated under reduced pressure. Hexanes was then added, stirred and then the mixture was passed through a celite pad. The filtrate was concentrated under reduced pressure to give the title compound (0.369 g, 90%) as an off-white solid. ¹H NMR (400MHz, CDCl₃) δ = 9.99 (s, 1 H), 7.61 (s, 2 H), 7.10 (d, *J* = 3.5 Hz, 1 H), 6.62 (d, *J* = 3.5 Hz, 1 H), 2.41 - 2.00 (m, 6 H). ¹³C NMR (101MHz, CDCl₃) δ = 191.9, 141.3, 139.4, 135.9, 130.0, 128.5, 128.3, 126.8, 112.2, 20.7. HRMS (ESI) *m/z*: [M+H]⁺ Calculated for C₁₃H₁₁BrOS 217.06816; Found 217.06815.

4-(5-(3-(tert-butyl)-4,5-bis(methoxymethoxy)phenyl)thiophen-2-yl)-3,5-dimethylbenzaldehyde (CHO-PhMe₂-Th-CatMOM₂). To a 25 mL round-bottom flask was added **CHO-PhMe₂-Th-Br** (0.500 g, 1.69 mmol), **MOM₂CatBpin** (0.643 g, 1.69 mmol), Na₂CO₃ (0.364 g, 3.43 mmol) and Bu₄NBr (0.056 g, 0.17 mmol). The flask was purge-pumped three times into the glovebox where 15 mg (0.013 mmol) of Pd(PPh₃)₄ was added. The flask was sealed with a rubber septum and removed from the glovebox where nitrogen-purged H₂O and toluene were added via syringe. A water-cooled, nitrogen-purged condenser was attached and the reaction mixture was heated to 85 °C for 16 h. The reaction was cooled to room temperature and then was transferred to a separatory funnel, diluted with EtOAc and washed with brine. The organic layer was separated, dried with Na₂SO₄ and concentrated under reduced pressure. The resulting residue was purified by flash chromatography (deactivated silica gel, gradient 0-15% EtOAc/hexanes) to give the title compound (0.77 g, 97%) of as a colorless oil which solidified

upon standing. ^1H NMR (400MHz, CDCl_3) δ = 10.00 (s, 1 H), 7.63 (s, 2 H), 7.33 (d, J = 2.3 Hz, 1 H), 7.30 (d, J = 2.0 Hz, 1 H), 7.28 (d, J = 3.5 Hz, 1 H), 6.79 (d, J = 3.5 Hz, 1 H), 5.26 (s, 4 H), 3.71 - 3.66 (m, 3 H), 3.56 (s, 3 H), 2.31 (s, 6 H), 1.52 - 1.44 (m, 9 H); ^{13}C NMR (101MHz, CDCl_3) δ = 192.3, 150.4, 145.7, 145.0, 143.9, 140.6, 139.5, 138.7, 135.7, 129.1, 128.4, 127.4, 122.7, 118.2, 112.0, 99.1, 95.4, 57.6, 56.3, 35.2, 30.4, 20.8; HRMS (ESI) m/z : $[\text{M}+\text{H}]^+$ Calculated for $\text{C}_{27}\text{H}_{32}\text{O}_5\text{S}$ 469.20432; Found 469.20365.

2-(4-(5-(3-(tert-butyl)-4,5-dihydroxyphenyl)thiophen-2-yl)-3,5-dimethylphenyl)-4,4,5,5-tetramethylimidazolidine-1,3-diol (BHA-PhMe₂-Th-Cat). OHC-PhMe₂Th-CatMOM₂ (0.416 g, 0.888 mmol) was stirred in ca. 5 mL of MeOH and 1 mL of 12 M HCl for 15 h at room temperature. The reaction was transferred to a separatory funnel, diluted with Et₂O and washed with brine. The organic layer was separated, dried with Na₂SO₄ and concentrated under reduced pressure to afford a slightly yellow residue that was used without further purification. To the residue was added BHA•H₂SO₄ (0.322 g, 1.31 mmol) and anhydrous K₂CO₃ (0.141 g, 1.02 mmol). The flask was sealed with a septum and purged under a stream of nitrogen for 1 h, then 6 mL of anhydrous, deoxygenated MeOH was added via syringe and the mixture was stirred at room temperature for two days. The mixture was poured into 200 mL of stirring brine. The white precipitate was filtered and collected by redissolving in Et₂O, the Et₂O was dried with Na₂SO₄, then concentrated under reduced pressure to afford the title compound as a white solid (0.347 g, 77%). ^1H NMR (400MHz, DMSO- d_6) δ = 9.62 (s, 1 H), 8.31 (s, 1 H), 7.75 (d, J = 3.5 Hz, 1 H), 7.23 (s, 2 H), 7.15 (s, 1 H), 6.96 (s, 1 H), 6.93 (s, 1 H), 6.83 (d, J = 3.5 Hz, 1 H), 6.78 (d, J = 3.5 Hz, 1 H), 5.34 (d, J = 3.5 Hz, 1 H), 4.47 (s, 1 H), 2.16 (s, 6 H), 1.37 (s, 9 H), 1.08 (s, 6 H), 1.06 (s, 6 H); ^{13}C NMR (101MHz, DMSO- d_6) δ = 145.4, 144.9, 144.1, 138.0, 137.7, 137.5, 136.1,

133.5, 133.3, 127.8, 125.5, 123.7, 121.5, 114.4, 110.1, 102.6, 52.7, 34.4, 30.7, 29.3, 20.6. HRMS (ESI) m/z: [M-H]⁻ Calculated for C₂₈H₃₆N₂O₄S 495.23230; Found 495.23131

NN-PhMe₂-Th-Cat. Iodine (50 mg, 0.20 mmol) dissolved in ca. 3 mL of Et₂O was added dropwise to a solution of **BHA-PhMe₂Th-Cat** (100 mg, 0.196 mmol) in 10 mL of Et₂O and 1 M, pH 7 phosphate buffer. After the addition of iodine, the reaction was transferred to a separatory funnel, washed quickly with 5 mL of saturated Na₂S₂O₃ solution which was quickly removed, then the organic layer was washed twice with 5 mL of brine each time. The organic layer was separated, dried with Na₂SO₄ and concentrated under reduced pressure to afford a blue residue (99 mg, 99%) that was used without further purification. HRMS (ESI) m/z: [M-H]⁻ Calculated for C₂₉H₃₅N₂O₄S 506.22448; Found 506.22387.

NN-PhMe₂-Th-SQ. **NN-PhMe₂Th-Cat** (133 mg, 0.262 mmol) was combined with Zn(OH)Tp^{Cum,Me} (181 mg, 0.262 mmol), sealed with a septum and purge-pumped three times; back-filling with nitrogen. 5 mL each of deoxygenated, anhydrous CH₂Cl₂ and MeOH were added via syringe and stirred at room temperature for 2 h under nitrogen. Then the septum was removed and the reaction was stirred in open air for 20 h, then concentrated under reduced pressure until precipitate was forming and then placed into a dry ice bath for 10 min. The precipitate was then filtered, collected with CH₂Cl₂ and concentrated under reduced pressure to afford the crude product (142 mg, 46%). X-ray quality crystals were grown from slow evaporation of a concentrated solution of the title compound from benzene. IR (solid) ν (cm⁻¹): 2552 (w, -BH). HRMS (ESI) m/z: [M+H]⁺ Calculated for C₆₈H₇₉BN₈O₄SZn 1179.54023; Found 1179.53780.

IV.8.2. Cross-conjugative Asymmetry.

4'-bromo-[1,1'-biphenyl]-3-carbaldehyde (*p*-Br-*m*-CHO). A 50 mL round-bottom flask containing 3-(4,4,5,5-tetramethyl-1,3,2-dioxaborolan-2-yl)benzaldehyde (1.85 g, 7.97 mmol), 1,4-dibromobenzene (4.50 g, 23.8 mmol), Na₂CO₃ (1.82 g, 17.2 mmol), Bu₄NBr (0.255 g, 0.791 mmol) and Pd(PPh₃)₄ (0.085 g, 0.074 mmol) in 5 mL of water and 15 mL of toluene, under a nitrogen atmosphere was fitted with a nitrogen-purged, water-cooled reflux condenser and then heated to 80 °C for 16 h. After which it was transferred to a separatory funnel, washed with ca. 50 mL of brine and extracted with ca. 50 mL of EtOAc. The organic layer was dried with Na₂SO₄ and concentrated under reduced pressure. The crude material was purified by silica gel flash chromatography with 10% EtOAc/hex (R_f = 0.34) as eluent to afford the title compound (1.440 g, 69%) of as a colorless solid. ¹H NMR (400 MHz, CDCl₃) δ = 10.10 (s, 2 H), 8.08 (t, *J* = 1.6 Hz, 1 H), 7.89 (td, *J* = 7.6, 1.3 Hz, 1 H), 7.84 (td, *J* = 7.6, 1.7 Hz, 1 H), 7.62 (td, *J* = 8.5, 1.8 Hz, 3 H), 7.53 - 7.49 (m, 2 H). ¹³C NMR (101 MHz, CDCl₃) δ = 191.9, 140.6, 138.3, 136.8, 132.5, 131.9, 129.5, 128.9, 128.5, 127.5, 122.2. Spectral data is consistent with that reported in literature.³⁸

3''-(tert-butyl)-4'',5''-bis(methoxymethoxy)-[1,1':4',1''-terphenyl]-3-carbaldehyde (*p*-MOM₂Cat-*m*-CHO). A 25 mL round-bottom flask containing MOM₂CatBpin (578 mg, 1.52 mmol), *p*-Br-*m*-CHO (404 mg, 1.55 mmol), Na₂CO₃ (325 mg, 3.07 mmol), Bu₄NBr (48 mg, 0.15 mmol) and Pd(PPh₃)₄ (17 mg, 0.015 mmol) in 2 mL of H₂O and 4 mL of toluene, under a nitrogen atmosphere was fitted with a nitrogen-purged, water-cooled condenser and then heated to 85 °C for 20 h. After which it was transferred to a separatory funnel, diluted with 30 mL of EtOAc and washed 2 times each with 20 mL of brine. The organic layer was separated, dried

with Na₂SO₄ and concentrated under reduced pressure. The crude material was purified by deactivate silica gel flash chromatography with 2 to 15% EtOAc/hex to afford the title compound (494 mg, 75%) of as a colorless solid. ¹H NMR (400 MHz, CDCl₃) δ = 10.09 (s, 1 H), 7.99 (d, *J* = 8.2 Hz, 2 H), 7.81 (d, *J* = 8.2 Hz, 2 H), 7.76 (t, *J* = 1.6 Hz, 1 H), 7.62 - 7.57 (m, 1 H), 7.55 (d, *J* = 7.4 Hz, 1 H), 7.30 (d, *J* = 2.3 Hz, 1 H), 5.27 (s, 2 H), 5.26 (s, 2 H), 3.69 (s, 3 H), 3.55 (s, 3 H), 1.49 (s, 9 H). ¹³C NMR (101 MHz, CDCl₃) δ = 191.7, 150.3, 147.0, 145.7, 143.6, 142.1, 140.1, 135.7, 135.2, 130.1, 129.2, 127.7, 127.2, 126.0, 119.4, 113.5, 99.0, 95.3, 57.4, 56.2, 35.2, 30.4. HRMS (APCI+) *m/z*: [M + Na]⁺ Calculated for C₂₇H₃₀O₅ 457.19855; Found 457.19809.

2-(3''-(tert-butyl)-4'',5''-dihydroxy-[1,1':4',1''-terphenyl]-3-yl)-4,4,5,5-

tetramethylimidazolidine-1,3-diol (*p*-Cat-*m*-BHA). *p*-MOM₂Cat-*m*-CHO (494 mg, 1.14 mmol) was dissolved in 10 mL of MeOH with 2 mL of 12M HCl and stirred for 2 days. Reaction was poured into 150 mL of stirring brine, then filtered through a Büchner funnel with filter paper. The solid was collected by dissolving it in CH₂Cl₂, drying with Na₂SO₄ and concentrating under reduced pressure. BHA•H₂SO₄ (419 mg, 1.70 mmol) and K₂CO₃ (158 mg, 1.14 mmol) were added and the flask was purge-pumped three times, filling with nitrogen. Anhydrous MeOH (5 mL) was added and the reaction stirred at room temperature for 20 h. The reaction mixture was concentrated under reduced pressure to ca. 1 mL of solution and precipitated into stirring brine. The precipitate was filtered through a Büchner funnel with filter paper. The solid was collected by washing with Et₂O, the organic layer was dried with Na₂SO₄ and concentrated under reduced pressure to give the title compound (377 mg, 70%) of as a colorless solid. ¹H NMR (400 MHz, DMSO-*d*₆) δ = 9.53 (s, 1 H), 8.19 (s, 1 H), 7.78 (s, 2 H), 7.69 - 7.67 (m, 1 H), 7.65 (d, *J* = 6.8 Hz, 2 H), 7.58 (d, *J* = 6.8 Hz, 2 H), 7.51 - 7.44 (m, 3 H), 7.01 (d, *J* = 2.0 Hz, 1

H), 6.95 (d, $J = 1.9$ Hz, 1 H), 4.56 (s, 1 H), 1.40 (s, 9 H), 1.10 (s, 6 H), 1.07 (s, 6 H). ^{13}C NMR (101 MHz, DMSO- d_6) $\delta = 145.5, 144.0, 142.0, 141.4, 140.9, 139.6, 136.0, 130.2, 129.4, 129.1, 126.1, 125.2, 124.7, 124.5, 115.8, 111.5, 90.1, 66.2, 34.5, 29.4, 24.4, 22.3, 17.2$. HRMS (APCI+) m/z : $[\text{M}+\text{H}]^+$ Calculated for $\text{C}_{29}\text{H}_{36}\text{N}_2\text{O}_4$ 477.27478; Found 477.27383.

***p*-Cat-*m*-NN.** To a solution of ***p*-Cat-*m*-BHA** (105 mg, 0.220 mmol) dissolved in 2 mL of Et_2O and 2 mL of 1M pH 7 phosphate buffer, was added I_2 (56 mg, 0.220 mmol) dissolved in 2 mL of Et_2O dropwise with vigorous stirring and allowing the I_2 color to disappear in between each drop. The reaction was transferred to a separatory funnel, diluted with 5 mL of Et_2O , and washed with ca. 10 mL of brine. The organic layer was separated, dried with Na_2SO_4 and concentrated under reduced pressure to afford the title compound (80 mg, 77%) of as a blue solid.

HRMS (APCI+) m/z : $[\text{M}+\text{H}]^+$ Calculated for $\text{C}_{29}\text{H}_{36}\text{N}_2\text{O}_4$ 474.2513; Found 474.25054

***p*-SQ-*m*-NN.** In a nitrogen-purged, 50 mL round-bottom flask, ***p*-Cat-*m*-NN** (159 mg, 0.336 mmol), $\text{Zn}(\text{OH})\text{Tp}^{\text{Cum,Me}}$ (237 mg, 0.342 mmol), and KOH (26 mg, 0.463 mmol) were dissolved in 10 mL of MeOH and 10 mL of CH_2Cl_2 and stirred under nitrogen for 2 h at room temperature. The reaction was opened to air and stirred overnight. The reaction was concentrated, then redissolved in MeOH with minimal CH_2Cl_2 and cooled to -78 °C. The precipitate was filtered and collected with CH_2Cl_2 to give a crude yield the product (262 mg, 68%) of as a dark green solid. X-ray quality crystals were grown from $\text{CH}_2\text{Cl}_2/\text{MeOH}$ layer-layer diffusion.

HRMS (APCI+) m/z : $[\text{M}]$ Calculated for $\text{C}_{68}\text{H}_{77}\text{BN}_8\text{O}_4\text{Zn}$ 1144.54578; Found 1144.54750

3'-bromo-[1,1'-biphenyl]-4-carbaldehyde (*m*-Br-*p*-CHO). A 100 mL round-bottom flask containing 4-formylphenyl boronic acid (1.097 g, 7.32 mmol), 1,3-dibromobenzene (4.29 g, 18.2 mmol), Na₂CO₃ (1.59 g, 15.0 mmol), Bu₄NBr (0.237 g, 0.735 mmol) and Pd(PPh₃)₄ (87 mg, 75 μmol) of in 8 mL of water, 8 mL of *i*-PrOH and 12 mL of toluene, under a nitrogen atmosphere was fitted with a nitrogen-purged, water-cooled reflux condenser and then heated to 80 °C for 16 h. After which it was concentrated under reduced pressure, diluted with EtOAc and washed with ca. 50 mL of brine. The organic layer was dried with Na₂SO₄ and concentrated under reduced pressure. The crude material was purified by silica gel flash chromatography with 10% EtOAc/hex (R_f = 0.33) as eluent to afford 1.30 g (68%) of the title compound as a colorless solid. ¹H NMR (400 MHz, CDCl₃) δ = 7.36 (t, 1H, *J* = 8 Hz), 7.55 (t, 1H, *J* = 2 Hz), 7.58 (s, 1H), 7.73 (d, 2H, *J* = 8 Hz), 7.79 (t, 1H, *J* = 2 Hz), 7.98 (d, 2H, *J* = 8 Hz), 10.08(s, 1H); ¹³C NMR (101 MHz, CDCl₃) δ = 123.35, 126.19, 127.94, 130.53, 130.63, 30.73, 131.59, 135.84, 142.03, 145.77, 191.97. Spectral data is consistent with that reported in literature.³⁹

3''-(tert-butyl)-4'',5''-bis(methoxymethoxy)-[1,1':3',1''-terphenyl]-4-carbaldehyde (*m*-MOM₂Cat-*p*-CHO). A 25 mL round-bottom flask containing MOM₂CatBpin (437 mg, 1.15 mmol), *m*-Br-*p*-CHO (300 mg, 1.15 mmol), Na₂CO₃ (244 mg, 2.30 mmol), Bu₄NBr (21 mg, 0.065 mmol) and Pd(PPh₃)₄ (7 mg, 0.006 mmol) in 3 mL of H₂O and 9 mL of toluene, under a nitrogen atmosphere was fitted with a nitrogen-purged, water-cooled condenser and then heated to 85 °C for 18 h. After which it was transferred to a separatory funnel, diluted with 10 mL of EtOAc and washed 2 times each with 10 mL of brine. The organic layer was separated, dried with Na₂SO₄ and concentrated under reduced pressure. The crude material was purified by deactivate silica gel flash chromatography with 2 to 15% EtOAc/hex to afford the title compound

(482 mg, 96%) as a colorless solid. ^1H NMR (400 MHz, CDCl_3) δ = 10.09 (s, 1 H), 7.99 (d, J = 8.2 Hz, 2 H), 7.84 - 7.79 (m, 2 H), 7.76 (s, 1 H), 7.64 - 7.58 (m, 2 H), 7.57 - 7.52 (m, 2 H), 7.01 (s, 1 H), 5.27 (s, 2 H), 5.26 (s, 2 H), 3.69 (s, 3 H), 3.55 (s, 3 H), 1.49 (s, 9 H); ^{13}C NMR (101 MHz, CDCl_3) δ = 191.7, 150.3, 147.0, 145.7, 143.6, 142.1, 140.1, 135.7, 135.1, 130.1, 129.2, 127.7, 127.2, 125.9, 119.4, 113.5, 99.0, 95.3, 57.4, 56.2, 35.2, 30.4; HRMS (APCI+) m/z : $[\text{M}+\text{H}]$ Calculated for $\text{C}_{27}\text{H}_{30}\text{O}_5$ 435.21660; Found 435.21623.

2-(3''-(tert-butyl)-4'',5''-dihydroxy-[1,1':3',1''-terphenyl]-4-yl)-4,4,5,5-

tetramethylimidazolidine-1,3-diol (*m*-Cat-*p*-BHA). *m*-MOM₂Cat-*p*-CHO (803 mg, 1.85 mmol) was dissolved in 5 mL of MeOH with 1 mL of 12M HCl and stirred for 18 h. Reaction was poured into 300 mL of stirring brine, then collected the precipitate by vacuum filtration. The solid was collected by dissolving it in Et_2O , drying with Na_2SO_4 and concentrating under reduced pressure. 681 mg (2.77 mmol) of $\text{BHA}\cdot\text{H}_2\text{SO}_4$ and 258 mg (1.87 mmol) of K_2CO_3 were added and the flask was purge-pumped three times, filling with nitrogen. 5 mL of anhydrous MeOH were added and stirred at room temperature for 2 days. Reaction mixture was concentrated under reduced pressure to ca. 1 mL of solution and precipitated into ca. 250 mL of stirring brine. The precipitate was filtered through a Büchner funnel with filter paper. The solid was collected by washing with Et_2O , the organic layer was dried with Na_2SO_4 and concentrated under reduced pressure to give the title compound (617 mg, 70%) as a colorless solid. ^1H NMR (400 MHz, $\text{DMSO}-d_6$) δ = 7.79 (s, 2 H), 7.70 - 7.62 (m, 3 H), 7.61 - 7.43 (m, 5 H), 7.01 (s, 1 H), 6.95 (s, 1 H), 4.56 (s, 1 H), 1.39 (s, 9 H), 1.09 (s, 12 H); HRMS (APCI+) m/z : $[\text{M}+\text{H}]^+$ Calculated for $\text{C}_{29}\text{H}_{36}\text{N}_2\text{O}_4$ 477.27478; Found 477.27361.

***m*-Cat-*p*-NN.** To a solution of ***m*-Cat-*p*-BHA** (100 mg, 0.196 mmol) dissolved in 10 mL of Et₂O and 10 mL of 1M pH 7 phosphate buffer, was added I₂ (50 mg, 0.196 mmol) dissolved in 3 mL of Et₂O dropwise, with vigorous stirring, allowing the I₂ color to disappear in between each drop, until the I₂ color persisted. The reaction was transferred to a separatory funnel, diluted with 5 mL of Et₂O, washed quickly with 5 mL of saturated Na₂S₂O₃ solution and then washed with two portions of 5 mL of brine. The organic layer was separated, dried with Na₂SO₄ and concentrated under reduced pressure to afford the title compound (68 mg, 69%) of as a blue solid.

HRMS (APCI+) *m/z*: [M] Calculated for C₆₈H₇₇BN₈O₄Zn 474.25131; Found 474.25064

***m*-SQ-*p*-NN.** In a nitrogen-purged, 50 mL round-bottom flask, ***m*-Cat-*p*-NN** (331 mg, 0.699 mmol) of, Zn(OH)Tp^{Cum,Me} (533 mg, 0.770 mmol) of, and KOH (40 mg, 0.71 mmol), were dissolved in 10 mL of MeOH and 10 mL of CH₂Cl₂ and stirred under nitrogen for 2 h at room temperature. The reaction was opened to air and stirred overnight. The reaction was concentrated, then dissolved in MeOH with minimal CH₂Cl₂ and cooled to -78 °C. The precipitate was filtered and collected with CH₂Cl₂ to give a crude yield of 400 mg (50%) of the product as a dark green solid. X-ray quality crystals were grown from CH₂Cl₂/MeOH layer-layer diffusion.

HRMS (APCI+) *m/z*: [M+H]⁺ Calculated for C₆₈H₇₇BN₈O₄Zn 1145.55251; Found 1145.55185

IV.9. REFERENCES

- (1) Aviram, A.; Ratner, M. A. Molecular Rectifiers. *Chem. Phys. Lett.* **1974**, *29* (2), 277–283.
[https://doi.org/10.1016/0009-2614\(74\)85031-1](https://doi.org/10.1016/0009-2614(74)85031-1).
- (2) Kondo, H.; Nara, J.; Kino, H.; Ohno, T. Dependence of the Conduction of a Single Biphenyl Dithiol Molecule on the Dihedral Angle between the Phenyl Rings and Its Application to a Nanorectifier. *J. Chem. Phys.* **2008**, *128* (6), 064701.
<https://doi.org/10.1063/1.2828531>.
- (3) Shil, S.; Misra, A. Electric Field Induced Tuning of Molecular Conformation to Acquire Spintronics Property in Biphenyl Systems. *RSC Adv.* **2013**, *3* (34), 14352.
<https://doi.org/10.1039/c3ra41706a>.
- (4) Jorgensen, W. L.; Ulmschneider, J. P.; Tirado-rives, J. Organic Radicals As Spin Filters. *J. Am. Chem. Soc.* **2010**, *132*, 3682–3684.
- (5) Stadler, R.; Geskin, V.; Cornil, J. A Theoretical View of Unimolecular Rectification. *J. Phys. Condens. Matter* **2008**, *20* (37), 374105. <https://doi.org/10.1088/0953-8984/20/37/374105>.
- (6) Tsuji, Y.; Staykov, A.; Yoshizawa, K. Orbital Views of Molecular Conductance Perturbed by Anchor Units. *J. Am. Chem. Soc.* **2011**, *133* (15), 5955–5965.
<https://doi.org/10.1021/ja111021e>.
- (7) Landauer, R. Electrical Resistance of Disordered One-Dimensional Lattices. *Philos. Mag.* **1970**, *21* (172), 863–867. <https://doi.org/10.1080/14786437008238472>.
- (8) Landauer, R. Spatial Variation of Currents and Fields Due to Localized Scatterers in Metallic Conduction. *IBM J. Res. Dev.* **2000**, *44* (1), 251–259.
<https://doi.org/10.1147/rd.441.0251>.

- (9) Tada, T.; Nozaki, D.; Kondo, M.; Hamayama, S.; Yoshizawa, K. Oscillation of Conductance in Molecular Junctions of Carbon Ladder Compounds. *J. Am. Chem. Soc.* **2004**, *126* (43), 14182–14189. <https://doi.org/10.1021/ja031736+>.
- (10) Caroli, C.; Combescot, R.; Nozieres, P.; Saint-James, D. Direct Calculation of the Tunneling Current. *J. Phys. C Solid State Phys.* **1971**, *4* (8), 916–929. <https://doi.org/10.1088/0022-3719/4/8/018>.
- (11) Combescot, R. A Direct Calculation of the Tunnelling Current. III. Effect of Localized Impurity States in the Barrier. *J. Phys. C Solid State Phys.* **1971**, *4* (16), 2611–2622. <https://doi.org/10.1088/0022-3719/4/16/026>.
- (12) Priyadarshy, S.; Skourtis, S. S.; Risser, S. M.; Beratan, D. N. Bridge-mediated Electronic Interactions: Differences between Hamiltonian and Green Function Partitioning in a Non-orthogonal Basis. *J. Chem. Phys.* **1996**, *104* (23), 9473–9481. <https://doi.org/10.1063/1.471690>.
- (13) Tada, T.; Yoshizawa, K. Quantum Transport Effects in Nanosized Graphite Sheets. II. Enhanced Transport Effects by Heteroatoms. *J. Phys. Chem. B* **2003**, *107* (34), 8789–8793. <https://doi.org/10.1021/jp021739t>.
- (14) Jiang, P.; Morales, G. M.; You, W.; Yu, L. Synthesis of Diode Molecules and Their Sequential Assembly to Control Electron Transport. *Angew. Chem. Int. Ed. Engl.* **2004**, *43* (34), 4471–4475. <https://doi.org/10.1002/anie.200460110>.
- (15) Coleman, L. B.; Cohen, M. J.; Sandman, D. J.; Yamagishi, F. G.; Garito, A. F.; Heeger, A. J. Superconducting Fluctuations and the Peierls Instability in an Organic Solid. *Solid State Commun.* **1973**, *12* (12), 1125–1132. [https://doi.org/10.1016/0038-1098\(93\)90282-R](https://doi.org/10.1016/0038-1098(93)90282-R).
- (16) Van Dyck, C.; Ratner, M. A. Molecular Rectifiers: A New Design Based on Asymmetric

- Anchoring Moieties. *Nano Lett.* **2015**, *15* (3), 1577–1584.
<https://doi.org/10.1021/nl504091v>.
- (17) Metzger, R. M. Unimolecular Rectifiers: Present Status. *Chem. Phys.* **2006**, *326* (1), 176–187. <https://doi.org/10.1016/j.chemphys.2006.02.026>.
- (18) Del Nero, J.; de Souza, F. M.; Capaz, R. B. Molecular Electronics Devices: A Short Review. *J. Comput. Theor. Nanosci.* **2010**, *7* (3), 503–516.
<https://doi.org/10.1166/jctn.2010.1386>.
- (19) Martin, A. S.; Sables, J. R. Molecular Rectification, Photodiodes and Symmetry. *Nanotechnology* **1996**, *7* (4), 401–405. <https://doi.org/10.1088/0957-4484/7/4/017>.
- (20) Ashwell, G. J.; Urasinska, B.; Tyrrell, W. D. Molecules That Mimic Schottky Diodes. *Phys. Chem. Chem. Phys.* **2006**, *8* (28). <https://doi.org/10.1039/b604092f>.
- (21) Kirk, M. L.; Shultz, D. A.; Zhang, J.; Dangi, R.; Ingersol, L.; Yang, J.; Finney, N. S.; Sommer, R. D.; Wojtas, L. Heterospin Biradicals Provide Insight into Molecular Conductance and Rectification. *Chem. Sci.* **2017**, *8* (8), 5408–5415.
<https://doi.org/10.1039/C7SC00073A>.
- (22) Kirk, M. L.; Shultz, D. A.; Stasiw, D. E.; Lewis, G. F.; Wang, G.; Brannen, C. L.; Sommer, R. D.; Boyle, P. D. Superexchange Contributions to Distance Dependence of Electron Transfer/Transport: Exchange and Electronic Coupling in Oligo(Para-Phenylene)- and Oligo(2,5-Thiophene)-Bridged Donor-Bridge-Acceptor Biradical Complexes. *J. Am. Chem. Soc.* **2013**, *135* (45), 17144–17154.
<https://doi.org/10.1021/ja4081887>.
- (23) Stasiw, D. E.; Zhang, J.; Wang, G.; Dangi, R.; Stein, B. W.; Shultz, D. A.; Kirk, M. L.; Wojtas, L.; Sommer, R. D. Determining the Conformational Landscape of σ and π

- Coupling Using Para -Phenylene and “Aviram–Ratner” Bridges. *J. Am. Chem. Soc.* **2015**, *137* (29), 9222–9225. <https://doi.org/10.1021/jacs.5b04629>.
- (24) Venkataraman, L.; Klare, J. E.; Nuckolls, C.; Hybertsen, M. S.; Steigerwald, M. L. Dependence of Single-Molecule Junction Conductance on Molecular Conformation. *Nature* **2006**, *442* (7105), 904–907. <https://doi.org/10.1038/nature05037>.
- (25) Xia, C.-J.; Zhang, Y.-T.; Liu, D.-S. Effect of Torsion Angle on the Rectifying Performance in the Donor-Bridge-Acceptor Single Molecular Device. *J. Theor. Comput. Chem.* **2012**, *11* (04), 735–743. <https://doi.org/10.1142/S0219633612500496>.
- (26) Vonlanthen, D.; Mishchenko, A.; Elbing, M.; Neuburger, M.; Wandlowski, T.; Mayor, M. Chemically Controlled Conductivity: Torsion-Angle Dependence in a Single-Molecule Biphenyldithiol Junction. *Angew. Chem. Int. Ed. Engl.* **2009**, *48* (47), 8886–8890. <https://doi.org/10.1002/anie.200903946>.
- (27) Ho, C. C.; Olding, A.; Smith, J. A.; Bissember, A. C. Nuances in Fundamental Suzuki–Miyaura Cross-Couplings Employing [Pd(PPh₃)₄]: Poor Reactivity of Aryl Iodides at Lower Temperatures. *Organometallics* **2018**, *37* (11), 1745–1750. <https://doi.org/10.1021/acs.organomet.8b00189>.
- (28) Gross, M. L.; Blank, D. H.; Welch, W. M. The Triazene Moiety as a Protecting Group for Aromatic Amines. *J. Org. Chem.* **1993**, *58* (8), 2104–2109. <https://doi.org/10.1021/jo00060a028>.
- (29) Organ, M. G.; Abdel-Hadi, M.; Avola, S.; Hadei, N.; Nasielski, J.; O’Brien, C. J.; Valente, C. Biaryls Made Easy: PEPPSI and the Kumada-Tamao-Corriu Reaction. *Chem. - A Eur. J.* **2007**, *13* (1), 150–157. <https://doi.org/10.1002/chem.200601360>.
- (30) Valente, C.; Belowich, M. E.; Hadei, N.; Organ, M. G. Pd-PEPPSI Complexes and the

- Negishi Reaction. *European Journal of Organic Chemistry*. WILEY-VCH Verlag June 25, 2010, pp 4343–4354. <https://doi.org/10.1002/ejoc.201000359>.
- (31) Rucareanu, S.; Schuwey, A.; Gossauer, A. One-Step Template-Directed Synthesis of a Macrocyclic Tetraarylporphyrin Hexamer Based on Supramolecular Interactions with a C₃-Symmetric Tetraarylporphyrin Trimer. *J. Am. Chem. Soc.* **2006**, *128* (10), 3396–3413. <https://doi.org/10.1021/ja057117d>.
- (32) Chen, X.; Jeon, Y. M.; Jang, J. W.; Qin, L.; Huo, F.; Wei, W.; Mirkin, C. A. On-Wire Lithography-Generated Molecule-Based Transport Junctions: A New Testbed for Molecular Electronics. *J. Am. Chem. Soc.* **2008**, *130* (26), 8166–8168. <https://doi.org/10.1021/ja800338w>.
- (33) Kenda, B.; Diederich, F. Supramolecular Aggregates of Dendritic Cyclophanes (Dendrophanes) Threaded on Molecular Rods with Steroid Termini. *Angew. Chemie Int. Ed.* **1998**, *37* (22), 3154–3158. [https://doi.org/10.1002/\(SICI\)1521-3773\(19981204\)37:22<3154::AID-ANIE3154>3.0.CO;2-W](https://doi.org/10.1002/(SICI)1521-3773(19981204)37:22<3154::AID-ANIE3154>3.0.CO;2-W).
- (34) Bedard, T. C.; Moore, J. S. Design and Synthesis of Molecular Turnstiles. *J. Am. Chem. Soc.* **1995**, *117* (43), 10662–10671. <https://doi.org/10.1021/ja00148a008>.
- (35) Zhang, J.; Pesak, D. J.; Ludwick, J. L.; Moore, J. S. Geometrically-Controlled and Site-Specifically-Functionalized Phenylacetylene Macrocycles. *J. Am. Chem. Soc.* **1994**, *116* (10), 4227–4239. <https://doi.org/10.1021/ja00089a012>.
- (36) Markussen, T.; Stadler, R.; Thygesen, K. S. The Relation between Structure and Quantum Interference in Single Molecule Junctions. *Nano Lett.* **2010**, *10* (10), 4260–4265. <https://doi.org/10.1021/nl101688a>.
- (37) Kirk, M. L.; Shultz, D. A.; Stasiw, D. E.; Habel-Rodriguez, D.; Stein, B.; Boyle, P. D.

- Electronic and Exchange Coupling in a Cross-Conjugated D-B-A Biradical: Mechanistic Implications for Quantum Interference Effects. *J. Am. Chem. Soc.* **2013**, *135* (39), 14713–14725. <https://doi.org/10.1021/ja405354x>.
- (38) Bonin, H.; Delbrayelle, D.; Demonchaux, P.; Gras, E. Base Free Aryl Coupling of Diazonium Compounds and Boronic Esters: Self-Activation Allowing an Overall Highly Practical Process. *Chem. Commun.* **2010**, *46* (15), 2677–2679. <https://doi.org/10.1039/b926547n>.
- (39) Capitosti, G. J.; Guerrero, C. D.; Binkley, D. E.; Rajesh, C. S.; Modarelli, D. A. Efficient Synthesis of Porphyrin-Containing, Benzoquinone-Terminated, Rigid Polyphenylene Dendrimers. *J. Org. Chem.* **2003**, *68* (2), 247–261. <https://doi.org/10.1021/jo026520p>.
- (40) Kozo Toyota; Subaru Kawasaki, and; Yoshifuji*, M. Preparation and Properties of Phosphaethynes Bearing Bulky Aryl Groups with Electron-Donating Substituents at the Para Position. **2004**. <https://doi.org/10.1021/JO049571Q>.

V. Evaluation of Coupling in Donor-Bridge-Acceptor Biradicals with Nonalternant π -System Bridges.

V.1. Introduction to Azulene and Theory.

V.1.1. Azulene vs. Naphthalene.

Based on their π -topology, conjugated molecules are classified as either alternant or nonalternant. These classifications indicate the electronic- and molecular orbital (MO) trends of a π -system. For example, consider a set of structural isomers with the formula $C_{10}H_8$: naphthalene and azulene. The structures of both compounds are shown in Figure V-1 with solutions of CH_2Cl_2 containing ~ 5 mg of each substance. These two molecules are both aromatic,

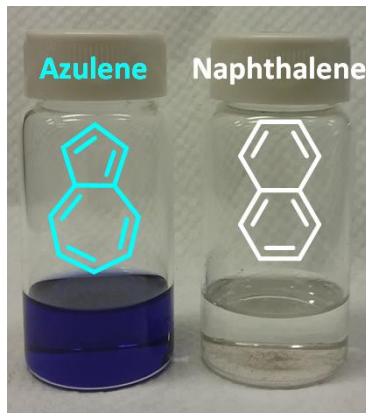


Figure V-1. Structures and CH_2Cl_2 solutions of the $C_{10}H_8$ isomers: azulene (left) and naphthalene (right).

as they satisfy the requirements for aromaticity: cyclic, conjugated, planar and have $(4n + 2) \pi$ electrons. However, as can be seen in Figure V-1, naphthalene is colorless while azulene is dark blue. These two molecules interact with light differently as a consequence of their inherently different electronic structures, despite being constitutional isomers.

V.1.2. Types of Alternant and Nonalternant Hydrocarbons.

To identify alternant/nonalternant hydrocarbons, one uses the “star” method as described by Ovchinnikov in 1978.¹ To implement the “star” method, every other atom in the π -system is “starred” and if this can be done so that no two starred atoms or no two unstarred atoms are

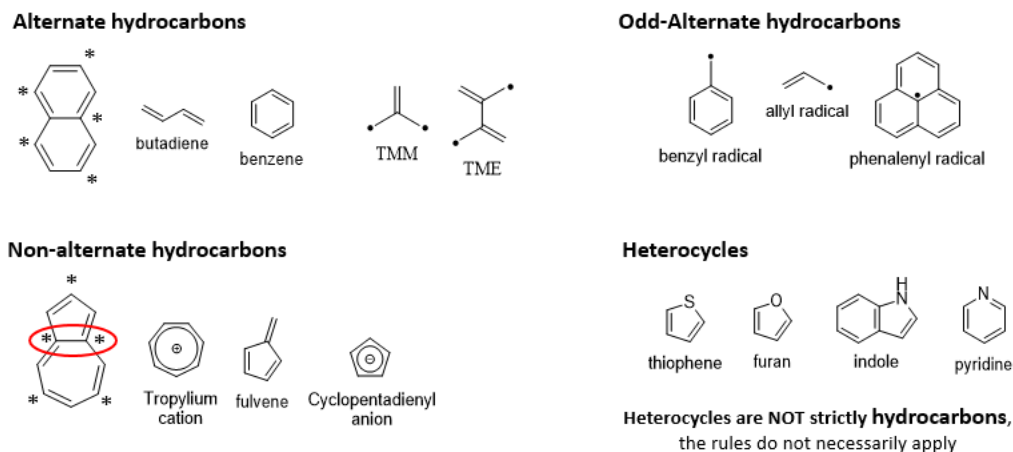


Figure V-2. Examples of even-alternant, odd-alternant, and nonalternant hydrocarbons, alongside heterocycles which are not part of any of these other classifications.

contiguous, then the π -system is alternant. However, if either two starred atoms or unstarred atoms are adjacent, then the π -system is nonalternant. As shown in Figure V-2, naphthalene satisfies the condition to be an alternant π -system while azulene does not and is therefore a nonalternant hydrocarbon π -system. Figure V-2 shows examples of even-alternant hydrocarbons (those which satisfy the star method and have an even number of carbon atoms in their π systems), which include: polyenes, benzene, and some biradicals. Odd-alternant hydrocarbons satisfy the star method and have an odd number of carbon atoms in their π -systems; all of these are going to be monoradicals such as the allyl, benzyl and phenalenyl radicals. Nonalternant hydrocarbons are those that will have two starred or unstarred atoms next to each other as shown for azulene in Figure V-2. Other common nonalternant hydrocarbons are shown such as the tropylium cation, cyclopentadienyl anion and fulvene. Any odd-membered ring in the π -system will immediately indicate that a system will be nonalternant. While some heterocycles may possess odd-membered rings in their π systems, most do not fit into either category of alternant or nonalternant hydrocarbon π systems because they are not strictly hydrocarbons. Adding heteroatoms into the π system disrupts the symmetry of the molecule, the number of electrons in

the π -system and the distribution of the electrons in the π -system due to heteroatom electronegativities being different from that of carbon.

V.1.3. Electronic Structure Differences between Alternant and Nonalternant Hydrocarbons.

The origin of the differences between alternant and nonalternant hydrocarbons arises in their electronic structures. This can be seen even at the simplest levels of calculation. Figure V-3A shows the simple Hückel-calculated MO energy levels for azulene and naphthalene. Because

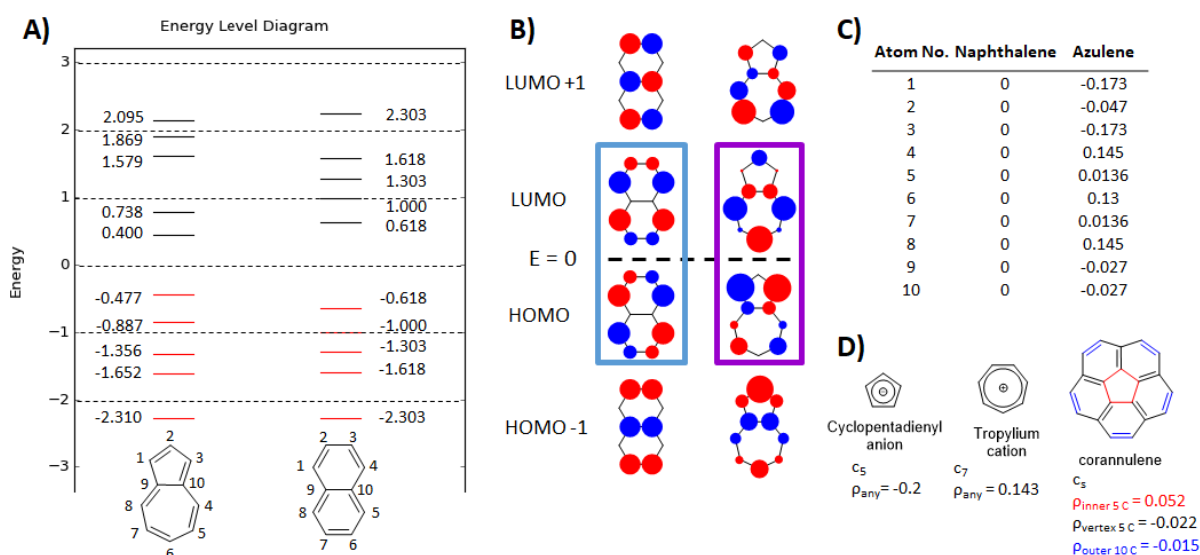


Figure V-3. A) Hückel-calculated energy level diagrams for azulene and naphthalene. B) HOMO-1, HOMO, LUMO and LUMO=1 molecular orbitals for naphthalene and azulene. C) Hückel-calculated charge densities for each carbon atom of naphthalene and azulene. D) Examples of nonalternant hydrocarbons where rotational symmetry dictates atom charge densities are equivalent or not equivalent.

there are no unpaired electrons in either of these structures there are no molecular orbitals at $E = 0$ energy; corresponding to nonbonding orbitals ($E = \alpha$). Both molecules have five bonding orbitals and five antibonding orbitals. However, in alternant hydrocarbons for every molecular orbital at $E = \alpha + x\beta$ there is a molecular orbital at $E = \alpha - x\beta$, but in nonalternant hydrocarbons this is not the case. Figure V-3B shows the HOMO and LUMO surrounded by a rectangle for naphthalene and azulene. As can be seen in naphthalene, the HOMO and LUMO are symmetric in the absolute value of their wavefunction coefficients: this is generally true for alternant

hydrocarbons; their matching orbital energies above and below the non-bonding energy are symmetric. Azulene's HOMO and LUMO are asymmetric and the same atoms have different wavefunction coefficients. Figure V-3C shows the Hückel calculated electron densities on each of the atoms in the π -system for naphthalene and azulene. Naphthalene is an example of the values of charge densities for even alternant hydrocarbons; each atom in the π -system contributes one electron and the charge densities are zero (electron densities = 1). For nonalternant hydrocarbons, the charge densities are only evenly distributed only if all the atoms in the π system can be related by rotational symmetry. In Figure V-3D the cyclopentadienyl anion and tropylium cation have atoms that can all be related by a C_5 and C_7 rotational axis, respectively and so each of the atoms in those π -systems have charge densities of 0.2 and -0.143, respectively. However, the nonalternant hydrocarbon corannulene cannot have all of its atoms related by the same rotational axis and so the five carbon atoms in the central ring have charge densities of +0.052 and the outer ten carbon atoms have charge densities of -0.015 and the five vertex carbon atoms which connect the inner and outer atoms are -0.022.

V.1.4. Breakdown of Rules for Understanding Conjugation, Electron-pushing and Spin-polarization in Nonalternant Hydrocarbons.

There are various qualitative "pen-and-paper" methods for understanding trends and concepts such as reactivity and conjugation in alternant hydrocarbons. However, in non-alternant hydrocarbons these same tried-and-true methods for alternant hydrocarbons generally fail,^{1,2} and similar constructs have remained elusive for non-alternant hydrocarbons.^{3,4} For example, Figure V-4 shows the breakdown of some of these common methods. Figure V-4A shows 1-methylene-naphthalene and 1-methylene-azulene radicals and a common technique of electron pushing to move the radical around the naphthalene and azulene rings. A technique that is taught early in

organic chemistry as a means to explain substituent effects in electrophilic aromatic substitution for benzene (an alternant π -system) derivatives. The radical is easily moved around to every other carbon atom in the π -system to show the resonance structures for the methylene-naphthalene radical which is where in the SOMO of naphthalene shown in Figure V-4B, has electron density. Furthermore, in Figure V-4C these positions are also the positions that get starred when using Ovchinnikov's star method,¹ or the positions that have all the same electron

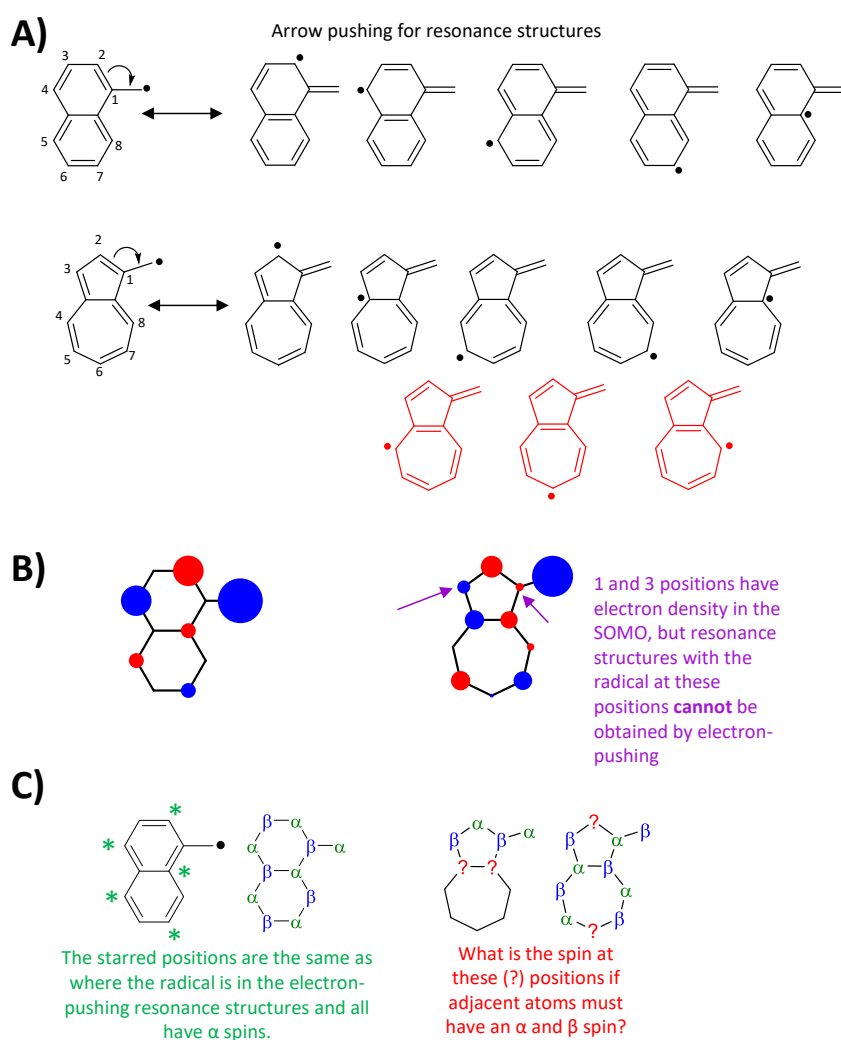


Figure V-4. The breakdown of some common pictorial analogies that work for alternant hydrocarbons, but not for nonalternant hydrocarbons. **A)** Electron/arrow-pushing to move a radical or charge around aromatic rings. **B)** SOMOs of 1-methylenenaphthalene and 1-methyleneazulene radicals showing discrepancies between the analogy and even low level of theory Hückel calculations. **C)** Application of the star method to naphthalene and spin polarization in naphthalene vs. azulene.

spin (α in this case). The same electron-pushing technique when applied to a non-alternant hydrocarbon will depend on which direction you start. In Figure V-4A the resonance structures in black are the result if the double bonds that get moved follow the ten-carbon perimeter of azulene. The red structures are the result if a figure-eight pattern is used for moving double bonds; moving the double bond between the 5- and 7-membered rings. Already this is different from naphthalene because in naphthalene and other alternant hydrocarbons, never will there be an instance where the radical (or anion or cation) will appear on two adjacent carbon atoms in the π -system. Now this could mean that perhaps there is electron density in the SOMO at all these positions, but Figure V-4B shows the SOMO for azulene and while this is technically true, even at the Hückel level, where at the 4- and 6 positions there is still electron density although the coefficients are very small ($|0.005|$ and $|0.06|$, respectively); and barely visible in the drawing. However, by using this arrow/electron pushing method, there is no way to draw a structure where the radical ends-up on the 1 or 3 positions and there is electron density in the SOMO at those positions which is greater than the barely-visible orbital coefficients at the 4,6- or even larger 8 positions. Furthermore, the star method clearly “fails” because this was discussed earlier as being the test to determine an alternant hydrocarbon versus a nonalternant hydrocarbon, but the spin polarization argument will also fail as shown in Figure V-4C as there will always be at least one position in a nonalternant hydrocarbon where attempting to assign α or β spins will be ambiguous.

An atom counting model has been proposed for the determining the presence or lack thereof quantum interference effects (e.g., negligible electron transport through the molecule) which in alternant hydrocarbons translates to cross-conjugation.^{3,5-7} This model is presented in in Figure V-5A for azulene. To determine if the connectivity across two positions of a ring system

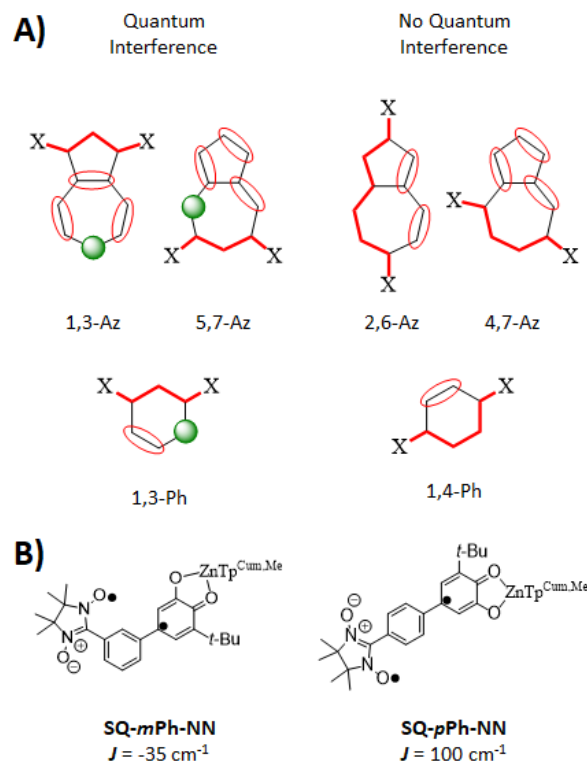


Figure V-5. **A)** Application of the atom counting model for predicting quantum interference in nonalternant hydrocarbons like azulene and alternant hydrocarbons such as benzene. **B)** SQ-B-NN molecules with alternant bridges that the atom counting model indicates quantum interference give $J < 0$ while those for which the atom counting model does not indicate quantum interference give $J > 0$.

will suffer from quantum interference, one highlights the shortest pathway between the two points, then circles adjacent pairs of atoms in the π -system. If there is an atom left without a partner, then there will be quantum interference, and if all remaining atoms are paired, then there will not be quantum interference (i.e., conjugation resulting in current flow).

In Figure V-5B, when an SQ-B-NN molecule containing an alternant hydrocarbon (phenyl) bridge, for which the atom counting model indicates quantum interference (*m*SQ-Ph-NN) the exchange coupling constants (J) are negative, indicating antiferromagnetic coupling, and when the atom counting model does not indicate quantum interference the exchange coupling constants (J) are positive, indicating ferromagnetic coupling. So, in Figure V-5A, 1,3- and 5,7- connectivities through azulene, the atom counting model suggests it will result in

quantum interference, which would suggest that an **SQ-Az-NN** across these positions would in theory have antiferromagnetically-coupled radicals ($J < 0$). On the other hand, 2,6- and 4,7 connectivities through azulene would not have quantum interference effects and an **SQ-Az-NN** at these positions would have ferromagnetically-coupled ($J > 0$) radicals. This atom counting model works for alternant hydrocarbons, but is still lacking empirical evidence to support its use in nonalternant hydrocarbons despite efforts to prove it, causing some results that will be discussed later as being in contention with each other.^{3,4}

V.1.5. The Dipole Moment of a Hydrocarbon and some Small Molecules.

Azulene is of interest for organic electronics 1) due to its unique photophysics which will be discussed in the next section and 2) because of its unusually large dipole for a molecule composed only of carbon and hydrogen. Of course, in order to have any dipole moment a molecule must lack multiple 3-fold or higher rotational axis, inversion symmetry and improper rotation axes. This constitutes a large variety of molecules and so the easiest way to express how the dipole moment of azulene compares is to provide examples of some small molecules of different classes. Figure V-6 shows a variety of molecules for comparison with azulene. First of all, azulene's dipole moment of 1.08 Debye arises from its resonance structure which is the cyclopentadienyl anion fused with the tropylium cation. As mentioned, azulene is a hydrocarbon -- It is composed only of carbon and hydrogen -- and for comparison, below it are several other hydrocarbons with various degrees of saturation -- some aromatic some not. Naphthalene, benzene, and cyclopropane do not have dipole moments because they either have inversion symmetry or improper rotation axes or both. Hexane is considered to have a dipole because some of its rotational isomers fit these criteria; although its dipole moment is very small (~0.1 Debye).

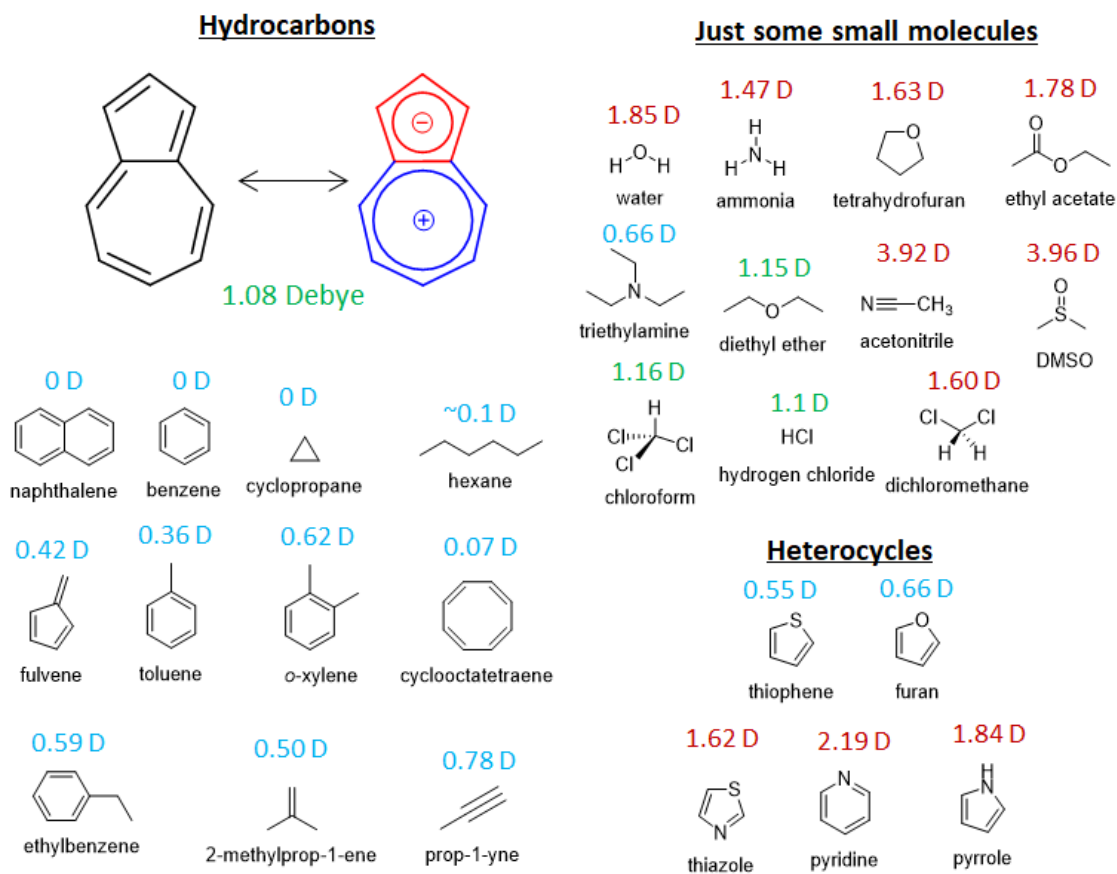


Figure V-6. The dipole moment of azulene, other hydrocarbons, some common small molecules and a few heterocycles.

Fulvene is another nonalternant hydrocarbon, however its dipole moment is still relatively small. The largest dipole moment of these hydrocarbons other than azulene is propyne at 0.78 Debye, which is still 0.3 Debye less than azulene. Some small molecules that contain heteroatoms such as oxygen, nitrogen, chlorine which are some of the most electronegative elements and are considered to be constituents of polar molecules only barely eclipse the dipole moment of azulene. Diethyl ether, chloroform, and hydrogen chloride are all within 0.08 Debye of azulene, while triethylamine is much less. Even among heterocycles, the dipole moment of azulene is greater than those of thiophene and furan. While azulene's dipole moment is much less than the molecules whose dipole moments are shown in red in Figure V-6, one must remember that all

these molecules possess one or more heteroatoms with electronegativity differences between their atoms much larger than the difference between carbon and hydrogen.

V.1.6. Violation of Kasha's Rule.

Azulene first garnered attention in 1955 when Beer and Longuet-Higgins published "Anomalous Light Emission of Azulene," in which they demonstrated that the fluorescence spectrum of azulene was the mirror image of its $S_0 \rightarrow S_2$ absorption (Figure V-7A).⁸ This is a violation of what has become known as Kasha's rule which states that the fluorescence spectrum for an organic molecule should be "approximately the mirror image of the absorption system at longest wavelengths." In other words, because internal conversion of $S_n \rightarrow S_1$ is typically so fast, emission occurs from the lowest excited state of a given multiplicity. So azulene, like other organic compounds, such as its isomer naphthalene, was expected to give fluorescence that was the mirror image of its $S_0 \rightarrow S_1$ absorption rather than the $S_0 \rightarrow S_2$ absorption. In fact, azulene shows no emission from its S_1 state, but strong S_2 emission. Kasha supported Beer and Longuet-Higgins's observations in 1956 with his own set of experiments to confirm that the emission was from azulene and not an impurity.⁹ In order to accomplish this, Kasha synthesized several alkylated azulenes for comparison with unsubstituted azulene to determine if the S_2 emission was observed with the alkylated derivatives with the hypothesis that it would be highly improbable that an impurity would survive through the purification of the azulene derivatives.

Many spectroscopic investigations and theoretical calculations went into identifying azulene's excited state dynamics and the focus of this chapter is not on azulene's photochemistry, but a brief summary will be provided. Figure V-7B shows the S_0 , S_1 , and S_2 states of naphthalene and azulene. Naphthalene, like most organic molecules, exhibits a quantum yield from fluorescence (Φ_F) of zero from its S_2 state, but a non-zero quantum yield from its S_1

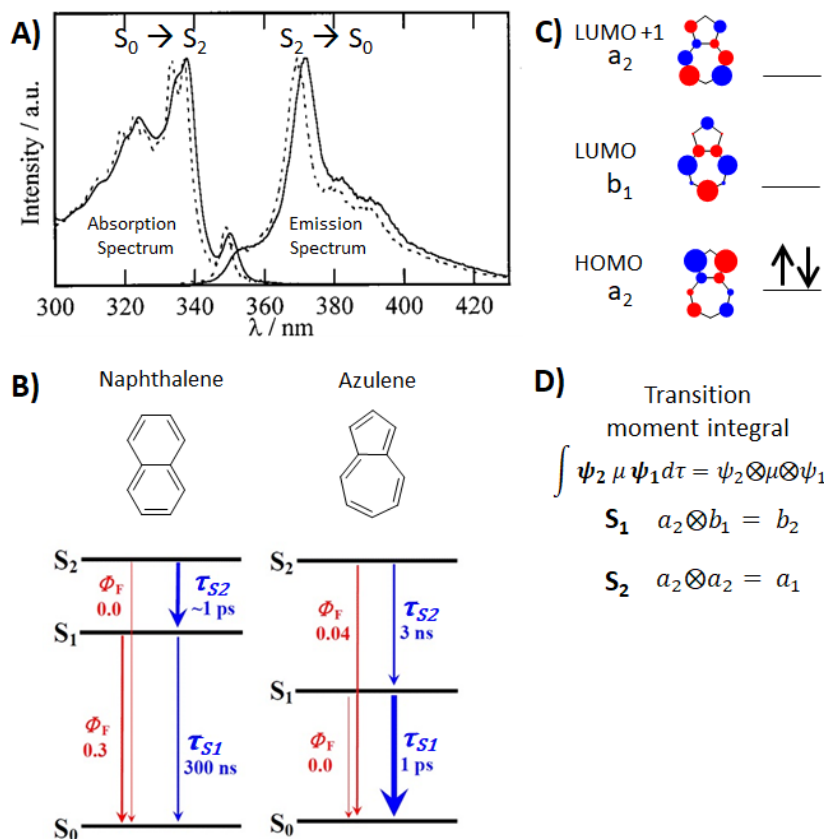


Figure V-7. **A)** S_2 state absorption and emission spectrum of azulene. **B)** Excited state dynamics of naphthalene and azulene. **C)** HOMO, LUMO and LUMO+1 of azulene with orbital symmetries in the C_{2v} point group. **D)** Transition moment integral and the products of the symmetries of the S_1 and S_2 states of azulene and naphthalene.

state. Azulene however exhibits a non-zero quantum yield from its S_2 state, but a quantum yield near-zero ($\Phi_F = 5 \times 10^{-6}$) for its S_1 state.^{10,11} In naphthalene the S_2 and S_1 states lie closer in energy and this facilitates fast non-radiative internal conversion from the S_2 state to the S_1 state. The lifetime for S_2 of naphthalene is ~ 1 picosecond ($k = 1/\tau$).¹⁰ Because the S_1 and S_0 states lie far apart in energy, there is relatively slow non-radiative internal conversion from the S_1 to S_0 state resulting in an S_1 lifetime of ~ 300 ns, which allows for some radiative decay in the form of fluorescence ($\Phi_F = 0.3$) from the S_1 state of naphthalene. Azulene however, has a very low-lying S_1 state which slows the rate of non-radiative internal conversion from the S_2 to S_1 state ($\tau_{S_2} = 3$ ns) allowing some of the energy to be dispersed in the form of fluorescence ($\Phi_F = 0.04$). The

low-lying S_1 state results in fast internal conversion to the S_0 state ($\tau_{S_1} = 1$ ps), with negligible fluorescence.

The extinction coefficients for naphthalene and azulene's S_1 - and S_2 absorptions vary greatly from each other. First of all, the S_1 transition for naphthalene occurs at 276 nm with an extinction coefficient of about $6000 \text{ M}^{-1} \text{ cm}^{-1}$ and its S_2 transition is at 220 nm with an extinction coefficient of $13000 \text{ M}^{-1} \text{ cm}^{-1}$. Azulene's S_1 transition occurs around 570 nm with an extinction coefficient of about $400 \text{ M}^{-1} \text{ cm}^{-1}$, an order of magnitude less than that of naphthalene. Azulene's S_2 transition occurs at 370 nm with an extinction coefficient of $5000 \text{ M}^{-1} \text{ cm}^{-1}$. Figure V-7C shows the HOMO, LUMO and LUMO+1 orbitals for azulene with their symmetries in the C_{2v} point group. Figure V-3B can be used as reference for naphthalene's corresponding orbitals. In C_{2v} symmetry azulene and naphthalene's orbitals possess the same symmetries and according to the transition moment integral in Figure V-7D the transitions for the S_1 states would transform as either b_1 or b_2 , depending on assignment of the axes; both of which are allowed transitions, transforming with the x- or y axes, respectively. The transition for the S_2 state for both molecules would transform as a_1 which transforms with the z-axis in C_{2v} , so it is also a dipole-allowed transition. However, naphthalene being an alternant hydrocarbon possesses a high degree of symmetry between the orbital coefficients in corresponding orbitals about $E = 0$ energy. The HOMO and LUMO of naphthalene have identical orbital coefficients on identical carbon atoms, they occupy the same space on the molecule. Azulene's HOMO has greater orbital coefficients in the 5-membered ring whereas its LUMO has greater orbital coefficients on the 7-membered ring. These orbitals occupy opposite sides of the molecule, as a result the transition moment integral is smaller for azulene than naphthalene due to poorer overlap and this is reflected in the difference in their extinction coefficients.

V.1.7. Organic Electronics.

As discussed, Azulene and other non-alternant hydrocarbons have unique properties that make them of interest for organic electronics, such as unique optical properties or high dipole moments.¹²⁻¹⁵ Despite this, basic attributes of aromatic molecules, such as what qualifies as a conjugated vs cross-conjugated pathway are not well understood for non-alternant hydrocarbons.^{3,4,6,7,16} Much research has been conducted on the optical properties of azulenes, and a few articles that will be discussed focused on polymers and oligomers of azulene as well as

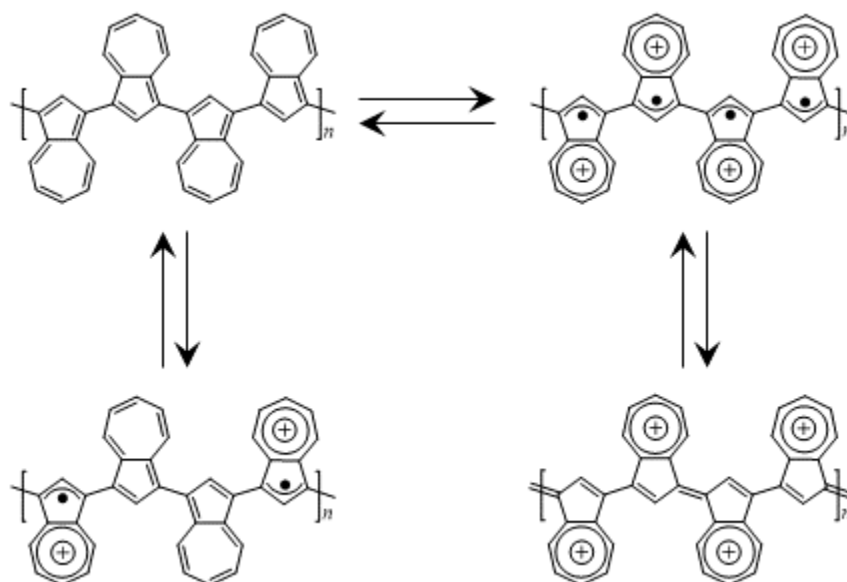


Figure V-8. *poly(1,3-azulene)* prepared by Wang, et al. with the radical cations and resonance structures attributed to the conductivity of polymers treated with either acid or iodine.

several articles that have attempted to discover the nature of conductance through several substituted azulenes in single-molecule devices.

V.1.8. Azulene Oligomers and Polymers.

Wang et al. reported the first polymer of azulene, *poly(1,3-azulene)*, in 2003.¹⁷ They reported that upon protonation with trifluoroacetic acid the polymer changed color from yellow-green to dark purple and became conductive (0.74 S/cm) versus treatment of the polymer with iodine resulted in conductivity of 1.22 S/cm. Both of which are significantly better than the

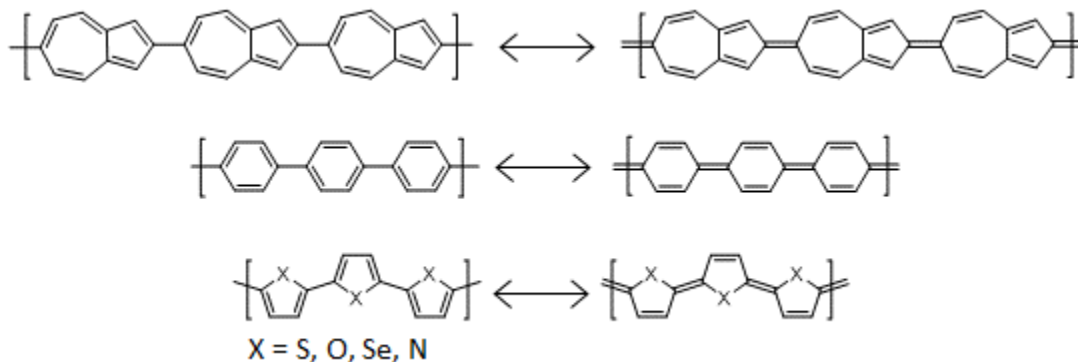


Figure V-9. The ability of *poly(2,6-azulene)* to have the quinoidal resonance structure like other conjugated polymers, such as *poly(phenylene)* and polymers of 5-membered heterocycles containing chalcogens and pnictogens.

untreated polymer which is not conductive at 10^{-11} S/cm. They hypothesized in both instances of treating *poly(1,3-azulene)* resulted in formation of the radical cation of the azulene units as shown in Figure V-8. The degree of protonation or oxidation controls the number of radical cationic azulene units that give rise to the higher conductivity vs. the neutral polymer. The presence of the radical cations is supported by the EPR spectrum which displays a singlet at $g = 2$. The relatively small shifts in the electronic absorption spectra versus other conducting polymers such as polythiophenes, was attributed to “*meta*-conjugation” (= cross-conjugation) through the polymer backbone.

2,6-Azulenenes are of interest for conducting organic polymers because they can adopt a quinoidal structure, similarly to *poly(phenylenes)* and polymers of 5-membered ring heterocycles containing chalcogens and pnictogens (*e.g.* polythiophene and polypyrrole) as shown in Figure V-9. Yamaguchi, et al. reported four terazulenenes with 2,6 connectivity with the difference being the orientation of the azulene ring to give one with head-tail head-tail connectivity (HTHT), one with heat-tail head-head (HTHH), one with head-head tail-tail (HHTT) and one with tail-tail head-tail (TTHT) as shown in Figure V-10 alongside their DFT calculated HOMO, LUMO and dipole moments.¹³ Interestingly the LUMOs for all four molecules are relatively similar and

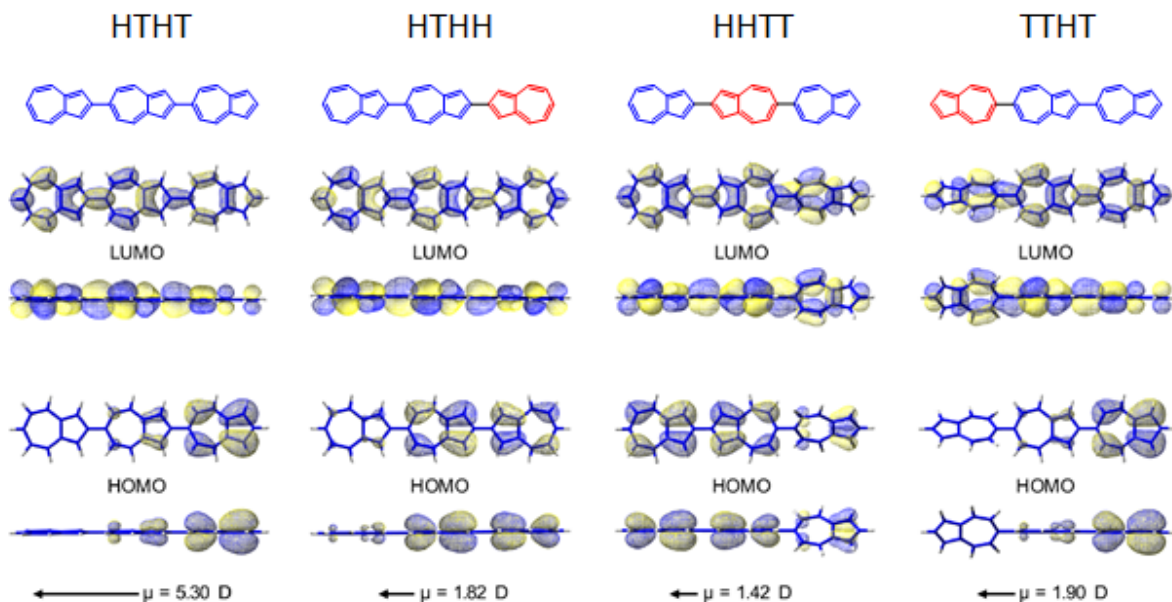


Figure V-10. Terazulenes from Yamaguchi et al. possessing different connectivities beside their DFT calculated HOMOs, LUMOs and dipole moments.

delocalized over all three azulene units, but the HOMOs for HTHT and TTHT are primarily localized to half the terazulenes whereas the HOMOs for HTHH and HHTT are more evenly delocalized over all three azulene units. Another interesting point is that the dipoles of all four terazulenes is greater than azulene and HTHT has a dipole of 5.30 Debye! This is greater than all of the molecules given as examples in Figure V-7; keeping in mind this is still a molecule composed only of carbon and hydrogen. There are not many organic molecules in the literature that exhibit dipole moments this large, a few examples from Song et al. are in Figure V-11, but it

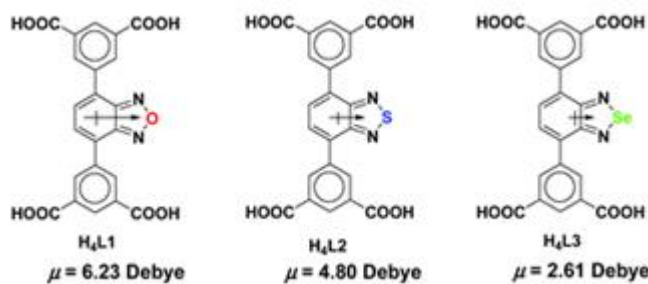


Figure V-11. Organic molecules with heteroatoms possessing dipole moments comparable to the terazulenes from Song et al.

should be noted that 1) only one of these molecules surpasses HTHT terazulene 2) the direction of the dipole in these molecules is perpendicular to the direction of connectivity and 3) these molecules contain electronegative heteroatoms to provide their dipoles.¹⁸

From device fabrication of the terazulenes with either gold or aluminum electrodes they were able to attribute different carrier motilities depending on the connectivity through the terazulenes. The HTHT terazulene exhibited primarily n-type (electron) carrier mobility, the HTHH however exhibited p-type (hole) carrier mobility with the exception of ambipolar mobility at elevated temperatures with aluminum electrodes.¹³ The exact opposite polarity just by changing one of the bonds. On the other hand, HHTT exhibited ambipolar mobility with a gold electrode, but only at room temperature and n-type mobility at elevated temperatures. TTHT exhibited purely n-type mobility similarly to HTHT.

V.1.9. Conductance Studies through Azulene Derivatives.

Xia et al. synthesized and studied the conductance for several derivatives of azulene with different connectivity in order to test the atom counting model that was presented earlier in this chapter.³ Their studies included the azulene derivatives shown in Figure V-12A, which with the thiochroman linkers were bridged between gold electrodes. Through the atom counting model, 1,3- and 5,7 linkages through azulene should exhibit quantum interference while 2,6- and 4,7 linkages should not (Figure V-6). Xia et al.'s conductance studies shown in the table of Figure V-12A, reveal that the conductance for 1,3-Az and 2,6-Az were experimentally the same ($32 \times 10^{-5} g_0$) when measured at 0.25 V and that the 4,7-isomer was only one-quarter of their value at $8 \times 10^{-5} g_0$. 1,3-Az and 4,7-Az contradict the atom counting model in that 1,3-Az would be expected to display lower conductance than 4,7-Az due to the presence of quantum interference. They also

present calculations^{19,20} which suggest that the conductance trend should be 1,3-Az > 2,6-Az ≈ 4,7-Az.

Schwarz et al. also synthesized and studied the conductance for several derivatives of azulene, but instead of making thiochroman-linked azulenes, they utilized *bis*(4-ethynylbenzenethiol) to anchor the azulene derivatives to gold electrodes (Figure V-12B).⁴ Their measured conductance for each azulene derivative are presented in the table of Figure V-12. Their data indicates that 2,6-Az and 4,7-Az exhibit experimentally identical conductance at $2.1 \times 10^{-3} g_0$ and 1,3-Az is three orders of magnitude less at $3.5 \times 10^{-6} g_0$. Their order for conductivity of azulene derivatives follows 2,6-Az ≈ 4,7-Az > 1,3-Az which is supported by

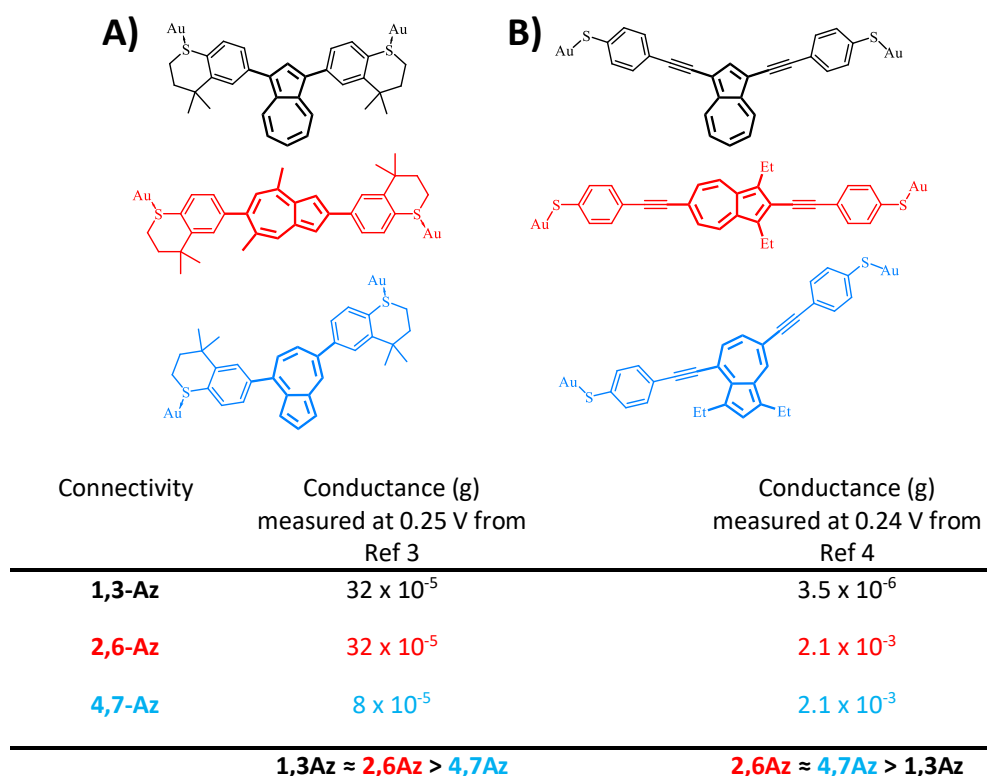


Figure V-12. Reported measured conductance values for the azulene derivatives synthesized by A) Xia et al. and B) Schwarz et al. with the order from greatest conductance to lowest conductance for both the measured and calculated conductance from each study.

their nonequilibrium Green's function calculations within the DFT framework (NEGF-DFT) calculations which give approximately the same result in terms of orders of magnitude.⁴

The studies conducted by Xia et al. and Schwarz et al. display different conductance results for azulene derivatives with the same connectivity at 0.25 and 0.24 V, respectively.^{3,4} Some of this discrepancy is to be expected, for example Schwarz et al.'s results are for all but 1,3-Az two orders of magnitude larger than the results reported by Xia et al. which can be explained by the fact that they used different electrode-anchoring groups. Xia et al. used the thiochroman and Schwarz et al. used 4-ethynylbenzenethiol groups which should give inherently different conductance. However, despite the orders of magnitude, the hierarchical trends of conductance displayed by the azulene derivatives are in disagreement. There is a large discrepancy between the experimentally-determined data and calculated conductance reported by Xia et al. which in turn are in contention with the experimental and calculated conductance reported by Schwarz et al.; although latter's experimental and calculated are consistent. Experimentally, 1,3-Az was determined to give the greatest conductance for Xia et al., but the lowest conductance of the series for Schwarz et al. Also, 4,7-Az displayed much lower conductance than 2,6-Az for Xia et al., but experimentally identical conductance was observed for 3,7-Az and 2,6-Az in the case of Schwarz et al. Furthermore, the calculations also do not support each other 1,3-Az is reported to have the largest conductance for Xia et al. while it is the lowest by several orders of magnitude for Schwarz et al.

These results noticeably demonstrate the challenges posed by azulene and nonalternant hydrocarbons for evaluating pathways through the molecule both experimentally and theoretically. An alternative method for evaluating non-alternant hydrocarbons with functional groups that are less susceptible to ambiguities during experimentation, such as precise geometric

information, and have reliably demonstrated consistency with other empirical evidence would be advantageous for developing the underlying theory of non-alternant hydrocarbons by elucidating their electronic structure.

V.2. Azulene Biradicals.

As discussed in Chapters III and IV donor-bridge-acceptor biradicals offer a unique opportunity for probing the electronic structure of a variety of molecules of interest for organic electronics by facilitating the availability of precise connectivity and geometric data from crystal structures for making detailed comparisons of structure-property relationships. The initial goal was to make the **1,3-SQAzNN** donor-bridge-acceptor molecule and evaluate the charge transfer bands in the absorption data and calculate the exchange coupling constant from variable temperature paramagnetic susceptibility plots from magnetometry following previous studies in order to divulge the contributing superexchange mechanisms resulting in observed coupling. However, as will be conferred during the synthetic discussion of **1,3-SQAzNN**, the synthesis of the desired donor-bridge-acceptor molecule was more challenging than anticipated. As a result, a different biradical (**1,3-SQ₂Az**) with its own utility was more easily accessed and synthesized first. although, its preparation and presentation will follow **1,3-SQAzNN**.

V.2.1. **1,3-NN₂Az** and **1,3-IN₂Az**

A rare example of magnetic communication through a nonalternant π -system was recently described by Haraguchi, et al. who reported differential magnetic exchange coupling of IN and NN covalently attached to the 1,3-positions of azulene (**1,3-IN₂Az** and **1,3-NN₂Az**, Figure V-13).¹⁶ Magnetic exchange interactions mediated by organic bridges have been a subject of intense theoretical and experimental research, and both the sign and magnitude of the exchange interaction is most often cast in terms of the active-electron approximation.²¹ As

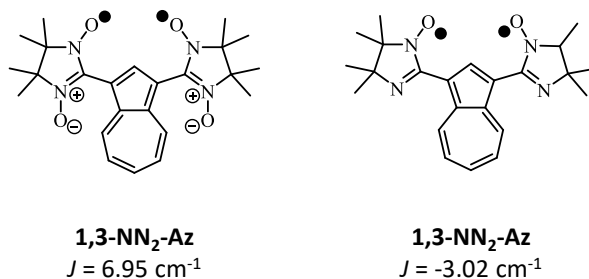


Figure V-13. 1,3-IN₂Az and 1,3-NN₂-Az.

discussed in Chapter I, Borden and Davidson classified biradicals as either nondisjoint or disjoint.² Within this active-electron approximation, nondisjoint biradicals possess substantial SOMO overlap densities and consequently have exchange integrals large enough to have the triplet lower in energy than the singlet. Thus, they are predicted to exhibit ferromagnetic exchange via Hund's 1st Rule.²²⁻²⁴ In marked contrast, disjoint biradicals have no SOMO overlap density and therefore possess negligible exchange integrals. These systems are therefore predicted to exhibit either antiferromagnetic- or very weak magnetic exchange interactions. Notably, disjoint and nondisjoint alternant π -system biradicals can be identified using Ovchinnikov's and Longuet-Higgins' "star/non-star" formalism in addition to spin-polarization methods, and a multitude of high-spin organic molecules, dendrimers, and polymers have been prepared based on this design strategy.^{1,25,26} However, as discussed earlier in this chapter, neither the active-electron approach nor the star/non-star method can account for exchange coupling in biradicals bridged by nonalternant π -systems. The results of Haraguchi et al. are notable since both **1,3-IN₂Az** and **1,3-NN₂-Az** are disjoint, yet **1,3-IN₂Az** exhibits weak antiferromagnetic coupling ($J = -3.02 \text{ cm}^{-1}$) while **1,3-NN₂-Az** exhibits weak ferromagnetic coupling ($J = +6.95 \text{ cm}^{-1}$).¹⁶ Interestingly, these two disjoint biradicals lack both spin delocalization into the bridging unit and superexchange pathways that are reflected by spectroscopic features.²⁷ As a result, more

structural types required to elucidate the mechanisms that control magnetic- and electronic coupling through nonalternant π -system bridges.^{28,29}

V.2.2 Symmetric and Asymmetric Biradicals for Evaluating Bridge-Modulated Coupling.

Other structural types would include both symmetric and asymmetric biradicals. **1,3-NN₂-Az** and **1,3-IN₂-Az** are both symmetric biradicals, but even in alternant hydrocarbons symmetric biradicals comprised of NNs or INs are disjoint and localized, giving small singlet-triplet gaps as a result of small magnetic exchange coupling constants. Furthermore, all radical species in the solid state have weak *intermolecular* through-space interactions, but radicals that have weak intramolecular interactions, like NNs and INs, these intermolecular interactions can significantly contribute to the observed magnetism. That said, DFT calculations for **1,3-NN₂-Az** suggest the intermolecular interactions are too weak to be interfering, but could have an effect on the observed magnetism of **1,3-IN₂-Az**.¹⁶ In Chapters III and IV, asymmetrical SQ-B-NN donor-bridge-acceptor biradicals have been used to elucidate the electronic structure of a variety of bridges.³⁰⁻³² The parent compound, **SQ-NN** or SQ-B-NN with a conjugated bridge are analogs of the quintessential smallest example of a nondisjoint, ferromagnetically coupled biradical, TMM as shown in Figure V-14A. Any SQ-B-NN with a cross-conjugated bridge is an analog to the archetypal disjoint biradical, TME (Figure V-14B) which exhibits a very small singlet-triplet gap demonstrated by magnetic susceptibility measurements of 2,3-dimethylenecyclohexane-1,4-diyl; a conformationally restrained version of TME.³³ In SQ-B-NN complexes with cross-conjugated bridges, a HOMO(B-NN) \rightarrow LUMO(B-NN) superexchange mechanism is responsible for the relatively strong, by comparison, antiferromagnetic coupling.²⁷

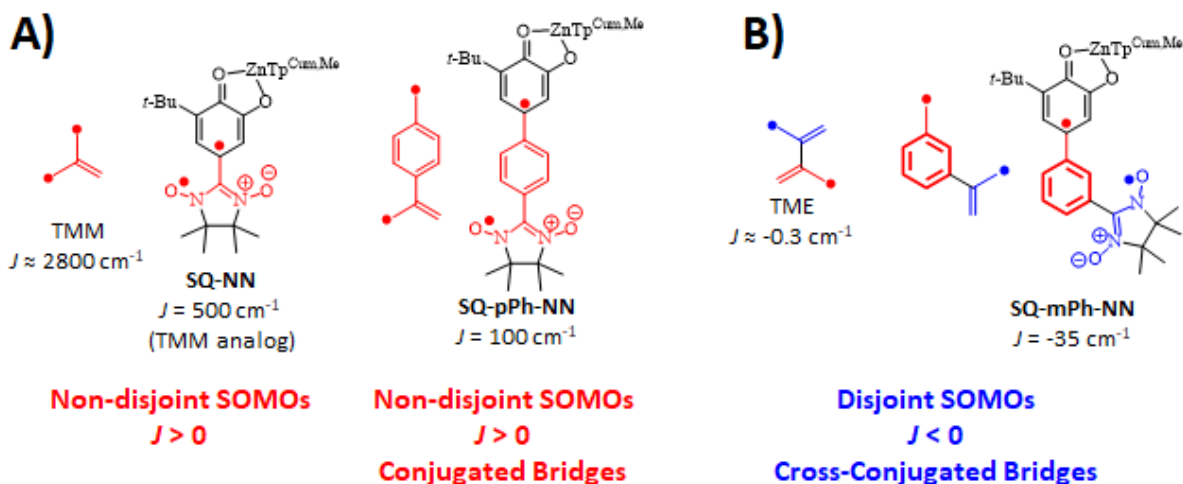


Figure V-14. SQ-B-NNs as analogs of TMM (A) or TME (B) allowing for delocalization of one radical while localizing the other resulting in nondisjoint SOMOs for SQ-NN and SQ-B-NNs with conjugated bridges or disjoint SOMOs for SQ-B-NNs with cross-conjugated bridges.

Figure V-15 shows another TME analog as the *bis*(NN), however separating two NNs by a bridge does not allow for delocalization of the radicals, overlap of the SOMOs and lack characteristic spectroscopic features for a coherent superexchange pathway. Thus, these molecules have small intramolecular J values. SQ-B-NNs with conjugated bridges allow for nondisjoint molecular orbitals and SQ-B-NNs with cross-conjugated bridges allow for delocalization of at least the SQ which allows for interaction of its SOMO with the HOMO (NN-Ph) \rightarrow LUMO (NN-Ph) transition.²⁷

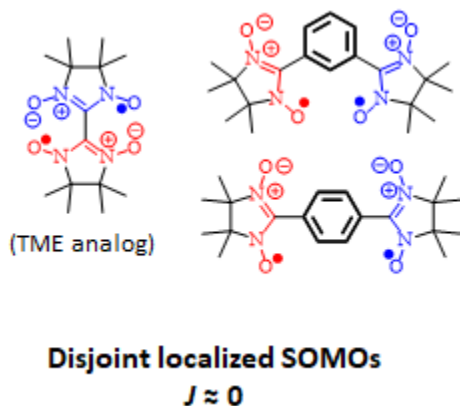


Figure V-15. Disjoint, localized symmetric NN biradicals that will exhibit small exchange coupling constants.

Other classes of biradicals allow for the delocalization of both radicals into a bridge. In such cases, this discussion will be limited to symmetrical biradicals with two SQs separated by a bridge as shown in Figure V-16 (*bottom*). For cross-conjugated bridges, the SQ SOMOs are non-disjoint just like TMM or will be analogous to the *m*-xylyl biradical and they will be ferromagnetically-coupled (Figure V-16A). If the two SQs are conjugated through a bridge, then

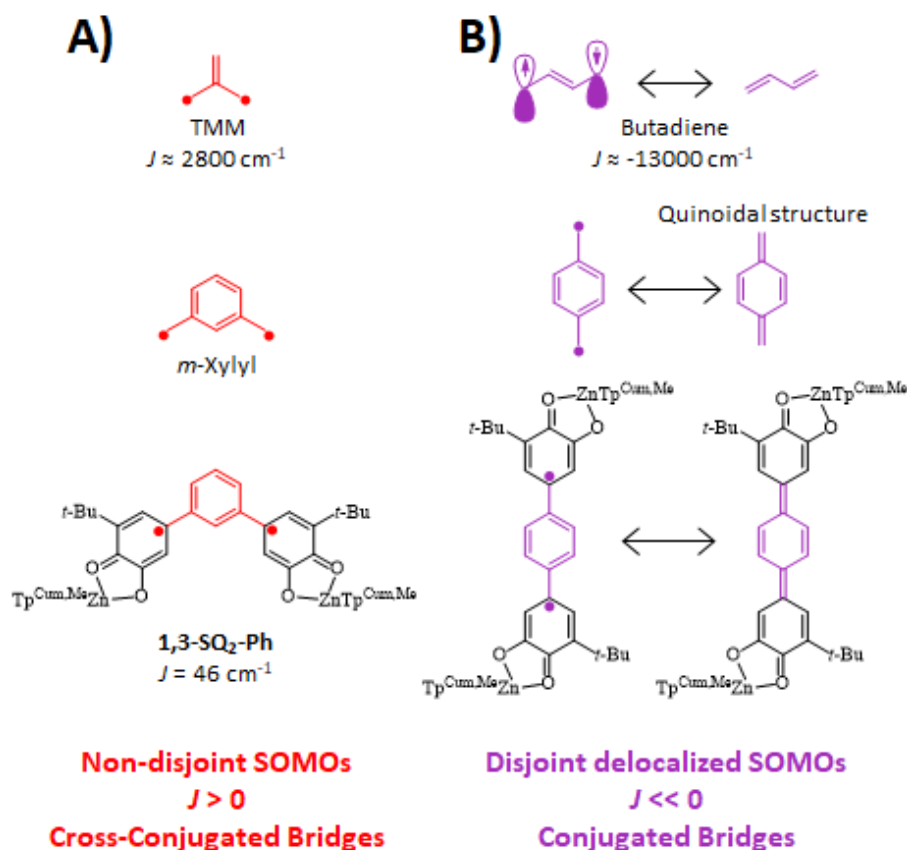


Figure V-16. Symmetrical SQ-B-SQ biradicals that are either **A)** cross-conjugated or **B)** conjugated through the bridge.

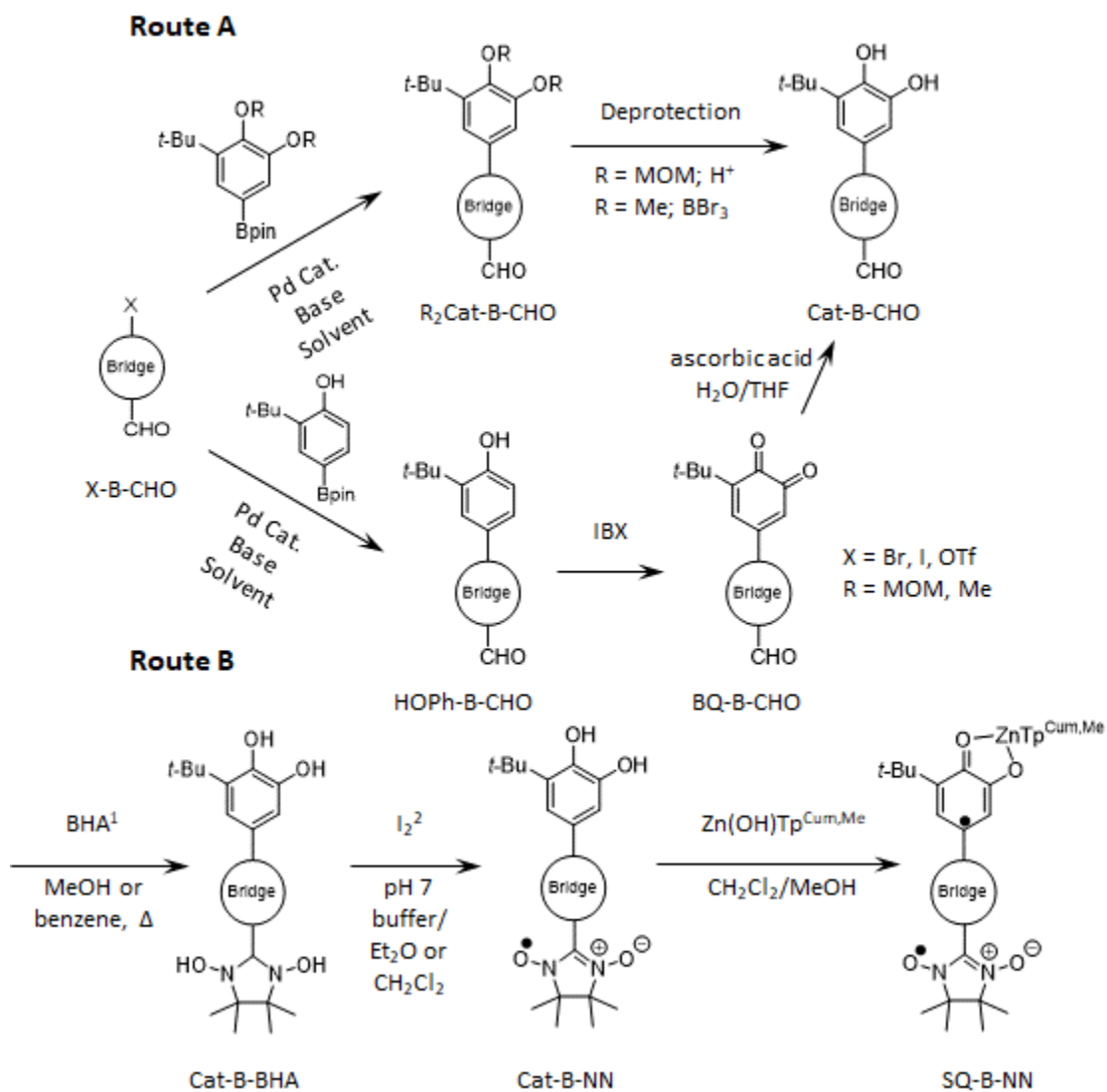
they will give rise to biradicals which have non-zero overlap integrals, thus forming a bonding interaction. In Figure V-16B, butadiene is shown with its resonance structure with two antiferromagnetically coupled unpaired electrons at the end carbons and bridged by an ethylene linker. Butadiene exchange coupling has been investigated and, like closed shell molecules should be, it has a large negative J consistent with the singlet state being much lower in energy

than the triplet (excited) state.³⁴ The analogy can be applied to the non-existent *para*-xylyl biradical which actually exists in its quinoidal structure form as 3,6-dimethylenecyclohexa-1,4-diene. The quinoidal structure being the consequence for delocalized disjoint biradicals with nonzero overlap integrals. The quinoidal structure would hold true for two SQs that are separated by a conjugated bridge as shown in the bottom of Figure V-16B. These molecules would be characterized by antiferromagnetic exchange coupling constants ($J < 0 \text{ cm}^{-1}$), and if the coupling between the radicals is strong enough they will be diamagnetic. If diamagnetic, they will neither display EPR signals nor paramagnetic susceptibilities, but they would display NMR spectra and X-ray crystallography will reveal the SQ-bridge bond lengths to be shorter and more C=C like as well as facilitate the SQ-B-SQ to exist in the same plane. There may be other spectroscopic features in the absorption spectra that are characteristic of conjugation between two SQs through a bridge and the formation of the quinoidal structure.

V.2.3. 1,3-SQ-Az-NN Synthesis.

As mentioned previously in the introduction to donor-bridge-acceptor biradicals, up to this point, all previously made SQ-B-NN biradicals followed Scheme V-1 and went through the Cat-B-CHO intermediate and most of them followed either route A or route B exactly. The final steps from Cat-B-CHO to SQ-B-NN have been very rigid, but this general synthesis has successfully, with little modification, produced over two dozen SQ-B-NN biradicals.^{27,30–32,35,36} Therefore, the original synthesis for **1,3-SQ-Az-NN** was designed with the same strategy. Scheme V-2 shows the original synthesis of **1,3-SQ-Az-NN**. Starting with azulene, the first step takes advantage of the large electron density at the 1 and 3 positions of azulene and utilizes a Vilsmeier-Haack reaction to install the formyl group. Care needed to be taken to either use azulene in excess or only add a stoichiometric amount of POCl₃ or over formylation would be

Scheme V-1. Generic route for all Shultz group **SQ-B-NN** biradicals up to this point.

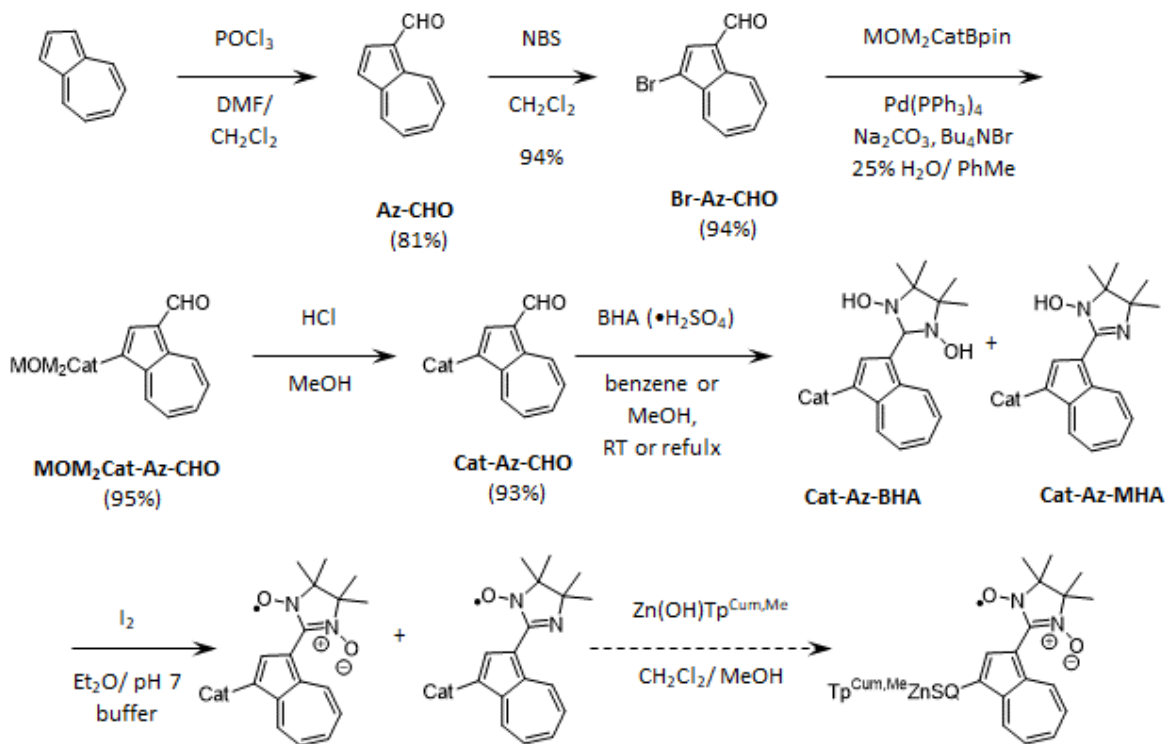


¹BHA•H₂SO₄/K₂CO₃ may be used instead of BHA.

²Cat-NN no bridge was made with NaIO₄.

accomplished readily. Bromination of the formylated azulene was facile with NBS and **Br-Az-CHO** was isolated as a stable, dark purple solid. The MOM-protected catechol was installed by a Suzuki coupling to give **MOM₂Cat-Az-CHO** in high yield. HCl in methanol was used to remove the MOM groups and upon precipitation into water gave a dark green powder which the ¹H-NMR (Figure V-17) indicated that the **Cat-Az-CHO** intermediate was synthesized in a high yield and purity. From this point, either BHA or BHA•H₂SO₄/K₂CO₃ were used to attempt the condensation reaction with the aldehyde; however, upon multiple attempts from room

Scheme V-2. The original proposed synthesis of **1,3-SQ-Az-NN**.



temperature to reflux in both benzene and methanol, the desired **Cat-Az-BHA** was not singularly isolatable. All reactions in methanol failed to produce the desired compound at all, but in benzene the desired compound was produced alongside the dehydrated monohydroxylamine (MHA) which gives iminonitroxide upon oxidation; albeit in a low yield of ca. 24%. Given that at least benzene produced the desired compound, the mixture was carried forward with hopes that it would be separable in a future. Oxidation of the mixture with iodine in Et_2O and phosphate buffer gave the expected overlapping 7 Gauss split 5-line- and 3 Gauss split 7-line EPR patterns for NN and IN, respectively. However, when the **Cat-Az-NN** and **Cat-Az-IN** were subjected to the $\text{Zn}(\text{OH})\text{Tp}^{\text{Cum,Me}}$, the splitting in the EPR signal remained the same and did not seem to indicate any reaction. TLC on basic alumina with 25% $\text{EtOAc}/\text{hexanes}$ also confirmed that no reaction had occurred. The complexation reaction was suspected to have failed due to the

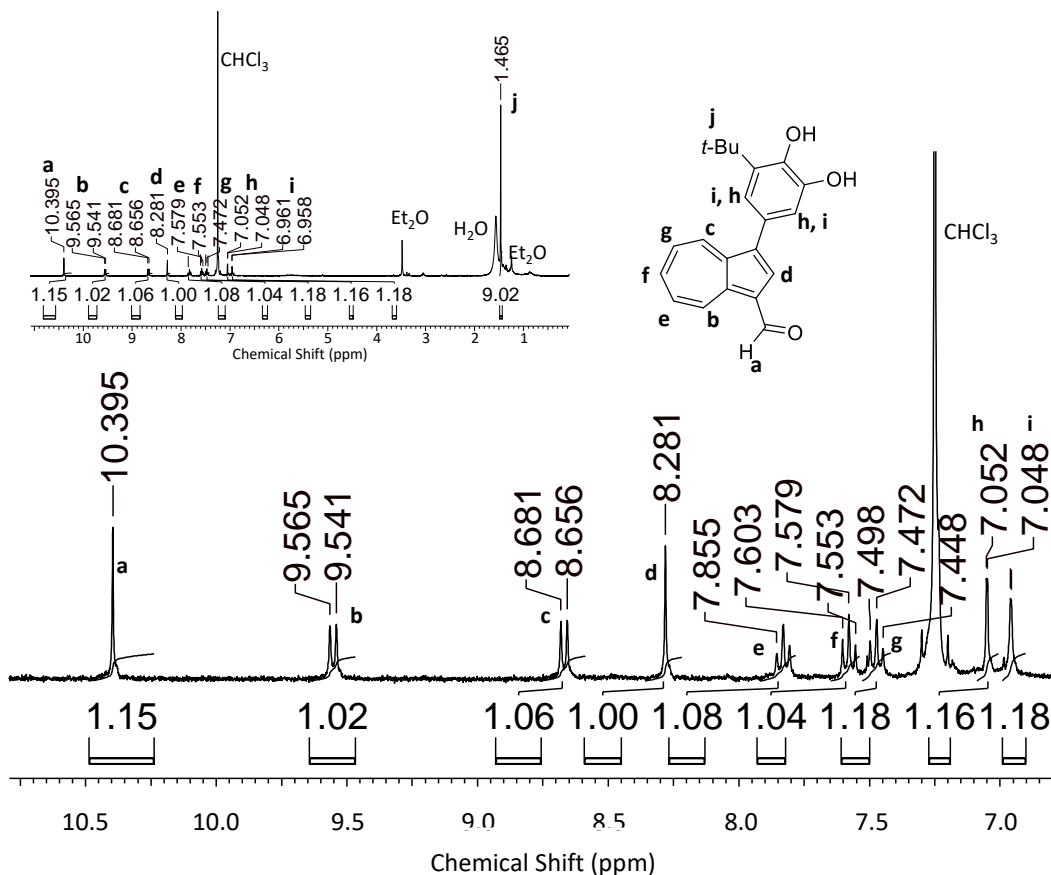


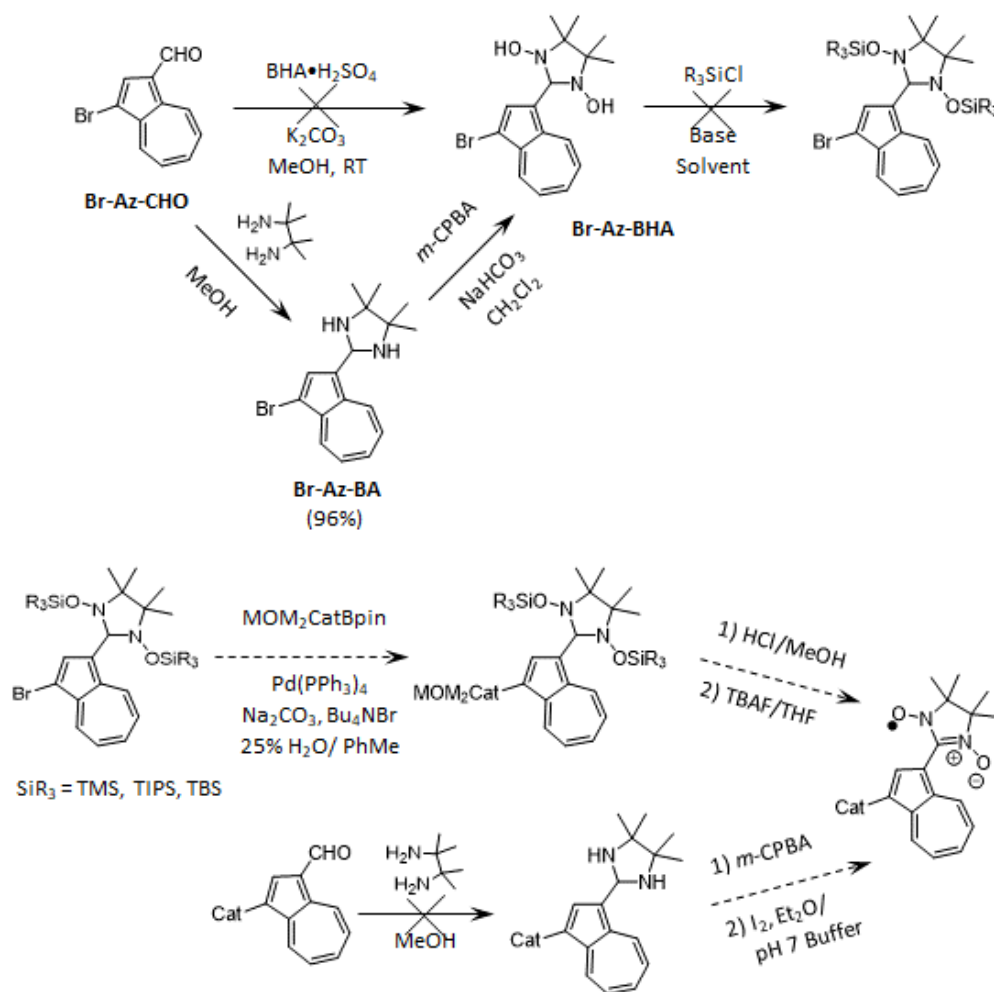
Figure V-17. Assigned ¹H-NMR spectrum of **Cat-Az-CHO**. Clean aromatic region with the full spectrum (*inset*) only showing residual solvent peaks.

Cat-Az-NN being produced both in a low yield and being impure with at least the **Cat-Az-IN**.

From here, the desire was to find a more effective means of producing **Cat-Az-BHA** both in high purity and yield. As Scheme V-1 indicated, there were not many options for arriving at **Cat-B-BHA** through our current methodology.

Given that the condensation reaction of **Cat-Az-CHO** with BHA was not proceeding as other **Cat-B-CHOs** had, it was believed that the electron-rich 5-membered ring of azulene and the electron-rich catechol together made the aldehyde carbonyl carbon too electron rich to allow for nucleophilic attack by the BHA nitrogen lone pairs. Scheme V-3 sought to condense a less electron-rich aldehyde with BHA first, protect the BHA with silyl groups, perform a Suzuki coupling and then globally deprotect the molecule to yield **Cat-Az-BHA**. This strategy for

Scheme V-3. Proposed use of silyl protecting groups for protecting Ar-BHA.



synthesizing NNs from silyl-protected BHAs has been implemented previously by several groups.^{37,38} Attempting to condense BHA with **Br-Az-CHO** also failed with the belief that it was just that the 5-membered azulene ring was too electron-rich. As an alternative, Rey et al. demonstrated that 2,3-dimethylbutane-2,3-diamine could be synthesized, condensed with an aryl aldehyde and then oxidized to the desired Ar-BHA with *m*-CPBA.³⁹ Given that the basicity of the amine is nearly 1000 times greater than the hydroxylamine, it was thought that the 2,3-dimethylbutane-2,3-diamine may be able to cyclize where the corresponding BHA could not. 2,3-dimethylbutane-2,3-diamine was prepared from 2,3-dinitro-2,3-dimethylbutane and the condensation was attempted on **Br-Az-CHO** which gave the desired *bis*(amino) (BA) compound

Table V-1. Attempted silyl protections of **Br-Az-BHA**.

Entry	R ₃ SiCl	Base	Catalyst	Solvent	Temp.	Result
1	TIPSCI	Imidazole	---	CH ₂ Cl ₂	RT	No Rxn
2	TIPSCI	Et ₃ N	---	CH ₂ Cl ₂	RT	No Rxn
3	TIPSCI	Imidazole	---	DMF	RT	No Rxn
4	TIPSCI	Imidazole	---	DMF	40 °C	Imino nitroxide precursor
5	TBSCI	Imidazole	---	DMAc	RT	No reaction
6 ^a	TBSCI	Imidazole	---	DMAc	40 °C	Product, slow rxn, 3 days, multiple eq. of TBSCI, 15% yield
7 ^b	TMSCI	Et ₃ N	---	THF	50 °C	Imino nitroxide precursor
8	TBSCI	Imidazole	NaI	DMAc	RT	No Rxn
9 ^c	TBSCI	Et ₃ N	DMAP	DMAc	RT	No Rxn

^a Reported for Ar-BHA in *J. Org. Chem.* **2017**, 82 (15), 7764–7773.

^b Reported for Ar-BHA in *J. Org. Chem.* **2013**, 78 (18), 9282–9290.

^c Reported for Ar-BHA in *J. Org. Chem.* **2014**, 79, 8348–8357.

(Br-Az-BA) in a high yield. From here, two equivalents of *m*-CPBA were used to oxidize the *bis*(amino) to the corresponding BHA and monitored by TLC and synthesis was confirmed via EPR by shaking an aliquot with NaIO₄. After an aqueous work-up and concentration, the next step was to protect the **Br-Az-BHA** with silyl protecting groups. From here the MOM₂Cat could be installed via Suzuki coupling with MOM₂CatBpin, then deprotection of the catechol could be performed with aqueous acid followed by deprotection of the silyl groups with TBAP which according to ref 37 provides the desired NN.³⁷ Unfortunately, after multiple attempts (Table V-1) with a variety of silyl protecting groups and conditions, the silyl protected **Br-Az-BHA** could not be synthesized in any appreciable yield. Entries 1-3, 5, 8, and 8 resulted in only starting materials, even after stirring for several days. Entries 4 and 7 provided the unprotected *iminonitroxide precursor*. *The only reaction that gave any yield was entry 6, but only after several days, multiple equivalents of silyl protecting reagent and gave just a 15% yield after isolation; this also was not reliably reproducible.*

Despite the failure of the silyl protection of **Br-Az-BHA**, the combination of peroxy acid oxidation followed by oxidation to NN led to a series of experiments for the expansion of interconverting Ar-BHAs, monohydroxylamines (MHA), INs and NNs. Parallel efforts to condense formylazulenes with BHA resulted in the synthesis where **MOM₂Cat-Az-CHO** was condensed with BHA and then was attempted to be deprotected with catalytic acid. The desired outcome was not achieved completely in that the acid also promoted a portion of the BHA to dehydrate to MHA as shown in the scheme of Figure V-18. Figure V-18A shows the EPR spectrum of this crude reaction mixture which has a very low concentration of a paramagnetic species which is approximately 70 Gauss wide; larger than either an NN or an IN. It appears to be a doublet ($I = 1/2$) of triplets ($I = 1$), which could imply it is a nitroxide radical interacting with the methine proton. We hypothesized that *m*-CPBA might convert a mixture of Ar-MHA and Ar-BHA entirely to Ar-BHA, but could it convert either Ar-IN or a mixture of Ar-IN and Ar-NN entirely to Ar-NN? Figure V-18 shows the EPR results from series of reactions that we had not performed in our group previously, but had some literature precedence.³⁹ Figure V-18B and C show for comparison, the experimental and simulated EPR spectra for **Az-NN** and **Az-IN**, respectively, that had been acquired previously when **Az-CHO** was refluxed in benzene and produced a mixture of the two monoradicals which gave clean EPR spectra, but were very low yielding Figure V-18D is the result from when the crude reaction mixture of **Az-BHA** and **Az-**

MHA was shaken for 30 seconds with NaIO₄ in Et₂O and water, which gave a mixture of the **Az-NN** and **Az-IN**. This result is how the components of the mixture were identified. When this EPR spectrum was simulated with the parameters for the simulation of the **Az-NN** and **Az-IN** individually, the best fit was 55% **Az-NN** and 45% **Az-IN**. If this mixture (Figure V-18D) was

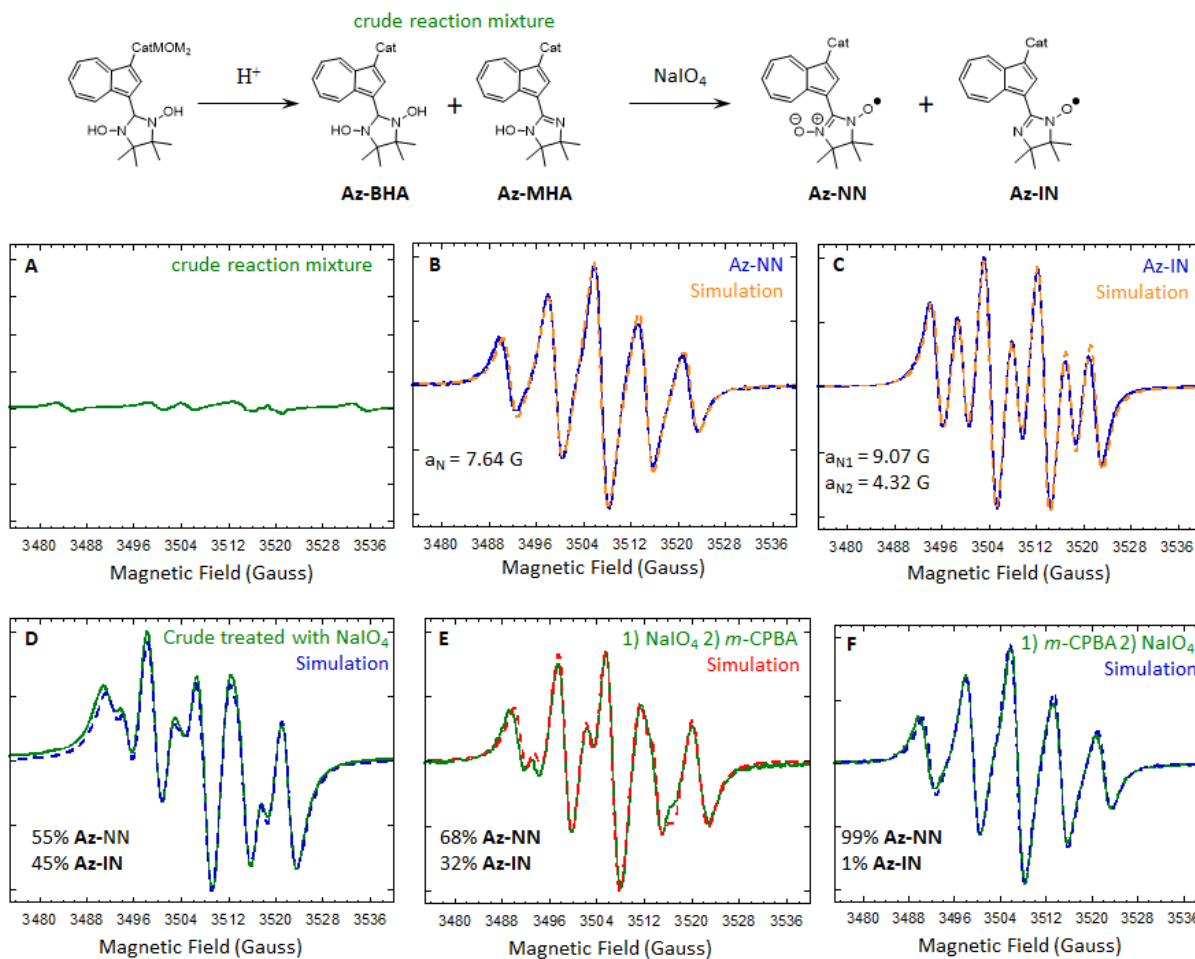


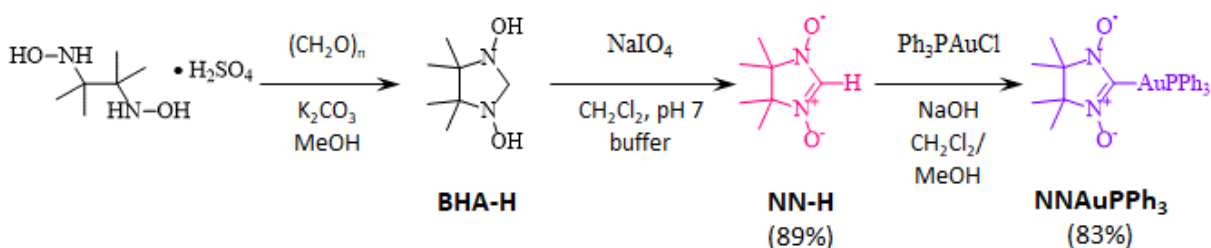
Figure V-18. EPR spectra and simulations of the attempted deprotection of MOM₂Cat-Az-BHA with catalytic acid giving A) the crude reaction mixture. B) The spectrum of **Az-NN**. C) The spectrum of **Az-IN**. D) Treatment of the crude mixture with NaIO₄. E) Treatment of the crude mixture with NaIO₄ then *m*-CPBA and F) treatment of the crude mixture with *m*-CPBA, then NaIO₄.

then treated with *m*-CPBA, it provided the spectrum in Figure V-18E and the best fit for this spectrum resulted in 68% **Az-NN** and 32% **Az-IN**. Perhaps with more *m*-CPBA or more reaction time, more or all of the IN could be converted to NN. However, if the crude reaction mixture (Figure V-18A) was shaken for 30 seconds with Et₂O and *m*-CPBA in aqueous NaHCO₃ and

then oxidized with NaIO_4 , the result was almost entirely **Az-NN** as shown in Figure V-18F. The simulation, still using the independent monoradical parameters, indicated that there was a very small amount ~1% of the **Az-IN** still remaining. These data suggest that Ar-MHAs or Ar-INs can have oxygen atoms transferred to them via peroxy acids to give the corresponding Ar-BHAs or Ar-NNs and that the oxygen atom transfer, qualitatively, seems to be more efficient for Ar-MHAs rather than Ar-INs, but additional experiments would be required to quantify this.

When Cat-B-BHA is oxidized with iodine to Cat-B-NN, care must be taken to only add the correct amount of iodine because if too much iodine is added, the result is the corresponding Cat-B-IN. This result is usually a death sentence for the current batch of material and the Cat-B-BHA oxidation must be attempted again with a fresh batch of material. The series of experiments in Figure V-18 indicate that there may be a way to return a decomposed Ar-BHA or Ar-NN to its desired form by transferring an oxygen back to the substrate. Despite these results, at this point, attempting to use this methodology to return Cat-B-MHA or Cat-B-IN to Cat-B-BHA or Cat-B-NN and have enough to include this on a large-scale synthesis of hundreds mg of material for it to be a sufficient amount to proceed still has its shortcomings. Particularly finding a way to remove excess *m*-CPBA from the reaction mixture without decomposing the desired monoradical, especially with a Cat-B-NN where Ar-NNs are typically somewhat stable to basic alumina, but not many other types of media; however, Cat-B-NNs do not run on basic alumina due to the catechol becoming deprotonated. These were issues that resulted in any attempts to try to isolate the **Cat-Az-NN** in the end. A future strategy may be to either attempt crystallizing as much of the *m*-CPBA out of cold CH_2Cl_2 as possible; the monoradical should have moderate solubility and then wash the remaining supernatant with pH 7-7.5 buffer solution in order to deprotonate any acids remaining, then extract the organic layer.

Scheme V-4. Synthesis of **NNAuPPh₃**.



Returning to the specific discussion of the synthesis of **1,3-SQ-Az-NN**. Given that most of the problems in the synthesis seemed to be arising from the condensation reaction to make any **Az-BHA**, not needing to arrive at this intermediate and going straight to **Az-NN** seemed like the best strategy. Okada et al. reported that an NN-gold(I) complex could be used to couple the NN moiety directly to an aryl iodide by palladium-mediated cross-coupling⁴⁰ and in a separate paper Haraguchi and Okada et al. reported the coupling of two NNs to 1,3-diiodoazulene to make the corresponding *bis*(NN).¹⁶ The steps to make **NN-H** are not well documented in literature and some methodology needed to be created in order to make it pure enough to be used directly in the synthesis of **NNAuPPh₃** in decent yield Scheme V-4. Paraformaldehyde in methanol with **BHA**• H_2SO_4 and K_2CO_3 , stirred for two days at room temperature provided the best results versus aqueous formaldehyde^{41,42} or as other literature preparations report: formic acid.⁴³ Once the **BHA-H** was synthesized oxidation with periodate seemed to be the most facile. Although, it was important to do it as a mixture of CH_2Cl_2 with aqueous pH 7 phosphate buffer. The organic phase has some flexibility, but CH_2Cl_2 seemed to give the resulting **NN-H** the best solubility because it is water soluble as well, and the reaction mixture still must be washed multiple times with CH_2Cl_2 in order to remove a sufficient amount of **NN-H**. This is simplified given that the **NN-H** is dark magenta when concentrated. The use of aqueous pH 7 phosphate buffer is less negotiable because without the buffer, if done just with water which is necessary to provide solubility for periodate, the **NN-H** will rapidly decompose into a yellow diamagnetic oil if

allowed to stir too long or upon concentration. The synthesis of the gold complex (**NNAuPPh₃**), and the characteristic EPR spectra for **NNAuPPh₃** and its precursor are shown in Figure V-19. There is a discrepancy in the original Okada. et al. paper, where they report the **NNAuPPh₃** complex as a doublet of quintets with the doublet coming from ³¹P(I = 1/2) hyperfine coupling. After numerous attempts to acquire the ten-line pattern both spectroscopically and by varying the synthetic parameters; including changing bases, solvents, removing the chloride from ClAuPPh₃ with AgOTf, adding a stronger phosphine ligand, tricyclohexylphosphine, and testing the reaction and having it seeming to work with iodobenzene and *p*-iodoanisole, an outside consultation with Prof. Andrzej Rajca was sought. Prof. Rajca is a chemist at the University of Nebraska who designs and prepares a variety of novel organic radicals and there was a possibility his group had attempted this synthesis. His response included images of an EPR spectrum, a TLC plate and the **NNAuPPh₃** in solution; all of which were consistent with our results. Thus, the published spectrum of **NNAuPPh₃** by Okada, et al. is incorrect.

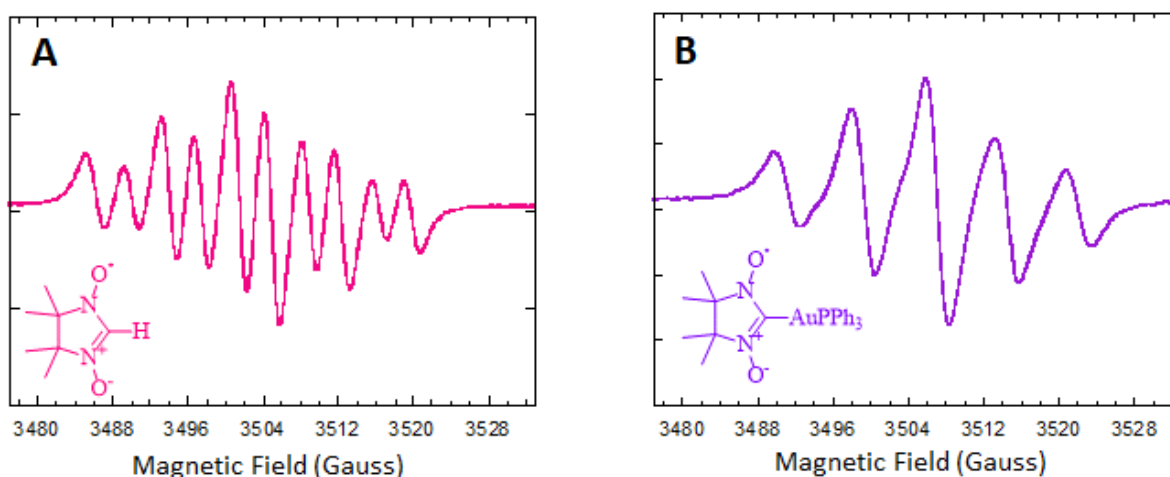
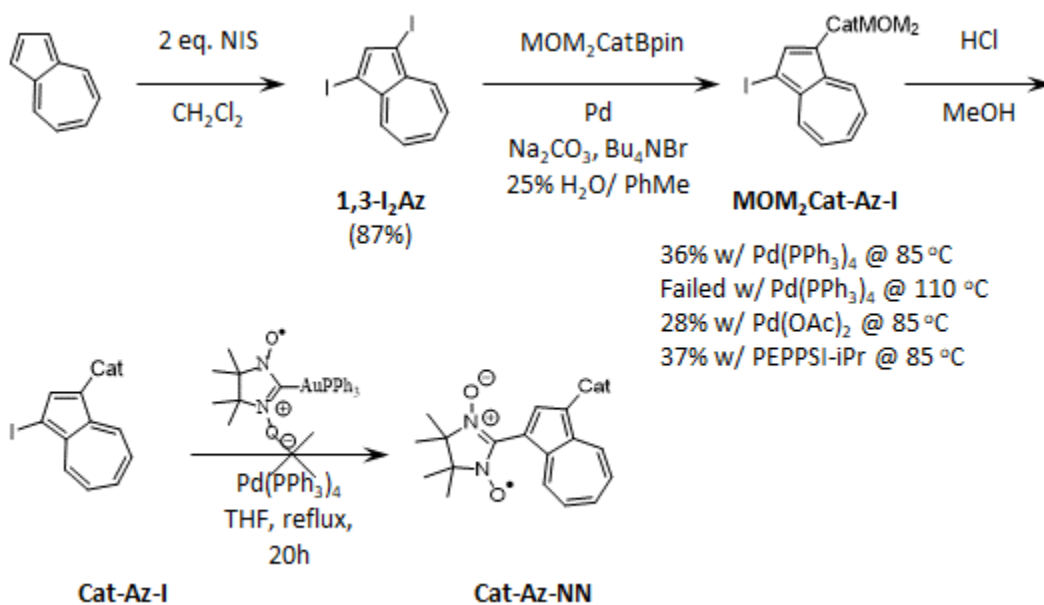


Figure V-19. EPR spectra of A) **NN-H** and B) **NNAuPPh₃**.

Scheme V-5 shows the original proposed synthesis for **SQ-Az-NN** by using **NNAuPPh₃**. In this synthesis, 1,3-diiodoazulene (**1,3-I₂Az**) is synthesized from azulene with 2 equivalents of NIS in Et₂O and then Suzuki coupled with 1 equivalent of **MOM₂CatBpin** to afford some of **MOM₂Cat-Az-I** in consistently low yields (28-36%). **MOM₂Cat-Az-I** was then deprotected with catalytic acid in methanol to give **Cat-Az-I** and then was used directly in the palladium-mediated cross-coupling with **NNAuPPh₃** in THF without further purification. **Cat-Az-I** was left unprotected in the cross-coupling, given that no base was required for this cross-coupling and it was done completely in anhydrous THF, we believed the chance of coordination of the catechol to palladium would be low. The first attempts at the cross-coupling reaction to install the NN were unsuccessful and the first one that worked at all was sluggish and took nearly a day to consume starting materials, the Okada et al. paper indicated that when these reactions work, reaction times were less than 6 h.⁴⁰ Unfortunately the result was also not the NN, but EPR revealed it to be the IN instead. Azulene can become rather expensive when attempting discover a viable synthetic pathway and being able to confidently bring-up larger amounts of pure

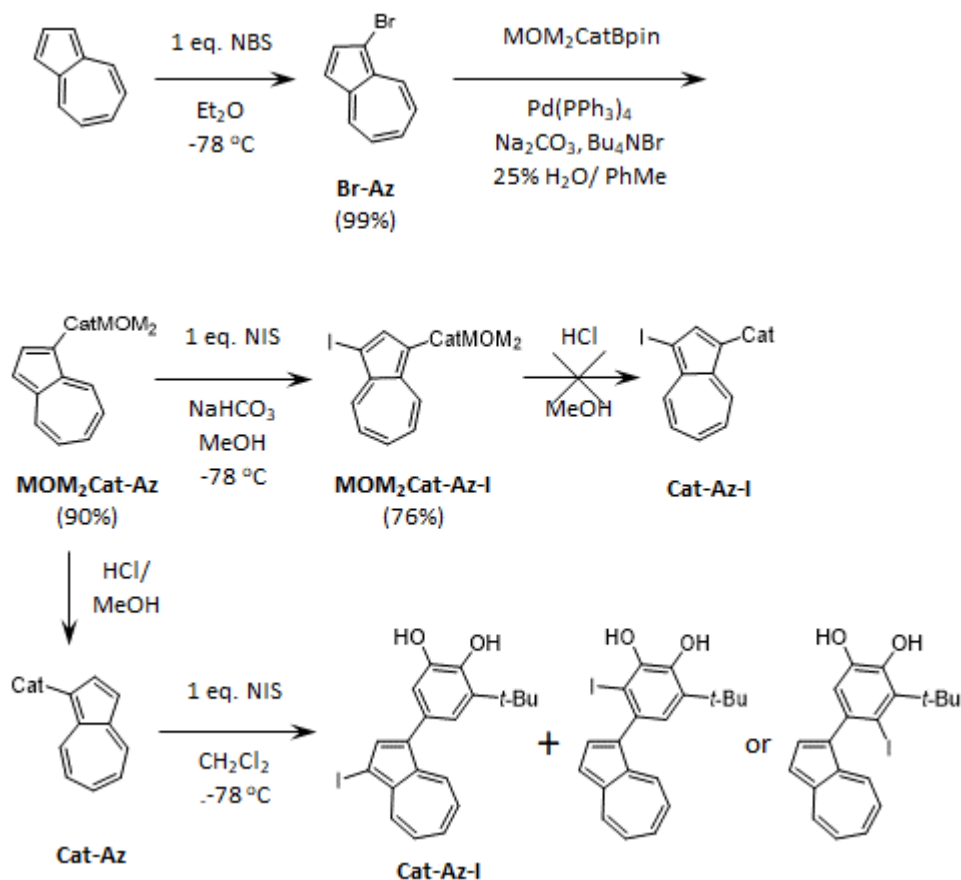
Scheme V-5. Original proposed method for implementing **NNAuPPh₃** for the synthesis of **1,3-SQ-Az-NN**.



material are helpful for performing many test reactions on a particular step, so given the low yielding Suzuki coupling, Scheme V-6 was developed as a more efficient means of making **Cat-Az-I**. Instead of attempting the Suzuki cross-coupling reaction with MOM₂CatBpin on di-haloazulene, azulene was first mono-brominated selectively with NBS at -78 °C in Et₂O. The temperature and solvent was vital to making bromoazulene in high yield because both of these limited the solubility of NBS and the temperature allowed azulene to react with NBS instead of some of the formed bromoazulene reacting with another equivalent of NBS to make 1,3-dibromoazulene and ending up with a difficult to separate mixture of azulene, bromoazulene and 1,3-dibromoazulene. The Suzuki cross-coupling reaction was then performed on bromoazulene to make **MOM₂Cat-Az** which was then iodinated with NIS in methanol in the presence of NaHCO₃. The bicarbonate is necessary to protect the MOM groups from HI which will begin to deprotect one of the MOM groups on the catechol. After the successful iodination, the overall yield for arriving at **MOM₂Cat-Az-I** with this route was 68% from azulene versus, at best, 32% with the **1,3-I₂Az** and mono MOM₂CatBpin Suzuki coupling.

When **MOM₂Cat-Az-I** was attempted to be deprotected with catalytic acid, the result was a blue material which had poor solubility in any organic solvent and water which could suggest this blue material was some macromolecule and that the acid catalyzed some polymerization reaction. Believing that it was the presence of the iodide at the 3-position because azulenes are known to be capable of being protonated at their 1- and 3 positions by strong acids,⁴⁴ **MOM₂Cat-Az** was attempted to be first deprotected and then iodinated. It was also suspected that this instability was probably why the installation of the NN via **NNAuPPh₃** did

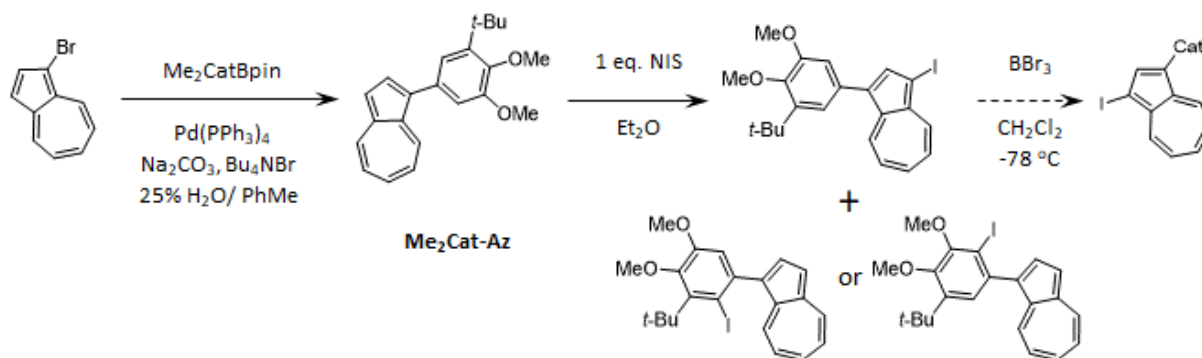
Scheme V-6. A more efficient route to **MOM₂Cat-Az-I**.



not proceed very well. Deprotection did not produce any insoluble blue material, but unfortunately without the MOMs the catechol ring became more susceptible to electrophilic aromatic substitution and the catechol ring started to become iodinated along with the azulene ring. The same strategy to synthesize **MOM₂Cat-Az-I** was attempted to make it with **Me₂Cat-Az-I** with the thought that using BBr_3 to deprotect the methyl groups and then cannula transfer the reaction mixture into stirring phosphate buffer solution would allow for deprotection, but not expose the molecule to a strong aqueous acid. This route did not go very far in that attempting to iodinate **Me₂Cat-Az** provided the same result as attempting to iodinate **Cat-Az** in Scheme V-7.

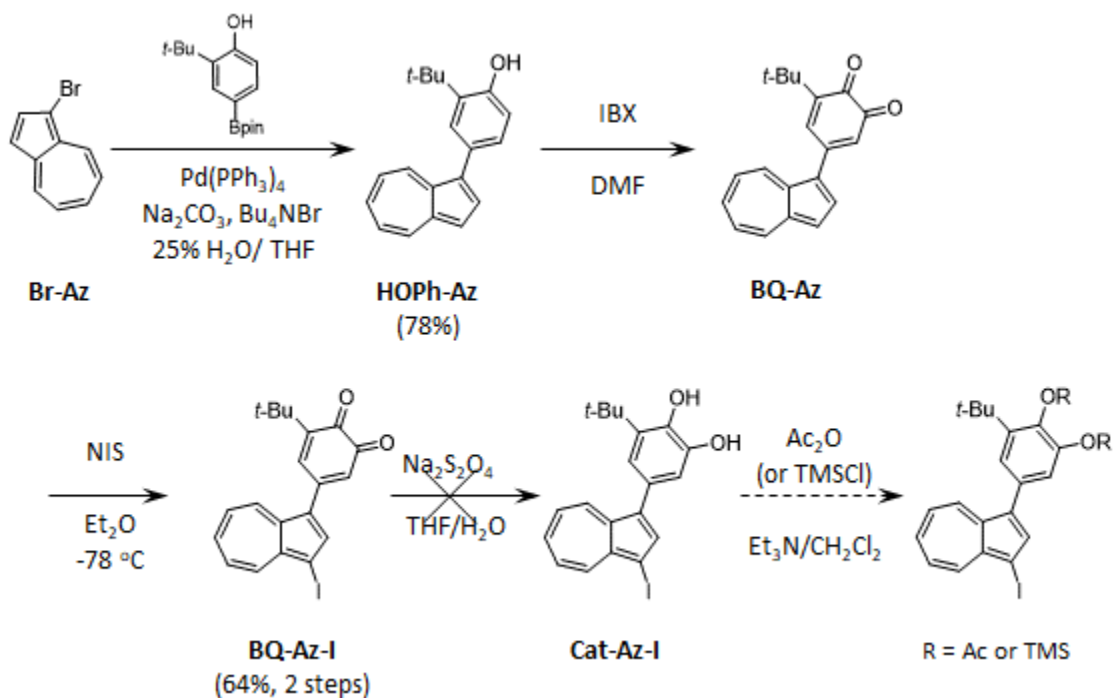
To combat the issue that a deprotected catechol or even one protected with methyl groups is too electron-rich to selectively iodinate the 3-position of azulene without iodinating the

Scheme V-7. Synthesis and attempted iodination of **Me₂Cat-Az**.



catechol ring, the catechol needed to be less electron-rich. The easiest way to make a catechol less electron rich is to oxidize it to the quinone, perform the iodination at the 3-position on azulene and then reduce the quinone to the corresponding catechol. To this end, Scheme V-8 was designed to make the quinone from the corresponding phenol via IBX oxidation, iodinate, then reduce to the catechol. DMF was chosen as the solvent for the IBX oxidation as this was considered to be the superior solvent by Magdziak et al.⁴⁵ Sodium dithionite was chosen as the reducing agent as through experience, it works much faster, more completely and is easier to remove than ascorbic acid which is the other common reducing agent that the Shultz group has used for quinones to catechols.^{31,32} The final step of this scheme is also to protect the **Cat-Az-I** with either acetate or TMS groups which are intended to help the palladium-mediated cross-coupling with **NNAuPPh₃** by ensuring that the catechol does not coordinate to palladium or participate in any other undesirable side reactions. Both of these protecting groups are labile under relatively weakly basic conditions; potentially conditions that are experienced during the final complexation of the catecholates with **Zn(OH)Tp^{Cum,Me}**.

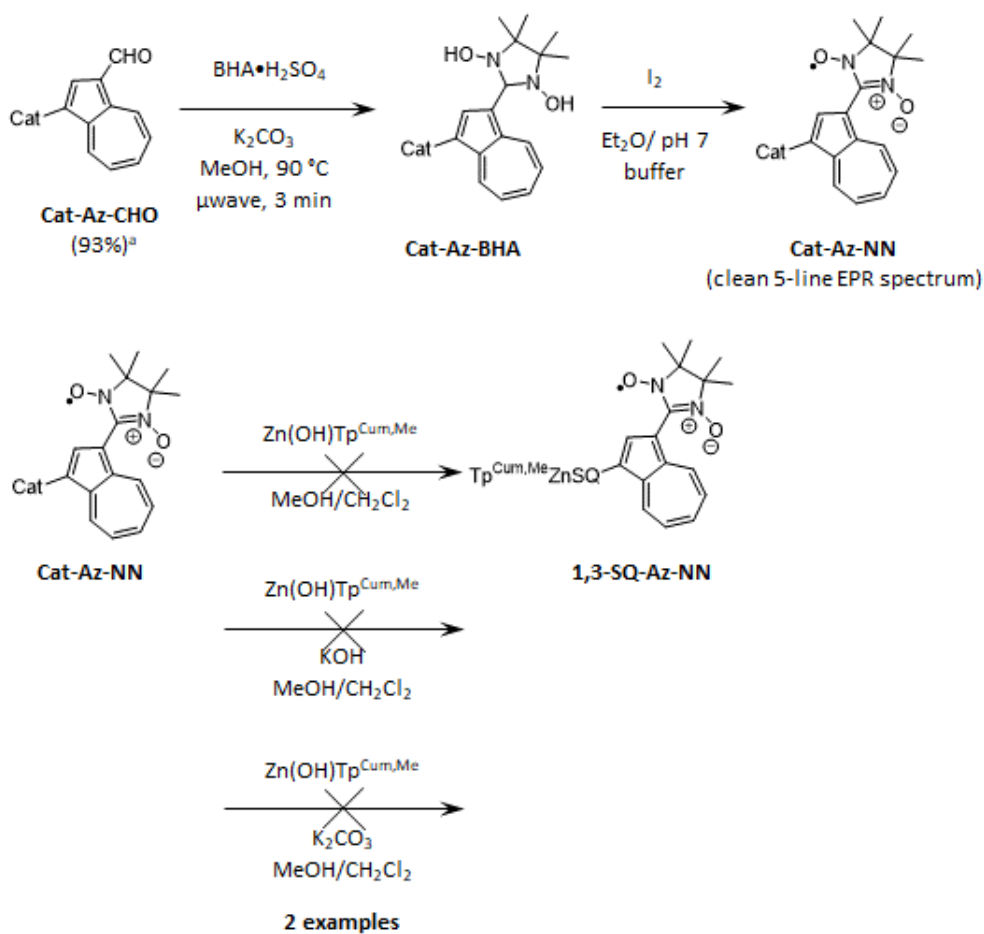
Scheme V-8. Synthesis of **BQ-Az-I**.



Oxidation of the **HOPh-Az** with IBX was complete in less than 2 h, worked-up and purified and then dissolved in Et_2O , cooled to -78°C and NIS was added. After concentration and purification to remove the succinimide, the **BQ-Az** was dissolved in 50/50 THF/ H_2O and $\text{Na}_2\text{S}_2\text{O}_4$ was added and the reaction was stirred for ca. 10 min to give a green-brown solution. Which was then subjected to an aqueous work-up in a separatory funnel, separated and concentrated. This residue was then used in the attempted protection of the catechol. During the protections, both with TMSCl and with Ac_2O , the TLC analysis of the reactions seemed to indicate very little product forming, even after stirring overnight. $^1\text{H-NMR}$ also indicated very little if any product. The TLC of any **Cat-Az** starting materials did not move far off of the baseline in even 50% EtOAc/hexanes, which should move even a mono-protected catechol.

Many of these attempts to make **1,3-SQ-Az-NN** were running in parallel and at about this time and going back to Scheme V-2 which had suffered from the failure of BHA to cyclize with **Cat-Az-CHO** or failed to give the desired product pure or in high yield, it was discovered that microwave heating a solution of **Cat-Az-CHO** with BHA•H₂SO₄ and either K₂CO₃ or NaHCO₃ in methanol to 90 °C for 3 minutes resulted in complete consumption of the starting material via TLC to the product, **Cat-Az-BHA** with no **Cat-Az-MHA** present as indicated from ¹H-NMR and EPR of an NaIO₄-oxidized aliquot. Attempting this reaction with other Cat-B-CHOs requires modifications to both temperature and time. For example, another subjected to 90 °C for 3 minutes; resulted in no reaction and only worked at 120 °C for 5 minutes. Interestingly, this Cat-

Scheme V-9. Microwave synthesis of **Cat-Az-BHA**, oxidation with I₂ and multiple attempted complexations with Zn(OH)Tp^{Cum,Me}.



B-CHO had been cyclized previously at room temperature overnight, where the **Cat-Az-CHO** would not condense with BHA at all at room temperature. Careful monitoring of these microwave-assisted cyclization reactions via TLC is necessary because they will further dehydrate and make the corresponding MHA. Scheme V-9 shows the microwave cyclization conditions and the oxidation of **Cat-Az-BHA** to **Cat-Az-NN** with iodine. Scheme V-9 also shows three different, four total, examples of attempted complexations of **Cat-Az-NN** with $\text{Zn(OH)Tp}^{\text{Cum,Me}}$, all of which did not exhibit the characteristic splitting pattern in EPR. The spectra should still be a five-line pattern, but instead of 7 Gauss splitting for the monoradical, it should be ~4 Gauss for a biradical, which even if the reaction is not complete begins to show. The TLC analysis on basic alumina also did not indicate biradical or even complexation occurring because on basic alumina, the Cat-B-NNs do not move from baseline and a complexed catecholate or semiquinone will run with an $R_f = 0.8-0.9$ in 50% EtOAc/hexanes, which is also where the uncomplexed $\text{Zn(OH)Tp}^{\text{Cum,Me}}$ will appear. It is also worth mentioning that frozen solution EPR spectra did not display a typical triplet spectrum nor did they display the forbidden $\Delta m_s = 2$ transition at half field. Given that the complexations seemed to be completely failing it seemed as though the catechol was no longer intact. Typically, catechols will become aerial oxidized to their corresponding quinones and can further decompose either by Diels-Alder reactions or by conversion into muconic anhydrides. However, this seemed improbable for this molecule because the **BQ-Az** which had been made in Scheme V-8 seemed to be very stable. Qualitative evidence being that a clean TLC was taken in 50% CH_2Cl_2 /hexanes of **BQ-Az** from a test tube after sitting for over a week. It was believable that the electron-rich **Cat-Az** could oxidize to **BQ-Az**, but TLC and IR data did not suggest it was the quinone. The **Cat-Az** material has always been green-brown where the **BQ-Az** is as a solid, purple, but it is solvatochromic: in

polar solvents or on a dry TLC plate it is blue, it is purple in intermediate polarity solvents and it is red in nonpolar solvents.

Given that something about this molecule seemed to be unstable and we had not identified where it was falling apart. It was decided that one more attempt with the installation of NN via **NNAuPPh₃** route in Scheme V-5 where the **Cat-Az-I** would be made with the **BQ-Az** route in Scheme V-8 would be tried before abandoning this project. When **BQ-Az** was remade, out of convenience, instead of dissolving it in THF/H₂O, adding dithionite and stirring, the **BQ-Az** was just dissolved in Et₂O with water in a separatory funnel, Na₂S₂O₄ was added and the separatory funnel was shaken until the solution became a clear blue-green. This was followed by a standard aqueous work-up and concentration under reduced pressure. However, after concentration, the residue was a green-brown color, not blue-green like it had been in the separatory funnel. Dissolving the residue in ether resulted in a green-brown solution with some insoluble brown material. TLC demonstrated what it always had with **Cat-Az** compounds, it remained on baseline or moved very little, even in polar solvent combinations. It seemed as though the **Cat-Az-I** was very unstable and would not survive concentration. Potentially, other **Cat-Az** compounds were also very unstable, which explained why the Zn(OH)Tp^{Cum,Me} complexations did not produce the desired result and that why the acetate or TMS protection from Scheme V-8 also did not produce the desired protected **Cat-Az-I**. In addition, other reactions seemed to encounter problems whenever free **Cat-Az** derivatives were either starting materials or products. To confirm this suspicion, more of a small amount of **BQ-Az-I** was synthesized, shaken in a vial with dithionite and the blue-green ether layer was removed and placed in a separate vial and analyzed via TLC in 50% EtOAc/hexanes which revealed one spot running with an R_f = 0.32 without baseline. This vial containing the blue-green solution was

allowed to sit overnight open to air by which time the Et₂O had mostly evaporated. Another TLC was taken which showed the spot at R_f = 0.32 was very faint and a green-brown spot was residing on the baseline. After another night of sitting, the TLC showed that none of the R_f = 0.32 spot was remaining; only a green-brown spot on baseline. A single catechol on azulene at the 1-position does not appear to be stable for very long. It also seemed that concentration was the most detrimental process for the **Cat-Az-I**, which would suggest the molecules are reacting with themselves. The numerous ¹H-NMR spectra that had been acquired of **Cat-Az** compounds had always had a disproportionately low signal-to-noise ratio for the amount of material that was in the NMR sample or had insoluble material present, and some of the ¹H-NMR that were acquired resulted in complex spectra with far more peaks than **Cat-Az**. Figure V-20 shows the aromatic region from the ¹H-NMR spectrum from allowing the **Cat-Az** to sit out in open air for

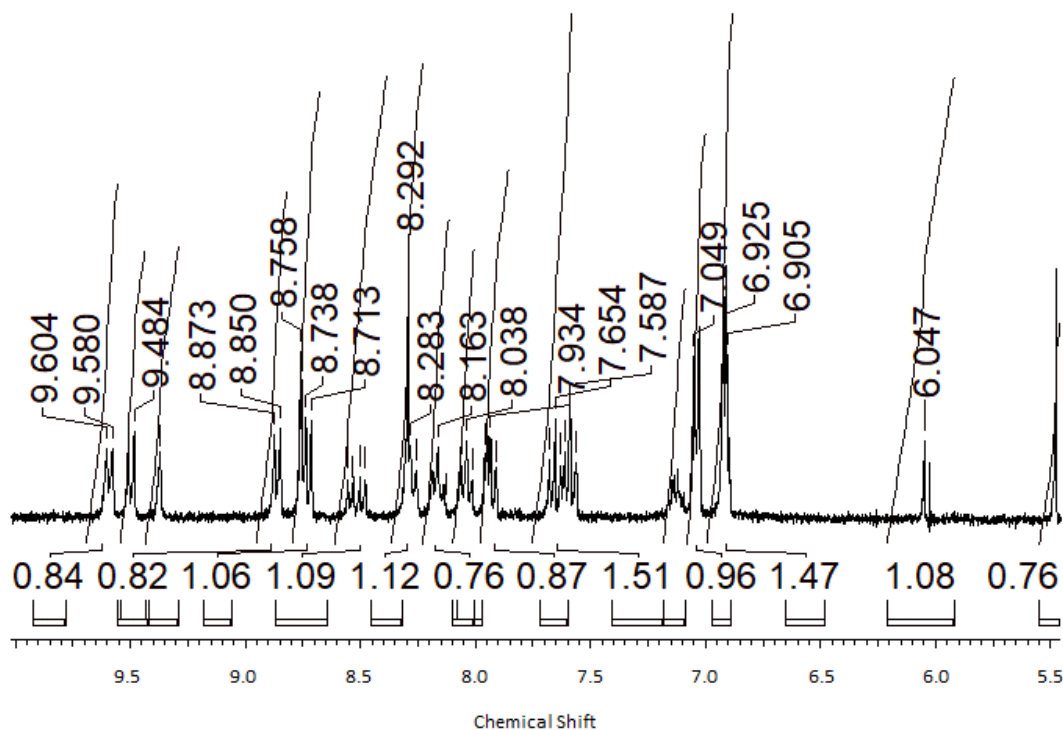
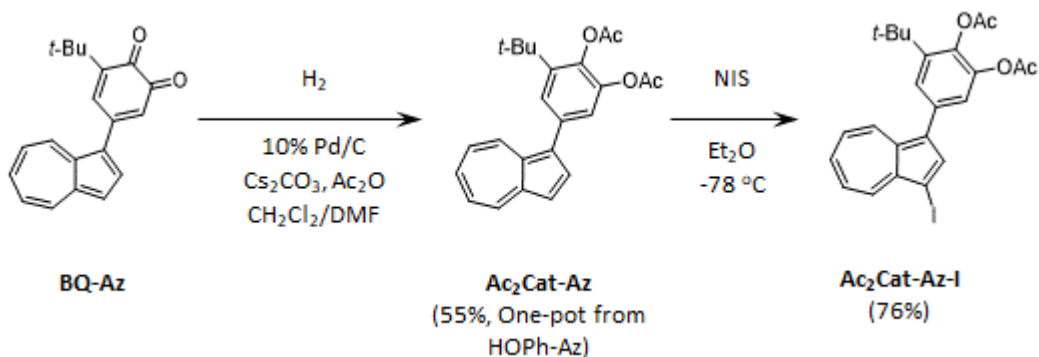


Figure V-20. Aromatic region from the ¹H-NMR spectrum from the reduction of **BQ-Az** to **Cat-Az** and allowing it to sit out for two days.

two days. There appears at least to be a doubling of azulene protons, but there are other signals mixed into the spectrum as well. The route of decomposition and the decomposition product or products remains elusive due to the complexity of the spectra. Interestingly, **Cat-Az-CHO** seemed to be relatively stable as indicated by the clean $^1\text{H-NMR}$ spectrum that was shown in Figure V-17. However, attempts to transform the aldehyde into other functional groups did not provide desirable results.

At this point the only way to synthesize **1,3-SQ-Az-NN** would be via a route where a **Cat-Az** compound was not isolated and did not exist in a high concentration with the intent to hinder the decomposition reaction and then generate the free catechol *in situ* during the complexation reaction with $\text{Zn(OH)Tp}^{\text{Cum,Me}}$. Scheme V-10 shows the result of an *in situ* generation of **Cat-Az** from **BQ-Az** by H_2/Pd reduction and then immediate protection of the catechol with acetates. This synthetic strategy was employed in Magdziak et al. to perform a one-pot conversion of several phenols to quinones via IBX oxidation in DMF and subsequent reduction with H_2 and 0.1 eq. of 10% Pd/C in the presence of 2.2 eq. of K_2CO_3 and 2.5 eq. of Ac_2O .⁴⁵ These reaction conditions were unsuitable to successfully prevent the decomposition of **Cat-Az** and the first attempt provided only a 13% yield of the desired compound in a one-pot conversion of **HOPh-Az** to **Ac₂Cat-Az**. The first modifications were that Cs_2CO_3 was used in

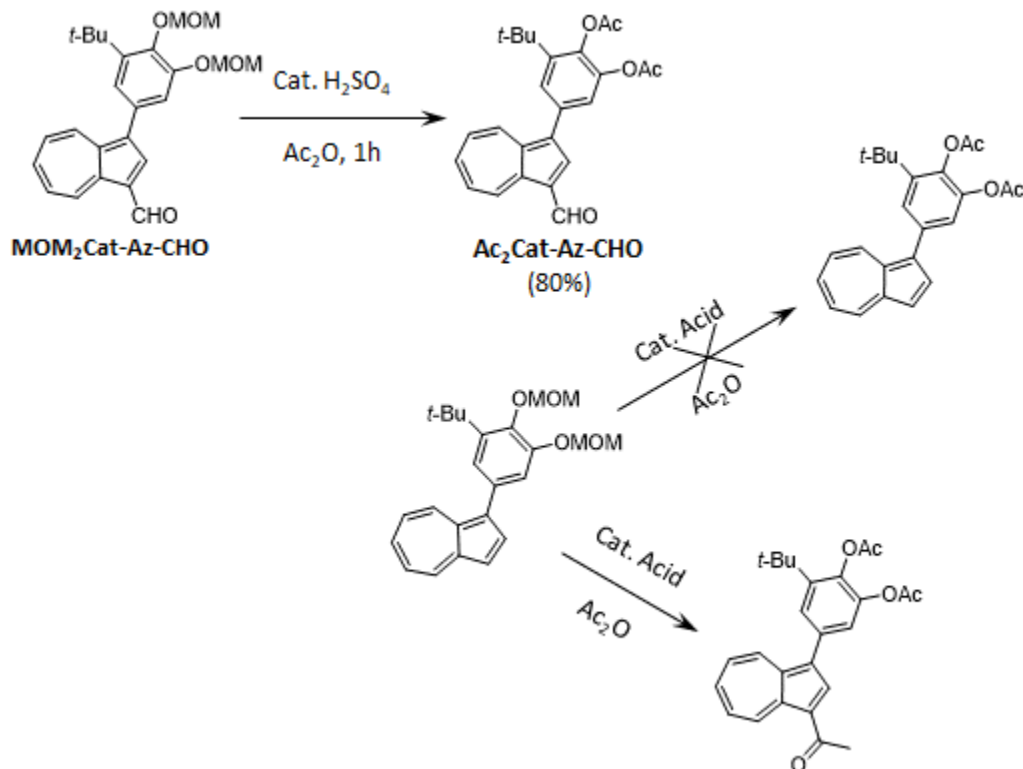
Scheme V-10. Pd/C hydrogen reduction and subsequent protection of **BQ-Az** to **Ac₂Cat-Az**, followed by iodination.



place of K_2CO_3 to increase the solubility of the base in organic solvents and 10 eq. of Ac_2O ; both of which were intended to quickly protect any **Cat-Az** that gets made. The result from these modifications were a 28% yield. During both of these reactions there was a green-brown spot on the baseline in the TLC in addition to the blue product. Since the decomposition of **Cat-Az** seemed to be concentration dependent, the hypothesis was that too much of a concentration of **Cat-Az** was being built-up between reduction of the quinone and protection. To combat this only 1% of 5% Pd/C was used in addition to the other modifications, but this reaction only gave a 7% yield. Given that this had the opposite of the desired effect, the hypothesis was reevaluated to be as some catechol was generated in low concentration and protected would then become deprotected by the excess carbonate and the free catechol would then decompose. The first thought was to generate the catechol as quickly as possible and allow it to become protected with 1 eq. of $\text{Pd}(\text{OAc})_2$ was used instead of Pd/C and the Pd was generated by the H_2 reduction. However, $\text{Pd}(\text{OAc})_2$ or 0.05, 0.1 0.2 or 1 eq. of 10% Pd/C resulted in either poor or variable yields. The hypothesis was still that either the concentration of **Cat-Az** was too high and it decomposed, or the Cs_2CO_3 was deprotonating the catechol, protecting it, but either the base directly or via adventitious H_2O making hydroxide was then deprotecting the catechol. Finally, to solve this, the reaction solution after the IBX oxidation was diluted with 10 times the volume with CH_2Cl_2 (*ca.* 50-80 mL) to reduce the solubility of the base and slow the hydrolysis of the acetates, which provided desirable results. With these modifications to the original procedure⁴⁵ **Ac₂Cat-Az** was synthesized in a 55% overall yield from **HOPh-Az** overnight after the solution containing the **BQ-Az**, 0.1 eq of 10% Pd/C, Ac_2O and Cs_2CO_3 was purged with H_2 . The iodination of **Ac₂Cat-Az** was accomplished easily with NIS in Et_2O in 76% yield.

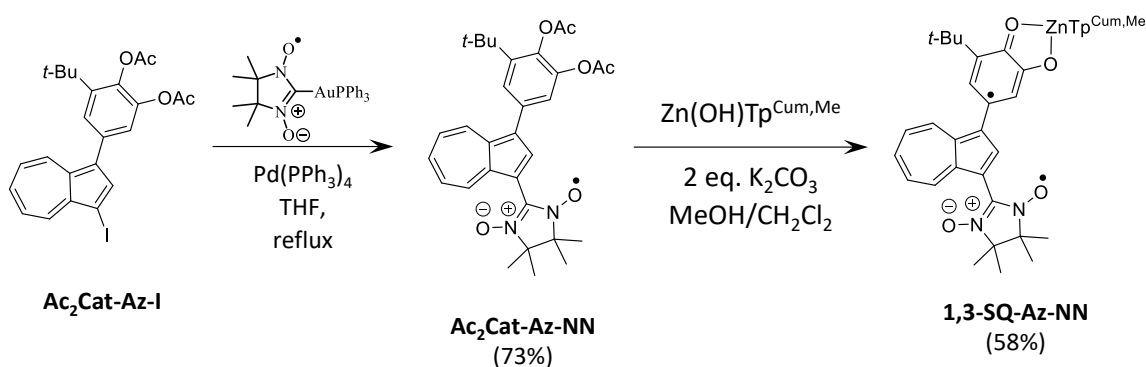
On a side note, parallel efforts to synthesize **Ac₂Cat-Az** in high yield led to the idea to replace the MOM groups with acetates in a single acid-catalyzed conversion. When this reaction

Scheme V-11. One-pot replacement of methoxymethyl groups with acetates.



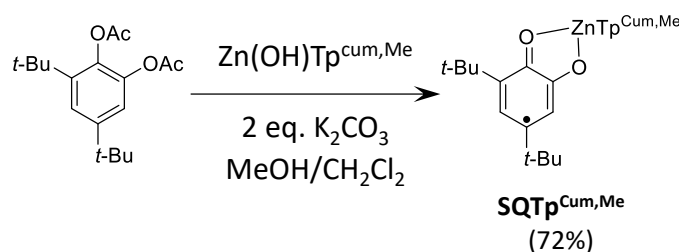
was attempted with **MOM₂Cat-Az-CHO**, as shown in Scheme V-11, the result was conversion to **Ac₂Cat-Az-CHO** in an 80% yield in less than 1 h using 3 drops of concentrated 18 M H_2SO_4 . Interestingly, concentrated 12M HCl in any amount was not acidic enough to produce the desired reaction and the result is that the MOM groups get removed and the solution turns from dark violet to green. However, when this methodology was attempted with **MOM₂Cat-Az** the MOMs were replaced with acetates, but the electron-rich 3-position of azulene became acylated as indicated by $^1\text{H-NMR}$. Attempting this with **MOM₂Cat-Az-I** also did not produce the desired product and instead led to many side products. Unfortunately, the substrate scope of this transformation as it seems to be somewhat limited, but is worth mentioning because this strategy could be used for other reactive catechols.

Scheme V-12. Synthesis of **Ac₂Cat-Az-NN** and **1,3-SQ-Az-NN**.



With **Ac₂Cat-Az-I** synthesized the final two steps were installation of the NN and SQ. Scheme V-12 shows the installation of the NN using the palladium-mediated cross-coupling with **NNAuPPh₃** which was complete within 4 h and gave a 73% yield of the desired compound as a seafoam green residue after purification on basic alumina. It is important to use basic alumina, as the compound will decompose completely before it elutes on neutral alumina or silica. As mentioned before, given the instability of free catechol containing azulene compounds, it was imperative that the protecting group for the catechol be able to be removed under the **Zn(OH)Tp^{Cum,Me}** complexation conditions. Acetates are perfect for this role in that they can be cleaved under mildly basic conditions using **K₂CO₃** in methanol, which conveniently were conditions that were already being used to deprotonate the catechols in order to facilitate the complexation. A test reaction was run on acetate-protected 3,5-di-*tert*-butylcatechol in the reaction solution of **K₂CO₃** in a 50/50 mixture of MeOH/CH₂Cl₂ (Scheme V-13). This complexation was run under a stream of nitrogen, but not a purge-pumped flask so that there

Scheme V-13. Test *in situ* acetate deprotection/ complexation.



would be some oxygen present to oxidize the complexed $\text{CatZnTp}^{\text{Cum,Me}}$ to the corresponding blue-green $\text{SQTp}^{\text{Cum,Me}}$ because given that this acetate-protected catechol and the $\text{Zn(OH)Tp}^{\text{Cum,Me}}$ are colorless, if the solution began to become blue-green, then the acetates had been cleaved, the $[\text{ZnTp}^{\text{Cum,Me}}]^+$ was complexed and the catechol was oxidized to the semiquinone. After about 20 min the reaction began to show faint blue-green, 1.5 h the color was more intense and the flask was then opened to air which resulted in the solution becoming very dark blue-green over the next couple of hours and the EPR spectrum displayed the doublet for the semiquinone proton and unresolved splitting for the *tert*-butyl protons.

When 50/50 MeOH/CH₂Cl₂ were added to a purge-pumped flask of **Ac₂Cat-Az-NN**, 2 eq. of K₂CO₃ and $\text{Zn(OH)Tp}^{\text{Cum,Me}}$, the result was a very faint spot of a pink compound by TLC on basic alumina running with the $\text{Zn(OH)Tp}^{\text{Cum,Me}}$, which is where the biradicals usually appear; however there was also a darker purple spot that turned blue once the TLC plate dried and a brown spot on baseline. The EPR spectra of the scrapings from the TLC plate of the pink and purple/blue spots showed clean 5-line, 7 Gauss splitting. Given the solvatochromic behavior and R_f of the purple/blue spot, this compound is believed to be **BQ-Az-NN** and the pink spot could not be further identified at this point other than that it was some NN in a very low concentration.

Regardless of this slightly negative result, the reaction was attempted again with the hypothesis that the acetates became deprotected too quickly and some decomposition occurred, as indicated by the brown spot on baseline and some amount of **Cat-Az** managed to get oxidized to the quinone which prevented its decomposition, which is not consistent with other observations in that the quinone was never observed for any other **Cat-Az** that seemed to have decomposed. On the second attempt, instead of combining the **Ac₂Cat-Az-NN** with the

Zn(OH)Tp^{Cum,Me} and K₂CO₃, the monoradical was purge-pumped, then dissolved in 20 mL of CH₂Cl₂ and then added dropwise at a rate of 1 drop per 6 seconds via cannula to a purge-pumped flask containing Zn(OH)Tp^{Cum,Me} and K₂CO₃ in mL of CH₂Cl₂ and 10 mL of methanol and 5 mL of CH₂Cl₂. The seafoam green **Ac₂Cat-Az-NN** solution turned to orange-brown as it entered the Zn(OH)Tp^{Cum,Me} and K₂CO₃ solution. Given the slow rate of addition, the transfer took approximately 3 h to complete. After addition, the brown-orange solution was opened to air and over the next 4 h, the orange-brown solution changed to a red-violet solution. The basic alumina TLC of the reaction revealed a dark red-violet spot running close to where the Zn(OH)Tp^{Cum,Me} does and a very faint purple spot, but no brown spot on baseline. Crystallizations were attempted after concentration, precipitation and collection of the red-violet solid. Figure V-21A shows the room temperature spectra of **Ac₂Cat-Az-NN** and **1,3-SQ-Az-NN**. **Ac₂Cat-Az-NN** is a typical NN EPR spectrum, but the **1,3-SQ-Az-NN** biradical is unusual in that it is not displaying the characteristic halving of the hyperfine coupling instead it appears to be dominated by monoradical NN with a five line pattern, split by *ca.* 7 Gauss with some biradical character

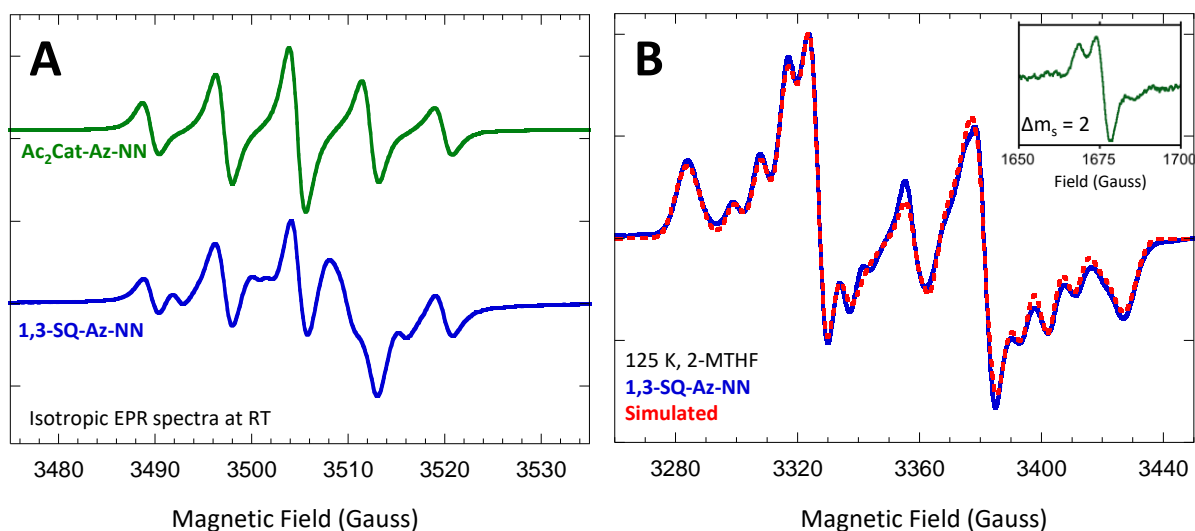


Figure V-21. A) Room temperature isotropic EPR spectra of **Ac₂Cat-Az-NN** monoradical (*top*) and **1,3-SQ-Az-NN** biradical (*bottom*). B) Anisotropic EPR spectrum and simulation of **1,3-SQ-Az-NN** in 2-MTHF at 125 K and the $\Delta m_s = 2$ half field transition (*inset*).

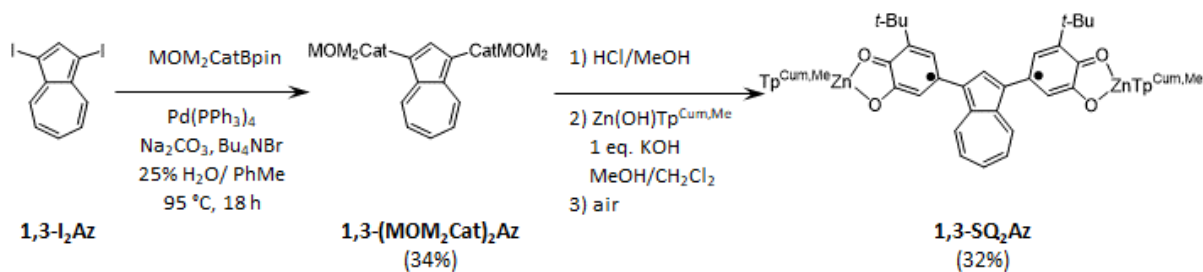
appearing in between the monoradical signal. Our group has encountered this before for any 1,3-substituted SQ-B-NN (discussed in Chapter III). Due to the steric bulk of the cumenyl groups they are capable of hindering the rotation of the NN at room temperature and give anisotropic EPR spectra at room temperature. The 125 K powder spectra of the red-violet solid in 2-MTHF at full field appears to be predominantly biradical and the forbidden $\Delta m_s = 2$ transition (*inset*) both with nitrogen hyperfine provide evidence that the bulk of the sample is the biradical. These data along with HRMS and X-ray crystallography confirmed the successful synthesis of **1,3-SQ-Az-NN**. Discussion of the powder EPR spectrum will occur in the results section of this chapter.

V.2.4. 1,3-SQ₂Az Synthesis.

The idea to synthesize **1,3-SQ₂Az** evolved out of the convenience of the low yielding reactions from Scheme V-5 where **MOM₂Cat-Az-I** was attempted to be synthesized by trying to Suzuki couple one **MOM₂Cat** onto **1,3-I₂Az**. A large portion of the remaining yield from those reactions was **1,3-(MOM₂Cat)₂Az**, the antepenultimate step to **1,3-SQ₂Az**. The utility of having a variety of different types of biradicals interacting through non-alternant systems for elucidating the electronic structure was discussed earlier in this Chapter (V.2).

Biradical ligand metal complex, **1,3-SQ₂Az** was synthesized as shown in Scheme V-14. The synthesis begins with the iodination of azulene at both the 1- and 3-positions with *N*-iodosuccinimide in accordance with literature procedure 1,3-diiodoazulene was subjected to

Scheme V-14. Synthesis of **1,3-SQ₂Az**.



Suzuki coupling with MOM₂CatBpin to give **1,3-(MOM₂Cat)₂Az**. The methoxymethyl (MOM) protecting groups were removed by catalytic HCl in MeOH at room temperature, and the resulting bis(catechol), **1,3-Cat₂Az** was complexed with Zn(OH) Tp^{Cum,Me} and subsequently oxidized with atmospheric O₂ to yield **1,3-SQ₂Az**. Which was confirmed via low temperature EPR, HRMS and X-ray crystallography.

V.2.4. Results.

X-Ray Crystallography. X-ray quality crystals of **1,3-SQ₂Az** were grown by slow evaporation of a CH₂Cl₂/MeOH solution, and the structure determined by X-ray diffraction is shown in Figure V-22 (*left*). The dioxolene C-O and C-C bond lengths are consistent with the semiquinone S = 1/2, anionic spin- and charge distribution (see Table V-2 for relevant bond lengths). Notably, the SQ-Az single bond lengths are ~1.46 Å consistent with substantial interaction between the SQ and Az π-systems. The torsion angles between the SQ and azulene bridging unit are 33.6° ± 0.5° as shown in the crystal structure, whereas the *meta*-phenylene-bridged biradicals have torsion angles of 32.2° ± 2.0°. ⁴⁶

The structure of **1,3-SQ-Az-NN** is shown in Figure V-22 (*right*). The dioxolene C-O and C-C bond lengths are consistent with the semiquinone S = 1/2, anionic spin- and charge distribution (see Table V-2 for relevant bond lengths). Notably, the SQ-Az single bond length is ~1.45 Å –

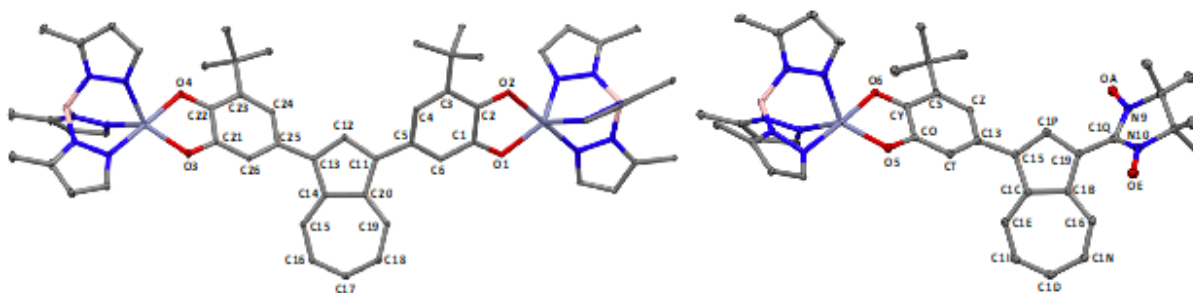


Figure V-22. Thermal ellipsoid plots (50% probability) and biradical ligand atomic numbering schemes for X-ray structures of **1,3-SQ₂Az** (left) and **1,3-SQ-Az-NN** (right).

Table V-2. Select **1,3-SQ₂-Az** and **1,3-SQ-Az-NN** bond lengths.^a

Moieties	1,3-SQ ₂ Az				1,3-SQ-Az-NN	
	Bond	Length (Å)	Bond	Length (Å)	Bond	Length (Å)
SQ C-O	C21-O3	1.296	C1-O1	1.300	CO-O5	1.298
	C22-O4	1.270	C2-O2	1.268	CY-O6	1.266
SQ rings	C21-C22	1.474	C1-C2	1.473	CO-CY	1.473
	C22-C23	1.444	C2-C3	1.446	CY-CS	1.449
	C23-C24	1.369	C3-C4	1.372	CS-CZ	1.365
	C24-C25	1.437	C4-C5	1.431	CZ-C13	1.445
	C25-C26	1.384	C5-C6	1.391	C13-CT	1.389
	C26-C21	1.395	C6-C1	1.400	CT-CO	1.407
SQ-Az bonds	C25-C13	1.463	C5-C11	1.463	C15-C13	1.451
NN bonds	---	---	---	---	N9-OA	1.288
					N10-OE	1.284
					N9-C1Q	1.371
					N10-C1Q	1.325
Az-NN	---	---	---	---	C19-C1Q	1.446

^aSee APPENDIX E for full list of structural parameters.

slightly shorter than the corresponding bonds in **1,3-SQ₂Az**. The torsion angle between the SQ ring and azulene bridging unit is $41.9^\circ \pm 0.5^\circ$, while the torsion angle between the ONCNO π -system of the NN radical and azulene bridging unit is $39.8^\circ \pm 2.0^\circ$.

Electron Paramagnetic Resonance (EPR) Spectroscopy. Support for a triplet-state of **1,3-SQ₂Az** biradical complex is provided by the frozen-solution EPR spectrum, Figure V-23A. The spectral features centered ~ 3340 G are consistent with the fine structure of a randomly-oriented triplet with a 5% monoradical impurity. Zero-field splitting (ZFS) parameters for the triplet determined by simulation are: $g_{xx} = 2.0040$, $g_{yy} = 2.0032$, $g_{zz} = 2.0054$; $|D/hc| = 0.00398$ cm⁻¹, and $|E/hc| = 0.00036$ cm⁻¹. The triplet signature $\Delta m_s = 2$ transition is present near half-field (Figure V-23A, *inset*). These ZFS parameters are very close to those of the *meta*-Ph-bridged complexes ($D \sim 0.004$ cm⁻¹ and $E \sim 0.0001$ cm⁻¹) which is expected due to the fact that in $S > 1/2$ organic species, ZFS parameters are determined by point dipole interactions (as opposed to spin-orbit interactions).⁴⁷

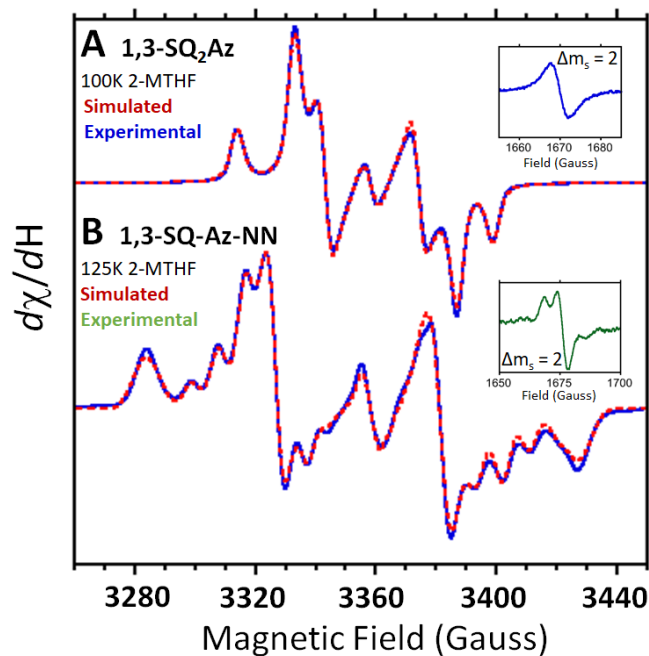


Figure V-23. X-band EPR spectra of **1,3-SQ₂Az** (A) and **1,3-SQ-Az-NN** (B) recorded at 100K and 125K, respectively in 2-methyltetrahydrofuran (2-MTHF). Simulations were executed using *Easyspin*.TM

The frozen solution triplet spectrum of **1,3-SQ-Az-NN** biradical complex is shown in Figure V-23B. As with **1,3-SQ₂Az**, the spectral features centered ~3340 G are consistent with the fine structure of a randomly-oriented rhombic triplet (relative $g_{xx} = 2.00606$, $g_{yy} = 2.00277$, $g_{zz} = 2.00518$; $|D/hc| = 0.00669 \text{ cm}^{-1}$, and $|E/hc| = 0.00044 \text{ cm}^{-1}$) with a 6% monoradical impurity and ¹⁴N hyperfine ($A_{N,xx} = 0.053 \text{ G}$, $A_{N,yy} = 8.76 \text{ G}$, $A_{N,zz} = 2.57 \text{ G}$), similar to the corresponding spectrum of **1,3-NN-Az**. The triplet signature $\Delta m_s = 2$ transition, possessing ¹⁴N hyperfine structure is present near half-field (Figure V-23B , *inset*).

The EPR spectral widths ($= 2D \sim r_e^{-3}$, where r_e is the interelectron separation)^{48,49} of **1,3-SQ₂Az** and **1,3-SQ-Az-NN** differ by a factor of ~50%, consistent with the shorter SQ---NN spin-spin distance compared to the SQ---SQ spin-spin distance, and consistent with the spectral trends for **1,3-IN₂-Az** and **1,3-NN₂-Az**.¹⁶ However, the room-temperature solution EPR spectrum of $S = \frac{1}{2}$ **1-SQ-Az** (Figure V-24) exhibits a ¹H-hyperfine pattern as indicated by additional splitting from the dashed blue lines in Figure V-24, strongly suggests delocalization into both the 5- and 7-membered rings of the azulene π -system, and such delocalization is required for “strong”

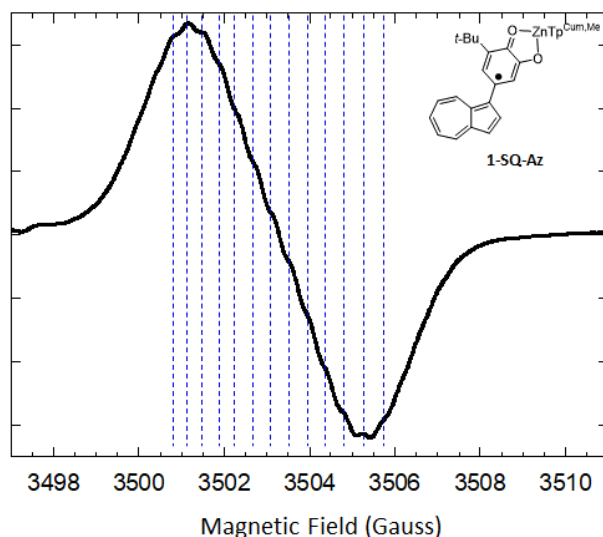


Figure V-24. Room-temperature solution spectrum of **1-SQ-Az**. Dashed blue lines show additional lines due to ¹H-hyperfine couplings.

magnetic exchange with the second radical be it a second SQ (a Donor-Bridge-Donor biradical, **1,3-SQ₂Az**), or an NN (a D-B-A biradical, **1,3-SQ-Az-NN**). With the number of discernable ¹H-hyperfine couplings shown by the dashed lines, when extrapolated to the whole spectrum, there would need to be at least 32 lines present because it must be a power of 2; therefore, that suggests coupling at least to 5 protons ($2^n = 2^5 = 32$). Of those at least five, two are probably catechol protons, two more are probably the protons at the 2- and 3-positions of azulene on the 5-

membered ring, but there still needs to be at least one more which could only be part of the 7-membered ring; indicating delocalization into both rings.

Electronic Absorption Spectroscopy. Figure V-25A shows the electronic absorption spectra of **SQ-NN** (*purple*), **Ph-NN** (*blue*) and 3,5-di-*tert*-butylsemiquinone (**ZnSQ**) (*gold*) as discussed in Chapter III, and can be seen the **ZnSQ** and **SQ-NN** possess the broad SQ $n \rightarrow \pi^*$ band at 12000 cm^{-1} with $\epsilon \approx 800 \text{ M}^{-1} \text{ cm}^{-1}$, **Ph-NN** and **SQ-NN** possess the NN $n \rightarrow \pi^*$ band around 18000 cm^{-1} with $\epsilon \approx 1500 \text{ M}^{-1} \text{ cm}^{-1}$ and then another band at approximately 30000 cm^{-1} . However, only the **SQ-NN** possesses a new band at 24000 cm^{-1} of the SQ SOMO \rightarrow B-NN LUMO transition that facilitates the interaction between the SQ and NN in **SQ-NN**, **pSQ-Ph-NN** (*red*) and conjugated pathways through other alternant hydrocarbon systems (biphenyl, naphthalene, thiophene). Figure V-25B shows the series of azulene compounds with the same strategy to reveal new absorption bands. Starting with unsubstituted azulene which possesses the visible $S_0 \rightarrow S_1$ absorption band at 17000 cm^{-1} ($\epsilon = 400 \text{ M}^{-1} \text{ cm}^{-1}$) and the $S_0 \rightarrow S_2$ absorption band at 29000 cm^{-1} ($\epsilon = 4000 \text{ M}^{-1} \text{ cm}^{-1}$). The visible band at 17000 cm^{-1} also possesses vibronic structure in non-polar solvents. The **1-SQAz** has several distinguishable bands at 12000 cm^{-1} ($\epsilon = 2500 \text{ M}^{-1} \text{ cm}^{-1}$),

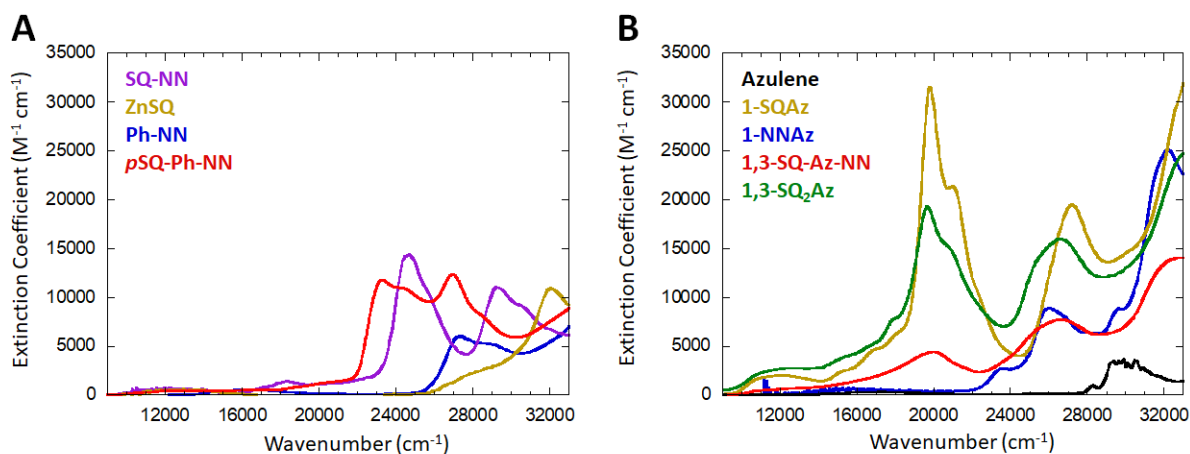


Figure V-25. Electronic absorption spectra of (A) **SQ-NN**, **ZnSQ**, **Ph-NN** and **pSQ-Ph-NN** and (B) azulene, **1-SQAz**, **1-NNAz**, **1,3-SQ-Az-NN** and **1,3-SQ₂Az**.

20000 cm^{-1} ($\epsilon = 31000 \text{ M}^{-1} \text{ cm}^{-1}$), 22000 cm^{-1} ($\epsilon = 21000 \text{ M}^{-1} \text{ cm}^{-1}$), 27000 cm^{-1} ($\epsilon = 20000 \text{ M}^{-1} \text{ cm}^{-1}$) and greater than 32000 cm^{-1} . There are several bands or a band with vibronic structure that appear as a shoulder on the low energy side of the band at 20000 cm^{-1} , which is similar to where the azulene visible band is at 17000 cm^{-1} , but the extinction coefficient for these bands in **1-SQAz** are 2000 to 7000 $\text{M}^{-1} \text{ cm}^{-1}$; over an order of magnitude larger than azulene's visible band ($\epsilon = 400 \text{ M}^{-1} \text{ cm}^{-1}$). Similarly, the band at 12000 cm^{-1} which is assumed to be the $n \rightarrow \pi^*$ band of the SQ given the energy, but with an extinction coefficient ($\epsilon = 2500 \text{ M}^{-1} \text{ cm}^{-1}$) that is about three times that of other semiquinones ($\epsilon = 800 \text{ M}^{-1} \text{ cm}^{-1}$). **1,3-SQ₂Az** possesses, as expected, essentially all of the same absorption bands of **1-SQAz**. In **1,3-SQ₂Az** the bands at 12000 cm^{-1} and the shoulder band(s) from 16000 cm^{-1} to under the 20000 cm^{-1} bands are stronger which in the case of the semiquinone $n \rightarrow \pi^*$ band is expected since there are now twice as many chromophores for that transition. However, in the case of the bands at 20000 cm^{-1} and 22000 cm^{-1} the intensity weakens for **1,3-SQ₂Az** relative to **1-SQAz** from 30000 and 21000 $\text{M}^{-1} \text{ cm}^{-1}$ to 20000 and 15000 $\text{M}^{-1} \text{ cm}^{-1}$ for each band, respectively. Given that corresponding orbitals (HOMO/LUMO, HOMO-1/LUMO+1, etc.) in azulene and non-alternant hydrocarbon systems are asymmetric, it could be that those bands involve transitions between inherently asymmetric orbitals. Having one semiquinone in **1-SQAz** removes the asymmetry between the orbitals by inducing asymmetry in the molecule; causing the transitions to become more allowed while a second semiquinone at the 3-position restores symmetry to the molecule and restores some of the asymmetry between the orbitals. The band at 27000 cm^{-1} in **1-SQAz** changes for **1,3-SQ₂Az**, but it is difficult to make comments on the changing strength of the absorption because a band moves to lower energy which appears to be a separate band that may be underneath the band

27000 cm^{-1} in **1-SQAz** because the band gets broader and asymmetric indicating that there are multiple bands together in this region.

The **1-NNAz** has several distinguishable bands at 15000 ($\epsilon \approx 600 \text{ M}^{-1} \text{ cm}^{-1}$), 23500 cm^{-1} ($\epsilon \approx 3000 \text{ M}^{-1} \text{ cm}^{-1}$), 26000 cm^{-1} ($\epsilon \approx 9000 \text{ M}^{-1} \text{ cm}^{-1}$), 29500 cm^{-1} ($\epsilon \approx 9000 \text{ M}^{-1} \text{ cm}^{-1}$) and 32000 cm^{-1} ($\epsilon \approx 25000 \text{ M}^{-1} \text{ cm}^{-1}$). The band at 15000 cm^{-1} is the azulene $S_0 \rightarrow S_1$ absorption band. **1,3-SQ-Az-NN** has three prominent bands at 20000 cm^{-1} , 26500 cm^{-1} and 32500 cm^{-1} ; as well as a broad, weak band around 12000 cm^{-1} with an extinction coefficient of less than 1000 $\text{M}^{-1} \text{ cm}^{-1}$, more reminiscent of other semiquinones. The band at 26500 cm^{-1} ($\epsilon = 7000 \text{ M}^{-1} \text{ cm}^{-1}$) could be the NN in that **1-NNAz** has a band at 26000 cm^{-1} with $\epsilon = 9000 \text{ M}^{-1} \text{ cm}^{-1}$; however this could also be a much weaker version of the bands at 27000 cm^{-1} that are in **1-SQAz** and **1,3-SQ₂Az** which are otherwise absent in **1,3-SQ-Az-NN**. Furthermore, the band at 20000 cm^{-1} in **1,3-SQ-Az-NN** may or may not be related to the 20000 cm^{-1} bands in **1,3-SQ₂Az** and **1-SQAz** because not only is it much weaker, $\epsilon = 4000 \text{ M}^{-1} \text{ cm}^{-1}$ vs. 20000 and 30000 $\text{M}^{-1} \text{ cm}^{-1}$ for **1,3-SQ₂Az** and **1-SQAz**, respectively, its shape is different. It lacks the shoulder at 22000 cm^{-1} which could be a consequence of the bathochromic shift of that band.

The electronic absorption spectra for **ZnSQ**, **Ph-NN**, **SQ-NN** and **pSQ-Ph-NN** (Figure V-25A) revealed the transitions that were involved in the superexchange mechanism by the presence of a new strong band ($\epsilon = 15000 \text{ M}^{-1} \text{ cm}^{-1}$) around 24000 cm^{-1} and there is great similarity between the other bands and bands present in the constituent molecule absorption spectra. This has held true for other bridges such as thiophene and naphthalene, but in the case of azulene and probably other nonalternant hydrocarbons the spectra are convoluted between **1-SQAz**, **1-NNAz**, **1,3-SQ₂Az**, **1,3-SQ-Az-NN** and even azulene; making these same comparisons

nearly impossible by visual inspection and necessitating the need for calculations and higher levels of theory in order to understand the nature of these transitions.

Magnetometry. To determine the sign and magnitude of intramolecular magnetic exchange coupling between the two SQ and between SQ and NN through the nonalternant azulene π -system, magnetic susceptibility measurements were performed on a SQUID magnetometer. Saturation magnetization experiments as shown in Figure V-26A at 2K gave $M_{\text{sat}} = 1.7$ Bohr magnetons, consistent with a triplet ground state (ferromagnetic coupling between the radicals). Paramagnetic susceptibility (χ_{para}) data measured between 2 and 300 K with an applied magnetic field of 0.7 T are shown in Figure V-26B. Fitting the plots of $\chi_{\text{para}} \cdot T$ vs. T resulted in an exchange coupling constant, $J = +38 \text{ cm}^{-1}$ and $J = +9 \text{ cm}^{-1}$ ($\mathcal{H} = -2J\hat{S}_1 \cdot \hat{S}_2$) for **1,3-SQ₂Az** and **1,3-SQ-Az-NN**, respectively. A positive J -value confirms ferromagnetic interaction between the two radicals through the nonalternant bridge giving a triplet ground-state. The J -value for **1,3-SQ₂Az** is very similar to those of **1,3-SQ₂Ph-X** with $J = +46 \text{ cm}^{-1}$ (X = H), $J = +36 \text{ cm}^{-1}$ (X = OMe) and $J = +35 \text{ cm}^{-1}$ (X = NMe₂).⁴⁶ **1,3-SQ-Az-NN** however is not similar to **1,3-SQ-Ph-NN** and its derivatives which gives -35 cm^{-1} , antiferromagnetically coupled radicals.²⁷ Not only is

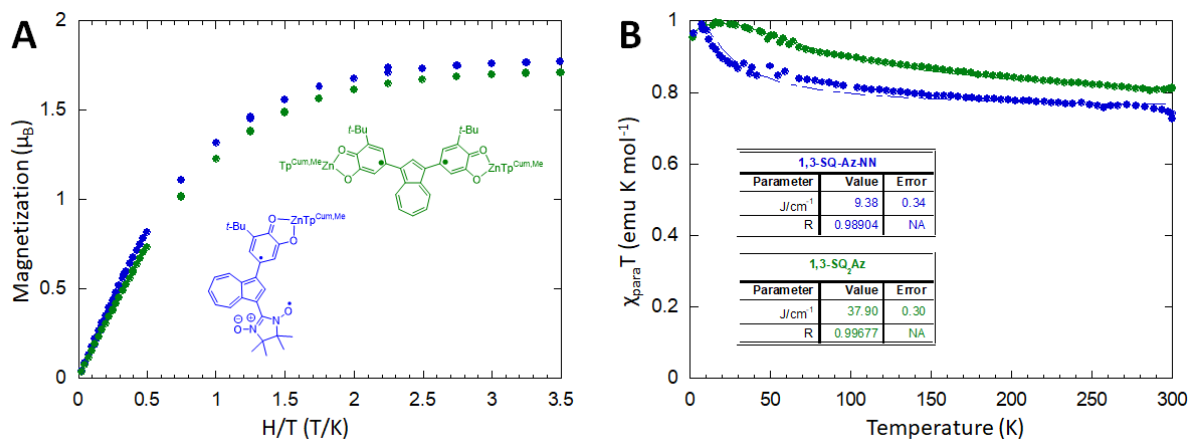


Figure V-26. Magnetic susceptibility (A) Saturation magnetization plots and (B) variable temperature paramagnetic susceptibility plots for **1,3-SQ₂Az** and **1,3-SQ-Az-NN**.

1,3-SQ-Az-NN much weaker, but more strikingly, it is the opposite sign of coupling indicating ferromagnetically coupled radicals. This is a clear demonstration of the greater complexity of electronic/magnetic coupling provided by a nonalternant π -system bridge compared to an alternant π -system bridge.

V.2.6. Discussion and Conclusions about Azulene Biradicals.

With Respect to Resonance Structures. In alternant hydrocarbon biradicals when two symmetric, delocalized radicals such as SQ are attached to identical positions as SQ and a NN, the observed exchange coupling is opposite in sign. In **1,3-SQ₂Ph-X** there is a $J = +35-50 \text{ cm}^{-1}$ for various derivatives and when one SQ is replaced with an NN radical to give **1,3-SQ-Ph-NN** (*m***SQ-Ph-NN**), $J = -35 \text{ cm}^{-1}$: the first ferromagnetic and the second antiferromagnetic.^{27,46} Meta through a phenyl ring is well known and accepted to be cross-conjugated and demonstrates what is called quantum interference in conductance experiments and calculations. **1,4-SQ-Ph-NN** (*p***SQ-Ph-NN**) has $J = +100 \text{ cm}^{-1}$ and while we have not measured it, **1,4-SQ₂Ph** would almost certainly be diamagnetic or strongly antiferromagnetically coupled as indicated by the short, double-bond style bond length of 1.42 \AA for a dioxolene dimer (**SQ₂**) that was synthesized. Once again, same connectivity, one with two semiquinones and one with SQ and NN, one is ferromagnetic and one is antiferromagnetic. Para through a phenyl ring is well known to be conjugated and a conductive pathway. However, when the molecule is **1,3-SQ₂Az** there is a $J =$

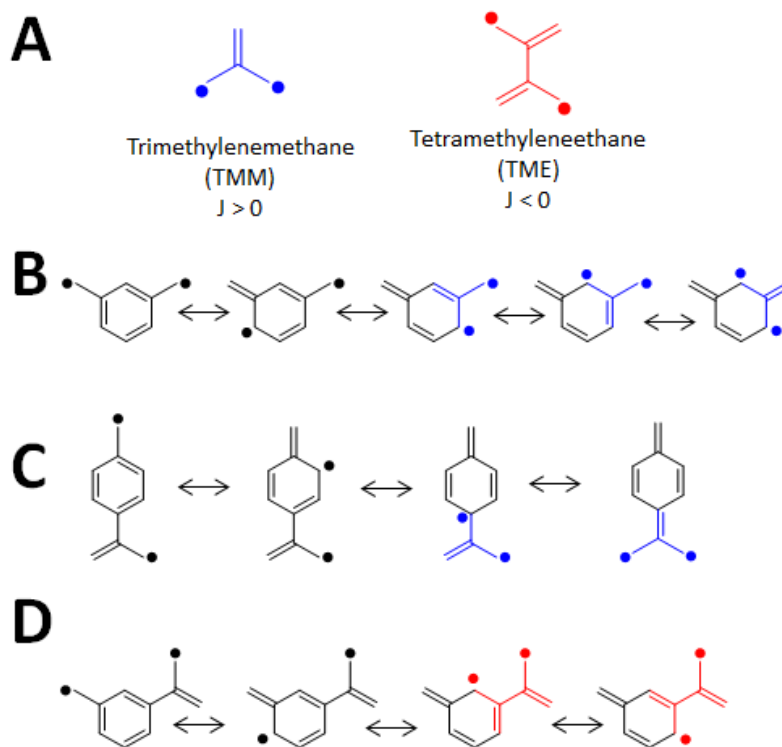


Figure V-27. Predicted and observed coupling in alternant hydrocarbons. (A) TMM and TME (B) symmetric, delocalized biradical (C) asymmetric one delocalized and one localized ferromagnetically and (D) antiferromagnetically coupled biradicals.

+38 cm^{-1} which can be compared to the **1,3-SQ₂Ph** compounds, but its analogous heterobiradical compound, **1,3-SQ-Az-NN** has a $J = +9 \text{ cm}^{-1}$: both are ferromagnetic, albeit the latter is weakly ferromagnetic, but regardless ferromagnetic; indicating the spins in the system do not use the same pathway or at least not a pathway that is understood in the context of our knowledge of alternant hydrocarbons. How do we reconcile these results for azulene?

Chapter I covered several topological methods for evaluating electron spins relative to each other for alternant hydrocarbons. These methods will be discussed here in the context of the magnetic data for **1,3-SQ₂Az** and **1,3-SQ-Az-NN** with alternant hydrocarbons (phenylene) for comparison. For simplicity, semiquinones will be modelled as methylene radicals because they can delocalize into the π system of the bridge and NNs will be modelled as allyl radicals bonded

at the 2-position because they possess a node at the central carbon and cannot delocalize into the bridge. Recall the classical examples of simple alternant biradicals: trimethylenemethane (TMM) and tetramethyleneethane (TME) (Figure V-27A). TMM is a classic biradical with nondisjoint molecular orbitals, the requirement for a triplet ground state and consequently has a ferromagnetic J -value, while TME has disjoint SOMOs indicating that the singlet-triplet gap will be small and in this case, a singlet ground state with an antiferromagnetic J -value. For biradicals of alternant hydrocarbons when resonance structures are drawn if some of those resonance structures contain the TMM substructure that molecule will have nondisjoint molecular orbitals and consequently ferromagnetically-coupled radicals (Figure V-27B and C). On the other hand, alternant hydrocarbons that have TME-containing resonance forms will be antiferromagnetically coupled (Figure V-27D). The important thing to note is that TMM is only in ferromagnetically-coupled alternant systems and can never be found in an antiferromagnetically-coupled system; while TME is only in antiferromagnetically-coupled nonalternant π -systems and can never be found in an alternant ferromagnetically-coupled biradical. Figure V-28A shows the resonance structures of a symmetric 1,3-azulene biradical with delocalized radicals (**1,3-SQ₂Az**). As can be seen, unlike the symmetric, delocalized biradical from Figure V-27B, the resonance structures of azulene contain not only TMM substructures, but also TME and the last one in the bottom right-hand corner contain both. There are more TME resonance structures, which may lead one to conclude that **1,3-SQ₂Az** may be antiferromagnetically coupled, but magnetometry reveals that this is not the case. Figure V-28B shows the resonance structures of the asymmetric biradical

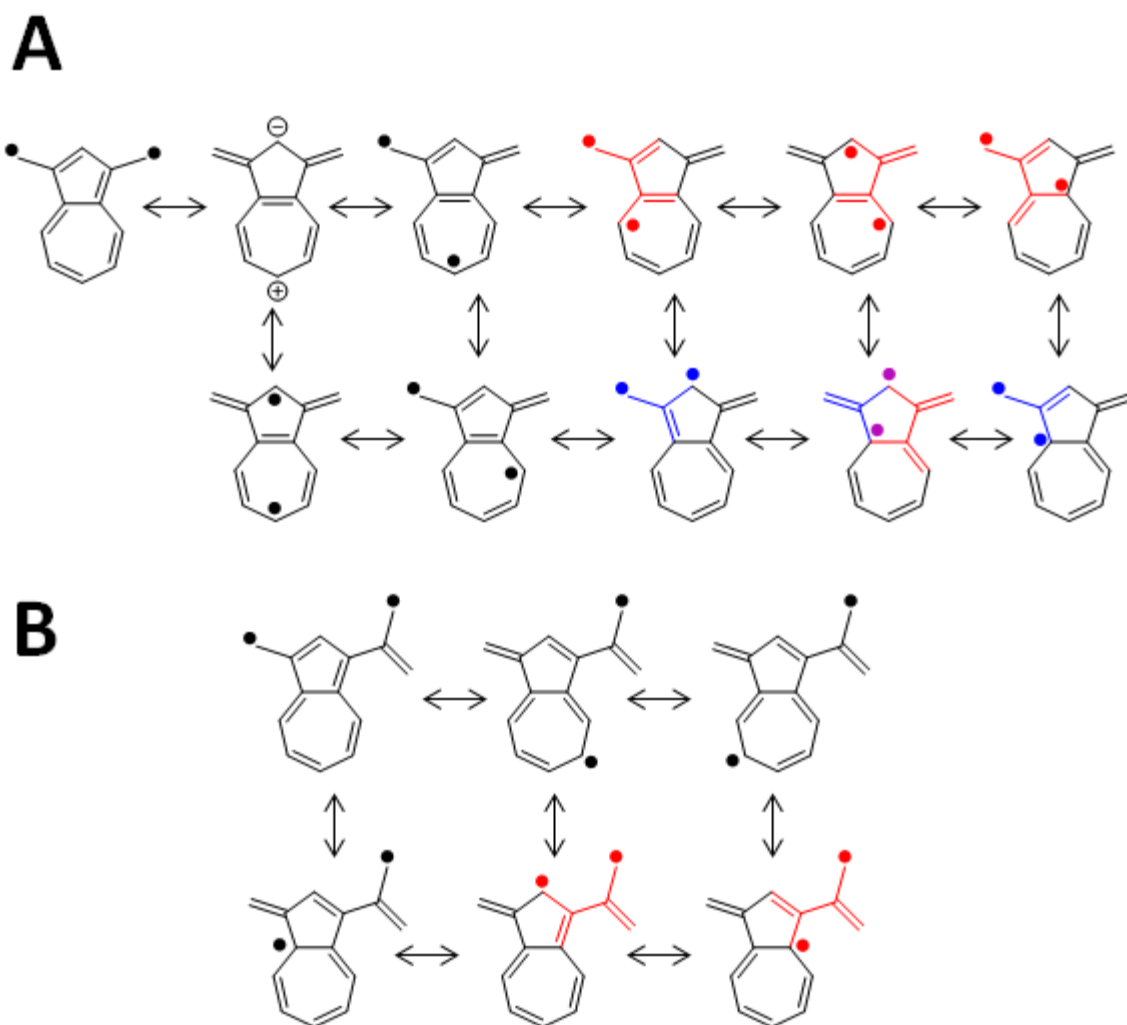


Figure V-28. (A) symmetric, delocalized biradical (B) asymmetric one delocalized and one localized biradicals 1,3- through azulene.

with methylene and allyl radicals (**1,3-SQ-Az-NN**). The resonance structures in this case only contain TME substructures, once again leading to the belief that **1,3-SQ-Az-NN** is antiferromagnetic, but once again this is not what the magnetometry reveals. Thus, this topological method which works well for alternant systems is insufficient to describe the observed coupling in azulene-bridged biradicals.

With Respect to Spin Polarization. Another topological method for predicting exchange coupling is to use a spin polarization argument.^{1,25,50,51} In a π -bond, the electrons in adjacent p-

orbitals must have opposite spins, such that in a conjugated π -system the spin densities alternate up, down. Figure V-29A shows this for symmetric, delocalized radicals at the 1,3 positions of a phenyl ring and azulene. The biradical having a *m*-phenyl bridge has both methylene radicals with the same spin (ferromagnetically coupled), and it does not matter which pathway through the π system is taken to get there – the spins alternate up and down. If you traverse the π -system across the 2-position the radicals are ferromagnetically coupled and if you travers the π system across the 6,5,4-positions the radicals are ferromagnetically coupled. Both routes give the same result as indicated by the blue double-headed arrows. For the azulene-bridged biradical, if you traverse the π -system through the 2-position (Path 2) the result is ferromagnetically coupled radicals as indicated by the blue double-headed arrow. However, if you traverse the π system through the 4,5-positions (Path 4,5), the result is antiferromagnetically coupled radicals as

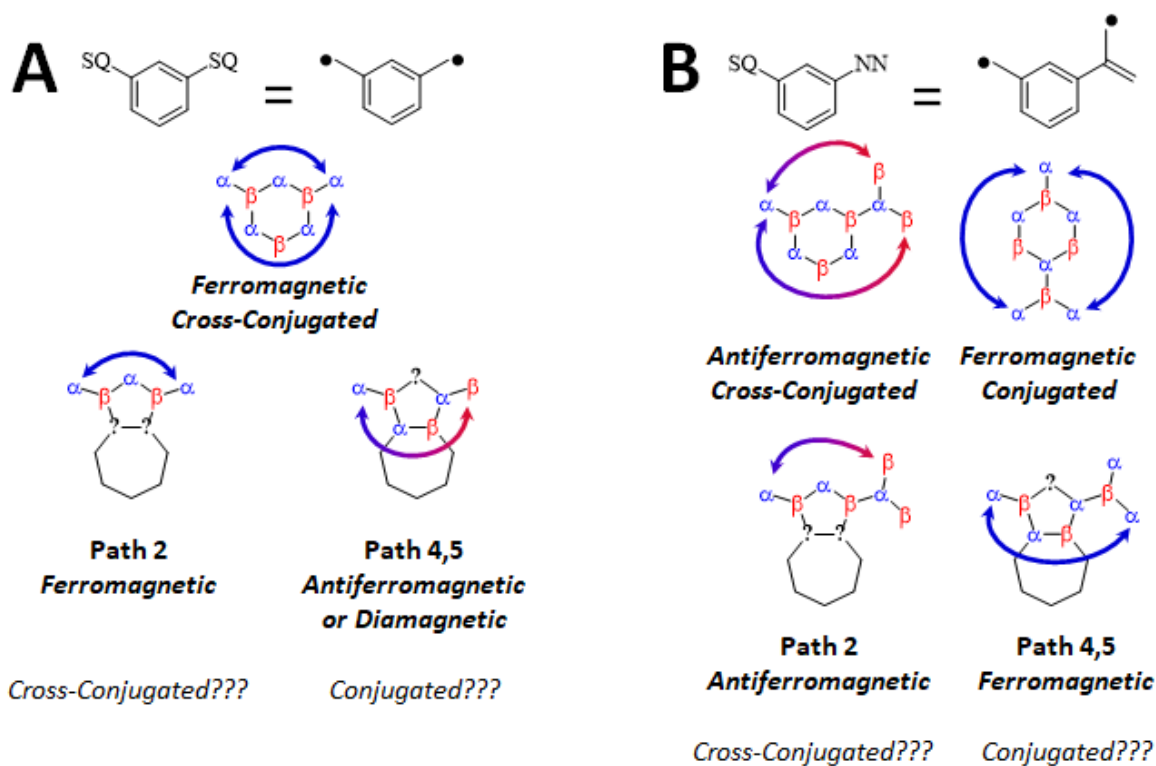


Figure V-29. Spin polarization through alternant and nonalternant hydrocarbons between two (A) symmetric, delocalized and (B) asymmetric, one delocalized and one localized radicals.

indicated by the blue-red double-headed arrow. In each case, either the 4- and 5-positions for Path 2 or the 2-position in Path 4,5 is left unknown as to the identity of the spin because neither α nor β spin is correct because then two of the same spin are next to each other. It is easy for us to say that Path 2 is correct because that gives ferromagnetically coupled radicals as is observed for **1,3-SQ₂Az** ($J = +38 \text{ cm}^{-1}$) and this is consistent with what is observed and known about **1,3-SQ₂Ph** compounds ($J = +35\text{-}50 \text{ cm}^{-1}$). But is this the only pathway through azulene? Is Path 2 stronger because it is shorter than Path 4,5? Is Path 4,5 diamagnetic and silent from magnetometry by formation of a quinoidal resonance structure (Figure V-28A, *only resonance structure with charges*)? Or is there another mechanism leading to the observed coupling? If Path 2 is the dominant pathway then **1,3-SQ-Az-NN** should give antiferromagnetic coupling, similarly to **1,3-SQ-Ph-NN** compounds. In Figure V-28B **1,3-SQ-Ph-NN** compounds give antiferromagnetic coupling and give that coupling whether you go through the 2-position or around the 6,5,4 positions as indicated by the blue-red double-headed arrows or by the blue double-headed arrows for **1,4-SQ-Ph-NN** compounds. As mentioned, for **1,3-SQ-Az-NN** going through the 2-position with a spin polarization method will give antiferromagnetic coupling, but going through the 4,5 path will give ferromagnetic coupling. The magnetic susceptibility data gives ferromagnetic ($J = +9 \text{ cm}^{-1}$) coupling. The sign of the exchange coupling parameter indicates that the coupling is not what was expected if azulene behaves like **1,3-SQ-Az-NN** compounds, but the magnitude of J is important because while **1,3-SQ₂Az** has a J value that is amongst J values for the phenyl analogs both in sign and magnitude. **1,3-SQ-Az-NN** is not only different in sign, but also in magnitude; it is much weaker than corresponding phenyl-bridged analogs. This result suggests nearly the opposite of **1,3-SQ₂Az** in that it is the longer pathway (Path 4,5) that gives the dominant coupling. “Dominant” seems to be a credible description

because of the magnitude of the coupling. It could be that the ferromagnetic pathway is being canceled by a slightly less than equivalent antiferromagnetic pathway. In alternant systems, ferromagnetic SQ-B-NN are indicative of conjugated connectivity through π -systems and antiferromagnetic SQ-B-NN are indicative of cross-conjugated connectivity. While it is unclear if these terms have the same meaning in nonalternant systems, they are going to be used to relate what is observed for azulene back to results for alternant systems. Exchange coupling through conjugated systems is greater in magnitude than that through cross-conjugated systems as shown by the cross-conjugated **1,3-SQ-Ph-NN** with $J = -35 \text{ cm}^{-1}$ and the conjugated **1,4-SQ-Ph-NN** with $J = +100 \text{ cm}^{-1}$, even though the radicals in the conjugated systems are an extra bond away. If Path 2 for **1,3-SQ-Az-NN** leads to antiferromagnetic coupling due to cross-conjugation, which would be supported by **1,3-SQ₂Az**, and Path 4,5 for **1,3-SQ-Az-NN** leads to ferromagnetic coupling due to a conjugated pathway and it is still true that the magnitude of exchange coupling through a conjugative pathway is greater than that through a cross-conjugative pathway for non-alternant hydrocarbons. This could be an explanation for $J = +9 \text{ cm}^{-1}$ for **1,3-SQ-Az-NN**. The problems with this explanation are that several assumptions about the similarities of alternant and nonalternant hydrocarbons are made and we do not know if two competing pathways for the sign of coupling are a linear combination or how this competition would be manifest. We know that **1,4-SQ-Az-NN** has a J value 2.9 times ($|100 \text{ cm}^{-1}/-35 \text{ cm}^{-1}|$) greater in magnitude than **1,3-SQ-Ph-NN**, but not necessarily what effect those pathways would have when occurring in the same molecule.

In the context of Donor-Bridge-Acceptor Biradicals. So far, the observed coupling through 1,3-azulene-bridged biradicals has been analyzed using simple resonance and spin polarization arguments, highlighting ambiguities and flaws of each approach. For the **SQ-B-NN**

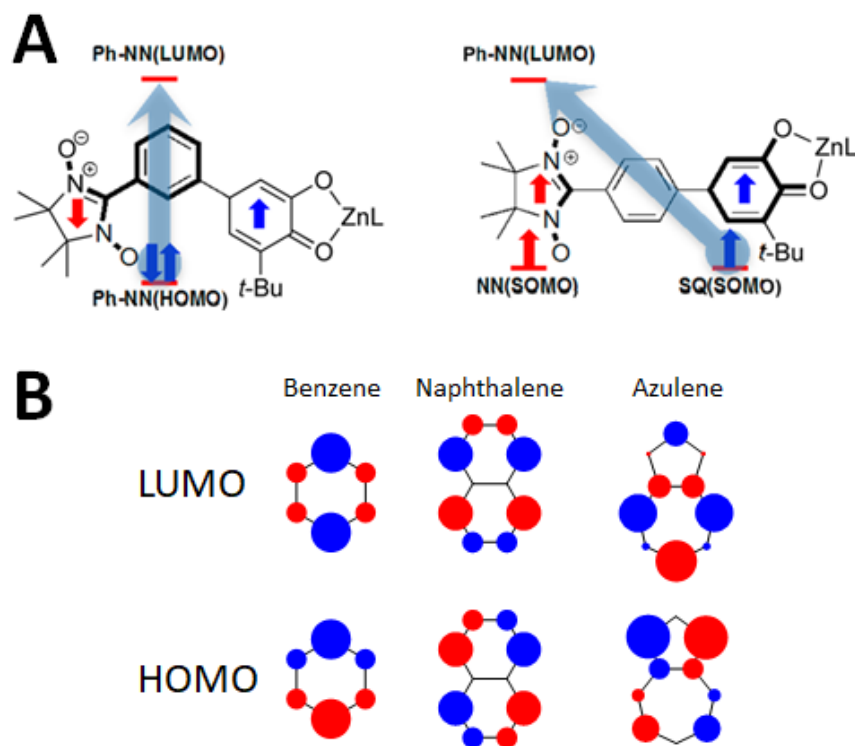


Figure V-30. (A) Dominant orbital interactions for 1,3-SQ-Ph-NN and 1,4-SQ-Ph-NN. (B) HOMO and LUMO of alternant hydrocarbons: benzene and naphthalene and nonalternant hydrocarbon: azulene.

structural motif the valence bond configuration interaction model described in Chapter III provides another opportunity to explain the unexpected ferromagnetic coupling in both **1,3-SQ₂Az** and **1,3-SQ-Az-NN**. Figure V-30A summarizes the molecular orbitals that are involved in the superexchange mechanism that is used to explain the observed coupling in these systems. For cross-conjugated systems (**1,3-SQ-Ph-NN**) the dominant orbitals involved in the superexchange pathway are the Ph-NN(HOMO) and the Ph-NN(LUMO) while for conjugated systems (**1,4-SQ-Ph-NN**) the dominant superexchange pathway involves the SQ(SOMO) and Ph-NN(LUMO). Figure V-30B shows the HOMOs and LUMOs for azulene, naphthalene and benzene. For benzene, only one set of its degenerate pair is shown because only this HOMO/LUMO set have non-zero orbital coefficients on atoms that are bonded to the radicals. As mentioned in the introductory sections of this chapter, one of the distinct electronic

differences between alternant and nonalternant hydrocarbons is that the HOMO and LUMO (and every pair of orbitals below and above) for alternant hydrocarbons are related by symmetry. The orbital coefficients on the same atoms have the same magnitude in corresponding orbitals. For nonalternant hydrocarbons there is no symmetry relation of the HOMO and LUMO. Both superexchange pathways in Figure V-30 make use of the bridge LUMO, but for azulene, the coefficients at the 1,3-positions are vanishingly small, such that both pathways are predicted to be weak. A third mechanism that has not been explored by us previously, involves Bridge-NN HOMO and SQ (SOMO) orbitals. This pathway would be ferromagnetic for **1,3-SQ-Az-NN** as it creates spin density on the bridge in an orbital that is orthogonal to the NN SOMO. However, this mechanism would predict antiferromagnetic coupling for **1,3-SQ-Az-SQ**. It may well be that all three superexchange pathways are operative but make different contributions for different biradicals. Exploration of these mechanism will be the focus of future work of our collaborators at the University of New Mexico.

In the context of related physical properties. Implementation of the atom-counting model for quantum interference and use in azulene seems to have some validity. Figure V-31 shows how the atom-counting model proposed by Markussen et al. works for 1,4-phenylene, 1,3-phenylene and 1,3-azulene with the latter two being predicted to display quantum interference.⁵² In SQ-B-NN molecules, antiferromagnetic coupling correlates with (weak) quantum interference conductance through the bridge, while ferromagnetic coupling correlates with normal (strong) conductance. While **1,3-SQ-Az-NN** is not antiferromagnetic it is the weakest ferromagnetically-

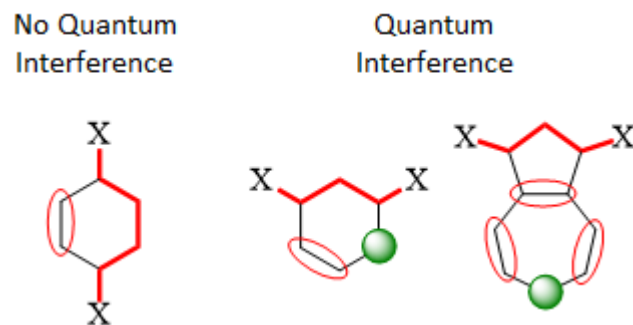


Figure V-31. Atom-counting model for the presence of quantum interference.

coupled biradical through a π -system that we have found for the radical-bridge bonds being so close and in the absence of torsion angles greater than 45° (SQ-Az = 41.9° and Az-NN = 39.8°). It is fairly close in ferromagnetic coupling strength to **NN-PhMe₂Th-SQ** from Chapter IV with a $J = +11 \text{ cm}^{-1}$, but this molecule has the SQ-bridge to bridge-NN connection points nearly three times further apart (6.74 \AA to 2.30 \AA) and contains a 68° intra-bridge torsion angle.

The conflicting conductance studies by Xia et al.³ and Schwarz et al.⁴ that were discussed in section V.1.6.2 which highlighted the complexities of elucidating conductance pathways in azulene can be rationalized in the context of two competing exchange pathways that **1,3-SQ-Az-NN** seems to indicate. To summarize, Xia et al. reported the relative order of the strength of conductance for azulene derivatives with different connectivity through azulene being $1,3\text{-Az} \approx 2,6\text{-Az} > 4,7\text{-Az}$ while Schwarz et al. reported the relative order for strength of conductance of $2,6\text{-Az} \approx 4,7\text{-Az} > 1,3\text{-Az}$ (Figure V-32) and their respective studies are supported by their own calculations.^{3,4} How does 1,3-azulene connectivity end-up giving one of the strongest conductance in one case and the weakest by several orders of magnitude in the other? The groups used different linkers as shown in Figure V-32 to connect their azulene derivatives to gold electrodes and it is probably the case that Xia et al.'s linkers facilitate conductance through the conductive or for lack of a better word, conjugated pathway through 1,3-azulene while Schwarz

et al.'s linkers were prejudicial toward the quantum interfering or cross-conjugated pathway. This would allow Xia et al. to have relatively strong conductance and Schwarz et al. to have relatively weak conductance with the same azulene connectivity. The respective linkers could be prejudicial to one path versus another due to their inherent electronics or the contact geometry of the molecule with the gold electrodes.⁵³

To conclude. Two azulene biradicals (**1,3-SQ₂Az** and **1,3-SQ-Az-NN**) and two azulene monoradicals (**1-SQAz** and **1-NNAz**) have been synthesized, characterized, their electronic properties and for the former two, magnetic properties investigated. **1,3-SQ₂Az** exhibits ferromagnetic coupling ($J = +38 \text{ cm}^{-1}$), similar to its 1,3-phenyl-bridged counterparts ($J \sim +40 \text{ cm}^{-1}$)⁴⁶ while **1,3-SQ-Az-NN** did not.²⁷ **1,3-SQ-Az-NN** exhibits weak ferromagnetic coupling ($J = +9 \text{ cm}^{-1}$) probably due to the presence of competing ferromagnetic and antiferromagnetic exchange pathways, where the ferromagnetic pathway is slightly stronger. The electronic absorption spectra for this series of compounds are complex did not provide a hint as to the orbital nature of the dominant exchange pathway. Instead, the electronic absorption spectra are exceedingly more complicated than those of **ZnSQ**, **SQ-NN**, **1,4-SQ-Ph-NN** and **Ph-NN**^{27,35} and will require higher levels of theory and calculation to elucidate the origin of the dominant exchange pathway and the observed coupling. This will be future work conducted by our collaborators at the University of New Mexico. As demonstrated, many of the normal pen-and-paper topological^{1,26,50} analogies for understanding electronic structure in alternant hydrocarbon-bridged biradicals fails to accurately or unambiguously predict coupling between two radicals appended to azulene, although the atom-counting model seems to have some validity for at least predicting quantum interference effects in azulene if not the observed coupling.^{3,5-7} However, these results provide context for the potential origin of the conflicting results that can be found in

literature for evaluating conductance pathways through azulene.^{3,4} In order to fully understand the exchange pathways through nonalternant hydrocarbons and azulene, higher level calculations and perhaps the synthesis of more compounds are necessary. Likely candidates to help with this understanding would be **5,7-SQ₂Az** and **5,7-SQ-Az-NN** because now the longer pathway is two more bonds further away than the shorter pathway than in **1,3-SQ-Az-NN**.

V.3. Ferrocene as Another Nonalternant Bridge.

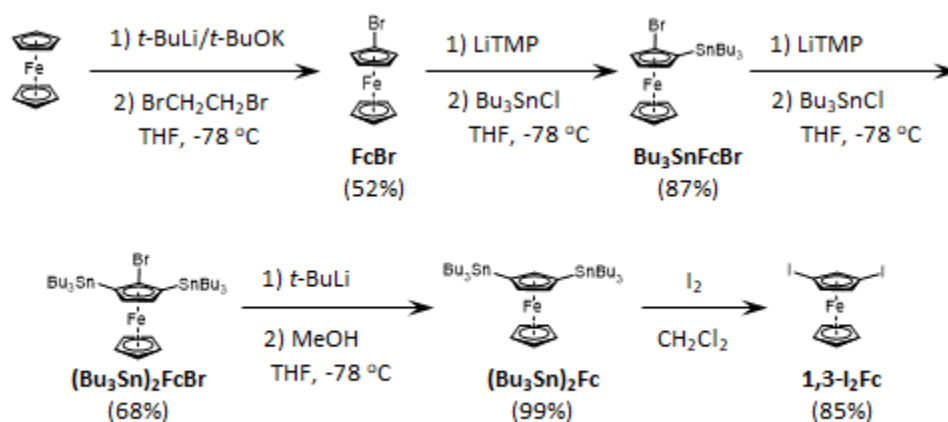
Another molecule that contains a non-alternant π -system is ferrocene as it possesses two cyclopentadienyl anions. Ferrocene has been the subject of a multitude of various studies for nearly 70 years.⁵⁴⁻⁵⁹ However, does ferrocene behave like azulene across its five-membered ring or will it behave differently? Like azulene, the goal was to synthesize the 1,3-SQ-B-NN containing ferrocene (**1,3-SQ-Fc-NN**); however, due to different synthetic challenges posed by ferrocene, the **1,3-SQ₂Fc** and **1,1'-SQ₂Fc** were synthesized instead by the argument for synthesizing symmetrical biradicals, the latter can be compared to existing symmetrically-substituted ferrocene biradicals containing verdazyl, NN, IN and tris(perfluorophenyl)methyl radicals.⁶⁰⁻⁶² However, this is the first synthesis of a 1,3-substituted biradical through one of ferrocene's cyclopentadienyl rings. The attempted syntheses of **1,3-SQ-Fc-NN** are presented in APPENDIX D.

V.3.1. 1,3-SQ₂Fc Synthesis.

The synthesis of **1,3-SQ₂Fc** follows the literature procedure for synthesizing 1,3-diiodoferrocene from 1-bromoferrocene as described by Zirakzadeh et al. (Scheme V-15) with a slight modification to the work-up.⁶³ Zirakzadeh et al. obtained their 1-bromoferrocene commercially, but in this case it was synthesized according to the literature procedure, with the

exception of purification, by Khobragade et al. who employed Schlosser's base to deprotonate ferrocene at low temperature and then quenched the lithiated ferrocene with 1,2-dibromoethane.^{63,64} Their purification involved silica flash chromatography in 100% hexane, but they mentioned that 1-bromoferrocene could not be separated by remaining ferrocene this way. When following this procedure, it was also found that the product was also contaminated with 1,2-dibromoethane. To remove these impurities, the crude material was subjected to Kugelrohr distillation for the 1,2-dibromoethane, during which some, but not all of the remaining ferrocene sublimed. To completely remove the unreacted ferrocene, the material was then washed twice by

Scheme V-15. Synthesis of 1,3-diiodoferrocene.

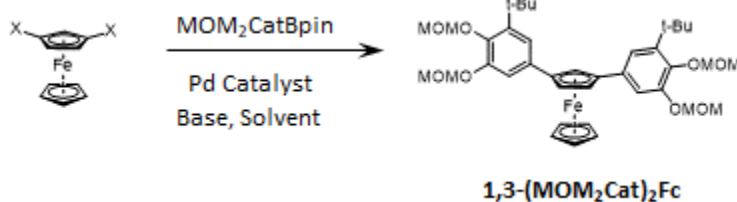


stirring with 0.1M FeCl₃ solution, removing the ferrocenium-containing aqueous layer, then washing with brine as prescribed by Inkpen et al. to give 1-bromoferrocene as a dark red-orange oil which solidified upon standing.⁶⁵ The next two steps in the synthesis according to Zirakzadeh et al. are to perform the same reaction twice by *ortho*-lithiating 1-bromoferrocene with the sterically hindered LiTMP and then quenching with tributyltin chloride; with purification in between the addition of the tin groups.⁶³ The purification in Zirakzadeh et al. was to use a silica column with 100% hexane as the eluent for both the mono- and di-stannylated products;⁶³ however when this was attempted, it was found that the product was contaminated with

unreacted ferrocene starting material and unreacted tributyltin chloride. All these compounds run at an $R_f \approx 0.9$, so achieving any separation with silica and non-polar solvents was nearly impossible. The alternative purification method that was used for **Bu₃SnFcBr** and **(Bu₃Sn)₂FcBr** was to use a reversed-phase silica column with ethanol as the eluent. While this was a slow process due to the more densely packed C18-silica gel and higher viscosity of alcohols, the ease of separation and the purity of the material that it furnished was superior. The replacement of the trialkyltin groups with iodine and purification of **1,3-I₂Fc** proceeded just as described.⁶³

From **1,3-I₂Fc**, MOM₂Cat groups could be installed via Suzuki cross-coupling with MOM₂CatBpin, which is where some issues were encountered. Table V-3 shows the results of Suzuki couplings that were attempted. Entry 1 shows the typical Suzuki coupling that have been employed for most of this document which had performed quite well with halo-bridges and MOM₂CatBpin, typically giving >85% yields, but in this instance it failed and only provided starting material. With knowledge of an article by Ho et al. which discusses the unusual reactive behavior of aryl iodides relative to aryl bromides in Suzuki couplings in the presence of phosphine ligands, entries 2-4 sought to remove the presence of the phosphine ligand by substituting the palladium catalyst with the *N*-heterocyclic carbene ligand of the PEPPSI-*i*Pr catalyst while using bases from Ho et al. which were reported to perform the best with aryl iodides.⁶⁶ Unfortunately none of these reactions provided the desired **1,3-(MOM₂Cat)₂Fc**. Entry 5 changed the solvent from toluene to THF which was the first instances where the reaction worked in a 41 and 13% yield, but then failed on an additional attempt. Indicating that these conditions were unreliable. In an attempt to use an aryl bromide, a portion of **(Bu₃Sn)₂Fc** was subjected to pyridinium tribromide to replace the trialkyltin groups with bromides and while the tin groups were successfully replaced with bromides, the yield was only 16% a big difference

Table V-3. Attempted palladium-mediate cross-couplings for 1,3-(MOM₂Cat)₂Fc.



Entry	1,3-X ₂ Fc	Pd Catalyst	Base/reagents	Solvent	Results
1	X = I	Pd(PPh ₃) ₄	Na ₂ CO ₃ /Bu ₄ NBr	25% H ₂ O/toluene	No Rxn
2	X = I	PEPPSI-iPr	Ba(OH) ₂ /Bu ₄ NBr	25% H ₂ O/toluene	No Rxn
3	X = I	PEPPSI-iPr	K ₂ CO ₃ /Bu ₄ NBr	25% H ₂ O/toluene	No Rxn
4	X = I	PEPPSI-iPr	CaCO ₃ /Bu ₄ NBr	25% H ₂ O/toluene	No Rxn
5	X = I	Pd(PPh ₃) ₄	K ₂ CO ₃	25% H ₂ O/THF	41%, 13%, No Rxn
6	X = Br	Pd(PPh ₃) ₄	Na ₂ CO ₃ /Bu ₄ NBr	25% H ₂ O/toluene	No Rxn
7	X = Br	PEPPSI-iPr	Na ₂ CO ₃ /Bu ₄ NBr	25% H ₂ O/toluene	No Rxn
8 ^a	X = SnBu ₃	Pd(PPh ₃) ₄	CsF	THF	Decomposition
9 ^a	X = SnBu ₃	Pd(PPh ₃) ₄	CuI	Toluene	No Rxn
10 ^b	X = SnBu ₃	Pd(PPh ₃) ₄	CsF	THF	Decomposition
11 ^b	X = SnBu ₃	Pd(PPh ₃) ₄	CuI	Toluene	No Rxn
12	X = I	Pd(OAc) ₂	Na ₂ CO ₃ /Bu ₄ NBr	25% H ₂ O/toluene	No Rxn
13	X = I	Pd(OAc) ₂	Na ₂ CO ₃	25% H ₂ O/THF	76, 93%

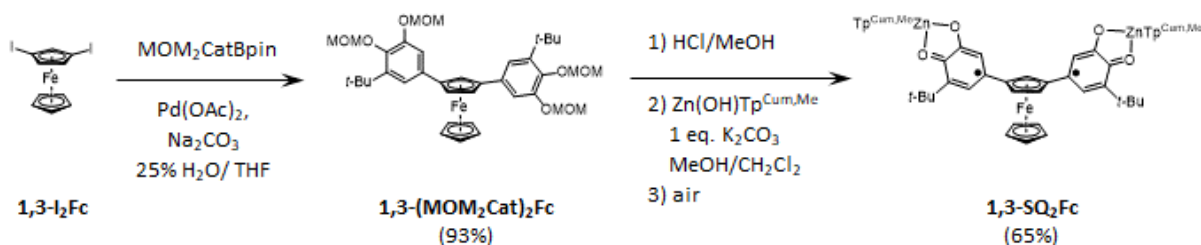
^a MOM₂CatBr was used instead of MOM₂CatBpin.

^b Ac₂CatBr was used instead of MOM₂CatBpin.

from 85% with iodides. Regardless, if the Suzuki coupling was successful, the yield could be dealt with. However, entries 6 and 7 both resulted in no reaction and attempts to use 1,3-dibromoferrocene were ceased after this 1) because of the 16% yield for it and 2) an article by Knapp et al. discusses the lack of reactivity of bromoferrocenes in Suzuki couplings. Entries 8-11 sought to change the electronics of the palladium cross-coupling by using (Bu₃Sn)₂Fc directly in a Stille cross-coupling with MOM₂CatBr in entries 8 and 9, then the acetate-protected catechol bromide (Ac₂CatBr) in entries 10 and 11 to further modulate the electronics. None of these reactions were successful and those that tried using CsF to facilitate the Stille resulted in

decomposition. Another catalyst used by Ho et al. was Pd(OAc)₂ with aryl iodides; no phosphine ligands, which was attempted in entries 12 and 13. Entry 12 used the previously highly successful 1:3 H₂O:toluene mixture, but this failed and provided starting materials.⁶⁶ It was noted that during this attempt, the clear orange reaction solution at the start had turned dark and there was black material coated onto the flask. Hypothesizing that this black material was palladium metal, indicating that Pd(OAc)₂ was successfully reduced, but was just not very soluble in the H₂O:toluene mixture, entry 13 was attempted with Pd(OAc)₂ in 1:3 H₂O:THF mixture. Since

Scheme V-16. Synthesis of **1,3-SQ₂Fc**.



THF is a coordinating solvent, it was thought that it may stabilize the activated palladium complex and keep it in solution to undergo the cross-coupling chemistry. Entry 13 resulted in a 76% yield on a small scale and then rose to 93% on a larger scale. It seems that Pd(OAc)₂ in H₂O/THF is a highly effective catalyst for Suzuki couplings involving aryl iodides as it has also been applied successfully to reactions presented in Chapter IV, APPENDIX C and APPENDIX D.

The final steps from **1,3-(MOM₂Cat)₂Fc** to **1,3-SQ₂Fc** (Scheme V-16) were to cleave the methoxymethyl groups with catalytic acid which was performed over 5 min in a microwave reactor at 90 °C to give the intermediate **1,3-Cat₂Fc** which was then complexed with Zn(OH)Tp^{Cum,Me} and oxidized aerobically to give **1,3-SQ₂Fc**.

V.3.2. 1,1'-SQ₂Fc Synthesis.

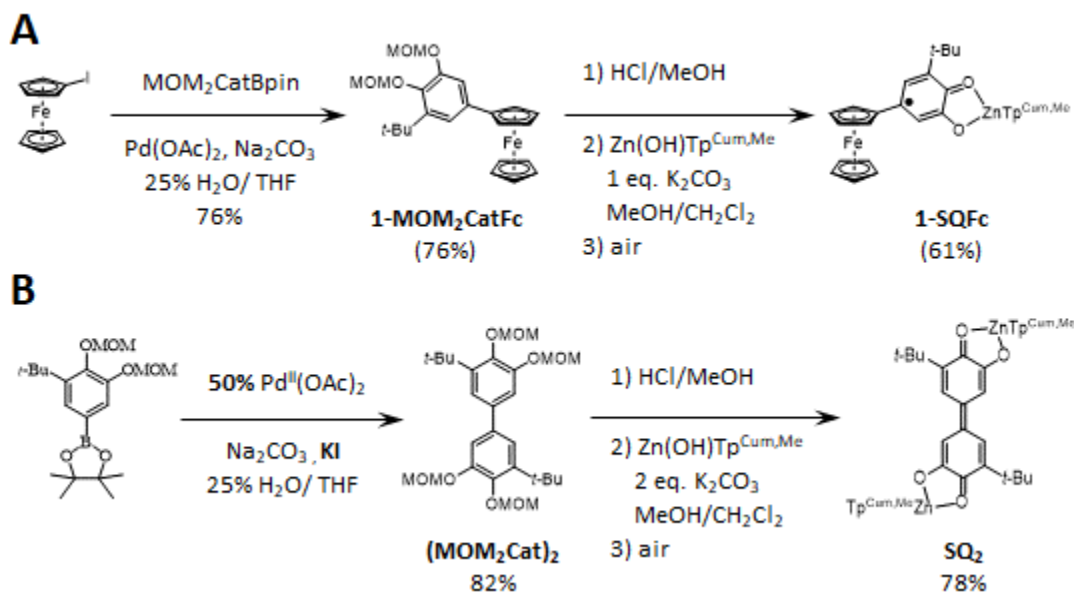
1,1'-diodoferrocene was synthesized via a combination of established literature procedures.^{64,67} Khobragade et al.'s procedure for the 1,1'-lithiation of ferrocene was superior to Butler et al., but the procedure by Butler et al. was preferred for producing pure 1,1'-diodoferrocene by the two step stannylation and replacement of the trialkyltin groups with iodides in overall 75% yield.⁶⁷ The synthesis of **1,1'-(MOM₂Cat)₂Fc** was easily accomplished from 1,1'-diodoferrocene using the Suzuki coupling methodology from the synthesis of **1,3-(MOM₂Cat)₂Fc**. This compound was then subsequently deprotected with catalytic acid over 5 min in a microwave reactor at 90 °C, then complexed with Zn(OH)Tp^{Cum,Me} and aeri ally oxidized.

V.3.3. 1-SQFc Synthesis.

It should also be mentioned that the **1-SQFc** monoradical was also prepared for comparison from 1-iodoferrocene by the same methods (Scheme V-17A) already discussed for **1,3-SQ₂Fc** and **1,1'-SQ₂Fc**.

During the X-ray analysis of the first batch of **1,3-SQ₂Fc**, it was discovered that a small fraction of an impurity (**SQ₂**) had crystallized much more easily than the desired ferrocene biradical, whose structure and intentional synthesis is shown in Scheme V-17B. The origin of this impurity in **1,3-SQ₂Fc** occurs during the Suzuki coupling to make **1,3-(MOM₂Cat)₂Fc** with Pd(OAc)₂. Because Pd(OAc)₂ is a pre-catalyst with palladium in the +2 oxidation state, it must be reduced to Pd⁰ before it can undergo oxidative addition with an aryl halide for the start of the Suzuki-coupling palladium cycle. In the absence of a reducing agent, the metallated aryl

Scheme V-17. Synthesis of **A**) **1-SQFc** monoradical and **B**) **SQ₂** dioxolene dimer.



substrates, in this case **MOM₂CatBpin**, can undergo transmetalation to the **Pd^{II}** twice and then reductively eliminate to give the **(MOM₂Cat)₂** dimer and **Pd⁰** for the Suzuki cross-coupling which should only have given approximately 2% of the impurity. However, it seemed to crystallize much more efficiently than **1,3-SQ₂Fc** and constituted a large number of the crystals. A second attempt to make **1,3-SQ₂Fc** was performed and after deprotection of the MOM groups, the product was washed with saturated **NaHCO₃** solution because it was hypothesized that due to resonance stabilization of the singly deprotonated conjugate base of **Cat₂** the **pK_a** of the catechol which is normally 10-11 would be much lower. Possibly low enough to become deprotonated by a weak base and could be extracted during an aqueous work-up. Conveniently, this strategy worked perfectly by removing the dimer impurity. Because of our strategy to utilize symmetrical SQ biradicals to aid in evaluating the electronic structure of non-alternant hydrocarbons, it is reasonable to have the no-bridge parent compound which is analogous to the **SQ-NN**, no-bridge parent. Being the simplest symmetrical SQ biradical which should be strongly antiferromagnetically coupled, its electronic structure can be probed via electronic absorbance

spectroscopy and either EPR or NMR depending on the strength of the coupling. For the intentionally synthesizing pure **SQ₂** for analysis, it was reasonable to attempt to use 1 eq. of **MOM₂CatBpin** with 2 eq. of **Na₂CO₃** and 0.5 eq. of **Pd(OAc)₂** in the 1:3 **H₂O:THF** mixture from the synthesis of **1,3-(MOM₂Cat)₂Fc**. Surprisingly, this was ineffective and TLC revealed only the starting materials and the clear, light orange solution did not change colors. In this instance it seemed like the **1,3-I₂Fc** or something from it had some mechanism for facilitating the transmetalation/reductive elimination steps. To this end, 1 eq. of potassium iodide was added to

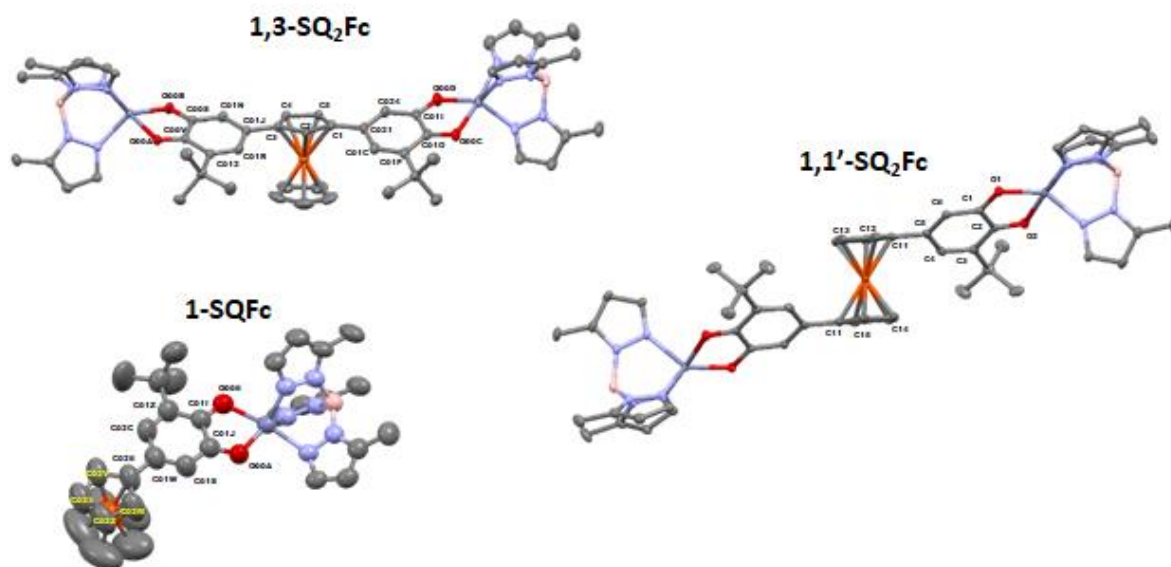


Figure V-32. Thermal ellipsoid plots (50% probability) and biradical ligand atomic numbering schemes for X-ray structures of **1,3-SQ₂Fc** (top left), **1,1'-SQ₂Fc** (right), and **1-SQFc** (bottom left). Cumenyl groups and hydrogens have been omitted for clarity.

give an iodide source which resulted in an immediate color change to dark red and TLC after 1 h indicated that the reaction was complete.

V.3.4. Ferrocene Results.

X-Ray Crystallography. X-ray quality crystals of **1,3-SQ₂Fc** were grown by slow evaporation of a **CH₂Cl₂/*i*-PrOH** solution, and the structure determined by X-ray diffraction is shown in Figure V-25 (*top left*). The dioxolene C-O and C-C bond lengths are consistent with the semiquinone S

Table V-4. Select **1,3-SQ₂Fc**, **1,1'-SQ₂Fc** and **1-SQFc** bond lengths.^a

Moiety	1,3-SQ ₂ Fc				1,1'-SQ ₂ Fc ^b		1-SQFc	
	Bond	Length (Å)	Bond	Length (Å)	Bond	Length (Å)	Bond	Length (Å)
SQ C-O	C00S-O00B	1.302	C01I-O00D	1.300	C1-O1	1.290	C01J-O00A	1.282
	C00V-O00A	1.263	C01O-O00C	1.269	C2-O2	1.270	C01I-O006	1.267
SQ rings	C00V-C00S	1.469	C01O-C01I	1.468	C1-C2	1.474	C01J-C01I	1.463
	C00S-C01N	1.395	C01I-C024	1.403	C2-C3	1.443	C01I-C01Z	1.405
	C01N-C01J	1.385	C024-C021	1.385	C3-C4	1.269	C01Z-C02C	1.369
	C01J-C01R	1.436	C021-C01C	1.428	C4-C5	1.428	C02C-C01W	1.408
	C01R-C012	1.364	C01C-C01F	1.364	C5-C6	1.377	C01W-C01S	1.368
	C012-C00V	1.454	C01F-C01O	1.452	C6-C1	1.405	C01S-C01J	1.447
SQ-Fc bonds	C01J-C3	1.457	C021-C1	1.465	C5-C11	1.467	C01W-C026	1.479

^aSee APPENDIX E for full list of structural parameters.

^b**1,1'-SQ₂Fc** has inversion symmetry so only one SQ-Cp ring data is shown.

= ½, anionic spin- and charge distribution (see Table V-4 for relevant bond lengths). X-ray quality crystals of **1,1-SQ₂Fc** and **1-SQFc** were grown by slow evaporation of a CH₂Cl₂/MeOH solution, and the structure determined by X-ray diffraction is shown in Figure V-32 (right and bottom left, respectively). For all three compounds the dioxolene C-O and C-C bond lengths are consistent with the semiquinone S = ½, anionic spin- and charge distribution (see Table V-4 for relevant bond lengths). The torsion angles between the SQ and ferrocene bridging unit varies over the three structures. As shown in the crystal structure **1-SQFc** has the highest degree of planarity with the torsion angle being 0.83° ± 0.02°. **1,3-SQ₂Fc** are 19.4° ± 2.5°, arising from a relatively large disparity between the two SQ-Fc bonds which are 16.9° and 21.9°. These torsions are also much smaller than the azulene-SQ torsion angles which were 33.6° ± 0.5° and the *meta*-phenylene biradicals with torsion angles of 32.2° ± 2.0°. ⁴⁶ **1,1'-SQ₂Fc** actually has the torsion angles with the most similarity between the azulene- and phenylene-bridged biradicals at 35.0° ± 0.4°.

Electron Paramagnetic Resonance (EPR) Spectroscopy. The isotropic room temperature spectrum of **1-SQFc** in 2-MTHF is shown in Figure V-33A. The spectrum was fit with *EasySpin* to a multiplet consisting of four proton hyperfine coupling constants and $g = 2.0068$ (DPPH reference). Two of the hyperfine coupling constants correspond to two inequivalent protons: $a_{H1} = 2.13$ G and $a_{H2} = 0.62$ G; and the other two correspond to two sets of two equivalent protons: $a_{H3} = 0.78$ G and $a_{H4} = 0.37$ G. The top-down view of **1-SQFc** in Figure V-33A shows that the single inequivalent proton hyperfine coupling constants; a_{H1} and a_{H2} , correspond to the

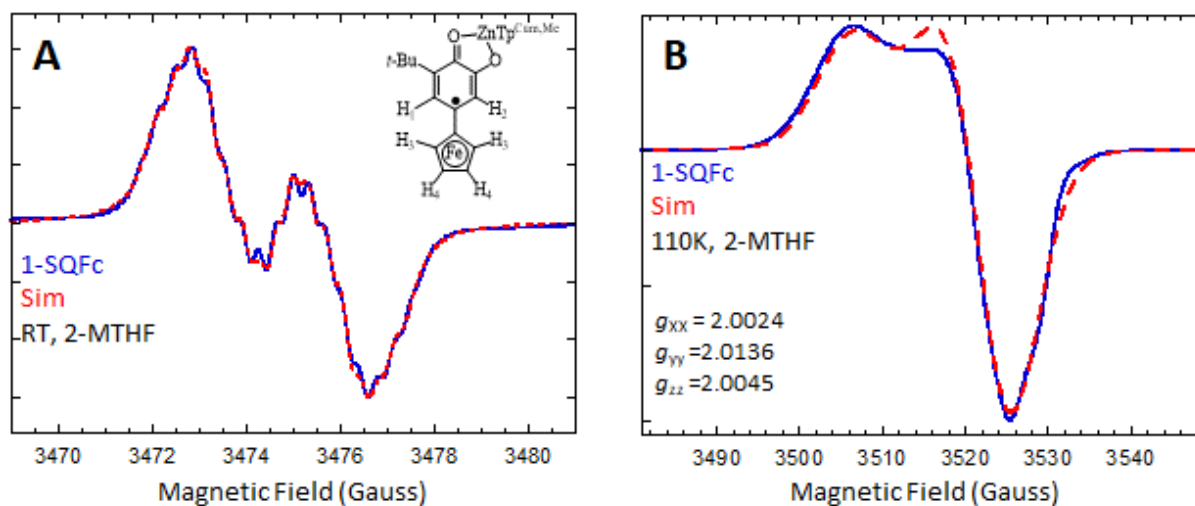


Figure V-33. A) Room temperature isotropic spectrum of **1-SQFc** in 2-MTHF. B) 110K powder spectrum of **1-SQFc**. Simulations were executed using *EasySpin*.TM

inequivalent protons on the SQ ring and the two sets of two equivalent proton hyperfine coupling constants; a_{H3} and a_{H4} , correspond to the two sets of equivalent protons on the one Cp ring which indicates delocalization of the radical into the π -system of the Cp ring. Figure V-33B shows the powder spectrum of **1-SQFc** in 2-MTHF at 110K and the g -tensors determined by simulation with *EasySpin* are $g_{xx} = 2.0024$, $g_{yy} = 2.0136$, $g_{zz} = 2.0045$.

Attempts to collect powder spectra for **1,3-SQ₂Fc** and **1,1'-SQ₂Fc** were unsuccessful. HRMS analysis as well as the discussed bond lengths (Table V-4) for X-ray analysis indicate that **1,3-SQ₂Fc** and **1,1'-SQ₂Fc** are the correct compounds. Furthermore, if the compounds do not contain SQ, there are several options for the identity of the material which would be indicated by IR spectroscopy: 1) mono-protonated, complexed Cat, but unoxidized would exhibit an O-H stretch and would be a salt and should exhibit poor solubility in organic solvents 2) it could be the quinone which would have strong C=O stretches in the 1650-1670 cm⁻¹ region or 3) it could be the muconic anhydride which would also have C=O stretches around 1800 cm⁻¹. The IR spectra of **1-SQFc**, **1,1'-SQ₂Fc** and **1,3-SQ₂Fc** are shown in Figure V-34. All three molecules look very similar, which they should as they should contain the exact same functional groups just with different placement. Most importantly, all three compounds display a B-H stretch at *ca.* 2550 cm⁻¹ as indicated by the black dashed line. To refute the possibilities that **1,3-SQ₂Fc** and

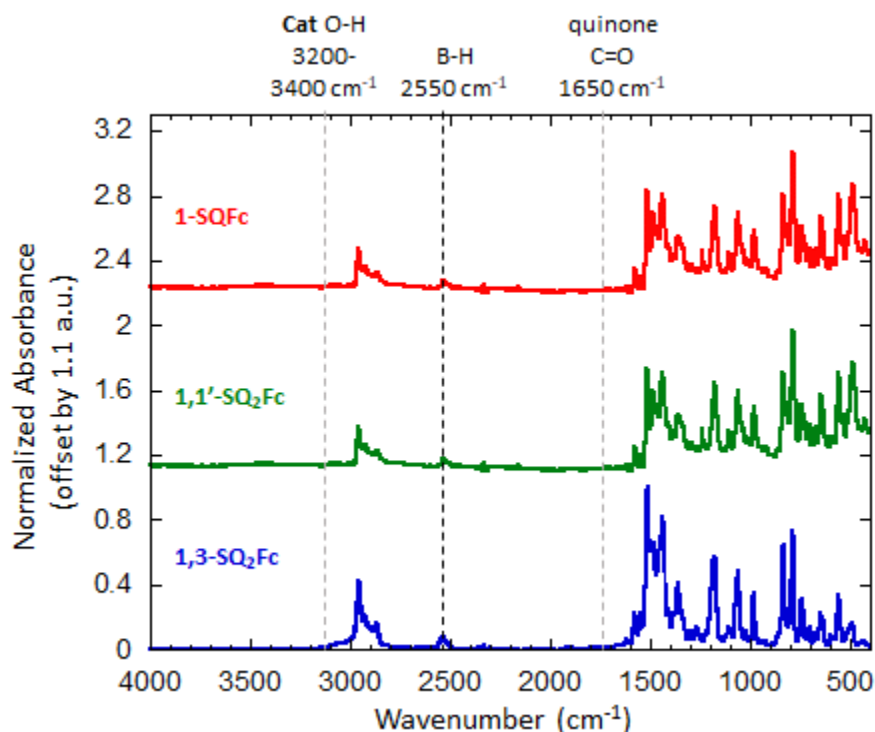


Figure V-34. IR spectra of **1-SQFc**, **1,1'-SQ₂Fc** and **1,3-SQ₂Fc**.

1,1'-SQ₂Fc may not contain SQs, first of all they have very good solubility in chlorinated and aromatic organic solvents and poor solubility in polar solvents (alcohols and MeCN) as well as aliphatic organic solvents, just like all other SQTp^{Cum,Me}-containing molecules; thus indicating they are probably not salts. In terms of the IR spectra there is not sign of a Cat O-H stretch in the 3200-3400 cm⁻¹ region (marked by one of the dashed gray lines). In the absence of hydrogen bonding solvents, free catechol O-H stretches are easily seen sharp peaks and for a complexed, protonated Cat, it is more resistant to broadening due to hydrogen bonding by virtue of the sterically-inhibiting [Tp^{Cum,Me}] ligand. To dismiss the quinone or muconic anhydride arguments, the quinone stretching frequency is marked on the IR spectra by the other dashed gray line at 1650 cm⁻¹ and from there to the B-H stretch at 2550 cm⁻¹ the baseline is relatively flat indicating no other stretches in between. The C=O stretches are very intense and even a small amount of quinone or anhydride would display a detectable band in those regions. It is possible that the exchange coupling through **1,3-SQ₂Fc** and **1,1'-SQ₂Fc** are much more negative in solution at the experimental temperatures and that the triplet states were not thermally populated at 110 K.

Electronic Absorption Spectroscopy. The absorption spectra for **1-SQFc**, **1,1'-SQ₂Fc** and **1,3-SQ₂Fc** are shown in Figure V-35A. The spectra for all three compounds have similar features; however the molar absorptivity for **1,1'-SQ₂Fc** and **1,3-SQ₂Fc** are nearly double that of **1-SQFc**. **1,1'-SQ₂Fc** is essentially a “doubled-up” spectrum of **1-SQFc** where it emulates most of the curvature in the monoradical spectrum particularly with the broad band centered at 10000 cm⁻¹ which trails off into the near-IR. **1,3-SQ₂Fc** has some spectral features that are more

different from **1-SQFc** than **1,1'-SQ₂Fc**, such as the area around that band at 10000 cm⁻¹ which is not as broad in the 13000-14000 cm⁻¹ region. This band is suspected to be a Fc → SQ based charge transfer band as indicated by Figure V-35B where it can be seen that when changing from a nonpolar solvent (toluene) to a polar solvent (DMSO) shifts the absorption band to lower energy by nearly 890 cm⁻¹. Neither the band centered around 17500 cm⁻¹ nor the band around 26000 cm⁻¹ are ferrocene-only bands as the only bands in this region for ferrocene are at 22700 cm⁻¹ and 30000 cm⁻¹ with extinction coefficients of 95 M⁻¹ cm⁻¹ and 54 M⁻¹ cm⁻¹, respectively (Figure V-28A *inset*). These are several orders of magnitude less than any of the bands observed

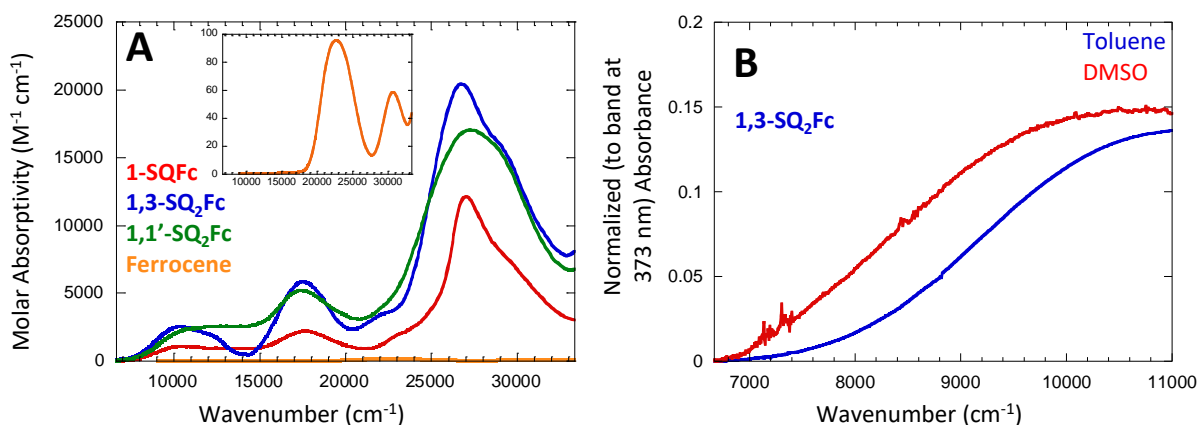


Figure V-35. Electronic absorption spectra of (A) **1-SQFc**, **1,3-SQ₂Fc** and **1,1'-SQ₂Fc**. (B) comparison of **1,3-SQ₂Fc** spectral feature at 10000 cm⁻¹ in DMSO and toluene .

in **1-SQFc**, **1,1'-SQ₂Fc** or **1,3-SQ₂Fc**; thus indicating the presence of strong SQ-Fc electronic coupling.

Magnetic Susceptibility. To determine the sign and magnitude of intramolecular magnetic exchange coupling between the two SQ rings through ferrocene, magnetic susceptibility measurements were performed on a SQUID magnetometer. Saturation magnetization experiments at 2K did not give $M_{\text{sat}} = 1.7$ Bohr magnetons, consistent with a singlet ground state (antiferromagnetic coupling of SQ spins). Paramagnetic susceptibility (χ_{para}) data measured between 10 and 300 K with an applied magnetic field of 0.7 T are shown in Figure V-36. Fitting

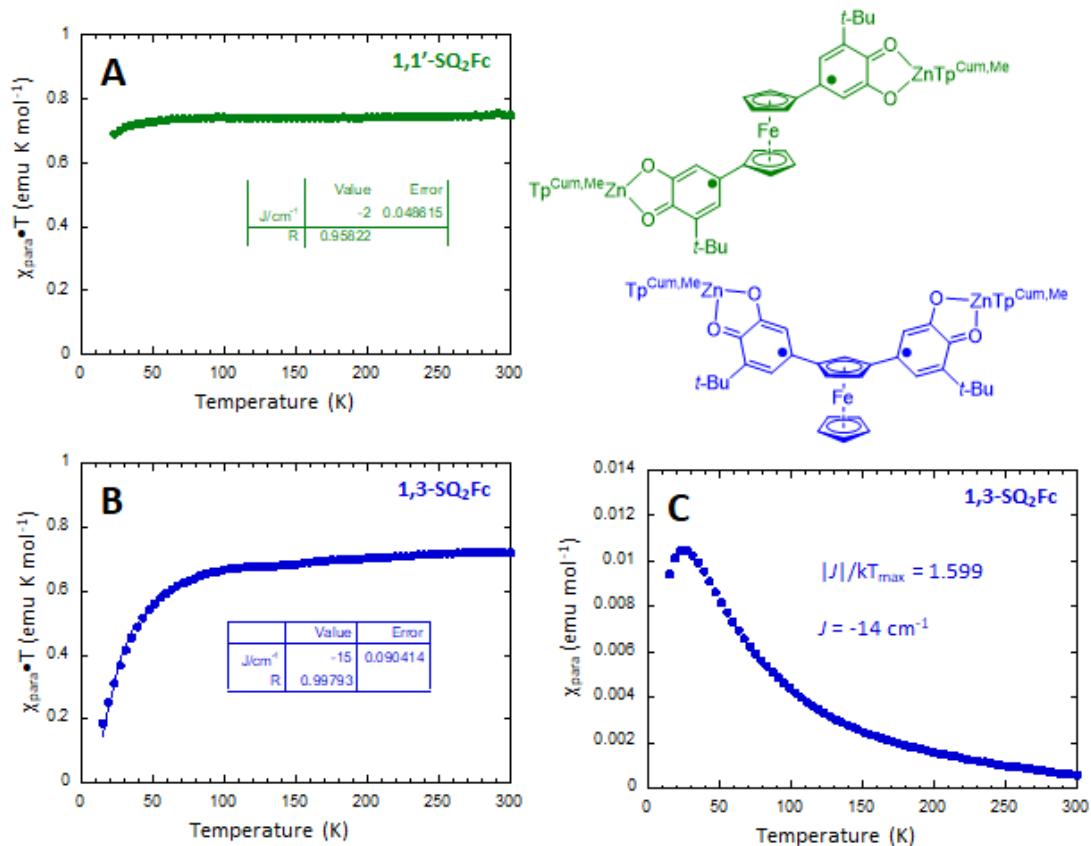


Figure V-36. Plots of paramagnetic susceptibility-temperature product ($\chi_{\text{para}} \cdot T$) vs. temperature for a crystalline sample of (A) $1,1'\text{-SQ}_2\text{Fc}$ and (B) $1,3\text{-SQ}_2\text{Fc}$. fit to the experimental $\chi_{\text{para}} \cdot T$ data gives an antiferromagnetic exchange parameter, $J = -2 \text{ cm}^{-1}$ and $J = -15 \text{ cm}^{-1}$, respectively indicating a singlet ground state ($\mathcal{H} = -2J\hat{S}_1 \cdot \hat{S}_2$). C) Plot of paramagnetic susceptibility- (χ_{para}) vs. temperature for $1,3\text{-SQ}_2\text{Fc}$ with $J = -14 \text{ cm}^{-1}$ by the mathematical relation between J and the temperature at which the magnetization is maximum (T_{max}).

the plot of $\chi_{\text{para}} \cdot T$ vs. T (Figure V-36A and B) resulted in an exchange coupling constant, $J = -15 \text{ cm}^{-1}$ for $1,3\text{-SQ}_2\text{Fc}$ and $J = -2 \text{ cm}^{-1}$ for $1,1'\text{-SQ}_2\text{Fc}$ ($\mathcal{H} = -2J\hat{S}_1 \cdot \hat{S}_2$). The negative J confirms a singlet ground state, consistent with the saturation plots. Furthermore, a plot of χ_{para} vs. T for an antiferromagnetic J reveals a maximum where the magnetization peaks and then begins to decrease. The temperature where the magnetization is at its maximum (T_{max}) can be related to the exchange coupling constant by the simple relation shown in Figure V-36C which in this case, gives $J = -14 \text{ cm}^{-1}$, consistent with the $\chi_{\text{para}} \cdot T$ vs. T plot for for $1,3\text{-SQ}_2\text{Fc}$ giving $J = -15 \text{ cm}^{-1}$.

These antiferromagnetic J values for **1,3-SQ₂Fc** and **1,1'-SQ₂Fc** should not be confused with the results that were obtained by Koivisto et al. who reported the synthesis of a 1,1'-bis(verdazyl)ferrocene with a large antiferromagnetic coupling because that antiferromagnetic coupling was due to the formation of a through-space dimerization of the stacked verdazyl radicals in the crystal structure.⁶⁸

Electrochemistry. SQ and ferrocene compounds are redox active and Figure V-37 shows the CV of **1-SQFc**. As expected, and as can be seen there are three distinct waves that correspond to the Cat/SQ, Fc/Fc⁺ and SQ/BQ couples which appear at *ca.* 0.9, 0.0 and 0.4 V, respectively. All three waves are highly reversible given the relatively equal intensities of both the oxidation and reduction sweeps. The reversibility of the Cat/SQ and Fc/Fc⁺ is not surprising.

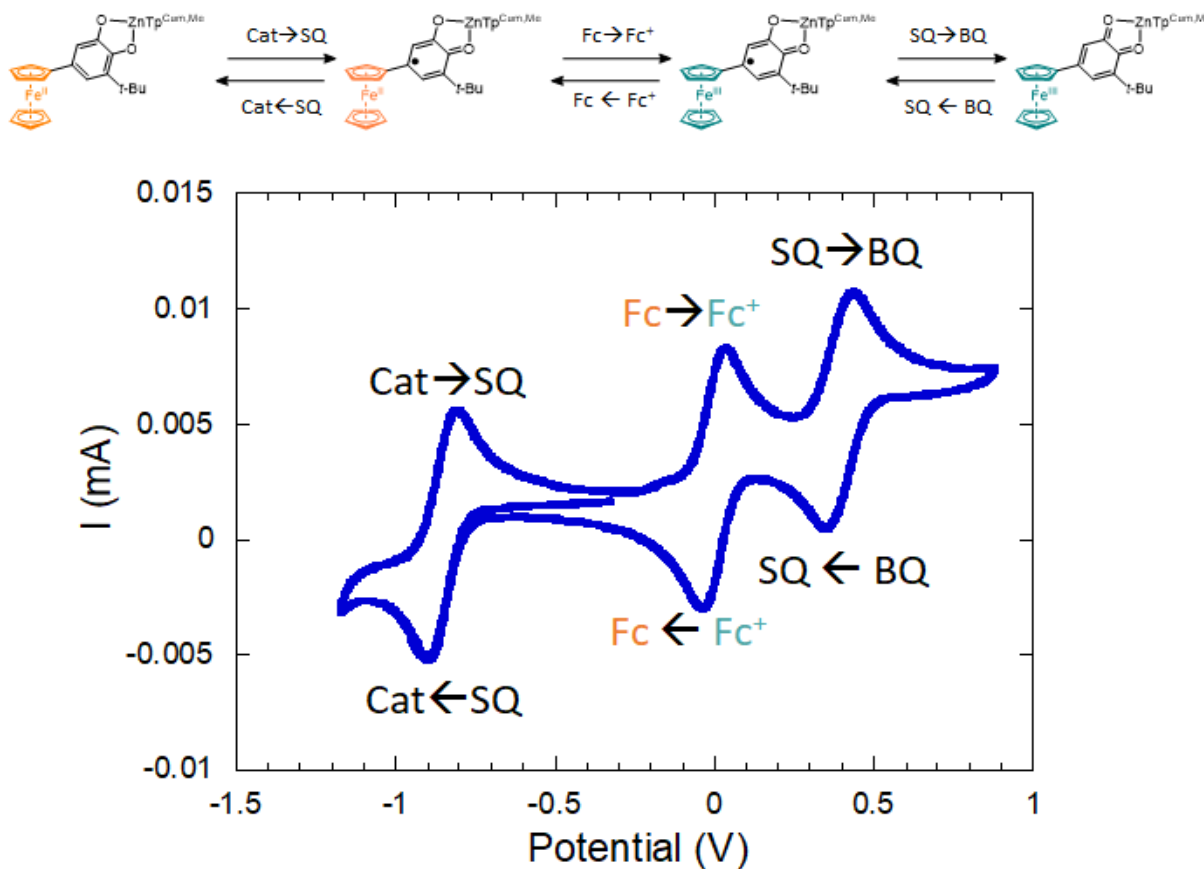


Figure V-37. Cyclic voltammogram of **1-SQFc** in MeCN with 0.1 M Bu₄NPF₆.

Fc/Fc⁺ is known to be highly reversible and electrochemistry data of **SQTp^{Cum,Me}**, **SQ-NN** and **pSQ-Ph-NN** display reversible Cat/SQ couples and the latter two display irreversible NN reduction waves.⁶⁹ However, the SQ/BQ couples of **SQ-NN** and **pSQ-Ph-NN** are less reversible in that their oxidation waves are of greater intensity than their reduction waves probably due to the BQ being poor ligands and the metal complex falls apart.⁶⁹ However, **1-SQFc**'s SQ/BQ couple is reversible indicating the **1-BQFc** is a better ligand.

The stronger the interaction between electroactive species connected by a bridge, the greater the redox splitting of the respective redox-active constituents. Since, in the symmetric SQ biradicals both redox active species are SQ, there should be two SQ waves for each couple. The stronger the interaction between the SQ radicals through the bridge, the greater the magnitude of the splitting. Figure V-38 shows the results of CVs acquired for several symmetric SQ biradicals. At the bottom of the series there are the **1-SQFc** CV shown in Figure V-37 and its precursor, **1-MOM₂CatFc** which should and does only show the Fc/Fc⁺ couple. Alongside this monoradical

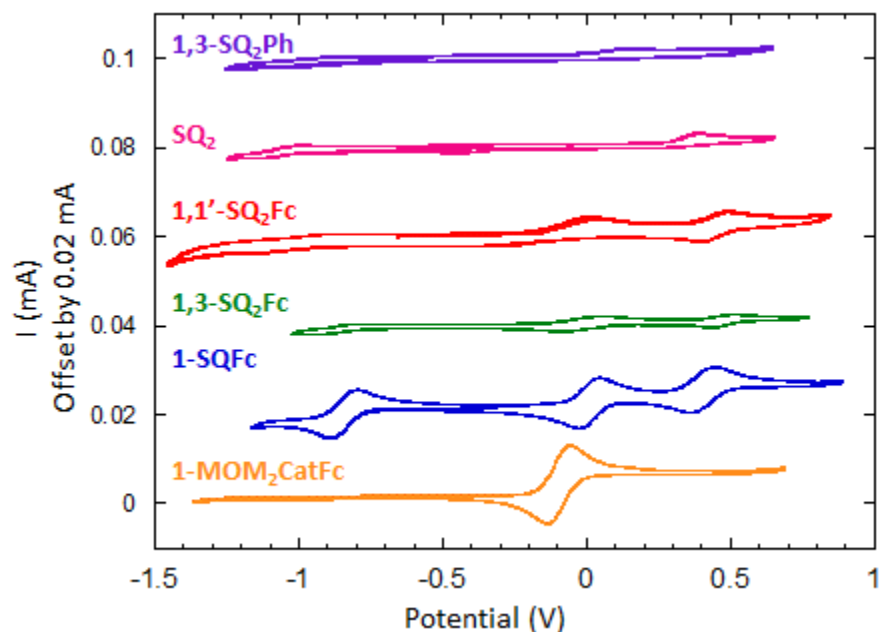


Figure V-38. Cyclic voltammogram of **1,3-SQ₂Ph**, **SQ₂**, **1,3-SQ₂Fc**, **1,1'-SQ₂Fc**, **1-SQFc** and **1-MOM₂CatFc** in MeCN with 0.1 M Bu₄NPF₆.

is shown the biradicals: **1,3-SQ₂Fc**, **1,1'-SQ₂Fc**, **SQ₂** and **1,3-SQ₂Ph**. Going up the series, the data becomes progressively worse. Some of the Fc/Fc⁺ couples for **1,3-SQ₂Fc** and **1,1'-SQ₂Fc** are visible, but the Cat/SQ and SQ/BQ couples are almost non-existent. They become even more diminished in **SQ₂** and **1,3-SQ₂Ph** and increasing the concentration of the biradicals did not improve the data.

The explanation for the well-behaved CV data from **1-SQFc** vs. the poor resolution and irreversible waves in the biradicals is illustrated in Figure V-39 where the “spacefill” crystal

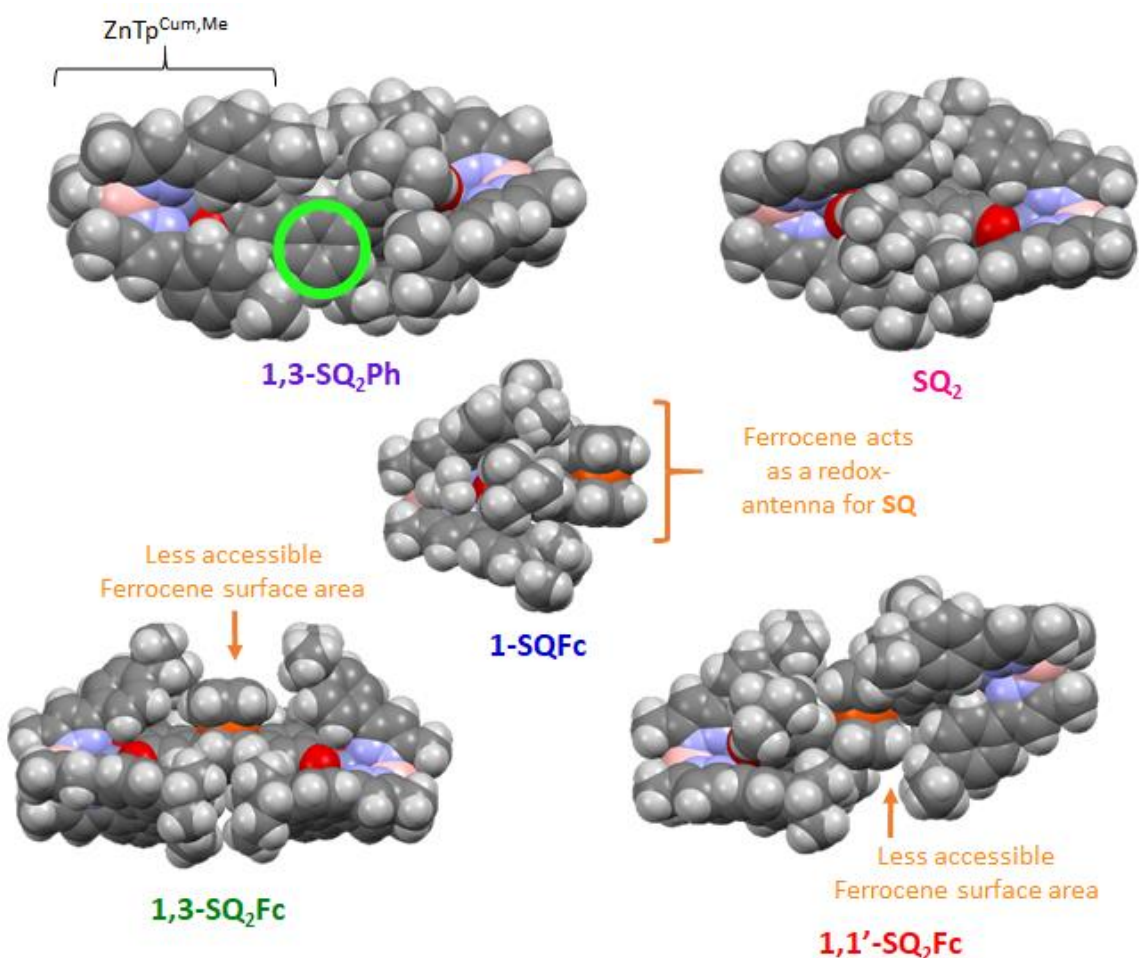


Figure V-39. Spacefilling models from the crystal structures of **1,3-SQ₂Ph**, **SQ₂**, **1,3-SQ₂Fc**, **1,1'-SQ₂Fc**, **SQ₂**, and **1-SQFc**. The $(\text{ZnTp}^{\text{Cum,Me}})^+$ ligands for each molecule are displayed horizontally. Red atoms are the oxygen atoms of the SQ. The green circle shows the six-carbon atoms of the phenyl ring bridge from **1,3-SQ₂Ph**.

structures for **1,3-SQ₂Ph**, **SQ₂**, **1,3-SQ₂Fc**, **1,1'-SQ₂Fc**, **SQ₂**, and **1-SQFc** are shown. We use the [Tp^{Cum,Me}]⁻ ligand because it provides steric bulk to insulate our biradicals from each other during magnetometry experiments; however, in the case of electrochemistry when the redox active species must get close enough to the electrode surface in order to transfer electrons, this results in slow heterogeneous electron transfer kinetics.⁷⁰ In **1,3-SQ₂Ph** and **SQ₂** the only redox active species are the SQ and the [Tp^{Cum,Me}]⁻ ligand shields almost all the surface area of the SQ. **1,3-SQ₂Ph** has most of the phenyl bridge also shielded as indicated by the green circle, outlining the six-carbon atoms of the phenyl rings. For **1-SQFc**, while the [Tp^{Cum,Me}]⁻ ligand still shields the SQ, the ferrocene sticks out the other end of the [Tp^{Cum,Me}]⁻ ligand exposing the iron and both Cp rings. The redox active ferrocene exhibits strong reversible oxidation/reduction waves in the **1-SQFc** compound, but **1-SQFc** also exhibits strong reversible oxidation/reduction waves for both Cat/SQ and SQ/BQ waves. This seems to indicate that having some exposed portion of either the bridge or having a redox-active bridge facilitates the electron transfer to and from the SQ. In the instances of **1,3-SQ₂Fc** and **1,1'-SQ₂Fc** adding the second [Tp^{Cum,Me}]⁻ ligand on the other side of the ferrocene (the steric bulk ensures it for **1,1'-SQ₂Fc**) significantly reduces the accessible ferrocene surface area. As indicated by the orange arrows in both molecules only one or a fraction of the Cp rings are now accessible for interaction with the electrodes for electron transfer, which is reflected in the reduced currents displayed for the Fc/Fc⁺ couples just below 0.0 V in Figure V-38 and **1,1'-SQ₂Fc** even shows irreversibility for the reduction of Fc⁺.

To still gain insight into the interaction between the two SQ radicals, instead the symmetrically substituted BQ of the bridges were synthesized by Ag₂O oxidation of the corresponding Cat compounds and differential pulsed voltammograms (DPV) were collected to observe the redox splitting of the BQ/SQ couple (Figure V-40). The BQ version of **SQ₂** was too

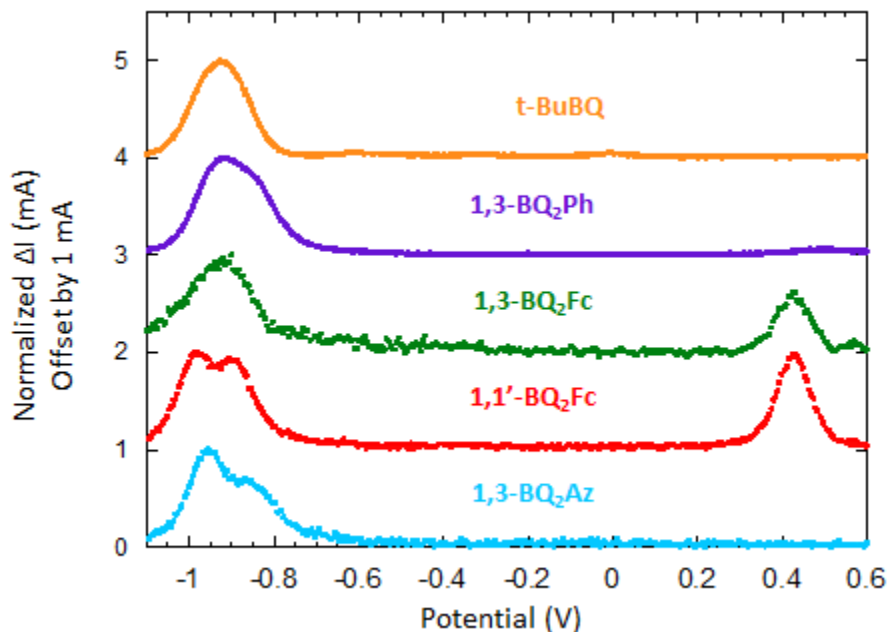


Figure V-40. Differential pulsed voltammograms of *t*-BuBQ, 1,3-BQ₂Ph, 1,3-BQ₂Fc, 1,1'-BQ₂Fc and 1,3-BQ₂Az collected in MeCN with 0.1 M Bu₄NPF₆.

unstable to collect data on, probably due to having a very electron deficient molecule and the ability of quinones to undergo Diels-Alder reactions with each other and susceptibility to nucleophilic addition reactions. Instead 3,5-di-*tert*-butylquinone (*t*-BuBQ) was used as a model compound. Only the SQ/BQ waves are observed for these molecules, further reduction to the Cat compounds requires very negative potentials and because the free SQ which are generated, are not very stable; anions counterbalanced by a non-coordinating cation (Bu₄N⁺). For the series of 1,3-BQ₂Ph, 1,3-BQ₂Fc, 1,1'-BQ₂Fc and 1,3-BQ₂Az all display DPV waves associated with the SQ/BQ couple at approximately -0.9 V with various degrees of redox splitting. 1,1'-BQ₂Fc and 1,3-BQ₂Az seem to display the greatest splitting while 1,3-BQ₂Fc displays the least. 1,3-BQ₂Ph displays some splitting due to the broadened wave relative to *t*-BuBQ. Both 1,1'-BQ₂Fc and 1,3-BQ₂Fc display the Fc/Fc⁺ DPV wave as well at 0.4 V, which has shifted by nearly 0.4 V relative to the respective SQ biradicals. This is probably a consequence of moving the BQ/SQ couple to

lower potential than the Fc/Fc⁺ couple in the BQ relative to the SQ compounds (0.4 V vs. -0.9 V).

V.3.5. Conclusions about Ferrocene.

1,3-SQ₂Fc is unlike both phenylene and azulene counterparts. From magnetometry there it exhibits an antiferromagnetic exchange coupling constant $J = -15 \text{ cm}^{-1}$, whereas the phenylene derivatives⁴⁶ and azulene exhibits ferromagnetic J -values from +35 to +50 cm^{-1} . **1,1'-SQ₂Fc** has no phenylene or azulene counterpart and must be compared to other 1,1'-ferrocene biradicals. 1,1'-bis(verdazyl)ferrocene is not very good comparisons as mentioned earlier because of the strong antiferromagnetic through-space interaction of the verdazyl radicals as shown in the crystal structure.⁶⁸ 1,1'-bis(nitronylnitroxide)ferrocene and 1,1'-bis(polychlorotriphenylmethyl)ferrocene biradical are better comparisons because both of these compounds were crystallized so that the radicals are approximately 180° apart by Cp rotation.^{60,62} **1,1'-SQ₂Fc** with a $J = -2 \text{ cm}^{-1}$ is in the same sign and magnitude as 1,1'-bis(nitronylnitroxide)ferrocene with a reported $J = -4 \text{ cm}^{-1}$ and 1,1'-bis(polychlorotriphenylmethyl)ferrocene with a reported $J = +7 \text{ cm}^{-1}$.^{60,62} **1,1'-SQ₂Fc** which should have more delocalization than 1,1'-bis(nitronylnitroxide)ferrocene and so it is unclear why the coupling is weaker for **1,1'-SQ₂Fc**. Ultimately, the coupling from one Cp ring to the other is not very strong in either direction either by competing pathways or just weak coupling.

A complicating factor for analyzing the exchange pathway through ferrocene is that there is the iron atom present which has five d-orbitals; each of which provides some contribution to the overall coupling mechanism in addition to the coupling through the Cp π system. The electronic absorption spectra for **1,3-SQ₂Fc**, **1,1'-SQ₂Fc**, **1-SQFc** and ferrocene are not very helpful for providing an apparent electronic transition for the coupling mechanism like

they are for **ZnSQ**, **SQ-NN**, **1,4-SQ-Ph-NN** and **Ph-NN**.^{27,35} What is seen is that all three semiquinone-ferrocene compounds seem to have strong interactions between the semiquinones and the ferrocene as indicated by the appearance of several strong bands at 10500, 17500 and 27000 cm^{-1} which have extinction coefficients an order of magnitude stronger than semiquinones for the band at 10500 cm^{-1} and several orders of magnitude stronger than any ferrocene bands for those at 17500 and 27000 cm^{-1} .

V.4. Nonalternant Hydrocarbon Experimental

V.4.1. Azulene Experimental.

Azulene-1-carbaldehyde. Prepared according to literature precedent:⁷¹ POCl_3 0.370 mL (3.97 mmol) was added dropwise to a stirring solution of DMF (1.5 mL, 20 mmol) and azulene (0.500 g, 3.90 mmol) of in 70 mL of CH_2Cl_2 at 0 °C. The reaction was stirred at room temperature for 20 h, overnight, during which the solution turned from dark blue to dark red. The reaction was added to a stirring solution of 30 mL of 2M NaOH, stirred for 5 minutes, and then transferred to a separatory funnel and washed with brine. The product was extracted with 20 mL of CH_2Cl_2 , dried with Na_2SO_4 , and concentrated under reduced pressure. The product was purified with a pad of silica by eluting first with 100% hexanes to collect remaining starting material and then following with 25% EtOAc/hexanes and collecting the magenta-colored band corresponding to the product, which was concentrated to give 0.494 g (81%) of the product as a dark magenta-colored solid. ^1H NMR (400MHz, CDCl_3) δ = 10.39 (s, 1 H), 9.63 (d, J = 9.8 Hz, 1 H), 8.55 (d, J = 9.8 Hz, 1 H), 8.31 (d, J = 3.9 Hz, 1 H), 7.90 (dd, J = 9.8, 9.8 Hz, 1 H), 7.67 (dd, J = 9.8, 9.8 Hz, 1 H), 7.57 (dd, J = 9.8, 9.8 Hz, 1 H), 7.37 (d, J = 3.9 Hz, 1 H). ^{13}C NMR (101MHz, CDCl_3) δ = 186.4, 145.9, 141.7, 140.2, 139.6, 138.9, 137.3, 129.3, 128.1, 125.8, 119.0, 118.9.

3-Bromoazulene-1-carbaldehyde. Az-CHO (0.493 g, 3.16 mmol) of was added to a 50 mL round-bottom flask with 40 mL of CH₂Cl₂ and NBS (0.591 g, 3.31 mmol) of was added slowly. The reaction was stirred for 18 h at room temperature after which the solvent was removed under reduced pressure. Hexanes was added to the crude mixture and stirred for 5 minutes and then passed through a pad of celite. The filtrate was concentrated under reduced pressure to afford the the title compound as a dark purple solid (0.736 g, 99%). ¹H NMR (400MHz, CDCl₃) δ = 10.30 (s, 1 H), 9.58 (d, *J* = 9.8 Hz, 1 H), 8.58 (d, *J* = 9.8 Hz, 1 H), 8.25 (s, 1 H), 7.94 (dd, *J* = 9.8, 9.8 Hz, 1 H), 7.70 (d, *J* = 9.8 Hz, 1 H), 7.65 (d, *J* = 9.8 Hz, 1 H). ¹³C NMR (101MHz, CDCl₃) δ = 185.2, 142.0, 141.0, 140.8, 139.2, 138.0, 137.6, 129.9, 128.5, 124.5, 105.9. HRMS (APCI+) *m/z*: [M + H]⁺ Calculated for C₁₁H₇BrO 234.97530; Found 234.97511.

3-(3-(*tert*-Butyl)-4,5-bis(methoxymethoxy)phenyl)azulene-1-carbaldehyde (MOM₂Cat-Az-CHO). A 50 mL round-bottom flask containing 3-bromoazulene-1-carbaldehyde (202 mg, 0.859 mmol), MOM₂CatBpin (327 mg, 0.860 mmol), Na₂CO₃ (228 mg, 2.15 mmol), Pd(PPh₃)₄ (10 mg, 0.009 mmol) and Bu₄NBr (28 mg, 0.087 mmol) of in 12 mL of toluene and 4 mL of H₂O, under nitrogen was fitted with a nitrogen-purged, water-cooled condenser and then heated to 80 °C for 20 h. After which it was transferred to a separatory funnel, diluted with 10 mL of EtOAc and washed 2 times each with 10 mL of brine. The organic layer was separated, dried with Na₂SO₄ and concentrated under reduced pressure. The crude material was purified by deactivate silica gel flash chromatography with 2 to 15% EtOAc/hex to afford 317 mg (91%) of the title compound as a dark solid. ¹H NMR (400MHz, CDCl₃) δ = 10.45 (s, 1 H), 9.62 (d, *J* = 9.8 Hz, 1 H), 8.72 (d, *J* = 9.8 Hz, 1 H), 8.36 (s, 1 H), 7.88 (dd, *J* = 9.8, 9.8 Hz, 3 H), 7.63 (dd, *J* = 9.8, 9.8 Hz, 1 H), 7.54 (dd, *J* = 9.8, 9.8 Hz, 1 H), 7.28 (d, *J* = 2.3 Hz, 1 H), 7.24 (d, *J* = 2.3 Hz, 1 H), 5.32 (s, 2 H), 5.27 (s, 2 H), 3.73 (s, 3 H), 3.56 (s, 3 H), 1.51 (s, 9 H). ¹³C NMR (101MHz, CDCl₃) δ =

186.3, 150.2, 145.2, 143.6, 141.4, 141.3, 141.1, 140.3, 137.7, 137.5, 132.4, 130.7, 129.3, 128.3, 124.5, 121.8, 115.8, 99.0, 95.3, 57.5, 56.2, 35.2, 30.5. HRMS (APCI+) m/z : $[M + H]^+$ Calculated for $C_{25}H_{28}O_5$ 409.20095; Found 409.20112.

3-(3-(*tert*-Butyl)-4,5-dihydroxyphenyl)azulene-1-carbaldehyde (Cat-Az-CHO). Aqueous HCl (12M, 2 mL) were added to a solution of 3-(3-(*tert*-butyl)-4,5-bis(methoxymethoxy)phenyl)azulene-1-carbaldehyde (130 mg, 0.318 mmol) of in 2 mL of MeOH and the reaction was stirred under nitrogen in the dark for 20 h. Reaction was then poured into ca. 250 mL of stirring water, stirred for 5 min and then filtered. The dark green solid was collected with Et_2O , dried with Na_2SO_4 and concentrated under reduced pressure to give the title compound (100 mg, 98%) of as a dark green solid. 1H NMR (400MHz, $CDCl_3$) δ = 10.40 (s, 1 H), 9.55 (d, J = 9.8 Hz, 1 H), 8.67 (d, J = 9.8 Hz, 1 H), 8.28 (s, 1 H), 7.83 (t, J = 9.6 Hz, 1 H), 7.58 (t, J = 9.6 Hz, 1 H), 7.47 (t, J = 9.6 Hz, 1 H), 7.05 (d, J = 1.6 Hz, 1 H), 6.96 (d, J = 1.6 Hz, 1 H), 1.47 (s, 9 H). ^{13}C NMR (101MHz, $DMSO-d_6$) δ = 186.4, 145.4, 143.6, 141.3, 140.7, 140.2, 140.1, 138.0, 137.0, 136.1, 132.7, 129.4, 128.7, 125.2, 124.2, 118.3, 113.9, 34.5, 29.4.

1,3-Dibromoazulene (1,3- Br_2 Az). Prepared according to literature procedure.⁷² NBS (139 mg, 0.78 mmol) was added to a 25 mL round-bottom flask containing a solution of azulene (50 mg, 0.39 mmol) of in ca. 10 mL of CH_2Cl_2 under nitrogen at 0 °C. The reaction was stirred for 3 h while warming to room temperature. The reaction was concentrated under reduced pressure, then the residue was redissolved in hexanes and passed through a pad of celite, then concentrated under reduced pressure to afford the title compound (105 mg, 94%) as a dark blue solid.

1,3-Diiodoazulene (1,3- I_2 Az). Prepared according to literature procedure.⁷³ *N*-iodosuccinimide (0.723 g, 3.21 mmol) was added to a 100 mL round-bottom flask containing a solution of

azulene (0.196 g, 1.53 mmol) of in ca. 50 mL of CH₂Cl₂ under nitrogen at 0 °C. The reaction was stirred for 3 h while warming to room temperature. The reaction was concentrated under reduced pressure, then the residue was redissolved in hexanes and passed through a pad of celite, then concentrated under reduced pressure to afford the title compound (0.506g, 87%) as a dark blue solid. ¹H NMR (400MHz, CDCl₃) δ = 8.21 (d, *J* = 9.4 Hz, 2 H), 8.02 (s, 1 H), 7.72 (t, *J* = 9.8 Hz, 1 H), 7.35 (dd, *J* = 9.8, 9.4 Hz, 2 H).

1,3-Bis(3-(*tert*-butyl)-4,5-bis(methoxymethoxy)phenyl)azulene (1,3-(MOM₂Cat)₂Az). 1,3-dibromoazulene (112 mg, 0.392 mmol) in 10 mL of argon-purged THF was cannula transferred into a 50 mL round-bottom flask, equipped with magnetic stir bar and a solution of MOM₂CatBpin (298 mg, 0.784 mmol), Pd(PPh₃)₄ (9mg, 8 μmol) and Cs₂CO₃ (516 mg, 1.58 mmol) in 5 mL each of argon-purged THF and H₂O, preheated to 55 °C. A nitrogen-purged reflux condenser was attached and the mixture was stirred at this temperature for 18 h. After cooling to room temperature, the reaction was transferred to a separatory funnel, diluted with Et₂O and washed with brine. The organic layer was separated, dried with MgSO₄ and concentrated under reduced pressure. The product was purified by silica gel (deactivated with 1% Et₃N in eluent) chromatography with 10% EtOAc/hexanes to afford 235 mg (96%) of the title compound as a blue oil. ¹H NMR (400MHz, CDCl₃) δ = 8.51 (d, *J* = 9.4 Hz, 2 H), 8.07 (s, 1 H), 7.56 (t, *J* = 9.8 Hz, 1 H), 7.30 (d, *J* = 2.3 Hz, 2 H), 7.27 (d, *J* = 2.3 Hz, 2 H), 7.10 (dd, *J* = 9.8, 9.4 Hz, 2 H), 5.30 (s, 4 H), 5.25 (s, 4 H), 3.71 (s, 6 H), 3.54 (s, 6 H), 1.50 (s, 18 H). ¹³C NMR (101MHz, CDCl₃) δ = 150.2, 144.8, 143.5, 138.9, 137.0, 136.4, 136.2, 132.0, 130.4, 123.2, 122.2, 116.2, 99.1, 95.5, 57.6, 56.3, 35.3, 30.6. HRMS (APCI+) *m/z*: [M + H]⁺ Calculated for C₃₉H₄₉O₈ 633.3427; Found 633.3429.

1,3-SQ₂Az. A solution of **1,3-(MOM₂Cat)₂Az** (75 mg, 0.12 mmol) in 5 mL of MeOH and 0.5 mL of 12 M HCl was stirred for 12 h at room temperature. The mixture was transferred to a separatory funnel, diluted with Et₂O and washed with brine. The organic layer was separated, dried with Na₂SO₄ and concentrated under reduced pressure. The crude product was carried into the next reaction without further purification, where KOH (14 mg, 0.25 mmol) and Zn(OH)Tp^{Cum,Me} (164 mg, 0.237 mmol) were combined with it in a 50 mL round-bottom flask and purge-pumped three times; backfilling with nitrogen. 20 mL of 1:1 deoxygenated, anhydrous MeOH:CH₂Cl₂ solution was added and the contents were stirred for 1.5 h under nitrogen, then opened and exposed to air for 18 h. The reaction solution was concentrated under reduced pressure leaving ca. 5 mL of MeOH. The mixture was then cooled and filtered through a Büchner funnel and the precipitate was washed with cold MeOH and dried to give 69 mg (34%) of the **1,3-SQ₂Az** as a red-violet solid. X-ray quality crystals were grown by slow evaporation of a mixture of minimal CH₂Cl₂ in MeOH. IR (solid) ν (cm⁻¹): 2533 (w, -BH). HRMS (APCI+) *m/z*: [M + H]⁺ Calculated for C₁₀₈H₁₂₁B₂N₁₂O₄Zn₂ 1797.8475; Found 1797.8394.

2-(3-Bromoazulen-1-yl)-4,4,5,5-tetramethylimidazolidine (Br-Az-BA). A solution of 19 mg (0.81 mmol) of **3-Bromoazulene-1-carbaldehyde**, 24 mg (0.13 mmol) of 2,3-dimethyl-2,3-diaminobutane hydrogen chloride and 12 mg (0.87 mmol) of K₂CO₃ in 2 mL of anhydrous MeOH was stirred under N₂ at room temperature for 16 h. The reaction was concentrated under reduced pressure, transferred to a separatory funnel, washed with brine and extracted with EtOAc. The organic layer was dried with Na₂SO₄ and concentrated under reduced pressure to afford 26 mg (96%) of the title compound as a dark blue solid. Deactivated silica TLC 66% EtOAc/hexanes: R_f = 0.59. ¹H NMR (400MHz, CDCl₃) δ = 8.68 (br. s., 1 H), 8.32 (d, *J* = 9.8 Hz,

1 H), 8.12 (s, 1 H), 7.64 (dd, $J = 9.8, 9.7$ Hz, 1 H), 7.31 - 7.18 (m, 2 H), 3.18 (br. s., 2 H), 1.26 (s, 12 H).

2-(3-bromoazulen-1-yl)-4,4,5,5-tetramethylimidazolidine-1,3-diol (Br-Az-BHA). 26 mg (0.078 mmol) of **2-(3-Bromoazulen-1-yl)-4,4,5,5-tetramethylimidazolidine** was dissolved in 10 mL of CH_2Cl_2 with 10 mL of saturated NaHCO_3 solution. The mixture was cooled to 0°C and 30 mg (0.17 mmol) of *m*-CPBA in 2 mL of CH_2Cl_2 was added dropwise. A color change from blue to green was observed. The reaction was stirred for 1 h after the addition was complete, then transferred to a separatory funnel, diluted with Et_2O and washed with brine. The organic layer was separated, dried with Na_2SO_4 and concentrated under reduced pressure to afford 28 mg of the crude product. This compound could not be successfully purified from impurities and side products.

1-Bromoazulene (Br-Az). Prepared according to literature procedure.⁷⁴ To a solution of azulene (154 mg, 1.20 mmol) in 30 mL of Et_2O at -78°C was added NBS (217 mg, 1.22 mmol) as a solid. The reaction was stirred for 15 min at -78°C and then warmed to room temperature and stirred overnight for 16 h. The reaction mixture was transferred to a separatory funnel and washed with 1 M NaOH, then brine. The organic layer was separated, dried with MgSO_4 and concentrated under reduced pressure to give a dark blue oil (244 mg, 99%), which was used without further purification.

1-(3-(*tert*-Butyl)-4,5-bis(methoxymethoxy)phenyl)azulene (Me₂Cat-Az). To a 50 mL round-bottom flask, equipped with magnetic stir bar, was added 1,3-diiodoazulene (162 mg, 0.782 mmol), Me₂CatBpin (252 mg, 0.787 mmol), Bu_4NBr (24 mg, 0.074 mmol) and Na_2CO_3 (165 mg, 1.56 mmol). The flask was purge-pumped 3 times and backfilled with nitrogen and transferred into the glovebox, where $\text{Pd}(\text{PPh}_3)_4$ (9 mg, 8 μmol) was added. Outside the glovebox, under

nitrogen, 8 mL and 4 mL of deoxygenated toluene and water were added, respectively. A nitrogen-purged reflux condenser was attached and the contents were heated to 85 °C for 16 h with stirring. The reaction was cooled to room temperature, transferred to a separatory funnel, washed with ca. 20 mL of brine and extracted with ca. 20 mL of ethyl acetate. The organic layer was separated, dried with Na₂SO₄ and concentrated under reduced pressure. The residue was purified by flash chromatography with 10% ethyl acetate/hexanes to give 160 mg (64%) of the product as a blue solid. ¹H NMR (400MHz, CDCl₃) δ = 8.55 (d, *J* = 9.8 Hz, 1 H), 8.34 (d, *J* = 9.4 Hz, 1 H), 8.01 (d, *J* = 3.5 Hz, 1 H), 7.59 (dd, *J* = 9.8, 9.8 Hz, 1 H), 7.43 (d, *J* = 3.5 Hz, 1 H), 7.31 - 7.25 (m, 2 H), 7.15 (dd, *J* = 9.8, 9.7 Hz, 1 H), 7.15 (dd, *J* = 9.8, 9.4 Hz, 1 H), 5.30 (s, 2 H), 5.25 (s, 2 H), 3.71 (s, 3 H), 3.55 (s, 3 H), 1.50 (s, 9 H). ¹³C NMR (101MHz, CDCl₃) δ = 150.1, 144.6, 143.3, 141.5, 138.0, 137.1, 136.9, 135.5, 135.0, 132.4, 131.2, 123.0, 122.8, 122.0, 117.2, 116.0, 99.0, 95.4, 57.4, 56.2, 35.2, 30.6.

1-(3-(*tert*-Butyl)-4,5-bis(methoxymethoxy)phenyl)-3-iodoazulene (MOM₂Cat-Az-I).

Method A; diiodoazulene Suzuki coupling:

A 50 mL round-bottom flask containing 1,3-diiodoazulene (581 mg, 1.53 mmol), MOM₂CatBpin (194 mg, 0.510 mmol) of, Na₂CO₃ (324 mg, 3.06 mmol), Pd(OAc)₂ (6 mg, 0.03 mmol) and Bu₄NBr (49 mg, 0.15 mmol) of in 12 mL of toluene and 4 mL of H₂O, under nitrogen was fitted with a nitrogen-purged, water-cooled condenser and then heated to 80 °C for 20 h. After which it was transferred to a separatory funnel, diluted with 10 mL of EtOAc and washed 2 times each with 10 mL of brine. The organic layer was separated, dried with Na₂SO₄ and concentrated under reduced pressure. The crude material was purified by deactivate silica gel

flash chromatography with 2 to 15% EtOAc/hex to afford the title compound (96 mg, 37%) as a dark blue-green oil. Overall yield from azulene is 32%.

Method B; bromoazulene Suzuki coupling then iodination:

A 25 mL round-bottom flask containing 1-bromoazulene (162 mg, 0.782 mmol), MOM₂CatBpin (297 mg, 0.781 mmol), Na₂CO₃ (165 mg, 1.56 mmol) and Pd(PPh₃)₄ (9 mg, 0.008 mmol) and Bu₄NBr (25 mg, 0.078 mmol) in 12 mL of toluene and 4 mL of H₂O, under nitrogen was fitted with a nitrogen-purged, water-cooled condenser and then heated to 80 °C for 20 h. After which it was transferred to a separatory funnel, diluted with 15 mL of Et₂O and washed 2 times each with 10 mL of brine. The organic layer was separated, dried with Na₂SO₄ and concentrated under reduced pressure. The crude material was purified by deactivated silica gel flash chromatography with 15% EtOAc/hexanes to afford 227 mg (0.597 mmol, 76%) of the un-iodinated compound as a dark blue oil. This compound was redissolved in 10 mL of MeOH with 210 mg (2.50 mmol) of NaHCO₃ and cooled to -78°C, under nitrogen. Then 139 mg (0.618 mmol) of *N*-iodosuccinimide was added as a solid. The reaction was stirred for 20 min at -78 °C, then warmed to room temperature over 1 h. The reaction was transferred to a separatory funnel, diluted with Et₂O, washed with 1 M NaOH and then brine. The organic layer was separated, dried with MgSO₄ and concentrated to give the title compound (299 mg, 0.590 mmol) as a blue-green oil. Overall yield from azulene is 74%. ¹H NMR (400MHz, CDCl₃) δ = 8.46 (d, *J* = 9.8 Hz, 1 H), 8.28 (d, *J* = 9.8 Hz, 1 H), 8.08 (s, 1 H), 7.65 (dd, *J* = 9.8, 9.7 Hz, 1 H), 7.33 - 7.16 (m, 3 H), 7.25 (d, *J* = 2.5 Hz, 1 H), 7.22 (d, *J* = 2.5 Hz, 1 H), 5.32 (s, 2 H), 5.27 (s, 2 H), 3.73 (s, 3 H), 3.57 (s, 3 H), 1.52 (s, 9 H). HRMS (APCI+) *m/z*: [M + H]⁺ Calculated for C₂₄H₂₇IO₄ 506.09485; Found 506.09515.

2-(3-(3-(*tert*-Butyl)-4,5-bis(methoxymethyl)phenyl)azulen-1-yl)-4,4,5,5-tetramethyl-4,5-dihydroimidazol-3-oxide-1-oxyl (MOM₂Cat-Az-NN). 1-(3-(*tert*-butyl)-4,5-

bis(methoxymethoxy)phenyl)-3-iodoazulene (10 mg, 0.020 mmol), **NNAuPPh₃** (19 mg, 0.030 mmol) and Pd(PPh₃)₄ (3 mg, 0.003 mmol) of were dissolved in ca. 5 mL of anhydrous, deoxygenated THF, under nitrogen. The flask was fitted with a water-cooled, nitrogen-purged reflux condenser and heated to 60 °C for 2 h. Basic alumina TLC with 50% EtOAc/hexanes as eluent confirmed completion. The reaction was concentrated under reduced pressure, then purified via basic alumina flash chromatography with 25% EtOAc/hexanes as eluent. The fractions containing product were concentrated to give the title compound (8 mg, 73%) of as a seafoam green residue.

4-(Azulen-1-yl)-2-(*tert*-butyl)phenol (HOPh-Az). To a pre-warmed to 55 °C solution of HOPhBpin (200 mg, 0.724 mmol), Pd(PPh₃)₄ (8 mg, 7 μmol) and Cs₂CO₃ (476 mg, 1.461 mmol) in ca. 20 mL of anhydrous, deoxygenated THF and 14 mL of H₂O was added a nitrogen-purged solution of **Br-Az** (150 mg, 0.724 mmol) in ca. 20 mL of THF via cannula. The flask was then fitted with a nitrogen-purged reflux condenser and stirred for 16 h. The reaction was cooled to room temperature then transferred to separatory funnel. The reaction was diluted with Et₂O and washed with brine. The organic layer was separated, dried with MgSO₄ and concentrated. The crude material was purified by silica chromatography with 10 to 30% CH₂Cl₂/hexanes as eluent. The product-containing fractions were combined and concentrated to afford the title compound in a 78% yield as a dark blue solid. ¹H NMR (400MHz, CDCl₃) δ = 8.51 (d, *J* = 9.8 Hz, 1 H), 8.33 (d, *J* = 9.4 Hz, 1 H), 7.99 (d, *J* = 3.9 Hz, 1 H), 7.57 (dd, *J* = 9.8, 9.8 Hz, 1 H), 7.53 (d, *J* = 1.9 Hz, 1 H), 7.43 (d, *J* = 3.9 Hz, 1 H), 7.33 (dd, *J* = 1.9, 8.0 Hz, 1 H), 7.12 (dd, *J* = 9.4, 9.8 Hz, 1 H), 6.82 (d, *J* = 8.0 Hz, 1 H), 4.79 (s, 1 H), 1.49 (s, 9 H). ¹³C NMR (101MHz, CDCl₃) δ =

153.1, 141.4, 138.0, 137.1, 136.3, 135.6, 135.0, 131.7, 129.8, 128.7, 128.6, 128.0, 122.8, 122.6, 117.2, 116.8, 34.7, 29.7. HRMS (APCI+) m/z: [M]⁺ Calculated for C₂₀H₂₀O 276.15087; Found 276.15097.

5-(Azulen-1-yl)-3-(tert-butyl)cyclohexa-3,5-diene-1,2-dione (BQ-Az). IBX (70 mg, 0.25 mmol) was added to a solution of **HOPh-Az** (62 mg, 0.22 mmol) in ca. 1 mL of DMF. The mixture was stirred for 2 h at room temperature, then transferred to a separatory funnel and extracted with 40 mL of CH₂Cl₂. The organic phase was washed twice with 50 mL of H₂O each time, then the organic phase was separated, dried with MgSO₄ and concentrated under reduced pressure. The product was purified by silica gel flash chromatography with 50% CH₂Cl₂/hexanes first, then 100% CH₂Cl₂ to elute the product. The fractions containing the product were concentrated under reduced pressure to afford the title compound (48 mg, 74%) as a dark violet solid. Which was taken directly into the following reaction.

3-(tert-Butyl)-5-(3-iodoazulen-1-yl)cyclohexa-3,5-diene-1,2-dione (BQ-Az-I). **BQ-Az** (48 mg, 0.17 mmol) was dissolved in ca. 30 mL of Et₂O and cooled to -78 °C. *N*-iodosuccinimide (44 mg, 0.20 mmol) was added and stirred for 20 min at -78 °C, then warmed to room temperature and stirred for 18 h. The reaction was transferred to a separatory funnel, washed with saturated NaHCO₃ solution, then brine, the organic layer was extracted, dried with MgSO₄ and concentrated under reduced pressure to afford the title compound (51 mg, 76%) as a dark violet solid.

5-(Azulen-1-yl)-3-(tert-butyl)-1,2-phenylene diacetate (Ac₂Cat-Az). IBX (144 mg, 0.514 mmol) was added to a solution of **HOPh-Az** (126 mg, 0.456 mmol) in ca. 3 mL of DMF. The mixture was stirred for 2 h at room temperature, then this solution was added dropwise via cannula to a stirring solution of 79 mg (0.74 mmol) of 10% Pd/C (101 mg, 0.500 mmol), Cs₂CO₃

(318 mg, 0.976 mmol) and Ac₂O (0.90 mL, 9.5 mmol) in 30 mL of CH₂Cl₂, which had H₂ bubbled through it for 30 min prior to addition and was under a H₂ atmosphere. More hydrogen gas was bubbled through the combined solution. After 1.5 h, TLC in 100% CH₂Cl₂ confirmed that the reaction was complete. Nitrogen was then bubbled through the solution for 30 min, then the solution was filtered through a pad of celite and washed with CH₂Cl₂. The filtrate was transferred to a separatory funnel where it was washed three times with 50 mL of water each time. The organic layer was separated, dried with MgSO₄ and concentrated under reduced pressure to afford a crude brown oil. The product was purified by a silica gel column, eluting with 50% CH₂Cl₂/hexanes to afford the title compound (60 mg, 39%) as a blue oil. ¹H NMR (400MHz, CDCl₃) δ = 8.58 (d, *J* = 9.8 Hz, 1 H), 8.37 (d, *J* = 9.8 Hz, 1 H), 8.01 (d, *J* = 3.5 Hz, 1 H), 7.62 (dd, *J* = 9.8, 9.8 Hz, 1 H), 7.51 (d, *J* = 2.3 Hz, 1 H), 7.44 (d, *J* = 3.5 Hz, 1 H), 7.35 (d, *J* = 2.3 Hz, 1 H), 7.21 (d, *J* = 9.8 Hz, 1 H), 7.17 (d, *J* = 9.8 Hz, 1 H), 2.40 (s, 3 H), 2.32 (s, 3 H), 1.43 (s, 9 H). ¹³C NMR (101MHz, CDCl₃) δ = 168.4, 168.2, 143.0, 142.8, 141.7, 139.4, 138.3, 137.3, 137.0, 135.5, 135.3, 135.2, 130.1, 125.8, 123.6, 123.2, 122.2, 117.4, 35.0, 30.3, 20.9, 20.8. HRMS (APCI+) *m/z*: [M+H]⁺ Calculated for C₂₄H₂₅O₄ 377.1753; Found 377.1752.

3-(*tert*-Butyl)-5-(3-iodoazulen-1-yl)-1,2-phenylene diacetate (Ac₂Cat-Az-I). Ac₂Cat-Az (48 mg, 0.17 mmol) of were dissolved in ca. 30 mL of Et₂O and cooled to -78 °C. *N*-iodosuccinimide (44 mg, 0.20 mmol) of was added and stirred for 20 min at -78 °C, then warmed to room temperature and stirred for 18 h. The reaction was transferred to a separatory funnel, washed with saturated NaHCO₃ solution, then brine, the organic layer was extracted, dried with MgSO₄ and concentrated under reduced pressure to afford 60 mg (70%) of the title compound as a green solid (70%). ¹H NMR (400MHz, CD₂Cl₂) δ = 8.48 (d, *J* = 9.8 Hz, 1 H), 8.30 (d, *J* = 9.8 Hz, 1 H), 8.08 (s, 1 H), 7.70 (dd, *J* = 9.8, 9.8 Hz, 1 H), 7.46 (d, *J* = 2.3 Hz, 1 H), 7.28 (d, *J* = 2.3 Hz, 1 H),

7.36 - 7.23 (m, 2 H), 2.37 (s, 3 H), 2.27 (s, 3 H), 1.39 (s, 9 H). ^{13}C NMR (101MHz, CDCl_3) δ = 168.3, 168.2, 143.3, 142.8, 140.5, 139.8, 139.6, 139.2, 136.4, 135.4, 133.8, 131.4, 127.2, 125.7, 124.7, 124.1, 122.2, 74.6, 35.0, 30.3, 20.9, 20.8 HRMS (APCI+) m/z: $[\text{M}+\text{H}]^+$ Calculated for $\text{C}_{24}\text{H}_{23}\text{IO}_4$ 503.07138; Found 503.06971.

3-(tert-Butyl)-5-(3-(4,4,5,5-tetramethyl4,5-dihydroimidazol-3-oxide-1-oxyl)azulen-1-yl)-1,2-phenylene diacetate (Ac₂Cat-Az-NN). In a 25 mL round-bottom flask, **Ac₂Cat-Az-I** (54 mg, 0.11 mmol), NNAuPPh_3 (74 mg, 0.12 mmol) and $\text{Pd}(\text{PPh}_3)_4$ (13 mg, 0.011 mmol) were combined under nitrogen. THF (5 mL) was added, a nitrogen-purged, water-cooled condenser was attached and the flask was heated to 60 °C. After 4 h, the reaction was observed to be complete by TLC on basic alumina with 33% EtOAc/hexanes, it was cooled to room temperature, and then concentrated under reduced pressure. The title compound was purified by basic alumina column chromatography with 25% EtOAc/hexanes as eluent to afford the dark seafoam green compound (43 mg, 73%). HRMS (APCI+) m/z: $[\text{M} + \text{H}]^+$ Calculated for $\text{C}_{31}\text{H}_{36}\text{N}_2\text{O}_6$ 532.2573; Found 532.2574.

1,3-SQ-Az-NN. A purge-pumped 50 mL flask containing **Ac₂Cat-Az-NN** (58 mg, 0.11 mmol) in 20 mL of CH_2Cl_2 was added dropwise via cannula at a rate of 1 drop per 6 seconds to a solution of $\text{Zn}(\text{OH})\text{Tp}^{\text{Cum,Me}}$ (76 mg, 0.11 mmol) of and K_2CO_3 (30 mg, 0.22 mmol) in 10 mL of CH_2Cl_2 and 5 mL of MeOH. The green **Ac₂Cat-Az-NN** solution became brown when added to the $\text{Zn}(\text{OH})\text{Tp}^{\text{cum,Me}}$ and K_2CO_3 solution and then became orange-red. The addition was complete after approximately 3 h at which point the reaction was opened to air and monitored by EPR. The reaction became red-violet and 77K EPR showed a triplet spectrum. The reaction was stirred open to air for 3 h and then concentrated under reduced pressure to remove the CH_2Cl_2 and the resulting precipitate in MeOH was collected via vacuum filtration. The red-violet solid was

collected from the filter paper in a separate flask by dissolving it with Et₂O, then being concentrated under reduced pressure to afford the crude biradical (71 mg, 58%) of as a red-violet solid. HRMS (APCI+) m/z: [M + H]⁺ Calculated for C₆₆H₇₅BN₈O₄Zn 1117.5332; Found 1117.5276. IR (solid) ν (cm⁻¹): 2533 (w, -BH). X-ray quality crystals were grown from CH₂Cl₂/i-PrOH layer-layer diffusion.

3-(*tert*-Butyl)-5-(3'-formylazulen-1'-yl)-1,2-phenylene diacetate (Ac₂Cat-Az-CHO). 3 drops of 18 M H₂SO₄ was added to a solution of **MOM₂Cat-Az-CHO** (62 mg, 0.16 mmol) in Ac₂O (ca. 10 mL) of and stirred for 3 h at room temperature. The reaction was transferred to a separatory funnel, diluted with a 50% Et₂O/hexanes mixture and washed liberally with brine. The organic layer was separated, dried with MgSO₄ and concentrated under reduced pressure. The crude residue was purified by silica gel column chromatography and the product was eluted with 20% EtOAc/hexanes to afford a dark violet oil (49 mg, 80%). ¹H NMR (400MHz, CDCl₃) δ = 10.42 (s, 1 H), 9.65 (d, *J* = 9.8 Hz, 1 H), 8.74 (d, *J* = 9.8 Hz, 1 H), 8.36 (s, 1 H), 7.90 (dd, *J* = 9.6, 9.6 Hz, 1 H), 7.66 (dd, *J* = 9.8, 9.6 Hz, 1 H), 7.57 (dd, *J* = 9.8, 9.6 Hz, 1 H), 7.47 (d, *J* = 2.3 Hz, 1 H), 7.33 (d, *J* = 2.3 Hz, 1 H), 2.41 (s, 3 H), 2.32 (s, 3 H), 1.43 (s, 9 H).

V.4.2. Ferrocene Experimental.

1,3-diiodoferrocene was prepared as described by Zirakzadeh et al. with modified purifications as described in the text.⁶³

Bromoferrocene. Prepared according to literature procedure.⁶⁵ A solution of ferrocene (5.27 g, 28.33 mmol) and KO^tBu (0.318 g, 2.83 mmol) of in 120 mL of THF was cooled to -78 °C. *t*-BuLi in pentane (25 mL of a 1.7M solution, 43 mmol) was added dropwise via cannula. This solution was stirred for 1 h at this temperature, then 1,2-dibromoethane (3.8 mL, 44 mmol) of was added and the reaction was warmed to room temperature. The reaction was transferred to a separatory funnel, washed with brine and extracted with Et₂O. The organic layer was dried with MgSO₄ and concentrated under reduced pressure. The excess 1,2-dibromoethane was removed by distillation, then the crude oil was redissolved in hexanes and the hexanes was washed twice with 100 mL of 0.1 M FeCl₃ for 2 minutes each. The organic layer was washed with brine, then separated, dried with MgSO₄ and concentrated under reduced pressure. The title compound solidified upon standing to afford 3.89 g (52%). ¹H NMR (700MHz, CDCl₃) δ = 4.42 (d, *J* = 1.7 Hz, 2 H), 4.24 (s, 5 H), 4.11 (d, *J* = 1.7 Hz, 2 H).

1,1'-Bis(tri-*n*-butylstannyl)ferrocene. Prepared by a combination literature procedures.^{63,64} To a solution of ferrocene (1.00 g, 5.36 mmol) in 10 mL of anhydrous hexanes and TMEDA (2.0 mL, 13 mmol) in an oven-dried 50 mL round-bottom flask at room temperature, was added *n*-BuLi (4.7 mL of a 2.5M hexanes solution, 11.75 mmol) dropwise. The solution was stirred for 18 h overnight. Then, to the orange suspension was added 10 mL of anhydrous THF and was cooled to -78 °C and 4.0 mL (12 mmol) of Bu₃SnCl was added dropwise. The reaction mixture was warmed to room temperature and concentrated under reduced pressure. The product was

purified by reversed-phase silica gel flash chromatography with 30% Et₂O/MeOH as eluent to afford the title compound (3.35 g, 82%) of as an orange-red oil.

1,1'-Diiodoferrocene. Prepared by a combination literature procedures.^{63,64} To a solution of 1,1'-bis(tri-*n*-butylstannyl)ferrocene (1.00 g, 1.31 mmol) in 130 mL (0.01M) of CH₂Cl₂ was added iodine (0.992 g, 3.91 mmol) and stirred for 16 h at room temperature. Saturated Na₂S₂O₃ solution (10 mL) and 5 mL of NaHCO₃ saturated solution were added simultaneously and stirred until the iodine color disappeared. The reaction was transferred to a separatory funnel, washed with brine, the organic phase was separated, dried with MgSO₄ and concentrated under reduced pressure. The residue was redissolved in ca. 30 mL of MeOH and 4 g of KF was added, stirred for 30 min, and then filtered through a pad of basic alumina. The filtrate was concentrated under reduced pressure, the residue was then redissolved in hexanes, filtered again through a pad of basic alumina and concentrated. The product was purified by a basic alumina column with hexanes as eluent to afford the title compound (0.522 g, 91%) of as an orange oil. ¹H NMR (400MHz, CDCl₃) δ = 4.39 (dd, *J* = 2.0, 2.0 Hz, 4 H), 4.19 (dd, *J* = 2.0 Hz, 4 H).

1,1'- Bis(3''-(*tert*-butyl)-4'',5''-bis(methoxymethoxy)phenyl)ferrocene (1,1'-MOM₂CatFc). To a 50 mL round-bottom flask, equipped with magnetic stir bar, was added 1,1'-diiodoferrocene (0.254 g, 0.580 mmol) of, MOM₂CatBpin (0.441 g, 1.16 mmol), Na₂CO₃ (0.162 g, 1.53 mol) and 1.2 mg (0.0053 mmol) of Pd(OAc)₂. The flask was purge-pumped three times and backfilled with nitrogen, then 10 mL of THF and 3 mL of H₂O were added. A nitrogen-purged reflux condenser was attached and the contents were heated to 60 °C for 18 h with stirring. The reaction was cooled to room temperature, transferred to a separatory funnel, washed with ca. 20 mL of brine and extracted with ca. 20 mL of EtOAc. The organic layer was separated, dried with MgSO₄ and concentrated under reduced pressure. The residue was purified by flash

chromatography (deactivated silica gel) with 20% ethyl acetate/hexanes to give the product (150 mg, 58%) as an orange-red oil. ^1H NMR (400MHz, CDCl_3) δ = 7.01 - 6.87 (m, 4 H), 5.20 (s, 4 H), 5.15 (s, 4 H), 4.78 - 4.49 (m, 4 H), 4.48 - 4.20 (m, 4 H), 3.66 (s, 6 H), 3.52 (s, 6 H), 1.41 (s, 18 H). ^{13}C NMR (101MHz, CDCl_3) δ = 149.8, 144.2, 142.9, 133.5, 118.8, 113.1, 98.8, 95.3, 87.3, 70.6, 68.2, 57.4, 56.2, 35.0, 30.5, 24.8. HRMS (APCI+) m/z: $[\text{M}]^+$ Calculated for $\text{C}_{38}\text{H}_{50}\text{O}_8\text{Fe}$ 688.2890; Found 688.2902.

1,1'-SQ₂Fc. 1,1'-MOM₂CatFc (150 mg, 0.217 mmol) was added to a microwave vial with 3 mL of MeOH and 1 drop of 2M HCl, purged with nitrogen for 20 minutes and heated in the microwave for 5 min at 90 °C (35 Watt maximum power). The reaction was then transferred to a separatory funnel, washed with brine and extracted with 50/50 Et₂O/hexanes. The organic layer was then washed with saturated NaHCO₃ solution, separated, dried with MgSO₄ and concentrated under reduced pressure. To this residue was added Zn(OH)Tp^{Cum,Me} (300 mg, 0.434 mmol) and K₂CO₃ (62 mg, 0.449 mmol) and the flask was purge-pumped with nitrogen three times. CH₂Cl₂ (5 mL) and 5 mL of MeOH were added and the contents were stirred under nitrogen for 1 h, then the septum was removed and the flask was stirred in open air for 16 h. The precipitate was filtered and then collected with CH₂Cl₂ to give a dark violet solid (293 mg, 73%). X-ray quality crystals were grown from CH₂Cl₂/MeOH slow evaporation. IR (solid) ν (cm⁻¹): 2550 (w, -BH). HRMS (APCI+) m/z: $[\text{M} + \text{H}]^+$ Calculated for $\text{C}_{108}\text{H}_{123}\text{B}_2\text{N}_{12}\text{O}_4\text{FeZn}_2$ 1853.8028; Found 1853.7966.

1,3- Bis(3'-(*tert*-butyl)-4',5'-bis(methoxymethoxy)phenyl)ferrocene (1,3-MOM₂CatFc). To a 25 mL round-bottom flask, equipped with magnetic stir bar, was added 1,3-diiodoferrocene (70 mg, 0.160 mmol), MOM₂CatBpin (122 mg, 0.321 mmol), Na₂CO₃ (54 mg, 0.51 mmol) and Pd(OAc)₂ (1 mg, 0.004 mmol). The flask was purge-pumped three times and backfilled with

nitrogen, then 10 mL of THF and 3 mL of H₂O were added. A nitrogen-purged reflux condenser was attached and the contents were heated to 60 °C for 18 h with stirring. The reaction was cooled to room temperature, transferred to a separatory funnel, washed with ca. 20 mL of brine and extracted with ca. 20 mL of EtOAc. The organic layer was separated, dried with MgSO₄ and concentrated under reduced pressure. The residue was purified by flash chromatography (deactivated silica gel) with 10% ethyl acetate/hexanes to give the product (103 mg, 93%) as an orange-red oil. ¹H NMR (400MHz, CDCl₃) δ = 7.23 (d, *J* = 1.5 Hz, 2 H), 7.19 (d, *J* = 1.5 Hz, 2 H), 5.26 (br. s., 4 H), 5.25 (br. s., 4 H), 4.92 (s, 1 H), 4.67 (s, 2 H), 3.99 (s, 5 H), 3.69 (s, 6 H), 3.58 (s, 6 H), 1.50 (s, 18 H). ¹³C NMR (101MHz, CDCl₃) δ = 149.9, 144.3, 143.0, 133.7, 119.0, 113.3, 98.9, 95.4, 87.4, 71.1, 67.4, 65.8, 57.5, 56.2, 35.1, 30.6. HRMS (APCI+) *m/z*: [M+H]⁺ Calculated for C₃₈H₅₀O₈Fe 689.2980; Found 689.2969.

1,3-SQ₂Fc. 1,3-MOM₂CatFc (150 mg, 0.217 mmol) was added to a microwave vial with 3 mL of MeOH and 1 drop of 2M HCl, purged with nitrogen for 20 minutes and heated in the microwave for 5 min at 90 °C (35 Watt maximum power). The reaction was then transferred to a separatory funnel, washed with brine and extracted with 50/50 Et₂O/hexanes. The organic layer was then washed with saturated NaHCO₃ solution, separated, dried with MgSO₄ and concentrated under reduced pressure. To this residue was added Zn(OH)Tp^{Cum.Me} (300 mg, 0.434 mmol) and K₂CO₃ (62 mg, 0.45 mmol) and the flask was purge-pumped with nitrogen three times. 5 mL of CH₂Cl₂ and 5 mL of MeOH were added and the contents were stirred under nitrogen for 1 h, then the septum was removed and the flask was stirred in open air for 16 h. The precipitate was filtered and then collected with CH₂Cl₂ to give a dark violet solid (290 mg, 73%). X-ray quality crystals were grown from CH₂Cl₂/EtOH slow evaporation. IR (solid) ν (cm⁻¹):

2550 (w, -BH). HRMS (APCI+) m/z: [M + H]⁺ Calculated for C₁₀₈H₁₂₃B₂N₁₂O₄FeZn₂ 1853.8028; Found 1853.7979.

1-(3'-(*tert*-Butyl)-4',5'-bis(methoxymethoxy)phenyl)ferrocene (MOM₂CatFc). To a 25 mL round-bottom flask, equipped with magnetic stir bar, was added 1-iodoferrocene (120 mg, 0.385 mmol), MOM₂CatBpin (146 mg, 0.384 mmol), Na₂CO₃ (61 mg, 0.58 mmol) and Pd(OAc)₂ (1 mg, 0.004 mmol). The flask was purge-pumped three times and backfilled with nitrogen, then 10 mL of THF and 3 mL of H₂O were added. A nitrogen-purged reflux condenser was attached and the contents were heated to 60 °C for 18 h with stirring. The reaction was cooled to room temperature, transferred to a separatory funnel, washed with ca. 20 mL of brine and extracted with ca. 20 mL of EtOAc. The organic layer was separated, dried with MgSO₄ and concentrated under reduced pressure. The residue was purified by flash chromatography (deactivated silica gel) with 5% ethyl acetate/hexanes to give the product (129 mg, 76%) as an orange-red oil. ¹H NMR (400MHz, CDCl₃) δ = 7.18 (d, *J* = 2.0 Hz, 1 H), 7.13 (d, *J* = 2.0 Hz, 1 H), 5.22 (s, 4 H), 4.55 (t, *J* = 1.8 Hz, 2 H), 4.27 (t, *J* = 1.8 Hz, 2 H), 4.07 (s, 5 H), 3.68 (s, 3 H), 3.56 (s, 3 H), 1.47 (s, 9 H). ¹³C NMR (151MHz, CDCl₃) δ = 149.9, 144.2, 142.9, 133.9, 118.9, 113.3, 98.9, 95.5, 86.8, 69.5, 68.5, 66.9, 57.5, 56.2, 35.1, 30.6. HRMS (APCI+) m/z: [M]⁺ Calculated for C₂₄H₃₀O₄Fe 436.1540; Found 436.1532.

1--SQFc. MOM₂CatFc (108 mg, 0.246 mmol) of was dissolved in 3 mL of MeOH with 2 drops of 2 M HCl in a microwave vial and heated in the microwave for 5 min at 90 °C (30 Watts maximum power). Reaction was transferred to a separatory funnel, washed with brine and extracted with Et₂O. The organic layer was separated and dried with MgSO₄ and concentrated. To the orange residue in a 50 mL round-bottom flask with a magnetic stir bar was added Zn(OH)Tp^{Cum,Me} (171 mg, 0.247 mmol) and KOH (14 mg, 0.249 mmol). The flask was purge-

pumped three times with nitrogen and then 5 mL each of anhydrous, deoxygenated CH_2Cl_2 and MeOH was added. The reaction was stirred for 1 h under nitrogen and then opened to air and stirred for 16 h. The precipitate was filtered and then collected with CH_2Cl_2 to give a dark violet solid (293 mg, 73%). X-ray quality crystals were grown from $\text{CH}_2\text{Cl}_2/\text{EtOH}$ slow evaporation. IR (solid) ν (cm^{-1}): 2550 (w, -BH). HRMS (APCI+) m/z : $[\text{M}]^+$ Calculated for $\text{C}_{59}\text{H}_{67}\text{BN}_6\text{O}_2\text{FeZn}$ 1019.4142; Found 1019.4115.

V.5.References.

- (1) Ovchinnikov, A. A. Multiplicity of the Ground State of Large Alternant Organic Molecules with Conjugated Bonds. *Theor. Chim. Acta* **1978**, *47* (4), 297–304.
<https://doi.org/10.1007/BF00549259>.
- (2) Borden, W. T.; Davidson, E. R. Effects of Electron Repulsion in Conjugated Hydrocarbon Diradicals. *J. Am. Chem. Soc.* **1977**, *99* (14), 4587–4594.
<https://doi.org/10.1021/ja00456a010>.
- (3) Xia, J.; Capozzi, B.; Wei, S.; Strange, M.; Batra, A.; Moreno, J. R.; Amir, R. J.; Amir, E.; Solomon, G. C.; Venkataraman, L.; Campos, L. M. Breakdown of Interference Rules in Azulene, a Nonalternant Hydrocarbon. *Nano Lett.* **2014**, *14* (5), 2941–2945.
<https://doi.org/10.1021/nl5010702>.
- (4) Schwarz, F.; Koch, M.; Kastlunger, G.; Berke, H.; Stadler, R.; Venkatesan, K.; Lörtscher, E. Charge Transport and Conductance Switching of Redox-Active Azulene Derivatives. *Angew. Chemie - Int. Ed.* **2016**, *55* (39), 11781–11786.
<https://doi.org/10.1002/anie.201605559>.
- (5) Zhao, X.; Geskin, V.; Stadler, R. Destructive Quantum Interference in Electron Transport: A Reconciliation of the Molecular Orbital and the Atomic Orbital Perspective. *J. Chem. Phys.* **2017**, *146* (9), 092308. <https://doi.org/10.1063/1.4972572>.
- (6) El-Nahas, A. M.; Staykov, A.; Yoshizawa, K. First-Principles Calculations of Electron Transport through Azulene. *J. Phys. Chem. C* **2016**, *120* (17), 9043–9052.
<https://doi.org/10.1021/acs.jpcc.6b00767>.

- (7) Tsuji, Y.; Stuyver, T.; Gunasekaran, S.; Venkataraman, L. The Influence of Linkers on Quantum Interference: A Linker Theorem. *J. Phys. Chem. C* **2017**, *121* (27), 14451–14462. <https://doi.org/10.1021/acs.jpcc.7b03493>.
- (8) Beer, M.; Longuet-Higgins, H. C. Anomalous Light Emission of Azulene. *J. Chem. Phys.* **1955**, *23* (8), 1390–1391. <https://doi.org/10.1063/1.1742314>.
- (9) Viswanath, G.; Kasha, M. Confirmation of the Anomalous Fluorescence of Azulene. *J. Chem. Phys.* **1956**, *24* (3), 574–577. <https://doi.org/10.1063/1.1742548>.
- (10) Wurzer, A. J.; Wilhelm, T.; Piel, J.; Riedle, E. Comprehensive Measurement of the S1 Azulene Relaxation Dynamics and Observation of Vibrational Wavepacket Motion. *Chem. Phys. Lett.* **1999**, *299* (3–4), 296–302. [https://doi.org/10.1016/S0009-2614\(98\)01288-3](https://doi.org/10.1016/S0009-2614(98)01288-3).
- (11) Bearpark, M. J.; Bernardi, F.; Clifford, S.; Olivucci, M.; Robb, M. A.; Smith, B. R.; Vreven, T. The Azulene S 1 State Decays via a Conical Intersection: A CASSCF Study with MMVB Dynamics. *J. Am. Chem. Soc.* **1996**, *118* (1), 169–175. <https://doi.org/10.1021/ja9514555>.
- (12) Nishimura, H.; Ishida, N.; Shimazaki, A.; Wakamiya, A.; Saeki, A.; Scott, L. T.; Murata, Y. Hole-Transporting Materials with a Two-Dimensionally Expanded π -System around an Azulene Core for Efficient Perovskite Solar Cells. *J. Am. Chem. Soc.* **2015**, *137* (50), 15656–15659. <https://doi.org/10.1021/jacs.5b11008>.
- (13) Yamaguchi, Y.; Takubo, M.; Ogawa, K.; Nakayama, K. I.; Koganezawa, T.; Katagiri, H. Terazulene Isomers: Polarity Change of OFETs through Molecular Orbital Distribution Contrast. *J. Am. Chem. Soc.* **2016**, *138* (35), 11335–11343.

- <https://doi.org/10.1021/jacs.6b06877>.
- (14) Liu, R. S. H. Colorful Azulene and Its Equally Colorful Derivatives. *J. Chem. Educ.* **2002**, *79* (12), 183–185.
- (15) Xin, H.; Gao, X. Application of Azulene in Constructing Organic Optoelectronic Materials: New Tricks for an Old Dog. *Chempluschem* **2017**, *82* (7), 945–956.
<https://doi.org/10.1002/cplu.201700039>.
- (16) Haraguchi, M.; Tretyakov, E.; Gritsan, N.; Romanenko, G.; Gorbunov, D.; Bogomyakov, A.; Maryunina, K.; Suzuki, S.; Kozaki, M.; Shiomi, D.; Sato, K.; Takui, T.; Nishihara, S.; Inoue, K.; Okada, K. (Azulene-1,3-Diyl)-Bis(Nitronyl Nitroxide) and (Azulene-1,3-Diyl)-Bis(Iminonitroxide) and Their Copper Complexes. *Chem. - An Asian J.* **2017**, *12* (22), 2929–2941. <https://doi.org/10.1002/asia.201701085>.
- (17) Wang, F.; Lai, Y.-H.; Kocherginsky, N. M.; Kostaschi, Y. Y. The First Fully Characterized 1,3-Polyazulene: High Electrical Conductivity Resulting from Cation Radicals and Polycations Generated upon Protonation. *Org. Lett.* **2003**, *5* (7), 995–998.
<https://doi.org/10.1021/ol0274615>.
- (18) Song, C.; Swager, T. M. Reactive Conducting Thiepin Polymers. *J. Org. Chem.* **2010**, *75* (4), 999–1005. <https://doi.org/10.1021/jo902079j>.
- (19) Hedin, L. New Method for Calculating the One-Particle Green's Function with Application to the Electron-Gas Problem. *Phys. Rev.* **1965**, *139* (3A), A796–A823.
<https://doi.org/10.1103/PhysRev.139.A796>.
- (20) Thygesen, K. S.; Rubio, A. Conserving GW Scheme for Nonequilibrium Quantum

- Transport in Molecular Contacts. *Phys. Rev. B - Condens. Matter Mater. Phys.* **2008**, *77* (11), 115333. <https://doi.org/10.1103/PhysRevB.77.115333>.
- (21) Kahn, O. O. *Molecular Magnetism*; VCH Publishers Inc.: New York, 1993.
- (22) Borden, W. T.; Iwamura, H.; Berson, J. a. Violations of Hund's Rule in Non-Kekule Hydrocarbons: Theoretical Prediction and Experimental Verification. *Acc. Chem. Res.* **1994**, *27* (4), 109–116. <https://doi.org/10.1021/ar00040a004>.
- (23) Borden, W. T. Effects of Electron Repulsion in Diradicals. *Diradicals* **1982**, *4587* (23), 1–72.
- (24) Salem, L.; Rowland, C. The Electronic Properties of Diradicals. *Angew. Chemie Int. Ed. English* **1972**, *11* (2), 92–111. <https://doi.org/10.1002/anie.197200921>.
- (25) Longuet-Higgins, H. C. Some Studies in Molecular Orbital Theory I. Resonance Structures and Molecular Orbitals in Unsaturated Hydrocarbons. *J. Chem. Phys.* **1950**, *18* (3), 265. <https://doi.org/10.1063/1.1747618>.
- (26) Misurkin, I. A.; Ovchinnikov, A. A. The Electronic Structures and Properties of Polymeric Molecules with Conjugated Bonds. *Russ. Chem. Rev.* **1977**, *46* (10), 967–987. <https://doi.org/10.1070/RC1977v046n10ABEH002185>.
- (27) Kirk, M. L.; Shultz, D. A.; Stasiw, D. E.; Habel-Rodriguez, D.; Stein, B.; Boyle, P. D. Electronic and Exchange Coupling in a Cross-Conjugated D-B-A Biradical: Mechanistic Implications for Quantum Interference Effects. *J. Am. Chem. Soc.* **2013**, *135* (39), 14713–14725. <https://doi.org/10.1021/ja405354x>.
- (28) Lahti, P. M.; Ichimura, A. S. Semiempirical Study of Electron Exchange Interaction in

- Organic High-Spin π -Systems. Classifying Structural Effects in Organic Magnetic Molecules. *J. Org. Chem.* **1991**, *56* (9), 3030–3042. <https://doi.org/10.1021/jo00009a020>.
- (29) Field, L. M.; Lahti, P. M. Coordination Complexes of 1-(4-[N - Tert -Butyl- N - Aminoxy]Phenyl)- 1H -1,2,4-Triazole with Paramagnetic Transition Metal Dications. *Inorg. Chem.* **2003**, *42* (23), 7447–7454. <https://doi.org/10.1021/ic0349050>.
- (30) Kirk, M. L.; Shultz, D. A.; Stasiw, D. E.; Lewis, G. F.; Wang, G.; Brannen, C. L.; Sommer, R. D.; Boyle, P. D. Superexchange Contributions to Distance Dependence of Electron Transfer/Transport: Exchange and Electronic Coupling in Oligo(Para-Phenylene)- and Oligo(2,5-Thiophene)-Bridged Donor-Bridge-Acceptor Biradical Complexes. *J. Am. Chem. Soc.* **2013**, *135* (45), 17144–17154. <https://doi.org/10.1021/ja4081887>.
- (31) Stasiw, D. E.; Zhang, J.; Wang, G.; Dangi, R.; Stein, B. W.; Shultz, D. A.; Kirk, M. L.; Wojtas, L.; Sommer, R. D. Determining the Conformational Landscape of σ and π Coupling Using Para -Phenylene and “Aviram–Ratner” Bridges. *J. Am. Chem. Soc.* **2015**, *137* (29), 9222–9225. <https://doi.org/10.1021/jacs.5b04629>.
- (32) Kirk, M. L.; Shultz, D. A.; Zhang, J.; Dangi, R.; Ingersol, L.; Yang, J.; Finney, N. S.; Sommer, R. D.; Wojtas, L. Heterospin Biradicals Provide Insight into Molecular Conductance and Rectification. *Chem. Sci.* **2017**, *8* (8), 5408–5415. <https://doi.org/10.1039/C7SC00073A>.
- (33) Matsuda, K.; Iwamura, H. Demonstration of the Degeneracy of the Singlet and Triplet States in 2,3-Dimethylenecyclohexane-1,4-Diyl by Measurement of Its Magnetic Properties †. *J. Chem. Soc. Perkin Trans. 2* **1998**, *0* (5), 1023–1026.

<https://doi.org/10.1039/a706301f>.

- (34) Rajca, A.; Coupling, S.; State, G.; Wroclawska, P. Organic Diradicals and Polyradicals: From Spin Coupling to Magnetism? *Chem. Rev.* **1994**, *94*, 871.
- (35) Kirk, M. L.; Shultz, D. A.; Depperman, E. C.; Brannen, C. L. Donor-Acceptor Biradicals as Ground State Analogues of Photoinduced Charge Separated States. *J. Am. Chem. Soc.* **2007**, *129* (7), 1937–1943. <https://doi.org/10.1021/ja065384t>.
- (36) Kirk, M. L.; Shultz, D. A.; Depperman, E. C.; Habel-Rodriguez, D.; Schmidt, R. D. Spectroscopic Studies of Bridge Contributions to Electronic Coupling in a Donor-Bridge-Acceptor Biradical System. *J. Am. Chem. Soc.* **2012**, *134* (18), 7812–7819. <https://doi.org/10.1021/ja300233a>.
- (37) Kolanji, K.; Ravat, P.; Bogomyakov, A. S.; Ovcharenko, V. I.; Schollmeyer, D.; Baumgarten, M. Mixed Phenyl and Thiophene Oligomers for Bridging Nitronyl Nitroxides. *J. Org. Chem.* **2017**, *82* (15), 7764–7773. <https://doi.org/10.1021/acs.joc.7b00435>.
- (38) Shinomiya, M.; Higashiguchi, K.; Matsuda, K. Evaluation of the β Value of the Phenylene Ethynylene Unit by Probing the Exchange Interaction between Two Nitronyl Nitroxides. *J. Org. Chem.* **2013**, *78* (18), 9282–9290. <https://doi.org/10.1021/jo4015062>.
- (39) Hirel, C.; Vostrikova, K. E.; Pécaut, J.; Ovcharenko, V. I.; Rey, P. Nitronyl and Imino Nitroxides: Improvement of Ullman's Procedure and Report on a New Efficient Synthetic Route. *Chemistry (Easton)*. **2001**, *7* (9), 2007–2014. [https://doi.org/10.1002/1521-3765\(20010504\)7:9<2007::AID-CHEM2007>3.0.CO;2-7](https://doi.org/10.1002/1521-3765(20010504)7:9<2007::AID-CHEM2007>3.0.CO;2-7).

- (40) Tanimoto, R.; Suzuki, S.; Kozaki, M.; Okada, K. Nitronyl Nitroxide as a Coupling Partner: Pd-Mediated Cross-Coupling of (Nitronyl Nitroxide-2-Ido)(Triphenylphosphine)Gold(I) with Aryl Halides. *Chem. Lett.* **2014**, *43* (5), 678–680. <https://doi.org/10.1246/cl.131162>.
- (41) Zhang, J.; Zhao, M.; Cui, G.; Peng, S. A Class of Novel Nitronyl Nitroxide Labeling Basic and Acidic Amino Acids: Synthesis, Application for Preparing ESR Optionally Labeling Peptides, and Bioactivity Investigations. *Bioorganic Med. Chem.* **2008**, *16* (7), 4019–4028. <https://doi.org/10.1016/j.bmc.2008.01.022>.
- (42) Boocock, D. G. B.; Darcy, R.; Ullman, E. F. Studies of Free Radicals. II. Chemical Properties of Nitronyl nitroxides. A Unique Radical Anion. *J. Am. Chem. Soc.* **1968**, *90* (21), 5945–5946. <https://doi.org/10.1021/ja01023a078>.
- (43) Wu, Y.; Bi, L.; Bi, W.; Li, Z.; Zhao, M.; Wang, C.; Ju, J.; Peng, S. Novel 2-Substituted Nitronyl Nitroxides as Free Radical Scavengers: Synthesis, Biological Evaluation and Structure-Activity Relationship. *Bioorganic Med. Chem.* **2006**, *14* (16), 5711–5720. <https://doi.org/10.1016/j.bmc.2006.04.016>.
- (44) Mikheev, Y. A.; Guseva, L. N.; Ershov, Yu, A. Mechanism of the Protonation of Azulenes in Aqueous Solutions of Acids. *Russ. J. Phys. Chem. A* **2013**, *87* (10), 1645–1653.
- (45) Magdziak, D.; Rodriguez, A. A.; Van De Water, R. W.; Pettus, T. R. R. Regioselective Oxidation of Phenols to o -Quinones with o -Iodoxybenzoic Acid (IBX). *Org. Lett.* **2002**, *4* (2), 285–288. <https://doi.org/10.1021/ol017068j>.
- (46) Sloop, J. C.; Shultz, D. A.; Coote, T.; Shepler, B.; Sullivan, U.; Kampf, J. W.; Boyle, P.

- D. Synthesis of and Structure-Property Relationships in Zinc Complexes of Bis-Metaphenylene Semiquinone Biradical Species. *J. Phys. Org. Chem.* **2012**, 25 (4), 314–321. <https://doi.org/10.1002/poc.1917>.
- (47) Atherton, N. M. (Neil M. *Principles of Electron Spin Resonance*; Ellis Horwood PTR Prentice Hall: New York, 1993.
- (48) Wasserman, E.; Snyder, L. C.; Yager, W. A. ESR of the Triplet States of Randomly Oriented Molecules. *J. Chem. Phys.* **1964**, 41 (6), 1763–1772. <https://doi.org/10.1063/1.1726156>.
- (49) Heisenberg, W. Über Die Spektra von Atomsystemen Mit Zwei Elektronen. *Zeitschrift für Phys.* **1926**, 39 (7–8), 499–518. <https://doi.org/10.1007/BF01322090>.
- (50) Coulson, C. A.; Rushbrooke, G. S.; Coulson, C. A. Mathematical Proceedings of the Cambridge Cambridge Philosophical Society: *Math. Proc. Cambridge Philos. Soc.* **1940**, 36 (02), 193–200. <https://doi.org/10.1017/S0305004100017163>.
- (51) Borden, W. T. Can a Square or Effectively Square Singlet Be the Ground State of Cyclobutadiene? *J. Am. Chem. Soc.* **1975**, 97 (21), 5968–5970.
- (52) Markussen, T.; Stadler, R.; Thygesen, K. S. The Relation between Structure and Quantum Interference in Single Molecule Junctions. *Nano Lett.* **2010**, 10 (10), 4260–4265. <https://doi.org/10.1021/nl101688a>.
- (53) Van Dyck, C.; Ratner, M. A. Molecular Rectifiers: A New Design Based on Asymmetric Anchoring Moieties. *Nano Lett.* **2015**, 15 (3), 1577–1584. <https://doi.org/10.1021/nl504091v>.

- (54) Kealy, T. J.; Pauson, P. L. A New Type of Organo-Iron Compound. *Nature*. Nature Publishing Group December 1951, pp 1039–1040. <https://doi.org/10.1038/1681039b0>.
- (55) van Staveren, D. R.; Metzler-Nolte, N. Bioorganometallic Chemistry of Ferrocene. *Chem. Rev.* **2004**, *104* (12), 5931–5986. <https://doi.org/10.1021/cr0101510>.
- (56) Xia, X.; Yu, H.; Wang, L.; Ul-Abdin, Z. Recent Progress in Ferrocene- and Azobenzene-Based Photoelectric Responsive Materials. *RSC Adv.* **2016**, *6* (107), 105296–105316. <https://doi.org/10.1039/C6RA16201K>.
- (57) Sun, R.; Wang, L.; Yu, H.; Abdin, Z.-; Chen, Y.; Huang, J.; Tong, R. Molecular Recognition and Sensing Based on Ferrocene Derivatives and Ferrocene-Based Polymers. *Organometallics* **2014**, *33* (18), 4560–4573. <https://doi.org/10.1021/om5000453>.
- (58) Saleem, M.; Yu, H.; Wang, L.; Zain-ul-Abdin; Khalid, H.; Akram, M.; Abbasi, N. M.; Huang, J. Review on Synthesis of Ferrocene-Based Redox Polymers and Derivatives and Their Application in Glucose Sensing. *Anal. Chim. Acta* **2015**, *876*, 9–25. <https://doi.org/10.1016/j.aca.2015.01.012>.
- (59) Astruc, D. Why Is Ferrocene so Exceptional? *Eur. J. Inorg. Chem.* **2017**, *2017* (1), 6–29. <https://doi.org/10.1002/ejic.201600983>.
- (60) Sporer, C.; Ruiz-Molina, D.; Wurst, K.; Kopacka, H.; Veciana, J.; Jaitner, P. Ferrocene Substituted Nitronyl Nitroxide and Imino Nitroxide Radicals. Synthesis, X-Ray Structure and Magnetic Properties. *J. Organomet. Chem.* **2001**, *637–639*, 507–513. [https://doi.org/10.1016/S0022-328X\(01\)00954-8](https://doi.org/10.1016/S0022-328X(01)00954-8).
- (61) Bryan D. Koivisto, †; Andrew S. Ichimura, *, ‡; Robert McDonald, §; Martin T.

- Lemaire, ‡; Laurence K. Thompson, ‡ and; Robin G. Hicks*, †. Intramolecular π -Dimerization in a 1,1'-Bis(Verdazyl)Ferrocene Diradical. **2005**.
<https://doi.org/10.1021/JA0566331>.
- (62) Elsner, O.; Ruiz-Molina, D.; Ratera, I.; Vidal-Gancedo, J.; Rovira, C.; Veciana, J. Ferrocene as a Ferromagnetic Coupler. Synthesis and Characterization of a Ferrocene Bridged Polychlorotriphenylmethyl Diradical. *J. Organomet. Chem.* **2001**, 637–639, 251–257. [https://doi.org/10.1016/S0022-328X\(01\)00912-3](https://doi.org/10.1016/S0022-328X(01)00912-3).
- (63) Zirakzadeh, A.; Herlein, A.; Groß, M. A.; Mereiter, K.; Wang, Y.; Weissensteiner, W. Halide-Mediated Ortho-Deprotonation Reactions Applied to the Synthesis of 1,2- and 1,3-Disubstituted Ferrocene Derivatives. *Organometallics* **2015**, 34 (15), 3820–3832.
- (64) Khobragade, D. A.; Mahamulkar, S. G.; Pospíšil, L.; Císařová, I.; Rulíšek, L.; Jahn, U. Acceptor-Substituted Ferrocenium Salts as Strong, Single-Electron Oxidants: Synthesis, Electrochemistry, Theoretical Investigations, and Initial Synthetic Application. *Chem. - A Eur. J.* **2012**, 18 (39), 12267–12277. <https://doi.org/10.1002/chem.201201499>.
- (65) Inkpen, M. S.; Du, S.; Driver, M.; Albrecht, T.; Long, N. J. Oxidative Purification of Halogenated Ferrocenes. *Dalt. Trans.* **2013**, 42 (8), 2813–2816.
<https://doi.org/10.1039/C2DT32779A>.
- (66) Ho, C. C.; Olding, A.; Smith, J. A.; Bissember, A. C. Nuances in Fundamental Suzuki–Miyaura Cross-Couplings Employing [Pd(PPh₃)₄]: Poor Reactivity of Aryl Iodides at Lower Temperatures. *Organometallics* **2018**, 37 (11), 1745–1750.
<https://doi.org/10.1021/acs.organomet.8b00189>.
- (67) Butler, I. R.; Wilkes, S. B.; McDonald, S. J.; Hobson, L. J.; Taralp, A.; Wilde, C. P. A

- Convenient Preparation of Iodoferrocenes. *Polyhedron* **1993**, *12* (2), 129–131.
[https://doi.org/10.1016/S0277-5387\(00\)81618-6](https://doi.org/10.1016/S0277-5387(00)81618-6).
- (68) Koivisto, B. D.; Ichimura, A. S.; McDonald, R.; Lemaire, M. T.; Thompson, L. K.; Hicks, R. G. Intramolecular π -Dimerization in a 1,1'-Bis(Verdazyl)Ferrocene Diradical. *J. Am. Chem. Soc.* **2006**, *128* (3), 690–691. <https://doi.org/10.1021/ja0566331>.
- (69) Shultz, D. A.; Vostrikova, K. E.; Bodnar, S. H.; Koo, H.-J. H.-J.; Whangbo, M.-H. M.-H.; Kirk, M. L.; Depperman, E. C.; Kampf, J. W. Trends in Metal-Biradical Exchange Interaction for First-Row M(II)(Nitronyl Nitroxide-Semiquinone) Complexes. *J. Am. Chem. Soc.* **2003**, *125* (6), 1607. <https://doi.org/10.1021/ja020715x>.
- (70) Gorman, C. B.; Smith, J. C.; Hager, M. W.; Parkhurst, B. L.; Sierzputowska-Gracz, H.; Haney, C. A. Molecular Structure-Property Relationships for Electron-Transfer Rate Attenuation in Redox-Active Core Dendrimers. *J. Am. Chem. Soc.* **1999**, *121* (43), 9958–9966. <https://doi.org/10.1021/ja990875h>.
- (71) Lash, T. D.; Lammer, A. D.; Idate, A. S.; Colby, D. A.; White, K. Preparation of Azulene-Derived Fulvenedialdehydes and Their Application to the Synthesis of Stable Adj - Dicarbaporphyrinoids. *J. Org. Chem.* **2012**, *77* (5), 2368–2381.
<https://doi.org/10.1021/jo2026977>.
- (72) Salman, H.; Abraham, Y.; Tal, S.; Meltzman, S.; Kapon, M.; Tessler, N.; Speiser, S.; Eichen, Y. 1,3-Di(2-Pyrrolyl)Azulene: An Efficient Luminescent Probe for Fluoride. *European J. Org. Chem.* **2005**, *2005* (11), 2207–2212.
<https://doi.org/10.1002/ejoc.200500012>.
- (73) Koch, M.; Blacque, O.; Venkatesan, K. Impact of 2,6-Connectivity in Azulene: Optical

Properties and Stimuli Responsive Behavior. *J. Mater. Chem. C* **2013**, *1* (44), 7400.

<https://doi.org/10.1039/c3tc31610f>.

(74) Anderson, A. G.; Nelson, J. A.; Tazuma, J. J. Azulene. III. Electrophilic Substitution 1-3.

J. Am. Chem. Soc. **1953**, *75* (20), 4980–4989. <https://doi.org/10.1021/ja01116a030>.

APPENDICES

APPENDIX A: Proposed High Spin and Soluble Polyradicals.

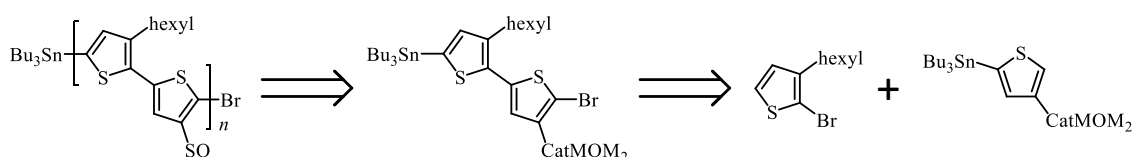
A.1. Introduction. As discussed in Chapter II.5. **pThSQ** was plagued by solubility issues at relatively low degrees of polymerization ($DP \approx 17$ units). **PoPE-SQ** also suffered from the low degrees of polymerization ($DP \approx 18$ units) and did not seem to have as strong of coupling between radical units that was indicated for **pThSQ** by hyperfine couplings in isotropic EPR. Alkyl chains are a common technique to afford solubility to macromolecules. Thiophene copolymers with alkyl chains at either just the 3- or 3- and 4-positions of thiophene have been utilized to afford better solubility to growing polymer chains during polymerization or to provide easier solution manipulation of resulting polymers. From the EPR spectrum of **pThSQ-025** it was observed that metallo-semiquinone pendant groups on a polythiophene could interact with each other to afford at least a majority bi- and triradicals in a polymer that was 17 units long with a random distribution of those units being radicals. This would suggest, by probability, that many of these radicals were able to interact over two or more diamagnetic thiophene units to provide the observed fractionating of the hyperfine coupling constants that were observed in a monoradical of the monomer, **ThSQ**. Given this, a trade-off for in a 100% of the BQ units being converted to SQ would be to have an alternating copolymer where every other unit would have a SQ radical and the units in between the radicals would be thiophenes with alkyl groups appended in order to provide the greater solubility. In theory, the trade-off would be that fewer units could be radicals for increased solubility which could overall provide a much higher working molecular weight which may overall have more units that are radicals. The information and ideas presented in this appendix is intended to overcome the solubility issues while still maintaining a relatively high-spin ferromagnetically coupled polyradical. Two polyradicals are presented 1) an AB copolymer whose units would consist of the existing **ThSQ** and 3-hexylthiophene for which

significant progress toward the copolymer monomer unit (AB) was made and whose synthesis is presented and 2) a hypothetically ideal and synthetically accessible copolymer consisting of two symmetric monomers, one with a delocalized conjugated radical and one that is a cross-conjugated solubilizing linker which are copolymerized with either a Stille or Suzuki polymerization.

A.2. Progress toward the synthesis of Poly(3-hexylthiophene-*alt*-3-SQthiophene) (P3HT-ThSQ).

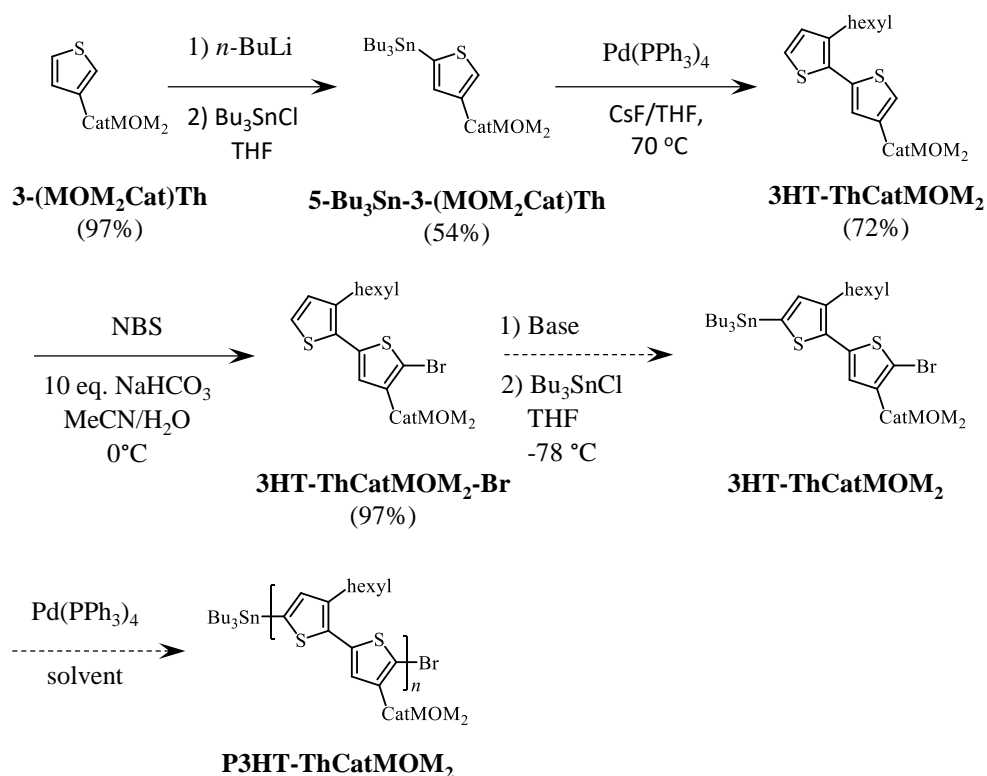
P3HT-ThSQ was designed to help circumvent some synthetic challenges that arise from having polymers that become very insoluble and to increase the likelihood that the resulting polymers would have greater degrees of polymerization. Since **pThSQ-025** seemed to indicate relatively strong interactions between multiple radicals and probably across multiple diamagnetic thiophene units in a DP = 17 polymer where only 3-4 of the units were randomly radicals, it was hypothesized that adding a conjugated spacer with solubilizing groups between each **ThSQ** unit would still allow relatively strong coupling between radicals.

Scheme A-1. Retrosynthesis of **P3HT-ThSQ**.



Scheme A-1 shows the retrosynthesis of **P3HT-ThSQ** with the proposed asymmetric 2,2'-bithiophene monomer to give appropriate head-tail couplings via Stille polymerization and the two thiophene subunits that compose the monomer. 3-hexylthiophene was selected as the solubilizing spacer because either 2-bromo-3-hexylthiophene or 3-hexylthiophene were commercially available from multiple sources. Scheme A-2 shows the synthetic pathway toward

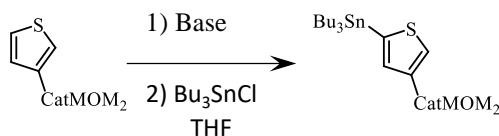
Scheme A-2. Synthesis of **P3HT-ThCatMOM₂**.



P3HT-ThSQ. The synthesis starts with **3-(MOM₂Cat)Th** from the **pThSQ** synthesis which is then selectively deprotonated at the 5-position and then quenched with **Bu₃SnCl**. This reaction was for unknown reasons challenging for **3-(MOM₂Cat)Th**. The reaction (Table A-1, Entry 1) provided variable yields from 30-54% over a series of four reactions, averaging 41% with no obvious reason for the variation and relatively low yields in comparison to similar reactions performed on 3-alkylthiophenes in literature.¹⁻⁸ Each of these reactions provided both product (**5-Bu₃Sn-3-(MOM₂Cat)Th**) and starting material and calculation of the total moles from the masses of **5-Bu₃Sn-3-(MOM₂Cat)Th** and recovered starting material consistently gave greater than 95% of the total moles of starting material used in the reaction. Since the reactions were giving product and starting material there are a few possibilities for why the yields are low-moderate: 1) incomplete deprotonation due to the acid-base equilibrium 2) deprotonation at a site

that does not react with Bu_3SnCl and instead gets protonated during work-up. Incomplete deprotonation due to acid-base equilibria did not make a lot of sense because the pKa of thiophene's 2 and 5 positions are in the low to mid-thirties; certainly a big enough difference

Table A-1. Syntheses of **5-Bu₃Sn-3-(MOM₂Cat)Th.**



Entry	Base	Temp. (°C)	(Time (h))	Result
1	<i>n</i> -BuLi	-78, RT ^a	0.25, 1 ^a	46, 32, 54, 30%
2	LiTMP	-78, RT ^a	0.25, 1 ^a	27%
3	LiTMP	-78	3.5	27%
4	<i>n</i> -BuLi/ TMEDA	-78, RT ^a	0.25, 1 ^a	43%
5	KO ^t Bu/ <i>n</i> -BuLi	-78	1	44%
6	KO ^t Bu/ <i>t</i> -BuLi	-30	3	34%
7	<i>t</i> -BuLi	-78	1 min	34%
8	2 eq. <i>t</i> -BuLi	-78	0.25	36%
9 ^b	<i>n</i> -BuLi	-78	1	53%, 55%
10 ^c	<i>n</i> -BuLi	-78	1	86%

Unless otherwise specified all reactions were performed in THF, 1.1 eq. of base was added and the reaction was stirred for the specified time and temperature, then cooled to -78 °C before adding Bu_3SnCl .

^a In Temp. column "-78, RT" corresponds to the Time column "0.25, 1" meaning at -78 °C for 15 min (0.25 h), then warmed to RT and stirred for 1 h.

^b Instead of MOM-protected catechol, methyl protected catechol was used.

^c Test reaction was performed on 3-hexylthiophene

from *n*-BuLi (butane pKa ca. 50) to fully deprotonate thiophene. Table A-1 summarizes attempts that were made to increase the yield. Entries 2 and 3 used LiTMP in order to increase the steric bulk of the base to force deprotonation at the exposed proton at the 5-position on thiophene with the only difference being the length of time which ended-up giving the same lower yield. LiTMP is a weaker base than *n*-BuLi and a weaker nucleophile, given that the yields decreased relative

to Entry 1, it was suspected that this may be due to the acid-base equilibrium. Acid-base reactions are very quick, so the equilibrium would have been established regardless of if the reaction was stirred for 1 h vs 3.5 h. Entries 4 and 5 intended to increase the strength of the base to facilitate complete deprotonation by using TMEDA and Schlosser's base, respectively. These did increase the yield, but only to just above the average of Entry 1's reactions. Entry 6

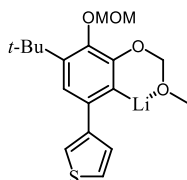


Figure A-1. *ortho*-lithiation directing MOM group

attempted slightly longer (3 h) and warmer (30 °C) reaction time and temperature to further force deprotonation, but this led to a yield decrease to 34%. Again starting material and product were only obtained. This result seemed to suggest deprotonation at another site which was unreactive to Bu_3SnCl and just was protonated during work-up. A potential hypothesis is shown in Figure A-1. Methoxymethyl groups are known to promote *ortho* lithiation, so it was thought that perhaps the proton *ortho* to the one MOM group was reacting as well and this site was unreactive to the Bu_3SnCl due to steric interactions with the MOM group and the thiophene ring. Entry 7 was performed to establish that the length of time was unimportant. By adding *t*-BuLi and allowing it to stir only 1 min before quenching with Bu_3SnCl and getting a 34% yield, which was within the range of previous reactions that had stirred for one or more hours with strong base. If the lithiation shown in Figure A-1 is occurring it may be possible to still deprotonate the thiophene 5 position in addition to the catechol proton on the same molecule. To this end, Entry 8 used two equivalents of *t*-BuLi, however this still only provided a 36% yield; not much difference from 1.1 eq. of *t*-BuLi for 1 min in Entry 7. Entry 9 was performed on the methyl-protected catechol analog to **3-(MOM₂Cat)Th**. Methoxy groups are not as strong at directing

ortho lithiation as MOM groups. This did seem to have some effect because two examples of this provided a 53 and 55% yield. Entry 11 is one final test reaction performed on 3-hexylthiophene which by ¹H-NMR indicated total conversion to the product and provided an isolated yield of 86%. It was decided that the moderate yields that were given were workable and that the best approach was to continue with the synthesis.

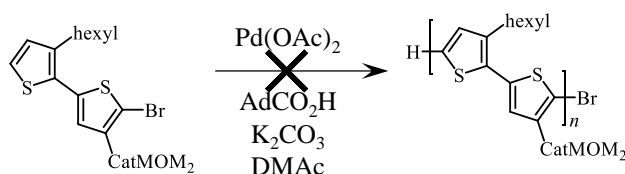
The stannylated product is then Stille cross-coupled with 2-bromo-3-hexylthiophene. The first cross-coupling was attempted with Pd(PPh₃)₄ in toluene at 100 °C which cleanly provided a 54% yield of the 2,2'-bithiophene (**3HT-ThCatMOM₂**). In an attempt to increase the yield, particularly given that the first step to make **5-Bu₃Sn-3-(MOM₂Cat)Th** was providing inconsistent and relatively poor yields, the toluene was replaced with THF at reflux and 2 eq. of CsF was included and two iterations of this Stille reaction provided 72 and 73% yields. Given that the reaction was consistent, clean and provided a decent yield, no further attempts were made to improve this reaction.

The selective bromination of a thiophene *ortho* to a MOM₂Cat at the 3 (in this case, 4 or 4' position for a 2,2'-bithiophene) position had already been accomplished in the synthesis of **pThSQ** and so a similar strategy was employed. For the bromination of 2,2'-bithiophene (**3HT-ThCATMOM₂**) to **3HT-ThCATMOM₂-Br**, NBS, instead of pyridinium bromide perbromide, was found to be a higher yielding brominating agent. And in order to protect the MOM groups from transient HBr, NaOAc was used instead of NaHCO₃ because of higher solubility in MeOH; 16 wt% vs 2.13 wt%, respectively. With NBS and 2 eq. of NaOAc to absorb HBr in MeOH a 96% yield was provided for the 5-bromo-2,2'-bithiophene (**3HT-ThCATMOM₂-Br**).

Similar 2,2'-bithiophene monomers have been prepared in literature and after bromination at the 5-position is the selective deprotonation at the 5' position with a lithium

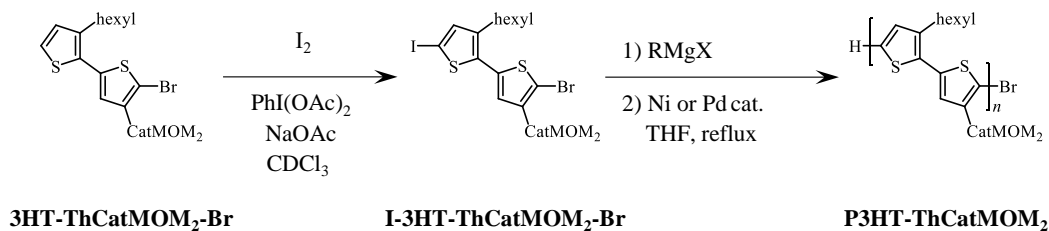
amide base, typically LDA, and quenching with Bu_3SnCl .⁹ Usually these sterically hindered lithium amide bases will deprotonate the thiophene ring without performing the lithium-halogen exchange side-reaction; however, in this case, approximately 33% was the desired product (**3HT-ThCatMOM₂**) and the remainder was the un-brominated 2,2'-bithiophene (**3HT-ThCatMOM₂**) by ¹H-NMR integrations. Similar results were observed with LiTMP was attempted as the base.

Scheme A-3. Attempted polymerization of **3HT-ThCATMOM₂-Br** with DArP.



Scheme A-3 shows the direct arylation polymerization (DArP) method that was used to synthesize **pThCatMOM₂**, was attempted on the 5-bromo-2,2'-bithiophene (**3HT-ThCATMOM₂-Br**) monomer. Unfortunately, DArP failed in this case, which given the variability to success that was observed for **pThCatMOM₂** is not altogether surprising. Another viable polymerization is either the Grignard metathesis (GRIM) or Reike polymerization which polymerize a 2,5-dihalothiophene, where the halogens are either symmetrical or the 2-position is a bromide and 5-position is an iodide. In these types of polymerizations, the 5-position halogen is exchanged with either magnesium (GRIM) or zinc (Reike) and then either a nickel or palladium catalyst is added to polymerize the metallated 5-position with the halogenated 2-

Scheme A-4. Synthetic procedure to make **P3HT-ThCatMOM₂** via GRIM.



position on another monomer to give very high head-tail configurations.^{10,11} Scheme A-4 shows the iodination of **3HT-ThCATMOM₂-Br** with I₂ and PhI(OAc)₂ in the presence of NaOAc in CDCl₃. Initially, this reaction was done in CDCl₃ in order to facilitate monitoring of the reaction's progress. However, after the reaction initially worked in CDCl₃, when it was attempted in CHCl₃, it failed. The iodine atoms in molecular iodine is not a strong enough electrophile to iodinate the 5-position on the thiophene, so PhI(OAc)₂ is added to oxidize molecular iodine into two equivalents of the hypohalite, AcOI. Hypohalites are strong electrophiles and will react with even weak nucleophiles so any impurities in the starting materials or solvents can destroy the reaction. Given that the iodination already worked in complete conversion with this starting material, it was probably the CHCl₃. It is known that CHCl₃ will photolyze in the presence of oxygen to give phosgene and HCl, so loss of reactivity is not unexpected. These reactions were done on small enough scale and concentrated enough that using CDCl₃ as the solvent was not exceedingly expensive in exchange for consistently successful reactions. Before attempting the GRIM polymerization, trials were performed to determine the rate of the magnesium-iodide exchange by adding *i*-PrMgCl and stirring for a period of time and quenching with MeOH. The best method was to add the *i*-PrMgCl and stir the reaction at room temperature overnight. However, two attempts to polymerize I-**3HT-ThCATMOM₂-Br** via the GRIM method were unsuccessful. Given that the magnesium-iodide exchange was working, it seemed as though there was an issue with the catalyst, solvent or reaction temperature.

A.3. Hypothetical High-Spin and Soluble polymer: Poly(phenanthrene semiquinone-*alt*-3,4-dialkylthieno[2,3-b]thiophene) (pPhenSQ-XBT).

A “better” polymer than the polymer presented in Section A.1., for reasons that will be explained, was conceived during the synthesis of **P3HT-ThSQ**. A constant struggle for designing high-spin polymers and their corresponding monomers is that the radicals which are usually in a pendant group in the resulting polymer must be able to delocalize into the polymer backbone enough to allow for the overlap of non-disjoint SOMOs with other radicals. Meaning that 1) the radicals must be conjugated with the polymer backbone 2) the radicals must be cross-conjugated with each other 3) defects must be minimized in order to prevent the failure of one of the preceding requirements. Few examples address the issue of conjugation of the radicals with the backbone by directly incorporating radicals into the backbone. Among those are Iwamura’s 1986 polycarbene¹², Racja’s dendritic triarylmethyl-based polyradicals^{13–15}, the tetrakis[3,5-bis(trifluoromethyl)phenyl]borate (TFPB) copolymer prepared by Yan et al. (Figure A-2A)¹⁶,

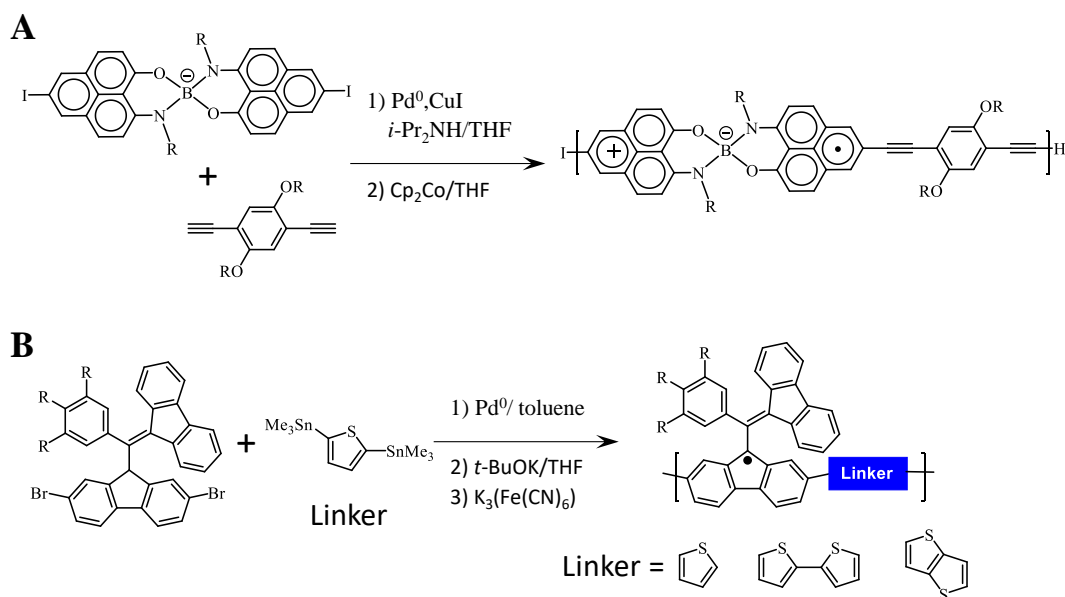


Figure A-2. Polyradicals prepared by A) Yan et al. and B) Swager et al.

and most recently in 2018, Swager's 1,3-*bis*(diphenylene-2-phenylallyl) (BDPA) radical-based copolymer with various conjugated linkers (Figure A-2B).¹⁷

Yan et al. reported ferromagnetic coupling between adjacent phenalenyl radical units with $S = 4$ for the polymers; however due to the phenalenyl SOMO having a node at the connection point, it cannot delocalize along the chain and so the ferromagnetic coupling is weaker than it could be if the SOMOs were non-disjoint and Swager's polymer should not be high-spin because adjacent radicals will be antiferromagnetically coupled due to the conjugated thiophene, 2,2'-bithiophene, and thieno[3-2-*b*]thiophene linkers, the symmetric design of the monomers in both examples is ideal for preventing defects, such as head-head and tail-tail coupling that break the ferromagnetic coupling between adjacent radicals and lower the overall spin of the polymer, because for symmetric monomers there is no such thing as head-head or tail-tail couplings and every monomer would be coupled the same, predictable way with the others. Both these polymers are also reported to be relatively stable in comparison to the other radical-in-backbone polymers that were mentioned, the TFPB polymer for "several weeks" in solid form and BDPA polymers are less stable with a reported 13% loss of EPR signal after 24 h in degassed toluene at room temperature.

Figure A-3 depicts some of the qualities that an ideal high-spin organic polyradical might have. The polyradicals must be synthetically accessible which mainly means that they can be synthesized, however straight-forward synthesis means that fewer steps and higher yields are preferable and that it can be relatively easily reproduced. Both TFPB and BDPA polymers have been made and are both fewer than ten steps from commercially available starting materials. In comparison to PoPE-SQ, pThSQ and P3HT-ThSQ which are fifteen, eleven and fourteen steps, respectively. Furthermore, the TFPB and BDPA polymers also dealt with the solubility issues by incorporating alkyl chains into their structures; the original attempt at the BDPA did not have these alkyl chains and suffered from poor solubility. PoPE-SQ and pThSQ both suffered from lack of solubility during their final steps, which also posed the issue for reproducibility. The MOM groups of both afford them better solubility during the polymerization and once there is a maximally soluble polymer while MOM-protected, the MOMs are removed and the catechol and

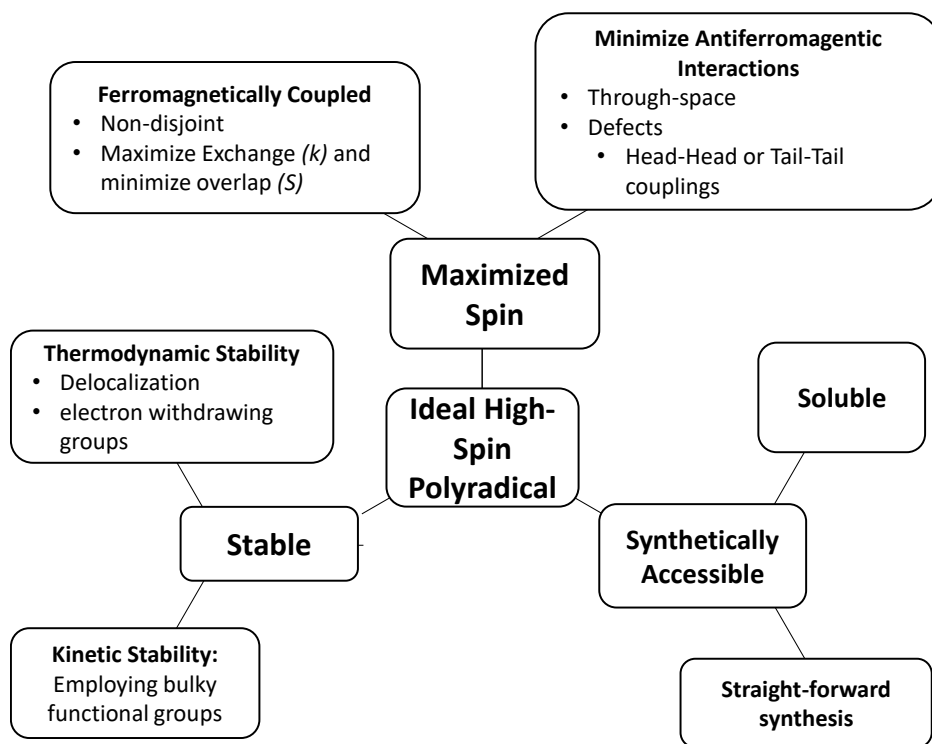


Figure A-3. Possible features of an ideal high-spin polyradical.

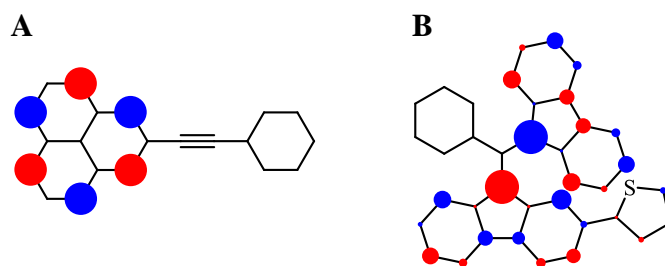


Figure A-4. Hückel SOMOs of A) phenalenyl and B) BDPA fragments from polyradicals.

quinone polymers are less soluble. P3HT-ThSQ was intended as the initial attempt to deal with the solubility issues, but is left incomplete. Another issue not shown, is that the polyradicals must be able to be purified easily; Yan *et al.* mentions that since Cp_2Co was used to oxidize the polymer to the polyradical, there may be some other paramagnetic species present.

Stability for TFPB and BDPA are more addressed by the choosing of radicals that tend to be more stable, but as mentioned before, TFPB was stable for several weeks whereas BDPA was observed to be decomposing in inert atmosphere after a day in solution. PoPE-SQ, pThSQ and P3HT-ThSQ are addressed two intertwined ways: by choosing the radical to be an *ortho*-semiquinone that is complexed to a metal complex. The metal stabilizes the semiquinone and the ancillary ligand of the metal complex provides that kinetic stability by helping to shield the radical against outside attack.

The TFPB polymer was mentioned before to have disjoint SOMOs due to the phenalenyl radicals having nodes at the connecting points with the alkynes and therefore cannot delocalize into the connecting units to allow the SOMOs of adjacent radicals to interact by a predictable and strong mechanism as can be seen in Figure A-4A. Therefore, the TFPB polymer will not have non-disjoint molecular orbitals which are necessary for maximizing the exchange integral. The BDPA polymer was not necessarily designed to be a high-spin polymer because the SOMOs in this instance are conjugated with each other and therefore will have greater overlap integrals which will result in antiferromagnetic coupling and minimization of the ground state spin. The

BDPA polymer could become a high-spin polymer by replacing the conjugated linkers with a cross-conjugated linker, which would allow delocalization of the radicals into the linkers, but make the radicals cross-conjugated with each other and create non-disjoint SOMOs on the linkers. However, even with a cross-conjugated linker the coupling between radicals would be relatively weak as can be seen in Figure A-4B due to very little electron density in the linker.

These design features were ideal and implemented to give the copolymer presented in Figure A-5. Utilizing the phenanthrene semiquinone (PhenSQ) as the radical unit the radical unit can be more easily implemented directly into the backbone of the polymer. Most likely attempts to do this with just a semiquinone would result in instability. With a radical unit directly in the backbone, the radical units must be connected by a cross-conjugated linker in order to facilitate the high-spin ground-state. *Meta*-phenylene could work, but introduces a twist into the polymer chain which could result in macrocycles during synthesis¹⁸ or position radical units close enough in the chain to result in through-space antiferromagnetic interactions which would lower the ground-state spin.¹⁹ A better cross-conjugated linker which has been used in organic electronics is thieno[2,3-b]thiophene.²⁰ Figure A-5 also shows both the “star” method and spin polarization

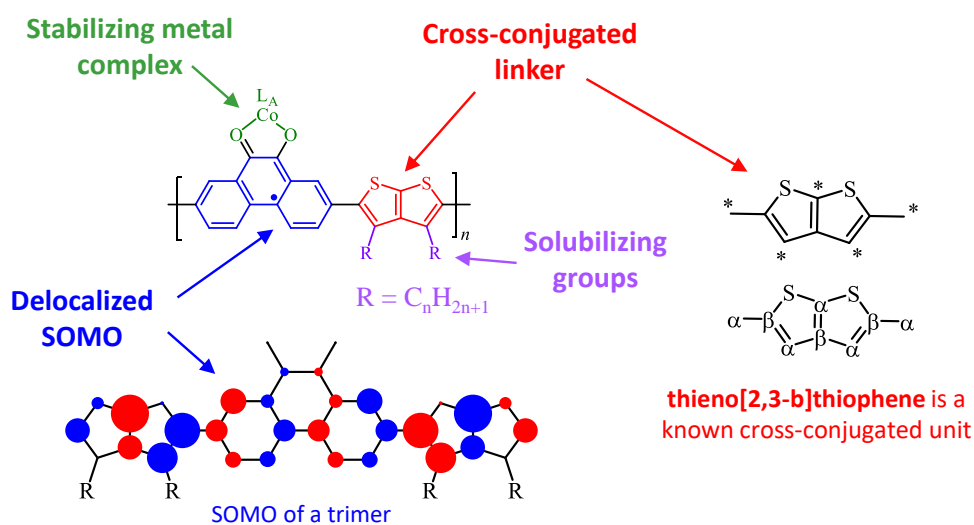
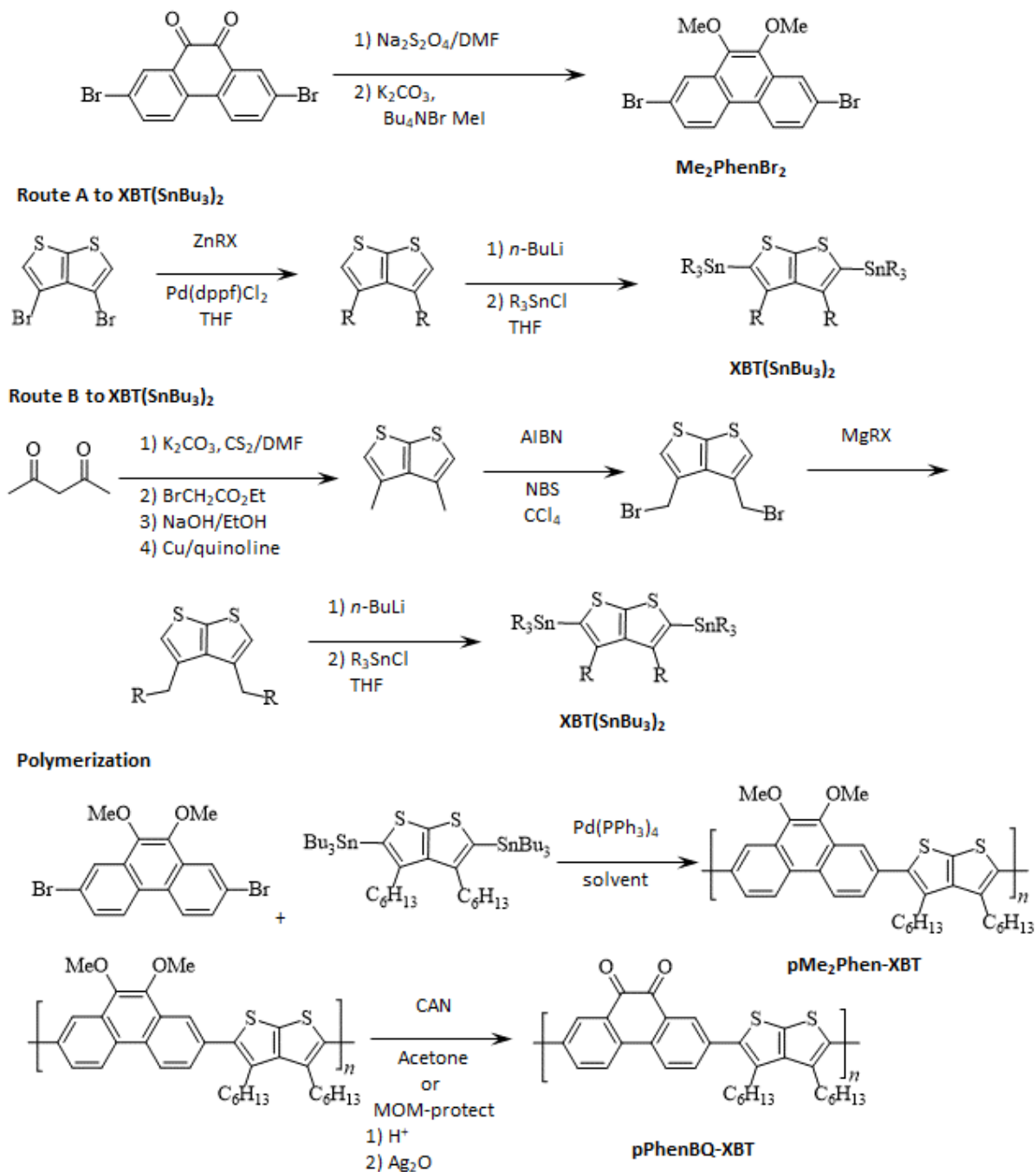


Figure A-5. Proposed high-spin, soluble polyradical, pPhenSQ-XBT.

in the form of α and β spins forming π bonds around the thiophene rings. Thieno[2,3-b]thiophene also has the open 3 and 4 positions that can be functionalized with solubilizing alkyl chains so that every other aromatic unit in the polymer chain will have two solubilizing units. PhenSQ also has a very delocalized SOMO when looking at a trimer consisting of bithiophene-PhenSQ-bithiophene. By Hückel MO theory, 68% of the electron density is located on the bithiophene, which may be less than or greater in reality, but regardless it is larger than what Hückel predicts for other polyradicals. So when this is applied to a polymer, each PhenSQ will have significant non-disjoint SOMO overlap with each adjacent PhenSQ SOMO. Finally, PhenSQ can still take advantage of the chemistry utilized by PoPE-SQ, pThSQ and P3HT-ThSQ by the redox reaction with CoL_A to produce and stabilize the semiquinones.

Scheme A-5 presents a prospective synthesis for **pPhenSQ-XBT**. Currently, the starting material, 2,7-dibromophenanthrene-9,10-dione is commercially available from Tokyo Chemical Industry (TCI) Co. Ltd. for \$380/ 5 grams; however if expense or discontinuation becomes an

Scheme A-5. Proposed synthesis of **pPhenBQ-XBT**; precursor to **pPhenSQ-XBT**.



issue it has been reported by the bromination of phenanthrene-9,10-dione with NBS in

concentrated H₂SO₄.²¹ The reduction with Na₂S₂O₄ in DMF and O-alkylation of 2,7-dibromophenanthrene-9,10-dione is also reported which are reported with a yield of 81%.²¹ Although, the desired compound, **Me₂PhenBr₂**, is known and reported by Müller et al.²² However, this procedure employs Me₂SO₄ as the methylating agent with aqueous NaOH as the base. Aqueous NaOH is typically used to quench Me₂SO₄ at the end of a reaction, but nonetheless Müller et al. reports an 80% yield of the desired compound, so this procedure should not be disregarded.²²

The synthesis of **XBT(SnBu₃)₂** exactly is not known, although the various transformations that would be required on thieno[2,3-b]thiophene are known. Two possible syntheses of **XBT(SnBu₃)₂** are presented in Scheme A-5. The fewest steps to the desired monomer is presented as Route A where commercially available 3,4-dibromothieno[2,3-b]thiophene (TCI, 1g for \$453) is Negishi cross-coupled to give the 3,4-dialkylthieno[2,3-b]thiophene.²³ Thieno[2,3-b]thiophene can be doubly deprotonated at the 2 and 5-positions and quenched with trialkyltin chloride^{20,24} to give the stannylated final product, **XBT(SnBu₃)₂**.

If Route A becomes challenging, poor yielding or 3,4-dibromothieno[2,3-b]thiophene is too expensive or discontinued, then Route B provides a viable alternative. Route B makes the thieno[2,3-b]thiophene rings from acetylacetone, carbon disulfide and ethyl 2-bromoacetate which are steps 1 and 2 in the first reaction arrow. Step 3 is the saponification of the esters that are now present at the 2 and 5 position to the carboxylic acids before decarboxylation with copper and quinoline in step 4 to give 3,4-dimethylthieno[2,3-b]thiophene as reported by Comel and Kirsch.²⁵ From here, Wu et al. reports the radical bromination of the methyl groups of with NBS and AIBN in CCl₄.²⁶ The bromomethyl groups can then undergo an S_N2 reaction with any Grignard reagent or other nucleophile of an alkyl chain to give the 3,4-dialkylthieno[2,3-

b]thiophene. The final step is again the double deprotonation and quenching with trialkyltin to give the final product.^{20,24}

From these two monomers the copolymerization is a Stille cross-coupling polymerization for which proper experimental parameters would need to be evaluated. An alternative to a Stille polymerization could be a Suzuki polymerization by replacing the bromides of **Me₂PhenBr₂** with 4,4,5,5-tetramethyl-1,3,2-dioxaborolane (Bpin) groups which is also reported²¹ and instead of stannylation, bromination at the 2- and 5-positions with bromine in acetic acid and chloroform²³. Another potential issue is that the methyl groups are removed via oxidative dealkylation with ceric ammonium nitrate (CAN), which could unintentionally oxidize the thieno[2,3-b]thiophene. If this happens, the methyl groups can most likely be replaced with MOM groups during the *O*-alkylation of phenanthrene-9,10-diol and should not pose additional problems during either the Stille or Suzuki polymerization. The MOM groups can be removed with catalytic acid and the phenanthrene-9,10-diol monomer units can be oxidized with Ag₂O.

As mentioned before the symmetry of the monomers obviates head-head and tail-tail couplings and should be able to produce a strongly coupled high-spin polyradical with decent solubility from a relatively short synthesis; potentially 4-8 steps depending on successful route to **pMe₂Phen-XBT**.

A.4. Experimental.

Tributyl(4-(3-(*tert*-butyl)-4,5-bis(methoxymethoxy)phenyl)thiophen-2-yl)stannane. *n*-BuLi solution (0.180 mL, 0.45 mmol) was added dropwise to a solution of **3-(3-(*tert*-butyl)-4,5-bis(methoxymethoxy)phenyl)thiophene** (0.138 g, 0.410 mmol) in ca. 20 mL of THF at -78 °C. The reaction was stirred for 15 min at -78 °C, then warmed to room temperature, stirred for 1 h

and then cooled to $-78\text{ }^{\circ}\text{C}$ before 0.130 mL (0.479 mmol) of Bu_3SnCl was added dropwise. The reaction was stirred, while warming to room temperature, overnight. 1 mL of MeOH was added and the reaction was concentrated under reduced pressure. The product was purified by silica gel chromatography with 100% hexanes for five column volumes, then 5% EtOAc/hexanes for seven column volumes to afford the title compound as a colorless oil (0.118 g, 46%). ^1H NMR (400 MHz, CDCl_3) δ = 7.66 (d, J = 1.2 Hz, 1 H), 7.36 (d, J = 1.2 Hz, 1 H), 7.29 (d, J = 2.3 Hz, 1 H), 7.27 (d, J = 2.3 Hz, 1 H), 5.26 (s, 2 H), 5.26 (s., 2 H), 3.70 (s, 3 H), 3.56 (s, 3 H), 1.68 - 1.58 (m, 6 H), 1.50 (s, 9 H), 1.41 (td, J = 7.3, 14.7 Hz, 6 H), 1.21 - 1.13 (m, 6 H), 0.95 (t, J = 7.2 Hz, 9 H). ^{13}C NMR (400 MHz, CDCl_3) δ = 150.3, 145.0, 143.8, 143.5, 137.7, 134.7, 131.4, 125.9, 119.1, 113.2, 99.0, 95.5, 57.5, 56.3, 35.2, 30.5, 28.9, 27.2, 13.6, 10.8.

4'-(3-(*tert*-Butyl)-4,5-bis(methoxymethoxy)phenyl)-3-hexyl-2,2'-bithiophene. A solution of tributyl(4-(3-(*tert*-butyl)-4,5-bis(methoxymethoxy)phenyl)thiophen-2-yl)stannane (0.982 g, 1.57 mmol), 2-bromo-3-hexylthiophene (0.344 mL, 1.73 mmol), $\text{Pd}(\text{PPh}_3)_4$ (18 mg, 0.016 mmol) of and CsF (0.477 g, 3.14 mmol) in 20 mL of THF contained in a 50 mL round-bottom flask, with a water-cooled condenser attached, under a nitrogen atmosphere to $85\text{ }^{\circ}\text{C}$ for 48 h. The reaction was cooled to room temperature and concentrated under reduced pressure. The produce was purified by silica gel column chromatography with 0-10% EtOAc/hexanes eluent to afford the title compound as a colorless oil (0.577 g, 73%). ^1H NMR (400 MHz, CDCl_3) δ = 7.35 (d, J = 1.2 Hz, 1 H), 7.33 (d, J = 1.2 Hz, 1 H), 7.29 (d, J = 2.0 Hz, 1 H), 7.27 (d, J = 2.0 Hz, 1 H), 7.21 (d, J = 5.1 Hz, 1 H), 6.97 (d, J = 5.5 Hz, 1 H), 5.25 (s, 2 H), 3.70 (s, 3 H), 3.56 (s, 3 H), 1.50 (s, 9 H). ^{13}C NMR 400 MHz, CDCl_3) δ = 145.3, 143.6, 142.5, 139.9, 136.7, 130.9, 130.3, 129.9, 125.4, 123.8, 119.7, 118.7, 112.8, 99.0, 95.4, 57.5, 56.3, 35.2, 31.6, 30.8, 30.5, 29.2, 29.1, 22.6, 14.0.

5'-Bromo-4'-(3-(*tert*-butyl)-4,5-bis(methoxymethoxy)phenyl)-3-hexyl-2,2'-bithiophene.

NBS (0.191 g, 1.07 mmol) was added to a solution of **4'-(3-(*tert*-butyl)-4,5-bis(methoxymethoxy)phenyl)-3-hexyl-2,2'-bithiophene** (0.506 g, 1.07 mmol) and NaOAc (0.178 g, 2.17 mmol) in ca. 20 mL of MeOH at 0 °C under a nitrogen atmosphere. The reaction was stirred at 0 °C for 1 h, then warmed to room temperature and concentrated under reduced pressure. The residue was redissolved in hexanes and washed with brine, the organic layer was extracted, dried with Na₂SO₄ and concentrated under reduced pressure to afford the title compound as a colorless oil (0.609 g, 98%).

3-(3-(*tert*-Butyl)-4,5-dimethoxyphenyl)thiophene. Me₂CatBpin (1.50 g, 4.68 mmol), Na₂CO₃ (0.996 g, 9.40 mmol) and Bu₄NBr (0.160 g, 0.496 mmol) were added to a 50 mL round-bottom flask, which was then purge-pumped three times with nitrogen and Pd(PPh₃) (97 mg, 0.084 mmol) was added. Toluene (9 mL), water (3 mL) and 3-bromothiophene (0.50 mL, 5.34 mmol) were added via syringe and a nitrogen-purged, water-cooled reflux condenser was attached and the contents were heated to 85 °C for 20 h. The reaction was cooled to room temperature, diluted with ca. 50 mL of EtOAc and washed with 50 mL of brine two times. The organic layer was separated, dried with MgSO₄ and concentrated under reduced pressure. The crude brown oil was purified by deactivate silica gel column chromatography with 10% EtOAc/hexanes to afford the title compound as a colorless to vaguely yellow oil (1.626 g, 97%). ¹H NMR (400 MHz, CDCl₃) δ = 7.42 - 7.33 (m, 3 H), 7.15 (d, *J* = 2.0 Hz, 1 H), 7.03 (d, *J* = 2.0 Hz, 1 H), 3.92 (s, 3 H), 3.91 (s, 3 H), 1.43 (s, 9 H).

A.5. References.

- (1) Lai, Y.-Y.; Tung, T.-C.; Liang, W.-W.; Cheng, Y.-J. Synthesis of Poly(3-Hexylthiophene), Poly(3-Hexylselenophene), and Poly(3-Hexylselenophene-*Alt*-3-Hexylthiophene) by Direct C–H Arylation Polymerization via *N*-Heterocyclic Carbene Palladium Catalysts. *Macromolecules* **2015**, *48* (9), 2978–2988.
<https://doi.org/10.1021/acs.macromol.5b00488>.
- (2) Kuo, C.-Y.; Huang, Y.-C.; Hsiow, C.-Y.; Yang, Y.-W.; Huang, C.-I.; Rwei, S.-P.; Wang, H.-L.; Wang, L. Effect of Side-Chain Architecture on the Optical and Crystalline Properties of Two-Dimensional Polythiophenes. *Macromolecules* **2013**, *46* (15), 5985–5997. <https://doi.org/10.1021/ma4007945>.
- (3) Koch, F. P. V.; Smith, P.; Heeney, M. “Fibonacci’s Route” to Regioregular Oligo(3-Hexylthiophene)S. *J. Am. Chem. Soc.* **2013**, *135* (37), 13695–13698.
<https://doi.org/10.1021/ja4057932>.
- (4) Jian, N.; Qu, K.; Gu, H.; Zou, L.; Liu, X.; Hu, F.; Xu, J.; Yu, Y.; Lu, B. Highly Fluorescent Triazolopyridine–Thiophene D–A–D Oligomers for Efficient PH Sensing Both in Solution and in the Solid State. *Phys. Chem. Chem. Phys.* **2019**, *21* (13), 7174–7182. <https://doi.org/10.1039/C9CP00672A>.
- (5) Li, J.; Qiao, X.; Xiong, Y.; Li, H.; Zhu, D. Five-Ring Fused Tetracyanothienoquinoids as High-Performance and Solution-Processable n-Channel Organic Semiconductors: Effect of the Branching Position of Alkyl Chains. *Chem. Mater.* **2014**, *26* (19), 5782–5788.
<https://doi.org/10.1021/cm502952u>.
- (6) Peng, L.; Yu, Y.; Lu, J.; He, P.; Wang, G.; Huang, M.; Zhao, B.; Pei, Y.; Tan, S.

- Development of S-Tetrazine-Based Polymers for Efficient Polymer Solar Cells by Controlling Appropriate Molecular Aggregation. *Dye. Pigment.* **2019**, *171*, 107717. <https://doi.org/10.1016/j.dyepig.2019.107717>.
- (7) Narayana, Y. S. L. V.; Baumgarten, M.; Müllen, K.; Chandrasekar, R. Tuning the Solid State Emission of Thin Films/Microspheres Obtained from Alternating Oligo(3-Octylthiophenes) and 2,6-Bis(Pyrazole)Pyridine Copolymers by Varying Conjugation Length and Eu³⁺/Tb³⁺ Metal Coordination. *Macromolecules* **2015**, *48* (14), 4801–4812. <https://doi.org/10.1021/acs.macromol.5b01004>.
- (8) Wang, R.; Zhao, Y.; Zhu, C.; Huang, X. New Synthesis of 3,6-Dibromophthalonitrile and Phthalocyanine Having Eight Thienyl Substituents at Peripheral α -Positions. *J. Heterocycl. Chem.* **2015**, *52* (4), 1230–1233. <https://doi.org/10.1002/jhet.2130>.
- (9) Lère-Porte, J. P.; Moreau, J. J. E.; Torreilles, C. Highly Conjugated Poly(Thiophene)s - Synthesis of Regioregular 3-Alkylthiophene Polymers and 3-Alkylthiophene/Thiophene Copolymers. *European J. Org. Chem.* **2001**, 1249–1258. [https://doi.org/10.1002/1099-0690\(200104\)2001:7<1249::AID-EJOC1249>3.0.CO;2-F](https://doi.org/10.1002/1099-0690(200104)2001:7<1249::AID-EJOC1249>3.0.CO;2-F).
- (10) Loewe, R. S.; Ewbank, P. C.; Liu, J.; Zhai, L.; McCullough, R. D. Regioregular, Head-to-Tail Coupled Poly(3-Alkylthiophenes) Made Easy by the GRIM Method: Investigation of the Reaction and the Origin of Regioselectivity. *Macromolecules* **2001**, *34* (13), 4324–4333. <https://doi.org/10.1021/ma001677+>.
- (11) McCullough, R. D.; Lowe, R. D.; Jayaraman, M.; Anderson, D. L. Design, Synthesis, and Control of Conducting Polymer Architectures: Structurally Homogeneous Poly(3-Alkylthiophenes). *J. Org. Chem.* **1993**, *58* (4), 904–912.

<https://doi.org/10.1021/jo00056a024>.

- (12) Iwamura, H. High-Spin Polycarbenes as Models for Organic Ferromagnets. *Pure Appl. Chem.* **1986**, *58* (1), 187–196. <https://doi.org/10.1351/pac198658010187>.
- (13) Rajca, A.; Utamapanya, S. Toward Organic-Synthesis of a Magnetic Particle - Dendritic Polyradicals with 15 and 31 Centers for Unpaired Electrons. *J. Am. Chem. Soc.* **1993**, *115* (9), 10688–10694.
- (14) Rajca, A.; Utamapanya, S.; Thayumanavan, S. Poly(Arylmethyl) Octet ($S = 7/2$) Heptaradical and Undecet ($S = 5$) Decaradical. *J. Am. Chem. Soc.* **1992**, *114* (5), 1884–1885. <https://doi.org/10.1021/ja00031a055>.
- (15) Rajca, A.; Rajca, S.; Wongsriratanakul, J. Very High-Spin Organic Polymer: π -Conjugated Hydrocarbon Network with Average Spin of $S \geq 40$. *J. Am. Chem. Soc.* **1999**, *121* (26), 6308–6309. <https://doi.org/10.1021/ja990881d>.
- (16) Yan, W.; Wan, X.; Xu, Y.; Lv, X.; Chen, Y. A Phenalenyl-Based Neutral Stable π -Conjugated Polyradical. *Synth. Met.* **2009**, *159* (17–18), 1772–1777. <https://doi.org/10.1016/j.synthmet.2009.05.025>.
- (17) Wang, P.; Lin, S.; Lin, Z.; Peeks, M. D.; Van Voorhis, T.; Swager, T. M. A Semiconducting Conjugated Radical Polymer: Ambipolar Redox Activity and Faraday Effect. *J. Am. Chem. Soc.* **2018**, *140* (34), 10881–10889. <https://doi.org/10.1021/jacs.8b06193>.
- (18) Shultz, D. a.; Hollomon, M. G.; Carolina, N. Preparation and EPR Spectroscopic Investigation of Conjugated Oligomers Containing Semiquinone Repeat Units. *Chem.*

- Mater.* **2000**, *12* (2), 580–585. <https://doi.org/10.1021/cm9907155>.
- (19) Juetten, M. J.; Buck, A. T.; Winter, A. H. A Radical Spin on Viologen Polymers: Organic Spin Crossover Materials in Water. *Chem. Commun.* **2015**, *51* (25), 5516–5519. <https://doi.org/10.1039/C4CC07119K>.
- (20) van Pruissen, G. W. P.; Brebels, J.; Hendriks, K. H.; Wienk, M. M.; Janssen, R. A. J. Effects of Cross-Conjugation on the Optical Absorption and Frontier Orbital Levels of Donor–Acceptor Polymers. *Macromolecules* **2015**, *48* (8), 2435–2443. <https://doi.org/10.1021/acs.macromol.5b00046>.
- (21) Kim, Y.-A.; Hwang, K.-I.; Kang, M.; Kim, N.-K.; Jang, S.; Kim, I.-B.; Kim, J.; Kim, D.-Y. Effect of Side Chains on Phenanthrene Based D-A Type Copolymers for Polymer Solar Cells. *Org. Electron.* **2017**, *44*, 238–246. <https://doi.org/10.1016/j.orgel.2017.01.014>.
- (22) Müller, M.; Reiss, H.; Tverskoy, O.; Rominger, F.; Freudenberg, J.; Bunz, U. H. F. Stabilization by Benzannulation: Butterfly Azaacenes. *Chem. - A Eur. J.* **2018**, *24* (49), 12801–12805. <https://doi.org/10.1002/chem.201803118>.
- (23) Heeney, M.; Bailey, C.; Tierney, S.; McCulloch, I. Monomers, Oligomers and Polymers of Thieno[2,3-b]Thiophene. Worldwide Applications 2006.
- (24) Lee, H.-S.; Lee, J. S.; Jung, A.-R.; Cha, W.; Kim, H.; Son, H. J.; Cho, J. H.; Kim, B. Processing Temperature Control of a Diketopyrrolopyrrole-Alt-Thieno[2,3-b]Thiophene Polymer for High-Mobility Thin-Film Transistors and Polymer Solar Cells with High Open-Circuit Voltages. *Polymer (Guildf)*. **2016**, *105*, 79–87. <https://doi.org/10.1016/j.polymer.2016.10.024>.

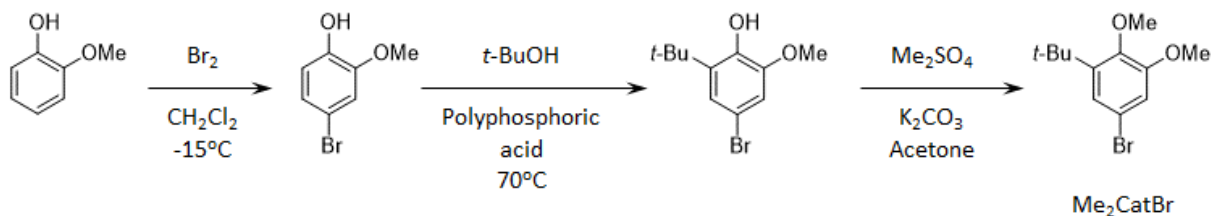
- (25) Comel, A.; Kirsch, G. Efficient One Pot Preparation of Variously Substituted Thieno [2,3-b] Thiophene. *J. Heterocycl. Chem.* **2001**, 38 (5), 1167–1171.
<https://doi.org/10.1002/jhet.5570380521>.
- (26) Wu, Y. X.; Cao, J.; Deng, H. Y.; Feng, J. X. Synthesis, Complexation, and Fluorescence Behavior of 3,4-Dimethylthieno[2,3-b]Thiophene Carrying Two Monoaza-15-Crown-5 Ether Groups. *Spectrochim. Acta Part A Mol. Biomol. Spectrosc.* **2011**, 82 (1), 340–344.
<https://doi.org/10.1016/j.saa.2011.07.058>.

APPENDIX B: MOM₂CatBpin – An Anthology

B.1. Introduction. For over two decades the syntheses of catechols to react with metal complexes followed by aerial oxidation to produce the corresponding semiquinone metal complexes, has been crucial to the success of Shultz group students. As a result, the synthesis of catechols has evolved over the years.

The earliest synthesis is for 5-bromo-1-(*tert*-butyl)-2,3-dimethoxybenzene (Me₂CatBr) began to appear around August 1994 according to DAS II-31. This original synthesis (Scheme B-1) utilized guaiacol as the starting material. The first step was bromination followed by treatment with *tert*-butanol and polyphosphoric acid to give moderate yields of the *ortho-tert*-butylated guaiacol, which was subsequently methyl protected by treatment with dimethylsulfate

Scheme B-1. Methyl protected catechol synthesis starting with guaiacol.

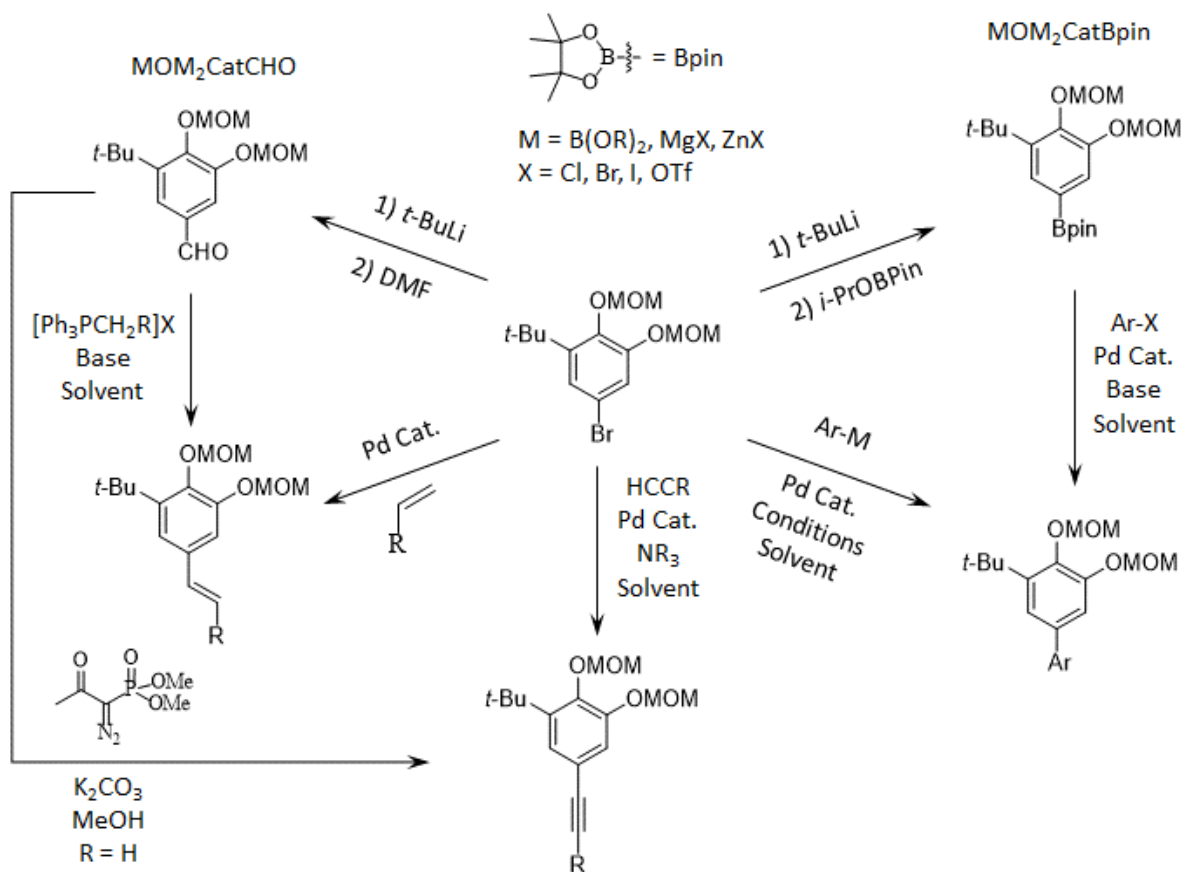


in acetone with K₂CO₃. However, methyl protecting group removal requires anhydrous and harsh, highly reactive conditions produced by the use of BBr₃ which can be unsuitable for some substrates and can pose challenges to work-up; not to mention that the reagent fumes vigorously. According to MGH II-38 in December of 1995, Me₂CatBr was deprotected with BBr₃ and reprotected with MOM protecting groups. It was also discovered at this time that the Cat-Br is unstable and should not be heated and should be used shortly after it is obtained. The first attempt was performed at room temperature and produced a mixture of the mono- and di-protected material. After refluxing for several hours the MOM-protected product was procured. This would become the preferred catechol protecting group and the primary intermediate for the group's syntheses became 5-bromo-1-(*tert*-butyl)-2,3-bis(methoxymethoxy)benzene

(MOM₂CatBr); as this compound can be transformed into a variety of compounds (Scheme B-2) and be deprotected under a variety of facile conditions including the most popular, catalytic aqueous acid.

Scheme B-2 shows some of the transformations of MOM₂CatBr that have been performed across its multiple decades as a primary synthetic starting material for Shultz group projects. The first semiquinone-nitronyl nitroxide (SQ-NN) donor-acceptor molecule was made by lithium-halogen exchange and quenching with DMF to give the corresponding aldehyde.¹ Then condensed with *N,N'*-(2,3-dimethylbutane-2,3-diyl)bis(hydroxylamine) (BHA) and oxidized to the NN with NaIO₄. MOM₂CatBr can and has been used directly in metal-catalyzed cross-coupling reactions with boronic acids and esters, Grignard reagents and zinc reagents (PH

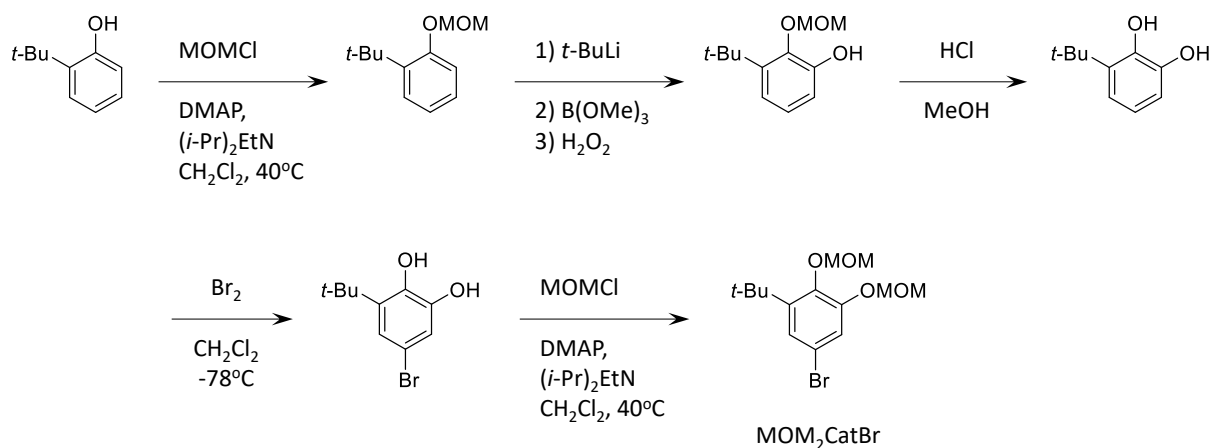
Scheme B-2. Some synthetic transformations of MOM₂CatBr



[Ph₃PCH₃]I to make MOM₂CatCH=CH₂. The numerous reactions performed on MOM₂CatBr are slightly more extensive than the routes used to make it over these years.

The lowest-yielding step of guaiacol synthesis in Scheme B-1 is the introduction of the *tert*-butyl group which was circumvented by starting with commercially available 2-*tert*-

Scheme B-3. Synthesis of MOM₂CatBr starting from 2-*tert*-butylphenol and making catechol via *ortho*-lithiation to a MOM protecting group.

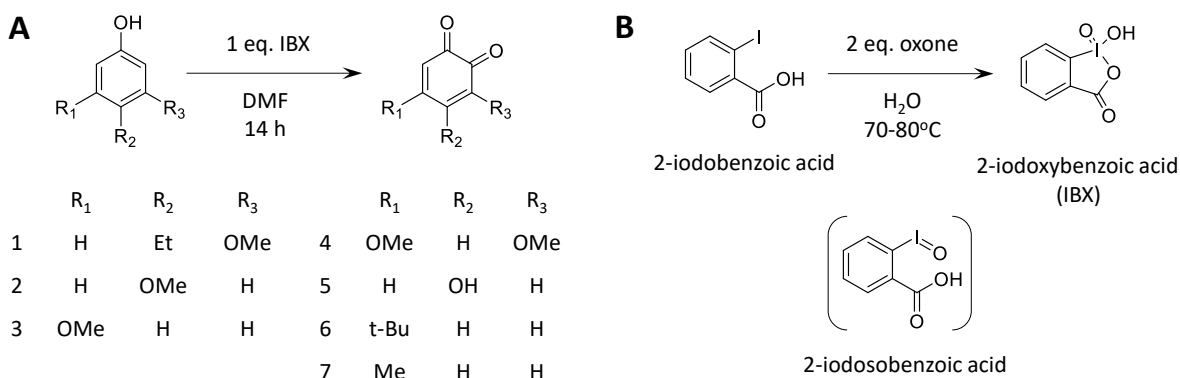


butylphenol, then starting with a MOM protection so that the second oxygen to make the catechol could be installed via the MOM-directed *ortho*-lithiation direction followed by quenching with B(OMe)₃ and H₂O₂ (Scheme B-3). The newly formed mono-protected MOM catechol was deprotected via aqueous acid and brominated. MOM₂CatBr was then generated via standard MOM protection conditions. The drawbacks to this synthetic route are that the second step uses *t*-BuLi in large amounts; being an early step to the synthesis of a major starting material for our syntheses. MOM₂CatBr is one of the first materials that new graduate students make in the Shultz group. Furthermore, there are two MOM protections that use a significant amount of highly carcinogenic MOMCl and two columns are implemented in purification; one after the introduction of the second oxygen to make the mono MOM-protected catechol and one after the MOM₂CatBr. Despite these disadvantages, this route maintained its status as the

primary route to MOM₂CatBr for over a decade and is still probably the best route for producing 100s of grams-scale quantities; although future, simpler routes typically provide enough material to last several months for most of our syntheses.

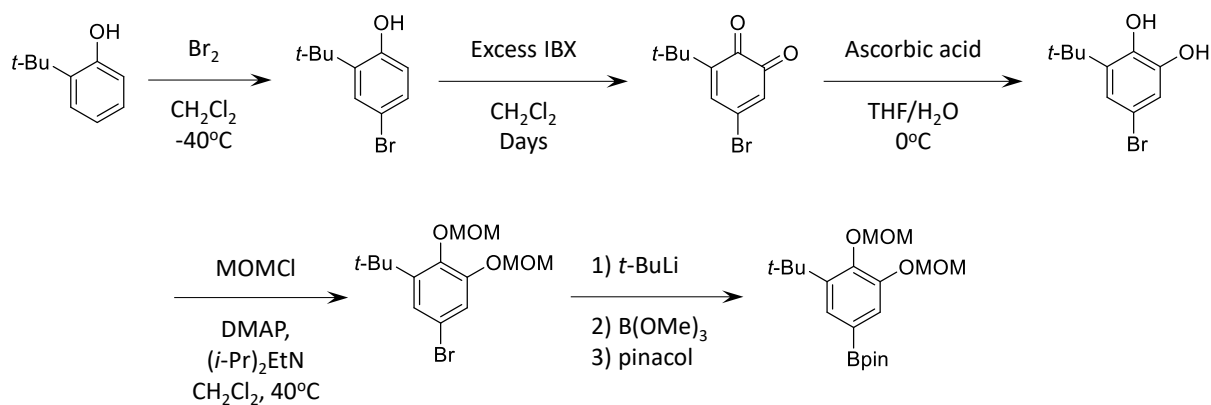
In 2002, Magdziak et al. published a paper on the selective synthesis of *ortho*-quinones from electron-rich phenols by oxidation with 1 eq. of iodoxybenzoic acid (IBX) (Scheme B-4A).³ They screened various solvents, but found DMF to be superior in that it required 14 h and proceeded in 85% yield (by NMR). This reaction fails for electron poor phenols and so the substrate scope is somewhat limited. While IBX is commercially available, it is rather expensive.

Scheme B-4. (A) IBX oxidation of electron-rich phenols. (B) IBX synthesis from 2-iodobenzoic acid and oxone in water.



Instead IBX can safely and easily be prepared by stirring a slurry of inexpensive 2-iodobenzoic acid and oxone in 70-80 °C water for 3 h and then precipitating by stirring for another 1.5 h at 0 °C (Scheme B-4B). This reaction can be used to make 10s to 100s of grams of IBX. Frigerio et al. introduced this method⁴ for preparing IBX in 1999 which is vastly favorable to previous synthetic methodology that used potassium bromate (KBrO₃) which is a shock-sensitive explosive and lead to past reports that IBX was explosive. IBX is also reported to begin decomposition in solvent between 95-100 °C or if left prolonged in water into 2-iodosobenzoic acid.⁴

Scheme B-5. IBX synthesis of MOM₂CatBr and MOM₂CatBpin.

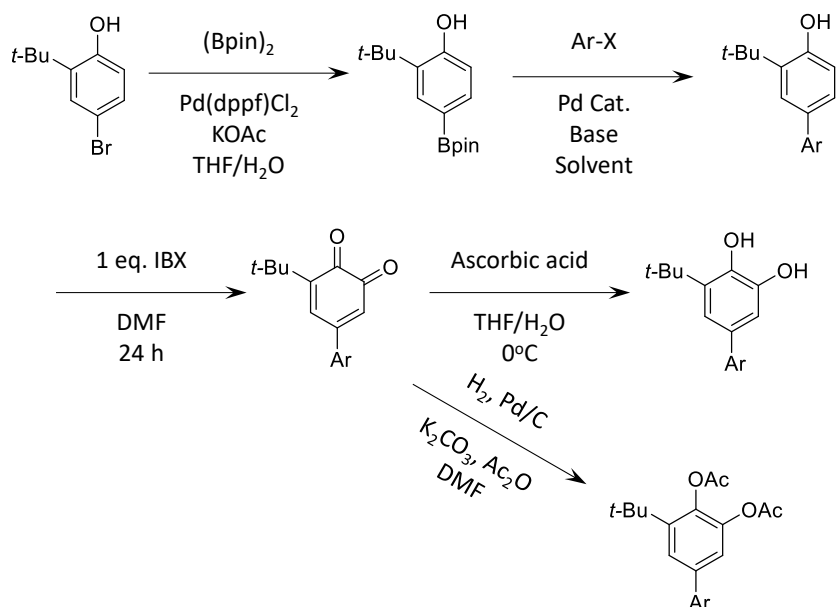


With the 2002 Magdziak et al. paper³ the synthesis of MOM₂CatBr and MOM₂CatBpin was redesigned (Scheme B-5) in 2013 to be less hazardous without the large amounts of carcinogen as the first step and pyrophoric reagent as the second step and more amenable to new and experienced students. Both DES and ZJY adopted this method. In this method, 2-*tert*-butylphenol was still the starting material which was then brominated and then subjected to the IBX oxidation in CH₂Cl₂, which took anywhere from 1-4+ days. CH₂Cl₂ was probably used for this step because DMF becomes very difficult to remove on larger scales. This oxidation step needed to be checked by ¹H NMR for completion and would occasionally require the addition of more IBX to drive the reaction to complete consumption the starting material. Work-up for the IBX reaction involved washing with saturated NaHCO₃ solution and then extracting with CH₂Cl₂. The quinone was then reduced to the catechol with ascorbic acid which could even be done by shaking in a separatory funnel. The catechol, which is unstable in ambient conditions, is then protected with MOMs. Upon work-up of this reaction the MOM₂CatBr is obtained as a dark red oil. Performing the lithium-halogen exchange and quenching with B(OMe)₃ followed by pinacol, would sometimes produce the MOM₂CatBpin in low yields (10-20%) as a yellow-orange oil after flash chromatography. Attempts to improve the yield of MOM₂CatBpin included

changing the quench to *i*-PrOBpin in case the pinacol cyclization was the issue. This did little to help, but simplified the reaction.

In DES and ZJY notebooks making MOM₂CatBpin became rare and almost completely faded probably due to poor yielding results and using a lot of starting material and column materials for little return. DES IV-35 began utilizing a Suzuki coupling with *bis*(pinacolato)diboron and 4-bromo-2-*tert*-butylphenol to make 2-(*tert*-butyl)-4-(4,4,5,5-tetramethyl-1,3,2-dioxaborolan-2-yl)phenol (PhOHBpin) in DMF (Scheme B-6). PhOHBpin

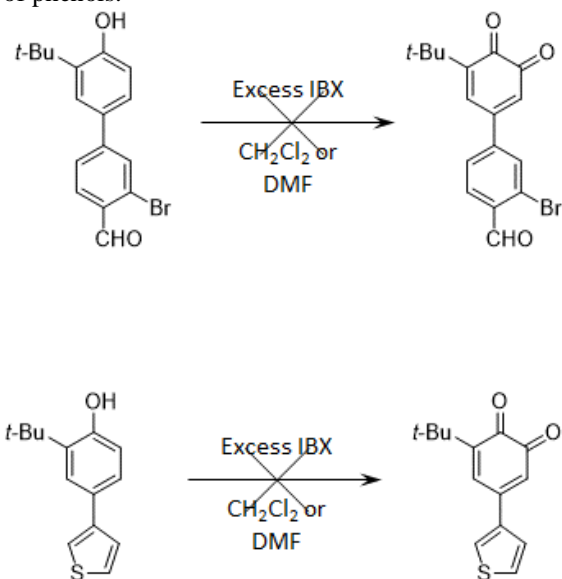
Scheme B-6. PhOHBpin synthetic procedure to prepare catechols.



could be used in subsequent Suzuki coupling to make the phenol-aryl bridge substrate. This could then be used with IBX in DMF to make the quinone and then reduced with ascorbic acid. DMF worked with this IBX oxidation because at this point in the syntheses, the amount of material is small enough that DMF can be washed away with water in a separatory funnel. The use of ascorbic acid as a reducing agent is important here as well. Other reducing agents that transform quinones to catechols, such as Na₂S₂O₄, will form an adduct with the aldehydes that are present in many of the group's donor-bridge-acceptor molecules. Without the aldehydes,

these sodium sulfoxide reagents work very efficiently. This protocol for making SQ-NNs enjoyed success using the generation of the quinone and reduction to catechol after the key carbon-carbon bond forming steps were complete; the Aviram-Ratner bicyclooctane bridged DBA biradical and several others were synthesized according to this protocol.^{5,6} The reduction for various quinones which is reported in Magdziak et al. and shown in Scheme B-6, is with Pd/C in a hydrogen atmosphere, which can be done in the presence of base and Ac₂O to immediately reduce the quinone and acetate protect the catechol for further reactions. This has

Scheme B-7. Challenging substrates for IBX oxidation of phenols.



not been a typical procedure for Shultz group biradicals because it is usually unnecessary and attempted cyclization with *bis*(hydroxylamine) (BHA) will form side-products in the presence of the acetates. However, in chapter **SQ-Az-NN** was synthesized using this procedure with some modifications because a free catechol on azulene results in decomposition (Chapter V).

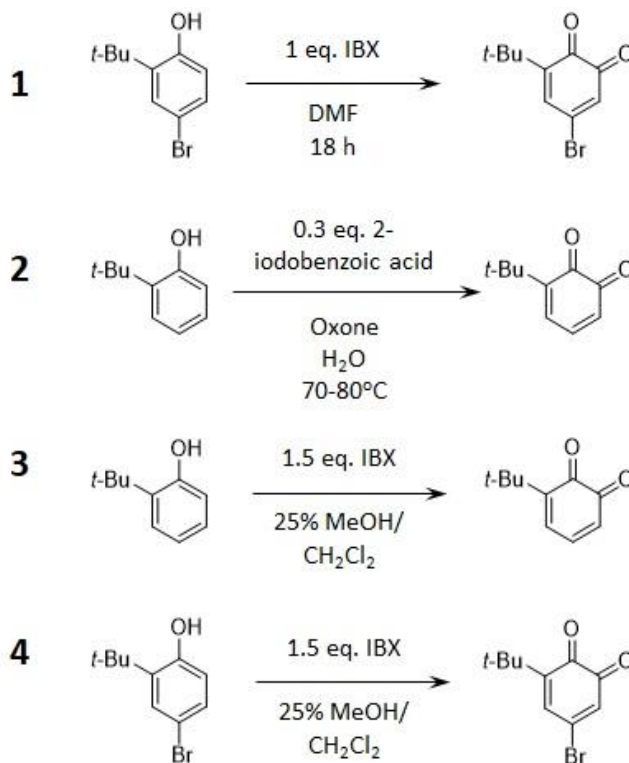
Unfortunately, the IBX oxidation of phenols to quinones is somewhat limited to electron-rich phenols and seems to have some inexplicable difficulty with other substrates. In PH IV-12 and PH IV-50, respectively both compounds shown in Scheme B-7 proved challenging for the

IBX oxidation; potentially the resulting quinones were too reactive. Both substrates yielded multiple products on TLC and ^1H NMR.

According to PH IV-60, mid-October and November of 2016, after a failed reaction to convert MOM_2CatBr to $\text{MOM}_2\text{CatBpin}$, Scheme B-5 was reexamined as a route to make $\text{MOM}_2\text{CatBpin}$, but needed some synthetic methodology work in order to make it viable. After examination of previous works detailed here, it seemed apparent that the synthesis was in peril after the introduction of IBX because the following products did not fit the physical description that they once had. MOM_2CatBr was previously reported as a light yellow oil (MGH II-38) and $\text{MOM}_2\text{CatBpin}$ was a colorless oil.⁷ After the introduction of IBX, MOM_2CatBr is a dark red oil and $\text{MOM}_2\text{CatBpin}$ is a yellow-orange oil after purification. In PH IV-58-98 the steps were reexamined starting with the IBX oxidation.

Going back to Magdziak et al., where they found more polar solvents seemed to work better with DMF being the best in terms of reaction time (14 h) and yield (85%), it was decided that CH_2Cl_2 may not be polar enough and over time the product could be decomposing because electron-rich quinones can be reactive and perform Diels-Alder reactions with themselves. The TLC of this IBX oxidation in CH_2Cl_2 consistently streaked up the plate; while other quinones, such as commercially available 3,5-di-*tert*-butyl-*o*-quinone would give one spot and so decomposition of the product would explain this observation. As shown in Scheme B-8 entry 1, 1 eq. of IBX was used on the phenol starting material in DMF and the reaction was complete within 18 h, without the need for additional IBX. DMF is a good solvent for IBX oxidations of phenols on a small scale, but even at 1 g of material, DMF can be very challenging to fully wash away with H_2O . The DMF could be removed by high vacuum, but any form of heating would need to be avoided to prevent the quinone from decomposing. Entry 2 in Scheme B-8 from PH

Scheme B-8. Phenol test reactions with IBX using different solvents.

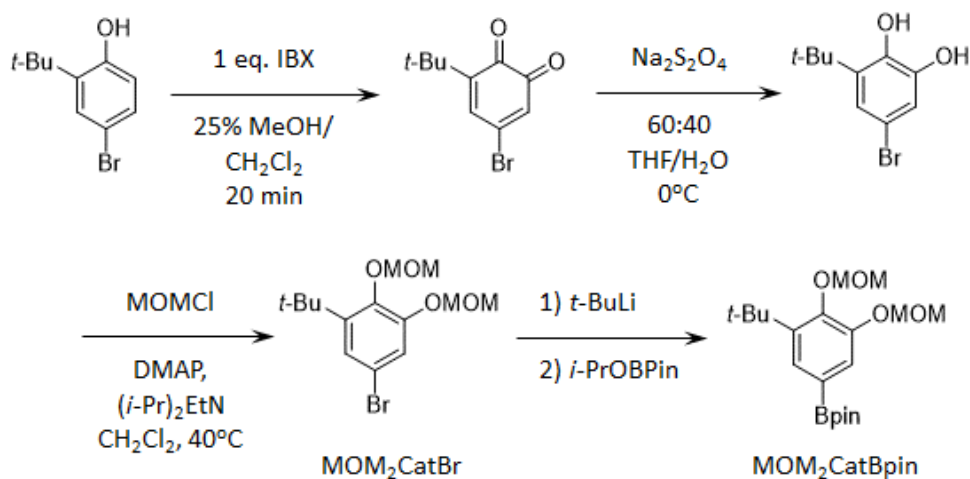


IV-66 was the attempted generation of catalytic IBX from 2-iodobenzoic acid in water which has been used to oxidize aliphatic alcohols and C-H activation of aromatic substituents.⁸ While the dark color of quinone formed, the reaction gave multiple products; probably due to the thermal instability of the product. From PH IV-68 shown in entries 3 and 4 of Scheme B-8 are attempts to increase the solvent polarity of CH₂Cl₂ by using it as a mixture with MeOH. In both of these reactions, IBX was added to a stirring solution of the phenol in the solvent mixture and within 1 min the reaction mixture changed colors from colorless to yellow to orange and to dark red. Dark red being the color reported in Magdziak et al. and the color our IBX oxidations in pure CH₂Cl₂ would become after 24 h. Entry 4 being the more desirable of the two, was analyzed by TLC after 2 h; a much shorter time than any reported IBX oxidation of phenol to quinone, however TLC revealed that the reaction was complete and ¹H NMR revealed that it was the desired product. Ideal TLC conditions for determining completion can be a variety of solvents and

mixtures including CH₂Cl₂, EtOAc/hexanes, Et₂O/hexanes; however, the most important point is to use an Et₃N treated TLC plate which makes the phenol run much slower than the quinone. However, it is important to note that quinones should *not* be chromatographed on Et₃N treated silica. This will result in undesirable side reactions probably produced from nucleophilic aromatic substitution that quinones can undergo with amines and other nucleophiles.

A scale-up of this IBX oxidation in PH IV-71 worked just as well and was analyzed by TLC after 1 h, which was also complete. However, a next-day attempted reduction with Na₂S₂O₄ in THF/H₂O failed and TLC of the quinone now indicated multiple spots on TLC. This confirmed that the quinone decomposes at room temperature on a short timescale and explains why the IBX oxidations that ran for multiple days do not work well. So, once the series of reactions shown in Scheme B-9 are started, up to MOM₂CatBr must be completed within the same day. The next round on PH IV-72 resulted in the reaction being carried to MOM₂CatBr with an overall yield from 4-bromo-2-*tert*-butylphenol of 67% and MOM₂CatBr as a light yellow oil after passing through a pad of silica. It was determined that the IBX oxidation of this phenol to quinone takes approximately 12 min in 25% MeOH/CH₂Cl₂, but running it for 20 min is

Scheme B-9. Redesigned synthesis using 25% MeOH/CH₂Cl₂ to accelerate the IBX oxidation of phenol.



common to ensure full completion of the reaction. An aqueous work-up with NaHCO_3 was the former method for removal of the iodobenzoic acid side products from the reaction, but this would sometimes form emulsions that were difficult to separate. The current method is flash chromatography on 12 g/g of phenol starting material of silica gel with 20% Et_2O / hexanes as eluent which is rather simple as the quinone can be observed moving through the column. Very short silica pads have also been used with hexanes as eluent, but the purity of the quinone increases with the column and is obtained as a dark solid. Increasing the purity and effectiveness of the IBX oxidation solved many of the other problems with the reaction. The reduction of the quinone to catechol is accomplished with $\text{Na}_2\text{S}_2\text{O}_4$ and occurs within 5 min and the reaction solution changes from highly colored to light yellow. The MOM protections proceed smoothly, but after work-up require a silica pad to remove some organic salts (probably $\text{HCl}\cdot(i\text{-Pr})_2\text{EtN}$).

The final step to make $\text{MOM}_2\text{CatBpin}$ now worked much better giving 60-70% yields routinely and 89% for a high. It was also no longer the yellow-orange oil, but a colorless solid at room temperature upon standing. Column chromatography was the common method for purifying $\text{MOM}_2\text{CatBpin}$, but it was found that having some solid $\text{MOM}_2\text{CatBpin}$ as a seed, the product could be selectively precipitated out of pentane in a $\sim 4^\circ\text{C}$ refrigerator over a night or two and be collected by decanting or pipetting off the pentane and drying the white solid that precipitates. This method of purification is superior to the flash chromatography that will routinely leave a faint yellow impurity in the product.

B.2. Experimental.

4-Bromo-2-*tert*-butylphenol. Dissolved 2-*tert*-butylphenol (30.05 g, 0.2000 mol) in ca. 250 mL of CH_2Cl_2 in a 500 mL oven-dried round-bottom flask. Attached an oven-dried addition funnel and a drying tube, then cooled the flask to -40°C in an ethylene glycol/ CO_2 bath. Methylene

chloride (~30 mL) was added to an addition funnel followed by addition of Br₂ (10.3 mL, 0.2004 mol). The Br₂/CH₂Cl₂ solution was added dropwise; stirred 1 h after the addition was complete, then warmed to room temperature. Water (50 mL) was added followed by NaHCO₃ (25.0 g, 0.298 mol) and the reaction stirred until evolution of CO₂ ceased. The reaction was transferred to a separatory funnel, washed with brine and then extracted the organic layer. Dried with MgSO₄ and concentrated under reduced pressure to give the title compound as a colorless oil (45.27 g, 99%).

5-Bromo-3-(*tert*-butyl)-*o*-quinone (BQ-Br). IBX (29.71 g, 106.1 mmol) was added to a stirred solution of 4-bromo-2-*tert*-butylphenol (18.70 g, 81.62 mmol) in 180 mL of 25% MeOH/CH₂Cl₂ in a room temperature water bath. Stirred for 20 min, then added 18 g of silica gel and concentrated to dryness under reduced pressure. Loaded the solid mixture onto a column of 224 g of silica gel and purified by flash chromatography using 10% Et₂O/hexanes as eluent. Concentrated to give the title compound as a dark solid (17.06 g, 86%).

5-Bromo-3-(*tert*-butyl)-catechol (CatBr). The quinone **BQ-Br** (17.06 g, 70.18 mmol) was dissolved in 90 mL of THF and 90 mL of H₂O, then Na₂S₂O₄ (15.88 g, 91.23 mmol) was added and stirred until the solution became light yellow. The reaction was transferred to a separatory funnel, extracted with hexanes and washed with brine. Separated and dried the organic layer with MgSO₄, then concentrated under reduced pressure to quantitatively give a yellow oil. No further purification was performed and the yellow oil was used directly in the next step.

5-Bromo-1-(*tert*-butyl)-2,3-bis(methoxymethoxy)benzene (MOM₂CatBr). **CatBr** from the previous step in 85 mL of CH₂Cl₂ and cooled to 0 °C under nitrogen. (*i*-Pr)₂EtN (85 mL, 490 mmol) and DMAP (0.100 g, 0.820 mmol) were added and the reaction was stirred for 10 min. A

1:1 (mol:mol by ^1H NMR integration) MOMCl/MeOAc solution (48 mL, 280 mmol) was added dropwise. A nitrogen-purged condenser was attached, and the reaction was heated to reflux overnight. After the reactions was cooled to room temperature, 100 mL of saturated NH_4Cl solution was added and the mixture was stirred for 20 min. Transferred reaction to a separatory funnel, washed with brined and extracted with CHCl_3 . The organic layer was separated and dried with MgSO_4 , filtered, and concentrated under reduced pressure. The dark red oil was loaded onto a silica pad and eluted with 20% Et_2O /hexanes, then concentrated to give the title compound as a yellow oil (20.14 g, 86%).

2-(3-(*tert*-Butyl)-4,5-bis(methoxymethoxy)phenyl)-4,4,5,5-tetramethyl-1,3,2-dioxaborolane (MOM₂CatBpin). MOM₂CatBr (5.96 g, 17.89 mmol) of in a 250 mL oven-dried round-bottom flask was purge-pumped 3x; backfilling with nitrogen. Then ca. 125 mL of anhydrous, deoxygenated THF was added and, under nitrogen, the flask was cooled to $-78\text{ }^\circ\text{C}$. Then *t*-BuLi in hexane (23 mL, 39 mmol) was added dropwise and the reaction was stirred for 10 min at $-78\text{ }^\circ\text{C}$ after the addition was complete. *i*-PrOBpin (4.4 mL, 22 mmol) was added dropwise, the reaction was stirred for 1.5 h at $-78\text{ }^\circ\text{C}$, and then the cold bath was removed and the reaction was allowed to warm to room temperature. The solvent was removed under reduced pressure, and the viscous orange oil was loaded onto a silica pad, eluted with 30% Et_2O /hexanes and concentrated. The resulting yellow oil was redissolved in minimal pentane and a piece of solid, existing MOM₂CatBpin was added and the product was precipitated out overnight in a $4\text{ }^\circ\text{C}$ refrigerator. The precipitate was washed gently with cold pentane which was pipetted off and then the title compound as a white solid was dried under a stream of nitrogen (6.05 g, 89%).

B.3. References.

- (1) Shultz, D. A.; Bodnar, S. H.; Vostrikova, K. E.; Kampf, J. W. *Inorg. Chem.* **2000**, *39* (26), 6091.
- (2) Kirk, M. L.; Shultz, D. A.; Zhang, J.; Dangi, R.; Ingersol, L.; Yang, J.; Finney, N. S.; Sommer, R. D.; Wojtas, L. *Chem. Sci.* **2017**, *8* (8), 5408–5415.
- (3) Magdziak, D.; Rodriguez, A. A.; Van De Water, R. W.; Pettus, T. R. R. *Org. Lett.* **2002**, *4* (2), 285–288.
- (4) Frigerio, M.; Santagostino, M.; Sputore, S. *J. Org. Chem.* **1999**, *64* (12), 4537–4538.
- (5) Stasiw, D. E.; Zhang, J.; Wang, G.; Dangi, R.; Stein, B. W.; Shultz, D. A.; Kirk, M. L.; Wojtas, L.; Sommer, R. D. *J. Am. Chem. Soc.* **2015**, *137* (29), 9222–9225.
- (6) Kirk, M. L.; Shultz, D. A.; Stasiw, D. E.; Lewis, G. F.; Wang, G.; Brannen, C. L.; Sommer, R. D.; Boyle, P. D. *J. Am. Chem. Soc.* **2013**, *135* (45), 17144–17154.
- (7) Shultz, D. A.; Hollomon, M. G.; Carolina, N. *Chem. Mater.* **2000**, *12* (2), 580–585.
- (8) Hussain, H.; Green, I. R.; Ahmed, I. *Chem. Rev.* **2013**, *113* (5), 3329–3371.

APPENDIX C: Progress Toward PhMeTh Twisted Rectifiers.

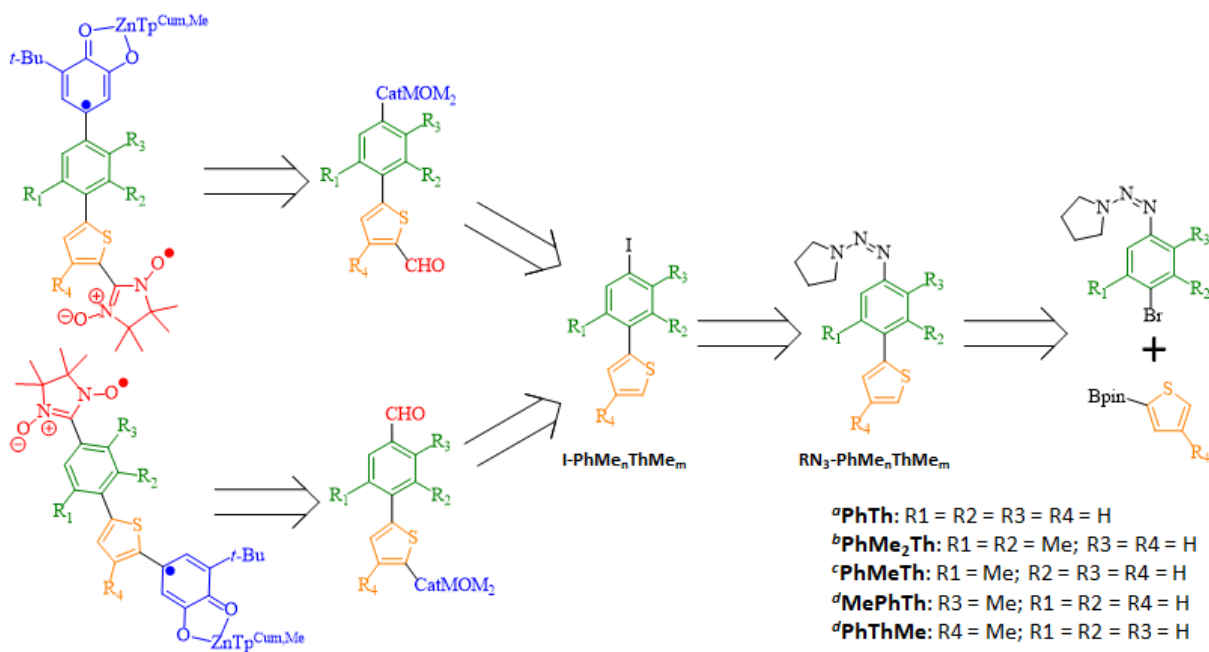
C.1. Introduction. During the syntheses of the **PhMe₂Th** torsional rectifiers discussed in Chapter IV, the first isomer that was successfully made, crystallized and had magnetometry data acquired on it was **SQ-PhMe₂Th-NN** which has an intra-bridge torsion of 82° indicating that the coupling would probably be minimal since the coupling varies by a function of the cosine of the torsion angles, squared.¹ The variable temperature paramagnetic susceptibility plots and fitting parameters supported this with a $J = 2 \text{ cm}^{-1}$. Given, that the bridge torsion would probably not differ greatly in **NN-PhMe₂Th-SQ** since the large torsion angle would not have any substituents varied that should greatly affect it, it was hypothesized that it too would give a low, ferromagnetic exchange coupling constant and the rectifying of this bridge would be minimal since if the donor and acceptor become completely decoupled, no rectification is observed.²

When this data was obtained, the desire was to have another set of compounds with a smaller intra-bridge torsion angle to help realize our goal of utilizing torsion to induce and evaluate molecular rectifiers. These compounds are the corresponding **PhMeTh** bridged biradicals, whose synthesis, as will be discussed, is rather simple employing the strategies used to synthesize **SQ-PhMe₂Th-NN** and **NN-PhMe₂Th-SQ**. The synthesis of these compounds was not completed because unfortunately while **SQ-PhMe₂Th-NN** took several months to provide crystals suitable for X-ray crystallography, **NN-PhMe₂Th-SQ** took nearly 1.5 years and newer X-ray instrumentation in order to provide a suitable structure.

C.2. Synthetic Discussion. It was realized that with the strategies implemented for the synthesis of **SQ-PhMe₂Th-NN** and **NN-PhMe₂Th-SQ**, at least five sets of isomers (Scheme C-1) could easily be synthesized from the same generic route from commercially available materials to

evaluate how intra-bridge, SQ-bridge, or NN-bridge torsion angles effect molecular rectifying behavior. Now it is possible to do so, but scientifically may or may not be worth doing so. In the retrosynthesis of Scheme C-1 the biradical complexes can be made by routine procedures from the corresponding **MOM₂Cat-B-CHO** molecules which have been made from **I-PhMe_nThMe_m** which has been made by the decomposition of triazene, **RN₃-PhMe_nThMe_m** in the presence of

Scheme C-1. Retrosynthesis of **PhMe_nTh**-bridged torsional rectifiers.



^a These isomers probably do not need to be synthesized because pyridine-thiophene (**PyTh**) from ref 3 serves as an analog.

^b Has been synthesized in Chapter IV.

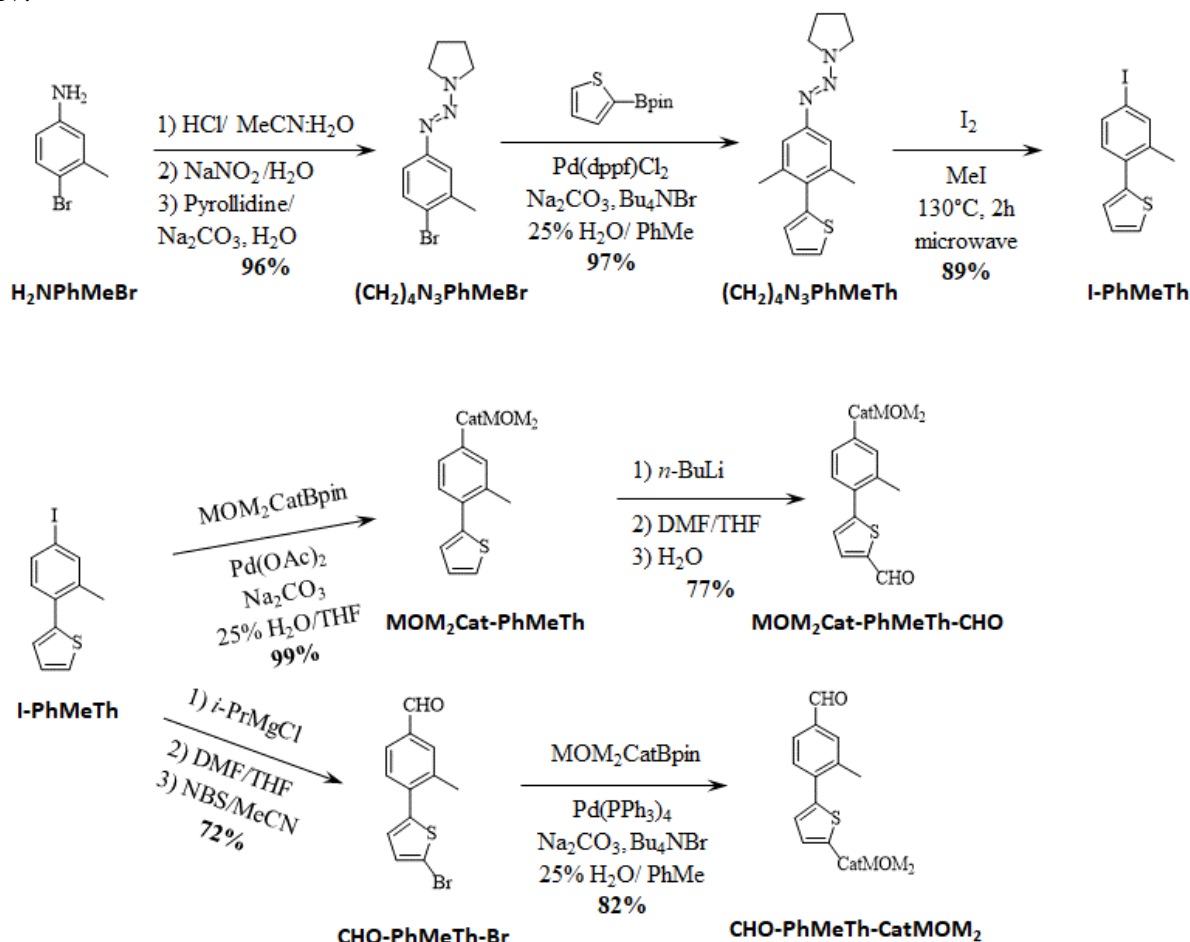
^c Synthesis is described in this APPENDIX.

^d May or may not be worth synthesizing depending on the results of **PhMe₂Th** and possibly **PhMeTh** if the latter's synthesis is completed and data is collected.

iodomethane at elevated temperature. **RN₃-PhMe_nThMe_m** could be made by Suzuki coupling with a thiophene-boropinacolate and the triazene of a corresponding, commercially available 4-bromoaniline (or commercially available aniline that is then brominated as described in Chapter IV) derivative. There are potentially five interesting sets of isomers that could be made with this synthetic procedure. The no methyl **PhTh** bridge is probably not worth making given that **PyTh**

satisfies this requirement closely enough.³ **PhMe₂Th**'s synthesis, characterization and data were discussed in Chapter IV. Progress toward the synthesis of **PhMeTh** is discussed as follows in this appendix. **MePhTh** and **PhThMe** are two sets of compounds for which synthesis has not begun, but if some **PhMe_nThMe_m** sets of compounds display rectifying behavior, these two sets of compounds could be used to evaluate the effect of donor-bridge and bridge-acceptor torsion

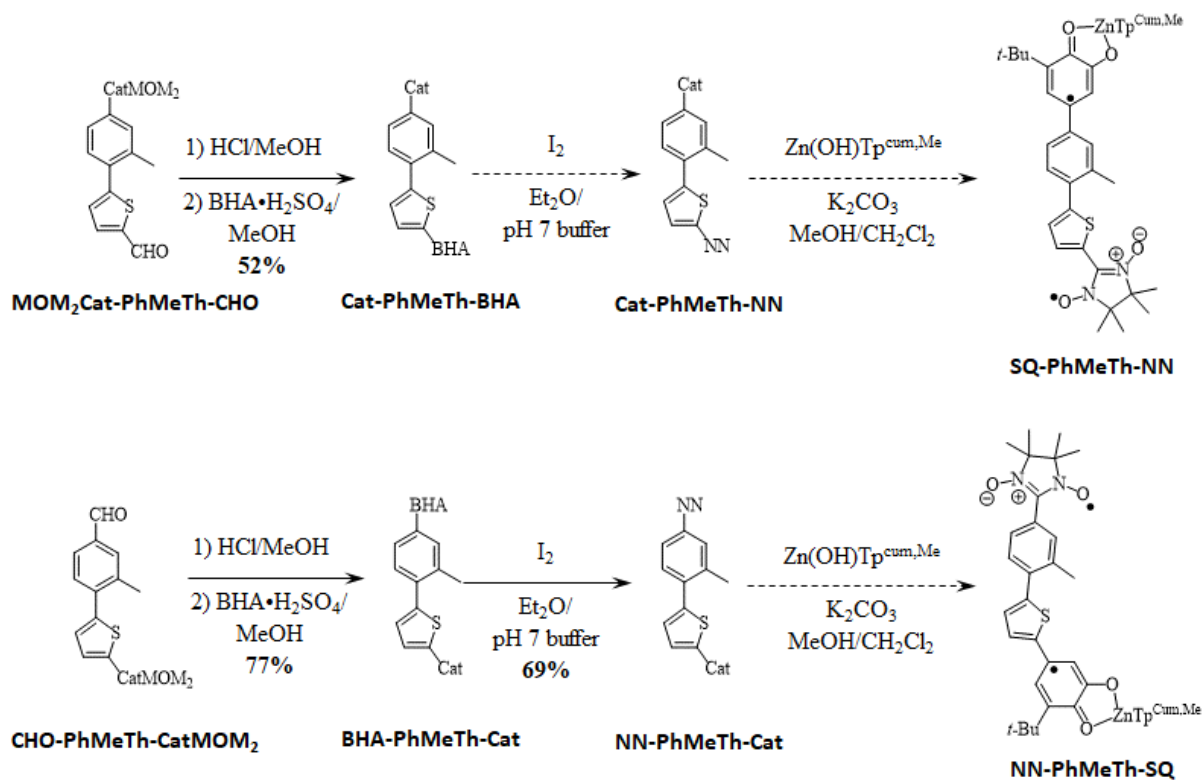
Scheme C-2. Synthesis of **PhMeTh** isomers up to MOM₂Cat-B-CHO by following the procedures from Chapter IV.



angles on the molecular rectification.

Scheme C-2 shows the synthesis of the **PhMeTh** bridge up to the MOM₂Cat-B-CHO of each isomer which were achieved in a few days by using the synthesis of the **PhMe₂Th** bridge discussed in Chapter IV as a model. Scheme C-3 shows the routine steps from MOM₂Cat-B-

Scheme C-3. Incomplete **PhMeTh**-bridge isomer steps from **MOM₂Cat-B-CHO** to **SQ-B-NN**.



CHO to SQ-B-NN. These steps were not completed, but **Cat-PhMeTh-BHA** and **NN-PhMeTh-Cat** were synthesized. The complexation and reduction of **NN-PhMeTh-Cat** to **NN-PhMeTh-SQ** was attempted, but proved unsuccessful. The EPR spectrum showed a large singlet and the nitronitroxide seemed to have disappeared. These syntheses were paused until crystal structures and magnetic data of both **PhMe₂Th** isomers from Chapter IV could be obtained as discussed in the introductory paragraphs of this appendix.

C.3. Experimental (*Incomplete*).

(E)-1-((4-Bromo-3-methylphenyl)diazenyl)pyrrolidine ((CH₂)₄N₃PhMeBr). 2-Bromo-3-methylaniline (3.97 g, 21.13 mmol) was added to a 100 mL round-bottom flask with 20 mL of MeCN, 20 mL of H₂O and 5 mL of 12 M HCl. The solution was cooled to -10 °C with an acetone/ice bath. A solution of NaNO₂ (1.628 g, 23.59 mmol) in 3 mL of H₂O was added dropwise; so that the temperature did not rise above 5 °C. The reaction was stirred for 30 min after the addition of NaNO₂, then it was poured into a 0 °C solution of Na₂CO₃ (11.208 g, 105.75 mmol) and pyrrolidine (2.8 mL, 34 mmol) in 120 mL of H₂O. The contents were stirred for 15 min, then the reaction was filtered through a Büchner funnel with filter paper, the solid orange product was collected by dissolving in Et₂O, drying with Na₂SO₄ and concentrating to give the title compound as an orange solid (4.57 g, 96%). ¹H NMR (400MHz, CDCl₃) δ = 7.45 (d, *J* = 8.6 Hz, 1 H), 7.30 (d, *J* = 2.3 Hz, 1 H), 7.12 (dd, *J* = 8.5, 2.3 Hz, 1 H), 3.78 (br. s., 4 H), 2.39 (s, 3 H), 2.03 (s, 4 H).

(E)-1-((3-Methyl-4-(thiophen-2-yl)phenyl)diazenyl)pyrrolidine ((CH₂)₄N₃PhMeTh). A 25 mL round-bottom flask containing 1.00 g (3.73 mmol) of (CH₂)₄N₃PhMeBr, 0.852 g (4.06 mmol) of 4,4,5,5-tetramethyl-2-(thiophen-2-yl)-1,3,2-dioxaborolane, 1.32 g (12.5 mmol) of Na₂CO₃, 90 mg (0.11 mmol) of Pd(dppf)Cl₂•CH₂Cl₂ and 62 mg (0.192 mmol) of Bu₄NBr in 8 mL of toluene and 3 mL of H₂O, under nitrogen was fitted with a nitrogen-purged, water-cooled condenser and then heated to 80 °C for 17 h. After which it was transferred to a separatory funnel, diluted with 10 mL of EtOAc and washed 2 times each with 10 mL of brine. The organic layer was separated, dried with Na₂SO₄ and concentrated under reduced pressure. The crude material was purified by deactivate silica gel flash chromatography with 0 to 10% EtOAc/hex to afford 0.977 g (97%) of the title compound as a yellow oil. ¹H NMR (400MHz, CDCl₃) δ = 7.39

(d, $J = 8.2$ Hz, 5 H), 7.32 (dd, $J = 4.9, 1.4$ Hz, 1 H), 7.35 - 7.28 (m, 2 H), 7.12 - 7.05 (m, 3 H), 3.81 (br. s., 4 H), 2.45 (s, 3 H), 2.04 (s, 4 H).

2-(4-Iodo-2-methylphenyl)thiophene (I-PhMeTh). Compound (CH_2)₄N₃PhMeTh (0.977 g, 3.60 mmol) was added to a microwave vial, dissolved in ca. 4 mL of MeI and purged with nitrogen for 10 min. The vial was placed in the microwave reactor and heated to 150 °C for 30 min. After which it was cooled to room temperature, concentrated under reduced pressure and purified via silica gel flash chromatography; eluting with 10% EtOAc/hex. The fractions were concentrated to give the product as a light yellow oil (0.964 g, 89%). ¹H NMR (400MHz, CDCl₃) $\delta = 7.65$ (d, $J = 2.0$ Hz, 1 H), 7.56 (dd, $J = 7.8, 2.0$ Hz, 1 H), 7.36 (dd, $J = 5.2, 1.2$ Hz, 1 H), 7.14 (d, $J = 7.8$ Hz, 1 H), 7.11 (dd, $J = 5.2, 3.6$ Hz, 1 H), 7.07 (dd, $J = 3.5, 1.2$ Hz, 1 H), 2.39 (s, 3 H).

2-(3'-(*tert*-Butyl)-4',5'-bis(methoxymethoxy)-3-methyl-[1,1'-biphenyl]-4-yl)thiophene (MOM₂Cat-PhMeTh). A 50 mL round-bottom flask containing compound **I-PhMeTh** (235 mg, 0.836 mmol), MOM₂CatBpin (319 mg, 0.838 mmol), Na₂CO₃ (222 mg, 2.09 mmol), Pd(OAc)₂ (2 mg, 0.009 mmol) and Bu₄NBr (32 mg, 0.099 mmol) in 8 mL of toluene and 3 mL of H₂O, under nitrogen was fitted with a nitrogen-purged, water-cooled condenser and then heated to 80 °C for 18 h. After which it was transferred to a separatory funnel, diluted with 10 mL of EtOAc and washed 2 times each with 10 mL of brine. The organic layer was separated, dried with Na₂SO₄ and concentrated under reduced pressure. The crude material was purified by deactivate silica gel flash chromatography with 2 to 15% EtOAc/hex to afford the title compound as a light yellow oil (430 mg, 100%).

5-(3'-(*tert*-Butyl)-4',5'-bis(methoxymethoxy)-3-methyl-[1,1'-biphenyl]-4-yl)thiophene-2-carbaldehyde (MOM₂Cat-PhMeTh-CHO). *n*-BuLi solution (1 mL, 2.5 mmol) was added

dropwise to a 25 mL round-bottom flask containing a solution of compound **MOM₂Cat-PhMeTh** (328 mg, 0.766 mmol) in 15 mL of THF at -78 °C. The reaction was stirred at this temperature for 1 h, then anhydrous DMF was added and stirred for 30 min while warming to room temperature. 0.5 mL of H₂O were added and the reaction was stirred for 3 h, then transferred to a separatory funnel, diluted with hexanes and washed with brine. The organic layer was separated, dried with Na₂SO₄ and concentrated under reduced pressure to afford 270 mg (77%) of the title compound as a colorless oil. ¹H NMR (400MHz, CDCl₃) δ = 9.91 (s, 1 H), 7.76 (d, *J* = 3.9 Hz, 1 H), 7.52 - 7.38 (m, 4 H), 7.20 (s, 3 H), 5.25 (s, 2 H), 5.24 (s, 2 H), 3.67 (s, 3 H), 3.53 (s, 3 H), 2.51 (s, 3 H), 1.39 (s, 9 H).

2-(5-(3'-(*tert*-Butyl)-4',5'-dihydroxy-3-methyl-[1,1'-biphenyl]-4-yl)thiophen-2-yl)-4,4,5,5-tetramethylimidazolidine-1,3-diol (Cat-PhMeTh-BHA). An aqueous solution of HCl (1 mL, 12 M) was added to a solution of compound **MOM₂Cat-PhMeTh-CHO** (270 mg, 0.594) in ca. 4 mL of MeOH and stirred overnight. The solution was transferred to a separatory funnel where it was extracted with Et₂O and washed with brine. The organic layer was separated, dried with MgSO₄ and concentrated. BHA•H₂SO₄ (220 mg, 0.893 mmol) and K₂CO₃ (86 mg, 0.622 mmol) were added, the flask was purge-pumped three times, 6 mL of anhydrous MeOH were added and the mixture was stirred at room temperature for two days. The reaction mixture was poured into ca. 100 mL of stirring brine and then the precipitate was collected via vacuum filtration. The precipitate was dissolved in Et₂O, dried with Na₂SO₄ and concentrated under reduced pressure to afford the title compound as a white solid (152 mg, 52%).

4-(5-Bromothiophen-2-yl)-3-methylbenzaldehyde (CHO-PhMeTh-Br). A solution of *i*-PrMgCl in THF (1.65M, 3.5 mL, 5.8 mmol) was added dropwise to a 0 °C cooled solution of **I-PhMeTh** (0.350 g, 1.17 mmol) in 15 mL of THF and stirred for 1 h at this temperature.

Anhydrous DMF (0.55 mL, 0.519 mmol) was added dropwise, then the reaction was stirred at 0 °C for 30 min, then warmed to room temperature and stirred for 2 h. 0.5 mL of H₂O was added and the reaction was stirred overnight. The reaction was concentrated under reduced pressure, then purified by silica gel flash chromatography with 100% hexanes. The fractions were concentrated and the formylated product (0.184 g, 0.907 mmol) was redissolved in ca. 10 mL of MeCN and NBS (0.180 g, 1.01 mmol) was added as a solid, the reaction was shielded from light and stirred for 18 h. The solution was concentrated under reduced pressure, the residue was redissolved in hexanes, filtered through a celite pad and concentrated to give the title compound as a colorless solid (0.235 g, 72%). ¹H NMR (400MHz, CDCl₃) δ = 9.99 (s, 1 H), 7.77 (s, 8 H), 7.72 (d, *J* = 7.8 Hz, 1 H), 7.51 (d, *J* = 7.8 Hz, 1 H), 7.09 (d, *J* = 3.9 Hz, 1 H), 6.93 (d, *J* = 3.9 Hz, 1 H), 2.52 (s, 3 H). ¹³C NMR (101MHz, CDCl₃) δ = 191.5, 142.9, 138.9, 136.3, 135.3, 132.0, 130.3, 130.1, 127.6, 127.2, 113.1, 21.1.

4-(5-(3-(*tert*-Butyl)-4,5-bis(methoxymethoxy)phenyl)thiophen-2-yl)-3-methylbenzaldehyde (CHO-PhMeTh-CatMOM₂). A 50 mL round-bottom flask containing **CHO-PhMeTh-Br** (300 mg, 1.02 mmol), MOM₂CatBpin (411 mg, 1.08 mmol), Na₂CO₃ (229 mg, 2.16 mmol), Pd(PPh₃)₄ (12 mg, 0.010 mmol) and Bu₄NBr (35 mg, 0.110 mmol) in 12 mL of toluene and 4 mL of H₂O, under nitrogen was fitted with a nitrogen-purged, water-cooled condenser and then heated to 80 °C for 16 h. After which it was transferred to a separatory funnel, diluted with 10 mL of EtOAc and washed 2 times each with 10 mL of brine. The organic layer was separated, dried with Na₂SO₄ and concentrated under reduced pressure. The crude material was purified by deactivate silica gel flash chromatography with 2 to 15% EtOAc/hex to afford the title compound as a light yellow oil (354 mg, 70%).

2-(4-(5-(3-(*tert*-Butyl)-4,5-dihydroxyphenyl)thiophen-2-yl)-3-methylphenyl)-4,4,5,5-tetramethylimidazolidine-1,3-diol (BHA-PhMeTh-Cat). A solution of 12M aqueous HCL (1 mL) was added to a solution of **CHO-PhMeTh-CatMOM₂** (414 mg, 0.883) in ca. 4 mL of MeOH and stirred overnight. The solution was transferred to a separatory funnel where it was extracted with Et₂O and washed with brine. The organic layer was separated, dried with MgSO₄ and concentrated. BHA•H₂SO₄ (228 mg, 0.926 mmol) of and K₂CO₃ (88 mg, 0.637 mmol) were added, the flask was purge-pumped three times, 6 mL of anhydrous MeOH were added and the mixture was stirred at room temperature for two days. The reaction mixture was poured into ca. 100 mL of stirring brine and then the precipitate was collected via vacuum filtration. The precipitate was dissolved in Et₂O, dried with Na₂SO₄ and concentrated under reduced pressure to afford the title compound as a white solid (347 mg, 77%).

2-(4-(5-(3-(*tert*-Butyl)-4,5-dihydroxyphenyl)thiophen-2-yl)-3-methylphenyl)-4,4,5,5-tetramethyl4,5-dihydroimidazol-3-oxide-1-oxyl (NN-PhMeTh-Cat). To a solution of **BHA-PhMeTh-Cat** (100 mg, 0.196 mmol) dissolved in 10 mL of Et₂O and 10 mL of 1M pH 7 phosphate buffer, was added I₂ (50 mg, 0.196 mmol) dissolved in 3 mL of Et₂O dropwise, with vigorous stirring, allowing the I₂ color to disappear in between each drop, until the I₂ color persisted. The reaction was transferred to a separatory funnel, diluted with 5 mL of Et₂O, washed quickly with 5 mL of saturated Na₂S₂O₃ solution and then washed with two portions of 5 mL of brine. The organic layer was separated, dried with Na₂SO₄ and concentrated under reduced pressure to afford the title compound as a blue solid (68 mg, 69%).

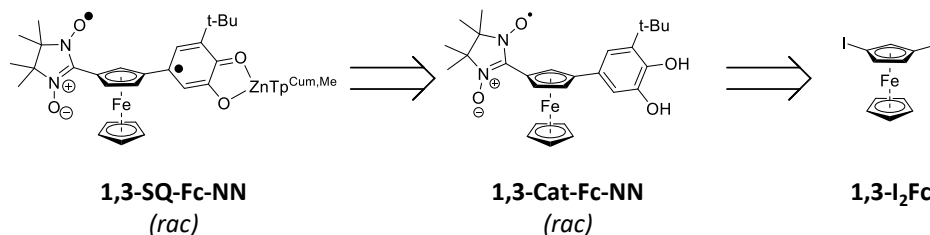
C.4. References

- (1) Stasiw, D. E.; Zhang, J.; Wang, G.; Dangi, R.; Stein, B. W.; Shultz, D. A.; Kirk, M. L.; Wojtas, L.; Sommer, R. D. Determining the Conformational Landscape of σ and π Coupling Using Para -Phenylene and “Aviram–Ratner” Bridges. *J. Am. Chem. Soc.* **2015**, *137* (29), 9222–9225. <https://doi.org/10.1021/jacs.5b04629>.
- (2) Aviram, A.; Ratner, M. A. Molecular Rectifiers. *Chem. Phys. Lett.* **1974**, *29* (2), 277–283. [https://doi.org/10.1016/0009-2614\(74\)85031-1](https://doi.org/10.1016/0009-2614(74)85031-1).
- (3) Kirk, M. L.; Shultz, D. A.; Zhang, J.; Dangi, R.; Ingersol, L.; Yang, J.; Finney, N. S.; Sommer, R. D.; Wojtas, L. Heterospin Biradicals Provide Insight into Molecular Conductance and Rectification. *Chem. Sci.* **2017**, *8* (8), 5408–5415. <https://doi.org/10.1039/C7SC00073A>.

APPENDIX D: Progress toward the Donor-Bridge-Acceptor, SQ-Fc-NN.

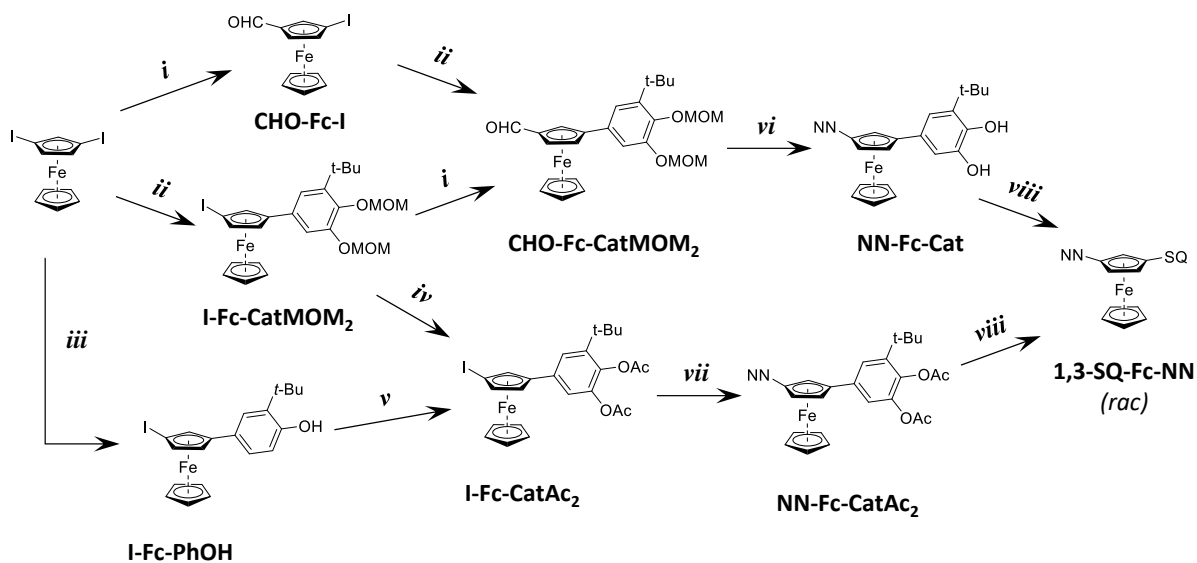
D.1. Synthetic Discussion. 1,3-Diiodoferrocene (**1,3-I₂Fc**) was synthetically accessible by the literature procedure by Zirakzadeh et al.¹ for the synthesis of **1,3-SQ₂Fc** in Chapter V and was therefore deemed a viable starting point for the synthesis of **1,3-SQ-Fc-NN** as shown in

Scheme D-1. Retrosynthesis of racemic **1,3-SQ-Fc-NN**.



Scheme D-1. It should be mentioned that asymmetrically substituted ferrocene derivatives are chiral and because this synthesis involves the asymmetric transformation of a symmetrically substituted ferrocene the subsequent products will be racemic mixtures. Scheme 2 shows several

Scheme D-2. Possible synthetic routes to the racemic mixture of **1,3-SQ-Fc-NN** biradicals.

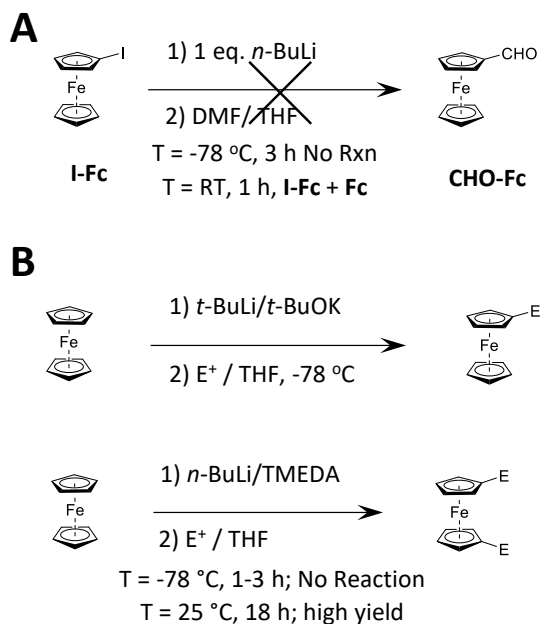


i) *n*-BuLi or *i*-PrMgCl, then DMF *ii*) MOM₂CatBpin, Pd(OAc)₂, Na₂CO₃, 25% H₂O/THF *iii*) HOPhBpin, Pd(OAc)₂, Na₂CO₃, 25% H₂O/THF *iv*) H⁺, then Ac₂O, Et₃N, CH₂Cl₂, 1h or 1 drop H₂SO₄, Ac₂O *v*) IBX, DMF, then Na₂S₂O₄, then Ac₂O, Et₃N, CH₂Cl₂ *vi*) H⁺, then BHA, then I₂, Et₂O, pH 7 buffer *vii*) NNAuPPh₃, Pd(PPh₃)₄, THF *viii*) Zn(OH)TP^{Cum,Me}, K₂CO₃, MeOH/CH₂Cl₂, then O₂.

possible routes for arriving at the racemic mixture of **1,3-SQ-Fc-NN** biradicals from **1,3-I₂Fc**. From 1,3-diiodoferrocene, the topmost route shows either lithium-halogen or magnesium-halogen exchange followed by quenching with DMF to afford the **CHO-Fc-I** racemate. From here the MOM₂Cat may be installed via Suzuki coupling with MOM₂CatBpin. Alternatively, if mono-formylation of **1,3-I₂Fc** becomes difficult, these steps can be done in reverse order with the MOM₂Cat being installed first, succeeded by metal-halogen exchange and followed by quenching with DMF. Either way the endpoint will be **CHO-Fc-CatMOM₂**. From here, the common steps to SQ-B-NN are employed in steps *vii* and *viii*.

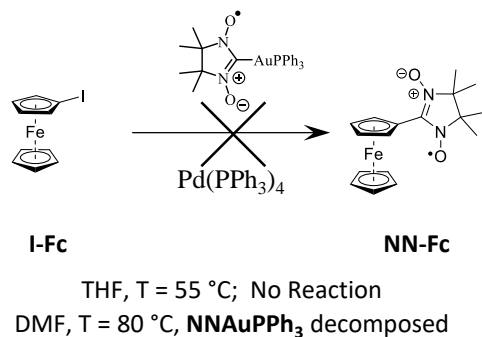
If for some reason the top routes are inaccessible either by reactivity or decomposition, of which some issues will be discussed later in this appendix, another alternative is presented that employs acetate protection of the catechol and the palladium-mediated cross-coupling reaction with **NNAuPPh₃** the latter being developed by Okada et al.² This other route can take **CHO-Fc-CatMOM₂**, remove the MOM groups and re-protect with acetates or employ a Suzuki coupling with HOPhBpin to give **I-Fc-PhOH**, which with IBX and the procedure presented by Magdziak et al.,³ may be used to oxidize the phenol to the quinone. However, in a modified procedure to the one presented by Magdziak et al.,³ the quinone will need to be reduced by either Na₂S₂O₄ or ascorbic acid, then protected with acetates to give **I-Fc-CatAc₂**. Catalytic hydrogenation with palladium on carbon cannot be used in this instance as the iodide will most likely react with the palladium; at best poisoning the catalyst and at worst producing undesired products. **I-Fc-CatAc₂** can be reacted with **NNAuPPh₃** and palladium catalyst to install the NN and finally **NN-Fc-CatAc₂** can be deprotected *in situ* and complexed with Zn(OH)Tp^{Cum,Me} to form **1,3-SQ-Fc-NN** as a racemic mixture.

Scheme D-3. **A)** lithium-halogen exchange method to make CHO-Fc and **B)** aggressive conditions employed for the deprotonation of ferrocene.



Test reactions were performed on iodoferrocene in an attempt to identify the easiest approach to make **1,3-SQ-Fc-NN**. Scheme D-3A shows the use of 1 eq. of *n*-butyl lithium to perform a lithium-halogen exchange on iodoferrocene and then quench with DMF at $-78\text{ }^{\circ}\text{C}$ to make **CHO-Fc**, which has been used efficiently to make aryl aldehydes from aryl halides. However, in the case of iodoferrocene the result was either starting material or ferrocene, the latter is more concerning in that it would suggest that **CHO-Fc** cannot be made like this. However, sluggish reactivity may be dealt with. Scheme D-3B shows two reactions that involve the deprotonation of ferrocene, requiring aggressive conditions for a successful reaction. The first reaction, at $-78\text{ }^{\circ}\text{C}$, Schlosser's base is used to increase the kinetic reactivity of *t*-BuLi to successfully deprotonate ferrocene, then follow by quenching with an electrophile, as was performed in Chapter 5 to make 1-bromoferrocene in a 52% yield. The second reaction shows the double deprotonation of ferrocene at the 1,1' positions which must be done with TMEDA, but at $-78\text{ }^{\circ}\text{C}$ for 3 h produces no reaction, but a high yield may be obtained by adding *n*-BuLi to

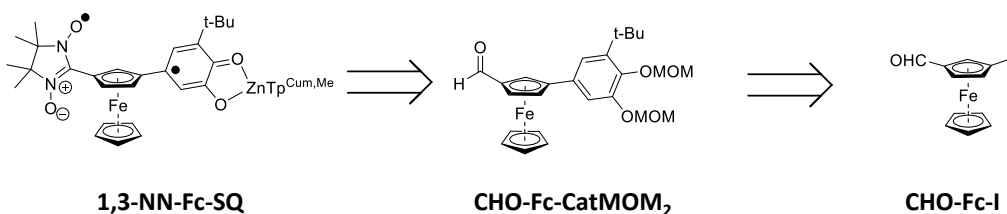
Scheme D-4. Unsuccessful palladium-mediated cross-coupling reaction of iodoferrocene with **NNAuPPh₃**.



the solution of ferrocene at room temperature and stirring overnight, then quenching the reaction with an electrophile, as was also done in Chapter 5 to make 1,1'-bis(tributylstannyl)ferrocene on route to 1,1'-diiodoferrocene.

Scheme D-4 shows the attempted palladium-mediated cross-coupling of iodoferrocene with **NNAuPPh₃** which despite working quite well in the case of aryl iodides and iodoazulenes as prescribed by Okada et al.^{2,4} failed to work with iodoferrocene. In an attempt to get the reaction warmed to perhaps facilitate some reactivity, the solvent was switched to DMF and heated at 80 °C. Unfortunately, this led to decomposition of **NNAuPPh₃** into the corresponding iminonitroxide and left iodoferrocene untouched. It is unclear if it was the temperature or solvent or both that led to the decomposition of the **NNAuPPh₃**. Okada et al.² screened only three palladium catalysts, including Pd(PPh₃)₂Cl₂, Pd₂(dba)₃•CHCl₃ and Pd(PPh₃)₄; determining that Pd(PPh₃)₄ was the best for this transformation, but only used THF as their solvent. It is conceivable that another catalyst/ solvent combination may provide the desired **NN-Fc** and make

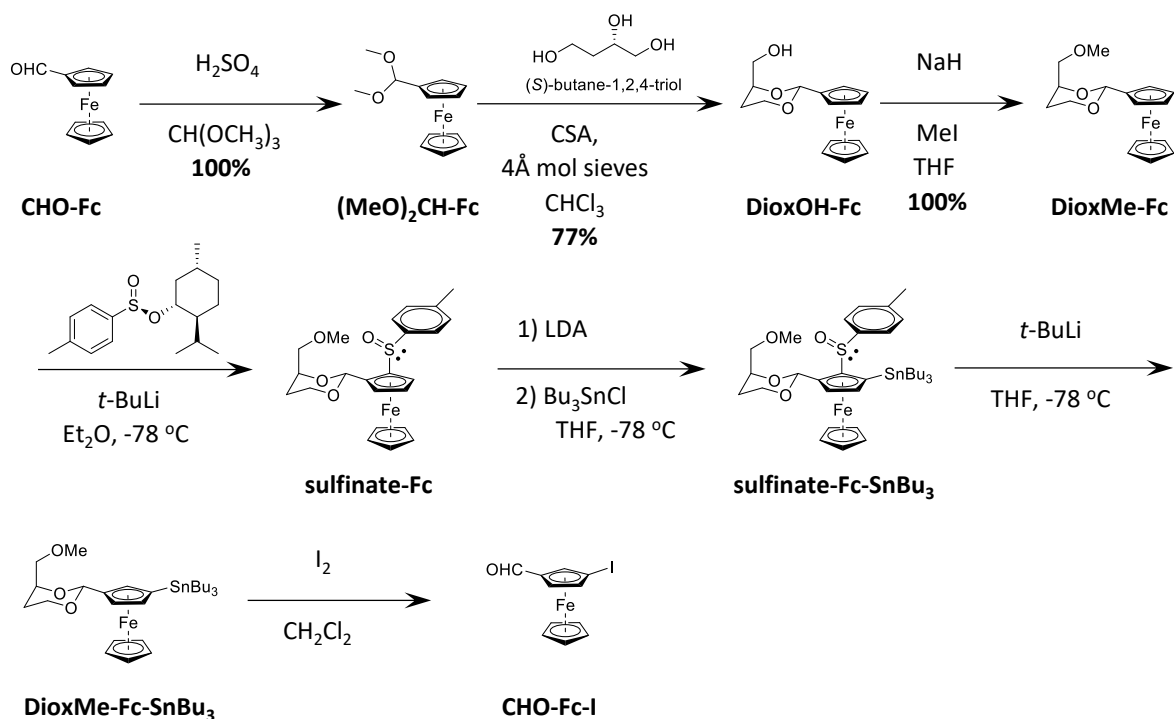
Scheme D-5. Retrosynthesis of enantiopure **1,3-NN-Fc-SQ** from CHO-Fc-I.



this the most viable route to making **1,3-SQ-Fc-NN**. Other catalysts such as Pd(dppf)Cl₂ or PEPPSI-*i*-Pr and solvents should be investigated for this transformation. It is worth mentioning that Pd(OAc)₂ was attempted in a test reaction on iodobenzene and this resulted in only starting material under conditions where Pd(PPh₃)₄ provided full conversion as indicated by TLC.

Unless these blockades are overcome, the synthetic routes presented in Scheme D-2 are going to be unsuccessful. Another synthesis presented in Scheme 5 shows the retrosynthesis of one enantiomer of **1,3-SQ-Fc-NN** (or in this case, **1,3-NN-Fc-SQ**, to introduce a convention to discuss each enantiomer) from enantiopure **CHO-Fc-I**. Given the shortcomings of the other reactions and that this route provides an enantiopure biradical, this route was pursued. Scheme D-6 shows the synthesis of **CHO-Fc-I** as described by Ferber et al.⁵ This synthesis starts from ferrocene-1-carbaldehyde and implements a chiral dioxane as a directing group for the enantioselective subsequent reactions. This chiral dioxane, precursor being (*S*)-butane-1,2,4-triol, must be installed by *trans*-acetalization of the dimethyl acetal of ferrocene-1-carboxyaldehyde ((**MeO**)₂**CH-Fc**) because the free aldehyde will not cyclize and higher temperatures should be avoided to prevent racemization of the (*S*)-butane-1,2,4-triol. Furthermore, the *trans*-acetalization reaction must be performed exactly as described⁶ and in the experimental section of this appendix which involves rigorous drying and scrupulously anhydrous conditions otherwise transient water will regenerate **CHO-Fc** from (**MeO**)₂**CH-Fc** rather than produce **DioxOH-Fc**.⁶ However, if done correctly, **DioxOH-Fc** can be obtained in decent yields after precipitation of the crude material from toluene. Important detail to mention is that while ref 6 reports the ¹H-NMR chemical shifts in CDCl₃, it is better to use DMSO-*d*₆ and use the chemical shifts in the experimental of this appendix because depending on the CDCl₃ that is used, very different NMR spectra can be obtained. Figure D-1 shows the ¹H-NMR spectra of

Scheme D-6. Synthesis of enantiopure **CHO-Fc-I** as described by Ferber et al.



DioxOH-Fc in DMSO- d_6 , CDCl_3 in green, which matches literature⁶ values and in red, CDCl_3 same bottle of chloroform, 2 months older different batch of **DioxOH-Fc**, but the same batch as the DMSO- d_6 NMR which is correct and shows the triplet for the proton on the alcohol at *ca.* $\delta = 4.65$. The DMSO and green CDCl_3 spectra are very similar as they have the correct number of peaks, integrations and splittings, but are starkly contrasted with the red CDCl_3 spectrum where the peaks are very broad, integrations are incorrect and some peaks are absent. It is known that chloroform decomposes over time in the presence of light and oxygen, usually it does not impact the collection of NMR spectra, but in this instance, it dramatically changes the acquired spectra. In fact, it is best to use DMSO for all $^1\text{H-NMR}$ spectra involving these ferrocene derivatives as another extreme example of this will be demonstrated later.

The methyl protection of the free alcohol consistently provides quantitative yields and proceeds without incident. The next reaction involves the stereoselective deprotonation of the

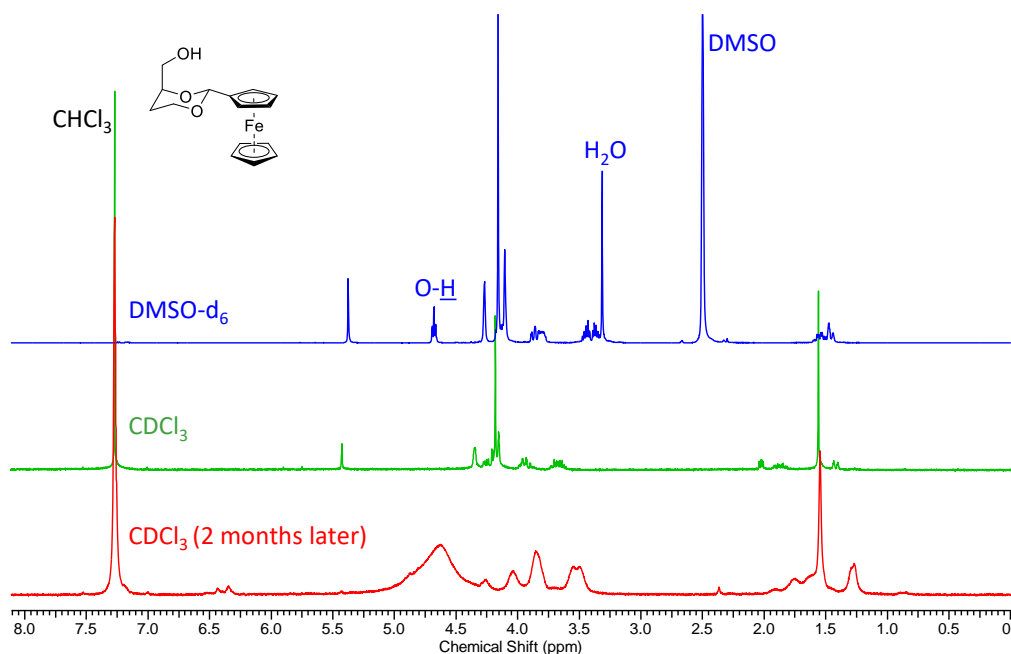


Figure D-1. $^1\text{H-NMR}$ spectra of **DioxOH-Fc** in DMSO-d_6 , CDCl_3 and aged CDCl_3 .

ferrocene proton *ortho* to the chiral dioxane so that the electrons from the methoxy oxygen can stabilize the lithiation at that position. This deprotonation is performed with *t*-BuLi in Et_2O , which for best results the Et_2O should be properly distilled from sodium/benzophenone and purged with argon immediately prior to this reaction. The lithiated ferrocene is quenched with a chiral sulfinate, which in turn is a strongly *ortho*-directs the next lithiation by LDA and successive quench with Bu_3SnCl to give **sulfinate-Fc-SnBu₃**. After this, the sulfinate is removed with *t*-BuLi and quenching with MeOH to protonate the ferrocene at the 2-position, giving **DioxMe-Fc-SnBu₃**. These reactions and purifications work as described by Ferber et al.⁵

The final step to **CHO-Fc-I** involves replacing the tributyltin group with iodine and removing the chiral dioxane. Ferber et al. does this with the addition of solid I_2 to a solution of **DioxMe-Fc-SnBu₃** in CH_2Cl_2 , which after they describe as being stirred overnight and purification on silica gel, gives **CHO-Fc-I**.⁵ In the replication their synthesis, it was found that the chiral dioxane was more robust and was not removed by what is probably transient HI

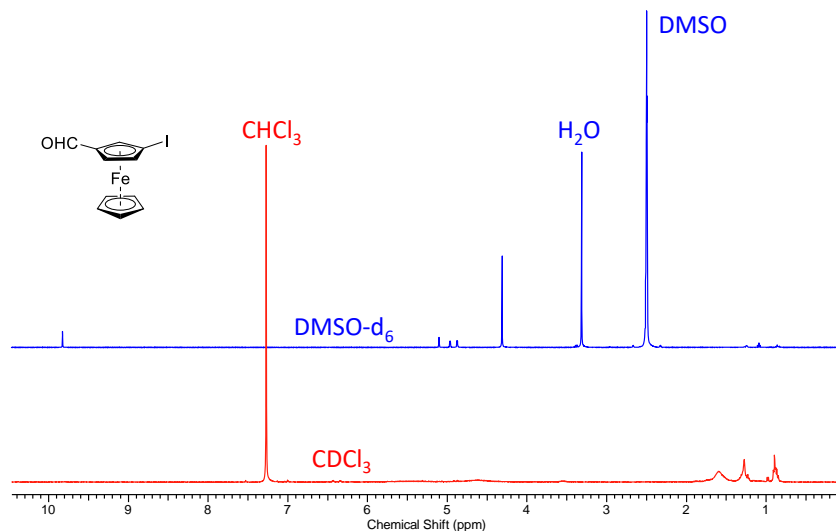
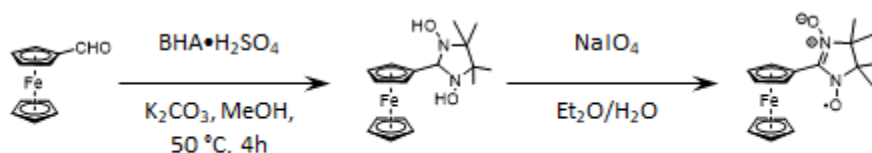


Figure D-2. $^1\text{H-NMR}$ Spectra of CHO-Fc-I in DMSO and CDCl_3 .

overnight and remained intact through purification. Also, after purification there were alkyl tin byproducts still remaining in the product. It was discovered that the tributyltin groups were replaced by iodine in less than 2 h after addition of iodine and the chiral dioxane could then be removed by stirring in MeOH with a couple drops of 12 M HCl in 30 minutes or less. After an aqueous work-up involving the neutralization of the acid with NaHCO_3 and concentration, the same purification for the synthesis of **1,3-I₂Fc** was performed to efficiently remove the tin byproducts. This involves stirring the crude material with KF in MeOH, followed by filtration through celite, concentration, dissolving the crude product in hexanes, filtration through celite again and eluting through a quick basic alumina column. A lengthier work-up, but one that easily and efficiently removes alkyl tin byproducts. Neutralization of the HCl with NaHCO_3 is very important as the next step involves KF and remaining acid will make highly toxic HF. Figure D-2 shows another example of acquiring $^1\text{H-NMR}$ spectra of these ferrocene derivatives in CDCl_3 versus DMSO-d_6 . Both spectra are from the same batch of **CHO-Fc-I**, as can be seen the DMSO

Scheme D-7. Successful route for ferrocene-1-nitronylnitroxide.



spectrum displays the appropriate protons where CDCl_3 seems to only show minor impurities with the product's peaks being broadened so much that they have vanished into the baseline.

From **CHO-Fc-I** to **1,3-NN-Fc-SQ** the synthesis is fairly rigid (Scheme D-4). The first step is a Suzuki coupling with $\text{MOM}_2\text{CatBpin}$ which for the iodoferrocene or any aryl iodide, $\text{Pd}(\text{OAc})_2$ is the best bet for a palladium catalyst⁷ and in $\text{H}_2\text{O}/\text{THF}$ as the THF seems to stabilize or solubilize the reactive palladium species instead of toluene where reactions generally do not proceed and give black palladium plated out on the sides of the flask (Chapter V). It is important to note that **CHO-Fc-CatMOM₂** is *not* a stable compound. It will begin to decompose over a period of days providing a dark brown solid from the orange-red oil of the product. Slightly decomposed product can be purified by passing through a silica pad as the dark brown material remains at baseline and there does not seem to be any organic-soluble decomposition components. This compound was successfully deprotected by heating with 0.05 eq. of *p*-TsOH in MeOH to 60 °C for several hours and monitoring closely by TLC. Deprotections that are performed over a longer period of time or with higher concentration of acids result in significant decomposition; producing a dark brown material that does not move on TLC. Unfortunately, despite a test reaction (Scheme D-7) that indicated ferrocenecarboxaldehyde could be cyclized with $\text{BHA}\cdot\text{H}_2\text{SO}_4$ and K_2CO_3 in MeOH at elevated temperature, the corresponding **BHA-Fc-Cat** compound could not be made easily due to significant decomposition to the dark brown solid. Figure D-3 shows the ^1H NMR of the reaction mixture in deuterated DMSO. The top (green) spectrum is just in DMSO and displays the characteristic methine proton at $\delta = 5.0$ indicating the

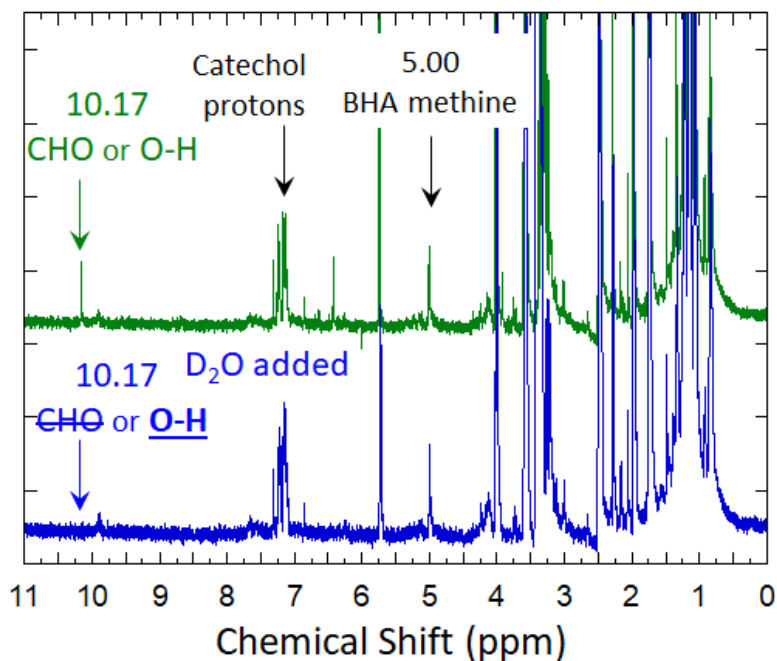


Figure D-3. $^1\text{H-NMR}$ of the BHA cyclization of 1,3-CHO-Fc-Cat using the reaction conditions from **Scheme D-5** taken in DMSO-d_6 (green) and with a drop of D_2O added.

cyclization is proceeding, it shows the presence of the aromatic catechol protons indicating that at least some of the catechol is intact and also a proton at $\delta = 10.17$. This latter proton can be only the aldehyde indicating the reaction is not complete, only an O-H indicating reaction completion, or a mixture of the two. The bottom (blue) spectrum is with a drop of D_2O added and shaken to exchange the proton if it is an O-H. Since this proton disappears in the bottom spectrum, it is just an O-H and the cyclization is complete. However, as can be seen by the rest of the spectrum there is significant decomposition. The product ferrocene protons are indistinguishable among the mess of decomposition signals and the catechol aromatic protons are also not alone. There are at least two other species that can be inferred just from the aromatic region. Attempted cyclizations with ferrocenecarboxaldehyde over longer periods of time at room temperature displayed a similar decomposition. A breakthrough would be either to get this cyclization to occur with less decomposition, given that these NMR spectra are proof-of-concept

that the cyclization can occur, this route could be successful by a brute-force method by using a large amount of starting materials and taking a large yield hit at this step. Alternatively, with being able to use **NNAuPPh₃** to install the NN onto **I-Fc-CatAc₂** would facilitate a successful route to the synthesis of **1,3-NN-Fc-SQ**; however, it will probably require a significant devotion to method development and severe reaction monitoring.

D.2. Experimental.

(Sp)-1-Formyl-3-(3'-(tert-Butyl)-4',5'-bis(methoxymethoxy)phenyl)ferrocene (CHO-Fc-CatMOM₂). A solution of **CHO-Fc-NN** (97 mg, 0.285 mmol), MOM₂CatBpin (177 mg, 0.308 mmol), Na₂CO₃ (84 mg, 0.793 mmol) and Pd(OAc)₂ (0.9 mg, 4 μmol) in 15 mL of deoxygenated 1:2 H₂O/THF solution under nitrogen was heated to 55 °C for 15 h. After which the reaction was cooled to room temperature and transferred to a separatory funnel. The reaction was diluted with Et₂O and washed with brine. The organic layer was separated, dried with Na₂SO₄ and concentrated under reduced pressure. The product was purified by Et₃N treated silica gel chromatography with 15→30% EtOAc/hexanes as eluent. The product-containing fractions were combined and concentrated to afford 106 mg (80%) of the title compound as a red oil. ¹H NMR (400MHz, CD₂Cl₂) δ = 9.97 (s, 1 H), 7.21 (d, *J* = 2.1 Hz, 1 H), 7.17 (d, *J* = 2.0 Hz, 1 H), 5.21 (s, 2 H), 5.21 (s, 2 H), 5.19 (d, *J* = 1.4 Hz, 1 H), 5.00 (t, *J* = 1.4 Hz, 1 H), 4.89 (d, *J* = 1.4 Hz, 1 H), 4.17 (s, 5 H), 3.63 (s, 3 H), 3.53 (s, 3 H), 1.45 (s, 9 H). ¹³C NMR (101MHz, CD₂Cl₂) δ = 193.7, 150.7, 145.8, 143.8, 132.2, 119.4, 113.9, 99.6, 96.0, 92.4, 80.4, 72.2, 71.7, 70.9, 67.7, 57.9, 56.7, 35.6, 30.9.

D.3. References.

- (1) Zirakzadeh, A.; Herlein, A.; Groß, M. A.; Mereiter, K.; Wang, Y.; Weissensteiner, W. Halide-Mediated Ortho-Deprotonation Reactions Applied to the Synthesis of 1,2- and 1,3-Disubstituted Ferrocene Derivatives. *Organometallics* **2015**, *34* (15), 3820–3832.
- (2) Tanimoto, R.; Suzuki, S.; Kozaki, M.; Okada, K. Nitronyl Nitroxide as a Coupling Partner: Pd-Mediated Cross-Coupling of (Nitronyl Nitroxide-2-Ido)(Triphenylphosphine)Gold(I) with Aryl Halides. *Chem. Lett.* **2014**, *43* (5), 678–680. <https://doi.org/10.1246/cl.131162>.
- (3) Magdziak, D.; Rodriguez, A. A.; Van De Water, R. W.; Pettus, T. R. R. Regioselective Oxidation of Phenols to o -Quinones with o -Iodoxybenzoic Acid (IBX). *Org. Lett.* **2002**, *4* (2), 285–288. <https://doi.org/10.1021/ol017068j>.
- (4) Haraguchi, M.; Tretyakov, E.; Gritsan, N.; Romanenko, G.; Gorbunov, D.; Bogomyakov, A.; Maryunina, K.; Suzuki, S.; Kozaki, M.; Shiomi, D.; Sato, K.; Takui, T.; Nishihara, S.; Inoue, K.; Okada, K. (Azulene-1,3-Diyl)-Bis(Nitronyl Nitroxide) and (Azulene-1,3-Diyl)-Bis(Iminonitroxide) and Their Copper Complexes. *Chem. - An Asian J.* **2017**, *12* (22), 2929–2941. <https://doi.org/10.1002/asia.201701085>.
- (5) Ferber, B.; Top, S.; Welter, R.; Jaouen, G. A New Efficient Route to Chiral 1,3-Disubstituted Ferrocenes: Application to the Syntheses of (Rp)- and (Sp)-17 α -[(3'-Formylferrocenyl)Ethyne]Estradiol. *Chem. - A Eur. J.* **2006**, *12* (7), 2081–2086. <https://doi.org/10.1002/chem.200500842>.
- (6) Riant, O.; Samuel, O.; Flessner, T.; Taudien, S.; Kagan, H. B. An Efficient Asymmetric Synthesis of 2-Substituted Ferrocenecarboxaldehydes. *J. Org. Chem.* **1997**, *62* (20), 6733–6745. <https://doi.org/10.1021/jo970075u>.

- (7) Ho, C. C.; Olding, A.; Smith, J. A.; Bissember, A. C. Nuances in Fundamental Suzuki–Miyaura Cross-Couplings Employing [Pd(PPh₃)₄]: Poor Reactivity of Aryl Iodides at Lower Temperatures. *Organometallics* **2018**, *37* (11), 1745–1750.
<https://doi.org/10.1021/acs.organomet.8b00189>.

APPENDIX E: Crystallographic Information.

Compound	<i>p</i> -SQ- <i>m</i> -NN	<i>m</i> -SQ- <i>p</i> -NN
Identification code	rds823	rds845
Empirical formula	C ₆₈ H ₇₇ BN ₈ O ₄ Zn	C ₆₈ H ₇₇ BN ₈ O ₄ Zn
Formula weight	1146.55 g/mol	1231.48 g/mol
Temperature/K	100(2) K	102(2) K
Crystal system	triclinic	triclinic
Space group	P-1	P-1
a/Å	12.9175(8)	14.9761(4)
b/Å	16.6444(11)	15.4385(4)
c/Å	18.4056(12)	16.9665(5)
α/°	110.608(2)°	100.1595(11)°
β/°	98.774(2)°	107.6979(10)°
γ/°	93.033(2)°	115.1722(9)°
Volume/Å ³	3636.3(4)	3162.52(15)
Z	2	2
ρ _{calc} /cm ³	1.047	1.293
μ/mm ⁻¹	0.384	0.528
F(000)	1216	1300
Crystal size/mm ³	0.132 x 0.153 x 0.512 mm	0.108 x 0.227 x 0.386 mm
Radiation	fine-focus sealed tube (MoKα, λ = 0.71073 Å)	fine-focus sealed tube (MoKα, λ = 0.71073 Å)
Reflections collected	137066	134545
Goodness-of-fit on F ²	1.075	1.037
Final R indexes	R1 = 0.0374, wR2 = 0.1031	R1 = 0.0462, wR2 = 0.1163
Largest diff. peak/hole / e Å ⁻³	0.420/-0.265	0.929/-1.301

Compound	SQ-PhMe ₂ Th-NN	NN-PhMe ₂ Th-SQ
Identification code	rds807	rds958
Empirical formula	C ₆₈ H ₇₉ BN ₈ O ₄ SZn	C ₆₈ H ₇₉ BN ₈ O ₄ SZn
Formula weight	1180.63 g/mol	1180.63 g/mol
Temperature/K	100(2) K	100(2) K
Crystal system	triclinic	monoclinic
Space group	P -1	P 1 21/c 1
a/Å	13.8004(8)	14.0225(4)
b/Å	14.1410(8) Å	38.7460(9)
c/Å	18.7598(11)	12.2208(3)
α/°	94.998(2)	90
β/°	110.749(2)	109.8920(10)
γ/°	94.118(2)	90
Volume/Å ³	3389.8(3)	6243.6(3)
Z	2	4
ρ _{calc} /cm ³	1.157	1.256
μ/mm ⁻¹	0.443	1.286
F(000)	1252	2504
Crystal size/mm ³	0.044 x 0.170 x 0.492 mm	0.023 x 0.084 x 0.155 mm
Radiation	fine-focus sealed tube (MoKα, λ = 0.71073 Å)	Incoatec IμS 3.0 microfocus sealed tube (Cu Kα, λ = 1.54178 Å)
Reflections collected	81297	96657
Goodness-of-fit on F ²	1.065	1.132
Final R indexes	R1 = 0.0446, wR2 = 0.0995	R1 = 0.0514, wR2 = 0.1130
Largest diff. peak/hole / e Å ⁻³	0.593 / -0.418	0.453/-0.401

Compound	1,3-SQ ₂ Az	1,3-SQ-Az-NN
Identification code	rds849	rds946
Empirical formula	C ₁₁₁ H ₁₂₆ B ₂ Cl ₆ N ₁₂ O ₄ Zn ₂	C _{68.50} H ₈₀ BCl ₅ N ₈ O ₄ Zn
Formula weight	2057.29 g/mol	1332.83 g/mol
Temperature/K	100(2) K	100(2) K
Crystal system	triclinic	triclinic
Space group	P-1	P-1
a/Å	12.3577(5)	12.0129(3)
b/Å	12.9693(6)	13.2970(3)
c/Å	33.4949(14)	21.9252(6)
α/°	97.2636(13)	103.3060(10)
β/°	95.6609(13)	101.2800(10)
γ/°	97.5826(14)	92.218(2)
Volume/Å ³	5242.2(4)	3329.49(15)
Z	2	2
ρ _{calc} /cm ³	1.303	1.329
μ/mm ⁻¹	0.668	2.784
F(000)	2160	1398
Crystal size/mm ³	0.050 x 0.322 x 0.455 mm	0.062 x 0.096 x 0.215 mm
Radiation	fine-focus sealed tube (MoKα, λ = 0.71073 Å)	Incoatec IμS 3.0 microfocus sealed tube (Cu Kα, λ = 1.54178 Å)
Reflections collected	154401	108098
Goodness-of-fit on F ²	1.041	1.057
Final R indexes	R1 = 0.0596, wR2 = 0.1429	R1 = 0.0653, wR2 = 0.1843
Largest diff. peak/hole / e Å ⁻³	1.639/-2.102	1.399/-1.316

Compound	1,3-SQ ₂ Fc	1,1'-SQ ₂ Fc
Identification code	rds940	rds927
Empirical formula	C _{110.91} H _{126.81} B ₂ Cl _{5.81} FeN ₁₂ O ₄ Zn ₂	C ₁₁₂ H ₁₃₀ B ₂ Cl ₈ FeN ₁₂ O ₄ Zn ₂
Formula weight	2106.24 g/mol	2200.13 g/mol
Temperature/K	100(2) K	100(2) K
Crystal system	triclinic	monoclinic
Space group	P -1	P 21/n
a/Å	14.3395(12)	12.1222(5)
b/Å	18.2664(15)	17.8809(8)
c/Å	23.2786(19)	25.7796(11)
α/°	71.655(2)	90
β/°	80.662(2)	91.2515(15)
γ/°	86.188(2)	90
Volume/Å ³	5710.0(8)	5586.6(4)
Z	2	2
ρ _{calc} /cm ³	1.225	1.308
μ/mm ⁻¹	0.732	0.801
F(000)	2206	2300.0
Crystal size/mm ³	0.216 x 0.321 x 0.563 mm	0.120 x 0.275 x 0.378 mm
Radiation	fine-focus sealed tube (MoKα, λ = 0.71073 Å)	fine-focus sealed tube (MoKα, λ = 0.71073 Å)
Reflections collected	148235	120431
Goodness-of-fit on F ²	1.045	1.034
Final R indexes	R1 = 0.0594, wR2 = 0.1605	R1 = 0.0558, wR2 = 0.1527
Largest diff. peak/hole / e Å ⁻³	1.802/-1.736	2.213/ -1.519

Compound	1-SQFc	
Identification code	FCSQ_	
Empirical formula	$C_{59.36}H_{66.73}BCl_{0.92}FeN_6O_2Zn$	
Formula weight	1060.85	
Temperature/K	296.65	
Crystal system	triclinic	
Space group	P-1	
a/Å	13.1791(10)	
b/Å	21.0759(16)	
c/Å	21.1546(16)	
$\alpha/^\circ$	79.432(4)	
$\beta/^\circ$	81.452(4)	
$\gamma/^\circ$	88.723(4)	
Volume/Å ³	5712.0(8)	
Z	4	
$\rho_{\text{calc}}/\text{cm}^3$	1.234	
μ/mm^{-1}	3.297	
F(000)	2230.0	
Crystal size/mm ³	0.44 × 0.33 × 0.05	
Radiation	CuK α ($\lambda = 1.54178$)	
Reflections collected	102083	
Goodness-of-fit on F ²	1.026	
Final R indexes	$R_1 = 0.0772$, $wR_2 = 0.2170$	
Largest diff. peak/hole / e Å ⁻³	0.41/-0.88	